



## City Research Online

### City, University of London Institutional Repository

---

**Citation:** Faghih, F. (2018). Structural performance of nano concrete-steel sandwich wall. (Unpublished Doctoral thesis, City, University of London)

This is the accepted version of the paper.

This version of the publication may differ from the final published version.

---

**Permanent repository link:** <https://openaccess.city.ac.uk/id/eprint/19774/>

**Link to published version:**

**Copyright:** City Research Online aims to make research outputs of City, University of London available to a wider audience. Copyright and Moral Rights remain with the author(s) and/or copyright holders. URLs from City Research Online may be freely distributed and linked to.

**Reuse:** Copies of full items can be used for personal research or study, educational, or not-for-profit purposes without prior permission or charge. Provided that the authors, title and full bibliographic details are credited, a hyperlink and/or URL is given for the original metadata page and the content is not changed in any way.



# **Structural Performance of Nano Concrete-Steel Sandwich Wall**

**Faezeh Faghieh**

Thesis submitted in fulfilment of the requirement for the degree of  
Doctor of Philosophy

City University of London  
School of Mathematics, Computer Science & Engineering

April 2018



*Dedicated to My Beloved Mother, Father and Brother*

# TABLE OF CONTENTS

LIST OF FIGURES .....	10
LIST OF TABLES .....	17
ACKNOWLEDGMENTS .....	19
DECLARATION .....	20
ABSTRACT.....	21
SYMBOLS.....	22
ABBREVIATIONS .....	24
LIST OF PUBLICATIONS .....	26

## CHAPTER 1 INTRODUCTION

---

1.1. BACKGROUND.....	27
1.2. AIMS AND OBJECTIVES.....	32
1.3. THESIS OUTLINE .....	33

## CHAPTER 2 LITERATURE REVIEW

---

2.1. INTRODUCTION.....	35
2.2. CARBON NANOTUBES (CNT) AND CARBON NANOFIBRES (CNF).....	35
2.2.1. Properties of CNT/Fs .....	37
2.2.2. Mechanical properties of CNT/F composites .....	40
2.2.2.1. Hybrid composites .....	48
2.2.2.2. Nanoconcrete.....	51
2.3. SELF-SENSING PROPERTIES OF NANOCOMPOSITES .....	54
2.3.1. Hybrid composites .....	63
2.3.2. Nanoconcrete .....	64
2.4. SELF-SENSING PROPERTIES OF SF REINFORCED COMPOSITES .....	67
2.5. STEEL-CONCRETE COMPOSITE (SC) WALLS.....	71
2.5.1. Failure modes of SC component.....	73
2.5.2. SC structural performance .....	74

2.5.2.1. SC with conventional headed stud connectors .....	75
2.5.2.2. Bi-Steel.....	79
2.5.2.3. SC with J-hook connectors.....	81
2.6. SUMMARY .....	83

## **CHAPTER 3 MECHANICAL AND ELECTRICAL PROPERTIES OF CNFRC**

---

3.1. INTRODUCTION.....	84
3.2. CARBON NANOTUBES (CNTS) VS. CARBON NANOFIBRES (CNFS)...	85
3.2.1. Review on the properties of CNF .....	85
3.3. CONCRETE DESIGN AND PREPARATION .....	86
3.3.1. Constituent materials .....	86
3.3.2. Mix design .....	88
3.3.3. Sample preparation .....	89
3.3.4. Dispersion of CNF in aqueous solution .....	90
3.4. EXPERIMENTAL PROGRAMME.....	93
3.4.1. Cylinder compression test.....	94
3.4.2. Split tensile test.....	95
3.4.3. Flexural test.....	96
3.5. GROUP A EXPERIMENT .....	97
3.6. GROUP B EXPERIMENT.....	100
3.7. TEST RESULTS – GROUP A.....	104
3.7.1. Compression test results .....	104
3.7.2. Split tensile test results .....	105
3.7.3. Flexural test results .....	107
3.8. TEST RESULTS – GROUP B .....	108
3.8.1. Compression test results .....	108
3.8.2. Split tensile test results .....	111
3.8.3. Flexural test results .....	113
3.9. SELF-HEALTH MONITORING OF CNFRC .....	117
3.9.1. SHM analysis method and the test set-up .....	117

3.9.2. Electrical resistance vs. strain .....	121
3.9.3. Electrical resistance variation of CNFRC .....	125
3.10. CONCLUSIONS .....	128

## **CHAPTER 4 STEEL-CONCRETE SANDWICH WALL EXPERIMENTAL PROGRAMME**

---

4.1. INTRODUCTION .....	130
4.2. EXPERIMENTAL PROGRAMME OUTLINE .....	130
4.3. DESIGN OF SC BEAMS.....	132
4.3.1. Flexural resistance of SC beam – Elastic approach – Full composite .....	134
4.3.2. Flexural resistance of SC beam – Elastic approach – Partial composite ..	136
4.3.3. Flexural resistance of SC beam – Plastic approach – Full composite .....	136
4.3.4. Flexural resistance of SC beam – Plastic approach – Partial composite ..	138
4.3.5. Shear resistance of SC beam.....	139
4.3.6. Designed SC beam capacity .....	140
4.4. SC BEAM LAYOUT .....	141
4.5. MATERIALS .....	144
4.5.1. PC.....	145
4.5.2. SFRC.....	145
4.5.3. CNFRC .....	146
4.5.4. Hybrid FRC (SF+CNF) .....	146
4.6. SC CONCRETE CORE MIX PROPORTIONS .....	147
4.7. SPECIMEN PREPARATION.....	148
4.7.1. Instrumentation .....	148
4.7.2. Self-health monitoring test set-up.....	151
4.7.3. Casting concrete.....	154
4.8. TEST SET-UP .....	157
4.9. SUMMARY .....	158

## CHAPTER 5 SC BEAM EXPERIMENTAL OBSERVATIONS AND DISCUSSION

---

5.1. INTRODUCTION .....	159
5.2. CONCRETE CORE MATERIAL PROPERTIES .....	159
5.3. FAILURE CRITERIA .....	161
5.4. CONTROL SAMPLE: SCB1 .....	162
5.4.1. Crack behaviour .....	163
5.4.2. DG measurements .....	167
5.4.3. Strain measurements .....	168
5.5. CATEGORY 1: SCB2-SCB4 .....	171
5.5.1. SCB2: SFRC .....	171
5.5.1.1. Crack behaviour .....	171
5.5.1.2. DG measurements .....	175
5.5.1.3. Strain measurements .....	176
5.5.2. SCB3: CNFRC0.5 .....	179
5.5.2.1. Crack behaviour .....	179
5.5.2.2. DG measurements .....	183
5.5.2.3. Strain measurements .....	184
5.5.3. SCB4: CNFRC1.0 .....	187
5.5.3.1. Crack behaviour .....	188
5.5.3.2. DG measurements .....	192
5.5.3.3. Strain measurements .....	192
5.5.4. Summary of category 1 SC beam test results .....	195
5.6. CATEGORY 2: SCB5 & SCB6 .....	198
5.6.1. SCB5: SF1.0% + CNF1.0% .....	198
5.6.1.1. Crack behaviour .....	199
5.6.1.2. DG measurements .....	203
5.6.1.3. Strain measurements .....	204
5.6.2. SCB6: SF1.5% + CNF0.5% .....	207
5.6.2.1. Crack behaviour .....	208
5.6.2.2. DG measurements .....	212

5.6.2.3. Strain measurements .....	212
5.6.3. Summary of category 2 SC beam test results .....	215
5.7. CATEGORY 3: SCB7 & SCB8 .....	217
5.7.1. SCB7: SF1.0% + CNF0.5% .....	217
5.7.1.1. Crack behaviour .....	218
5.7.1.2. DG measurements .....	222
5.7.1.3. Strain measurements .....	223
5.7.2. SCB8: SF0.5% + CNF1.0% .....	226
5.7.2.1. Crack behaviour .....	226
5.7.2.2. DG measurements .....	230
5.7.2.3. Strain measurements .....	231
5.7.3. Summary of category 3 .....	234
5.8. SEM ANALYSIS OF SC CONCRETE CORE .....	234
5.9. OVERVIEW OF THE RESULTS .....	246
5.10. CONCLUSIONS .....	252

## **CHAPTER 6 SELF-SENSING PROPERTIES OF CNF REINFORCED CONCRETE**

---

6.1. INTRODUCTION .....	254
6.2. EXPERIMENTAL PROGRAMME OUTLINE .....	254
6.3. ELECTRICAL RESISTANCE OF CONCRETE FOR SC BEAMS .....	256
6.4. SC BEAM RESULTS .....	258
6.4.1. SCB3: CNFRC0.5 .....	258
6.4.1.1. Electrode T .....	259
6.4.1.2. Electrode B .....	262
6.4.1.3. Electrode M .....	263
6.4.2. SCB4: CNFRC1.0 .....	264
6.4.2.1. Electrode T .....	264
6.4.2.2. Electrode B .....	266
6.4.2.3. Electrode M .....	268
6.4.3. SCB5: SF1.0% + CNF1.0% .....	269

6.4.3.1. Electrode T .....	269
6.4.3.2. Electrode B .....	271
6.4.3.3. Electrode M .....	273
6.4.4. SCB6: SF1.5% + CNF0.5% .....	274
6.4.4.1. Electrode T .....	274
6.4.4.2. Electrode B .....	276
6.4.4.3. Electrode M .....	278
6.4.5. SCB7: SF1.0% + CNF0.5% .....	279
6.4.5.1. Electrode T .....	279
6.4.5.2. Electrode B .....	280
6.4.5.3. Electrode M .....	282
6.4.6. SCB8: SF0.5% + CNF1.0% .....	283
6.4.6.1. Electrode T .....	283
6.4.6.2. Electrode B .....	285
6.4.6.3. Electrode M .....	288
6.5. CONCLUSIONS .....	289

## **CHAPTER 7 FINITE ELEMENT ANALYSIS OF SC BEAMS**

---

7.1. INTRODUCTION .....	291
7.2. FE METHOD .....	291
7.2.1. Fiber beam-column element .....	292
7.2.2. Theory behind the FE model .....	293
7.2.3. Shear-based fiber beam-column element.....	298
7.3. SC BEAM FE MODEL.....	300
7.3.1. Material constitutive model .....	300
7.4. FE MODEL VALIDATION OF SCB5 - SCB8 SPECIMENS.....	302
7.4.1. SCB5 model.....	303
7.4.2. SCB6 model.....	304
7.4.3. SCB7 model.....	306
7.4.4. SCB8 model.....	307
7.5. PARAMETRIC STUDY .....	309

7.5.1. Steel plate thickness.....	310
7.5.2. Tie bar spacing.....	312
7.6. A CASE STUDY ON SC BEAM .....	314
7.7. CONCLUSIONS .....	315

## **CHAPTER 8 CONCLUSIONS AND RECOMMENDATIONS**

---

8.1. INTRODUCTION.....	317
8.2. SUMMARY OF KEY FINDINGS .....	317
8.3. RECOMMENDATIONS FOR FUTURE WORK.....	323
8.4. LIMITATIONS OF THE WORK .....	324

<b>REFERENCES.....</b>	<b>325</b>
------------------------	------------

## **APPENDICES**

---

APPENDIX A: SC BEAM MATERIAL TEST PHOTOS

APPENDIX B: SEM IMAGES

APPENDIX C: FE SENSITIVITY STUDY ON SCB6

APPENDIX D: THEORETICAL SC BEAM MID-DISPLACEMENT



## LIST OF FIGURES

Figure 2.1. Schematic illustration of CNT/Fs .....	36
Figure 2.2. Schematic demonstration of (a–c) formation of cup-stacked CNF structure; and (d) platelet CNF structure (Feng et al., 2014) .....	39
Figure 2.3. The dispersion mechanism of polycarboxylate-based superplasticiser to carbon nanotube-nanofibre (Han et al., 2014).....	43
Figure 2.4. Typical load-CMOD curves of 28 days cement paste with CNTs, cement paste with PVA microfibres and hybrid cement paste (Metaxa et al. 2010).....	49
Figure 2.5. The commonly used fixing style and layout of electrodes in self-sensing concrete (Han et al., 2014) .....	57
Figure 2.6. Sketch of polarization in concrete (Han et al., 2014) .....	59
Figure 2.7. Left: normalised measured strain and electrical resistance vs. time for different load frequencies; Right: normalised measured strain and measured electrical resistance vs. time .....	61
Figure 2.8. Wire mesh configuration inside short column tested by Howser et al. (2011) .....	66
Figure 2.9. Stress-strain and resistivity-strain relationship of a carbon-ECC specimen during AC monotonic load testing (Hou and Lynch, 2005).....	69
Figure 2.10. SC in submerge tube tunnel application (Wright and Oduyemi, 1991b). 71	
Figure 2.11. Failure modes of double skin composite beam (Wright et al., 1991b)....	74
Figure 2.12. (a) Bi-steel panel (Pryer and Bowerman, 1998); (b) SC system with J-hook connector (Liew and Soheli, 2009) .....	74
Figure 3.1. Sample preparation .....	90
Figure 3.2. (a) Weighing CNF; (b) sonication of Water + HRWR + CNF using ultrasonic processor.....	91
Figure 3.3. Dispersion of CNF in Water + HRWR.....	93
Figure 3.4. Cylinder uniaxial compression test.....	95
Figure 3.5. Split tensile test set-up .....	96
Figure 3.6. Flexural test set-up.....	97
Figure 3.7. Appearance of CNF-water solution in concrete matrix in: (a) fresh concrete; (b) hardened concrete .....	99
Figure 3.8. Slump test of Group B materials .....	101
Figure 3.9. Water+HRWR+CNF mixture after sonication .....	103
Figure 3.10. Effect of CNF on concrete colour.....	103

Figure 3.11. Compressive stress-strain relationship – Group A .....	104
Figure 3.12. Compressive failure of: (a) PC-A; (b) CNFRC-A-0.5; (c) CNFRC-A-0.75 .....	105
Figure 3.13. Split tensile failure of cylinders - Group A .....	106
Figure 3.14. Group A – four-point bending load-displacement graphs for: (a) PC; (b) CNFRC-A-0.5; (c) CNFRC-A-0.75 .....	107
Figure 3.15. Compressive strength results – Group B .....	109
Figure 3.16. Compressive stress-strain relationship – Group B .....	110
Figure 3.17. Group B sample failure after compression test .....	111
Figure 3.18. Split tensile strength results – Group B .....	112
Figure 3.19. Split tensile failure of cylinders - Group B .....	112
Figure 3.20. Flexural strength results for Group B .....	113
Figure 3.21. Group B – four-point bending load-displacement graphs .....	114
Figure 3.22. Flexural beam test samples after failure .....	116
Figure 3.23. Copper mesh electrodes used for self-health monitoring test .....	118
Figure 3.24. (a) Electrode configuration in the beam samples; (b) concrete strain gauge attached to the beam .....	119
Figure 3.25. Mesh embedment inside: (a) fresh concrete; (b) hardened concrete .....	119
Figure 3.26. (a) Schematic diagram of four-probe wiring on beam samples; (b) equivalent circuit diagram for direct-current four-pole method .....	120
Figure 3.27. Electrical connection to power supply .....	121
Figure 3.28. Flexural beam test set-up for obtaining self-health monitoring results ..	121
Figure 3.29. Time history results for PC and CNFRC0.25 .....	122
Figure 3.30. Time history results for CNFRC0.5 .....	123
Figure 3.31. Time history results for CNFRC0.75 .....	123
Figure 3.32. Time history results for CNFRC1.0 .....	124
Figure 3.33. ERV vs. strain for all concrete types .....	126
Figure 4.1. Schematic sketch of beam subsection taken from structural wall (drawing is not to scale) .....	131
Figure 4.2. Schematic illustration of SC wall section .....	131
Figure 4.3. (a) SC beam section; (b) equivalent steel section; (c) forces acting in section; (d) linear stress distribution .....	134
Figure 4.4. Force distribution in SC section - fully plastic stage .....	137

Figure 4.5. (a) Shear diagram; (b) moment distribution diagram for simply supported beam under four-point bending .....	141
Figure 4.6. SC beam dimensions.....	143
Figure 4.7. SC beam as received from fabricator prior to concrete cast .....	143
Figure 4.8. Concrete types used for SC beam experiments .....	144
Figure 4.9. End-hooked steel fibre used in SFRC.....	145
Figure 4.10. Location of steel strain gauges .....	148
Figure 4.11. Tie bar: (a) before surface sanding; (b) after surface sanding. ....	149
Figure 4.12. Strain gauge attachment to tie bar .....	150
Figure 4.13. Strain gauge wire numbering map .....	150
Figure 4.14. Strain gauges attached to the bottom steel plate .....	151
Figure 4.15. Schematic illustration of two probe method adopted in SC beam experiment.....	152
Figure 4.16. Copper mesh electrode poles .....	152
Figure 4.17. Power supply connection to copper meshes .....	152
Figure 4.18. Locations of copper electrodes inside the SC beam .....	153
Figure 4.19. Securing copper electrodes in place within the SC beam.....	154
Figure 4.20. SC beam concrete casting .....	156
Figure 4.21. SC beam four-point bending test set-up .....	157
Figure 4.22. DG set-up.....	158
Figure 5.1. Concrete cube compressive strength at 14d and 28d for SCB1-SCB8....	159
Figure 5.2. Concrete split tensile strength at 14d and 28d for SCB1-SCB8 .....	160
Figure 5.3. Concrete density for SCB1-SCB8 .....	160
Figure 5.4. Concrete appearance inside SCB3 sample.....	161
Figure 5.5. Load-displacement curve for SCB1.....	163
Figure 5.6. Crack development for SCB1 .....	164
Figure 5.7. Flexural crack locations for SCB1 .....	164
Figure 5.8. Steel plate local buckling of SCB1 .....	165
Figure 5.9. Fractured tie bars in SCB1 .....	166
Figure 5.10. SCB1: (a) beam at the end of the test; (b) bottom plate plastic deformation at C6; (c) top plate deformation at C6 .....	167
Figure 5.11. Crack map of SCB1 by the end of four-point bending test .....	167
Figure 5.12. DG measurements for SCB1 .....	168

Figure 5.13. Measured strain for: (a) inner tie bars; (b) outer tie bars for SCB1.....	169
Figure 5.14. Measured strain in tension steel plate for SCB1.....	170
Figure 5.15. Load-displacement curve for SCB2.....	171
Figure 5.16. Crack progression for SCB2.....	173
Figure 5.17. Close view of steel fibre at the crack interface.....	174
Figure 5.18. SCB2: (a) specimen after failure; (b) crack map of failed specimen ....	174
Figure 5.19. Fractured tie bars crossing C4 .....	175
Figure 5.20. DG measurements for SCB2 .....	175
Figure 5.21. Measured strain for: (a) inner tie bars; (b) outer tie bars for SCB2.....	177
Figure 5.22. Measured strain in tension steel plate for SCB2.....	178
Figure 5.23. Load-displacement curve for SCB3.....	179
Figure 5.24. Fractured tie bars in SCB3 (east shear span) .....	181
Figure 5.25. Crack progression for SCB3 .....	182
Figure 5.26. SCB3: (a) specimen after failure; (b) crack map of failed specimen ....	183
Figure 5.27. DG measurements for SCB3 .....	183
Figure 5.28. Fracture of a tie bar close to G7 for SCB3 .....	184
Figure 5.29. Measured strain for: (a) inner tie bars; (b) outer tie bars for SCB3.....	185
Figure 5.30. Measured strain in tension steel plate for SCB3.....	186
Figure 5.31. Load-displacement curve for SCB4.....	187
Figure 5.32. Crack progression for SCB4.....	189
Figure 5.33. Fractured tie bar in SCB4 .....	190
Figure 5.34. (a) Enlarged view of C5 and C7 for SCB4; (b) tie bars crossing C5 and C7 after demolition of the concrete core.....	191
Figure 5.35. Final crack pattern for SCB4 .....	191
Figure 5.36. DG measurements for SCB4 .....	192
Figure 5.37. Strain measurements for: (a) inner tie bars; (b) outer tie bars for SCB4.....	194
Figure 5.38. Measured strain in tension steel plate for SCB4.....	195
Figure 5.39. Load-displacement curve for beams in category 2.....	198
Figure 5.40. Crack progression for SCB5.....	200
Figure 5.41. Schematic map of crack pattern for SCB5 after the test.....	201
Figure 5.43. Closer view of the shear crack for SCB5 .....	203
Figure 5.42. Fractured tie bars in SCB5 (east shear span) .....	203

Figure 5.44. DG measurements for SCB5 .....	204
Figure 5.45. Measured strain for: (a) inner tie bars; (b) outer tie bars for SCB5 .....	206
Figure 5.46. Measured strain in tension steel plate for SCB5 .....	207
Figure 5.47. Crack progression for SCB6 .....	209
Figure 5.48. Crack pattern for SCB6 at the end of the test .....	211
Figure 5.49. Concrete shear crack view for SCB6 .....	211
Figure 5.50. DG measurements for SCB6 .....	212
Figure 5.51. Measured strain for SCB6: (a) inner tie bars; (b) outer tie bars .....	213
Figure 5.52. Measured strain in tension steel plate for SCB6 .....	215
Figure 5.53. Load-displacement curve for category 3 .....	217
Figure 5.54. Crack progression for SCB7 .....	219
Figure 5.55. SCB7: (a) after the test; (b) crack map after the test .....	222
Figure 5.56. DG measurements for SCB7 .....	223
Figure 5.57. Measured strain for SCB7: (a) inner tie bars; (b) outer tie bars .....	224
Figure 5.58. Measured strain in tension steel plate for SCB7 .....	225
Figure 5.59. Crack progression for SCB8 .....	227
Figure 5.60. Close observation of (a) shear crack C5; (b) tie bar fractured at C5 .....	229
Figure 5.61. SCB8: (a) after the test; (b) crack map after the test .....	230
Figure 5.62. DG measurements for SCB8 .....	230
Figure 5.63. Measured strain in tie bars for: (a) outer bars; (b) inner bars for SCB8 .....	232
Figure 5.64. Measured strain in tension steel plate for SCB8 .....	233
Figure 5.65. Example of samples taken from SCB4 beam for SEM analysis .....	235
Figure 5.66. SEM micrographs of SCB3 core sample with 0.5% CNF .....	236
Figure 5.67. SEM micrographs of SCB4 core sample with 1.0% CNF .....	237
Figure 5.68. Surfactant concentration effect on nanotube dispersion .....	238
Figure 5.69. SEM micrographs of SCB5 core sample with 1.0% SF + 1.0% CNF ...	240
Figure 5.70. SEM micrographs of SCB6 core sample with 1.5% SF + 0.5% CNF ...	241
Figure 5.71. SEM micrographs of SCB7 core sample with 1.0% SF + 0.5% CNF ...	243
Figure 5.72. SEM micrographs of SCB8 core sample with 0.5% SF + 1.0% CNF at 10000× magnification .....	244
Figure 5.73. (a) Scanning Electron Microscope Image of CNF Clump in Normal Cement (1670× Magnification), (b) Scanning Electron Microscope Image of Well Dispersed CNF in a Uniform Self-Consolidating Cement (9410× Magnification). ..	245

Figure 5.74. (a) SEM images of fractured surface of hardened silica fume paste SF-3, indicating the uniform dispersion of CNFs. (b) SEM images of fractured surface of hardened silica fume paste SF-3, indicating the uniform dispersion of CNFs. (Yazdanbakhsh, 2012).....	245
Figure 5.75. Normalised load-displacement curve for all tested SC beams under four-point bending.....	246
Figure 5.76. Crack map for all tested SC beams under four-point bending.....	251
Figure 6.1. Electrical resistance of concrete core for all SC beams before loading ..	256
Figure 6.2. Electrode positions for SCB3 .....	259
Figure 6.3. Damaged wires of Electrode B at east shear crack for SCB3.....	259
Figure 6.4. Electrode T results for SCB3 .....	260
Figure 6.5. ERV vs. strain for Electrode T: (a) stage 1; (b) stage 2.....	261
Figure 6.6. ERV vs. strain for electrode T for SCB3 .....	261
Figure 6.7. Electrode B results for SCB3.....	262
Figure 6.8. ERV vs. strain for Electrode B in SCB3.....	263
Figure 6.9. Electrode M results for SCB3 .....	264
Figure 6.10. Electrode positions for SCB4 .....	264
Figure 6.11. Electrode T results for SCB4.....	265
Figure 6.12. ERV vs. strain for electrode T for SCB4 .....	266
Figure 6.13. Electrode B results for SCB4.....	267
Figure 6.14. ERV vs. strain for Electrode B in SCB4.....	268
Figure 6.15. Electrode M results for SCB4.....	269
Figure 6.16. Electrode positions for SCB5 .....	269
Figure 6.17. ERV vs. strain for Electrode T for SCB5 .....	270
Figure 6.18. Electrode T results for SCB5 .....	271
Figure 6.19. Electrode B results for SCB5.....	272
Figure 6.20. ERV vs. strain for Electrode B for SCB5 .....	273
Figure 6.21. Electrode M results for SCB5.....	274
Figure 6.22. Electrode positions for SCB6 .....	274
Figure 6.23. Electrode T results for SCB6.....	275
Figure 6.24. ERV vs. strain for Electrode T for SCB6 .....	276
Figure 6.25. Electrode B results for SCB6.....	277
Figure 6.26. ERV vs. strain for Electrode B for SCB6 .....	277

Figure 6.27. Electrode M results for SCB6.....	278
Figure 6.28. Electrode locations for SCB7 .....	279
Figure 6.29. Electrode T results for SCB7 .....	280
Figure 6.30. Electrode B results for SCB7.....	280
Figure 6.31. ERV vs. strain for Electrode B for SCB7 .....	281
Figure 6.32. Electrode M results for SCB7 .....	283
Figure 6.33. Electrode positions for SCB8 .....	283
Figure 6.34. Electrode T results for SCB8 .....	284
Figure 6.35. ERV vs. strain for Electrode T in SCB8.....	285
Figure 6.36. Electrode B results for SCB8.....	286
Figure 6.37. ERV vs. strain for Electrode B for SCB8 .....	287
Figure 6.38. Electrode M results for SCB8.....	288
Figure 7.1. Fiber beam element; distribution of control sections and section subdivision into fibers .....	292
Figure 7.2. Reinforced concrete membrane elements subjected to in-plane stress (Hsu and Mo, 2010) .....	296
Figure 7.3 Stress states in (a) fixed-angle theory and; (b) rotating-angle theory (adopted from Hsu and Mo, 2010).....	297
Figure 7.4. Concrete material model used in FE analysis.....	301
Figure 7.5. Steel material model used in FE analysis .....	302
Figure 7.6. Validation of FE model with experimental result for SCB5 .....	303
Figure 7.7. Strain measurements for SCB6: FE model vs. Test .....	304
Figure 7.8. Validation of FE model with experimental result for SCB6 .....	305
Figure 7.9. Strain measurements for SCB6: FE model vs. Test .....	305
Figure 7.10. Validation of FE model with experimental result for SCB7 .....	306
Figure 7.11. Validation of FE model with experimental result for SCB7 .....	307
Figure 7.12. Validation of FE model with experimental result for SCB8 .....	308
Figure 7.13. Strain measurements for SCB8: FE model vs Test .....	308
Figure 7.14. Parametric study results for varying parameter $t_p$ .....	311
Figure 7.15. Parametric study results for varying parameter S .....	313
Figure 7.16. Schematic drawing of tested specimen SP1-3 (Sener et al., 2016) .....	314
Figure 7.17. FE study on tested SC beam by Sener et al. (2016).....	315

## LIST OF TABLES

Table 2.1. Properties of Carbon Nanotubes and Carbon Nanofibres .....	38
Table 2.2. Percentage increase of 28-day compressive strengths over control samples (Yazdani and Mohanam, 2014) .....	51
Table 2.3. Percentage increase of flexural strengths over control samples (Yazdani and Mohanam, 2014) .....	51
Table 2.4. Summary of past studies on CNF reinforced cementitious composites and resulting improvement in mechanical properties .....	53
Table 2.5. Summary of past studies on CNT reinforced cementitious composites and resulting improvement in mechanical properties .....	54
Table 2.6. Gauge factor and correlation coefficient of the test conducted by Teomete and Kocyigit (2013) .....	70
Table 3.1. Properties of silica fume .....	87
Table 3.2. Properties of CNF used for the experiment .....	87
Table 3.3. Summary of tests conducted to obtain mechanical properties of concrete .	94
Table 3.4. Group A mix proportions (kg per m <sup>3</sup> of concrete) .....	98
Table 3.5. Group B mix proportions in kg per m <sup>3</sup> of concrete .....	101
Table 3.6. Water+HRWR+CNF sonication properties – Group B .....	103
Table 3.7. Compressive strength – Group A .....	104
Table 3.8. Split tensile strength – Group A .....	105
Table 3.9. Nanoconcrete vs. traditional sensor .....	117
Table 3.10. Initial electrical resistance of CNFRC prior to loading .....	122
Table 3.11. GF for CNFRC .....	127
Table 3.12. GF found in literature .....	128
Table 4.1. Moment capacity and shear capacity of the designed control SC beam (SCB1) with PC .....	141
Table 4.2. SC beam design parameters .....	142
Table 4.3. End-hooked steel fibre properties .....	146
Table 4.4. Mix proportions for SC beam samples (per m <sup>3</sup> of concrete) .....	147
Table 5.1. Summary of test results for SCB1-SCB8 .....	248
Table 6.1. CNFRC electrical resistivity .....	257
Table 7.1. Concrete material properties used in the FE models .....	301



Table 7.2. FE steel material model properties.....	302
Table 7.3. Validation of FE model with test results for SCB5 .....	304
Table 7.4. Validation of FE model with test results for SCB6 .....	305
Table 7.5. Validation of FE model with test results for SCB7 .....	307
Table 7.6. Validation of FE model with test results for SCB8 .....	308
Table 7.7. Parameters for parametric study .....	309
Table 7.8. Details of SC beam SP1-3 tested by Sener et al. (2016).....	314

## **ACKNOWLEDGMENTS**

I would like to express my sincere thanks and deepest gratitude towards my supervisor Professor Ashraf Ayoub for his endless supervision, patience, encouragement, and invaluable support throughout the preparation of this thesis. His professionalism, commitment, and self-less time were indispensable for the completion of this thesis.

I also wish to show my gratefulness towards Dr Brett McKinley and Philip Beckwith for their technical succour and assistance at City University of London concrete laboratory for supporting the experimental part of this research. I also want to thank Russell Bailey for his collaboration in conducting the SEM imaging of experiment samples at the NanoVision centre, Queen Mary University of London. I am especially grateful to Ahmad Bazgir for his support and help during my experiments and his companionship.

I am thankful to City University of London for the financial support offered throughout my studies.

A deep and heartfelt thanks to my friends, for all their help and support during the various stages of my PhD years, but most importantly for their invaluable friendship.

Finally, I would like to express my sincere love and gratitude to my devoted and loving family, especially my mother and father. Their endless love, support and prayers helped me get through the difficult times and achieve this work. I warmly thank my brother for his never-ending support for keeping me optimistic and brave. Without the support of family, unquestionably none of this would have been possible.

## DECLARATION

I certify that this project is wholly my own work and that all material extracted from other sources is clearly referenced.

I grant powers of discretion to the University Librarian to allow this thesis to be copied in whole or in part without further reference to me. This permission covers only single copies made for study purposes, subject to normal conditions of acknowledgements.

*Faezeh Faghieh*

---

## ABSTRACT

Concrete is extensively used in the construction of infrastructures, however formation and development of cracks undermines the integrity of the structure. Thus, both improving the mechanical properties of this construction material as well as structural health monitoring of structures are essential tasks to be tackled.

The research covered in this thesis is concerned with mechanical properties of carbon nanofiber reinforced concrete and the effect of this type of concrete on structural performance of the composite steel-concrete sandwich (SC) system. The use of nanofibers such as Carbon Nanofiber (CNF) within cementitious materials is found to be effective in enhancing the mechanical properties of the cementitious material as well as enhancing the sensing ability of the cementitious composites. Despite the abundant experimental work on nanofiber reinforced cementitious composites by researchers, their use within concrete has not been fully addressed. Therefore, the significance of this research is to assess mechanical properties of nanoreinforced concrete along with its sensing capability.

The steel-concrete sandwich system consists of thick concrete core with exterior steel faceplates acting as reinforcement. The steel faceplates are anchored to the concrete core with shear connectors. This study presents the structural performance of the SC element with fiber reinforced concrete (FRC) core using both single fiber and hybrid fiber (i.e. consisting of two types of fibers) in the core. For this study carbon nanofiber and steel fiber, which is conventionally used in practice, are used for the FRC. Static tests were conducted on eight SC beams with different concrete types. In addition to studying the structural performance of the SC element with fiber reinforced concrete, the self-sensing capability of beams with CNF reinforced concrete core were assessed. Furthermore, finite element analysis was conducted to evaluate the effect of some design parameters on the behaviour of SC element.

The outcome of this thesis enhances the current knowledge on the use of nanofibers in civil engineering industry as nano reinforcement and nanofilaments within cementitious materials, typically concrete and it will contribute to the understanding of the effect of CNF on concrete mechanical properties. This research laid the groundwork for additional in-depth study on using carbon nanofiber reinforced concrete within structural members and determination of their effect as nanofilaments on the self-sensing capability of the structural element.

## SYMBOLS

$a$	Shear span
$A_s$	Cross-sectional area of transverse shear reinforcement
$b$	Modular ratio
$B$	Steel plate width
$b_c$	Beam width
$d$	Beam depth
$d_{bar}$	Diameter of tie bar
$d_{stud}$	Diameter of shear stud
$E_c$	Concrete modulus of elasticity
$E_{cm}$	Secant modulus of concrete
$E_s$	Steel modulus of elasticity
$f_{cf}$	Flexural strength
$f_{ck}$	Characteristic cylinder strength of concrete
$f_{ct}$	Split tensile strength
$f_{u-bar}$	Ultimate strength of tie bars
$f_{us}$	Ultimate strength of steel plate
$f_{u-stud}$	Ultimate strength of shear studs
$f_y$	Steel plate yield strength
$f_{y-bar}$	Yield strength of tie bars
$f_{ys}$	Ultimate tensile strength of tie bars
$f_{y-stud}$	Yield strength of shear stud
$h_c$	SC concrete depth
$I$	Electrical current
$L_{stud}$	Length of shear studs
$L$	four-point bending flexural span
$M_{pl}$	Plastic moment capacity
$n_c$	Number of connectors in the compression plate between the position of maximum moment and the support or the point of contraflexure.
$N_{cs.Rd}$	Compression force generated in compression plate
$N_{cu.Rd}$	Compression force generate in concrete in compression zone

$n_t$	Number of connectors in the tension plate between the position of maximum moment and the support
$N_{t,Rd}$	Tension force generated in tension plate
$P_{Rd}$	Design shear resistance of welded headed stud
$P$	Applied load
$D$	Beam mid-span deflection
$R$	Electrical resistance
$s$	Stud spacing
$S$	Tie bar spacing
$t_c$	Compression steel plate thickness
$t_p$	Steel plate thickness
$t_{sc}$	Overall SC thickness
$t_t$	Tension steel plate thickness
$V$	Voltage
$V_{cd}$	Shear capacity of the concrete
$V_u$	Ultimate shear capacity
$V_f$	Volume fraction of fibres
$x$	Depth of neutral axis from the interface between the compression plate and concrete
$\gamma_a$	Partial safety factor for steel
$\gamma_c$	Partial safety factor for concrete
$\gamma_v$	Partial safety factor for connector
$\varepsilon_{y-bar}$	Yield strain of the tie bars
$\varepsilon_{y-plate}$	Yield strain of the steel plates
$\sigma_c$	Compression stress in top steel plate
$\sigma_t$	Tension stress in bottom steel plate
$\sigma_u$	Ultimate tensile strength of shear studs
$\rho$	Reinforcement ratio
$\tau_{Rd}$	Nominal transverse design shear resistance

## **ABBREVIATIONS**

AC	Alternating Current
ACI	American Concrete Institute
BS EN	British Standard European Norm
BS	British Standards
CA	Coarse Aggregate
CB	Carbon Black
CF	Carbon Fibre
CMOD	Crack Mouth Opening Displacement
CNF	Carbon Nanofibre
CNFR	Carbon Nanofibre Reinforced Concrete
CNT	Carbon Nanotube
C-S-H	Calcium-Silicate-Hydrate
DC	Direct Current
DG	Digital Displacement Gauge
DSC	Double Skin Composite
ECC	Engineered Cementitious Composite
ERV	Electrical Resistance Variation
FA	Fine Aggregate
FCR	Fractional Change in Resistance
FE	Finite Element
FEAP	Finite Element Analysis Programme
FRC	Fibre Reinforced Concrete
GF	Gauge Factor
HRWR	High Range Water Reducer
HSC	High Strength Concrete
MWCNT	Multi-Wall Carbon Nanotube
MWNT	Multi-Wall Carbon Nanotube
PC	Plain Concrete
PVA	Polyvinyl Alcohol
RC	Reinforced Concrete
SC	Steel-Concrete Composite

SCB	Steel Composite Beam
SCC	Self-Consolidating Concrete
SEM	Scanning Electron Microscopy
SF	Steel Fibre
SFRC	Steel Fibre Reinforced Concrete
SHM	Structural Health Monitoring
SP	Superplasticizer
SWCNT	Single-Wall Carbon Nanotube
UHPC	Ultra-High-Performance Concrete
UHSC	Ultra-High Strength Concrete
W/B	Water to Binder ratio



## LIST OF PUBLICATIONS

- Paper 1: Faghih, F. and Ayoub, A. (2014) Finite Element Modeling of Carbon Nanofibre Concrete Structural Members. In: *Structures Congress 2014, 3<sup>rd</sup>–5<sup>th</sup> April, Boston Massachusetts, United States, pp.1048-1058.*
- Paper 2: Faghih, F., and Ayoub, A. (2015) Structural Behaviour of Fibre Reinforced Steel Concrete Composite Walls. In: *23<sup>rd</sup> Conference on Structural Mechanics in Reactor Technology (SMiRT-23), Manchester, United Kingdom. August 10-14, Division X.*
- Paper 3: Faghih, F. and Ayoub, A. (2015) Structural Behaviour of The CNF Reinforced Concrete Steel Composite Walls. In: *SECED 2015 Conference: Earthquake Risk and Engineering towards a Resilient World, 9<sup>th</sup>-10<sup>th</sup> July, Cambridge, UK.*
- Paper 4: Faghih, F., Das, D., Gendy, S. and Ayoub, A. (2016) Structural Behavior of Fibre-Reinforced Steel-Concrete Composite Elements under Hazard Loads. In: *The 2016 Structures Congress (Structures16), 28<sup>th</sup> August – 1<sup>st</sup> September, Jeju Island, Korea.*
- Paper 5: Faghih, F., Das, D. and Ayoub, A. (2017). Seismic behavior of fibre reinforced steel-concrete composite systems. *Procedia Engineering*, 171, 899-908. Doi number: 10.1016/j.proeng.2017.01.386.
- Paper 6: Faghih, F. and Ayoub, A. (2017) Behaviour of Fibre Reinforced Steel Concrete Double Skin Composite Systems Under Extreme Load Events. In: *1st International Conference on Nuclear Power Plants: Structures, Risk & Decommissioning (NUPP2017), 6<sup>th</sup> February, Croydon, United Kingdom.*

# CHAPTER 1

## INTRODUCTION

---

### 1.1. BACKGROUND

Nanotechnology is one of the most active research areas that encompass a number of disciplines with both novel science and useful applications including civil engineering and construction materials in the past two decades. The interest in nanotechnology concept for cement composites is steadily growing.

Cementitious materials such as concrete are typically characterised as quasi-brittle materials, with low tensile strength and low strain capacity, and hence affecting long-term durability of structures. One of the most important issues in designing and maintaining massive concrete structures like offshore and nuclear power plants is concrete cracking which is due to the low tensile strength of concrete. This can destroy the structural aesthetic and lead to deterioration of the structure.

During recent decades, discrete short fibres are widely used to control cracking of concrete. The concrete with incorporated fibres is known as Fibre Reinforced Concrete (FRC). Fibres are also described as distributed three-dimensional reinforcements. These fibres can be considered at multi-scale levels from nano to macro scale. Macro fibres (typically defined as fibres with diameters  $> 500 \mu\text{m}$ ) can bridge macro cracks and improve post-peak toughness. Fine microfibres (typically defined as fibres with diameter  $< 50 \mu\text{m}$ ) on the other hand, bridge the microcracks which delay the process by which the microcracks coalesce to form macrocracks. Steel fibres are one of the most researched fibres in the past decades available in both macro scale and micro scale. They proved to be effective in increasing the tensile properties of concrete and enhancing structural performance of structural elements when appropriate dosage and fibre type is used. This type of fibre is also being widely used in the industry for different applications. Another type of fibre reinforced concrete is the hybrid fibre reinforced concrete, in which two or several types of fibres, likely in different scales, are included

in the matrix. The use of hybrid fibres is also being researched recently using different fibres for different applications. In this type of FRC, the purpose is to take an advantage of benefits from variety of fibres. One idea is to use fibres at different scales (e.g. nano/micro/macro). This would allow the material to benefit from different fibres at different structural level.

Cracks in cement based materials initiate from the nanoscale where microfibres are not effective. Therefore, the development of fibres at the nanoscale has opened a new field of research within cementitious materials in the past two decades.

Nano-particles such as carbon nanotubes and carbon nanofibres (CNT/Fs) exhibit unique properties with remarkable mechanical, physical and electrical properties and hence they have been gaining extensive scientific attention during the past years and they are applied in many fields to fabricate new materials with novelty functions. As Sanchez and Ince (2009) describe carbon nanofibres; they are unique as they combine microscopic length (from 200 nm to 100  $\mu\text{m}$ ) with a nanoscopic diameter (1–200 nm), with greater strength to weight ratio than steel.

Up to date, the use of such nanofilaments in cementitious materials has shown great advantages such as increasing the strength, modulus, and durability of the material as well as increasing electrical conductivity characteristics of the material. These properties are achieved under the condition of good dispersion and uniform distribution of the fibres within the right dosage. Previous studies have addressed the appropriate dispersion method which is reviewed in this research.

Despite the efforts made to date in integrating CNTs and CNFs in cementitious materials, only a few have considered concrete material. Moreover, in the research area of cementitious materials, less studies considered integration of CNFs compared to CNTs. Nonetheless, the material properties of Carbon Nanofibre Reinforced Concrete (CNFRC) and their structural use has not yet been fully achieved. Moreover, Yazdanbakhsh (2012) has suggested that carbon nanofilaments should be incorporated into concrete rather than in only cement paste and the mechanical properties of the produced concrete should be investigated by different mechanical tests. Little attention has focused on the effect of CNT or CNF on concrete properties, and more specifically, on the behaviour of structural elements constructed with CNFRC. Since CNFs have about 100 times lower production cost compared to CNTs while offering similar

benefits, they are considered to be more suitable for mass production. Thus, due to lack of research on using CNF in cementitious materials and suitability of CNF for mass production compared to CNT, this study has focused on the mechanical properties of CNFRC to better understand the effect of CNF on concrete.

Essentially, the aim of all researchers to enhance the mechanical properties of concrete is to enhance the behaviour of the structural elements. Cracking behaviour of concrete in enormous yet indispensable structures such as containment structures for nuclear power plants is of high importance. Recently a structural system known as Steel Plate Composite (SC) system has become popular for use on safety-related structures because of the advantages it offers. SC walls are sandwich systems consisting of two steel plates covering concrete core in between the two plates. The composite action between steel plates and concrete is developed by the shear connectors. They are faster to build, highly flexible with improved efficiency, enhanced site safety, and greater accuracy. The use of FRC in SC systems could potentially be advantageous in many aspects such as performance enhancement of the structure under normal loading conditions as well as in the case of hazard loads. It is the intention of this study to bring light to improving the structural behaviour of SC walls using FRC, focusing on carbon nanofibre reinforced concrete, which is a pressing need, especially with respect to unforeseen loadings such as earthquake and blast to which infrastructures are exposed. Primarily it is essential to analyse the behaviour of SC element infilled with FRC under normal loading condition, hence, this research is concerned with the behaviour of SC element under static loading. Moreover, having known that hybrid fibres could benefit from different fibres and be more advantageous over singly fibre reinforced concrete, the idea of using combined nano and macro scale fibre was developed for this study. Thus, the use of hybrid fibres at different scales, which was the combination of nanofibres studied in this research and steel fibres which are promising macro fibres in the structural engineering industry, was aimed for this study to be further investigated at the structural level.

A civil structure should meet the requirements of safety, durability, serviceability, and sustainability for long-term operation. The structure may slowly deteriorate in its performance during its long-term service, or it could be severely damaged when subjected to natural disasters (i.e earthquake, strong winds, etc.). To evaluate the safety and durability of a structure during its service life Structural Health Monitoring (SHM)

is essential. This technology provides a way to ensure the serviceability and sustainability of the structure. Structural monitoring is conventionally performed by using resistance strain gauges, metal strain gauges, optic sensors, piezoelectric ceramics, fibre reinforced polymer bar sensors, embedded or attached sensors or detectors. Since the strain gauges can monitor the condition of a structure at a specific point, in order to monitor a structure, a high number of strain gauges would be needed which increases the costs. The drawback of these conventional sensors are low durability, limited life, and unfavourable compatibility with concrete structures as well as high cost, limited sensing volume, and degradation of the structural performance of the concrete when sensors or detectors are embedded.

Developing self-sensing concrete also referred as smart concrete has become a new field of research to apply in civil structures to eliminate issues that arise from using sensors. Smart concrete is introduced as an alternative to conventional sensors which is promising for solving the durability and incompatibility issue between conventional sensors and concrete structures owing to its capability of detecting its inside stress, strain, cracking and damage (Han et al., 2014). Smart concrete structures which function as both the structure and the sensor can potentially perform full-scale monitoring of the structure, which is very difficult or impossible for the conventional point-measurement monitoring techniques to do. Initially, the potential of a self-sensing concrete was recognised in traffic detection and the development of self-sensing concrete has increasingly been paid attention ever since.

The self-sensing concrete can be used in different forms in a structure. They can be used in bulk form or they can be used only in key positions of the structure. The former has simpler construction technology, while the latter can achieve higher monitoring efficiency and lower construction cost.

The self-sensing of the concrete has become possible due to the potential of the cementitious matrix to be electrical conductive. The electrical conductivity of cementitious materials ranges from  $1 \times 10^{-8}$  to  $1 \times 10^{-4} (\Omega \cdot \text{cm})^{-1}$ , which is similar to the range of semiconductors (Hou and Lynch, 2005). Therefore, cementitious materials have the potential to conduct electricity which is a desirable property of cementitious materials. The electrical conductivity of cementitious materials can be enhanced with the inclusion of conductive fillers including conductive fibres such as nano particles,

Carbon Fibre (CF), Carbon Black (CB) and Steel Fibre (SF) in the matrix by providing additional paths for electrical current to travel through the cement matrix. Such conductive fibres simultaneously act as nano reinforcement to the mechanical properties and efficiently increase the bulk material electrical conductivity by accommodating the flow of free ions in the porous matrix material.

Researchers to date have focused on the use of Carbon Black (CB) fibres, Carbon Fibres (SF), carbon nanotubes (CNT) and carbon nanofibre (CNF) as functional fillers within cement paste for strain sensing purposes. Considering the fact that typical aggregates that are used in concrete are electrically insulating in nature, they will interrupt the electron flow through the conductive network by creating obstacle. Therefore, it is expected that there is a need for a higher dosage of functional fillers to achieve expected self-sensing ability when aggregates, especially coarse ones are included in the composite (Han et al., 2014). Literature review indicates that there is lack of information or experimental research covering the effect of nanofibres on the self-sensing properties of concrete. Due to this fact, it is important to expand the study of self-sensing capability of cement mortar and cement paste further into the study of self-sensing capability of concrete. This study seeks to shed light on the self-sensing capability of nano-reinforced concrete as well as its damage sensing capability when used in a structural member. To the researcher's knowledge, the use of CNFRC in a structural element and its damage sensing capability has not been addressed up to date.

The focus of this research is on the self-sensing capability of an SC member, here a beam element. Such SC beam element, which is assumed to be part of an SC wall, are used within complex structures such as containment structures for nuclear power plants, offshore oil platform structures and submerged tube tunnels which require complex 3D distributed monitoring and clusters of 2D and 1D monitoring. It should be noted that access to all locations in these types of construction is an issue for constant health monitoring of the whole structure, while health monitoring of such structures is very crucial. With this premise, the need for improving the health monitoring of such structures benefiting from nanofibre filaments has been the main inspiration which has led to the conduction of this research within this area using the advanced nanotechnology on SC system. Currently, the use of smart concrete could be a major advantage in civil engineering whose main purpose is the early assessment of structural damage.

## 1.2. AIMS AND OBJECTIVES

The aim of this research is to study the mechanical performance of CNFRC and its self-sensing capability as well as to study the structural performance of SC elements with CNFRC and hybrid FRC. Also, the self-sensing properties of the SC element was aimed to be investigated to analyse the effect of CNFRC on this property. This research mainly seeks to:

- (i) Gather and interpret information on the mechanical properties of CNFRC material.
- (ii) Study the self-sensing capability of CNFRC material and determine if CNF at a specified dosage, would effectively overcome challenges associated with the formation of conductive network in concrete due to the presence of coarse aggregate.
- (iii) Determine the structural performance of CNFRC in SC structural element.
- (iv) Determine the structural performance of SC element infilled with CNFRC and hybrid FRC.
- (v) Investigate the self-sensing performance of CNFRC as a smart concrete within SC structural element.
- (vi) Investigate the effect of some design parameters on the structural performance of the SC element.

The specified aims of this research are achieved through the following objectives:

- Conducting a literature review that covers the following tasks:
  - Reviewing mechanical behaviour of the nanofibre reinforced cementitious materials.
  - Defining the main issues when using nanofibres within cementitious materials.
  - Identifying successful methods developed to overcome issues with using nanofibres within the cementitious matrix.
  - Establishing the current understanding of the structural health monitoring capability of fibre reinforced cementitious composites.
  - Reviewing the structural advantageous and performance of SC system and its role in civil engineering.

- Reviewing past and recent research on SHM of structures with smart concrete or smart cementitious sensors.
- Experimentally investigating the effect of CNF on mechanical properties of concrete at different fibre volume fractions.
- Experimentally investigating the self-sensing capability of CNFRC material and its capability to sense its own damage.
- Studying the relationship between the applied strain and electrical resistance of the CNF reinforced concrete.
- Experimentally investigating the effect of FRC on the structural performance of SC beams.
- Experimentally investigating the capability of SC beams infilled with smart concrete in sensing its own damage.
- Developing a simple 2D beam element model for SC beam, incorporating the CNFRC material properties for the purpose of parametric study to find the effect of design parameters on the behaviour of SC element.

### 1.3. THESIS OUTLINE

This thesis comprises eight chapters. A brief overview of each chapter is given below.

**Chapter 2** reviews the available literature on CNT/CNF reinforced cementitious composites and their mechanical properties accompanied by the associated issues with their addition to the cement matrix. The successful methods to overcome the existing issue are reviewed. Also, literature on self-sensing properties of cementitious composites with CNT/CNF is described. The SC construction system is introduced and a brief review of recent research conducted on this system is also presented.

**Chapter 3** reports the experimental programme to study the mechanical properties of CNFRC concrete with different dosages considering two material categories. The experimental outcome and findings are then discussed and compared with previous research findings. This is followed by examining the self-sensing capability of the CNFRC.

**Chapter 4** gives a comprehensive detail of methodology and experimental programme conducted on SC beams for current research, which was carried out at the engineering laboratory of City University of London. The experimental programme comprises



testing eight full-scale SC beam members infilled with fibre reinforced concrete with different fibre combinations under four-point bending test. A description of the design process of the test specimens and the materials used is given in this chapter in line with a description of the construction of the specimens, concrete mix designs, material properties, instrumentation, and the test set-up.

**Chapter 5** describes the experimental observations conducted on eight SC beams with different FRC cores categorised into three categories. An extensive discussion on the results and findings is presented in this chapter, which reports on the effect of different FRC on the structural performance of SC beams.

**Chapter 6** presents and analyses the results from the self-sensing analysis conducted on carbon nanofibre reinforced concrete SC beams. The results for each beam is thoroughly discussed separately.

**Chapter 7** presents finite element study conducted on SC beams using 2D beam element. The chapter includes a summary of the theory behind the beam element formulation, validation of FE models using the experimental data, and the results of a parametric study conducted on SC beams to evaluate the effect of some design parameters on the structural performance of the SC beam with FRC core.

**Chapter 8** summarises the concluding remarks of this research according to findings of each section. Recommendations for future research are also presented.

## CHAPTER 2

### LITERATURE REVIEW

---

#### 2.1. INTRODUCTION

This chapter includes relevant literature on the recent research aiming to study the effect of nanofibres on cementitious materials as reinforcing fibre. This section deals with issues regarding the use of nanofibres as well as approaches to deal with such issues. In addition to the mechanical performance of nano-reinforced cementitious composites, the self-sensing properties of the material are also reviewed. Available literature on steel-concrete-steel sandwich wall system is also discussed later in this chapter as this was the structural element to be studied in this research.

#### 2.2. CARBON NANOTUBES (CNT) AND CARBON NANOFIBRES (CNF)

In the world of nanotechnology, Carbon Nanotubes (CNTs) and Carbon Nanofibres (CNFs) are recognised as two of the most promising nanomaterials because of their unique mechanical properties. CNT is a sheet of graphite rolled up into a tube structure. There are two common types of CNT raw materials that can be used as smart materials. These are Single-Wall Carbon Nanotubes (SWCNT); a single sheet that has been rolled up, and Multi-Wall Carbon Nanotubes (MWCNT); a number of sheets that have been rolled up. Unlike CNTs, CNFs have exposed edge planes along their surface. These edges, which are present along the circumference of the fibre, can be used to help anchor the fibre in the matrix and prevent interfacial slip that allows for a better bond with the cement matrix (Kang et al., 2006; Shah, 2011). The morphologies of SWCNT, MWCNT, and CNF are shown in Figure 2.1 (Kang et al., 2006).

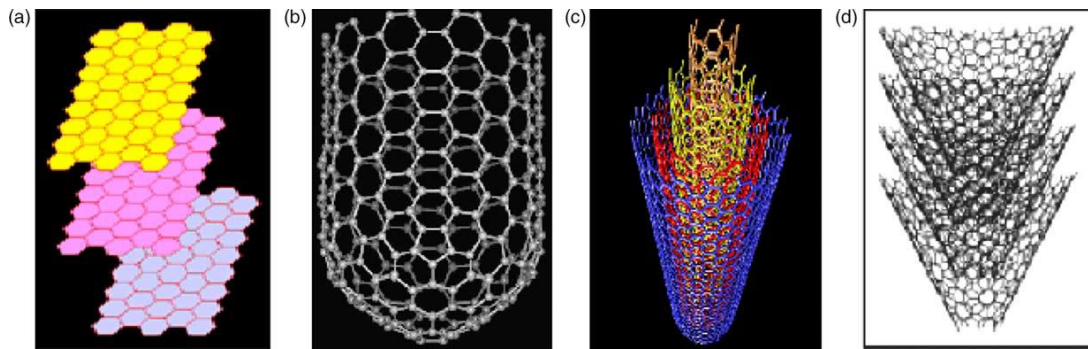


Figure 2.1. Schematic illustration of CNT/Fs: (a) carbon nano-walls; (b) structure of SWCNT; (c) structure of MWCNT; and (d) structure of a four-nano-cone-stacked CNF (Kang et al., 2006)

Carbon nanofibres (CNFs) have been investigated in both fundamental scientific research and practical applications and the research has proved that both CNT and CNF composites are able to be applied in fields such as electrical devices, electrode materials for batteries, reinforcement of composites, self-sensing devices and as sensors (Feng et al., 2014). Electrical conductivity plays a vital role in these applications which is greatly dependant on the dispersion of these nanofilaments in the matrix material. The dispersion issue will be discussed later in this section.

Concrete, a cementitious material, is a nano-structured, multi-phase, composite material that is composed of an amorphous phase, nanometer to micrometer size crystals, and bound water. At the amorphous phase, Calcium-Silicate-Hydrate gel (C-S-H) is formed which is the *glue* that holds concrete together and is itself a nanomaterial. The properties of concrete exist in, multiple length scales (nano- to micro- to macro scale) ‘where the properties of each scale derive from those of the next smaller scale’ (Sanchez et al., 2010). Initially, the main factor which is thought to increase the characteristics of cement concrete modified with carbon nanotubes and nanosilica as Yakovlev et al. (2017) state ‘is the structural modification of C-S-H concerning both the composition and the morphology of new products’ (p.1268). In addition to enhancement in the microstructure of the cementitious composite, previous research has shown that nanoscale cracking can be controlled by incorporating highly dispersed CNTs at low amounts. Thus, the mechanical properties of the material are enhanced by effectively arresting the cracks at the nanoscale. These researches will be outlined in the following sections.

Addition of CNT/Fs as nanofilaments forms a continuous conduction net and reduce the electrical resistance, decrease the shrinkage cracking, improve the durability and freezing resistance and does not induce large amount of water demand (Kang et al., 2006). Nanotubes as concrete fillers make concrete impenetrable to water, salt, etc. adding centuries to the useful life. This can greatly increase the durability of concrete (Shah, 2011). A summary of the effect of incorporating nanoscale fibres such as CNT/Fs in concrete can be described as follows:

- Lower density than plain concrete,
- Higher compressive strength compared with plain concrete with similar admixtures,
- Higher thermal conductivity than plain concrete,
- Higher electrical conductivity than plain concrete,
- Reduced porosity (by 18% - 50%, depending on the fibre content),
- More homogenous pore wall structure,
- Increased durability compared with plain concrete.

Structural and electrical characteristics of CNT/Fs make them advantageous for developing unique and revolutionary smart composite materials. CNT/Fs have high strength as well as high thermal and electrical conductivities, and ‘therefore’ can provide structural and functional capabilities simultaneously, including actuation, sensing, and generating power.

### **2.2.1. Properties of CNT/Fs**

Carbon NanoTubes (CNTs) are extremely small and their diameter is usually less than 20 nm (Yazdanbakhsh, 2012). In 1997, Salvetat and Kuik reported that CNTs have an elastic modulus of more than 1 TPa with elastic strain capacity of 12%, which is 60 times higher than that of steel. Kang et al. (2006) also classified nanotubes mechanically as the stiffest known fibres with a measured Young’s as high as 1–1.4 TPa. Yu et al. (2000) reported that the tensile strength and modulus of the MWNTs ranges from 11-63 GPa, and 270-950 GPa respectively. The maximum strain of SWCNT is >10%, which is greater than most structural materials (Kang et al., 2006). It should be noted that the direct measurement of the mechanical properties of CNTs is very difficult due

to their extremely small size and the mentioned values have been obtained mostly through theoretical calculations and estimations.

Carbon nanofibres, on the other hand, are relatively large compared to CNTs. ‘CNFs are unique as they combine microscopic length (few 100  $\mu\text{m}$ ) with nanoscopic diameter (50–200 nm), have a strength to weight ratio greater than steel, and could offer a similar benefit at a lower cost than CNTs (Yazdanbakhsh, 2012). Compared to CNTs, vapor grown CNFs have a lower production cost (about 100 times lower than SWCNTs) and are suitable for mass production. Additionally, unlike CNTs, CNFs present numerous exposed edge planes along the surface, which in turn create potential sites for advantageous physical interaction.’ Ozkan et al. (2008) were successful in performing direct mechanical measurements on CNFs. The CNF that they investigated had a tensile strength between 2 and 5 GPa with an average modulus of elasticity of 300 GPa.

These strong mechanical properties of CNT/Fs are due to the C–C covalent bonding and the seamless hexagonal network. ‘Thermal conductivity of CNT/Fs is also very high in the direction of the nanotube axis, typically about 1750–5800 W/mK’ (Kang et al., 2006). CNT/Fs properties are summarised in Table 2.1.

Table 2.1. Properties of Carbon Nanotubes and Carbon Nanofibres

Fibre Type		Typical Characteristics					
		Physical Properties			Mechanical Properties		Cost
		Diameter (nm)	Length	SSA	Young's Modulus	Tensile strength	
CNT	SWCNT	0.3-2	>200 nm	>300 $\text{m}^2/\text{g}$	1 TPa	60 GPa	~£110/g* (EliCarb)
	MWNT	20-80	1-20 $\mu\text{m}$	250-300 $\text{m}^2/\text{g}$			~£50/g* (EliCarb)
CNF		60-200	20-100 $\mu\text{m}$	50-60 $\text{m}^2/\text{g}$	400 Gpa	7 Gpa	~ £0.43/g**

\* Thomas Swan & Co. Ltd – Elicarb (R)

\*\* Applied Science, Inc – Pyrograf Products

Concerning the above table, it can be argued that the market price of CNT/CNFs is high at the moment for any commercial application and to be used in large concrete structures which would need tonnage quantities of nanofibres. According to Nadarajah et al.

(2008), the accelerating advances in the methods of producing these nano reinforcements are leading us to promising future for CNT/F-reinforced cementitious composites. It should be noted that the starting prices for carbon fibres were also prohibitively high during their initial stage of development but have come down significantly in time (Siddique and Mehta, 2014). From the cost point of view, the CNF has lower production cost and it is about 300 times cheaper than SWCNTs, and 150 times cheaper than MWCNTs, and is already produced in ton-per-year quantities making the applications practicable based upon the current material cost (Sanchez et al., 2010).

CNF can be mainly prepared by two approaches: catalytic thermal chemical vapour deposition growth and electro-spinning followed by heat treatment (Feng et al., 2014). Two types of CNF can be prepared by catalytic thermal chemical vapour deposition, namely, the cup-stacked CNF also known as conical CNF which was first discovered by Ge and Sattler (1994) and the second type is the platelet CNF (Figure 2.2). On the other hand, in most cases, the CNFs prepared by the electro-spinning method are prone to form web or mat structures which is a good form to be used as electrode materials for batteries.

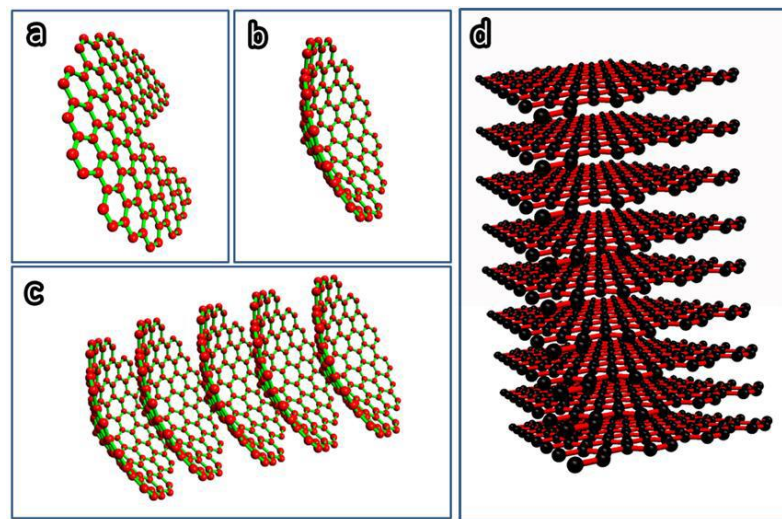


Figure 2.2. Schematic demonstration of (a–c) formation of cup-stacked CNF structure; and (d) platelet CNF structure (Feng et al., 2014)

There are two major problems that arise when CNT/Fs are used to reinforce any kind of material. The first issue is dispersion of fibres in the material. The very high surface areas of CNT/Fs cause them to adhere together strongly due to electrostatic effects and

Van der Waals forces. This attraction results in the formation of agglomerations in the form of entangled ropes and clumps that are very difficult to detangle (Yazdanbakhsh et al., 2009). The second difficulty to be tackled is achieving an optimal interfacial bond between fibres and matrix, which is difficult due to the atomically smooth and nonreactive surface of these filaments (Lourie and Wagner, 1998).

While the research on reinforcing cementitious materials with CNT/Fs is relatively new, growing number of studies have exclusively used CNTs in cement composites. The number of studies giving attention to CNFs reinforced composites is limited. Also, it should be mentioned that most researchers have been addressing dispersion issues of CNT/Fs in cement paste and the mechanical properties of the nano cementitious composite, while their effect in concrete matrix remains unknown. In the following sections first, an overview of past studies on the effect of CNT/Fs on the mechanical properties of the cementitious composite material as well as methods used to tackle the dispersion issues are presented followed by electromechanical properties of such nano-reinforced cementitious composites.

### **2.2.2. Mechanical properties of CNT/F composites**

The nano-reinforced cementitious composite could only benefit from the outstanding properties of the nanofibres when they are properly dispersed within the matrix. Mainly two approaches are identified for the dispersion of the CNF in polymer matrix: the melt mixing process and the sonication process in low velocity solutions (Feng et al., 2014). The melt mixing method can be categorised into extrusion or roll mill (Sanchez et al., 2011), Haake torque rheometer, and mini-max molder techniques. This method (melt mixing) is generally mentioned to be used more widely due to its simplicity, availability and lower cost. In this method, a high shear mixing condition is required. The issue with this method is the decrease in the aspect ratio of the nanofibres during this method which affects the composite properties adversely.

Recently most researchers focus on mixing nanofibres in an aqueous solution. The difficulty in dispersing nanofibres in liquid media has been overcome using various methods such as surface modification of fibres, using surfactants in combination with sonication, and also implanting or growing the fibres directly on non-hydrated cement grains. To enhance the interfacial bond, surface modification is found as the most common way. In this method, the surface of CNT/Fs can be functionalised to chemically

react with cement hydration products, thereby creating a stronger interfacial bond (Li et al., 2005).

According to Tchoul (2007), a basic and common method of functionalising is to oxidise the fibres in nitric acid or a mixture of nitric and sulfuric acids while the acid-treated CNT/F solution is being heated or sonicated. This method was adopted and investigated by Li et al. (2005), who studied carbon nanotubes treated in a mixed solution of sulfuric acid and nitric acid and due to the presence of carboxylic acid groups on the surfaces of carbon nanotubes, chemical reactions took place between the carboxylic acid and the Calcium-Silicate-Hydrate (C-S-H). The compressive strength of the cement paste increased up to 19%, while the flexural strength was increased up to 25%. Also, the failure strain was significantly increased. As Li et al. (2005) describe:

‘The interaction leads to a strong covalent force on the interface between the reinforcement and matrix in the composites, and therefore increases the load-transfer efficiency from cement matrix to nanotubes.’ (p.1244)

In contrast to the idea of functionalisation of nano fibres, Yazdanbakhsh et al. (2010) stated that although acid treatment results in CNF/Ts that are more soluble than pristine fibres, if not controlled properly it can damage or shorten CNFs–CNTs or even dissolve them. These negative effects are thought to be the reason that the first efforts to use acid-treated CNTs did not result in remarkable improvements in the mechanical properties of hardened cement paste.

Hence, alternative methods were further investigated for good dispersion such as using surfactants combined with sonication (i.e. ultrasonication). This is a well-researched topic that proved to be an effective dispersion method for CNT/Fs. ‘In an ultrasonic processor, electrical voltage is converted to mechanical vibrations, which are transferred to the liquid medium (water or solvent) and lead to formation and collapse of microscopic bubbles’ (Parveen et al., 2013, p.4). During this process (known as cavitation), a high level of energy is released as millions of shock waves are created which leads to dispersion of nanomaterials in the liquid. The analysis of the influence of dispersion on mechanical properties of hardened cement in the composition of fine aggregate concrete, conducted by Yakovlev et al. (2017), showed that the increase in strength is in direct proportion to the duration of ultrasonic processing of dispersion.



With the effectiveness of the ultrasonication method, some researchers combined the two method of surface modification with sonication. Amongst them, Cwirzen et al. (2008) used CNTs functionalised with carboxyl groups along with sonication process to disperse CNTs in water, while polyacrylic acid polymers were used as surfactant. Using a mix containing only 0.045% volume fraction of CNTs, they observed a significant increase (as high as 50%) in compressive strength of the cement composite.

Similarly, Kowald (2004) investigated the influence of surface-modified MWNTs (by oxidation nitric or sulphuric acid) on the mechanical properties of cement mortar. Dispersion of MWCNT was done by sonication of the CNTs within the mixing water for 15 minutes and then adding the superplasticizer (SP) to wrap around the dispersed CNTs and sonicated for another 2 minutes. For 0.5 wt.% of superplasticiser wrapped MWNTs (untreated) the compressive strength was increased by 8% after 7d and 12% after 14d. When 1.0 wt % of MWNTs was added the water to cement ratio was necessarily increased from 0.22 to 0.26. The samples containing the MWNTs oxidised in nitric acid showed a very bad workability which leads to a loss in the mechanical strength of the composite. The samples with the MWNTs oxidised in sulphuric acid showed no in- or decrease in their compressive strength compared to the samples without MWNTs. Their result showed contrary results to Cwirzen et al. (2008), who stated the effectiveness of combined mixing method. This suggests that the surface treatment method has not been a promising method to be further investigated, therefore, researchers focused on the use of sonication.

Yazdanbakhsh et al. (2009 & 2010) investigated the dispersion and interfacial bond of CNF fibres and cementitious composite at CNF/cement weight ratio of 0.4% through experiments. Two different CNFs were used. CNFs were dispersed in a water-surfactant solution and ultrasonically processed for 15 minutes. As the experimental results showed, non-ionic surfactant was more effective in deagglomeration of the CNFs in water. However, the addition of non-ionic surfactant was found incompatible with cement hydration to cement paste and it increased the amount of entrapped air remarkably. It was found that a polycarboxylate-based superplasticiser (i.e. weaker surfactant also known as water reducing admixture) could properly disperse a relatively high concentration (more than 1.0%) of CNFs in water. The dispersion mechanism of polycarboxylate-based superplasticiser to carbon nanofibre is demonstrated in Figure 2.3 (Han et al., 2014).

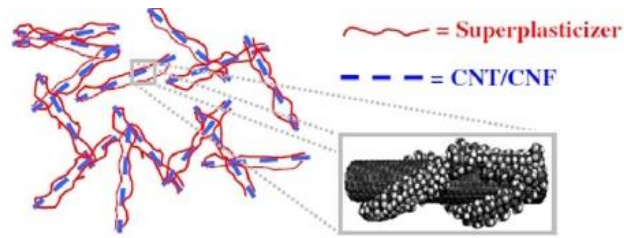


Figure 2.3. The dispersion mechanism of polycarboxylate-based superplasticiser to carbon nanotube-nanofibre (Han et al., 2014)

Transmission electron microscopy (TEM) observations revealed that CNFs in the dispersion were shorter than minimum length specified by the manufacturer, which suggested that some of the fibres break during sonication as mentioned by Ozkan et al. (2008) as well. They advised that a hydration-compatible surfactant may not always be the solution to the problem of producing cementitious composites with uniformly distributed and well-bonded CNT/Fs, and according to their suggestion, approaches such as surface functionalising and implantation on cement grains should be further investigated. As Yazdanbakhsh et al. (2010) describe:

‘These fibres are much more dispersible, and their physical properties can be controlled during functionalising by parameters such as the period of treatment and the concentration or intensity of the functionalising agent. Moreover, more dispersible CNFs require less sonication, which would be another advantage since long period of sonication can break and shorten the fibres.’ (p.94)

It was shown that although the established methods of incorporating CNT/Fs in cement paste (using superplasticiser and ultrasonic processing) results in a well-dispersed nanofilament in a water-superplasticiser, but the Scanning Electron Microscopy (SEM) image of hardened cement paste showed relatively high concentration of CNFs at some fractured areas and it does not maintain a sufficiently good dispersion of nanofilaments in cementitious materials and relatively rapid reagglomeration occurs when the solution is added to cement (Yazdanbakhsh and Grasley, 2011; Yazdanbakhsh, 2012).

Therefore, Yazdanbakhsh (2012) proposed and studied the effectiveness of silica fume in maintaining a good dispersion and a novel and effective method of using silica fume to immobilise and stabilise the nanofilaments already dispersed in cement paste and preventing them from migrating towards each other. He found that the effect of the presence of silica fume on dispersion could be remarkable if silica fume is used in

sufficient proportions in cement paste. It can physically restrain the CNFs and prevent the reagglomeration of CNFs in fresh cement to a great extent, and thereby stabilise the distribution of CNFs in fresh cement paste. For silica fume to cement mass ratios up to 0.2, the quality of the stabilised CNF dispersion varied roughly linearly with silica fume content. It was suggested that this novel dispersion stabilisation method is simple and practical and can be readily implemented in the concrete construction industry due to the existing familiarity with silica fume as a concrete additive.

The researcher (Yazdanbakhsh, 2012) continued his study and tested CNF- cement paste beams under flexural loading at 1.0 wt% of cement and w/c ratios of 0.25 and 0.4. High range polycarboxylate-based water reducing admixture (superplasticizer) was used as the surfactant for dispersion of CNFs in water. Some samples were also made by using silica fume for better dispersion as it was suggested by the author. The dispersion method used was ultrasonically processing the CNFs in a water-superplasticizer solution. The results showed that the strength of the paste increased by more than 250% and Young's modulus was increased by 68% when the cement paste had normal strength ( $w/c = 0.4$ ), and when the specimen was not moist cured in the first 24 hours (a situation that can occur frequently in concrete construction industry). CNFs were also very effective in preventing shrinkage cracks that occur in the absence of moist curing. As Yazdanbakhsh (2012) stated:

‘It is possible that strictly using the methodologies described in this dissertation on concrete rather than cement paste might very well create a highly crack-resistant material.’ (p.120)

According to Nam et al. (2010), the surfactant applied in the sonication process can act as air entraining agent, therefore causing entrapped pores in the cement matrix and ultimately degrading the mechanical properties of the cement composites. Silica fume, due to its extremely fine particle size, similar to CNT, was considered to act effectively as means of overcoming such problem caused by surfactants. Kim et al. (2014) focused on the enhancing effect of CNTs on mechanical and electrical properties of cement composites by incorporation of silica fume. The SEM images showed that the dispersion of CNTs in the cement matrix was strongly affected during the mixing process by the presence of silica fume. It was stated that silica fume was hydrated with cement and developed C-H-S crystals) and possibly CNTs were anchored by C-S-H, and some

CNTs were embedded under the surface of hydration products. When silica fume at 10-20% was used, CNTs were dispersed individually hence increasing compressive strength, while at higher silica fume dosage CNTs were dispersed as clumps which was not satisfactory.

Silica fume forms additional C-S-H during the hydration reactions of Portland cement hence improving hardened properties of the material. The study by Sanchez and Ince (2009) on the effect of silica fume on the dispersion enhancement of the CNF in cement composite revealed that silica fume particles due to their small size disrupted the individual CNF (Pyrograf III- PR-19-LHT) fibre-fibre interaction that held them as clumps during the dry mixing. This resulted in an overall greater, though not complete (due to re-agglomeration upon water addition) dispersion of the CNFs throughout the cement paste. Although some defects such as CNF pockets and SF agglomerates were reported in the composites, no overall loss in strength was observed suggesting that the CNFs embedded in the paste acted to offset the effect of defects. No significant effect of CNF addition on the compressive strength was observed for all CNF concentrations. However, post-failure behaviour for the 2 wt.% CNF composites exhibited a fair level of mechanical integrity of the composites compression failure with greater water penetration resistance. According to authors, performance enhancements of cement composites are expected if better dispersion of the CNFs in the cement paste can be achieved. Surface treatment of CNFs, optimum physical blending, and/or the use of surfactants are recommended by authors as the potential approaches.

Similar mechanical investigation on nanofibres with more complex dispersion method was carried out on MWNTs by Rhee and Roh (2013) who examined the effect of adding MWNTs to the mortar and its effect on normal strength concrete. For dispersing the MWNTs, three stages were used; 1) mechanical ball-milling for 7h; 2) dispersed solution was diluted in water using sodium naphthalene sulfonate formaldehyde (SNSF) condensate as superplasticiser, and 3) ultrasonic bath for 20 min. The well-dispersed MWNT-water solution was used as the typical mix-water addition during the mixing process. Increasing the wt% of the MWNTs resulted in reduced workability. Cylinder compressive tests showed an increase in strength by 72% at 1.0 wt%. Particularly for small amounts of MWNT addition (0.25 wt%), a significant increase in the compressive strength was observed for both the well-dispersed and the just-stirred case. No significant changes were observed in the splitting tensile strength, elastic modulus, or

Poisson ratio with variation in the MWNT wt%. Mortar flexural tests showed no improvement of the specimen mechanical behaviour with the addition of the MWNTs. Hence, it was thought that the compressive strength enhancement may have originated from the interaction at the aggregate surface and from the ability of the MWNT to hold the mixing water owing to its large outer surface area. Thus, sorption and diffusion of water were reduced by MWNTs which enhances the concrete's strength. An improvement in delaying the water penetration into the concrete with well-dispersed MWNT was also reported.

Despite the great improvement found in compressive strength by Rhee and Roh (2013), Camacho-Ballesta et al. (2016) observed 7.7% improvement in compressive strength of 0.25% CNT reinforced cement paste. The dispersion was completed by mixing CNT and distilled water in a high-shear mixer for 10 min and afterwards an ultrasound treatment was applied for 5 min. Also, the flexural strength was improved by 19.4% when 0.5% fibre dosage was used. The difference in the results could be attributed to different mixing method.

On the other hand, the flexural strength capacity of the material was studied by Tyson et al. (2011), who conducted small-scale flexural tests on CNT and CNF reinforced cement paste. 0.1 wt% and 0.2 wt% (by weight of cement) for each fibre type were used. It was found that addition of both CNT and CNF improves peak displacement up to 150% (specimen with 0.2 wt% CNF) which is crucial for structural applications in which higher ductility and strain capacity is needed. In addition, the elastic modulus of cement paste was increased from 15 GPa to 24 GPa by addition of 0.2% CNF. Both concentrations of CNF outperformed CNTs for displacement at failure, which was attributed to the higher aspect ratio of CNFs (i.e., approximately 1,000 for CNFs and 150 for CNTs). CNF/c mass ratio of 0.1% showed highest fracture toughness at all ages compared to other samples and increased the flexural strength of hardened cement paste by over 80%. They observed a significant decline in flexural strength when the CNF to cement mass ratio (CNF/c) was increased from 0.1% to 0.2% which was attributed to poor dispersion. Overall, CNFs were recognised more effective as reinforcement due to their large interaction with cement matrix as well as enhanced dispersion achieved when using CNF. Regardless of good dispersion of CNT and CNF fibres in aqueous solution, the SEM observation of fractured surface revealed poor dispersion within the cement matrix. As authors state, the reason to poor dispersion within the hydrated cement paste

is unknown. However, it is thought to be due to size and agglomeration of cement grains. The hydration process of the hard cement grains occurs from the outside surface inward, toward the centre. As the cement hydrates, areas that were previously hard cement grains missing nanofilaments become hydrated C-S-H without any CNTs or CNFs. Authors suggested further studies needs to be conducted on the change in microstructural properties of CNT/F reinforced cementitious composites.

Konsta-Gdoutos et al. (2010) studied the effective dispersion of different length MWCNTs in water. Suspensions were prepared by mixing the MWCNTs in an aqueous solution containing different amounts of surfactant and the resulting dispersions were sonicated at room temperature. Successful nanofibre dispersion was achieved; thus, the application of ultrasonic energy was found necessary for proper dispersion. Also, there exists an optimum weight ratio of surfactant to MWCNTs close to 4.0. It was also shown that the ultrasonication process does not change the performance of the surfactant alone. Experimentation of different nanocomposites revealed that a higher concentration of short MWCNTs (0.08 wt.%) is needed to achieve effective reinforcement while a lower concentration (0.048 wt.%) of long MWCNTs is required to attain the same level of mechanical performance. Both short fibres and long fibres increased the flexural strength of the cement paste by 25%. Also, Young's modulus of both nanocomposites was most increased by 45% to a value of about 13GPa. In addition, the nanoindentation results suggest that MWCNTs can strongly reinforce the cement paste matrix at the nanoscale by increasing the amount of high stiffness C-S-H and decreasing the porosity. Authors believe that only a small amount of effectively dispersed CNTs is needed to achieve an enhanced reinforcing effect of the cementitious matrix and the production of low-cost nanocomposites. Regarding the effective dispersion, a successful method was reported by Metaxa et al. (2013) who dispersed CNFs (0.048 wt%) by initially adding CNFs to a water/surfactant solution then subjecting the solution to an intensive sonication. For complete dispersion, under the conditions employed in the research, the application of an ultrasonic energy close to 2800 kJ/l was found to be most effective, compared to 2100 kJ/l and 3500 kJ/l. An excessive amount of surfactant showed lower flexural strength enhancement. A surfactant to CNF ratio close to 4.0 was found to be optimal as opposed to ratios of 2.0 and 6.0. The best nanocomposite sample exhibited a 50% and 75% increase in flexural strength and Young's modulus, respectively. It was concluded that the addition of CNF to cement paste offers a significant property

enhancement to the cementitious nanocomposites, mainly increased flexural strength and stiffness, and crack control at the nanoscale.

Gdoutos et al. (2016) conducted a fracture mechanics experiment study on the 0.1 wt.%, 0.2 wt.% MWCNT reinforced cement mortar and 0.1 wt.% CNF cement mortar prisms. 0.1 wt.% MWCNT had 86.7% higher flexural strength and 92.4% higher Young's modulus than the normal cement mortar. In their study, CNF showed better performance than those MWCNT samples, which the authors stated that besides good dispersion, the diameter, and the length of the CNF was responsible for better performance. The addition of 0.1% wt. CNF to the mortar resulted in an increase of 105.9% in flexural strength and 94.3% increase in modulus of elasticity. Overall, the nano-reinforced mixes exhibited less brittle behaviour.

#### **2.2.2.1. Hybrid composites**

In addition to all the effort made by researchers to investigate the effect of nanofibres on cementitious materials, the idea of using hybrid fibres was developed and investigated by Metaxa et al. (2010). They studied the characteristics of hybrid fibre reinforced cement paste containing nano-scale fibre (CNF) and micro-scale fibres (PVA) in proportions of 0.048% and 0.54% of cement weight respectively. Cement paste reinforced with CNF at the concentration as low as 0.048%wt of cement improved Young's modulus by 75%. During the early stages of loading, the pre-peak mechanical behaviour of the hybrid mixes was mainly controlled by the CNFs since nanofibres were effectively reinforcing the matrix at the nanoscale level providing the material with the ability to carry higher load in comparison to plain paste, while microfibres due to their larger diameter efficiently bridged the larger scale pores and cracks and enhanced the load carrying capacity of the material after fracture, improving the ductility and post-peak behaviour of cement paste (see Figure 2.4). Cement paste reinforced with PVA microfibres exhibited less than 10% increase in flexural strength and Young's modulus, while a tremendous increase on the fracture toughness of the matrix was achieved. Overall, it was concluded that the incorporation of hybrid fibres resulted into a stronger and tougher composite compared to the singly-reinforced composites or plain cement paste.

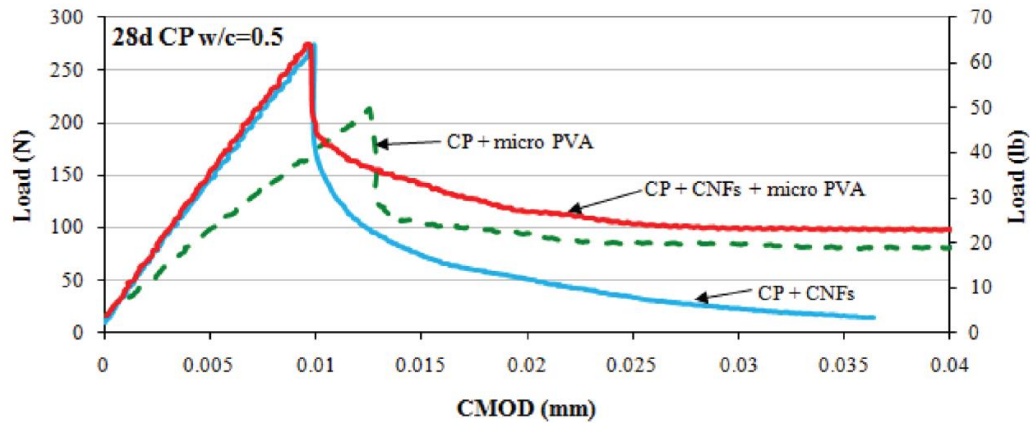


Figure 2.4. Typical load-CMOD curves of 28 days cement paste with CNTs, cement paste with PVA microfibres and hybrid cement paste (Metaxa et al. 2010)

Use of hybrid nanofibre reinforced cementitious composites was further developed. Peyvandi et al. (2013) also investigated the properties of hybrid reinforcement systems comprising CNF, micro steel fibres (SF) and micro PVA and came to a comparable conclusion as Metaxa et al. (2010) that the complementary action of nano- and micro-scale fibre reinforcement in concrete (rather than each of them individually) render desired benefits to concrete material properties since they function at different scales. In their study, High Strength Concrete (HSC) and Ultra-High-Performance Concrete (UHPC) were considered due to the relatively high cementitious binder content and packing density, which favours the dispersion and interfacial interactions of discrete reinforcement system. It was found that nanofibres contribute to the interfacial stress transfer from fibres to the cementitious matrix and enhance the bonding and pull-out behaviour of micro-scale fibres. CNF/PVA made a better contribution to the engineering properties of UHPC than HSC; this was attributed to the higher compaction density and reduced porosity of UHPC. Amongst all tested hybrid materials, CNF/SF combination in UHPC outperformed other materials with 46% higher flexural strength than plain concrete and compressive strength of 154 MPa (3.9% gains over plain concrete).

The improvement in the performance of the hybrid composite could also be seen in studies of Hunashyal et al. (2011) on the behaviour of cement mortar composite bars reinforced with carbon fibres (CFs at 2.25 wt.%) and MWCNTs (at 0.5 wt.%) under direct tension. First, the MWCNTs were pre-dispersed in acetone by means of an



ultrasonic probe. Then the acetone was allowed to evaporate. Next, CFs were pre-dispersed in a fraction of the water required; sonication was carried for 10 minutes. Next dispersant Hydroxyethyl cellulose (HEC) of quantity 0.06% by weight of cement was added to the pre-dispersed mixture and again sonicated for about 10 minutes with continuous stirring. From the results, it was observed that the hybrid composite (i.e. cement mortar+CF+MWCNT) mainly contributed in increasing the tensile strength and tensile load carrying capacity of the composite by 54%, while singly-reinforced composites with CF and MWCNT enhanced this property by 38% and 19% respectively. Also, failure strain capacity of the hybrid composite was 44% higher as compared with plain bars, indicating ductile failure mode of the specimen. Authors concluded that the addition of nanofibres, to plain bars (with or without CF) will increase tensile strength. This proved their ability to become an ideal reinforcing material and as the authors stated 'it can be used for the construction of structures subjected to seismic, impact, dynamic, and so forth, loadings' (p.5).

The first researcher to consider the effect of nanofibre on the performance of steel was Willie and Loh (2010) who studied the effect of including nanometre sized particles on bond behaviour between steel fibres and UHPC matrix while preserving the workability of the concrete mix. MWNTs were chosen with a low concentration of 0.022% wt. of cement. The aim was to design a hybrid fibre-reinforced UHPC. To tackle dispersion issue, MWNTs were mixed in diluted superplasticizer solutions. Dispersion quality was compared by SEM and the solution showed only individual and small bundles of MWNTs, hence considered as the best dispersion method. MWNTs showed no significant influence on compressive strength and bending strength. However, pull-out test results showed that the bond behaviour of steel fibres significantly increased with the addition of low concentrations of MWNTs within the concrete mix.

At the University of Texas, Yazdani and Mohanam (2014) studied the compressive strength and flexural strength of cement mortar reinforced with 0.1% and 0.2% of both CNT and CNF with water/cement ratios of 0.35-0.50. Mixing technique used was ultrasonication of fibres in water-surfactant mixture. 30 min and 15 min sonication were used for CNT and CNF respectively. Higher compressive strength was achieved in the CNF samples at lower w/c ratios of 0.35 and 0.45. It was apparent that the best combination for compressive and flexural strength production was CNF composites

(0.1%-0.2%) with w/c ratio of 0.35. The percentage increase of compressive strengths and flexural strength over control samples are summarised in Table 2.2 and Table 2.3.

Table 2.2. Percentage increase of 28-day compressive strengths over control samples (Yazdani and Mohanam, 2014)

	<b>Dosage of CNT/CNF</b>			
<b>W/C ratio</b>	0.1% CNT	0.2% CNT	0.1% CNF	0.2% CNF
<b>0.35</b>	154	37	200	217
<b>0.45</b>	54	27	68	36

Table 2.3. Percentage increase of flexural strengths over control samples (Yazdani and Mohanam, 2014)

	<b>Dosage of CNT/CNF</b>			
<b>W/C ratio</b>	0.1% CNT	0.2% CNT	0.1% CNF	0.2% CNF
<b>0.35</b>	53	27	42	50
<b>0.45</b>	14	22	8	19

The SEM imaging results revealed that although the dispersion of aqueous medium was visually uniform, the dispersion was not fully achieved when mixed with the cement. Having said that, it was suggested that both CNT and CNF are promising reinforcing materials for cementitious products.

#### 2.2.2.2. Nanoconcrete

Gao et al. (2009) investigated the mechanical properties of concrete and Self-Consolidating Concrete (SCC) containing 0.16%-2.5% CNF by volume of binder. They also studied the electrical properties of CNF concrete which will be discussed in the next section. Three types of CNF used in their study were: 1) PR-19-XT-PS, 2) PR-19-XT-PS-OX; an oxidised version of PR-19-XT-PS which is more conductive, and 3) PR-19-XT-LHT-OX; produced by heat-treating the fibre at 1500°C. This is the most conductive fibre due to heat treatment.

The cylinder compressive strength of the concrete increased by 42.7% for 0.16% CNF concentration. The optimum concentration for first, second and the third type of CNF in SCC was found to be 0.5%, 2.0%, and 1.0% respectively, which increased the

compressive strength by 13.5%, 24.4% and 21.4% correspondingly compared to plain SCC. From the ductility point of view, oxidised and heat-treated CNFs performed better. The authors believe that using SCC improves CNF dispersal and increases the electrical sensitivity of the concrete.

Similar to Gao et al. (2009) studies, Sivakumar (2011) studied SCC reinforced with 0.5%, 1.0%, 1.5%, and 2.0% of CNF by volume of binder. CNF were mixed with water using a blender and superplasticiser was then added. The characteristic compressive strength of the concrete increased by 29.4% for 1.0% CNF which was less than what was found by Gao et al. (2009). Both flexural strength and split tensile strength increased with 0.5% and 1.0% then decreased for higher volume fractions. The maximum variation for the split tensile strength in their study was as low as 0.6%.

Recently alternative type of concrete was considered for the research on nanoconcrete by Meng and Khayat (2016) who investigated mechanical properties of UHPC with carbon nanofibre. 0.5% micro steel fibre, 5% silica fume and 0-0.3% CNF were used. The compressive strength slightly increased by 5-8 MPa. The direct tensile strength and flexural strength was increased by 56% and 46% respectively for 0.3% CNF concrete and the energy absorption was increased by 108%.

Regarding the structural performance of the nanomaterials, the only research up to date, has been conducted by Howser et al. (2011). Short shear critical columns built with 1% dosage of CNF reinforced self-consolidating concrete (SCCNFC) were tested under reversed cyclic load. Steel fibre reinforced SCC (SCSFC) and SCC columns with no fibres (SCRC) were also tested for comparison purposes. A definite yielding of longitudinal steel occurred in both the SCRC and SCCNFC columns with visible compression strut, while steel fibre reinforced column failed with one dominant shear crack. This was attributed to the absence of transverse shear ties. The ultimate normalised capacity, deflection, and ductility of SCCNFC column was respectively 30.7%, 34.9%, and 35.1% higher than the SCRC column. It was concluded that the addition of carbon nanofibres to concrete increased the strength and ductility of a short column.

A summary of some findings to date on CNT/CNF reinforced cementitious composites and their effect on the mechanical properties are given in Table 2.4 and Table 2.5.

Table 2.4. Summary of past studies on CNF reinforced cementitious composites and resulting improvement in mechanical properties

Type	wt. %	Matrix	Dispersion Technique	Compression	Flexure	Tension	Reference
CNF	0.16 vol. %	Concrete/ SCC	Waring blender	42.7%	-	-	Gao et. al. (2009)
CNF	0.1	Cement mortar	Sonication + SP*	-	105.9 %	-	Gdoutos et al. (2016)
CNF	0.048	Cement paste	Sonication + SP	-	50%	-	Metaxa et al. (2013)
CNF	0.1	Cement paste	Sonication + Silica fume + SP	-	250%	-	Yazdanbakhsh (2012)
CNF	0.1	Cement mortar	Surfactant + Sonication	200%	42%	-	Yazdani and Mohanam (2014)
	0.2			217%	50%		
CNF	0.2	Cement paste	HRWR	-	-	22%	Gay and Sanchez (2010)
			Silica fume+HRWR	-	-	26%	
CNF	0.1	Cement paste	Sonication + SP	-	55.5%	-	Tyson et al. (2011)
	0.2				38.8%		

\*SP=Superplasticiser

From Table 2.4 and Table 2.5, it is evident that the material mechanical property enhancement has been various. This reveals that the effect of nanofibres is dependent on many variables such as matrix, dispersion method, volume fraction of fibres, and type of fibres. From the obtained results, it is concluded that the use of superplasticiser and silica fume together with sonication has been a successful method in dispersion of nano particles and achieving improvement in the mechanical properties of the material.

Table 2.5. Summary of past studies on CNT reinforced cementitious composites and resulting improvement in mechanical properties

Type	wt. %	Matrix	Dispersion Technique	Compression	Flexure	Tension	Reference
MWNT	0.5	Cement mortar	Acetone + ultrasonication	-	-	19%	Hunashyal et al. (2011)
MWNT	0.5	HS concrete	Sonication + SP*	12%	-	-	Kowald (2004)
MWNT	0.5	Cement mortar	Surface treated by acid	19%	25%	-	Li et al. (2005)
MWCNT	0.08	Cement	SP solution + Sonication	-	25%	-	Metaxa et al. (2010)
MWNT	0.1	Cement mortar	Sonication + SP	-	86.7%	-	Gdoutos et al. (2016)
MWNT	0.2	Cement paste	Sonication + SP	-	269%	-	Abu Al-Rub et al. (2012)
MWNT	0.08	Cement paste	Sonication + SP	-	25%	-	Konsta-Gdoutos et al. (2010)
CNT	0.1	Cement mortar	Surfactant + Sonication	154%	53%	-	Yazdani and Mohanam (2014)
	0.2			37%	27%		
MWNT	0.25	Cement paste	Shear mixing + sonication	7.7%	9.7%	-	Camacho-Ballesta et al. (2016)
	0.5			0%	19.4%		
MWNT	0.25	Concrete	SP-basket mill-diluted in water-sonicated	50%	-	-	Rhee and Roh (2013)
	1.0			72%			

\*SP=Superplasticiser

### 2.3. SELF-SENSING PROPERTIES OF NANOCOMPOSITES

Structural health monitoring (SHM) is the process of implementing a damage detection and characterisation strategy for engineering structures aimed at providing accurate and timely information concerning structural health condition and performance. The information obtained from monitoring is generally used to plan and design maintenance activities, increase the safety, verify hypotheses, reduce uncertainty, and widen the knowledge concerning the structure being monitored. Cumulative damage and the

degradation of structure or material resistance could be mentioned as the common reasons for the failure of conventional concrete structures and infrastructures such as bridges, power station and other structures under different load, fatigue or erosion effect or material aging. Hoheneder (2012) stated that:

‘The constant monitoring of infrastructure will allow for a more educated approach to future designs. Currently, the standard approach to the maintenance of infrastructure is to wait until damage is visual and reactively fix the issues as they arise. Allowing for constant health monitoring during construction, setting, and the service life of the structure will allow for more proactive maintenance designs that target flawed areas as well as allow for future infrastructure to be designed to avoid these known flaws, saving money and resources while also increasing public safety.’ (p.2)

Traditionally, strain sensors (such as optical fibre sensors, electrical resistance strain gauges, and piezoelectric ceramics) have been widely used in SHM. However, the cost and durability of traditional sensors motivates researchers to develop new sensors. The technologies used to perform the SHM are continuously developing. Recently, concrete that has self-monitoring ability and high mechanical properties is attractive for guaranteeing the safety of structures. Self-monitoring function is achieved by correlating the variation of the applied stresses or strains with the variation of the electrical resistance property of the material. According to Materazzi et al. (2013), ‘the deformation or tension state can be estimated through the resistance or electrical resistivity changes allowing the emergence and spread of damage and micro-fractures to be monitored’ (p.3).

Since the birth of nanotechnology and development of cementitious materials, advanced methods have emerged for structural health monitoring, providing measurable electrical responses to applied strain. Incorporating conductive nanomaterials (such as carbon nanofibre, carbon fibre, or carbon black) within concrete, results in developing a material that can be conductive and piezoresistive (resistance changes with strain), which is so-called *smart concrete*. Smart materials are those that sense and respond to changes in strain, temperature, moisture and/or electric or magnetic shield (Mo and Howser Roberts, 2013). Electric conductive concrete has strain sensing of damage, in which strain or stress variations in the structure member could be analysed by

performing resistivity measurements, making the evaluation of early damage (i.e. impending of cracking) of concrete members possible, therefore the need for embedding sensors is eliminated (Ding et al., 2013). A building material with high mechanical performance and piezoresistivity indicate the possibility to make a long continuous sensor and transforming the structures themselves into infinite sets of potential sensors, thus enlarging the sensitive volume to its maximum extent and measure strain over a large structure for SHM (Kang et al., 2006).

Furthermore, the application of smart concrete would benefit most cases of interest in the SHM of large concrete structures, such as tall buildings, bridges, plants and more, in which traditional testing techniques based on local inspections can become especially troublesome due to the structures' large spatial extents and the use of traditional sensors becomes almost prohibitive because of maintenance and access difficulties (Materazzi et al., 2013).

Conductive fibres are important for piezoresistivity and they are typically used at a volume fraction below the percolation threshold; this refers to the volume fraction above which the fibres touch one another to form a continuous electrical path (Wen and Chung, 2003). Non-connected nanofibres can also contribute to conductance through tunnelling transport of electrons. It is reported that the tunnelling resistance has an important role in electrical conductivity of the composite and the maximum tunnelling distance for CNT is reported about 1.8 nm (Li, Thostenson, and Chou, 2007). In sensors with fibre volume fraction below the percolation threshold, the conductivity will be highly dependent on the degree of fibre dispersion. Also, surface treatment methods and the polymer types are extremely important for the enhancement of the electrical properties of the nanocomposite (Feng et al., 2014).

By increasing the dosages of conductive admixtures in concrete, the concrete conductivity increases. Having said that, increasing fibre content declines the workability of fresh concrete which is an important precondition for structural concrete in the practice. Therefore, the upper limit of the dosage of conductive materials is determined mainly by the workability and not by the conductivity. Ding et al. (2013) emphasises this matter by stating that:

‘The electric characteristics of the concrete must be made suitable for the application without clear degrading of the workability of fresh concrete and mechanical behaviours of hardened concrete.’ (p.234)

The electrical conductivity of the fibres (CNT/Fs) within cement-based materials enables the DC electrical resistivity of the composites to change in response to strain, damage, or temperature, allowing sensing (Mo and Howser Roberts, 2013). So, the monitoring signal of this kind of sensors is resistance signal, where the resistance (volumetric or surface resistance) is calculated by synchronously collected current and voltage signals (Han et al., 2007). Electrodes of appropriate materials are used for measuring the conductivity of the material with various configurations as described by Han et al. (2014) in Figure 2.5.

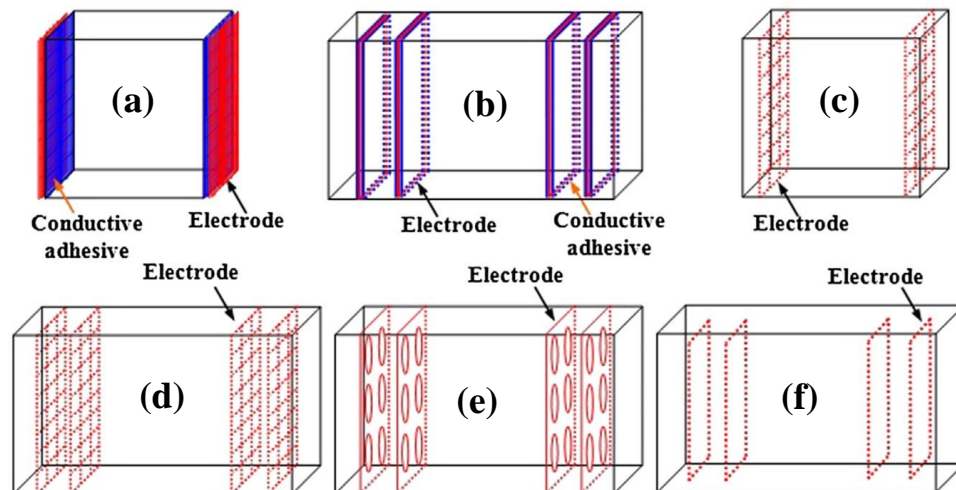


Figure 2.5. The commonly used fixing style and layout of electrodes in self-sensing concrete (Han et al., 2014)

The electrodes could be attached to the surface as shown in layouts (a) and (b) in Figure 2.5. In this method, the attached electrodes could easily be debonded from the surface in practical applications. Four schemes of (c)-(f) shown in Figure 2.5 uses embedded mesh within the material. The measurement methods are two-probe method and four-probe method. In the two-probe method, the two electrodes act as both the current pole and the voltage pole, whereas the four-probe method uses inner electrodes as voltage poles and the outer poles as a current pole (Han et al., 2014).

Wen and Chung (2007) studied sensing properties of 0.5% carbon fibre reinforced cement paste using different measurement methods. They found that for strain sensing,



embedding the electrodes in four-probe configuration is superior to four-probe method with contact electrodes. Also, they observed that two-probe method showed higher electrical resistance and the contribution of the embedded contact in the resistance was 9%. Thus, four-probe method was suggested as more accurate sensing measurement method. The researchers (Wen and Chung, 2001) found decreased transverse and longitudinal resistivity upon uniaxial compression of cement paste with 0.5% carbon fibre using four-probe method with contact electrodes in the specimen perimeter. The decrease was reversible in the elastic regime. In a companion research (Wen and Chung, 2000), they reported that both transverse and longitudinal resistivity increase upon uniaxial tension. The magnitude of the gage factor (defined as the fractional change in electrical resistance per unit strain) was reported higher for compression than tension also it was stated that using silica fume in the paste increased the gauge factor. Overall it was concluded that the resistivity in any direction relative to the stress axis can be used to indicate strain or stress in the stress axis.

Similar to the findings of the Wen and Chung (2001), the advantageous of using silica fume was also reported by Cao and Chung (2001) in lowering the electrical resistance of carbon fibre reinforced cement mortar. Kim et al. (2014) found that adding silica fume in CNT reinforced cement paste enhances the electromagnetic shielding effectiveness of CNT/cement composites causing the CNTs to have noticeable impact on the electrical properties of the cement composites and decreasing its electrical resistance.

The effect of polarization on the electrical resistance of the material was raised by Li, Xiao, and Ou (2006) who investigated the electrical properties of carbon black (CB), at the scale of 120nm, filled cement composites. They mentioned that the moisture content of the samples had significant influence on polarization which led to increased resistance of the cement-based composites. During polarization, ions existed in electrolyte filled in pores would move to the surface of the electrode contacts, which induced an electric field in the opposite direction to the applied field. Therefore, the resistance increased up to a balanced state. On the other hand, the amount of carbon black in the matrix was stated to weaken the polarization electric field by the leakage of charges through the conductive paths of the carbon black fibres and higher carbon black content could effectively reduce the polarization effect.

Han et al. (2014) describe the polarization effect (shown in Figure 2.6) as the movement and aggregation of the ions in the cement concrete matrix when constant electrical field is applied and the electrical conduction will be dominated by ionic conduction mechanism. Ways to nullify the polarization effect are suggested to be using alternating current (AC) signals or applying the direct current (DC) voltage potential well ahead of loading the composite to allow the resistance to plateau off.

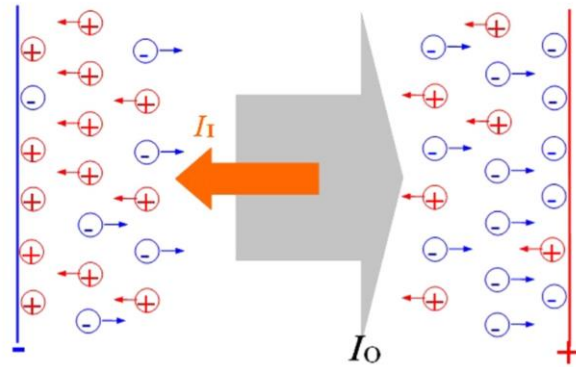


Figure 2.6. Sketch of polarization in concrete (Han et al., 2014)

Han et al. (2007) investigated the Carbon Fibre (CF) cement paste sensors ( $V_f = 3$  vol.%). Two measuring methods of pasted copper foil using silver paint and embedded copper gauze were compared. It was observed that the Fractional Change in Resistance (FCR) of specimens with embedded electrode was relatively smooth, but resistance of specimens with pasted electrode was relatively high, which was attributed to the poor bond between the copper foil and carbon fibre cement paste. However, under compression, the contact resistance diminished because the bond between the copper foil and carbon fibre cement paste improved. It was concluded that the copper gauze electrode is more suitable for carbon fibre cement paste. Regarding the mesh size, bigger mesh sizes did not affect the compressive strength of the material while fine mesh resulted in lower compression strength. In terms of durability, the copper gauzes were found to be effective since the resistivity of the material hardly changed after 1 year.

Moreover, two electrode layouts of direct-current two-pole and direct-current four-pole were studied. The experiment showed that the resistance measured by the four-pole method was less than that obtained by the two-pole method. The contact resistance between electrode and carbon fibre cement paste was the cause of the difference

between the resistance measured by these two methods, and the direct-current four-pole method eliminated it. Therefore, the four-pole layout was introduced suitable for measuring the resistance of carbon fibre cement paste sensors. The area of the voltage pole and mesh size of gauze electrode did not affect the resistivity of the specimens. Also, the spacing between the current pole and voltage pole did not influence the resistivity when more than 7.5 mm.

Further on the effect of CF on electrical properties of cementitious composite, Azhari and Banthia (2012) studied both CF and carbon nanotube as the conductive filler in cement paste. The hybrid cementitious sensors contained both carbon fibre at 15% and MWCNT at 1% by the volume. 10% improvement in conductivity was observed for the hybrid sensor. Cylindrical samples showed nonlinear decrease in resistivity under linear compressive load. The rate at which the resistivity decreased was higher initially, which was thought to be due to internal micro-cracks. In the hybrid sensor, the CNT bridged the pathway between CF and created more uniform conduction path, which in turn helped to increase the accuracy and repeatability of the cement-based sensor. In both sensors creation of micro-cracks was signified by a steady increase in the resistivity which then changed to a sudden upsurge when microcracks coalesced and failure occurred. Thus, in addition to strain sensing, the material was capable of damage-sensing as well. Researchers further extended their research and studied the tensile strain sensing of CF sensors (Azhari and Banthia, 2017). They found that the two-probe measurement technique resulted in twice as much resistivity as the four-probe method. Embedded electrodes were found more robust than the pasted electrodes. During each loading cycle, the resistivity values increased with the increase in tensile load. The 20% CF sensors' electrical resistivity changed, in a reversible manner, corresponding to the applied cyclic load, increasing with the increase in tensile strain and vice versa similar to the 15% CF sensor. It was found that above the percolation threshold (estimated at 0.5%), the sensors were more sensitive to tension than to compression, while below the percolation threshold (reported 0.5 to 1%) sensors were more sensitive to compression than to tension.

The capability of CNT-cement based material and their electrical response for measuring dynamically varying strain in concrete structures was explored by Materazzi et al. (2013) in the typical frequency range of large civil structures for the first time. For this purpose, prismatic specimens were prepared using two copper wires directly embedded in the samples (i.e. two-probe method). The specimen's response to both sinusoidal compression loads and axial loads with forward/backward sweep variation of the frequency was measured. Good correlation was qualitatively observed between axial strain and electrical resistance and normalised input and output were almost perfectly overlapped (see Figure 2.7). The results demonstrated that the sensors' output (i.e. electrical resistance) retains all dynamic features of the input (i.e. applied stress). Moreover, it was concluded that the sensors are apt to measure rapidly varying strain responses. Thus, CNT-cement composites provide useful information for SHM to the dynamic range.

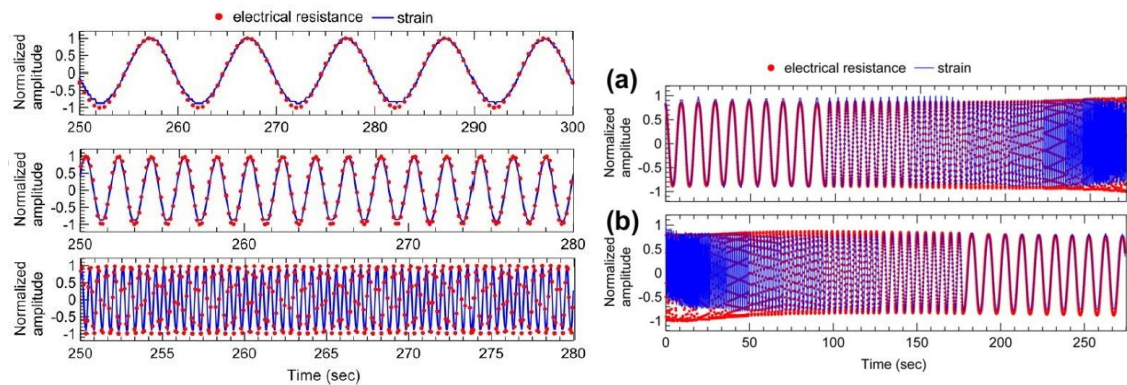


Figure 2.7. Left: normalised measured strain and electrical resistance vs. time for different load frequencies; Right: normalised measured strain and measured electrical resistance vs. time: (a) test with forward sweep of the frequency from 0.1 Hz to 5.0 Hz and (b) test with backward sweep of the frequency from 5.0 Hz to 0.1 Hz (Materazzi et al., 2013)

Further results on the damage-sensing capability of CNT-cement mortar and CNF-cement mortar was established in research conducted by Dalla et al. (2016) where 0.6 wt.% CNT loading and 0.2 wt.% and 0.6 wt.% CNF loading was adopted. It was suggested that a CNT loading of 0.6 wt.% is the percolation threshold to obtain a continuous conductive network of carbon nanotubes throughout the material volume. Also, piezoresistive behaviour of both types of mortar was analysed and they showed fully recoverable electrical resistance varying in an inverse relation to applied compressive stress. Three-point bending test on small prismatic mortar samples showed

that both fibres gave remarkable damage sensing capability to the mortar shown by dramatic resistivity jumps at maximum loading level, thus providing valuable warning sign.

Loh and Gonzalez (2015) tested MWNT mortar cubes subjected to cyclic compression load. Specimens exhibited bilinear sensitivity to applied compressive strains. At low strains (i.e., up to -0.2%), the sensitivity was extremely high; when compressive strain exceeded -0.2%, another linear least-squares best-fit line was fitted to the 'high strain' region. Given that it was unlikely that samples were damaged, from the researcher's perspective, it was assumed that compression up to -0.25% strains allowed fibres to begin to come into contact with one another, thereby facilitating significantly better electrical current transport. After this point, additional compression would yield less significant changes in particle contacts, thereby reducing the relative change in resistance to result in lower sensitivities.

Camacho-Ballesta et al. (2016) also investigated the performance of MWCNT cement paste for strain sensing. It was observed that from the lowest CNT addition (0.05 wt.%) to the highest (0.5 wt.%), FCR was well correlated with the stress applied to the specimen under compression. All current intensity consisting a different range of 0.1 mA, 1 mA, and 10 mA, made it possible to establish the correlation between resistance variation and compressive strain. However, sensitivity was enhanced when the current intensity increased. The best performance as strain sensor was obtained for the 0.05% CNT composite, reaching values of gauge factor up to 240 with  $R^2$  Pearson's coefficient above 0.99.

In expansion of previous researches, other materials were considered as matrix by D'Alessandro et al. (2016). They investigated sensing properties of MWNT reinforced cement paste, mortar, and concrete. Both mechanical mixing and sonication process were considered. Sonication method was more successful in achieving a desirable level of dispersion as well as better signal quality in electrical resistance measurements. The percolation threshold was found to be 1% for concrete specimens as well as mortar specimens. Pastes had larger gauge factor than mortar and concrete. The relative increase in electrical conductivity grew when ranging from paste to mortar and concrete and the reason was due to aggregates, which reduced the electrical conductivity. However, they were ineffective above the percolation threshold. Authors stated that the

fabrication process presented might be potentially suitable for casting full-scale self-sensing structural components.

CNT and CNF reinforced cement paste with 0.05%, 0.1%, 0.3%, and 0.5% dosages were tested for sensing capability by Samsal et al. (2017). The electrical resistance increased by time during hydration which was due to microstructure changes in the matrix. The electrical resistance of oven-dried CNF-cement paste was greater than CNT samples, unlike the undried samples. Increasing the filler content resulted in increased electrical conductivity. In CNF-pastes the conductivity increased with increasing applied voltage. The gage factor reported for 0.05% CNT composite and 0.1% CNF composites were 189 and 228 respectively. The piezoresistive strain sensitivity of nanocomposites containing CNF (0.1%) showed better sensing sensitivity than CNT nanocomposite. It was also found that resistivity for both nanocomposite types decreases from 2.5 V to 5 V and after that.

Galao, Baeza, Zornoza and Garces (2014) studied strain sensing and damage sensing of prismatic cement paste specimen reinforced with 0.5%, 1% and 2% CNF by mass of cement under compressive strain. The FCR was reversible during the elastic behaviour. Composites with 2% CNF was the most sensitive with gage factor of around 50 which was almost thrice the lower CNF dosages. A linear relationship between electrical response and compressive stress was reported which became parabolic after the damage detection and the linear stage (i.e. yield point). Therefore 2% CNF reinforced cement paste was suggested to be sensitive to its own structural damage.

### **2.3.1. Hybrid composites**

It was found by the researchers that the use of hybrid fibres is effective in enhancing the electrical conductivity of the cementitious composite (Noiseux-Lauze and Akhras, 2013; Konsta-Gdoutos and Aza, 2014). Noiseux-Lauze and Akhras (2013) studied hybrid CNT/CNF nano cement sensors. The electrical conductivity of the hybrid specimens (0.2% CNF/0.2% CNT) was significantly higher than single CNT or CNF cement composites. The relationship between strain and resistivity was fairly linear and a gauge factor of approximately 70 was measured.

Furthermore, Konsta-Gdoutos and Aza (2014) studied the self-sensing properties of cementitious composite reinforced with CNT and CNF at an amount of 0.1 wt.% and

0.3 wt.% of cement using four-probe method. Nanocomposites reinforced with CNF exhibited higher resistivity compared to samples with CNT. This was attributed to different aspect ratio of the fibres, 'which results in a lower amount of individual carbon nanofibre reinforcing the matrix. Another plausible explanation could be differences in the electrical conductance between CNTs and CNFs' (p.166). Also, a higher dosage of fibres for both CNF and CNT showed a decrease in electrical resistivity, which was thought by the authors to be due to insufficient dispersion and presence of agglomerates in the matrix, which in turn impairs the composite's conductivity. The piezoresistivity behaviour of both materials was studied and the average change in electrical resistance (i.e. ERV) of 5% for 0.1 wt.% nanofibre and 1.5% for 0.3 wt.% of nanofibres were reported. It was concluded that due to an increased change in resistivity which indicated the amplified sensitivity of the material in strain sensing, cement paste with 0.1 wt.% CNTs and CNFs were sensitive and can be considered to be a piezoresistive sensor.

### **2.3.2. Nanoconcrete**

On the effect of nanofibres on concrete electrical properties, Rhee and Roh (2013) found that 'the electrical conductivity of MWNT concrete increased up to an optimal value, which corresponded to 1.0 wt% MWNT, and then decreased as the wt% MWNT increased further. This feature could be used as an embedded sensor to transmit the internal information inside the concrete, such as the rebar corrosion rate, water penetration and crack development.' (P.960)

Ding et al. (2013) added nano-carbon black and carbon fibre (CF) as electrically conductive materials into concrete. The flexural strength of concrete beams increased ranging from 10% to 19%. Also, compressive strength of the material was increased for nano-carbon black and CF reinforced concrete ranging between 2.2% and 6.2%, which was not considered a significant improvement. The relationship between FCR and the strain of initial geometrical neutral axis of concrete beams showed correspondence. A low value of correlation coefficient (0.5) was found for normal concrete beam with no admixture, while high correlation coefficient of higher than 0.9 was found for some fibre reinforced concrete with specific fibre content, the highest correlation coefficient (0.978) was observed for 1.0% CF sample. Hence, these were found suitable for self-diagnosing of the damage.

To investigate the self-sensing ability of CNF concrete Gao et al. (2009) tested compressive cylindrical specimens using the four-probe method to determine the volume electrical resistance of the concrete. Different types of CNF had the optimal performance at different concentrations. Minimum concentration of 1.5% was recognised for first CNF type to be effective in detecting electrical resistance variation (ERV). This concentration was higher than that which was efficient for the cement paste or mortar (around 0.3%) as mentioned previously. For second type (i.e. oxidised) the electrical resistance was almost the same for 1%-2% concentrations. At last, the third type of CNF, which was heat treated exhibited the highest electrical sensitivity at 1% concentration with 80% reduction in electrical resistance, while this value decreased rapidly when the concentration of CNF was increased to 1.5%, 2%, and 2.5%. It was concluded that 'If the actual concentration is higher than the threshold, the tunnel conductivity effect of CNF will decrease, and the electrical resistance does not change with increasing strain' (p.7). Overall, it was specified that well-dispersed CNF in the appropriate concentration allows for the greatest ERV of concrete with increasing strain and consequently may be used in applications that require strain monitoring and make concrete itself a sensor.

Mullapudi et al. (2013) used the pulse velocity method to characterise properties of concrete containing CNFs. Measuring the pulse velocity in the longitudinal axis of the cylinder, compressive strength, and dynamic modulus of elasticity of the concrete increased with the curing time of the mixture and the pulse velocity test results exhibited linear correlation with compression test results as well as linear correlation with the dynamic modulus of elasticity. Because of this, the pulse velocity test results could be used to predict compressive strengths and elastic properties of the specimens.

During loading, pulse velocity was measured along the transverse direction of cylinders. As the loading increased, the compressive strain along the longitudinal direction increased. Due to Poisson's effect, with the increase of the compressive strain of the concrete along the longitudinal axis of the cylinder, the tensile strain along the transverse direction increases, this causes damage to the cylinder. It was shown that the pulse velocity has a direct correlation with the strength and the relationship of both strength-pulse velocity and dynamic modulus of elasticity-pulse velocity can be described by linear equations. The ERV of plain SCC was random, while the ERV of CNF reinforced concrete increased with the increase of the stress and strain. It was



concluded that appropriate amount of CNF uniformly dispersed in the cement paste is tightly bound to the hydrate products and the transmission of the CNF's high tensile strength and electrical conductivity to the surrounding cement matrix is possible. However, CNF in excess of the threshold concentration will cause the fibres to attract each other and clump together in localised weak zones resulting in the reduction of the ultimate strength of the concrete.

The self-sensing performance of a nanoconcrete structural element was first studied by Howser et al. (2011). They measured the electrical properties of a 500mm short concrete column constructed with CNF concrete. The voltage and current were measured using the four-probe method as shown in Figure 2.8. The electrical readings showed a great correlation between the peaks in the applied horizontal force, strain, and resistance plots for the CNF reinforced column and little correlation between the resistance plots and the force or strain plots for the plain concrete and SF reinforced columns was recorded. It was concluded that when an appropriate dosage of CNF is used, self-consolidating CNF reinforced concrete can be used as a reversible strain sensor and can be used for self-structural health monitoring.

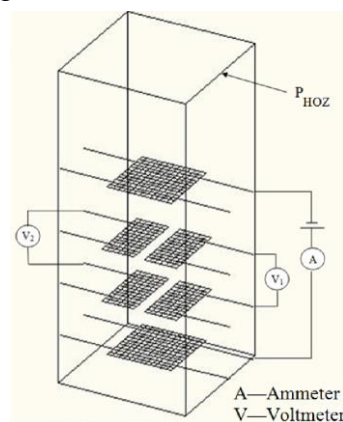


Figure 2.8. Wire mesh configuration inside short column tested by Howser et al. (2011)

To accommodate the measurement of internal strain in structural element, a carbon nanofibre reinforced cementitious material as an aggregate was developed by Howser and Mo (2016). The use of such aggregate in the concrete was tested for the primary purpose of strain monitoring. The so-called carbon nanofibre aggregate (CNFA) can be embedded in reinforced or pre-stressed concrete structures to determine the localised damage. These samples were chosen to be sized in  $2.54 \times 2.54 \times 2.54$  cm cubes satisfying the nominal maximum size of the coarse aggregate according to ACI. CNF was used in

0.25%, 0.50%, 0.75%, 1.0%, 1.25%, 1.50%, and 1.75% by weight of cement dosages. In the mortar mix, HRWR and silica fume were used as admixtures. Extreme fibre clumping was observed for mixes with 1.0%-1.75% CNFs (by weight of cement) and the optimal concentration was likely less than 1.0% CNFs by weight of cement. By the ERV evaluation of the mixes, a CNF concentration with 0.70% exhibited the largest change in ERV. It was found that ERV increases simultaneously with the stress and strain when subjected to compression and also a cyclic stress and strain can be assessed from the ERV-versus-time relationship. The peaks and valleys of all three relationships coincided during cyclic loading. This finding was similar to the findings of Howser et al. (2011) on the short column, while in their study the whole structure was made with nanoconcrete. In addition, small reinforced beam samples were tested under four-point load flexural test using CNFA and it was concluded that the CNFAs are capable of detecting localised catastrophic damage in reinforced concrete structures since, at the time of the sudden crack development in the beam and the sudden load drop, the ERV in CNFA was also suddenly dropped.

#### **2.4. SELF-SENSING PROPERTIES OF SF REINFORCED COMPOSITES**

Apart from self-sensing properties of the carbon filaments (i.e. carbon black, carbon fibre, and carbon nanofibre), some researchers investigated the effect of steel fibre on the electrical properties of cementitious materials. There are limited studies on the effect of steel fibre on the piezoresistivity of concrete or cementitious composite. In steel fibre reinforced cementitious composites, an important parameter is the steel fibre diameter. The large diameter of steel fibres compared to nanofibres is believed to be the cause of the inferior performance of the steel-fibre cement-based material. It was found by Chen and Chung (1996) that a stainless-steel fibre with a diameter of 60  $\mu\text{m}$  renders piezoresistivity to the cement-based material under compression, however, this phenomenon was noisy, and the resistivity did not vary smoothly with strain.

Wen and Chung (2003) conducted a comparative study between the steel fibre (8 $\mu\text{m}$  diameter) and carbon fibre (15 $\mu\text{m}$  diameter) reinforced cement as piezoresistive strain sensors. Steel fibres at dosages of 0.72 vol% and 0.36 vol% and carbon fibre at the dosage of 0.5 vol% were used. Overall carbon fibre paste was a better piezoresistive strain sensor than stainless steel-fibre paste. The results of carbon black showed less noisy response and it was totally reversible under both tension and compression

compared to steel fibre samples. For 0.72% steel fibre samples, the resistivity was dependant on the load history and this dependency is stated to be undesirable for practical strain sensing. Because the steel fibre volume fraction was above the percolation threshold (0.27-0.36 vol%), the electrical resistivity of both steel fibre pastes was much more conductive than the carbon fibre paste (percolation threshold: 0.5-1.0 vol%). The piezoresistivity is dominated by the effect of strain on the fibre-fibre contact when steel fibre is used, whereas that in carbon fibre paste is dominated by the effect of strain on the fibre-matrix contact. Overall an inferior behaviour was observed for steel fibre pastes and since the diameter of steel fibre was smaller than that of carbon fibre, this inferior performance of steel fibre cement was related to the difference in piezoresistive mechanism.

For structural element health monitoring, with similar aim as Howser and Mo (2016), Sun et al. (2014) developed a cement-based strain sensor to evaluate the use of such sensor for structural health monitoring of ultra-high strength concrete (UHSC) column. The sensor was made as a prism with 40×40×160mm with the use of 0.5% brass-coated straight steel fibre and four-probe method was used with galvanised welded wire mesh electrodes. The prismatic sensor was tested under cyclic compressive loading and a general trend of decreasing ERV ( $=\Delta R/R_0$ ) upon loading and decreasing  $\Delta R/R_0$  upon unloading was found. The electrical conduction of the sensor is related to both ionic conduction and electronic conduction. The ionic conductor is the electrolyte solution within the matrix which electrons cannot pass through it. Therefore, the presence of water at the fibre-matrix interface will cause these parts of the interface not to contribute to the piezoresistivity. If water is removed by oven-drying the sensor sample, larger interface can contribute to the piezoresistivity. UHSC were subjected to both cyclic and monotonic compressive load. For both cases, it was found that  $\Delta R/R_0$  was sensitive to the stress even though the sensitivity decreased when the stress increased to a certain level (70 MPa). The piezoresistive behaviour of the embedded sensor was classified into three phases for the monotonic loading case. These phases were: 1) high sensitive; linear phase, 2) medium sensitive; nonlinear phase, and 3) low sensitive; linear phase. It was observed that the bond between the cementitious sensor and the UHSC failed beforehand and the bond surface was the plane of weakness within the column. Thus, it caused the column failure before the stress reached the compressive strength of the UHSC.

Similar to Sun et al. (2014), Hou and Lynch (2005) had suggested a three-stage process during the progression of the damage in a carbon-engineered cementitious composite (ECC) specimen containing 0.4% volume fraction of carbon fibres as well as another set with steel fibres with a volume fraction of 0.1% tested under direct tensile load. The chosen fibre volumes were close to the lower bound of the percolation thresholds. Despite the nonlinear stage reported by Sun et al. (2014), Hou and Lynch (2005) observed linear relationship between mechanical strain and electrical resistivity for all stages. Throughout the three stages; development of a dense field of microcracks with slow increase in electrical resistivity, damage localisation with strain softening and change in material gage factor, and further localisation of the damage resulting in a macroscopic crack and increased gage factor occurred respectively (Figure 2.9).

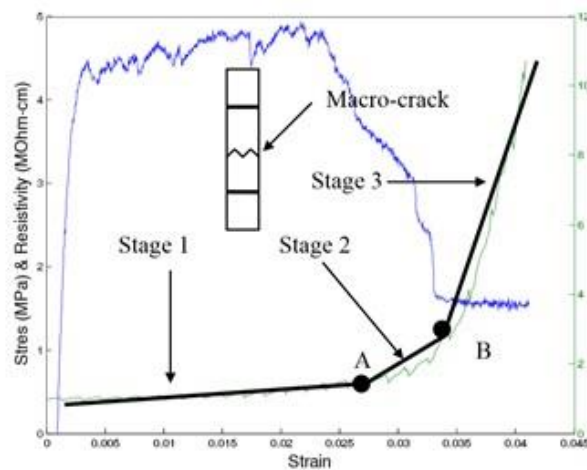


Figure 2.9. Stress-strain and resistivity-strain relationship of a carbon-ECC specimen during AC monotonic load testing (Hou and Lynch, 2005)

A scaled bridge pier to 1/3<sup>rd</sup> of the realistic structural element of ECC was laterally loaded. The base of the column was facilitated with two electrical probes to measure resistivity. A strong linearity was noted between the mechanical deformation and the electrical resistance in both the positive and negative direction (tension and compression). They concluded that using ECC to self-sense its strain is feasible, even when steel reinforcement is included in the structure.

The sensing capability of steel fibre reinforced cement-based mixture was investigated by Teomete and Kocyigit (2013) using split tensile test. Steel fibres with 6mm length were used at 0.2%, 0.5%, 0.8%, 1% and 1.5% volume fractions. The gauge factor, which

represents the sensitivity of a gauge and the correlation coefficient of best fit line to the ERV versus strain data is summarised in Table 2.6 below. The highest gauge factor was observed for 0.8% fibre concentration.

Table 2.6. Gauge factor and correlation coefficient of the test conducted by Teomete and Kocyigit (2013)

<b>Fibre volume fraction</b>	<b>Gauge Factor</b>	<b>Correlation coefficient</b>
0%	3	0.92
0.2%	9	0.94
0.5%	100	0.98
0.8%	5195	0.96
1%	95	0.99
1.5%	2589	0.98

The percolation threshold is stated to be 1% at which higher fibre volume fraction than 1% did not increase the electrical conductivity. On the other hand, the increase of fibre percentage over percolation threshold would result in an increase in voids in the sample which affects the electrical contact and will result in an increase in the electrical resistance. When fibres are at a low percentage (0.2%) or a high percentage (1.5%), the formation of voids dominates, and electrical resistance increases and for the midrange of fibre volume fraction, the formation of conductive path dominates.

Shi, Lu and Bai (2017) studied ECC with PVA fibre under four-point bending. Steel fibre and Carbon Black (CB) fibre were also utilised to improve the conductivity of mortar. 0.58% volume fraction of micro steel fibre with a diameter of 39  $\mu\text{m}$  and length of 8 mm. Carbon black with 30 nm size at 1.0% by weight of the cementitious material was used. CB samples showed better strain hardening behaviour than SF sample while the stiffness of SF sample was higher. The electrical resistance for SF sample was lower. It was observed that the resistance increased dramatically with the crack density and the increasing rate tended to be mild in the post-crack state.

Overall, the use of micro steel fibres could be effective in self-sensing capability of the cementitious composites, however, the size of the steel fibre and fibre volume fraction affects this property. Nonetheless, the use of nanofibres was found to be more effective in self-sensing of materials by providing higher gauge factor and more stable response.

## 2.5. STEEL-CONCRETE COMPOSITE (SC) WALLS

Construction methods are of importance in infrastructure construction and advanced methods are being developed to reduce the construction cost mainly by shortening the time needed to build the structure. One of the methods used in many industries including nuclear power plants is modularisation with prefabrication and pre-assembly. In this method, modules may be fabricated at a factory or at a workshop at the plant site, and multiple modules can be fabricated while civil engineering work is progressing at the site in preparation for receiving the modules. Modularisation allows construction tasks that were traditionally performed in sequence to be completed in parallel. This reduces site congestion and can shorten the construction schedule as well as reducing on-site workforce requirements. In the mid-1990s, a concrete-filled double steel-plate wall (i.e. SC wall) was proposed for nuclear power plants in Japan to promote rationalisation of modular construction techniques (Nie et al., 2013). Recently, this modular construction system has become popular in infrastructure applications.

Steel plate composite construction is a sandwich system in which two steel plates encase the concrete in the middle (see Figure 2.10). The composite action is provided by the shear studs. The SC system originally devised for use in submerged tube tunnels over 25 years ago by a team of local consultants in Cardiff, UK. The two face plates act as permanent formwork during construction providing impermeable skins, which are highly suited for marine and offshore applications (Liew et al., 2009).

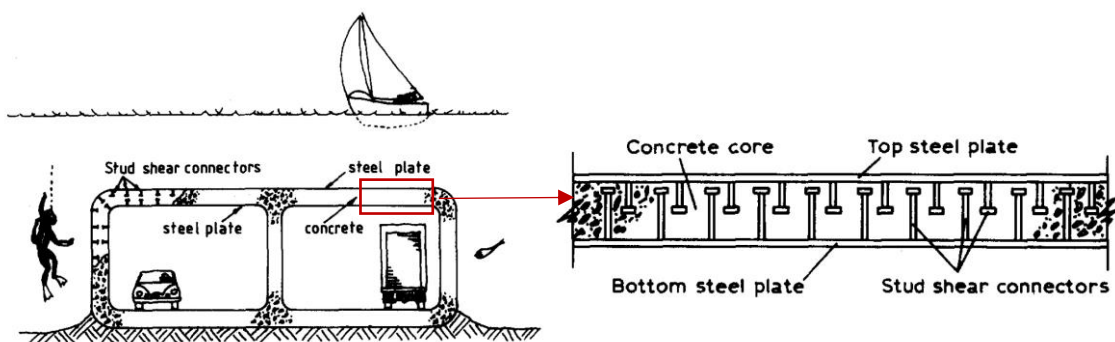


Figure 2.10. SC in submerge tube tunnel application (Wright and Oduyemi, 1991b)

One of many advantages of SC system over the conventional RC construction is the elimination of the time and workmanship required for constructing the formwork, placing rebars and removing the formworks as the steel plates act as formwork itself

and sections can be modularised and prefabricated off-site. Using SC system reduces the cost of reinforcement with savings resulting from less workmanship required for the construction process. Takeuchi et al. (1998) conducted a feasibility study and they found that in SC structural system a decrease in the amount of steel by about 20% is possible and additional formworks become unnecessary for this type of construction compared to RC structures. The construction period was also estimated to be 2-5 months shorter than RC buildings.

SC enables the building to maintain a highly seismic condition (Takeuchi et al., 1998). According to Oduyemi and Wright (1989) and Liew et al. (2009), this form of construction combines the advantages of both steel and reinforced concrete and is thought to give increased impact and blast resistance in installations subject to such loads. SC system application is diverse including nuclear containments, liquid and gas retaining structures, submerged tunnel linings, building cores, the basement of multi-storey buildings, bridge deck, floating breakwater, and offshore structures which all are required to be blast resistant (Liew et al., 2009; Wright et al., 1991b).

Wright et al. (1991b) describe the SC System as a strong and efficient structure with following advantageous over conventional reinforced concrete sections:

- ‘(i) The steel skins act as permanent formwork obviating the need shutters.
- (ii) The steel plates and shear connectors are easily site fabricated and expensive detailing, bending and fixing of bar reinforcement is avoided.
- (iii) The steel plates act as a waterproofing membrane and respond in a truly biaxial manner to applied loads.’ (p.99)

Westinghouse AP 1000 SC wall modules are being used in nuclear power plant industry as well as Bechtel’s proprietary design for SC wall modules. In nuclear power plant infrastructure, the SC modules have been proposed for use primarily as shear wall structures inside and outside containment. The loads that should be considered acting on these structures are dead load, live load, pressure loads, seismic loads, blast loads, and thermal loads. As Braverman et al. (1997) mentions:

- ‘An individual wall section would primarily experience in-plane axial compression, in-plane and out-of-plane shear loads and bending about two perpendicular in-plane axes.’ (p.3)

For research studies covering SC systems, particular emphasis is given to research focusing on properties of out-of-plane flexural strength, shear strength, and bending stiffness. The review of research presented hereafter covers an array of applications ranging from high-rise buildings to infrastructures such as power plants and tunnel construction applications under static loads. The performance of the SC system under seismic load, blast load, and impact load is out of the scope of this research.

### 2.5.1. Failure modes of SC component

The basic failure modes of a steel composite beam are described as stated below and represented in Figure 2.11 (Oduyemi and Wright, 1989; Wright et al., 1991a):

- i. *Flexural failure*: concrete crushing is preceded by steel yielding. The steel plates may yield in tension and buckling is prevented in compression.
- ii. *Vertical shear failure (i.e. diagonal tension failure)*: if the shear capacity of concrete alone plus the shear capacity of the long studs is insufficient, the concrete may fail in vertical shear close to the support or any point load. This may be resisted by long stud shear connectors welded to one steel skin with the head anchored in the concrete near to the other skin. These act in a similar way to the links in a reinforced concrete beam.
- iii. *Longitudinal shear (i.e. horizontal slip failure)*: the most likely failure, in which due to inadequate composite connection, shear connectors (i.e. shear bond between the steel plates and concrete core) fail and composite action terminates. In RC elements, this failure is prevented by well-anchored deformed or ribbed reinforcement. In SC elements, it is the shear connectors that resist these forces and they must, consequently, be carefully designed.
- iv. *Concrete compression failure*: compression concrete crushing may occur if the section is over-reinforced. As with reinforced concrete sections, it is beneficial to provide sufficient compression steel so that the tension steel yields before the concrete crushes. This results in a ductile 'under-reinforced' section.
- v. *Steel plate buckling*: it is also possible that top steel plate in compression buckles away from concrete. The likelihood of this will depend upon the steel plate thickness, the pull-out resistance of the connectors and their spacing in both directions.



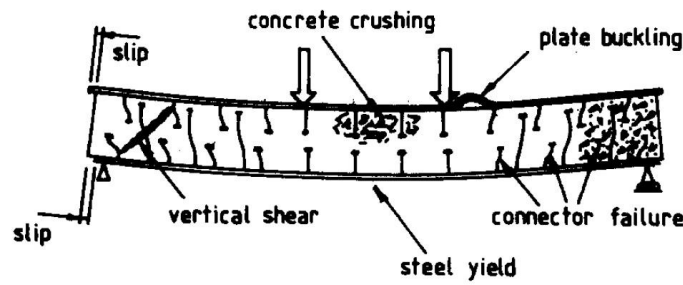


Figure 2.11. Failure modes of double skin composite beam (Wright et al., 1991b)

### 2.5.2. SC structural performance

Different types of mechanical shear connectors are being used and some are proposed and under investigation to achieve the best composite action and shear resistance between steel faceplates and concrete. The most common form of the shear connectors is the conventional headed shear studs. Although the installation of the studs on steel plates implies no restriction on the core thickness and making the casting of the concrete easier, this form of construction could be costly in time and labour due to temporary works and welding of individual connectors (Liew and Soheli, 2009; McKinley and Boswell, 2002). In the United Kingdom, Tata Steel (Tata Steel construction) has developed a patented modular wall system called Bi-Steel (Figure 2.12.a) in order to improve the method of construction. Bi-steel, however, implies dimensional restriction; therefore, to be able to achieve a thin core and a through connectors to prevent tensile separation of the face plates, J-hook connectors (Figure 2.12.b) were proposed, which is recently studied by Liew and Soheli (2009, 2012). Other possible types of shear connectors including rolled sections such as: Bent-up bars, Angle sections, T-sections, were considered non-viable according to McKinley (2002), since it was found that the amount of welding necessary to connect a rolled section is large in comparison to studs and bars, which again increases the cost of the end product.

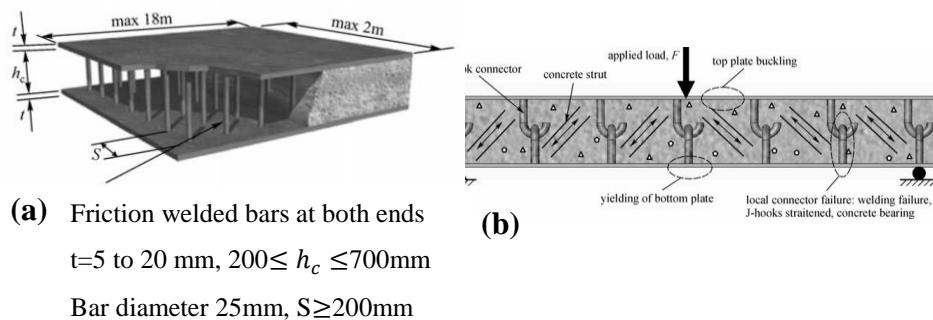


Figure 2.12. (a) Bi-steel panel (Pryer and Bowerman, 1998); (b) SC system with J-hook connector (Liew and Soheli, 2009)

### 2.5.2.1. SC with conventional headed stud connectors

Basic design methodology for Double Skin Composite (DSC) elements subjected to bending and axial load for applications of DSC construction was first defined by Wright et al. (1991a). A research study was conducted at University of Wales College of Cardiff, UK and Scale model tests (Wright et al., 1991b) were carried out on beam, column, and beam-column specimens to determine basic behavioural characteristics to be used to formulate design guidance. Also, a limited number of full-scale tests were carried out and validated both the applicability of the model scale tests and the proposed design methods. Due to similarities of DSC and RC construction, the authors have developed a design method based on three British Standards Institution (BS) guides. ‘The basic design is carried out using BS8110, steel plate strength is evaluated using BS5400 and the connection designed to either BS5400 or BS5950 Pt.3’ (p.113). Researchers (Oduyemi and Wright, 1989; Wright et al., 1991b) investigated the effect of main variables such as steel skin thicknesses, spacing and length of shear connectors, and concrete strength on the behaviour of SC walls. They found that weak concrete displays more flexible load-slip characteristic but with comparatively lower ultimate capacity. They reported that ductility increases as the tension steel area decreases. Inadequate bottom shear connection resulted in increased end slip, shear connection failure as well as reduced bottom steel strain below the yield strain, indicating that the bottom steel plate was unable to develop its full yield force.

Low strength concrete does not change the fundamental failure mode, but it induces earlier concrete crushing in over-reinforced sections and earlier horizontal shear failure with few connectors (Wright et al, 1991b). In their tests, when no long shear studs were provided, the vertical shear was the primary cause of the collapse. Also, providing long studs attached to the compression plate resulted in considerably more shear cracks. Therefore, it was advised that the long shear studs should always be attached to the tension plate. The ration of stud spacing/plate thickness higher than 50 showed buckling adjacent to and outside the two symmetrical load points, where the moment is at its highest with a coexistent shear force.

Bending and shear strength and deformation of SC walls were investigated by Ozaki et al. (2001). They found that as the value of the steel plate ration (section thickness/ plate thickness) decreased, the initial stiffness and the cracking strength increased

inconsiderably, while the yield strength and maximum shear strength increased conspicuously. Decreasing the height of the wall also increased the shear strength. The shear span ratio had little influence to shear yielding strength. For the case where, axial force was applied to the SC wall, the cracking strength and bending yielding increased remarkably, and shear strength increased to some extent.

Varma et al. (2011a) studied the out-of-plane shear behaviour of SC elements. Bending tests on beams that were representative of large-scale SC walls (of safety-related nuclear facilities) in the longitudinal and transverse directions was conducted. All specimens with no tie bars failed in a sudden and brittle manner due to shear failure. Modes of failure observed were vertical shear failure, however, one specimen failed in interfacial (horizontal) shear mode at the steel plate/concrete interface, because it was designed with an insufficient number of studs in the shear span resulting in low level of composite action between the steel plates and the concrete. Flexural cracks appeared as soon as the load was applied, which took place at about 5-10% of the maximum load, indicating the quick transition of un-cracked section to cracked section. Amongst specimens with tie rods, two demonstrated flexural cracking in the mid-span, and diagonal shear cracking leading to eventual shear failure and one with  $a/d = 5.5$  developed flexural yielding failure. Including tie rods increased the shear strength of specimens and altered failure mode. The out-of-plane shear strength of the tested specimens with or without shear reinforcement was predicted reasonably using ACI code equations for RC beams.

An experimental investigation to study the shear behaviour of SC beams without any shear reinforcement was conducted by Sener, Varma and Seo (2016). Overall, 5 beams were tested. Beam 1 was the control beam. Beam 2 had increased longitudinal stud spacing. Beam 3 had larger plate thickness (smaller plate slenderness ratio) and beam 4 had smaller shear span, while beam 5 had geometrical dimension twice as other beams to investigate the influence of scale and size on out-of-plane shear behaviour and strength. All beams except beam 2 failed in diagonal-tension. This was in contrast with Varma et al. (2011a) results, where the beam with no shear reinforcement had shear failure. Beam 2 had an interfacial shear failure due to fracture of stud anchors resulting from excessive horizontal shear at the steel faceplate-concrete interface. This sample had significantly lower stiffness due to interfacial slip (i.e partial composite action). Beam 3 had 10% higher shear strength with increased stiffness due to the thicker plate

which resulted in smaller crack width. Beam 4 showed more arching action due to lower shear span-to-depth ratio and the shear strength was increased by 12% when the shear span-to-depth ratio was reduced from 3.2 to 2.5. The behaviour of Beam 5 with full-scale geometric dimensions as used in nuclear facility construction was slightly different from the behaviour of the small-scale specimens, but the final out-of-plane failure mode was similar. The failure of the large-scale sample was accompanied with the excessive widening of shear cracks and slight horizontal extension towards the support.

Bruhl and Varma (2017) experimentally investigated eight one-third-scale SC wall sections in four-point bending. All beams failed due to rupture of the tension steel faceplates under the loading point. All specimens exhibited deformation ductility larger than 7.0. Specimen built from the most ductile steel achieved maximum moment at larger curvature. They found that higher steel plate strength resulted in higher moment capacity, however, ductility was inversely related to face-plate strength. Thicker steel plates resulted in higher stiffness, higher moment capacity, and higher ductility. Tie bar diameter was inversely related to strength and ductility while it had no influence on stiffness. However, this effect was attributed to the configuration of the specimens which had holes through the faceplates for fastening threaded tie bars.

In addition to the consideration of the mechanical loading on the SC elements, Booth (2008) investigated the out of plane response of SC steam generator compartment walls within the nuclear facility subjected to simultaneous thermal and mechanical loads. The loading due to internal pressure (equal to that caused by 69 kPa internal pressure) was simulated on simply supported beam using four-point loading. Thermal loading was applied by heating the top faceplate of the beam specimen to 149°C. Concrete vertical shrinkage cracks at locations directly adjacent to through rod as well as longitudinal surface cracks extending in the longitudinal direction the entire length of the beam on both sides were observed. Exposure to elevated temperatures caused extension of existing vertical shrinkage cracks as well as originating numerous cracks (typically 25.4 mm in length) extending down from the top of the specimen leading to an expected “fully cracked” behaviour, with a commensurate reduction of flexural stiffness. But, specimens exhibited elastic behaviour (with concrete cracking) up to and including the peak load. The specimen experienced no local buckling or shear connector failure. The

specimens resisted moments and shears for pressures in excess of 207 kPa, over 3 times the expected design pressure of 69 kPa. It was concluded that SC wall modules tested could be safely used for applications involving the typical levels of simultaneous thermal and mechanical loads specified for nuclear steam generator compartment walls.

In SC walls, shear connectors serve two important functions namely, preventing local buckling of the steel plate before yielding in compression and developing composite action. Zhang et al. (2014) investigated the effect of shear connectors on the composite action and local buckling of SC walls. ‘The critical buckling stress could be predicted using Euler’s column equation with an effective length coefficient (K) of 0.7, which corresponds to the pinned-fixed end conditions’ (p.232). The results of normalised strain versus the normalised plate slenderness ratios ( $s/t_p \times \sqrt{f_y/E}$ ;  $s$ =stud spacing,  $t_p$ =plate thickness,  $f_y$ = plate yield strength,  $E$ =Young’s Modulus of plate) obtained from a parametric FE study in ABAQUS followed the trend of the Euler column curve with pinned-fixed end conditions. It was stated that when normalised  $s/t_p$  ratios is less than 1.0, yielding in compression occurs prior to local buckling. Plate slenderness ( $s/t_p$ ) and reinforcement ratio ( $2t_p/T$ ;  $T$ =section thickness) are two important ratios defining the level of slenderness and composite action of the SC system respectively and are used for the design of members. When the number of studs were quadrupled the partial composite action increased from 60% to only 70%, which is neither economical nor structural efficient. SC wall sections also with lower reinforcement ratio develop composite action more rapidly, while higher reinforcement ratio could give very low levels of % composite section. It was found that the flexural section stiffness ( $EI$ ) does not decrease significantly (by 10%) as a consequence of the level of partial composite action and can be calculated reasonably using equation developed by Varma et al. (2011b) which is based on cracked transformed section properties and full composite action (i.e. no interfacial slip).

Studies on different type of connector, namely bi-directionally inclined connector (i.e. truss configuration) was considered in the parametric Finite Element (FE) analysis studies of Anandavalli et al. (2013) conducted on SC system under static load employing solid, plate and beam elements. The parametric study was carried out by varying plate thickness, inclination angle, and diameter of the connectors. Displacement was reduced by increasing plate thickness. Increasing inclination of the angle showed

29.5% decrease in displacement, whereas load carrying capacity had marginal decrease of about 7%. Increasing the spacing of the connectors above 225mm, resulted in increased displacement of the beam. However, the load carrying capacity had marginal change with varying connector spacing. The diameter of the connectors less than 12mm had a negligible effect on displacement response, while the connection with 16mm diameter had highest deflection value. However, 12mm diameter was found optimum since welding 16mm connector is only practical to thick steel plates.

#### **2.5.2.2. Bi-Steel**

For the construction of Bi-Steel, in a factory environment, round bright steel bar is rotated at high speed and opposite external force is applied to the face plates generating frictional heat that fuse the bar and the plates together hence bars are friction-welded to both plates simultaneously. This system is also capable of resisting the internal pressures caused by the pouring concrete. The application of this system according to Tata Steel is mentioned to be in the construction of RC shear walls and cores, high integrity blast protection buildings, and as an alternative to concrete retaining walls in specialist applications.

Design methods for Bi-Steel beams under static loading were established through research carried out by Xie et al. (2007). The functions of the bar connectors were to resist longitudinal and transverse shear and to prevent plate buckling, which can only occur outwards. Beam failure modes were; tension plate failure, bar tension failure, concrete shear failure and bar shear failure. The load vs. deflection curves confirmed that tension plate yielding leads to the most ductile failure. Design checks for plate forces, bar shear strength, bar tension forces, and transverse shear resistance (transverse shear is resisted in two parts: the shear resistance provided by the concrete acting with the steel, and the shear resistance provided by the steel bar connectors acting with the concrete) were suggested with proposed formulas. Tension tests on embedded bars and standard push tests with embedded bars were also conducted to better understand the behaviour of connecting bars (Xie and Chapman, 2006). Beam tests showed that the slip at the top plate was negligible, and the effect of bottom plate slip on plate forces was shown to be small enough to be neglected. However, the effect of slip on deflection was significant and deflection was reported with three quantifiable components of bending, slip, and vertical shear strain.

A comparative study was carried out by Mckinley (2002) on the behaviour of DSC panels and the Bi-Steel through testing sixteen wide-beams at City University of London. Elastic and early plastic deformations and load characteristics of both systems were similar, while Bi-Steel withstood larger deformation before failure. Studded specimens failed by compression plate studs being pulled out of concrete, whereas Bi-Steel failed through compression plate local buckling. The onset of local buckling occurred earlier as the bar spacing to plate thickness ratio increased. Also, from the measured strain it was found that at the time of buckling, the forces in compression plate agrees with the Euler analysis ( $L_e=0.7$ ). Increased concrete strength affected local buckling behaviour and resulted in increased ultimate failure load and deflection. Further loads could be applied before the buckling stresses were reached within the steel since higher strength of concrete reduces the steel plate stresses and increases panel capacity. Specimen with  $s/t_p < 30$  failed by the yielding of compression plate before buckling occurred. This limit range is comparable to the limit defined by Wright et al. (1991b), who found that  $s/t_p > 50$  would result in local buckling of the steel plate. A small amount of slip was recorded at the tension plate interface for specimens.

A finite element (FE) model was developed by Foundoukos and Chapman (2008) and a parametric study was conducted which enabled the comparison and verification of the proposed design equations for transverse shear capacity. A 2D beam was modelled with two-dimensional, plane stress, reduced integration, solid elements in ABAQUS. Contact interaction was defined between the bar and concrete blocks. Friction coefficients between the steel plates and concrete and between the steel bars and concrete were also defined. The truss contribution was increased for bar spacing to concrete depth  $s_x/h_c < 1$  and it was reduced for  $1 < s_x/h_c < 2$ , however, the concrete contribution to transverse shear remained approximately constant. Varying the tension plate thickness ratio ( $\rho = t_t/h_c$ ) revealed that thicker plates result in an increase in the un-cracked concrete area and therefore the concrete contribution increases for increasing plate thickness. The transverse shear capacity decreased with increasing concrete depth. Based on FE results, the effect of beam span varying from 1200 to 3600mm was a small reduction in shear strength. Overall, the parametric studies showed good agreement with the predictions based on the design guide equations for transverse shear capacity.

### 2.5.2.3. SC with J-hook connectors

Liew and Soheli (2009) tested the SC beams with the proposed J-hook shear connectors with lightweight concrete core ( $1400 \text{ kg/m}^3$ ) for use in structural decking. The use of J-hook connectors is not restricted by the core thickness and minimum core thickness can be as thin as 50 mm unlike Bi-Steel in which the core thickness must not be too thin ( $\geq 200 \text{ mm}$ ). From push-out tests on connectors, it was confirmed that the shear transfer capability of J-hook connector is superior to the conventional headed stud connector in achieving composite action between the steel plate and concrete core. The concrete core of some specimens was reinforced with either PVA or steel fibres. Connectors spacing varied (80-300 mm) providing either partial or full composite action. Initial tension cracks normally appeared at about 50% of the peak loads. Extensive shear cracks appeared in all beams. However, the shear cracking did not cause abrupt failure, indicating that the interconnected J-hooks provided effective force transfer mechanism between the steel and concrete. Beams with flexural failure mode (i.e. yielding of the bottom steel plate) were extremely ductile and had a higher maximum load than other beams. Partially composite beams failed due to J-hook connectors bearing on concrete rather than by yielding of the bottom steel plate. This is attributed to the fact that the total longitudinal shear transfer capacity of the J-hook connectors was less than the yield strength of the steel plate. The capacity of the shear connector was influenced by the concrete strength, which in turn affected the load carrying capacity of the beams. The ultimate load carrying capacity of the specimens with lightweight concrete was lower than that of the specimens with normal concrete.

The use of fibres in lightweight concrete increased the load carrying capacity by about 25%, which makes it closer to that using normal weight concrete. The presence of fibres in the concrete increased the ductility of the sandwich beam in terms of the post-peak load-displacement as well as increasing the connectors' (J-hook) bearing capacity as found from the push-out test and thus they enhanced the effectiveness of the connectors to develop composite action. Fibres helped to prevent brittle failure of the concrete core in particularly at the large deflection range. An increase in volume fraction of fibres provided a higher post cracking stiffness because of a better crack-arresting mechanism and higher tension stiffening, thus resulting in a smaller beam deflection at a particular load level. The inclusion of 1% fibre (steel or PVA) in the core was found best.



Sohel and Liew (2011) expanded their study into investigating the performance of SC slabs. Patch load was applied at the centre of the slab panels of 1000×1000mm. Normal weight concrete slab had local punching –shear failure within the concrete core around the loaded perimeter. The punching was not apparent in the lightweight concrete core specimens. At the post-yield region, buckling of the top steel plate was observed for all specimens. The addition of 1% volume fraction of fibres increased the load–deflection stiffness and the first peak load. This is because fibres increased the concrete tensile and flexural capacity as well as shear capacity hence leading to an overall increase in its punching resistance as well as flexural capacity. It was concluded that the shank diameter of the J-hook connector has a direct influence on the shear capacity of the connectors hence affecting the moment capacity of the SC section. Also, increasing the plate thickness increased the stiffness and load carrying capacity of the slabs.

The impact test by dropping free weights on these sandwich beams (Liew et al., 2009; Soh el et al., 2007) revealed that the proposed J-hook connectors provide an effective means to interlock the top and bottom steel faceplates, preventing them from separation during impact. The beams did not fail completely under the applied impact load and they did not show separation or buckling of the steel faceplates, whereas the beam with overlapping stud shear connectors experienced tensile separation of the face plates leading to local buckling of the top faceplate and large displacement after impact. Specimens with FRC core ( $V_f = 1\%$ ) exhibited an improved performance in stiffness and structural integrity after impact. Since additional energy is absorbed by the stretching of the fibres in the concrete core, the overall deflection of the SC sandwich beams with FRC core can be reduced accordingly. Overall, ultra-lightweight concrete core exhibited brittle behaviour and it may crack into many pieces at the impact event. Using 1% to 2% volume fraction of fibre (PVA or SF) in the concrete core could reduce the cracks significantly and enhance the overall integrity of the sandwich beams.

Sohel et al. (2012) investigated J-hook connectors and headed studs in SC beams using lightweight concrete (LWC) and high-performance ultra-lightweight cement composite (ULCC) as the core material. Specimens with a short shear span, showed inclined cracks bridging the point load (cracks with 45°) and bottom faceplate (cracks with less than 45°). For these short span samples, J-hook connectors showed premature weld failure. ULCC showed some degree of ductility before reaching maximum load. J-hook connectors and headed studs showed similar load-deflection behaviour up to peak load.

One of the advantages of using J-hooks over headed studs was stated to be the interlocking between steel faceplates by the coupling of the J-hooks, which is not possible in case of headed studs. Separation during casting of concrete is prevented by this interlocking system and it may enhance the vertical shear resistance of the section. By increasing the shear span the failure tended to be governed by flexure with more ductile behaviour by yielding of tension steel faceplate. As expected the flexural capacity of the beams were governed by number of shear connectors since it is dependent on the composite action provided by shear connectors.

## **2.6. SUMMARY**

This chapter reviews diverse areas of research conducted in the fields of nano-reinforced cementitious composites, especially focusing on the carbon nanotubes and carbon nanofibres, self-sensing properties of nanocomposites, as well as the structural performance of SC wall systems investigated by various researchers.

From the literature, it was concluded that the best dispersion method for nano concrete would be the use of silica fume and superplasticiser along with sonication, which was adopted in this research to accomplish the aims of the study. Very limited studies were found regarding the use of nano-reinforced concrete and their effect on the structural performance of members. Hence, this area of research was further investigated in this study. From earlier researches, it was concluded that the use of hybrid reinforced composites was effective in both enhancing the mechanical properties as well as the electrical conductivity of the material, and this finding encouraged this research to further investigate the use of hybrid fibre reinforced concrete consisting of both nano- and macro-sized fibres. Moreover, the research on the use of FRC for SC core material was very limited.

To summarise, by taking into account the conducted researches up to date and their outcome, this research programme expand upon previous researched by studying the mechanical performance of nano-reinforced concrete, their self-sensing properties as well as the structural performance of SC members infilled with various FRC including nanofibres.

## CHAPTER 3

# MECHANICAL AND ELECTRICAL PROPERTIES OF CNFRC

---

### 3.1. INTRODUCTION

Nanotechnology has been applied to cementitious materials in the last decade and successfully enhancing some material properties of the material such as durability and strength as well as introducing new capabilities of the material. Short fibres are widely used in concrete to control cracking introducing fibre-reinforced concrete (FRC). The randomly oriented fibres in the concrete matrix are thought to control cracks better than rebars since they are more closely spaced in the concrete matrix. The efficiency of these fibres is, however, dependant on the geometry, size, and material properties of the fibres. Conventional fibres which are being used in FRC are in macro-size. Research on micro-sized fibres (e.g. PVA/polyvinyl alcohol and micro steel fibres) showed improvement in the mechanical properties of cement-based materials by delaying the transformation of microcracks into macro forms, however, the crack growth could not be stopped. This encouraged the use of nano-size fibres for concrete reinforcement in order to prevent the transformation of nano-cracks into micro-cracks. Recently, it is found that the use of nanoparticle in cement paste is effective in improving mechanical, electrical, and thermal properties of the cementitious matrix. Despite the findings, the effect of nanofibres on building material; concrete, is uncertain up to date. This chapter will address the first two aims of the research outlined previously and it will shed light on the mechanical properties of nanoconcrete and its electrical properties (i.e. self-sensing property) for SHM through experiments. A conclusion upon the performance of CNFRC is then drawn.

### 3.2. CARBON NANOTUBES (CNTS) VS. CARBON NANOFIBRES (CNFS)

Carbon nanofibres are the most interesting nanofibres in materials science world. Carbon nanotubes (CNTs) and carbon nanofibres (CNFs) are both categorised as nanofibres. The primary differences between the CNTs and CNFs are morphology, size, ease of processing, and price. Carbon nanofibres, due to their structure are also known as stacked-cup carbon nanotubes. Their unique morphology is in a way that graphene planes are canted from the fibre axis, which results in exposed edge planes on the exterior surfaces of the fibre. On the other hand, CNTs typically are an assembly of cylinders of graphite sheets that are concentric. The difference in the morphology of the two fibres makes CNF more attractive as reinforcing fibre because it is expected to form a better bond with the matrix around the fibre due to the rough edge of the fibre. According to carbon nanofibre manufacturer, Pyrograf products, a summary of the benefits of using CNF over CNT are:

- Easier to disperse,
- Easier to process,
- Easier to functionalise,
- Lower overall cost of use.

Concluding the benefits of CNF over CNT to be used as a fibre in the concrete matrix, the carbon nanofibre was selected to be used as the nanofibre for the purpose of this research, to assess the properties of a nano-reinforced concrete.

#### 3.2.1. Review on the properties of CNF

Carbon nanofibres are known to be the strongest material with 2.5-3.5 GPa characteristic strength (Ozkan et al., 2009; Bal and Saha, 2015), high specific modulus ~500 GPa of individual nanofibres, electrical conductivity ~103 S/cm, thermal conductivity ~1900 W/(m.K) and huge specific surface area (SSA) of up to 1000 m<sup>2</sup>/g together with their low manufacturing cost (Bal and Saha, 2015). Thus, CNF becomes an eye-catching structural material.

For the purpose of this research, heat treated carbon nanofibre; Pyrograf-III PR-19-XT-LHT CNFs (provided by Applied Sciences Inc.) were used as it was received from the manufacturer. These fibres are heat-treated to temperatures of 1500°C, which carbonises chemically vapour deposited carbon present on the surface of the fibre to a

short-range ordered structure. This heat treatment produces nanofibres which generally provide the highest electrical conductivity in nanocomposites (Go et al., 2009), hence they are considered to be more suitable for producing smart concrete. Manufacturer of the CNF fibres claimed that ‘because the fibres are produced in a vapour phase, they generally become entangled during growth, producing a mesh-like configuration. This raw form is then de-bulked to provide the customer with a product that is uniform in bulk density allowing accurate compounding into final products’ (Applied Sciences Inc., 2013). The de-bulked form is denoted as XT. ‘The loose bundle of the “XT” carbon nanofibre requires much less energy to achieve dispersion, thus allowing greater retention of fibre length during processing’ (Applied Sciences Inc., 2013).

Having chosen the nanofibre for this research, the concrete was then designed, and experiments were programmed. The following sections will address the experimental procedure.

### **3.3. CONCRETE DESIGN AND PREPARATION**

#### **3.3.1. Constituent materials**

Concrete mix is made of binder materials, aggregates, water and additives and fibres if required. In this experimental study, cement and silica fume were used as binder materials. The concrete constituent materials, their type, and properties are described below.

- Cement: Type I Portland cement,
- Silica Fume: Dry undensified silica fume Grade 940U (Elkem Materials, Inc.) was used (see Table 3.1 for its properties). Silica fume acts physically as a filler and chemically as a highly reactive pozzolan. According to the findings of previous researchers (Kim et al., 2014; Sanchez and Ince, 2009, Yazdanbakhsh and Grasley, 2014; Yazdanbakhsh, 2012) silica fume enhances and stabilises the dispersion of CNFs in cement paste. These particles prevent CNFs from moving and restrain the fibres such that the CNFs could hardly agglomerate. Hence, due to the benefits of silica fume towards the dispersion of CNF in the cementitious paste, this nanoparticle additive is partially used as a binder. From the electrical properties perspective, Wen and Chung (2001), Cao and Chung (2001), and Howser and Mo (2016) found that using silica fume increases the sensitivity of cement paste and

improves their damage sensing capability, which could be attributed to better dispersion of the nanofibres. On the other hand, according to ACI 234R-06, silica fume concrete is more cohesive than ordinary concrete; consequently, increasing water demand. Hence, it is necessary to maintain the water-cementitious material ratio. Accordingly, High Range Water Reducer admixtures (HRWRs) are used to obtain the required performance and workability.

Table 3.1. Properties of silica fume

	SiO <sub>2</sub>	Retention on 45µm sieve	Mean particle size (µm)	Bulk density (undensified) (kg/m <sup>3</sup> )	SSA (m <sup>2</sup> /g)
<b>Silica Fume (Elkem 940U)</b>	> 90%	< 1.5%	0.15	200-350	15-30

- Aggregate: Sharp sand was used as fine aggregate and gravel was used as coarse aggregate (maximum size of 10mm and 20mm were used for different mixes).
- Carbon Nanofibre: Heat treated carbon nanofibre; Pyrograf-III PR-19-XT-LHT CNFs (provided by Applied Sciences Inc., Ohio) were used as it was received from the manufacturer. A summary of physical properties of CNF is presented in Table 3.2.

Table 3.2. Properties of CNF used for the experiment

CNF Fibre	Average diameter (nm)	Average length (µm)	Bulk density (kg/m <sup>3</sup> )	SSA (m <sup>2</sup> /g)	Appearance
<b>Pyrograf-III PR-19-XT-LHT</b>	150	50-200	32	20-30	Black solid, fluffy agglomerates/powder

- Superplasticizer/HRWR: Another constituent used was a surfactant. A high-range polycarboxylate-based water-reducer admixture (superplasticizer) provided by Sika under the commercial name ViscoFlow 1000 was used with the density of 1.075 kg/l (at +20°C). This admixture was chosen as part of the concrete constituents to accommodate dispersion of CNF in water. This material was found to be essential in accommodating the dispersion of nanotubes in water in previous researches (e.g. Gay and Sanchez, 2010; Metaxa et al., 2013; Willie and Loh, 2010;

Yazdanbakhsh, 2012). The HRWR not only makes the dispersion of CNFs in aqueous solution feasible but also maintains the increased water demand caused by the addition of the silica fume.

### 3.3.2. Mix design

Initially, a concrete mix was designed (Teychenne et al., 1997) as a normal strength concrete with a characteristic strength ( $f_c$ ) of 40 MPa and target mean compressive strength ( $f_m$ ) of 53 MPa. The target mean strength was obtained from characteristic strength, taking into account a margin ( $m$ ) which ( $f_m=f_c+m$ ) with 5% defective level as specified in BS5328. The flow process of the design can be summarised as below:

Stage 1: the target strength was calculated leading to the water/cement ratio.

Stage 2: The workability was considered leading to the water content amount.

Stage 3: the results of stage 1 and stage 2 was combined to obtain the cement content.

Stage 4: The total aggregate content was obtained.

Stage 5: the proportion of fine aggregate (FA) and coarse aggregate (CA) was obtained. This depends on the maximum size of aggregate, the workability level, the grading of fine aggregate and w/c ratio.

In the mix design, the presence of high range water reducer was taken into account to calculate the water quantity since HRWR reduces the water demand. Also, the amount of water in the HRWR was accounted for in obtaining the required water for the mix. Several trial concrete mixtures (both PC and CNFRC) were made to achieve the suitable mix proportions with acceptable workability limit. Also, cube compression tests were conducted according to BS EN 12350-1:2000 on trial samples to record the compressive strength of the mix. The final mix proportion which was chosen to be used for this research was selected based on the desired workability (slump value of 60-130 mm) and concrete strength ( $\geq 40$  MPa). The experiment was carried out with the obtained mix proportion for the first set of experiments referred to Group A in this work. The W/C ratio for this group was 0.4 and the coarse aggregate used had maximum size of 20mm. Followed by the experimental findings of Group A, the mix proportion and methods were further modified, and Group B was then designed with W/C ratio of 0.4 and maximum coarse aggregate size of 10mm. The main difference between Group A and Group B mixes was the maximum coarse aggregate size, superplasticiser quantity, and the mixing procedure. It should be noted that considering the unique target workability

level (i.e. slump value) for both mix designs, due to different aggregate size used in each group (10mm vs. 20mm), the aggregate proportion for the two Group A and Group B varied. The FA to CA proportion for Group A and Group B was 0.55 and 1.04 respectively. Therefore, the fine aggregate content for Group B was higher than Group A to compensate for the smaller coarse aggregate size.

### 3.3.3. Sample preparation

For mixing the constituents, an electric concrete mixer was used, and the following points were considered for mixing the constituents. The chemical admixture in liquid form such as HRWR should not come in contact with dry cement, therefore, the HRWR was added to the water prior to the mixing. This also accommodated the CNF dispersion in water. An important issue regarding mixing of the materials is that finely divided mineral admixtures such as silica fume should be introduced into the mixer with the cement and other components of the concrete mixture. As the suppliers of the silica fume advised, the micro silica powder should be added at the first opportunity, but not into an empty mixer, also it should not be charged into a wet mixer ahead of the other materials because of the tendency of the admixture to stick to the sides of the mixer and to the blades or fins. Likewise, they should not be introduced into the mixer along with the mixing water because of their tendency to ball and lump under such conditions. As suggested by manufacturers batching the silica fume alone or first can result in head packing or balling in the mixer and it must always be added with the coarse aggregate. Thus, the silica fume was added as soon as the aggregate was mixed. For all the CNFRC samples, the CNF dispersion was completed in advance to concrete mixing and one consistent dispersion method was used in this study. The dispersion method, as well as mixing steps for Group A and Group B, will be described in the following sections.

After mixing concrete was complete, a slump test was performed for each batch (Figure 3.1(a)). Whenever the desired slump value was achieved, the concrete was poured in the metal moulds of different moulds (cube, cylinder, and prism) and vibrated on a vibration table to diminish excess air in the mixture (Figure 3.1(b)). Samples were then covered with wet cloth and left to rest as shown in Figure 3.1(c). After 24h, they were removed from the mould and cured in a water tank at room temperature for 28 days before testing (see Figure 3.1(d)).





Figure 3.1. Sample preparation: (a) slump test; (b) vibration; (c) samples covered with wet cloth; (d) curing in water tank

### 3.3.4. Dispersion of CNF in aqueous solution

Prior to mixing the concrete constituents for CNFRC samples, the CNF was mixed with the aqueous solution. The dispersal property of nanofibres, such as carbon nanofibres, is the main issue encountered when they are used in cementitious materials. For the optimum dispersion of CNF in concrete, chemical dispersion method along with ultrasonication was adopted in this experimental study. Given that the HRWR should not be added to the paste during paste mixing, it was first manually mixed with water (Water + HRWR). Second, the CNF was added to the aqueous solution and ultrasonication was performed on the mixture (Water + HRWR + CNF) to achieve a good dispersion of the nanofibres in water. Using HRWR yields the best possible dispersion of CNFs in water during ultrasonic processing (Yazdanbakhsh et al., 2012). It is expected that the HRWR is capable of suspending nanofibres in aqueous solution through steric stabilisation owing to its polymeric nature. After completing sonication, the final dispersed product was used and added during the mixing process of the concrete constituents at the stage in which water was added. As discovered by previous research on cementitious paste, reviewed in Chapter 2, the adopted technique was found to be the optimum feasible method, which is also used by many researchers for mixing the nanofibres into cementitious materials compared to other methods. This method was

used for all CNFRC mixtures in this research and the steps that were followed can be summarised as follows.

- Water + HRWR; stirred manually
- CNF was added; stirred manually for about 2 minutes
- Sonication; until dispersion achieved

A 20-kHz ultrasonic processor (Vibra-Cell, Model VCX 750, Sonics & Materials) was used to disperse the nanofibres with a 139 mm long titanium alloy solid probe with 13mm diameter. The processor was set to operate at an amplitude of 50% at 20s time intervals to prevent overheating of the solution. The amplitude of probe tip was kept constant for an effective process. The CNFs were initially weighed out in a glass container (Figure 3.2(a)). Then, an aqueous solution of Water + HRWR, which was previously mixed manually, was added to the CNF container and the solution was stirred manually. The manually mixed solution of Water + HRWR + CNF was then sonicated as shown in Figure 3.2(b).

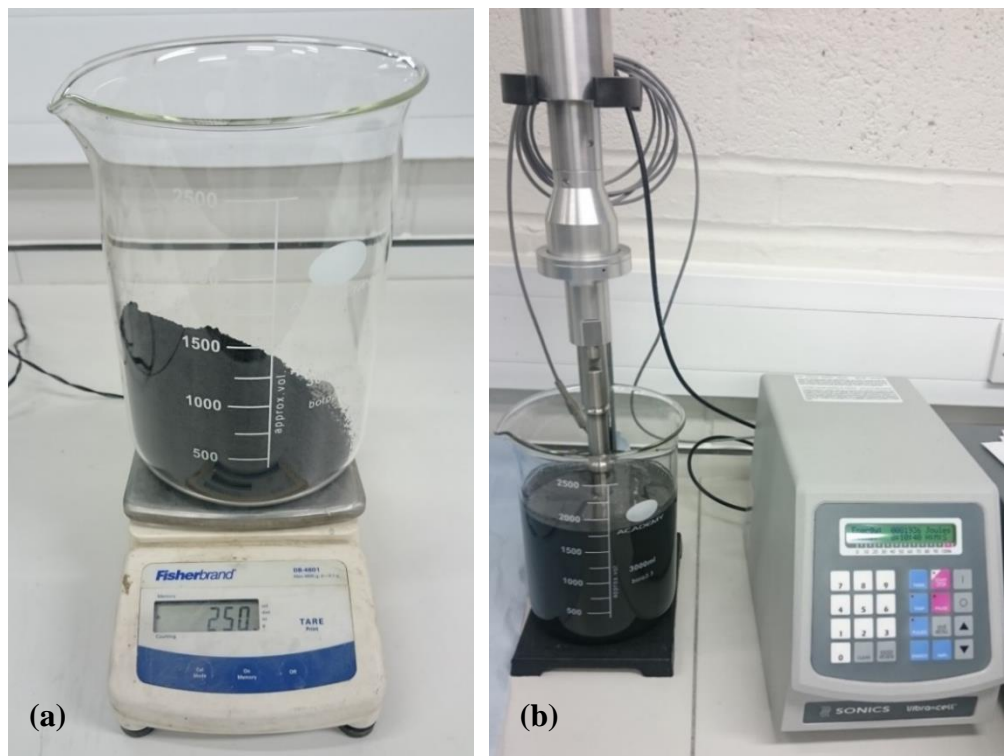


Figure 3.2. (a) Weighing CNF; (b) sonication of Water + HRWR + CNF using ultrasonic processor

While manually mixing CNF with Water + HRWR, large dark spots of CNF and agglomeration of the fibres were clearly visible; more apparent on the surface of the solution as shown in Figure 3.3(a), which indicated poor dispersion by only stirring. The sonication time was selected based on previous research reports. For mixing CNT, sonications from 30 min to 120 min have been reported (Nochaiya and Chaipanich, 2011; Sivakumar, M., 2011; Sobolkina et al., 2012). But, dispersion of CNF in aqueous solution is easier than CNT and requires less ultrasonic energy as they have much lower surface area compared to CNTs (Yazdanbakhsh et al., 2009). Due to this reason, the sonication of CNTs has been for a longer duration compared to CNF dispersion process. This has been twice in some studies (e.g. Tyson et al., 2011).

Several researchers (Manzur and Yazdani, 2010; Metaxa et al., 2013; Peyvandi et al., 2013; Yazdanbakhsh, 2012) reported that good dispersion of CNF could be satisfactorily be completed within 10-20 mins with an amplitude set at 50%. For this research, therefore, sonication was continued for an average of 15 min at room temperature based on the suggestion found in literature. However, the sonication process was controlled and optimised according to each mix design depending on the quantity of the CNF to be mixed with water. This was to avoid fibre breakage that might occur as a result of long sonication process. During sonication process, the black clumps started to vanish (Figure 3.3 (b)). After the sonication, the solution was visibly clear with no CNF clump, and a clear, consistent, homogeneous black fluid was the product of the dispersion process carried out, which was regarded as an indication of satisfactory dispersion of CNF in the solution as depicted in Figure 3.3(c).

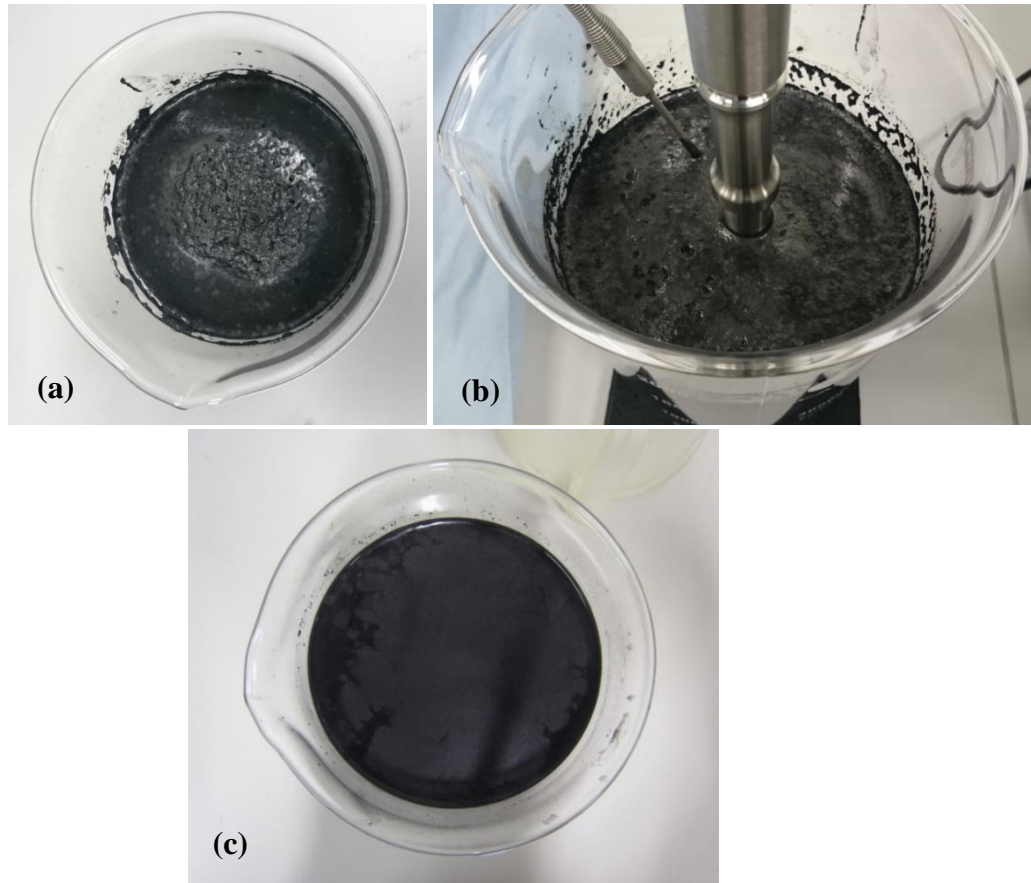


Figure 3.3. Dispersion of CNF in Water + HRWR: (a) before sonication; (b) during sonication; (c) after sonication

### 3.4. EXPERIMENTAL PROGRAMME

In the first phase of the experimental study, two groups of materials were prepared and tested namely Group A and Group B. for each group, the fundamental mechanical properties were obtained by conducting compressive test, split tensile test, and flexural test. This section describes the procedure for each test conducted for obtaining mechanical properties of different types of concrete. Table 3.3 summarises these experiments. All tests were carried out using ADVANTEST 9 (Controls Group) testing machine.

Table 3.3. Summary of tests conducted to obtain mechanical properties of concrete

Test Type	Specimen	# of Sp*	Sp* Dim. (mm)	Standards	The aim of conducting the test was to obtain:
<b>Compression</b>	Cube	min 3	100×100×100	BS EN 12390-3:2002	<ul style="list-style-type: none"> <li>• Cube Compressive strength</li> </ul>
<b>Compression</b>	Cylinder	min 3	Ø100× H200	BS EN 12390-3:2002	<ul style="list-style-type: none"> <li>• Cylinder Compressive strength</li> <li>• Post-peak behaviour</li> </ul>
<b>Flexure</b>	Prism	min 3	100×100×500	BS EN 12390-5:2000	<ul style="list-style-type: none"> <li>• Flexural strength</li> <li>• Ductility</li> </ul>
<b>Split Tensile</b>	Cylinder	min 3	Ø100× H200	BS EN 12390-6:2009	<ul style="list-style-type: none"> <li>• Split tensile strength</li> </ul>

\*Sp=Sample

#### 3.4.1. Cylinder compression test

In this experiment, cylindrical specimens were tested under uniaxial compression. The compression test was conducted according to BS EN 12390-3:2002. Since studying the post-peak behaviour of the material was an objective of this research, the load was applied in displacement control manner with the help of displacement transducers. Displacement transducers were attached to cylinders in equal angular distances of 120° (Figure 3.4(a)). The transducers which had an initial length of 100mm were hammered into concrete in a way that the centre point of the transducer length was aligned with the centre point of the cylinder's height. All three transducers were tightened to the concrete and they were fixed in place with an elastic band around all three transducers. The displacement of each transducer was recorded during the test by the ADVANTEST system and strain was calculated accordingly. The rate of the applied displacement was chosen to be 1µm/s.

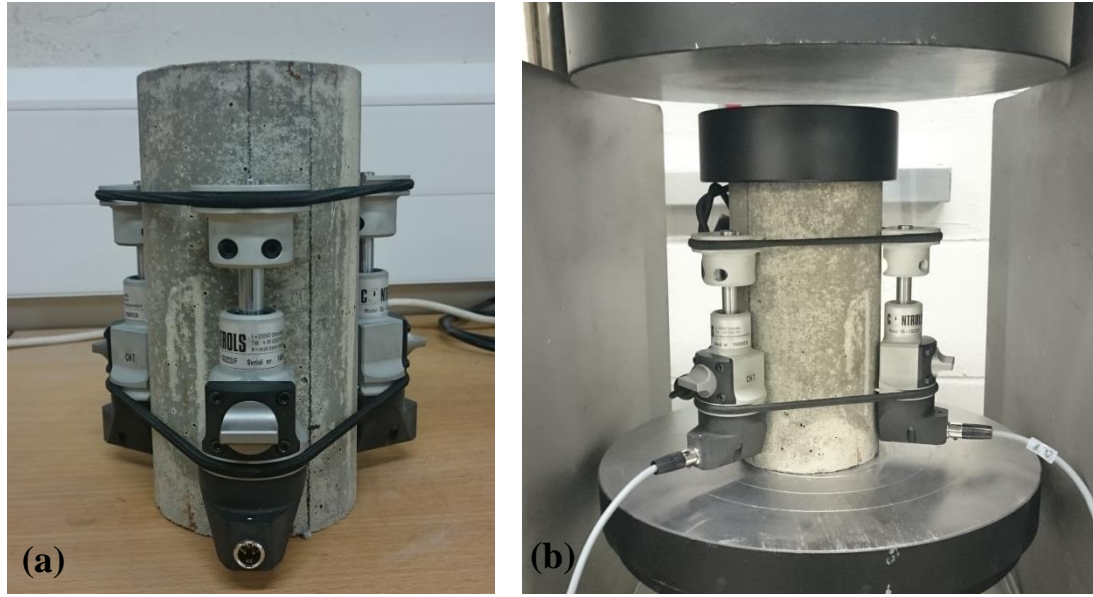


Figure 3.4. Cylinder uniaxial compression test: (a) displacement transducer attachment; (b) test set-up

### 3.4.2. Split tensile test

The tensile strength of cementitious materials is one of the most important mechanical properties which is considered crucial to engineers. However, the uniaxial tension tests of concrete is a difficult task, therefore splitting tension tests are usually conducted on cylindrical specimens by compressing the cylinder through a line load applied along its length which can be conducted in a standard concrete compression testing machine (Figure 3.5). Then, the maximum tensile strength could be calculated. For this study, the split tensile test was conducted on cylinders according to BS EN 12390- 6:2009 which recommends a constant rate of loading within the range of 0.04 MPa/s to 0.06 MPa/s. According to this guidance, a constant loading rate of 1260 N/s was used for the test. The splitting tensile strength is given in BS-EN 12390- 6:2009 as:

$$f_{ct} = \frac{2 \times F}{\pi \times L \times d} \quad (\text{Eq. 3.1})$$

Where:

$f_{ct}$  is the tensile splitting strength, in MPa or N/mm<sup>2</sup>;

$F$  is the maximum load, in N;

$L$  is the length of the line of contact of the specimen, in mm;

$d$  is the designated cross-sectional dimension, in mm.





Figure 3.5. Split tensile test set-up

### 3.4.3. Flexural test

Four-point bending test represents materials' flexural strength which is one of the main mechanical properties of a material. This can give us an indication of material's flexibility and ductility which is of great importance in the design of structural members. Properties with high importance obtained from this test are the maximum flexural load, maximum displacement, and ductility.

The four-point flexural beam test was conducted according to BS EN 12390-5:2000 on samples of 100×100×500mm. The test set-up is shown in Figure 3.6. The clear span was set to 300 mm and the upper bearer distance was set to 100 mm. Two displacement transducers at the center of the beam on both front side and back side of the beam were used to measure relative displacement at mid-span as displayed in Figure 3.6. This test provides a clear means of comparing the post-cracking tensile behavior of various fibre reinforced concretes as well as examining the ductility and energy dissipation capacity of the material. The test was conducted with displacement control manner at the rate of 0.1µm/s.

According to BS EN 12390-5:2000 the flexural strength (or maximum tensile stress in the lower fibre of the beam under loading) can be obtained by the following equation:

$$f_{cf} = \frac{F \times l}{b \times h^2} \quad (\text{Eq. 3.2})$$

Where:

$f_{cf}$  is the flexural strength, in MPa or N/mm<sup>2</sup>;

$F$  is the maximum load, in N;

$l$  is the distance between the supporting rollers, in mm;

$b$  and  $h$  are the beam's width and height dimensions respectively, in mm.

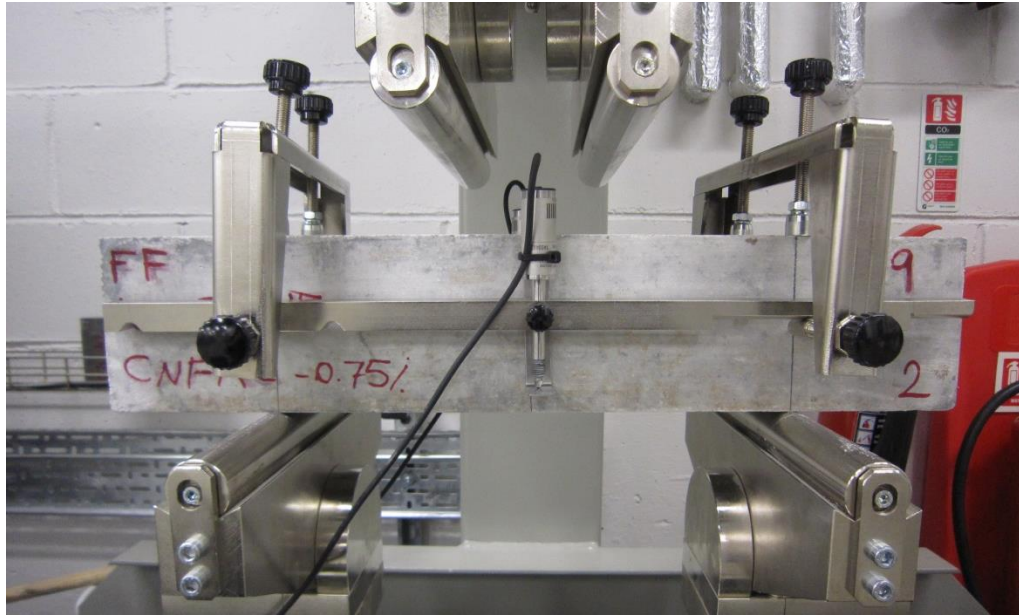


Figure 3.6. Flexural test set-up

### 3.5. GROUP A EXPERIMENT

In this category three different concrete batches were prepared which were: 1) PC (Plain Concrete; which was the control mixture with no fibres); 2) Carbon Nanofibre Reinforced Concrete (CNFRC) with 0.5% and 3) 0.75% CNF by binder volume, which are denoted as CNFRC-A-0.5, and CNFRC-A-0.75 respectively. For each batch, three beam samples and six cylinders were made. These samples were tested under four-point bending, uniaxial compression, and split tensile forces. The composition of mixtures is presented in Table 3.4. Coarse aggregate with the maximum size of 20mm was used for this group. Silica fume was used at 10% wt. of the cement and the HRWR was used at 1.0% wt. of the Binder ( $B = \text{cement} + \text{silica fume}$ ). Water to binder ratio ( $W/B$ ) was kept constant at 0.37.



Table 3.4. Group A mix proportions (kg per m<sup>3</sup> of concrete)

Concrete Mix	W/B	CA (kg)	FA (kg)	Binder (B)		CNF		HRWR (kg)	W (kg)	Slump (mm)
				C (kg)	Silica Fume (kg)	%	(kg)			
PC-A	0.37	1313.8	726.2	380.8	38.1	0	0.0	2.73	155	180
CNFRC-A-0.5	0.37	1313.8	726.2	380.8	38.1	0.5	0.96	2.73	155	175
CNFRC-A-0.75	0.37	1313.8	726.2	380.8	38.1	0.75	1.44	2.73	155	170

Notation: CA= coarse aggregate, FA= fine aggregate, C=cement, CNF= carbon nanofibre, HRWR= high range water reducer, W= water

The mixing method which was adopted for this mix was recommended by Elkem (providers of silica fume). According to Elkem, this method is optimum for the mixing and dispersion of micro silica into a concrete mix. The method used is as follows:

- All coarse aggregate and 50% of the fine aggregate were put into the mixer and mixed (1 minute).
- When evenly mixed, silica fume was added slowly and mixed (2 minutes).
- 50% of the water was added and mixed (2 minutes).
- Once evenly mixed (a uniform grey color obtained) the cement was added and mixed in (2 minutes).
- Chemical admixtures (HRWR) diluted with 50% of the remaining water was added to the mixture and mixed (1 minute).
- Then 50% of the sand was added and mixed.

For making CNFRC samples, the CNF was mixed with (HRWR+50% water) and added to the mix at step (e). During the process of mixing the CNFRC and filling the moulds, it was observed that the CNF-water solution did not fully dissolve with other constituents. Figure 3.7(a) demonstrates this phenomenon for the beam sample of CNFRC-A-0.5 while it was being vibrated on the vibration table. This can be described as the migration of CNF in the bleed water, creating a layer of black CNF-water solution intermixed with cement paste at the upper surface of the concrete especially at the corners of the mould.

In addition to the visible appearance of the black CNF-water solution in fresh concrete, the black patterns of the CNF mixtures were visible on the surface of the hardened concrete when the concrete was removed from the moulds after 24 hours as shown in

Figure 3.7(b). Because white cement was used in the mixture, the final product was white concrete, hence, the black pattern was clearer on the surface of the concrete. The reason for such issue could be associated with the mixing method used, in which the water was split into two batches and the CNF was mixed with 50% of the water only. Therefore, the addition of the Water+HRWR+CNF into the wet mixture did not mix well with the initial 50% of water which was added, resulting in non-uniform mixing.

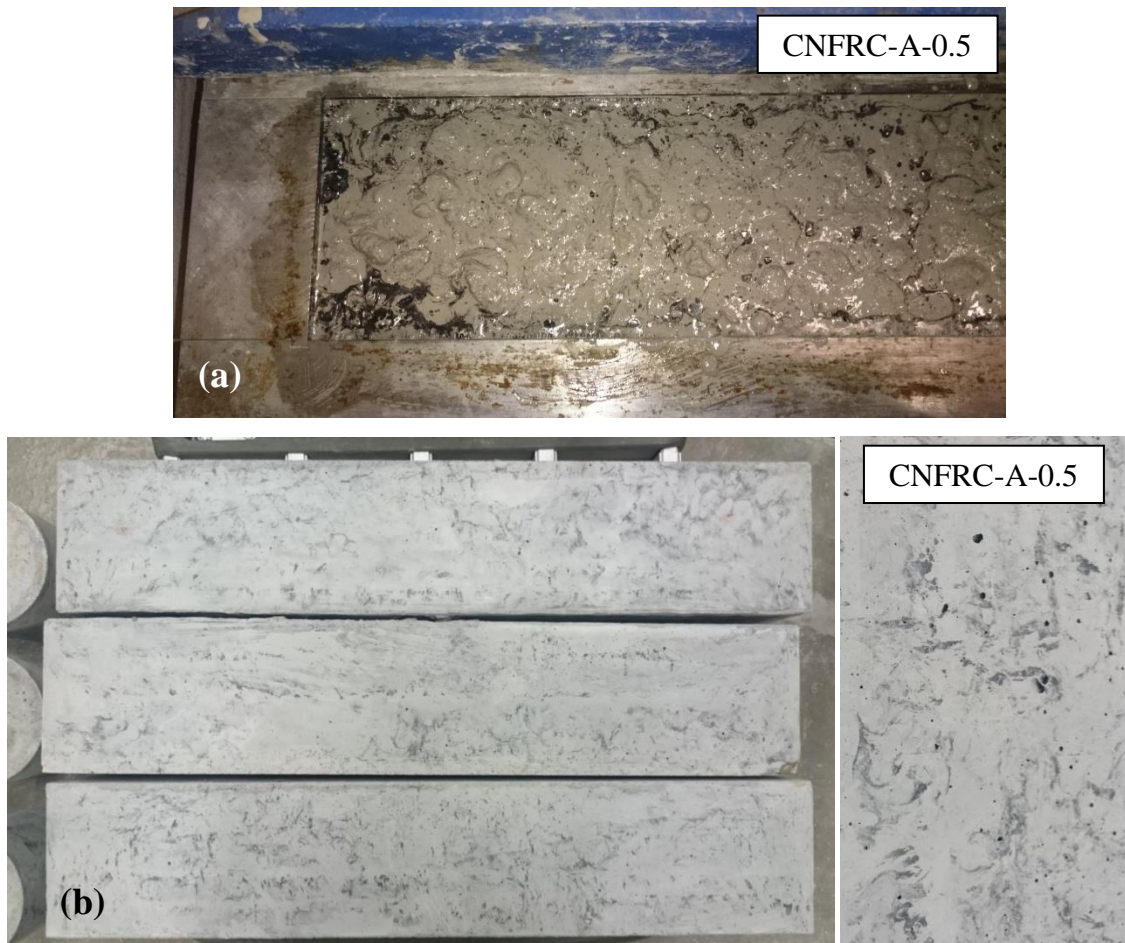


Figure 3.7. Appearance of CNF-water solution in concrete matrix in: (a) fresh concrete; (b) hardened concrete

Another possible reason could be attributed to the CNF/Water ratio<sup>1</sup>. Yazdanbakhsh (2012) used a maximum CNF/water value of 1.14% in his study on CNF paste, and it was found to be sufficient. In this study, CNFRC-A-0.5 and CNFRC-A-0.75 had CNF/Water ratios of 1.3% and 1.9% respectively. This could suggest that these ratios are high, and the smaller ratios would be more suitable, in other words, more water is required for better dispersion. Therefore, it could be more effective to disperse the CNF

<sup>1</sup> In this ratio, the amount of water mixed with CNF is considered.

with the entire amount of water designed to be used in the mix. Also, the slump values for these samples were higher than what was expected as the mixture was initially designed for. This was thought to be the effect of the HRWR on the mix.

Followed by the test conducted on Group A and considering the stated matters, Group B was proposed with different mixing procedure considering higher CNF/Water ratio, as well as adjusting the amount of HRWR, aiming for lower slump.

### **3.6. GROUP B EXPERIMENT**

A total of five concrete mixtures, incorporating different contents of CNF, were produced in this set of experiments to evaluate the effect of carbon nanofibres. The Plain Concrete (PC) mixture was dealt as the control mixture with no fibres. CNFRC concrete were produced incorporating 0.25%, 0.5%, 0.75%, and 1.0% CNF by binder volume. These samples are denoted as CNFRC0.25, CNFRC0.5, CNFRC0.75, and CNFRC1.0, which indicates the concrete type followed by the fibre percentage used for the mix. Three samples of beams and six cylinders were replicated in each test. Mechanical properties of the material under flexure, uniaxial compression, and split tensile forces were established. Also, self-health monitoring of the beam samples under flexure were studied for this group.

The content of the mixture was kept constant in all mixtures with W/B ratio of 0.37. For this group, coarse aggregate with a maximum size of 10 mm was used. The reason for using smaller aggregate as opposed to Group A was to better accommodate the embedment of wire mesh in beam moulds, which were used to analyse the self-sensing capability of the concrete. To obtain higher slump, the HRWR amount was used at 0.5 wt.% of the binder. The CNF/Water mass ratio for all fibre reinforced samples varied from 0.4% - 1.7 %. Details of concrete mixture proportions are presented in Table 3.5 and the slump test for each CNFRC batch is depicted in Figure 3.8.

Table 3.5. Group B mix proportions in kg per m<sup>3</sup> of concrete

Concrete Mix	W/B	CA (kg)	FA (kg)	Binder (B)		CNF		HRWR (kg)	W (kg)	Slump (mm)
				C (kg)	Silica Fume (kg)	%	(kg)			
PC	0.37	918	955.5	360	36	0.0	0.0	2	146	85
CNFRC0.25	0.37	918	955.5	360	36	0.25	0.63	2	146	125
CNFRC0.5	0.37	918	955.5	360	36	0.5	1.26	2	146	90
CNFRC0.75	0.37	918	955.5	360	36	0.75	1.90	2	146	70
CNFRC1.0	0.37	918	955.5	360	36	1.0	2.50	2	146	50

Notation: CA=coarse aggregate, FA= fine aggregate, C=Cement, CNF= carbon nanofibre, HRWR= high range water reducer, W= water

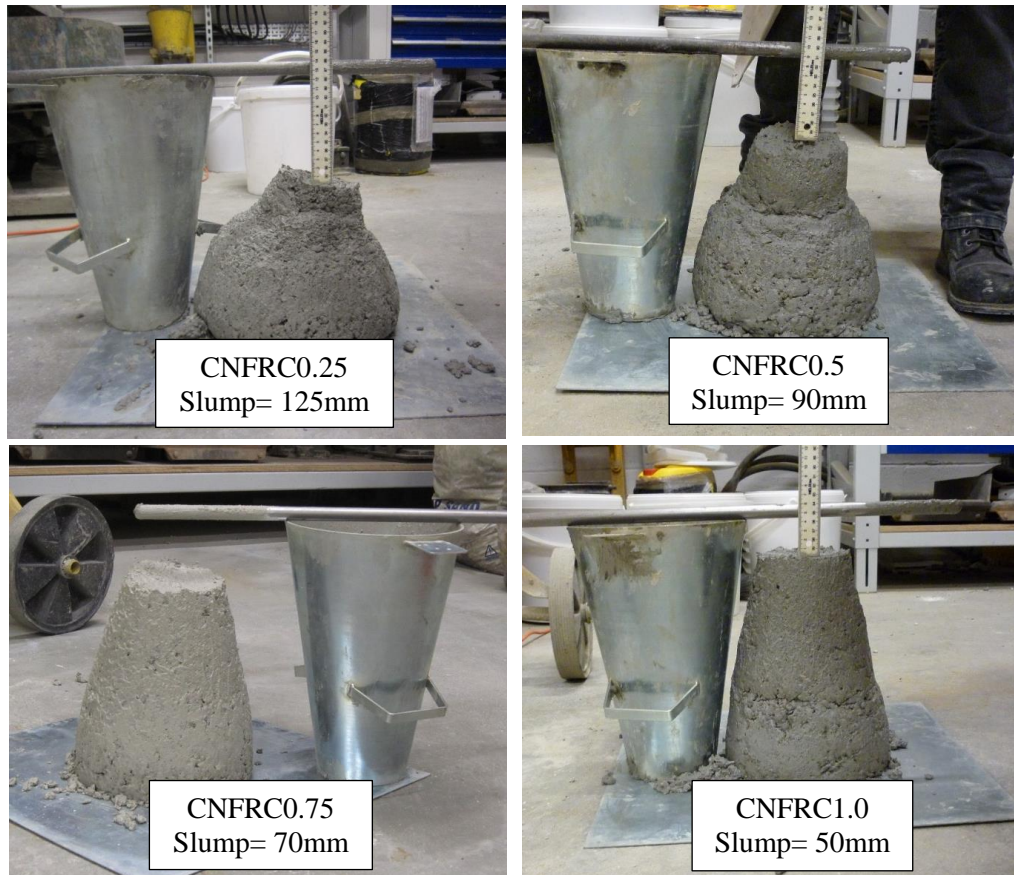


Figure 3.8. Slump test of Group B materials

From Table 3.5, it can be noted that the CNF concentration affected the workability of the concrete and the slump value of the concrete with 0.25% CNF was the highest amongst the CNFRCs. Since the nanomaterials adsorb the HRWR and water, which is adverse for the workability, increasing fibre dosage caused decreased slump value. As Meng and Khayat (2016) claimed, this adverse effect is dominant when the content of nanomaterial is more than 0.05% by binder weight which was the case for this experimental program.

Considering the modifications and following the mixing recommendation as explained in section 3.3.3, the mixing procedure was followed as below:

- a. Coarse aggregate and fine aggregate were added to the mixer and mixed well (2 minutes).
- b. Silica fume was added and mixed (2 minutes).
- c. Once evenly mixed (a uniform grey colour obtained) cement was added and mixed well (2 minutes).
- d. Water was then added under low speed to the mixer and mixed well till the paste uniformity was enhanced (3-5 minutes).

For CNFRC concrete the CNF diluted and sonicated with all Water+HRWR was used at step (d). The Water+HRWR+CNF mix for CNFRC0.25 is shown in Figure 3.9. Details of sonication for each CNFRC batch are presented in Table 3.6. Following this method of mixing there was no sign of black solution on the surface of the samples hence it was considered that Water+HRWR+CNF solution was blended in the concrete matrix satisfactorily and a homogeneous paste was obtained. The surface of the hardened concrete was clear of any black marks, those which were apparent in Group A samples. However, the CNF concrete had darker colour compared to plain concrete. As shown in Figure 3.10, concrete with a higher percentage of CNF had a darker shade than others and CNFRC1.0 had the darkest appearance.



Table 3.6. Water+HRWR+CNF sonication properties – Group B

CNF %	CNF/W (%)	W+HRWR (ml)	Sonication Energy (J)	t (s)	Watt (J/s)	(Watt/ml)
<b>0.25</b>	0.43	2426.5	36375	270	134.72	0.056
<b>0.50</b>	0.86	2640	91777	600	152.96	0.058
<b>0.75</b>	1.30	3058.7	86330	600	143.88	0.047
<b>1.0</b>	1.71	4068.4	134814	540	244.1	0.060

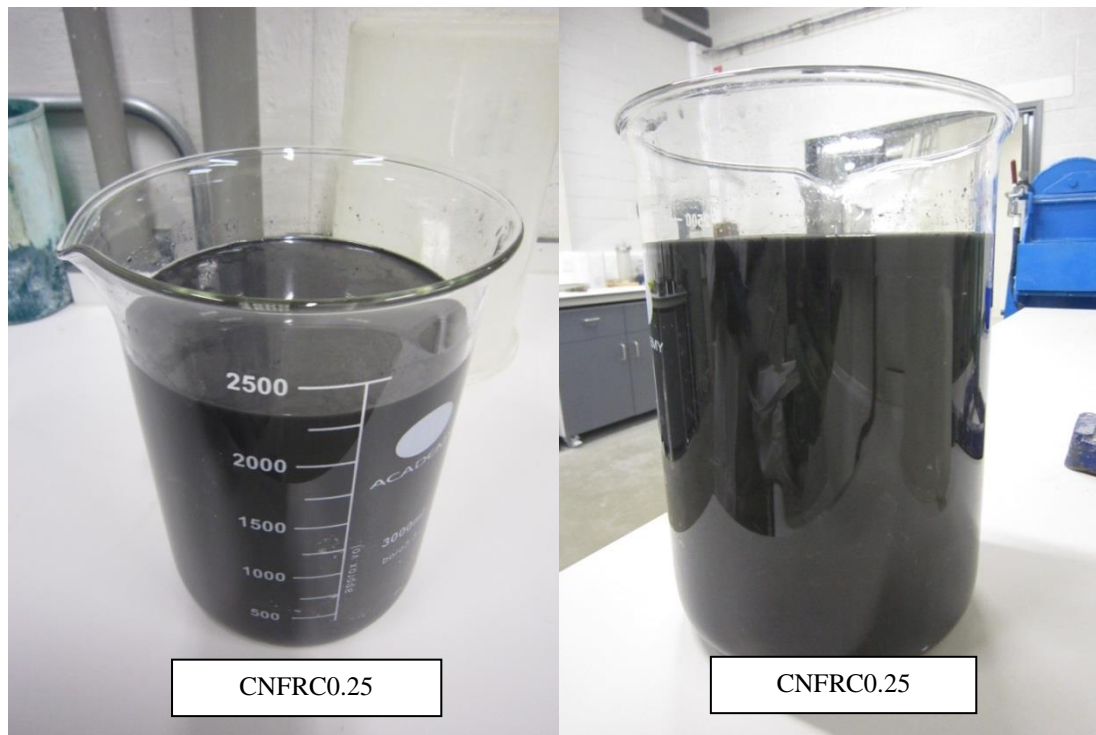


Figure 3.9. Water+HRWR+CNF mixture after sonication

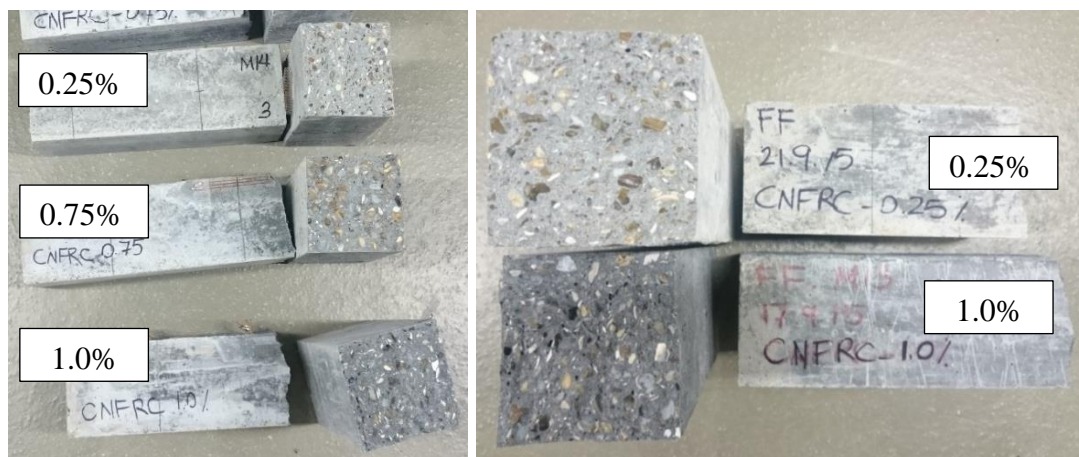


Figure 3.10. Effect of CNF on concrete colour

### 3.7. TEST RESULTS – GROUP A

Materials in this group were tested under flexure load, compression, and split tensile load and the results are presented in the following sections.

#### 3.7.1. Compression test results

Stress-strain diagram for cylinders tested under compression in a displacement control manner is shown in Figure 3.11 and Table 3.7. From the figure and the table it is evident that both CNFRC were stronger than PC (by 13% and 7.6% for 0.5% CNF and 0.75% CNF respectively) and they both showed a very similar behaviour in terms of strength and strain capacity. CNFRC-A-0.5 has shown remarkable strain capacity compared to PC, which was 69% higher than PC.

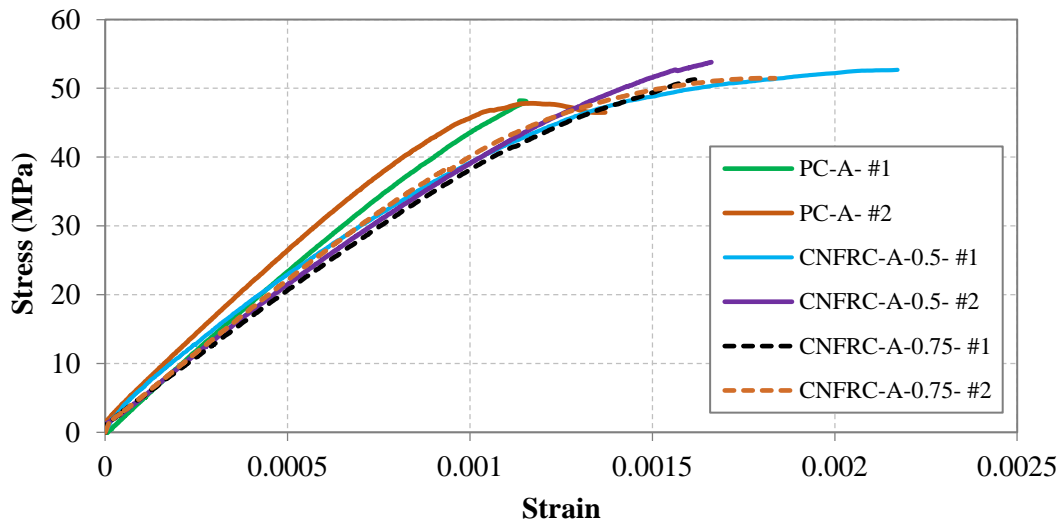


Figure 3.11. Compressive stress-strain relationship – Group A

Table 3.7. Compressive strength – Group A

Concrete Type	PC-A	CNFRC-A-0.5	CNFRC-A-0.75
<b>Compressive Strength</b>	47.82 MPa	54.07 MPa	51.47 MPa

The failure of concrete samples in this category under compression load was very brittle for all concrete types. The cylinders had an explosive failure due to the high strength of concrete at the maximum strength (see Figure 3.12) and could not reach the post-peak phase. This behaviour of the samples was similar to high strength concrete and ultra-

high strength concrete, in which the material shows a brittle explosive failure due to compact nature of the concrete and its high strength. The nanofibres for this type of failure were not so effective to prevent the explosive failure and macro fibres are required to control this behaviour and allow the concrete material to have a post-peak response. However, the nanofibres were effective in increasing the compressive strength.



Figure 3.12. Compressive failure of: (a) PC-A; (b) CNFRC-A-0.5; (c) CNFRC-A-0.75

### 3.7.2. Split tensile test results

The results of split tensile strength are presented in Table 3.8. Split tensile strength of concrete with the addition of 0.5% and 0.75% CNF to plain concrete was increased by 13% and 21% respectively. The failure of samples is shown in Figure 3.13. The failure pattern showed a brittle failure of PC with concrete spalling, while both CNFRC-A-0.5 and CNFRC-A-0.75 developed cracks along the length of the sample without splitting the cylinder into two pieces. This could represent better performance of concrete under tension.

Table 3.8. Split tensile strength – Group A

Concrete Type	PC-A	CNFRC-A-0.5	CNFRC-A-0.75
Split Tensile Strength	3.8 MPa	4.3 MPa	4.6 MPa



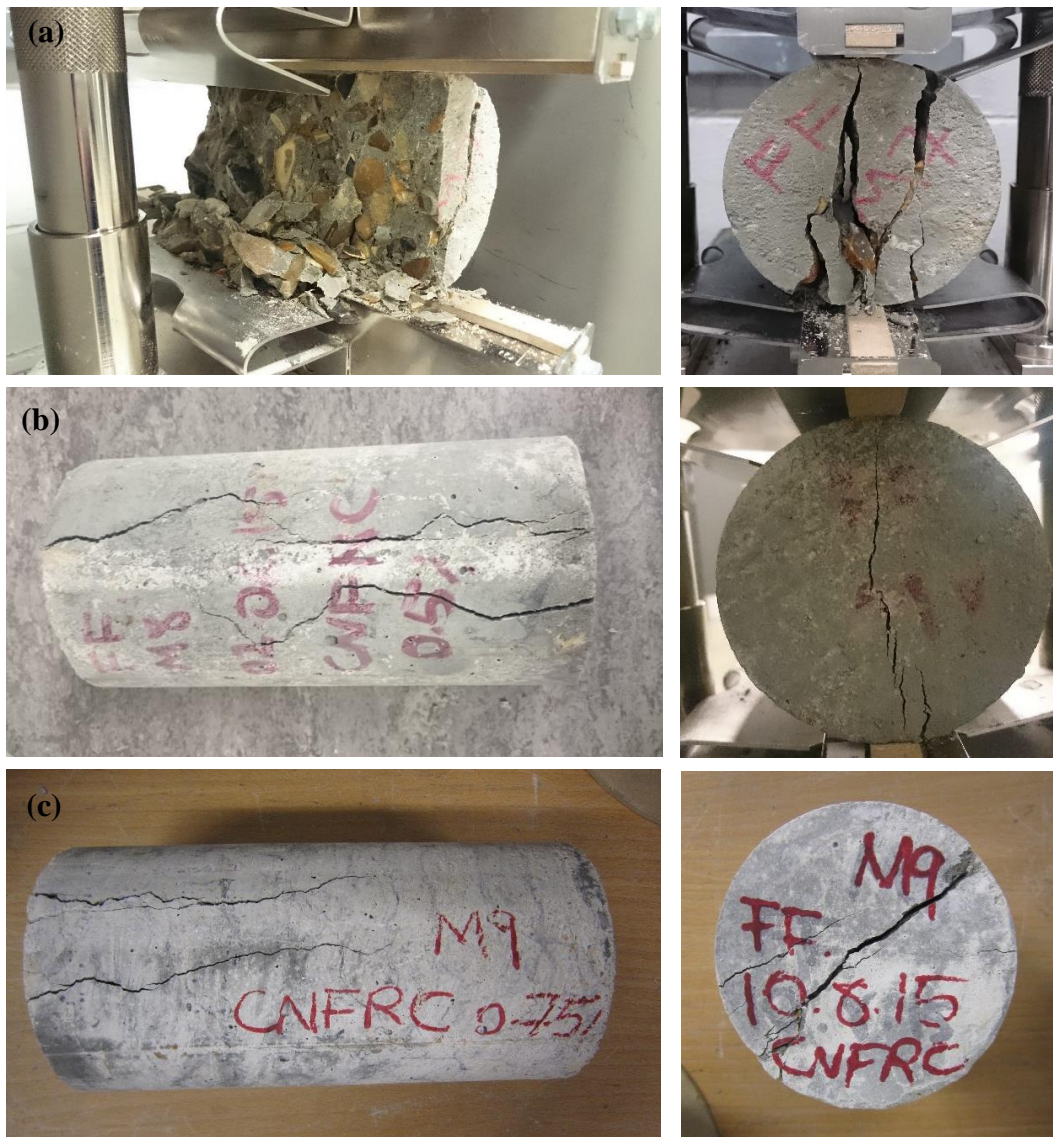


Figure 3.13. Split tensile failure of cylinders - Group A: (a) PC; (b) CNFRC-A-0.5; (c) CNFRC-A-0.75

### 3.7.3. Flexural test results

Load-displacement graphs for each concrete type are shown in Figure 3.14. All beam samples under four-point bending failed with central crack, where the beam was split into two pieces by the end of the test. From the graphs, it is evident that CNFRC had higher flexural strength than PC. With 0.75% of fibres, the concrete strength was slightly higher than samples with 0.5% of fibres. However, from the ductility point of view, both CNFRC performed better than PC. For PC samples, followed by reaching the maximum strength of the material, the beam crack developed quickly and propagated to the top surface resulting in breakage of the sample. PC beams struggled to maintain the post-peak behaviour of the concrete under flexural load, while samples of CNFRC-A-0.5 showed the best performance reaching the highest displacement of 500 $\mu$ m, which was about 16 times larger than PC. CNFRC-A-0.75 showed slight post-peak behaviour as well. It can be concluded that the CNFRC has better integrity when fibres are used. This was also reflected in the split tensile performance of the material.

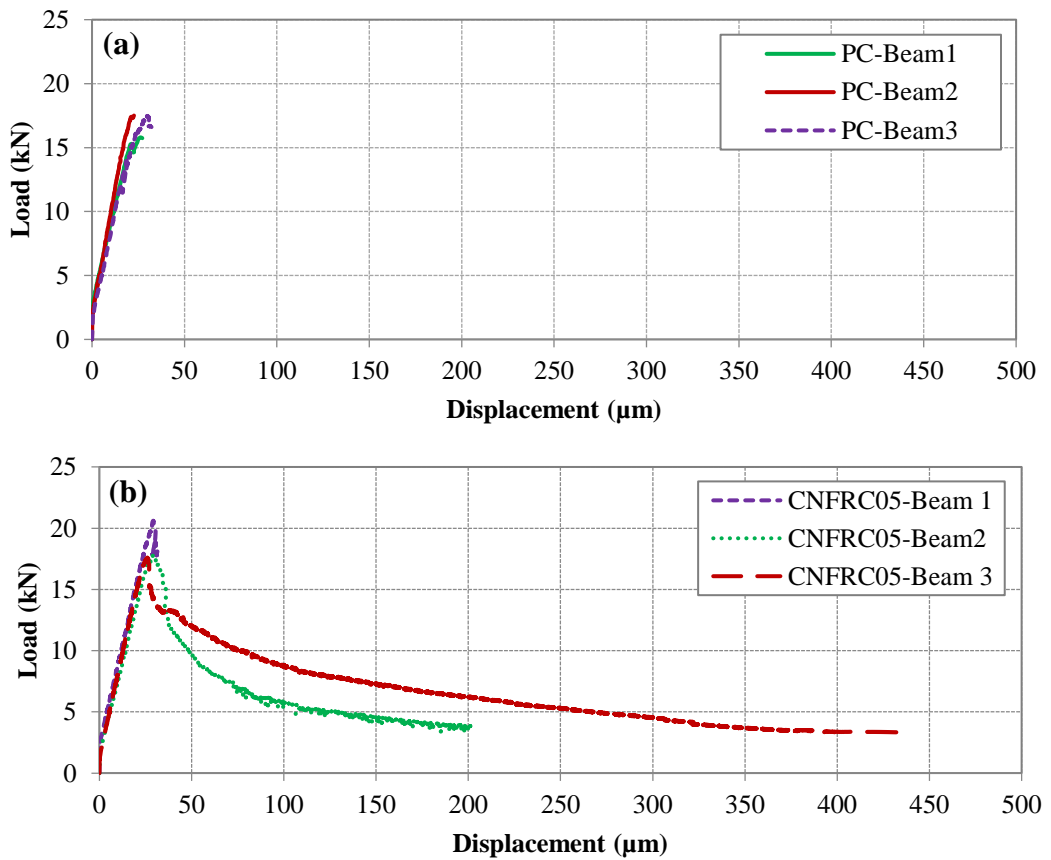


Figure 3.14. Group A – four-point bending load-displacement graphs for: (a) PC; (b) CNFRC-A-0.5; (c) CNFRC-A-0.75

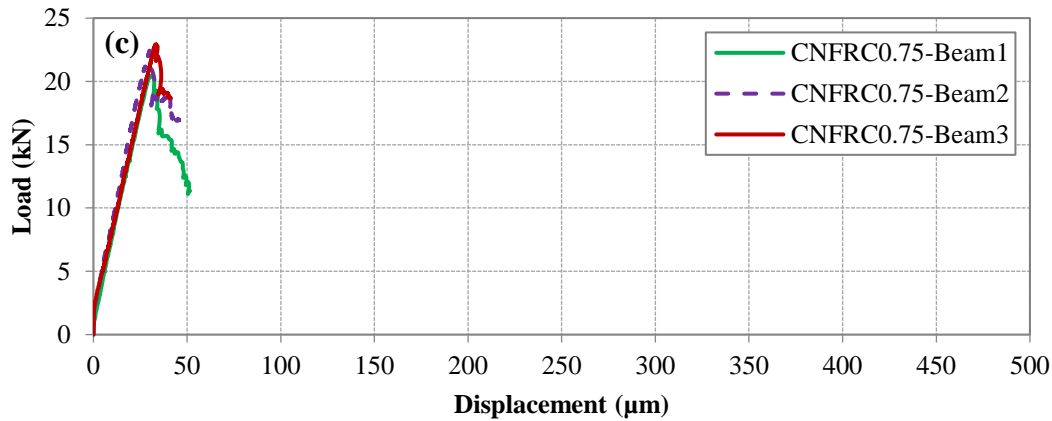


Figure 3.14. (continued)

Higher ductility observed for 0.5% CNF reinforced samples could be due to better dispersion of CNF achieved within the aqueous solution due to lower CNF/W ratio (1.3%) which was less than that for CNFRC-A-0.75 (CNF/W=1.9%).

### 3.8. TEST RESULTS – GROUP B

This section presents the mechanical properties of Group B materials. The results from compression, split tensile, and flexural tests are discussed in the following sections.

#### 3.8.1. Compression test results

The compressive strength of cylinders for all types of concrete is shown in Figure 3.15 and the graph in Figure 3.16 presents the stress-strain relationship for all concrete types. For each type, the results of two representative samples are presented. Since the strength of the concrete is dependent on the calcium silicate hydrate (C-S-H) component of the concrete, the nanofibres are expected to reinforce the nanoscale properties of the C-S-H, hence increasing the compressive strength. At the interface, CNF possesses an intimate bonding with the cement matrix due to the Van der Waals forces. The large aspect ratio and stacked-up cone shape and rough edges of the fibres give themselves filament abilities to block and diver micro-cracks, which can slow down crack propagation and formation of the crack network. As stated by Han et al. (2015) the increase in compressive strength can be related to two effects:

- *Bridging effect* of the CNF for micro-cracks,
- *Filler effect* for accelerating the hydration reactions of the cementitious materials as well as filling in the voids, which in turn results in less porosity and higher compaction.

From Figure 3.15, with the addition of only 0.25% of CNF fibres to the concrete, the compressive strength was increased by 30.5%. As the fibre dosage increased, the compressive strength increased as well. However, there was an inflection point at 0.5% CNF content, at which the compressive strength of concrete was decreased by 8.5%. This decrease could be an indication of the presence of fibre clumps in concrete matrix and poorer dispersion quality of the CNF solution compared to other CNFRC samples. Although CNFRC0.5 was less effective on enhancing plain concrete post-peak behaviour (Figure 3.16), but it improved the strength by 19.5%, which is comparable to findings of Sanchez et al. (2010) who found an increase in compressive strength of plain mortar from 30 MPa to 36 MPa (by 20%) using CNF at 0.5% wt. of cement (with  $W/C=0.365$ ). Compared to the results obtained by Kowald (2004), who used 0.5% CNT in high-strength concrete and found 12% increase in compressive strength, it can be stated that the CNF incorporated concrete in this study showed slightly better performance than CNT. Li et al. (2005) also obtained a 19% enhancement in compressive strength of mortar by using 0.5% MWCNT. On the other hand, Rhee and Roh (2013) found 50% increase in compressive strength by adding only 0.25% MWCNT to the concrete. This increased enhancement could be attributed to different dispersion method used in their research (which involved basket milling in addition to sonication).

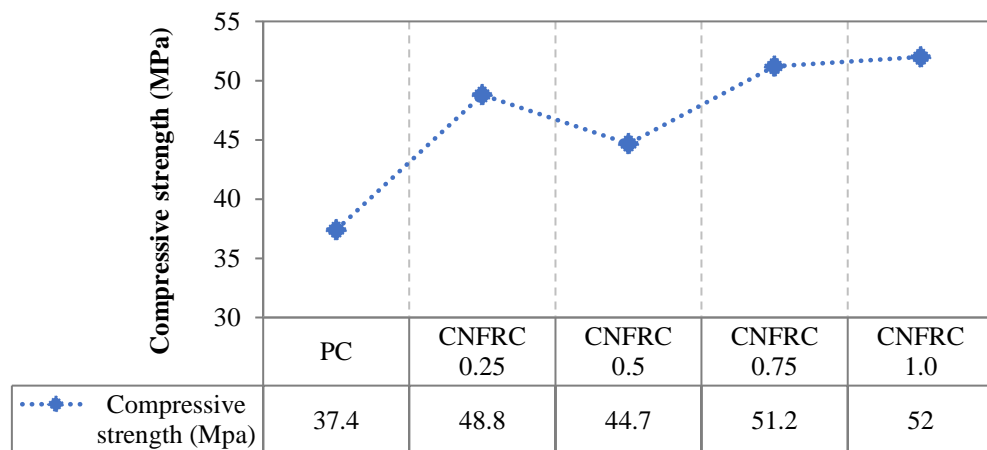


Figure 3.15. Compressive strength results – Group B

In this study, the maximum strength was achieved by the addition of 1.0% fibre, with 39% increase in strength. It is worth mentioning that the results for CNFRC0.75 were very close to CNFRC1.0, hence the effect of fibre at a dosage higher than 0.5% became inconspicuous in the case of this experimental program. In the review of the previous

work on the compressive strength of CNF composites, it was found that 1.0% CNF by volume of binder increases the cylinder compressive strength by 26.9% (Sivakumar, 2001) which was lower than what was achieved in this research. However, Gao et al. (2009) found that the addition of 0.16% CNF to a self-consolidating concrete increases the compressive strength by 40%. The reason for higher enhancement found by them could be the type of the concrete used in their study, suggesting that SCC could possibly better accommodate the dispersion of the fibres when mixed with the cementitious materials and hence achieving a more uniform mixture because of its higher fluidity (due to higher HRWR and water content) resulting in higher strength enhancement. This is, however, a premise that needs to be further studied in the future.

From the post-peak behaviour of the cylinders, it can be seen that CNFRC0.75 and CNFRC1.0 had similar behaviour and they outperformed other materials. CNFRC0.5 reached higher strain despite lower strength compared to CNFRC0.25. Figure 3.17 shows specimens of Group B after failure. From the figure, PC and CNFRC0.25 showed the most damage and concrete was broken into pieces, however, CNFRC0.75 and specially CNFRC1.0 showed the least damage and mainly on the concrete surface. It can be concluded that samples with higher fibre dosage (0.75% and 1.0%) were more successful in attaining their integrity and mainly surface damage was observed. The reason for this is because the fibres enhanced the compressive performance of concrete by better filler effect (i.e. creating compacter concrete by filling the voids in the matrix) at higher fibre dosage.

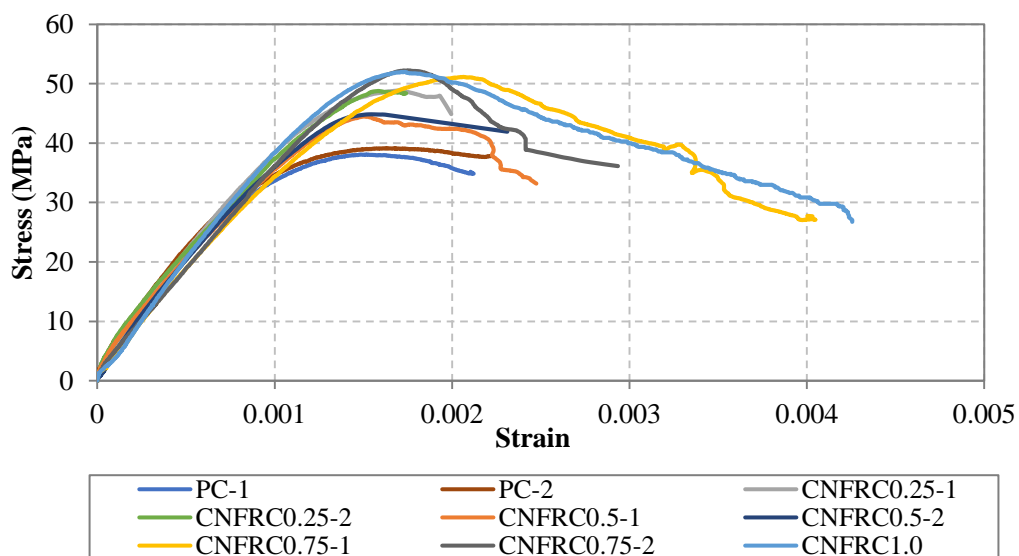


Figure 3.16. Compressive stress-strain relationship – Group B



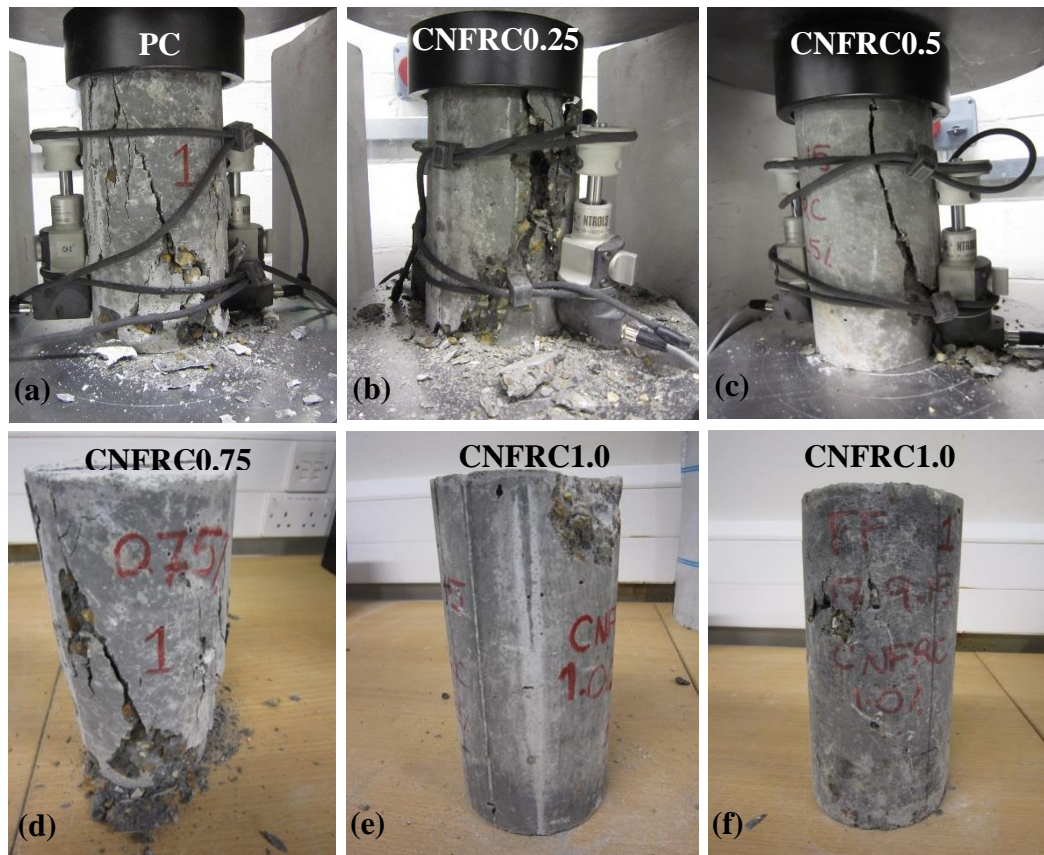


Figure 3.17. Group B sample failure after compression test: (a) PC; (b) CNFRC0.25; (c) CNFRC0.5; (d) CNFRC0.75; (e) CNFRC1.0; (f) CNFRC1.0

### 3.8.2. Split tensile test results

The average split tensile strength of all samples for each concrete type is shown in Figure 3.18. No significant changes were observed in the splitting tensile strength with variation in the CNF percentage. However, compared to PC this mechanical property was increased by 24.2% when 1.0% CNF was added to the concrete. Amongst the CNFRC samples, both 0.75% and 1.0% CNF fibre had the greatest effect on the concrete and their effect was almost similar. Addition of 0.25% CNF in the concrete resulted in 22.2% increase in split tensile strength, which is close to the findings of Gay and Sanchez (2010) who found 26% increase in tensile strength of the reinforced cement paste with 0.2% CNF. It can be suggested that the effect of CNF within concrete could compete with its effect in cement paste or cement mortar. On the other hand, the direct tensile strength of 0.3% (wt. of binder) CNF reinforced UHPC tested by Meng and Khayat (2016) showed 56% increase in the strength and Sivakumar (2011) achieved 66.6% increase in split tensile strength of SCC with 1.0% CNF by volume of binder.

The different results obtained by these researchers could be due to the different concrete type used in their study, namely UHPC (which is more compact than PC) and SCC (which has higher fluidity than PC) respectively. As mentioned beforehand, this comparison suggests that the effect of CNF could vary within different concrete types and further study regarding this issue is recommended.

All samples failed by a crack through the centre of the cylinders and splitting the cylinder into two pieces as shown in Figure 3.19.

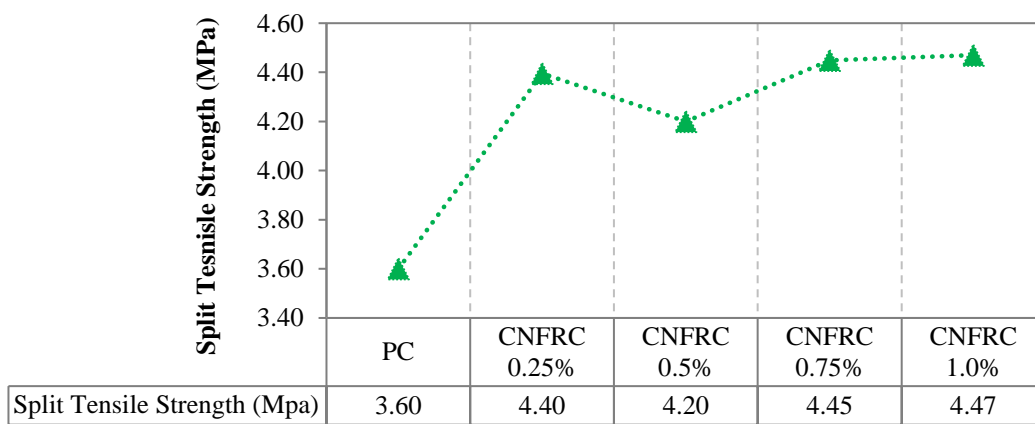


Figure 3.18. Split tensile strength results – Group B



Figure 3.19. Split tensile failure of cylinders - Group B: (a) CNFRC0.25; (b) CNFRC0.75

### 3.8.3. Flexural test results

The flexural strength of each sample was calculated according to Eq. 3.2 (section 3.4.3) and the average strength is presented in Figure 3.20. From this figure, the change in the flexural strength shows the same general trend as compressive strength and split tensile strength for CNFRC with an inflection point at 0.5% fibre dosage. From three samples that were tested, the load-displacement relationship of one beam from each mix, representing the behaviour of the concrete is shown in Figure 3.21.

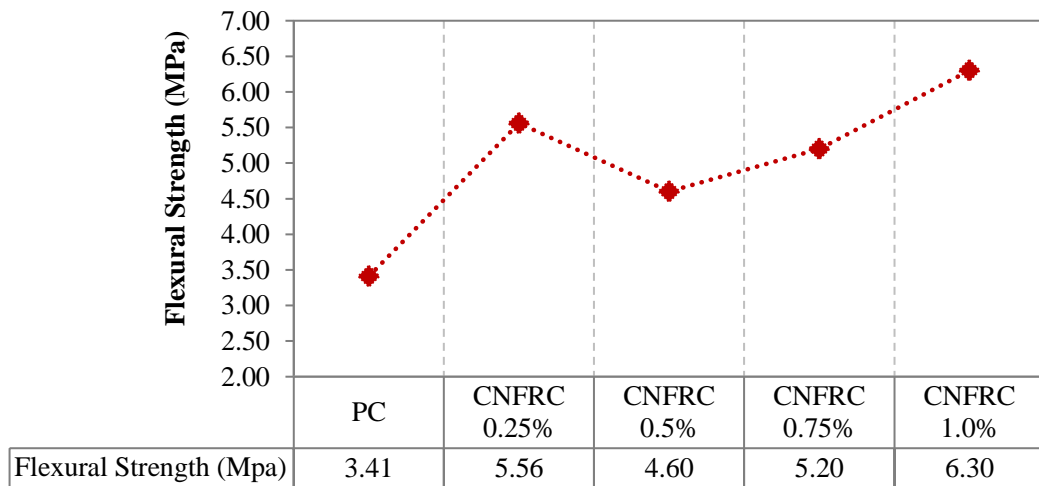


Figure 3.20. Flexural strength results for Group B

According to both Figure 3.20 and Figure 3.21, it is evident that addition of CNF has increased the flexural strength of the plain concrete by 63%, 35.3%, 52.5%, and 85% respectively with fibre dosage of 0.25%, 0.50%, 0.75% and 1.0%. From reviewing previous researches, 55.5% increase in the flexural strength of the cement paste was found with the addition of CNF at 0.1 wt.% of cement (Tyson et al., 2011). This fibre dosage was close to the CNFRC0.25 of this research with an equivalent CNF dosage at 0.17 wt.% of cement. It is seen that both results are somewhat close considering the higher fibre volume fraction used in CNFRC0.25 might be the reason for higher effect (63%) on the flexural strength. When Tyson et al. (2011) doubled the amount of fibre dosage (0.2 wt.%), the flexural strength decreased by 30%. This phenomenon also occurred in this study between CNFRC0.25 and CNFRC0.5; in which the flexural strength decreased by 17.3% as the amount of fibre was doubled.



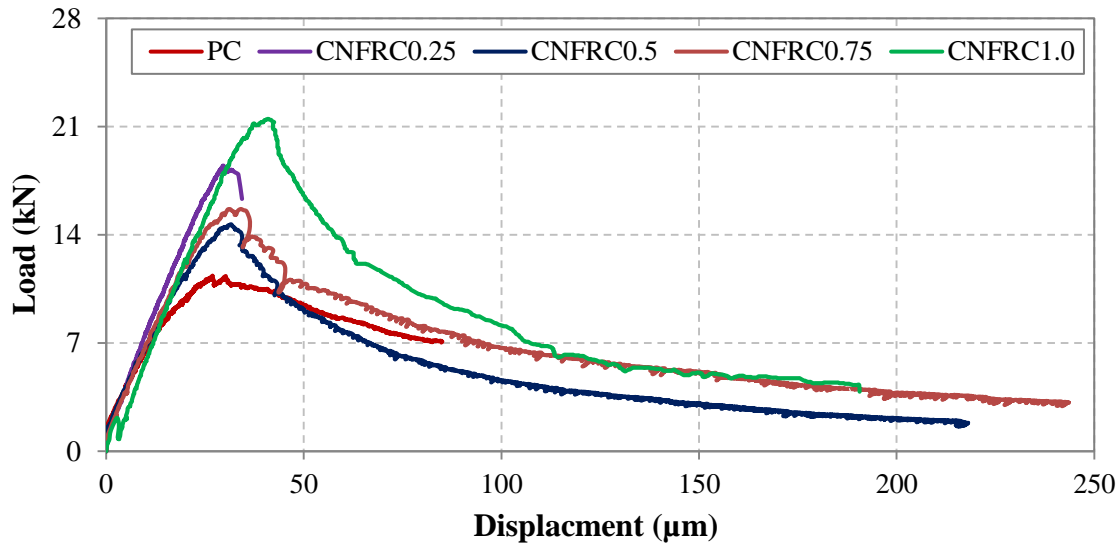


Figure 3.21. Group B – four-point bending load-displacement graphs

Li et al. (2005) achieved 25% increase in the flexural strength of cement mortar by the addition of 0.5% MWCNT. The results obtained in this study for an equivalent amount of CNF in concrete was 35.3%, which suggests that CNF could compete with CNT and perform better than CNT within concrete matrix.

From the strength point of view, it is evident that the concrete with 1.0% fibre was the strongest with the flexural strength of 6.30 MPa. The performance of CNFRC1.0 in this study outperformed the results found by Sivakumar (2011), who found an increase of 38% in flexural strength of SCC when 1% CNF by volume of binder was used. Also, Meng and Khayat (2016) reported 46% increase in flexural strength of UHPC reinforced with 0.5% micro steel fibre and 0.3% CNF. This enhancement in flexural strength could be of great advantage for the behaviour of concrete members at the structural level. Overall, the trend of change in compressive strength, flexural strength, and split tensile strength from 0.5% to 1.0% in this study agrees with the findings of Sivakumar (2011) for CNF reinforced SCC who found an increasing trend in all mechanical properties.

Interestingly, contrary to what one might presuppose that the 0.25% fibre addition could have the least effect on the behaviour of the material as opposed to higher fibre concentrations; it was more effective than 0.5% and 0.75% fibre concentrations in the concrete matrix in increasing the flexural strength. A possible reason is that due to the lower fibre concentration, agglomeration of fibres was greatly prevented, and better dispersion was achieved for this material. However, according to the load-displacement

graph, CNFRC0.25 did not show great ductility compared to other CNFRCs. The material showed more brittle behaviour after reaching the maximum strength followed by sample breakage regardless of its higher strength capacity.

CNFRC0.5, CNFRC0.75, and CNFRC1.0 showed relatively high displacement capacity compared to PC which means that these materials had higher ductility. This is because the material was successful in attaining its load carrying capacity resulting in higher ductility while the crack propagated towards the top surface of the beam. This can be attributed to better nano-crack and micro-crack control due to a higher concentration of fibres as opposed to CNFRC0.25. During the post-peak stage, CNFRC1.0 showed higher load level than other samples and at the mid-span deflection of 0.12 mm, the capacity of the sample reached the same capacity as CNFRC0.75. At this stage, both CNFRC0.75 and CNFRC1.0 had higher loading capacity compared to CNFRC0.5, hence higher energy dissipation was obtained for 0.75% and 1.0% CNF samples. On the other hand, it is interesting to note that the highest displacement achieved by 0.5% CNF reinforced concrete was higher than 1.0% CNF sample.

Although it was assumed that better dispersion of 0.25% fibres caused higher flexural strength than 0.5% and 0.75% fibre, it should be emphasised that the dispersion of other samples was also satisfactory since there was an apparent improvement in the behaviour of the concrete in terms of strength, ductility, and energy dissipation capacity, which was manifested by the post-peak behaviour. This is due to the presence of higher fibre dosage. Overall, it is believed that the CNF embedded in the paste along with the network created by CNF inside of the pockets (referring to clumps that might not have been fully dispersed, and be formed inside the paste followed by being introduced into concrete matrix) may have limited the propagation of the cracks when 1.0% fibre is used, allowing specimen to retain some significant flexural capacity over the plain concrete.

Figure 3.22 shows the failure of CNFRC beam samples after the test. It can be seen that the crack developed in sample CNFRC0.5 is very thin and the beam has remained intact. This failure explains the load-displacement behaviour of the beam and its higher ductility. Also, CNFRC1.0 showed thin crack width towards the top of the beam. CNFRC0.25 had the full breakage shortly after reaching the maximum strength and the beam was split into two pieces (Figure 3.22(a)).

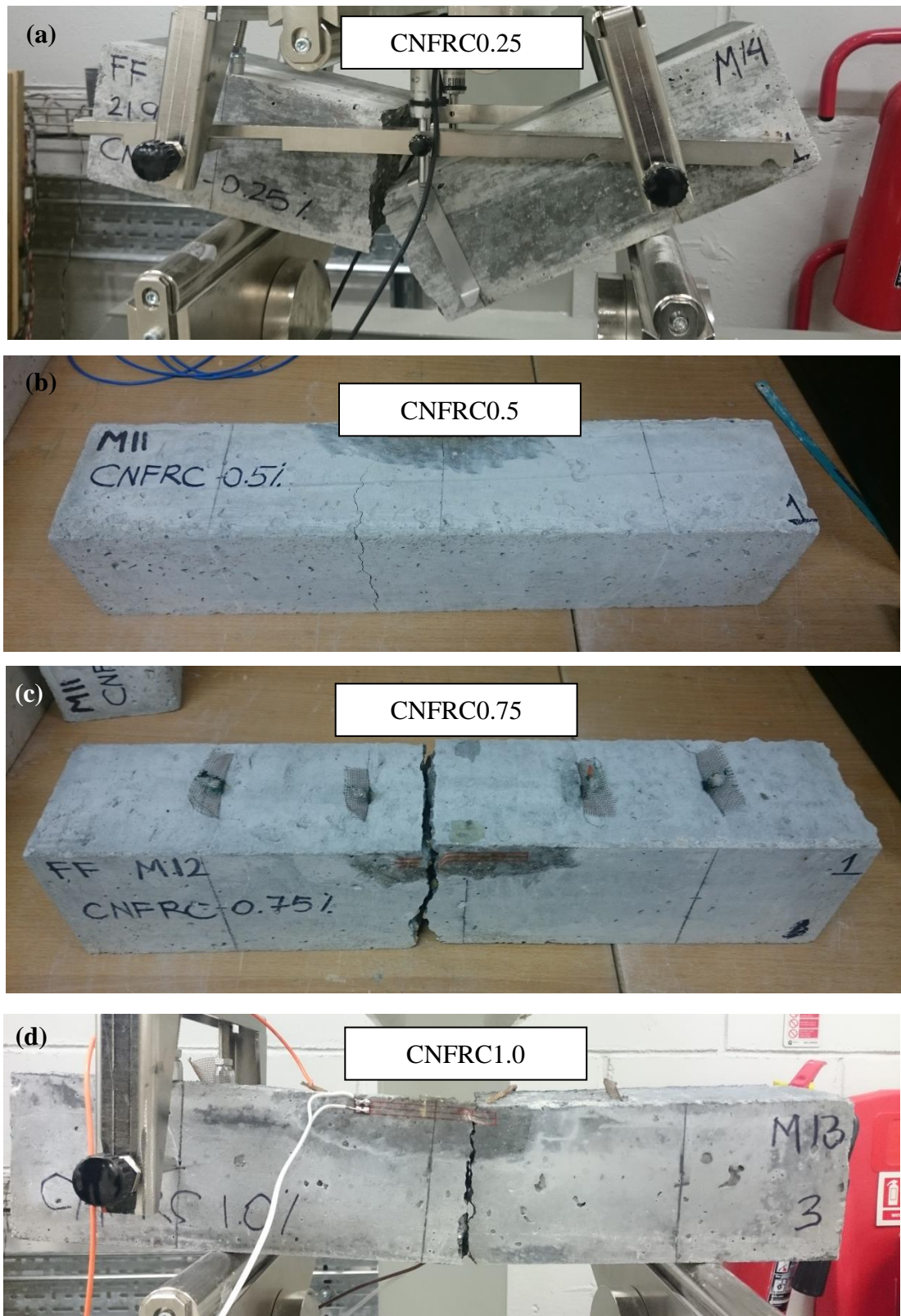


Figure 3.22. Flexural beam test samples after failure: (a) CNFRC0.25; (b) CNFRC0.5; (c) CNFRC0.75; (d) CNFRC1.0

### 3.9. SELF-HEALTH MONITORING OF CNFRC

The self-sensing capability of the nanoconcrete is based on its piezoresistivity<sup>2</sup>. CNF reinforced concrete is a material with discontinuous conductive nanofibres (CNF) which creates an electromagnetic field and transforms the concrete into a conductive material. Electrically conductive concrete allows performing resistivity measurements, which could be used to analyse the strain or stress variations in the structure member. Advantages and disadvantages of the nanotechnology-modified concrete versus traditional sensors are summarised in Table 3.9. To accomplish the objective of this study regarding the self-sensing capability of nanoconcrete, self-health monitoring test was conducted on beam samples of Group B.

Table 3.9. Nanoconcrete vs. traditional sensor

	<b>Nanoconcrete</b>	<b>Traditional sensor</b>
<b>Placement</b>	<ul style="list-style-type: none"> <li>• Internal</li> <li>• Structure itself in an infinite set of sensors</li> <li>• Enlarging the sensitive volume to its maximum extent</li> </ul>	<ul style="list-style-type: none"> <li>• Externally attached</li> <li>• Wired to the data acquisition system</li> </ul>
<b>Durability</b>	<ul style="list-style-type: none"> <li>• More durable</li> </ul>	<ul style="list-style-type: none"> <li>• The service life is generally short</li> </ul>
<b>Application</b>	<ul style="list-style-type: none"> <li>• Large concrete structures e.g. tall buildings, bridges, dams</li> </ul>	<ul style="list-style-type: none"> <li>• This technique based on local inspection could be troublesome because of maintenance and access difficulties in large spatial extents</li> </ul>

#### 3.9.1. SHM analysis method and the test set-up

Different methods are being used for SHM analysis of cementitious nanocomposites namely two-probe method and four-probe method as discussed in Chapter 2. For the effective measurement of the sensitivity of the concrete during the flexural beam tests, direct-current four-probe method was adopted, which previously has shown to successfully evaluate accurate electrical resistance of cementitious material (Azhari & Banthia, 2017; Han et al., 2007; Wen and Chung, 2007). In this method, overall four electrodes are embedded in the matrix (i.e. nanoconcrete), where two outer electrodes

<sup>2</sup> The piezoresistive effect is a change in the volume electrical resistivity of a semiconductor or metal when mechanical strain is applied or it is subjected to a force.

act as the current pole and the two inner electrodes act as the voltage pole. Electrodes could be either wires wrapped around the sample having surface contact or being embedded inside the sample. Embedding the electrodes ensures a better connection with sensing material as opposed to using wires wrapped around the specimen, having only surface contact with the sensing material. Extensive investigation of electrode types (Azhari and Banthia, 2017; Han et al., 2007) recommends that copper mesh has a better interaction with the cement composite owing to its high conductivity, small openings, and thus, it provides a better interface. Therefore, for this research, all four electrode contacts were made with woven copper wire mesh (#16 mesh) to have the utmost conductivity, with 1.233 mm aperture, and 0.355 mm wire diameter and the embedment method was used for more accurate results. Figure 3.23 shows the copper mesh used as the electrode for this experimental program. The copper electrodes had the following dimensions:

- Current pole: 90mm×50mm
- Voltage pole: 90mm×65mm

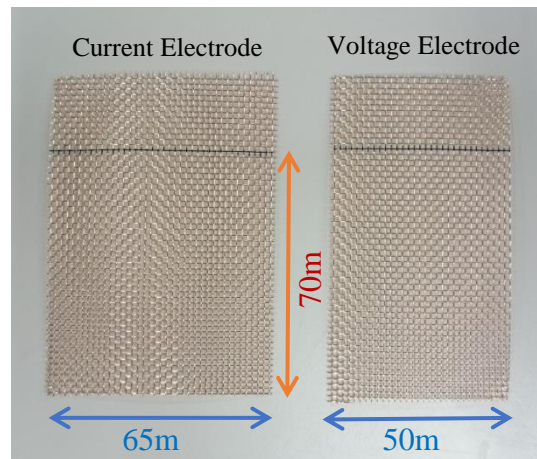


Figure 3.23. Copper mesh electrodes used for self-health monitoring test

The area of voltage pole can be decreased without affecting the results; hence the size of the mesh was slightly smaller in this study to minimise the influence of electrodes on mechanical properties of the concrete. The height of the embedded electrodes inside the concrete was 70 mm, and 20 mm was left out from the concrete surface to accommodate wiring connection to the electrical power supplier and voltmeter. The area of the current electrode embedded in concrete was 70×65 mm and the area of the voltage electrode embedded in concrete was 70×50 mm. These electrodes were placed symmetrically with respect to the centre along the length of the beam specimens at four planes that



were all perpendicular to the horizontal axis. Figure 3.24(a) illustrates the mesh arrangement in beam samples. The outer electrodes (325mm apart) were the current pole for passing current and the inner electrodes (125mm apart) were the voltage poles for measuring the voltage. They were incorporated into the specimen immediately after pouring the concrete mix in moulds (Figure 3.25). Prior to the test, a concrete strain gauge (PL-60-11, by TML) was attached to both sides of the beam at the centre towards the top surface of the beam as shown in Figure 3.24(b). The strain gauge was used to measure the compressive strain of the top fibres of the beam during loading. The results were then used to correlate the electrical readings with measured strain.

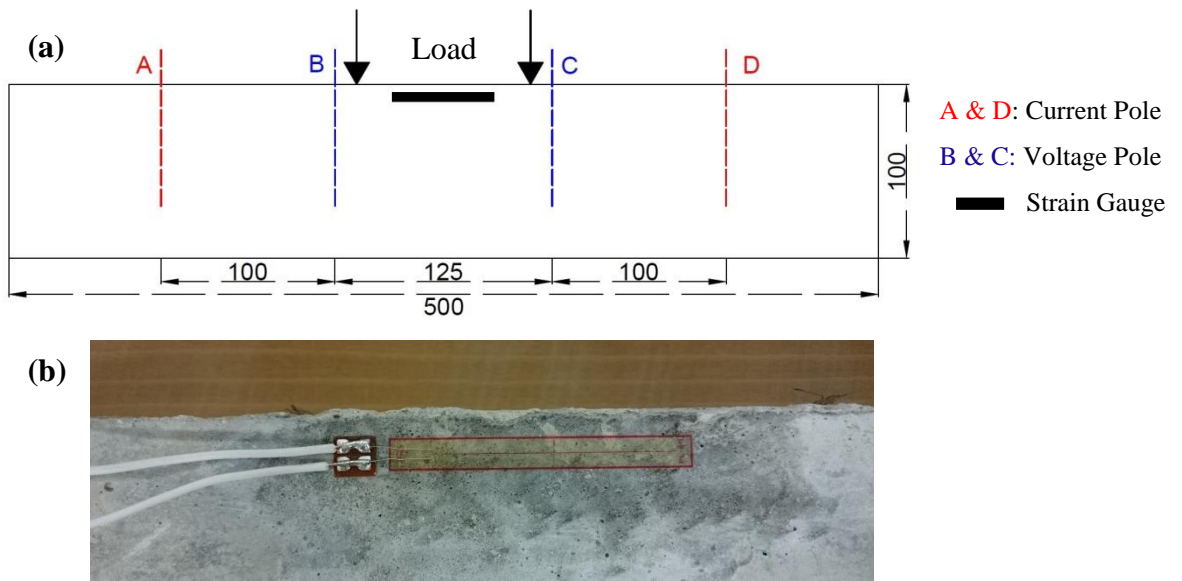


Figure 3.24. (a) Electrode configuration in the beam samples; (b) concrete strain gauge attached to the beam

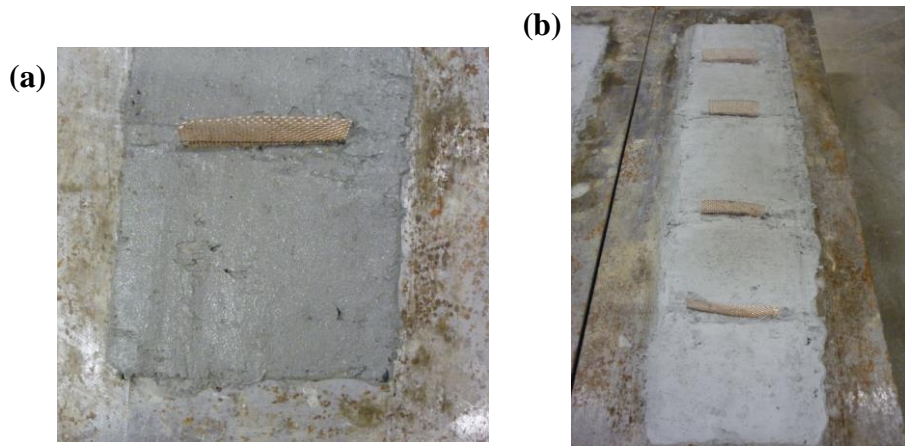


Figure 3.25. Mesh embedment inside: (a) fresh concrete; (b) hardened concrete

To create the current circuit within concrete (see Figure 3.26(a)), a copper wire was soldered to the copper mesh that was left outside the sample surface. The wires connected to the outer electrodes were connected to a power supply unit capable of supplying direct current (DC) up to 30V. Since the electrical resistance of the concrete varied with elapse of time due to the polarization of positive and negative charges, DC was applied for approximately 15 minutes prior to testing to let the electrical resistance stabilise in concrete. The current was kept constant throughout the test at 1mA. The inner electrodes were connected to a data logger to record the voltage. Data was set to be recorded at every 1 second. Consequently, the electrical resistance between the two middle electrodes could be calculated based on ohms' law:

$$R=V/I \quad (\text{Eq. 3.3})$$

'V' is the voltage (volts, v), recorded by data logger, 'I' is the current (Amp, A), kept constant at 1 mA, and 'R' is the resistance (Ohm,  $\Omega$ ), which was calculated. The diagram of the test set-up along with its equivalent circuit diagram developed from an illustration by Han et al. (2007) is shown in Figure 3.26(b). The electrical resistance of CNFRC ( $R_{BC}$ ) was obtained from the measured voltage ( $V_C$ ) by incorporating the Ohm's law (i.e.  $R_{BC} = V_C/I$ ). The wiring connections on beam sample are shown in Figure 3.27 and the beam set-up in the testing frame is shown in Figure 3.28.

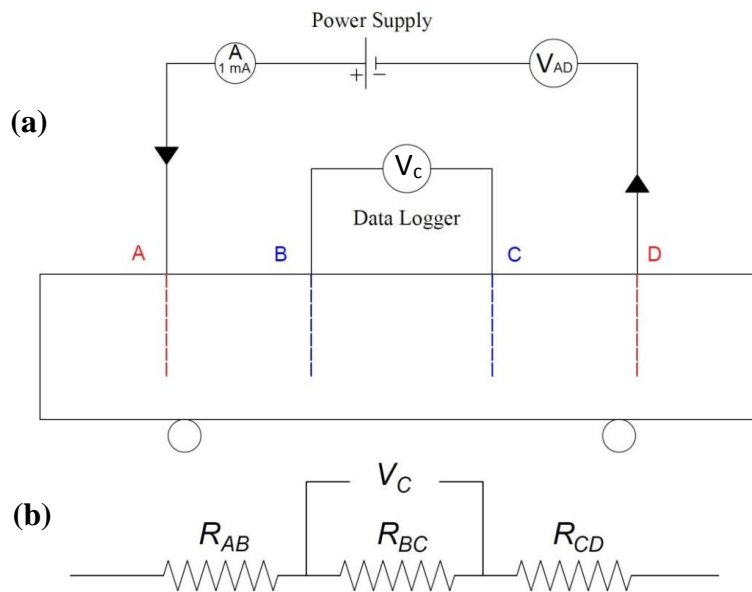


Figure 3.26. (a) Schematic diagram of four-probe wiring on beam samples; (b) equivalent circuit diagram for direct-current four-pole method

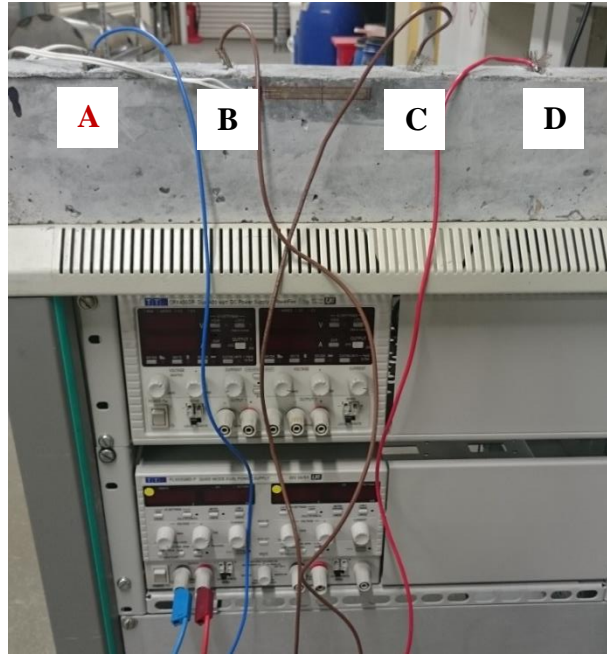


Figure 3.27. Electrical connection to power supply

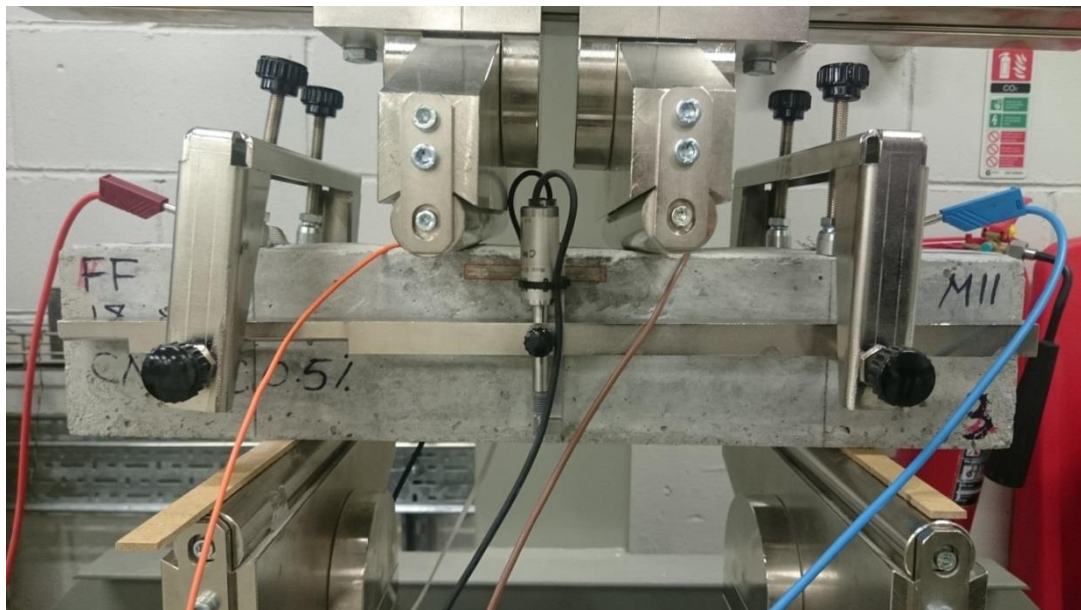


Figure 3.28. Flexural beam test set-up for obtaining self-health monitoring results

### 3.9.2. Electrical resistance vs. strain

To investigate the self-health monitoring capability of CNFRC and quantify this property for each sample, the following time histories are plotted and compared for each concrete type.



- Load vs. time
- Compressive strain vs. time
- Measured electrical resistance vs. time

These plots are shown in Figure 3.29 to Figure 3.32 for PC, CNFRC0.25, CNFRC0.5, CNFRC0.75, and CNFRC1.0 respectively. Additionally, the average value of initial electrical resistance for CNFRC samples after stabilisation of electrical circuit for 15 min prior to loading, is tabulated in Table 3.10. From the results, increasing the fibre dosage decreased the electrical resistance of the concrete evidently. As can be seen from Figure 3.29 the electrical resistance of plain concrete was random, and no relation could be detected between the resistance and strain. However, a good correlation was qualitatively observed for CNFRC concrete between strain and electrical resistance during loading.

Table 3.10. Initial electrical resistance of CNFRC prior to loading

	CNFRC0.25		CNFRC0.5		CNFRC0.75		CNFRC1.0	
<b>Initial R (k<math>\Omega</math>)</b>	8.76	8.80	7.9	8.33	5.86	5.86	4.07	4.30
<b>Average (k<math>\Omega</math>)</b>	8.78		8.12		5.86		4.19	

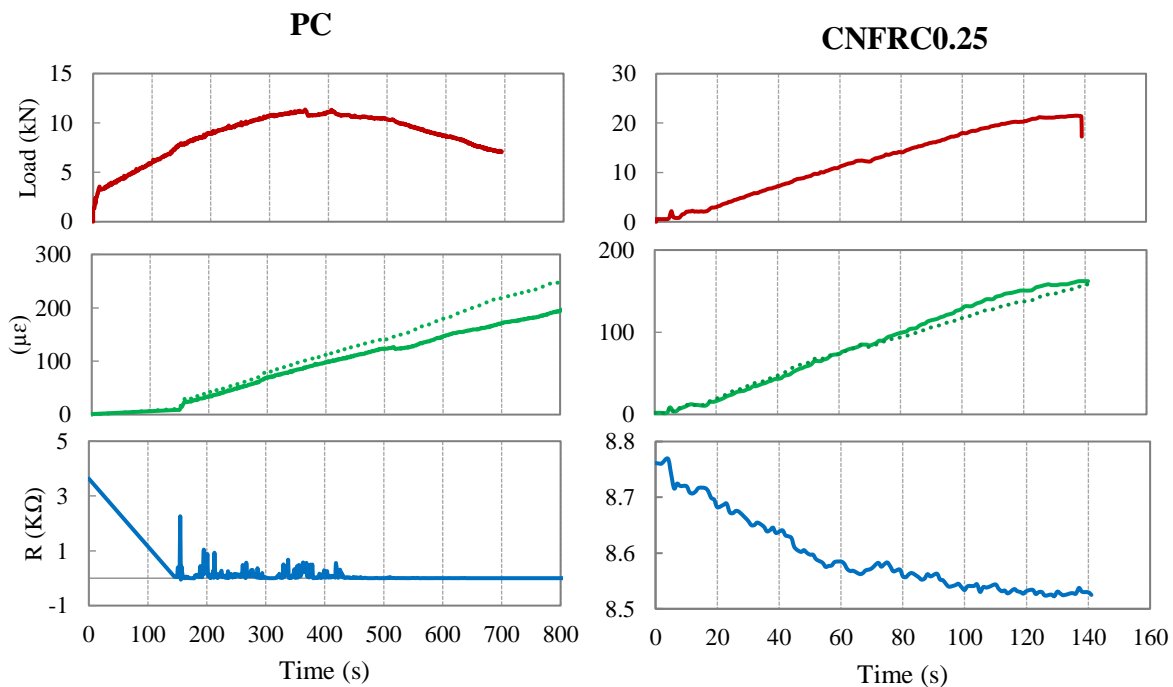


Figure 3.29. Time history results for PC and CNFRC0.25

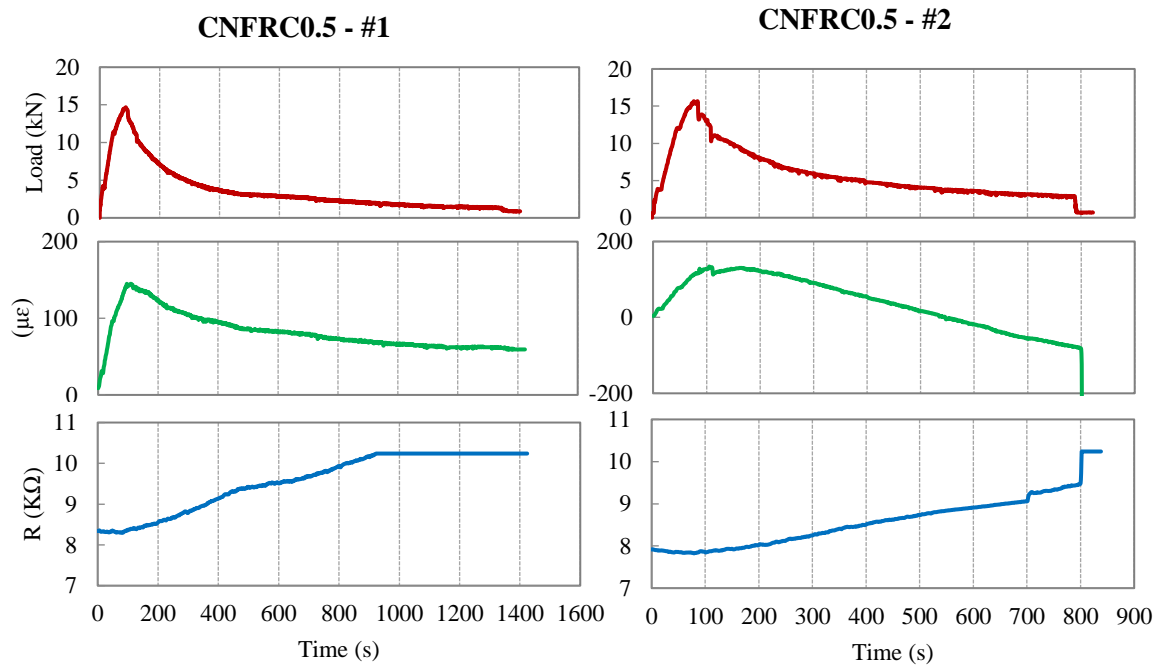


Figure 3.30. Time history results for CNFRC0.5

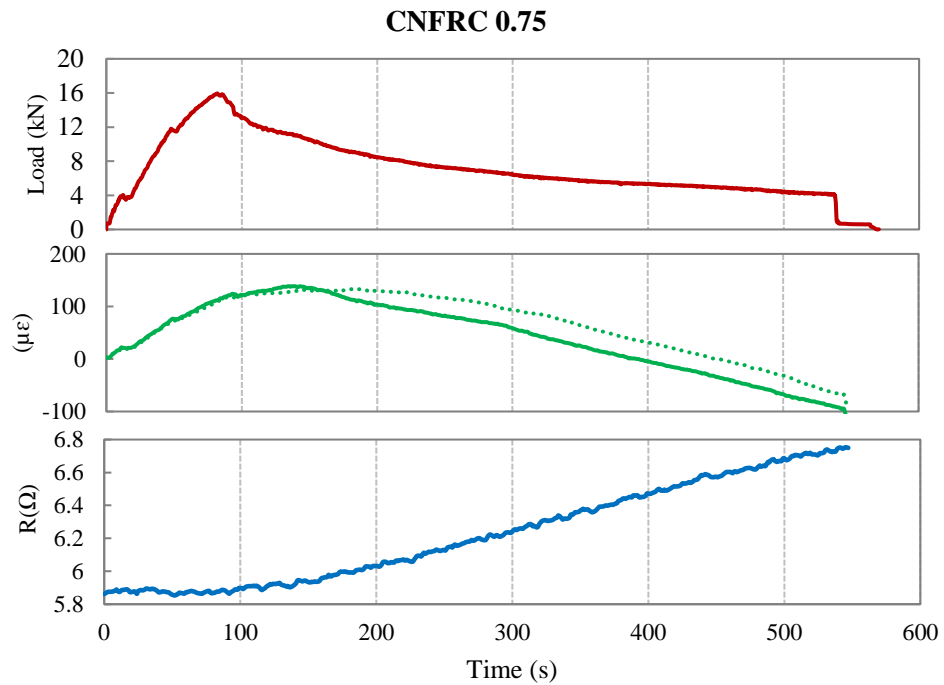


Figure 3.31. Time history results for CNFRC0.75

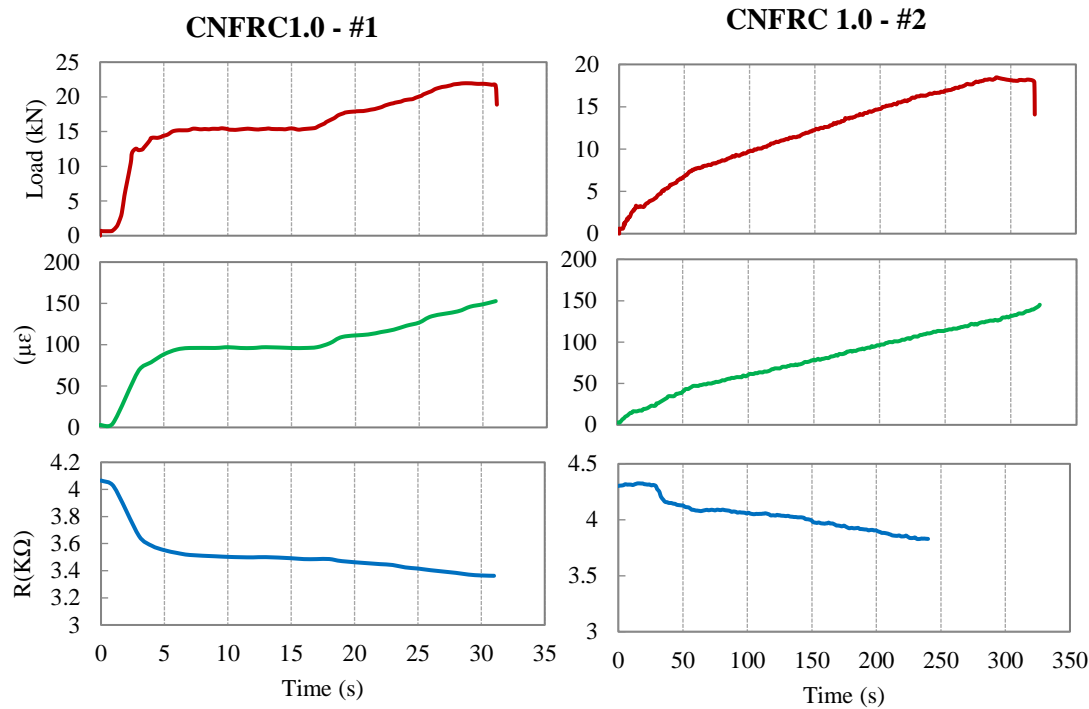


Figure 3.32. Time history results for CNFRC1.0

Considering the CNFRC0.25 results, as the load increased, the compressive strain measured by the strain gauge in the centre of the beam at the top, also increased, while the calculated resistance was decreasing inversely proportional to the strain. Both CNFRC0.5 (Figure 3.30) and CNFRC0.75 (Figure 3.31) results showed similar behaviour regarding the relationship between resistance of the material with the load and strain. The variation in resistance ( $R$ ) value was varying with strain following the same trend. The change in resistance was however in reverse to the strain. For all samples, a trend was found in which with increasing compressive strain, the resistance decreased and with decreasing compressive strain, the resistance increased. This is because under compressive stress the fibres in the concrete get closer to each other as the material is compressed, hence the conductive network becomes stronger resulting in decreased electrical resistance. On the other hand, the conductive network becomes weak either due to the fibres getting apart from each other by reducing compressive stress (for e.g. unloading specimen) or due to micro-cracks interrupting the circuit, thus the resistance increases gradually. The decrease in electrical resistance for samples can be spotted during the post-peak stage of samples that successfully reached the post-peak stage. This could be due to the development of micro-cracks during this stage.

During the testing of sample CNFRC1.0 (#2) the beam reached its highest load carrying capacity very quickly and it fractured within 30 seconds (Figure 3.32). Despite the short duration of the test, the change in electrical resistance was promptly responsive to the change in the strain. This result can confirm that the CNFRC is apt to measure rapidly varying strain responses. This also manifests the potential of CNFRC as damage sensor, by a dramatic change in the resistance, at loading instances as early as the maximum load, hence providing timely failure warnings. This phenomenon was also claimed for cement paste by Materazzi et al. (2013).

The results presented here can thus contribute to extending the known strain-sensing capability of the CNF cementitious composites to the CNF reinforced concrete (CNFRC). To better understand the relation between the strain and the electrical resistance, electrical resistance variation (ERV) is analysed for each concrete and presented in the next subsection.

### 3.9.3. Electrical resistance variation of CNFRC

Piezoresistivity of the CNFRC is expressed using fractional change in resistance also known as Electrical Resistance Variation (ERV). This would also help to better understand the effect of different dosages of CNF on the electrical sensitivity of the concrete. As explained in section 3.9.1, the initial voltage ( $V_0$ ) was recorded and the initial electrical resistance ( $R_0$ ) was calculated. Subsequent voltage values were recorded every second at the same time as the strain was recorded during the test. Therefore, each strain value, at every time point,  $i$ , had corresponding values of voltage recorded as  $V_i$ . The electrical resistance  $R_i$  and ERV were calculated as follows:

$$R_0 = V_0 / I \quad (\text{Eq. 3.4})$$

$$R_i = V_i / I \quad (\text{Eq. 3.5})$$

$$ERV = (R_i - R_0) / R_0 \quad (\text{Eq. 3.6})$$

ERV vs. strain is plotted and presented in Figure 3.33 for all concrete types. The linear function for the best fit linear trend line, correlating the ERV and the strain is also presented in this figure along with the correlation coefficient ( $R^2$ ). The correlation coefficient of the best-fit line ( $R^2$ ) to the data is a measure of the linear distribution of the data. If the data has a strong linear distribution, ( $R^2$ ) is closer to 1.

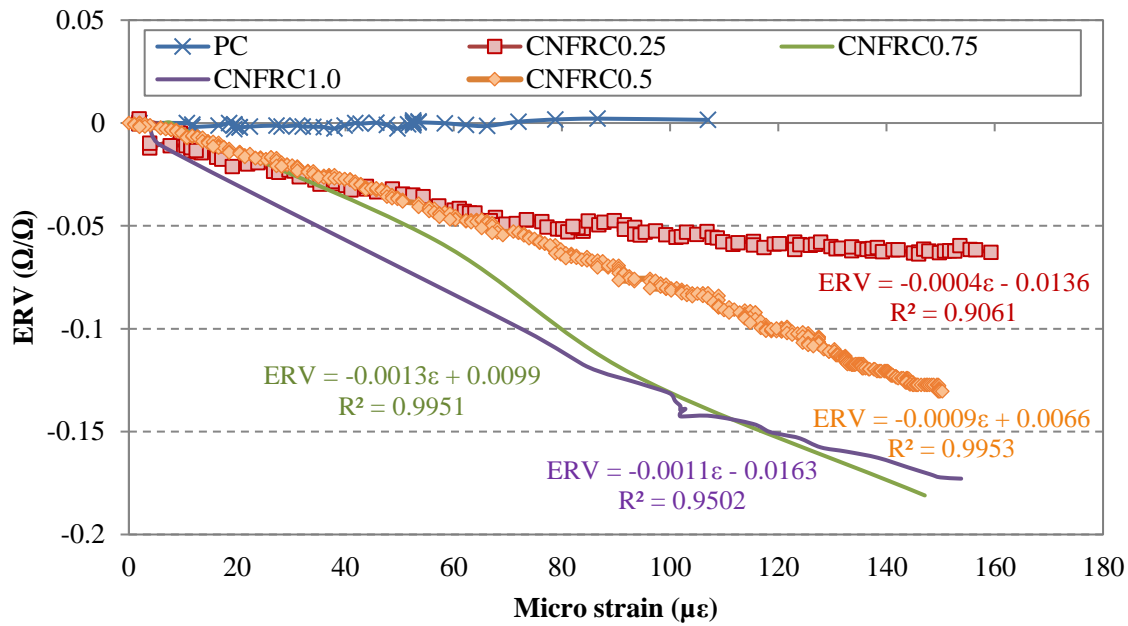


Figure 3.33. ERV vs. strain for all concrete types

From the plot above, it is apparent that when loading samples started, the strain started to increase and the absolute value of ERV increased from zero simultaneously with the strain. The ERV had negative sign since the resistance decreased under the compressive strain and the absolute value of the ERV is of importance to this discussion, henceforward the ERV sign is neglected in the magnitude comparisons. The maximum ERV for CNFRC cases occurred near the strain of  $150\mu\epsilon$ . It is evident that ERV was constant for PC, showing no variation in resistance, while it was increasing for all volume fractions of CNF as the compressive strain increased. The maximum electrical resistance variation was directly related to CNF concentration and according to the figure, it can be concluded that the tunnel conductivity effect of the CNFRC increases with increasing the fibre concentration as the maximum ERV value increased from 0.06 to 0.17 when fibre dosage increased from 0.25% to 1.0%.

The ERV versus strain relationship for CNFRC0.25 exhibited deviation from the perfect linear behaviour at a strain of about  $70\mu\epsilon$ , while other CNFRC maintained their original slope and an almost linear relationship between ERV and compressive strain could be detected for 0.5%, 0.75% and 1.0% CNFRC. This can be determined from the  $R^2$  coefficient values for CNFRCs, which was the smallest ( $R^2 = 0.902$ ) for CNFRC0.25. On the other hand, other CNF concentrations showed a very good linear correlation coefficient (i.e.  $R^2$  closer to 1).

The ERV was comparatively steady when the fibre concentration was 0.75% and 1.0% and the maximum ERV for these were 0.17 and 0.19 respectively. This was close to the values found in the literature (Gao et al., 2009) for SCC where using CNF fibres at 0.70%, 1.0% and 2.0% lead to a maximum ERV value of 0.20, 0.21 and 0.25 respectively. In another study (Camacho-Ballesta et al., 2016), the maximum ERV for 0.25% and 0.5% CNT cement paste was 0.05 and 0.14 respectively which are close to the values found in this study for 0.25% CNF ( $ERV_{max} = 0.06$ ) and 0.5% CNF ( $ERV_{max} = 0.13$ ) in concrete. The close values of the ERV for specific fibre volume fractions of these studies, considering different matrix used, could lay down the foundation of a finding which suggests that from a certain volume fraction of CNF (i.e. nanofibres) in concrete (could be any type of concrete), there exists a specific range of conductivity that can be expected from the material, subjected to satisfactory dispersion of the nanofibres. However, this hypothesis needs to be further investigated with more experiments.

In addition to ERV, the Gauge Factor (GF) of each concrete type was calculated and compared with previous literature. Gauge factor is a performance measure of a strain gauge which is defined as the electrical resistance variation (ERV) per unit strain and it can be determined by the following equation:

$$GF = \frac{(R_i - R_0)/R_0}{\varepsilon} \quad (\text{Eq. 3.7})$$

This value is a demonstration of strain sensitivity of a strain gauge and represents the slope for the resistivity versus strain curve. Gauge factor is a good indicator to show the sensitivity of the sensor as it is used in other research studies to better demonstrate the effect of conductive fillers within cementitious material. ‘The higher the GF, the more sensitive the strain gauge is’ (Teomete and Kocyigit, 2013). Therefore, in this experiment, the gauge factor was calculated and used for comparison to better understand the performance of the CNF concrete as a sensor. The GF obtained in this study is tabulated in Table 3.11 and Table 3.12 reviews previous GF found by researchers.

Table 3.11. GF for CNFRC

Concrete	CNFRC0.25	CNFRC0.5	CNFRC0.75	CNFRC1.0
GF	644.9	664.2	759.9	1264.4

Table 3.12. GF found in literature

Researcher	Nano fibres %	GF
<b>D'Alessandro et al.</b>	1.0% CNT in cement composite	130
<b>Noiseux-Lauze and Akhras</b>	0.1% CNT in cement composite	70
<b>Camacho-Ballesta et al.</b>	0.05% CNT in cement composite	240
	0.1% CNT in cement composite	180
	0.5% CNT in cement composite	140
<b>Loh and Gonzalez</b>	MWNT-based ink solution to develop thin film over cement composite surface	118
<b>Samsal et al.</b>	0.05% CNT in cement matrix	189
	0.1% CNF in cement matrix	228

From the above results, it can be observed that the GF obtained for all CNFRC in this research was higher than the previous research conducted on nanofibre cementitious composites. One reason could possibly be the higher volume fraction of fibres used in this study as well as using CNF in the matrix (instead of CNT) could have had a better effect for this purpose. Another reason could be the use of silica fume in the mixture which has previously proved to enhance the electrical properties of nanocomposites. Generally, the wide range of reported GFs is a consequence of different fibre types and properties, admixture additions, preparation methods, resistivity measurement techniques, and load testing procedures among others.

Overall, it can be concluded that the CNFRC has a self-sensing capability and it has the potential for structural health monitoring since a good correlation between resistance and strain was found.

### 3.10. CONCLUSIONS

This chapter outlined the experimental study carried out on carbon nanofibre reinforced concrete. Mechanical properties of concretes which were designed (categorised in two groups) for this study were presented. Compressive strength, split tensile strength, and flexural strength were investigated and presented for CNFRC with varying volume fraction of fibres and results were compared to plain concrete. Moreover, the self-

sensing capability of CNFRC was investigated and electrical resistance variation was studied against the applied compressive strain.

The Group A results showed that the flexural strength, split tensile, and compressive strength of concrete (with 20mm CA) was increased by 31.3%, 21%, and 7.6% respectively when 0.75% CNF was used. However, the failure of samples was very brittle. With regards to the ductility, samples with 0.5% CNF in this group showed the best performance by achieving high displacement under four-point bending. On the other hand, the results of Group B showed that CNF at dosages of 0.25%, 0.5%, 0.75% and 1.0% by binder volume could affect all mechanical properties of the concrete. It was concluded that CNFRC1.0 performs better than all other mixes in terms of enhancing the mechanical strength, while all CNFRC0.5, CNFRC0.75, and CNFRC1.0 showed good ductility under four-point flexural test.

Overall, the use of CNF as fibres within concrete was found to improve the mechanical properties of the plain concrete as well as making the concrete a smart concrete which can sense its own strain variation. It was concluded that increasing the nanofibre content of the concrete decreases the electrical resistance of the matrix. In addition, analysing the ERV of CNFRC, it was found that a linear relationship exists between the ERV and compressive strain, which has higher sensitivity at higher fibre dosage (i.e. 1.0%).

Thus, CNFRC has great potential, due to both enhanced mechanical and electrical properties, to be used in structural elements. Since it was the intention of this research to study the structural performance of CNFRC structural elements, steel-composite sandwich wall (i.e. SC wall) which was selected for this research were constructed using CNFRC. From the observed enhanced performance of the CNFRC, two materials from Group B (with improved mixing procedure and less brittle sample failure) were chosen to be used for further experimental investigation carried out on SC elements, which were CNFRC1.0 (that outperformed other samples in all aspects) and CNFRC0.5 (which showed great ductility with least damage to the sample). The next chapter will address the experimental programme for conducting the structural SC element experiments.



## CHAPTER 4

### STEEL-CONCRETE SANDWICH WALL EXPERIMENTAL PROGRAMME

---

#### 4.1. INTRODUCTION

In light of the results obtained from the previous chapter on mechanical properties of CNFRC as well as their sensing capability, the findings were noteworthy and motivated the experimental study followed in this chapter. This chapter reports on the experimental programme which was designed to study the performance of SC walls with different fibre reinforced concretes subjected to four-point flexural loading. This chapter contains the details of the experimental programme, specimen design procedure, instrumentation, specimen preparation and the test set-up.

#### 4.2. EXPERIMENTAL PROGRAMME OUTLINE

The experimental investigations in this chapter focus on the out-of-plane flexural behaviour of a typical SC wall in a structure subjected to the postulated loading. In the nuclear structure, SC walls are used in containment structures which are subjected to an internal pressure at specific sections. In such structures, the concrete thickness is typically between 600 mm to 1500 mm to provide adequate radiation shielding. In marine or offshore structures, also the SC walls are subjected to lateral loads in the form of lateral pressure. A simple rectangular compartment structure, about 8m by 8m in plan, as shown in Figure 4.1, where the sides are made from SC composite walls, was considered. The height of such structures reaches about 21m. The experimental investigation in this research focus on the structural behaviour of the compartment in the central region along the structural height, where the effects of restraint at the top and the bottom are negligible. The complete wall section can be simplified into a partial section of the wall, which simplifies the structural analysis problem to a 2D problem (Figure 4.1(b)). Furthermore, the 2D compartment section was further simplified to a

1D beam (Figure 4.1(c)), that does not account for the effects of interaction with the end walls. This simplification led to two approximations in the experimental research: (i) the beam ends were simply supported, and (ii) the effects of force/moment interaction due to the end forces and moments induced by the end walls could not be included. Therefore, in this research, samples were designated as a beam element subjected to four-point flexural loading. Eight SC beams were designed and tested as part of this research program.

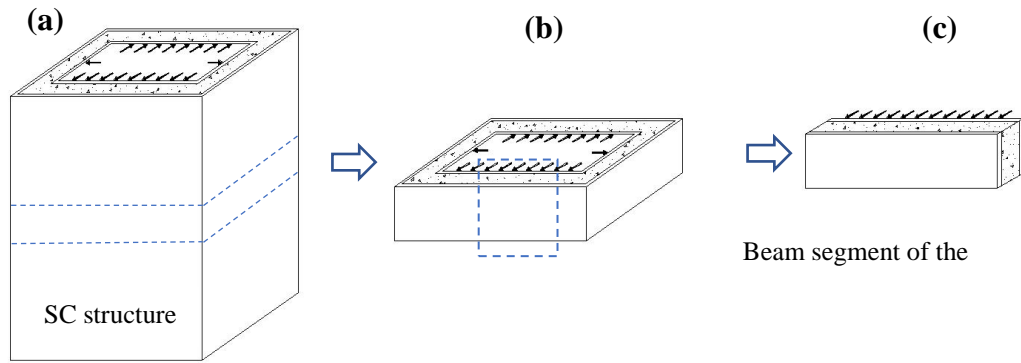


Figure 4.1. Schematic sketch of beam subsection taken from structural wall (drawing is not to scale)

Beam specimens were identified as SCB1 through SCB8. The samples were constructed and tested under four-point flexural loading. The SC sandwich beam samples used in this study consisted of two steel plates which were connected by tie bars to serve as an out of plane shear reinforcement. In this system, the plates are anchored to concrete using headed shear studs, providing composite action between concrete and steel plate. The use of tie bars connecting the plates also eases specimen handling and constructing as the beam itself acts as a mould. A schematic section of a typical SC wall is shown in Figure 4.2. All beams were intended to have identical dimensions while the type of the concrete core varied for each beam to evaluate the effect of FRC on the performance of the beam.

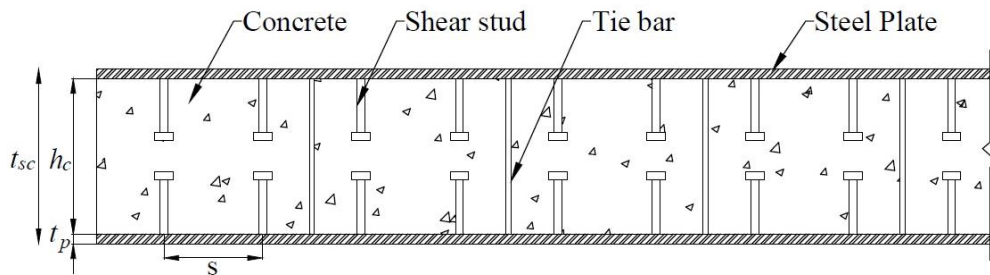


Figure 4.2. Schematic illustration of SC wall section

All eight samples were categorised into three categories (Category1 – Category3) according to their concrete core type which will be presented in section 4.4. Each beam was then prepared, tested and the results for each test were recorded. Also, for each SC beam sample, the mechanical properties of the concrete core were obtained by conducting the material test. Furthermore, investigation of self-sensing properties of SC beam concrete core was undertaken, aimed at studying the operation of smart concrete in predicting the strain induced in a structural element.

### 4.3. DESIGN OF SC BEAMS

Guidelines for designing an SC element are presented in different sources and various requirements are introduced into the design considerations as a result of experimental investigations conducted by researchers. The Japanese design code for SC walls (JEAC-4618) and the S. Korean code for SC walls (KEPIC-SNG) are the published practice codes specifically for SC walls which were not considered in this research due to inaccessibility. Primarily, Wright and Oduyemi (1991a) and Roberts et al. (1996) made some imperative and key design recommendations through experimental research on SC beams subjected to bending and transverse shearing forces. Also, other accessible resources including the report on properties and in-service performance of double skin composite construction for submerged tube tunnels (Burgan, 1997), the report on assessment of INCA steel-concrete-steel sandwich technology (Weitzenböck and Grafton, 2010), the SC wall design for nuclear facilities introduced in AISC N690-Appendix N9 (2013), EC4:1994-Design of composite steel and concrete structures, and the US code provisions ACI 349M-06 were considered. The key recommendations that were taken into account for the design of SC beams for this research are summarised as follows:

- ‘Opposite faceplates shall be connected using tie system,
- The tensile strength contribution of concrete infill to the available strength of SC wall shall be ignored,
- The reinforcement ratio should be  $0.015 < \rho = \frac{2t_p}{t_{sc}} < 0.05$ ,’ (AISC N690-Appendix N9)
- ‘For steel plates forming the skin of a sandwich panel carrying significant loads (bending, tensile, or compression) a minimum thickness of 3 mm should be used for each face,

- The tie-systems shall have spacing no greater than the section thickness.’ (INCA report, 2010)
- To avoid plate buckling:
  - $\frac{\text{Stud spacing}}{\text{Plate thickness}} = 40$ , (Wright and Oduyemi, 1991a)
  - $\frac{\text{Stud spacing in compression region}}{\text{Compression plate thickness}} \leq 40$  (Burgan, 1997)
- To avoid plate buckling around connector (Wright and Oduyemi, 1991a):
  - Stud  $\varnothing < 2 \times$  steel plate thickness; tension zone,
  - Stud  $\varnothing < 2.5 \times$  steel plate thickness; compression zone,
- To avoid shear stud pull-out of the studs (Wright and Oduyemi, 1991a):
  - Head  $\varnothing = 1.5 \times$  shank  $\varnothing$ ,
  - Head thickness =  $0.4 \times$  shank  $\varnothing$ .

To achieve a comprehensive insight into the effect of FRC on structural performance of SC beams in terms of cracking behaviour and failure mode, knowing that shear mode of failure is the one to be avoided in the structural design and with the aim of altering this failure mode by enhancing the material properties, the beam was initially designed to be shear-critical with plain concrete (with characteristic cylinder compressive strength of 55 Mpa). Therefore, the effect of FRC on enhancing the performance of a shear-critical structure could be better observed and analysed. This design was achieved by controlling the vertical shear reinforcement ratio (tie bar diameter;  $d_{\text{bar}}$ , and tie bar spacing;  $S$ ) and keeping these parameters within the range that would result in a beam with lower shear capacity than the moment capacity. The design assumptions were:

- Concrete resists no tension (AISC-Appendix N9),
- Concrete core and steel plates are fully bonded,
- Steel plates do not contribute to the transverse shear capacity.

For the design of the SC panels, four design conditions were checked and each approach is described in the following subsections. The aim was to achieve an SC beam which had higher flexural capacity than shear capacity. The analysis methods are as follows:

- ✓ Flexural resistance
  - Elastic Approach
    - *Full composite*
    - *Partial composite*

- Plastic approach
  - Full composite
  - Partial composite
- ✓ Shear resistance

#### 4.3.1. Flexural resistance of SC beam – Elastic approach – Full composite

As noted in the title of the analysis method, it is assumed that full composite action is achieved and compression plate buckling is prevented due to closely spaced shear studs, providing lateral restraint. Materials are assumed to be in elastic range and linearly distributed throughout the section. Flexural resistance can be obtained using cracked-transformed composite section (Booth, 2008; Burgan, 1997; Liew and Sohel, 2009; Varma et al., 2009). The un-cracked concrete (in compression) in the SC section is first transformed to an equivalent steel section. Based on the full interaction assumption, this is done by dividing the width of the beam by the modular ratio ( $b$ ) expressed in Eq. 4.1.

$$b = \frac{E_s}{E_c} \quad (\text{Eq. 4.1})$$

$E_s$  = Steel modulus of elasticity

$E_c$  = Concrete modulus of elasticity

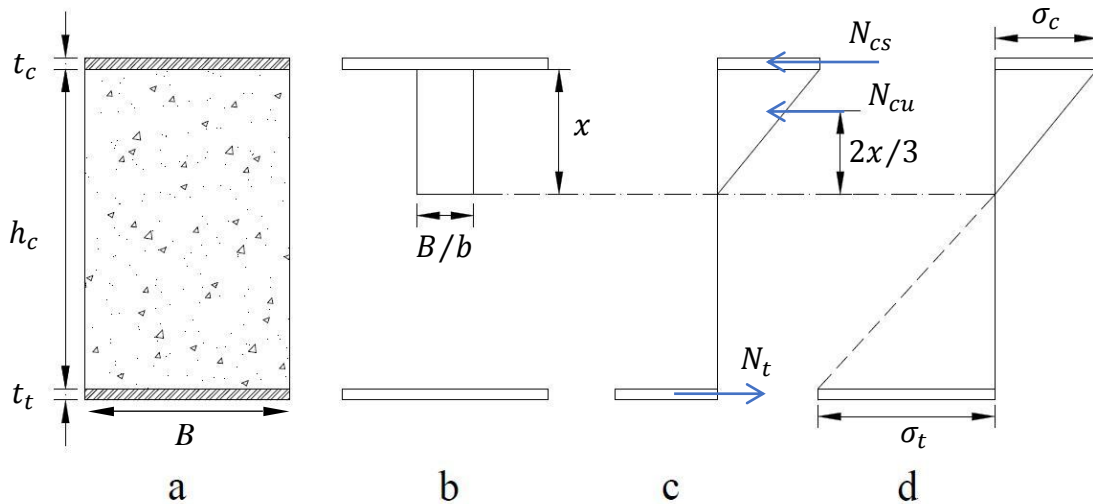


Figure 4.3. (a) SC beam section; (b) equivalent steel section; (c) forces acting in section; (d) linear stress distribution

Liew and Soheli (2009) expressed that the position of the neutral axis ( $x$ ) shown in Figure 4.3, can be determined as follows:

$$x = -b(t_c + t_t) + \sqrt{[b^2(t_c + t_t)^2 - b(t_c^2 - 2t_t h_c - t_t^2)]} \quad (\text{Eq. 4.2})$$

Taking moments about the line of  $N_{cu}$  action, the flexural resistance of the SC beam is:

$$M = \sigma_c B t_c \left( \frac{x}{3} + \frac{t_c}{2} \right) + \sigma_t B t_t \left( h_c - \frac{x}{3} + \frac{t_t}{2} \right) \quad (\text{Eq. 4.3})$$

Since the stress distribution is linear,  $\sigma_c$  and  $\sigma_t$  have the following relation:

$$\sigma_c = \sigma_t \frac{x+t_c/2}{h_c-x+t_t/2} \quad (\text{Eq. 4.4})$$

Assuming that the first yield occurs at the tension plate (i.e.  $\sigma_t = \sigma_y$ ) the moment resistance of the SC beam can be calculated substituting Eq. 4.4 in Eq. 4.3:

$$M = B t_c \left( \frac{x}{3} + \frac{t_c}{2} \right) \sigma_y \frac{x+t_c/2}{h_c-x+t_t/2} + \sigma_y B t_t \left( h_c - \frac{x}{3} + \frac{t_t}{2} \right) \quad (\text{Eq. 4.5})$$

To obtain a full composite action, an adequate number of shear studs must be provided. According to EC4: part 1.1 (6.3.2), the total shear resistance of shear connectors to the shear forces transferred by steel plates depends on the number of headed shear studs and their characteristic strength. For full composite action:

$$\text{For compression plate; } N_{cs.Rd} \leq n_c P_{Rd} \quad (\text{Eq. 4.6})$$

$$\text{For tension plate; } N_{t.Rd} \leq n_t P_{Rd} \quad (\text{Eq. 4.7})$$

Where:

$N_{cs.Rd}$  = Compression force generated in compression plate

$n_c$  = Number of connectors in the compression plate between the position of maximum moment and the support or the point of contraflexure.

$N_{t.Rd}$  = Tension force generated in tension plate

$n_t$  = Number of connectors in the tension plate between the position of maximum moment and the support or the point of contraflexure.

$P_{Rd}$  = Design shear resistance of welded headed stud connectors which is the lesser of (BS EN 1994-1-1:2004):

$$P_{Rd} = 0.8 \sigma_u \left( \frac{\pi d^2}{4} \right) / \gamma_v \quad (\text{Eq. 4.8})$$

$$P_{Rd} = 0.29 \alpha d^2 \sqrt{(f_{ck} E_{cm})} / \gamma_v \quad (\text{Eq. 4.9})$$

$\sigma_u$  = Ultimate tensile strength of shear studs

$d$  = Diameter of the stud shank

$f_{ck}$  = Characteristic cylinder strength of concrete

$E_{cm}$  = Secant modulus of concrete

$$\alpha = 0.2 (h_s/d + 1) \quad \text{for } 3 \leq h_s/d \leq 4$$

$$= 1.0 \quad \text{for } h_s/d > 4$$

$h_s$  = Overall height of the stud.

$\gamma_v = 1.25$ ; is the partial safety factor for connector recommended by BS EN 1994-1-1:2004.

Satisfying Eq. 4.6 and Eq. 4.7 means that the studs are providing enough shear strength to resist the force generated in compression and tension plates respectively and full bond is achieved.

#### 4.3.2. Flexural resistance of SC beam – Elastic approach – Partial composite

Reducing number of studs to less than required number of studs for full composite action will result in a partially composite beam. Thus, the moment resistance is reduced due to less number of connectors compared to the full composite case. The maximum tensile force and tensile stress at the tension plate with partial composite are:

$$N_{t.Rd(\max)} = n_t P_{t.Rd} \quad (\text{Eq. 4.10})$$

$$\sigma_t = n_t P_{t.Rd} / B t_t \quad (\text{Eq. 4.11})$$

Substituting Eq. 4.11 into Eq. 4.4 and substituting the result into Eq. 4.3, the moment resistance for a partially composite beam can be calculated as follows:

$$M = n_t P_{t.Rd} \left[ \left( \frac{t_c}{t_t} \right) \left( \frac{x+t_c/2}{h_c-x+t_t/2} \right) \left( \frac{x}{3} + \frac{t_c}{2} \right) + \left( h_c - \frac{x}{3} + \frac{t_t}{2} \right) \right] \quad (\text{Eq. 4.12})$$

#### 4.3.3. Flexural resistance of SC beam – Plastic approach – Full composite

In this approach, the plastic moment resistance is determined by assuming (EC4-part 1.1):

- i. A rectangular stress block of depth  $x_c$  for the concrete (Figure 4.4), where  $x$  is the depth of the plastic neutral axis from the interface of the compression plate and the concrete,
- ii. The concrete beneath the plastic neutral axis does not contribute to the resistance of the section,
- iii. The forces in the steel plates depend on the material yield strength and on the strength of the shear connectors to transfer the shear loads from the steel plates to the concrete core,
- iv. No local buckling in compression plate.

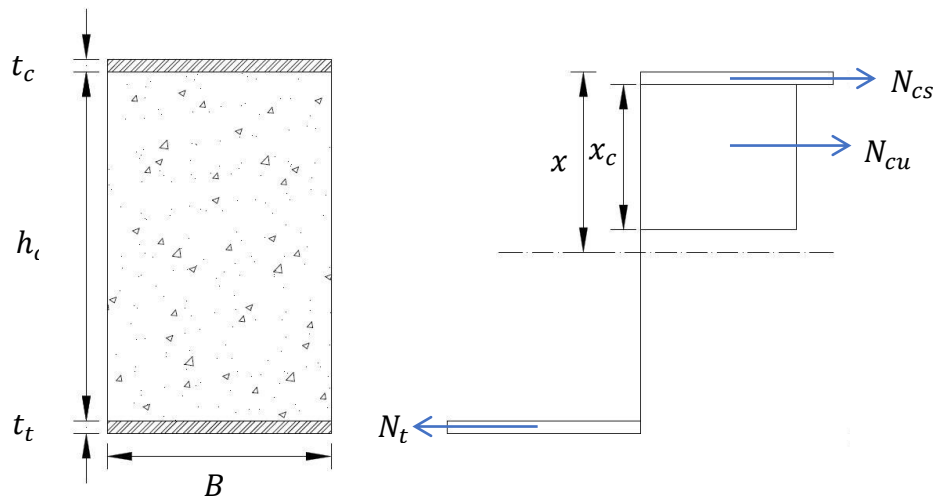


Figure 4.4. Force distribution in SC section - fully plastic stage

As stated in BS EN 1992-1-1:2004 the compressive force in concrete is:

$$N_{cu.Rd} = \frac{0.85f_c}{\gamma_c} B x_c \quad (\text{Eq. 4.13})$$

By satisfying the equilibrium condition and equating the tensile and compressive forces, the plastic neutral axis depth ( $x$ ) can be determined:

$$N_{t.Rd} = N_{cs.Rd} + N_{cu.Rd} \quad (\text{Eq. 4.14})$$

$$N_{cs.Rd} = \sigma_y B t_c \quad (\text{Eq. 4.15})$$

$$N_{t.Rd} = \sigma_y B t_t \quad (\text{Eq. 4.16})$$

Substituting Eq. 4.13, Eq. 4.15, and Eq. 4.16 in Eq. 4.14, gives:



$$x_c = 1.176\gamma_c\sigma_y(t_t - t_c)/f_c \quad (\text{Eq. 4.17})$$

Taking the moments about the centre of the compression steel plate, the plastic moment of resistance of the section is:

$$M_{pl} = N_{t.Rd} \left( h_c + \frac{t_t}{2} + \frac{t_c}{2} \right) - N_{cu.Rd} \left( 0.5x_c + \frac{t_c}{2} \right) \quad (\text{Eq. 4.18})$$

The moment capacity is reached when the neutral axis moves near to lower surface of the compression plate (i.e.  $x_c = 0$ ) and the tension steel plate is fully yielded. If the two faceplates have the same thickness (i.e.  $t_c = t_t = t$ ), therefore, from Eq. 4.18 the plastic moment of resistance can be written as:

$$M_{pl} = N_{t.Rd}(h_c + t) \quad (\text{Eq. 4.19})$$

#### 4.3.4. Flexural resistance of SC beam – Plastic approach – Partial composite

If the longitudinal forces in steel plates;  $N_{t.Rd}$ (tensile force) and  $N_{cs.Rd}$ (compressive force) are controlled by the shear connector capacity, the SC beam is termed as partially composite and the reduced number of shear connectors, correspondingly reduces the moment resistance. Substituting Eq. 4.13 in Eq. 4.14, the depth of the plastic neutral axis becomes:

$$x_c = 1.176\gamma_c(N_{t.Rd} - N_{cs.Rd})/Bf_c \quad (\text{Eq. 4.20})$$

The tensile force in tension steel plate is:

$$N_{t.Rd} = n_p P_{t.Rd} \quad (\text{Eq. 4.21})$$

Taking into account the reduced tensile force in steel plate given by Eq. 4.21 and the new plastic neutral axis depth (Eq. 4.20) and substituting in Eq. 4.18, the moment resistance for partial composite is given by:

$$M_{pl} = n_p P_{t.Rd} \left( h_c + \frac{t_t}{2} + \frac{t_c}{2} \right) - \left( \frac{0.85f_c}{\gamma_c} B x_c \right) \left( 0.5x_c + \frac{t_c}{2} \right) \quad (\text{Eq. 4.22})$$

If the two faceplates have the same thickness (i.e.  $t_c = t_t = t$ ), Eq.4.21 becomes:

$$M_{pl} = n_p P_{t.Rd}(h_c + t) \quad (\text{Eq. 4.23})$$

#### 4.3.5. Shear resistance of SC beam

Tie bar systems in SC beam serve as out-of-plane shear reinforcement (or transverse shear reinforcement). Two different methods are presented in the literature for calculating the shear resistance of SC cross-section. First, the overall out-of-plane shear strength ( $V_u$ ) for SC section that is only subjected to flexure and shear can be conservatively estimated from provisions given for shear strength of reinforced concrete beams (EC2, ACI 349M-06) which is the total of the shear resistance of the concrete core ( $V_{cd}$ ) and the shear resistance of the tie bars ( $V_{sd}$ ). This method is also suggested by INCA (2010), AICS-N9 (2013), and Liew and Soheli (2009) which is as follows:

$$V_u = V_{cd} + V_{sd} \quad (\text{Eq. 4.24})$$

Where according to EC2:

$$V_{sd} = 0.9 h_c \frac{A_s}{S} f_{ys} \quad (\text{Eq. 4.25})$$

$A_s$  = Cross sectional area of transverse shear reinforcement

$f_{ys}$  = Yield strength of transverse shear reinforcement

$S$  = Tie bar spacing

And;

$$V_{cd} = [C_c k_c \eta_1 (100 \rho_1 f_{ck})^{1/3}] B h_c \quad (\text{Eq. 4.26})$$

$$k_c = 1 + \sqrt{200/h_c} \leq 2.0,$$

$$\rho_1 = \frac{t_t}{h_c},$$

$$C_c = \frac{0.18}{\gamma_c},$$

$$\eta_1 = 0.4 + 0.6 \rho / 2200 \leq 1.0; \rho \text{ is the concrete density in kg/m}^3$$

Second approach to determine the shear resistance according to Burgan (1997) and Roberts et al. (1996) is:

$$V_{pl.Rd} = \tau_{Rd} B h_c \quad (\text{Eq. 4.27})$$

$$\tau_{Rd} = \frac{f_{ck}}{20 \gamma_c} + \frac{0.5 n_0 A_s f_{ys}}{B S \gamma_a} \quad (\text{Eq. 4.28})$$

$\tau_{Rd}$  = Nominal transverse design shear resistance

$n_0$  = Number of tie bars across SC section acting as transverse reinforcement

$f_{ys}$  = Ultimate tensile strength of tie bars

$\gamma_a = 1.15$  is the partial safety factor for steel recommended by BS EN 1994-1-1:2004

The factor 0.5 in the second term of Eq. 4.27 is due to the unlikeliness of mobilising the full resistance of the concrete and stud connectors simultaneously. Moreover, the contribution of the steel plates is relatively small and neglected in this formula.

Two other formulas (Eq. 4.29 and Eq. 4.30) which are an empirical formula obtained by Adams & Zimmerman (1987) were suggested for the calculation of the shear strength which takes into account the presence of the steel plates by including the tension plate reinforcement ratio ( $\rho$ ). The second formula (Eq. 4.30) is also used by McKinley (2002) to calculate the shear resistance of a double skin composite slab. These formulas are:

$$V_u = \frac{3.39 \times f_c^{0.8} \times B \times d \times \rho^{0.54}}{(a/d)^{1.29}} \quad (\text{Eq. 4.29})$$

$d$  = Beam depth (mm)

$\rho$  = Reinforcement ratio (tension plate)

$a$  = Shear span (mm)

And;

$$V_u = \frac{1.35 \times f_c^{0.8} \times B \times d \times \rho^{0.5}}{(a/d)^{1.3}} \quad (\text{Eq. 4.30})$$

$d$  = Depth between the centroid of steel plates (mm)

$\rho$  = Connection ratio (connector shear strength/steel plate tensile strength)

$a$  = Shear span (mm)

#### 4.3.6. Designed SC beam capacity

The results of moment capacity and shear capacity of the designed control beam (SCB1) with plain concrete are shown in Table 4.1. According to the calculations for the SC beam with plain concrete (PC) with cube compressive strength of 50 MPa, the load level (2P, Figure 4.5) at which shear capacity of the beam is reached, was lower than that at which the moment capacity is reached. Therefore, the beam was shear critical and shear failure was the expected mode of failure.

Table 4.1. Moment capacity and shear capacity of the designed control SC beam (SCB1) with PC

Moment capacity				
Analysis Method	Elastic		Plastic	
	Full composite	Partial composite	Full composite	Partial composite
Moment (kNm)	39.1	28.7	41.7	30.5
$2P = 2 \times M/a$ (kN)	173.7	127.6	185.3	135.6
Shear capacity				
Formula	$V = V_{cd} + V_{sd}$	$V_{pl.Rd} = \tau_{Rd} B h_c$	$V_u = \frac{3.39 \times f_c'^{0.8} \times B \times d \times \rho^{0.54}}{(a/d)^{1.29}}$	$V_u = \frac{1.35 \times f_c'^{0.8} \times B \times d \times \rho^{0.5}}{(a/d)^{1.3}}$
P (kN)	42.7	48.4	55.1	57.9
2P (kN)	85.4	96.8	110.1	115.8

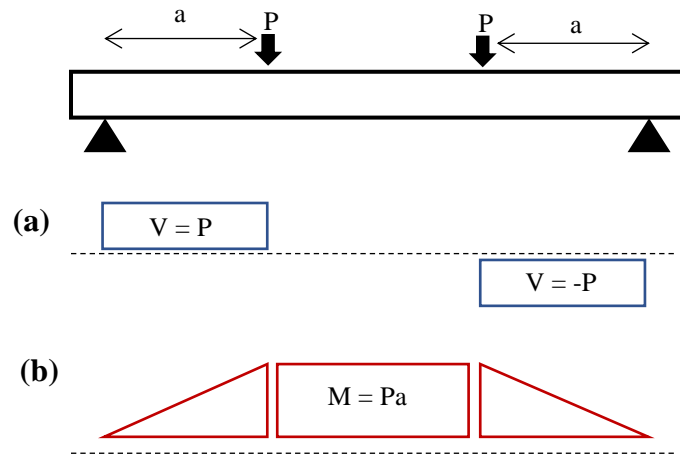


Figure 4.5. (a) Shear diagram; (b) moment distribution diagram for simply supported beam under four-point bending

#### 4.4. SC BEAM LAYOUT

The final designed beam was fabricated by Arromax Structures Limited. The tie bars ( $\phi = 6$  mm) and shears studs ( $\phi = 10$  mm) were welded to two steel faceplates according to the designed dimensions. Specification of SC beam layout and its components are shown in Figure 4.6 and geometrical details are presented in

Table 4.2. The fabricated SC beam by the manufacturer prior to concrete casting is shown in Figure 4.7.

Table 4.2. SC beam design parameters

Parameter	Dimension	Description of the parameter
B	120	Plate width (mm)
$t_p$	5	Plate thickness (mm)
$h_c$	220	Concrete core thickness (mm)
$t_{sc}$	230	Overall SC thickness = $h_c + (2 \times t_p)$ (mm)
$s$	180	Stud spacing (mm)
S	180	Tie bar spacing (mm)
$\rho$	4.3%	Reinforcement ratio = $2t_p/t_{sc}$
$d_{stud}$	10	Diameter of shear stud (mm)
$L_{stud}$	80	Length of shear studs (mm)
$d_{bar}$	6	Diameter of tie bar (mm)
$f_{ys}$	309	Yield strength of steel plate (MPa)
$\epsilon_{y-plate}$	1545	Yield strain of the steel plates ( $\mu\epsilon$ )
Plate elongation	35%	Plate elongation
$f_{us}$	457	Ultimate strength of steel plate (MPa)
$f_{y-stud}$	350	Yield strength of shear stud (MPa)
$f_{u-stud}$	450	Ultimate strength of shear studs (MPa)
$f_{y-bar}$	385	Yield strength of tie bars (MPa)
$f_{u-bar}$	495	Ultimate strength of tie bars (MPa)
$\epsilon_{y-bar}$	1925	Yield strain of the tie bars ( $\mu\epsilon$ )
Tie bar elongation	15%	Tie bar elongation

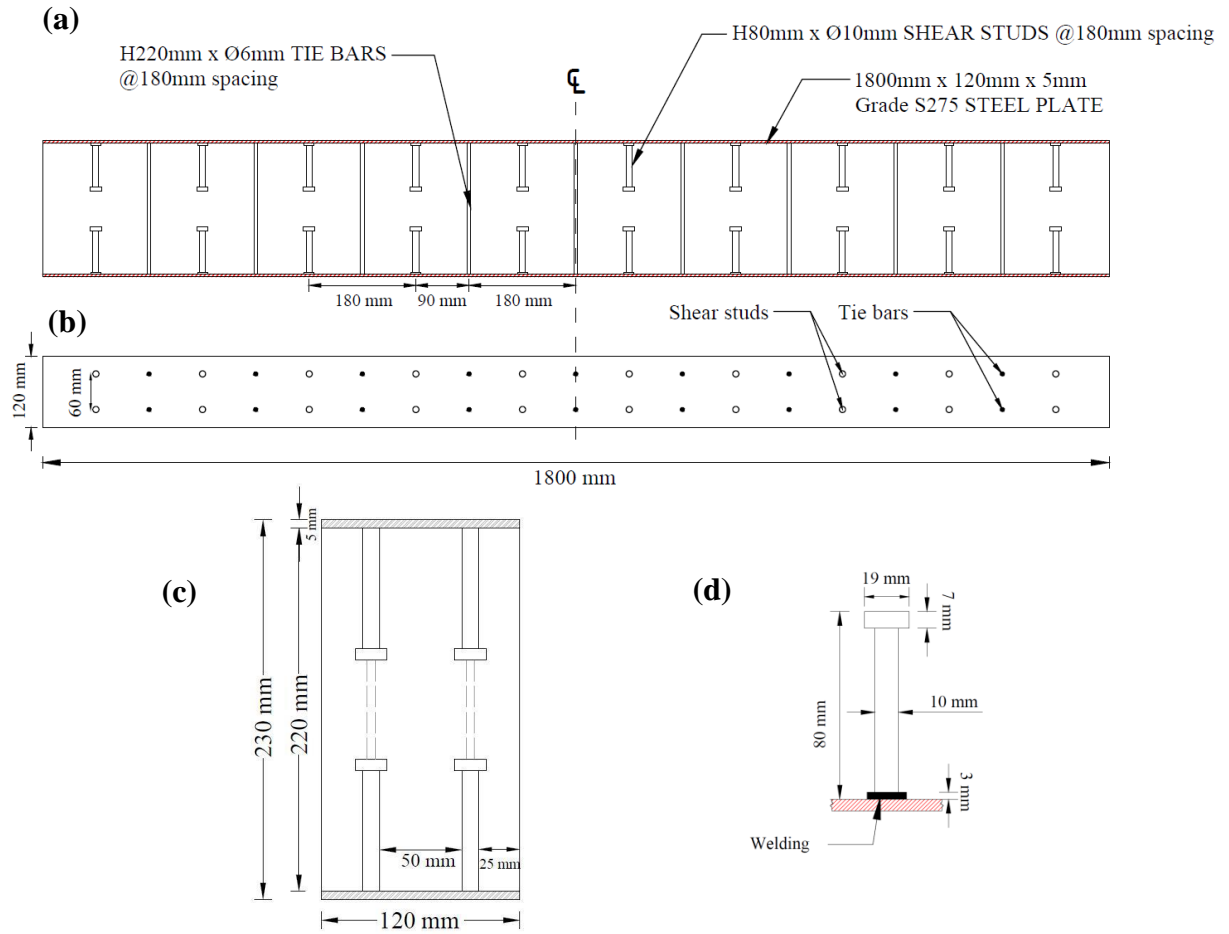


Figure 4.6. SC beam dimensions: (a) SC beam elevation; (b) shear stud and tie bar layout on both steel plates; (c) SC beam section; (d) shear stud details



Figure 4.7. SC beam as received from fabricator prior to concrete cast

#### 4.5. MATERIALS

To address the aim of this study on the effect of FRC on the structural performance of SC wall systems, SC beam elements were prepared for experiment with fibre reinforced concrete (FRC) core. The FRC consisted of single FRC, and hybrid FRC, in which a combination of macro and nano-scale fibres was used. The use of hybrid FRC was aimed at further clarifying the effect of fibres of different scales (nano and macro) on the structural performance of the SC beam.

To make up the hybrid FRC in this study, and to accompany the nanofibre (CNF) studied in this research, the well-known and most researched macro fibre was selected. Steel fibre has been studied extensively for the past decades and used in the industry, therefore, this type of fibre which was promising to be an efficient fibre in improving both material properties of concrete and structural performance of concrete elements was used as the macro fibre for this experimental investigation. Also, one control sample was constructed with plain concrete for comparison purposes. All concrete types used for the beams are summarised in Figure 4.8. Each material is further explained in the following subsections.

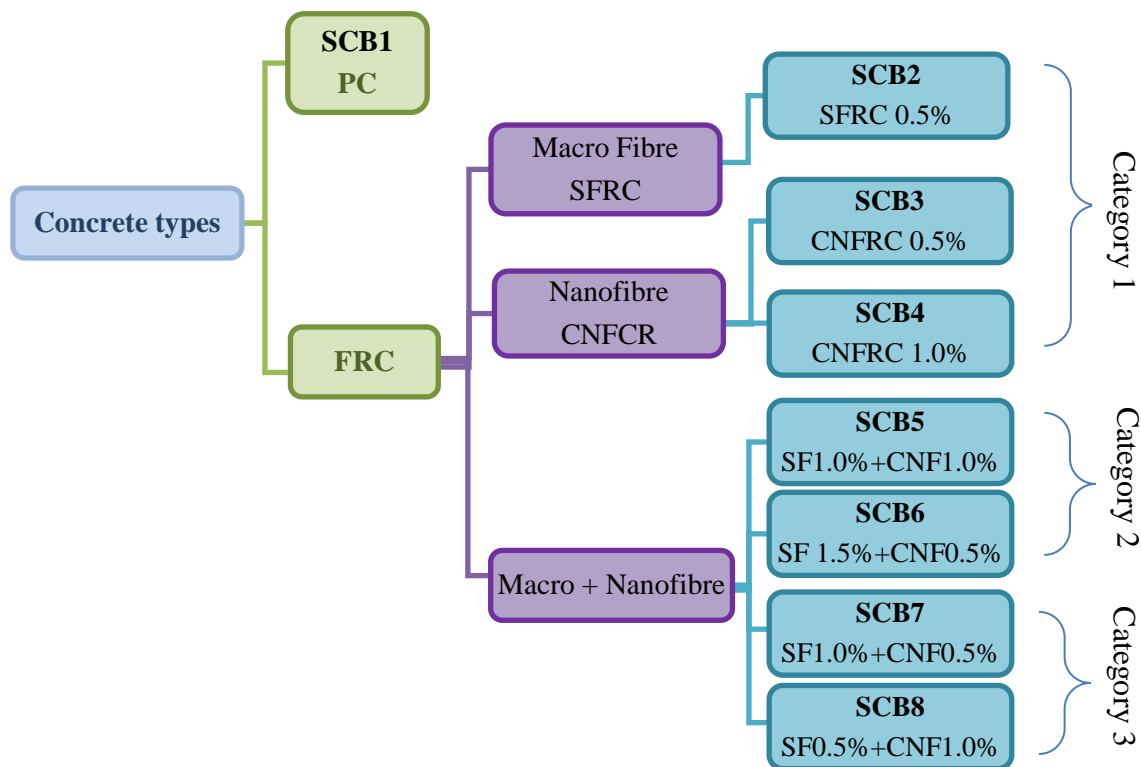


Figure 4.8. Concrete types used for SC beam experiments

#### 4.5.1. PC

The concrete mix proportion was adopted from the previously developed mixture of plain concrete similar to *Group B* presented in the previous chapter. Mix proportions and constituents are presented in Table 4.4 at the end of this section.

#### 4.5.2. SFRC

The SFRC beam was constructed using end-hooked steel fibres. This type of steel fibre is commonly used in the industry due to its success in bridging the cracks and enhancing mechanical properties of the concrete. This type of fibre was chosen for this research since according to the previous research conducted (Bazgir, 2016), using end-hooked fibres showed great improvement in all mechanical properties of the concrete. Bazgir (2016) reported an enhancement of 7% and 25.2% in the flexural strength of concrete with 0.5% and 1.0% steel fibre dosage respectively. Also, the split tensile strength was enhanced by 22% and 53% correspondingly. Thus, end-hooked steel fibres were selected for the experimental programme of this research.



The fibres were supplied under commercial name Dramix 4D by Bekaert Maccaferri. The geometry of the end-hooked steel fibre used is illustrated in Figure 4.9. These fibres are originally glued together for mixing purposes to prevent fibre balling during the mixing process. The glue is water sensitive and the fibres will break up into individual fibres and will spread throughout the concrete mix providing a homogenous fibre reinforced concrete. In the case of SFRC, the steel fibres were added to the mix before the water was introduced to the mix and mixed well with the constituents and then the water was added at the last stage. The fibres had the nominal properties tabulated in Table 4.3. The volume fraction ( $V_f$ ) of steel fibre used was 0.5% by volume of concrete. Refer to Table 4.4 for mix proportions.



Figure 4.9. End-hooked steel fibre used in SFRC



Table 4.3. End-hooked steel fibre properties

Fibre properties	Length (l) 	Diameter (d) 	Aspect ratio (l/d)	Tensile strength	Young's Modulus
End-hooked steel fibre	35 mm	0.55 mm	65	1800 MPa	200 GPa

#### 4.5.3. CNFRC

For the preparation of the CNFRC, the same CNF that was chosen for this study was used (i.e. Pyrograf-III PR-19-XT-LHT) as it was received from the supplier (Table 3.2). The same method was followed for dispersion of nanofibres as explained in section 3.3.4. The fibres were initially dispersed in Water+HRWR solution using sonication method, and then the final aqueous solution was mixed with concrete mixture during mixing procedure. CNF contents used were at volume fractions of 0.5% (CNFRC0.5) and 1.0% (CNFRC1.0) by binder volume. Refer to Table 4.4 for mix proportions.

#### 4.5.4. Hybrid FRC (SF+CNF)

This selection of FRC is concerned with the effect of fibres at two different scales of macro and nano size. This is primarily because fibres depending on their size act at different scale and have different role in enhancing mechanical properties of the concrete. This issue has not been studied at the structural level yet, and only a few studies (e.g. Peyvandi et al., 2013) have conducted material tests on the use of fibres at two scales in concrete including nano size fibres. Therefore, it was intended to analyse the use of both fibres in concrete mixture. Total fibre dosage used was 1.5% and 2.0% with various combination of nano and macro fibre concentrations as shown in Figure 4.8. Classification of fibres according to Mehta and Monterio (2014) based on their volume fraction is:

- Low volume fraction (<1%)
- Moderate volume fraction (> 1% and < 2%)
- High volume fraction (> 2%)

In this study, low to moderate volume fractions of steel fibres were used at 0.5%, 1.0%, and 1.5% loadings in combination with 0.5% and 1.0% volume fraction of CNF.

#### 4.6. SC CONCRETE CORE MIX PROPORTIONS

Concrete was prepared in a single batch for each beam specimen labelled SCB1 through SCB8. For each batch, 6 cubes and 6 cylinders were also prepared. Uniaxial compression tests were performed on cubes at the age of 14 days and 28 days (i.e. SC beam testing day) as described in section 3.4.1 to quantify the compressive strength of the concrete core, whereas split tensile test was performed on cylinders at the age of 14 days and 28 days (i.e. SC beam testing day) following the test method described in section 3.4.2 to quantify the tensile strength of concrete core. The same concrete mix proportions were used for all concrete types, however, due to using different fibres at different dosages the workability of the mixture was influenced depending on the fibre  $V_f$ , therefore, the workability was enhanced after the slump test, by adjusting water demand whenever needed. The mix proportions for each SC beam are shown in Table 4.4. The mixing method used was unique to which was found more operative (for Group B materials) in previous experimental programme discussed in Chapter 3.

Table 4.4. Mix proportions for SC beam samples (per m<sup>3</sup> of concrete)

SC Beam Sample	Fibre				HRWR  (kg)	CA  (kg)	FA  (kg)	Binder (B)		W/B	Slump  (mm)
	SF		CNF					C  (kg)	Silica Fume  (kg)		
	$V_f$ (%)	kg	$V_f$ (%)	kg							
SCB1	-	-	-	-	2	918	955.5	360	36	0.30	80
SCB2	0.5	39	-	-	2	918	955.5	360	36	0.30	30
SCB3	-	-	0.5	1.26	2	918	955.5	360	36	0.29	90
SCB4	-	-	1.0	2.5	2	918	955.5	360	36	0.29	95
SCB5	1.0	78	1.0	2.50	2	918	955.5	360	36	0.32	46
SCB6	1.5	117	0.5	1.26	2	918	955.5	360	36	0.39	54
SCB7	1.0	78	0.5	1.26	2	918	955.5	360	36	0.32	50
SCB8	0.5	39	1.0	2.5	2	918	955.5	360	36	0.32	40

Notation: B: binder (cement + silica Fume), CA=coarse aggregate, FA= fine aggregate, C=Cement, CNF= carbon nanofibre, HRWR= high range water reducer, W= water.

## 4.7. SPECIMEN PREPARATION

The beam sample preparation process before conducting the test is summarised below:

- i. Attaching tie bar strain gauges,
- ii. Placing and fixing electrodes inside the beam (if applicable),
- iii. Placing the SC beam in the wooden mould,
- iv. Mixing and casting concrete and curing samples for 28 days,
- v. Attaching steel and concrete strain gauges on the steel plate and concrete surface,
- vi. Loading beam into test frame and prepare the test set-up,
- vii. Conducting the test.

### 4.7.1. Instrumentation

Strain gauges were used for monitoring strain during the test both inside and on the surface of the beam. Small steel strain gauge FLK-6-11 (6mm long, with a resistance of  $120\Omega$  and a gauge factor of 2.12) provided by Techni Measure were affixed on tie bars and the bottom plate at different locations as shown in Figure 4.10. Also, concrete strain gauge PL-60-11, provided by Techni Measure was used for measuring concrete compressive strain at the top-centre of the beam. Total of 16 strain gauges were attached to tie bars located in the shear span (2 gauges on 8 tie bars: one at  $1/4^{\text{th}}$  of the tie bar length from the top and the other at  $1/4^{\text{th}}$  of the tie bar length away from bottom) and total of 6 gauges were attached to outer surface of the bottom steel plate.

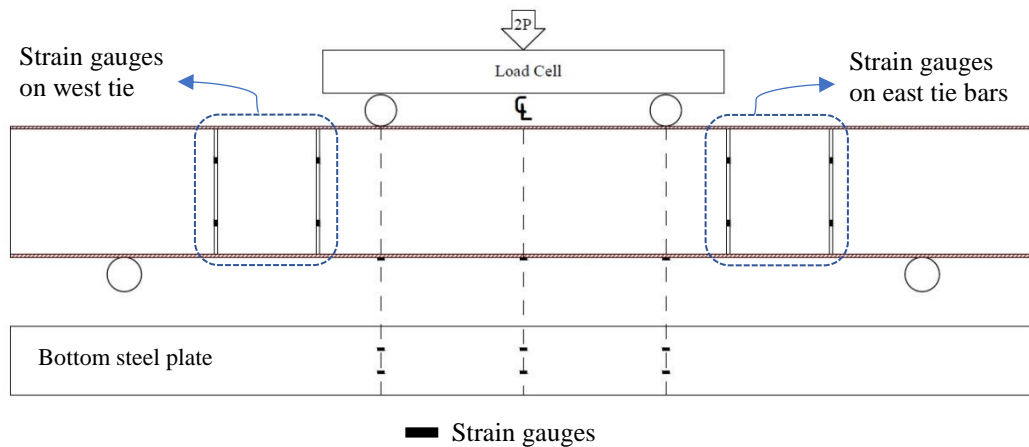


Figure 4.10. Location of steel strain gauges

Initially, the surfaces of the tie bars were smoothed with three different grades of sandpaper. The smooth surface was then cleaned with acetone to remove any dirt particles from the surface (Figure 4.11). The gauges were then attached in position using superglue. Terminals with appropriate size, matching the gauge size, were glued beneath each gauge. Gauge wires were soldered to the terminal along with wires to be connected to the data logger. The gauges were then covered with a thick layer of rubber sealant to protect gauges during casting and prevent any damage that might happen when in contact with concrete. The resistance of each gauge was then measured separately through the attached wires by a multimeter, to ensure the measured resistance was identical to the resistance of the gauge itself. This check was also done after concrete casting to examine the intactness of the gauges. The procedure of attaching the strain gauges to the tie bars is shown in Figure 4.12.

Each wire connected to a strain gauge was numbered and annotated from G1 to G24 to collect data accordingly. G1-G16 represents gauges on tie bars within the SC beam, G17-G22 represents the strain gauges of the bottom steel plate and G23 represents the concrete gauge. The position of steel strain gauges and their numberings are illustrated in Figure 4.13 and Figure 4.14. This arrangement was consistent for all of the beams.



Figure 4.11. Tie bar: (a) before surface sanding; (b) after surface sanding.

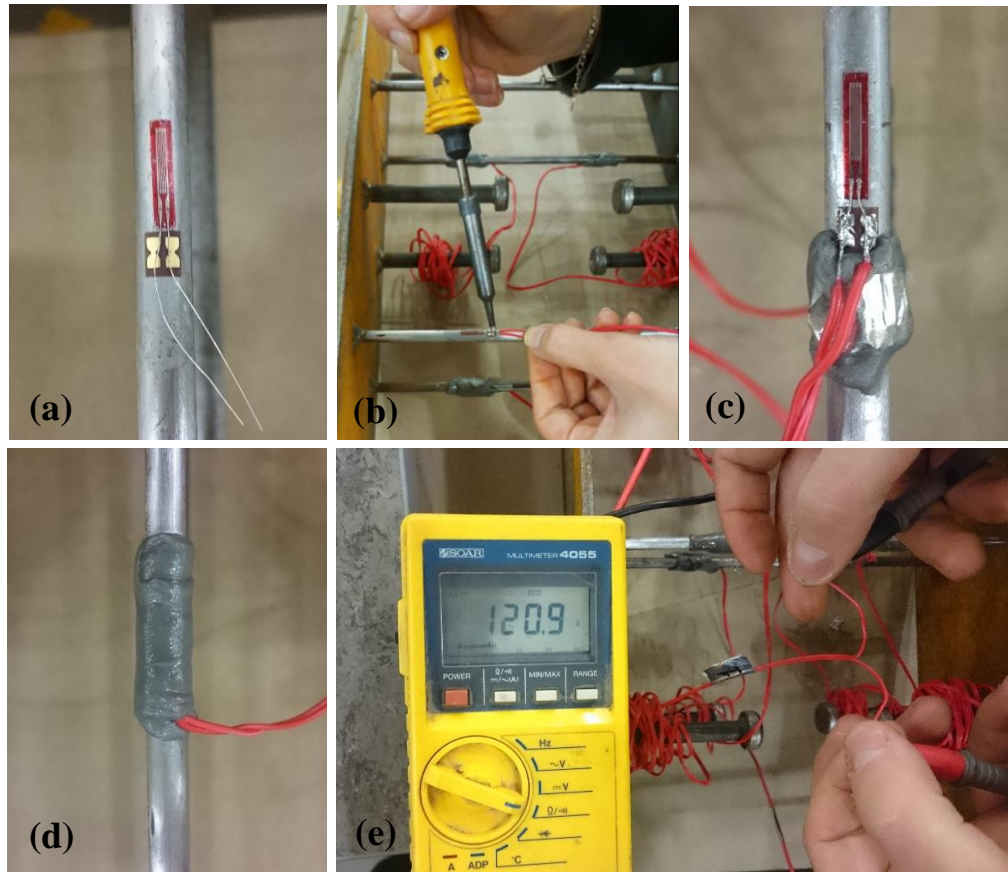


Figure 4.12. Strain gauge attachment to tie bar: (a) gauge and terminal glued to the tie bar; (b) soldering the wires to the strain gauge; (c) wired strain gauge; (d) covering strain gauge with rubber material; (e) measuring gauge resistance.

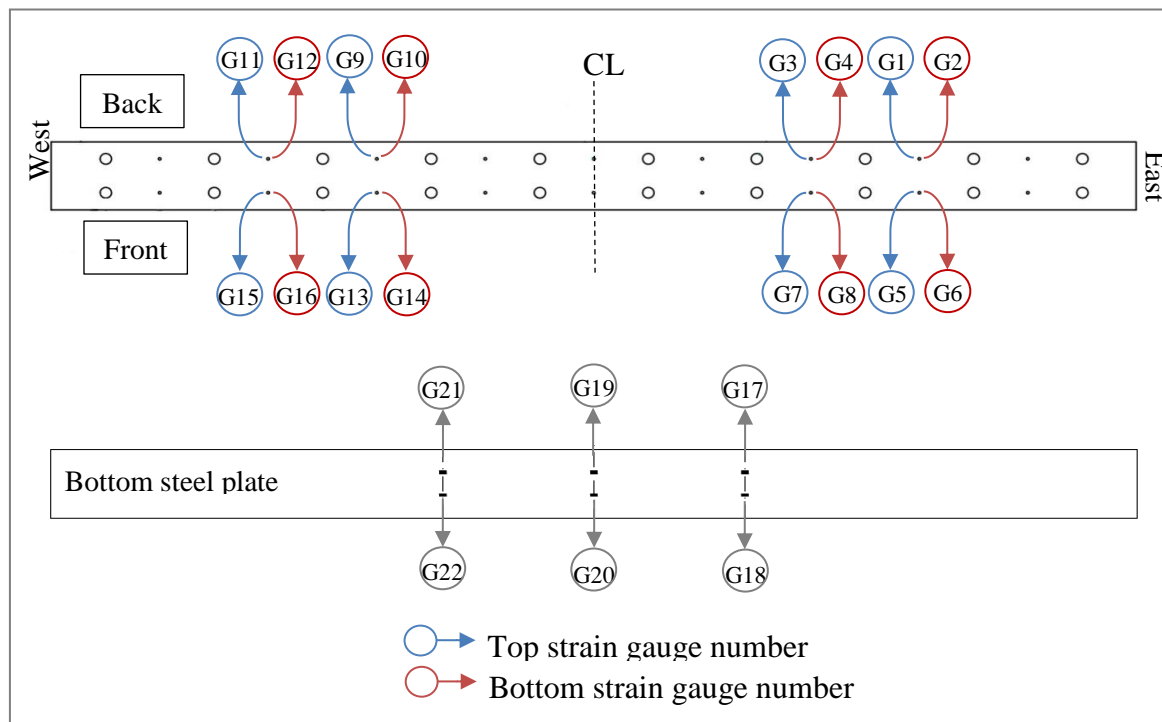


Figure 4.13. Strain gauge wire numbering map

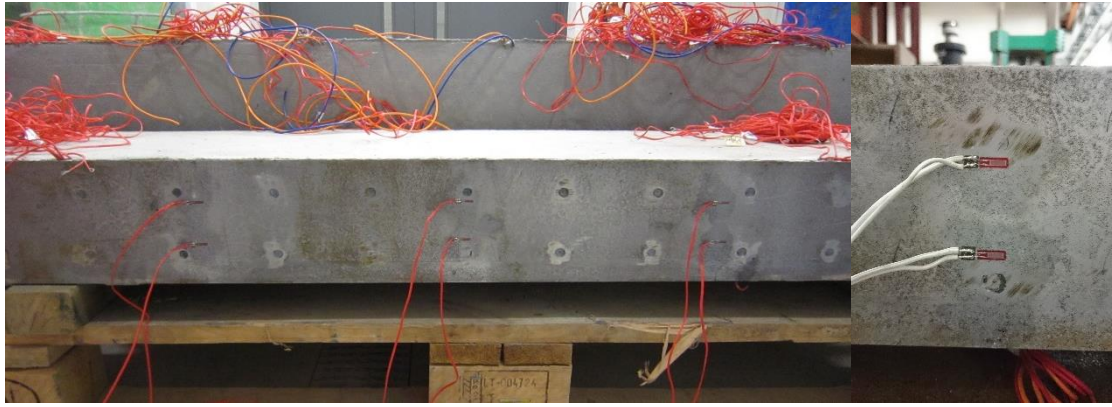


Figure 4.14. Strain gauges attached to the bottom steel plate

#### 4.7.2. Self-health monitoring test set-up

As part of this study, the aim was to study the self-strain sensing and self-damage sensing property of the nanoconcrete. To further understand the behaviour of such smart concrete in a structural element, SCB3 to SCB8, which were reinforced with CNFs, were studied for self-health monitoring capability of the concrete. For this purpose, the electrical resistance of SC beam concrete core at three different locations was monitored. The direct-current two-probe method, in which only two poles are embedded in the matrix was used. This method was chosen against the four-probe method because it was more feasible to place the electrodes within the beam due to space limitations. Adopting this method, two poles of 40mm×40mm copper wire mesh (#16) with 1.233mm aperture, and 0.355mm wire diameter were used and they acted as both current electrode and voltage electrode. Constant DC was applied to the electrode well ahead of loading the beam so as to allow the resistance to plateau off due to complete polarization and eliminate the effect of polarization on the electrical resistance response during loading. The voltage between the two poles (concrete voltage) was recorded throughout the test with the data logger and the electrical resistance of the material was then calculated according to Ohm's law ( $R=V/I$ ).

Two copper wires were soldered to each copper mesh (Figure 4.16). The red and blue wires were connected to the positive (+) and negative (-) poles of a power supply to generate the constant current between the two meshes. To measure the voltage between the two poles, orange wires were connected to channels logged into the data logger which was connected to a PC, automatically recording the voltage value every 1 second.



As demonstrated in Figure 4.15, the two copper electrodes were located parallel to each other to create the electrical circuit within the concrete. The connection of wires to the power supply prior to testing is shown in Figure 4.17.

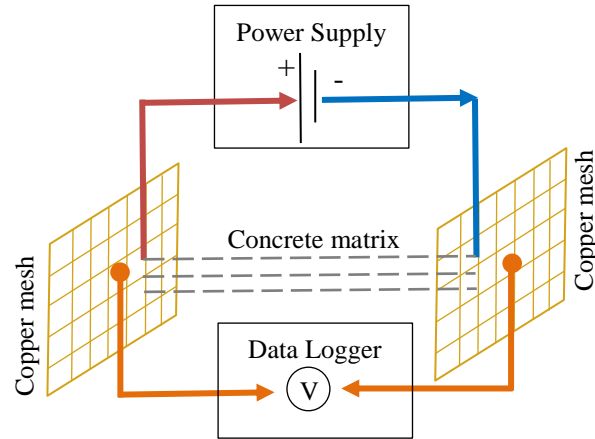


Figure 4.15. Schematic illustration of two probe method adopted in SC beam experiment

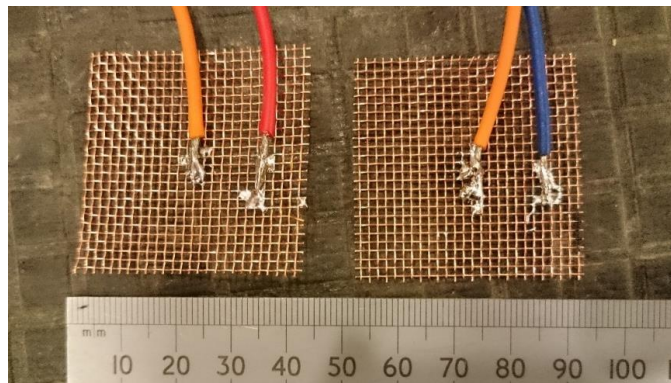


Figure 4.16. Copper mesh electrode poles

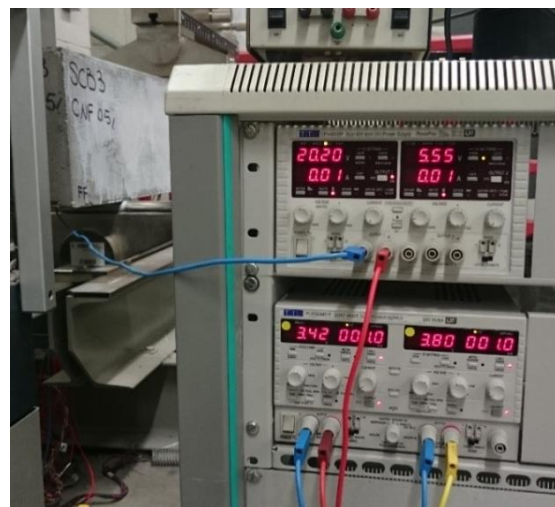


Figure 4.17. Power supply connection to copper meshes

The location of electrodes in the SC beam is shown in Figure 4.18 and described below with the current used for each electrode:

- M: located at the top mid-span of the beam: applied  $I = 0.01$  A,
- B: located at lower half of the beam, representing the bottom electrode; applied  $I = 3$  mA,
- T: located at upper half of the beam, representing the top electrode; applied  $I = 3$  mA.

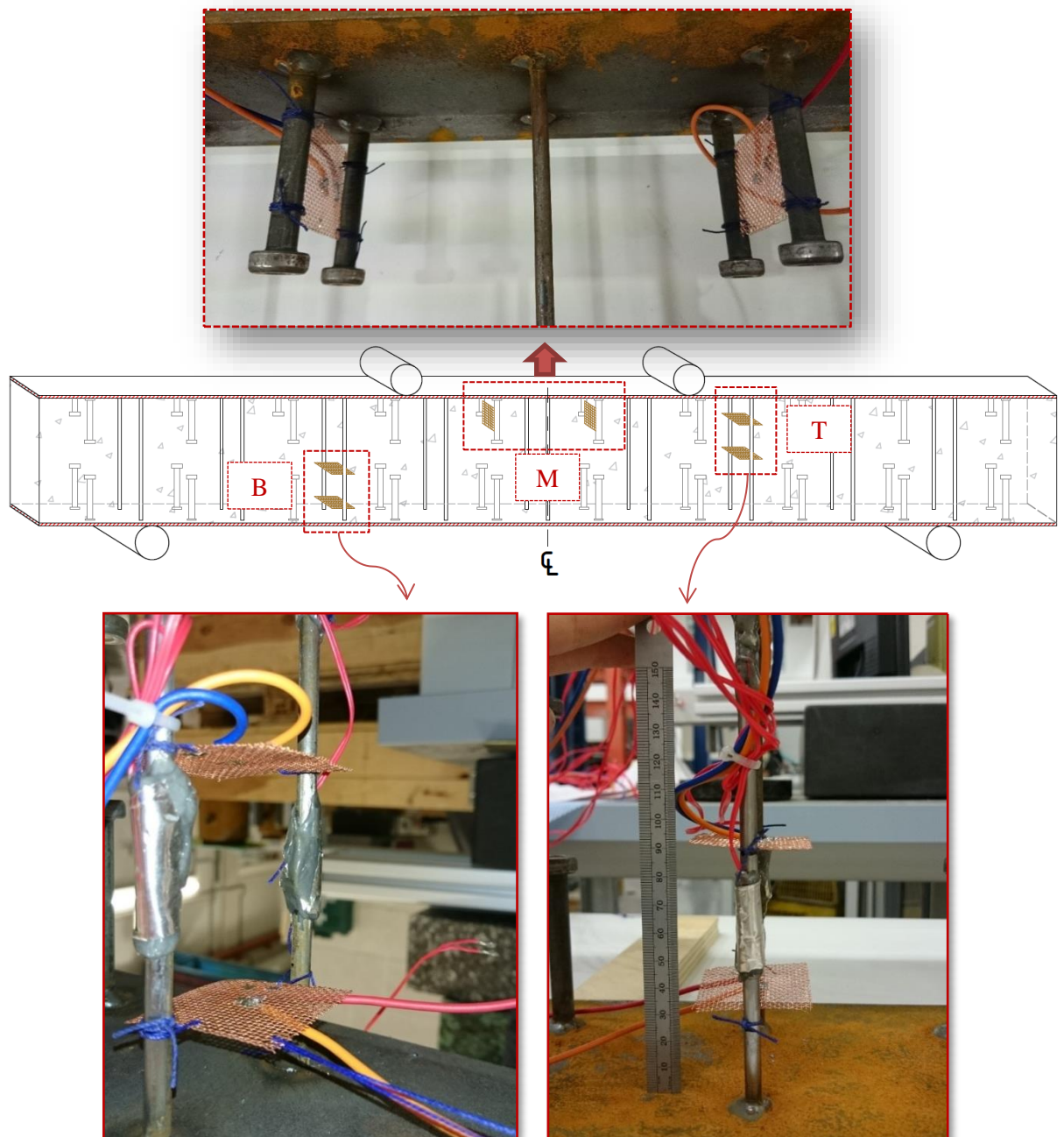


Figure 4.18. Locations of copper electrodes inside the SC beam



The copper meshes were secured in place by using non-conductive strings, tying corners of the mesh to the tie bars and shear studs accommodating enough gap between the electrode mesh and the steel bar to prevent metal contact and electric conduction through steel components of the beam (Figure 4.19). The two meshes at location 'M' (i.e. the top centre of the beam) were placed in between the shear studs so the two poles were 180 mm away from each other. The concrete strain gauge was located in the middle point of the front face of the beam towards the top plate (i.e. corresponding to the centre of the two poles location) oriented in the longitudinal direction. The two electrode meshes at locations 'B' and 'T' were positioned 60mm away from each other and placed in between the tie bars. This setting was chosen so that the strain gauges of the adjacent tie bars were at the mid-length of the two meshes (Figure 4.18).

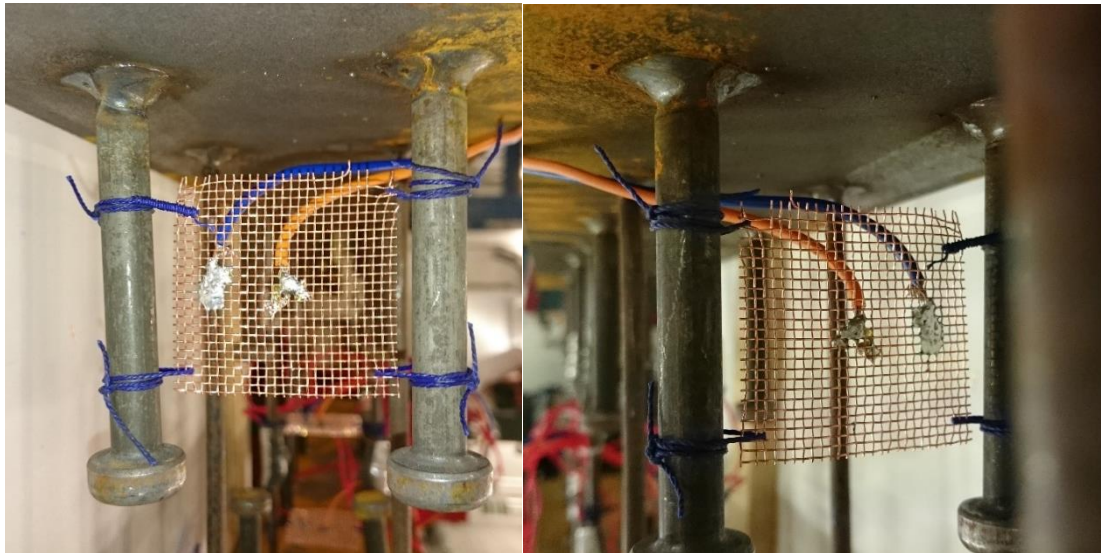


Figure 4.19. Securing copper electrodes in place within the SC beam

#### 4.7.3. Casting concrete

The steel plates of the beam were acting partially as a formwork itself and they made the concrete casting and removal from formwork easy. A wooden mould was made consisting of a base to cover one face of the beam and additional wood plates were secured at the ends to enclose the sides of the beam as shown in Figure 4.20(a). Bracing was installed in the centre to prevent uplift during the cast. Prior to placing the concrete, only the wooden base of the formwork was treated with oil. Concrete was poured in layers and a handheld electric flexible shaft vibrator was used to achieve a good compaction of concrete (Figure 4.20(b)). Concrete was poured around the electrodes

with caution to keep them in place securely. The top surface of the beam was finished (Figure 4.20(c)) and the sample was covered with a plastic cover (Figure 4.20(d)) to avoid water evaporation. The sample was left inside the mould for two days and then removed after making sure that the concrete was set, and the de-moulding process would not damage the specimen. The beam was then cured for 28 days with spraying water on the surface of the concrete every 3 days. With each beam preparation, 6 cubes and 6 cylinders were also prepared for obtaining mechanical properties of the concrete.

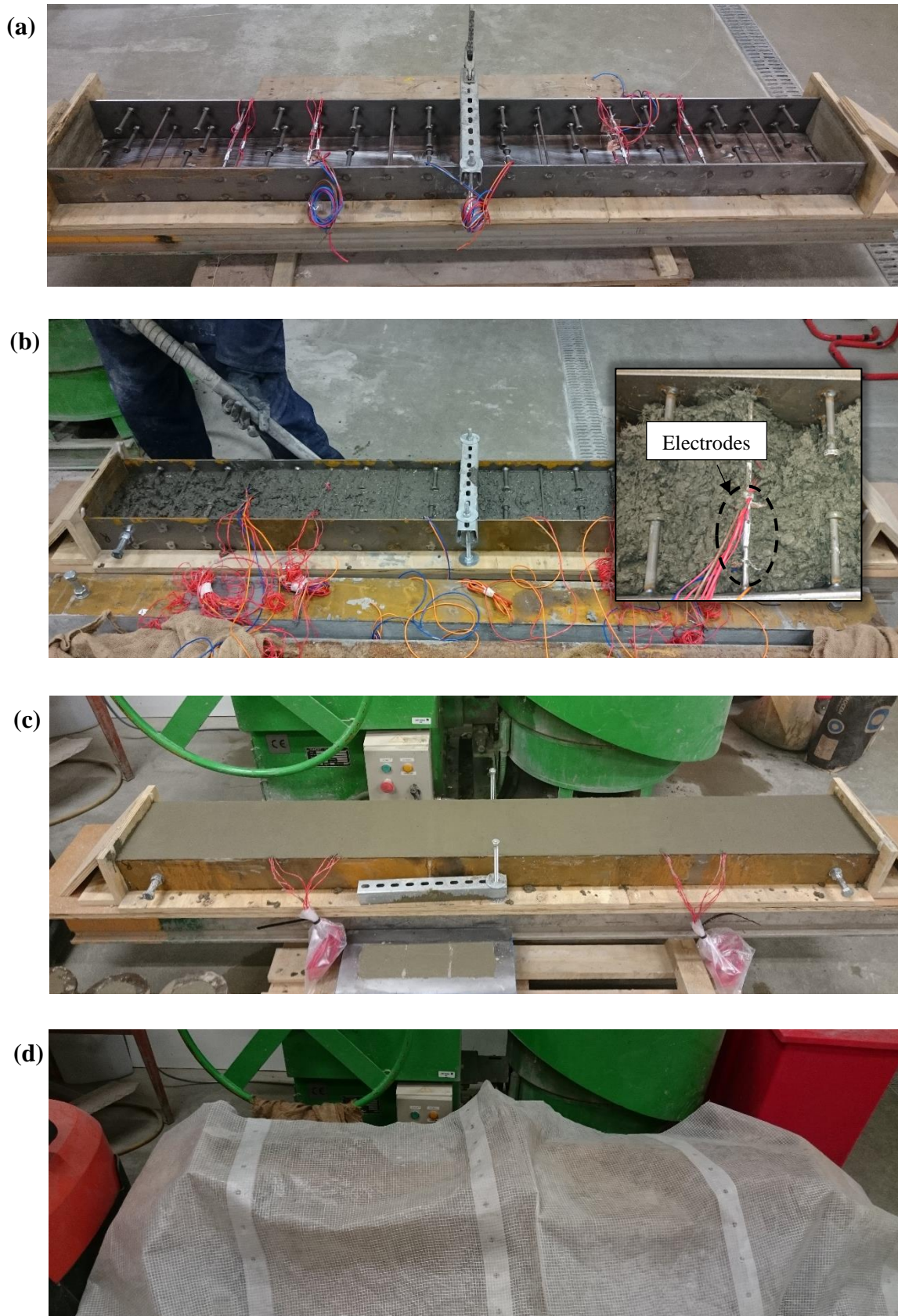


Figure 4.20. SC beam concrete casting



#### 4.8. TEST SET-UP

After 28 days of curing, the beam was painted in a white colour to better track the formation of cracks during the test, and then it was loaded in the testing frame. Universal, open structure flexural frame with maximum loading capacity of 300kN from CONTROLS Group was used for conducting the four-point bending test on SC beams. The beam span was 1400 mm with a 200 mm overhang. The shear span was 450 mm and the load bearing distance was 500 mm (Figure 4.21(a)). Strain gauge wires, numbered from G1-G23 were connected to 23 channels of a data logger connected to a PC, logging the strain output automatically at every 1 second. The load was applied in a load control manner with a rate of 80 N/s up to 50kN. Afterwards, the load was applied in a displacement control manner with the rate of  $2\mu\text{m/s}$  for higher precision.

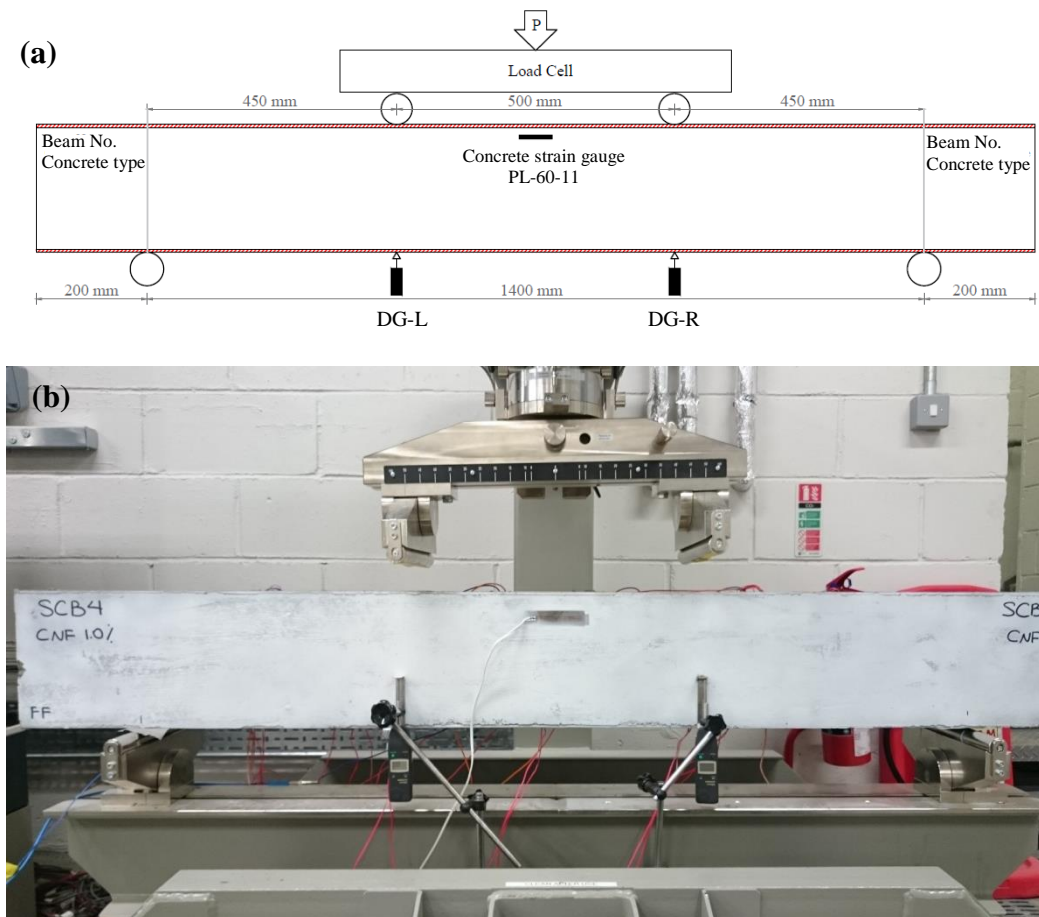


Figure 4.21. SC beam four-point bending test set-up: (a) schematic illustration; (b) experiment set-up

As illustrated in Figure 4.21(b) and Figure 4.22 the displacements were measured using Digital Displacement Gauges (DG) located in the lower part of the beam corresponding to the point loads that were acting at the top. These DGs had 30mm stroke and the measured values were recorded by hand during the test.



Figure 4.22. DG set-up

#### 4.9. SUMMARY

An experimental programme was designed to accomplish aims (iii) to (v) of this research study assigned in Section 1.2. The experimental programme consisted of four-point bending test of SC beam elements (representative of a wall section) with different concrete core materials. A total of eight SC beams were fabricated with both plain concrete, single fibre reinforced concrete (SF or CNF) and hybrid fibre reinforced concrete (SF+CNF). Strain gauges were attached to concrete, steel tie bars, and tension steel plate to measure the strain during the test. Also, DGs were located at the bottom of the beam to measure the beam displacement at load points. To analyse the self-health monitoring capability of SC beams with smart concrete core (CNFRC), two-probe direct-current method was implemented using copper mesh electrodes at three different locations of the beam. The experimental output was recorded continuously from the load frame, DGs, strain gauges and copper electrodes during the test. The data was collected after each test and the results were obtained. The analysis of the results will be presented in the following two chapters.

## CHAPTER 5

### SC BEAM EXPERIMENTAL OBSERVATIONS AND DISCUSSION

#### 5.1. INTRODUCTION

The experimental investigations reported here aimed at studying the structural performance of steel-concrete-steel sandwich structural element subjected to four-point flexural load using different types of fibre reinforced concrete infill. Eight SC beams were tested following the experimental programme presented in Chapter 4. This chapter first presents the material properties of each concrete type, followed by the observed response of all eight SC beams in terms of load-displacement behaviour, crack pattern, tie bar and tension steel plate strain throughout the test, and the failure mode.

#### 5.2. CONCRETE CORE MATERIAL PROPERTIES

The test results for cubes tested under uniaxial compression and for cylinders under split tensile test at the age of 14 days and 28 days (i.e. SC beam testing day) for each concrete batch are presented in Figure 5.1 and Figure 5.2 respectively. The results are the average value of three tested samples. Figure 5.3 presents the density of each concrete batch. Photos of specimens at the end of each test are collected in Appendix A.

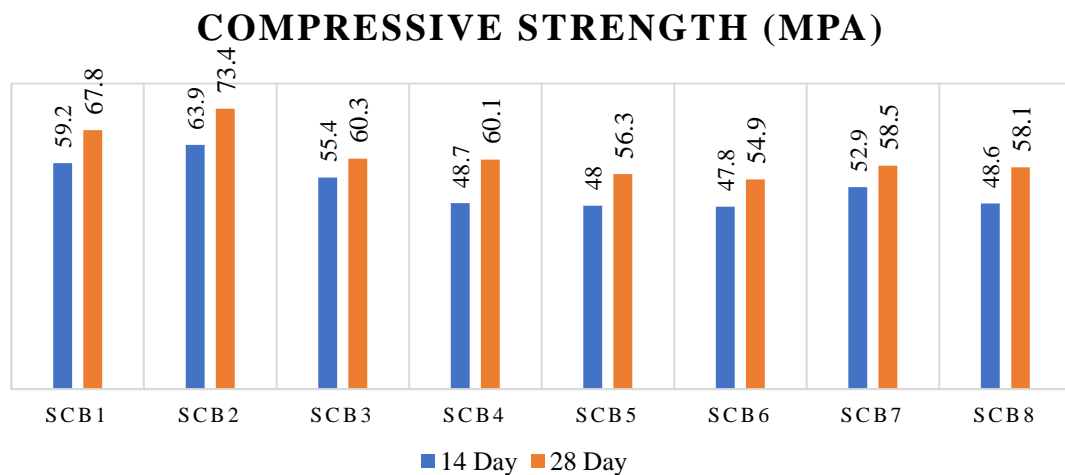


Figure 5.1. Concrete cube compressive strength at 14d and 28d for SCB1-SCB8

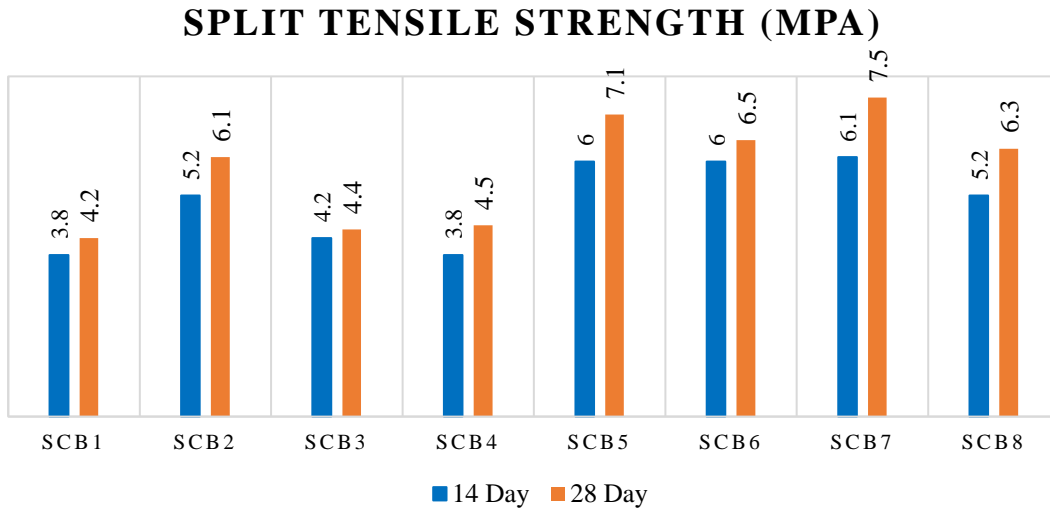


Figure 5.2. Concrete split tensile strength at 14d and 28d for SCB1-SCB8

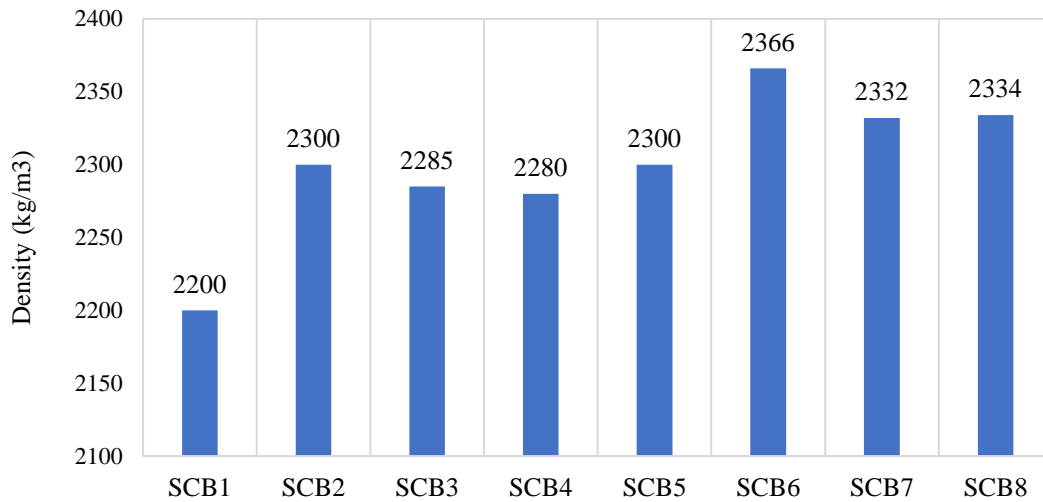


Figure 5.3. Concrete density for SCB1-SCB8

From Figure 5.1, the compressive strength of hybrid FRC materials incorporating CNF+SF was less than PC and CNFRC, which is most likely attributed to the higher water content (i.e. ranging  $W/B=0.32-0.39$ ) used in these mixes for adjusting the workability. Having said that, these materials had the highest split tensile strength due to the fibre bridging effect. The use of hybrid fibres was more effective in enhancing the split tensile strength since the steel fibres could bridge the cracks at the macro scale, at which the nanofibres are ineffective.

Figure 5.3 shows that with the addition of fibres the concrete density increased. This effect was the most when 1.5% SF was used in the mix for SCB6. Therefore, the use of

high dosage of steel fibre could lead to a higher self-weight of the concrete material while the effect of CNF on the concrete self-weight was less.

The compressive strength of CNFRC with 0.5% (SCB3) and 1% (SCB4) did not show any improvement, which is thought to be due to carbon admixture clusters that might appear after being added to the cement and other concrete constituents. Figure 5.4 shows the cylinder sample for SCB3 after the split tensile test. It could be observed that at some parts the concrete had darker appearance and at some parts lighter appearance was evident, hence it is possible that a good dispersion was not achieved in some sections.

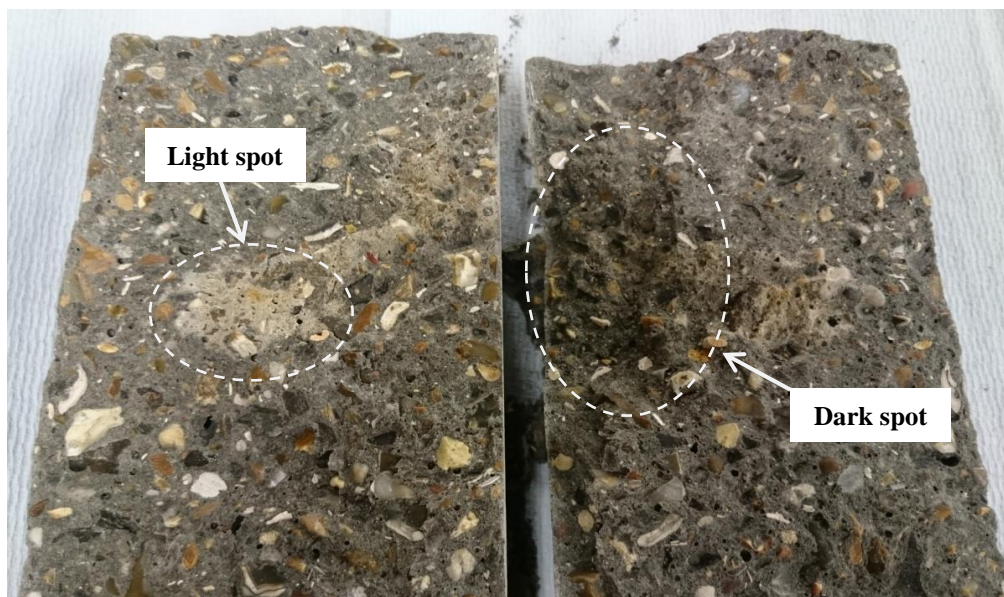


Figure 5.4. Concrete appearance inside SCB3 sample

### 5.3. FAILURE CRITERIA

Failure can be categorised according to two observations. The first observation is the load vs. displacement curves of SC samples and second observation is according to the measured strain of steel plates and the tie bars. These failure criteria are:

- *Shear failure:*
  - 1<sup>st</sup> observation: **brittle** failure at the peak loads and severe load drop at the post-peak stage occurs along with diagonal concrete crushing,
  - 2<sup>nd</sup> observation: measured strain in tie bars exceeds the yield strain; this could be an indication of a highly likely shear failure depending on the yielding of steel plates.



- *Flexure failure:*
  - 1<sup>st</sup> observation: **very ductile** behaviour due to yielding of the tension steel plate, hence an elastic-plastic load-displacement curve is obtained,
  - 2<sup>nd</sup> observation: when the steel plate has excessive yielding strain prior to any minor yielding of tie bars and tie bars do not undergo significant yielding.
- *Flexure-shear failure:*
  - 1<sup>st</sup> observation: **non-ductile** behaviour which results in a yield plateau in the load-displacement curve at the peak load followed by a brittle shear failure and a negative post-peak stiffness after failure,
  - 2<sup>nd</sup> observation: when both steel plate and tie bars undergo yielding almost simultaneously and the post-peak behaviour of the beam shows a non-ductile behaviour.

The load-displacement curves for all SC beams are presented, compared with the control sample SCB1, and discussed in detail in three different categories according to the aforementioned concrete infill categories used as follows:

- Category 1: SCB2-SCB4
- Category 2: SCB5-SCB6
- Category 3: SCB7-SCB8

The first category includes SCB2 to SCB4 samples with single FRC concrete core. The second category includes SCB5 and SCB6 which had hybrid FRC with overall  $V_f$  of 2.0%, and the third category includes SCB7 and SCB8 which had hybrid FRC concrete with total  $V_f$  of 1.5%. The initial behaviour, crack initialisation, crack progression, peak strength, post-peak behaviour, ductility, maximum displacement and failure mode are compared for all samples and will be discussed in the following sections.

#### 5.4. CONTROL SAMPLE: SCB1

Specimen SCB1 infilled with PC was the control specimen and the behaviour of other beams are compared to this sample to analyse the effect of different fibres on the structural performance of the beam. The load-displacement curve of the beam is shown in Figure 5.5. The load capacity of the beam was reached at  $P_{\max} = 169.6$  kN with the corresponding mid-span deflection of  $D = 7.6$  mm.

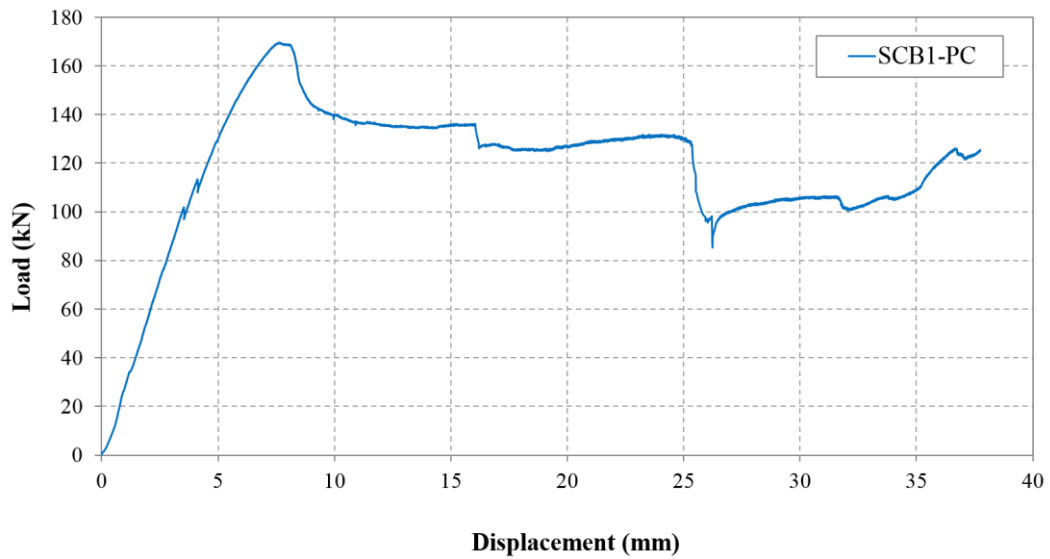


Figure 5.5. Load-displacement curve for SCB1

#### 5.4.1. Crack behaviour

Crack pattern and crack progression of SCB1 is shown in Figure 5.6. As the load was acting on the beam, initially hairline vertical cracks denoted as C1 to C4 started to appear at 11% of the ultimate load at  $P = 18.8$  kN, from the bottom of the beam in the flexural span and close to DGs. The location of these cracks was coinciding with the shear stud position as shown in Figure 5.7. It can be stated that the shear studs appeared to have acted as crack inducers. This phenomenon has also been captured in previous experimental investigations by Wright and Oduyemi (1991b). These tension cracks reduce the strength and stiffness of shear studs on the bottom plate since they are located in the cracked tension concrete zone. While shear studs in the uncracked concrete zone (top plate) remain stronger. The first diagonal cracks, as Xie et al. (2007) state:

‘develop from a tensile crack at a bar. These diagonal cracks do not have any discernible effect on the beam deflection or bar tension. As the load increases diagonal cracks occur independently of the tension cracks, when the principal tensile stress reaches a sufficient magnitude. The independent diagonal cracks appear first in the concrete tension region at about  $45^\circ$  to the beam axis, influenced predominantly by the transverse shear stress.’ (p.743)

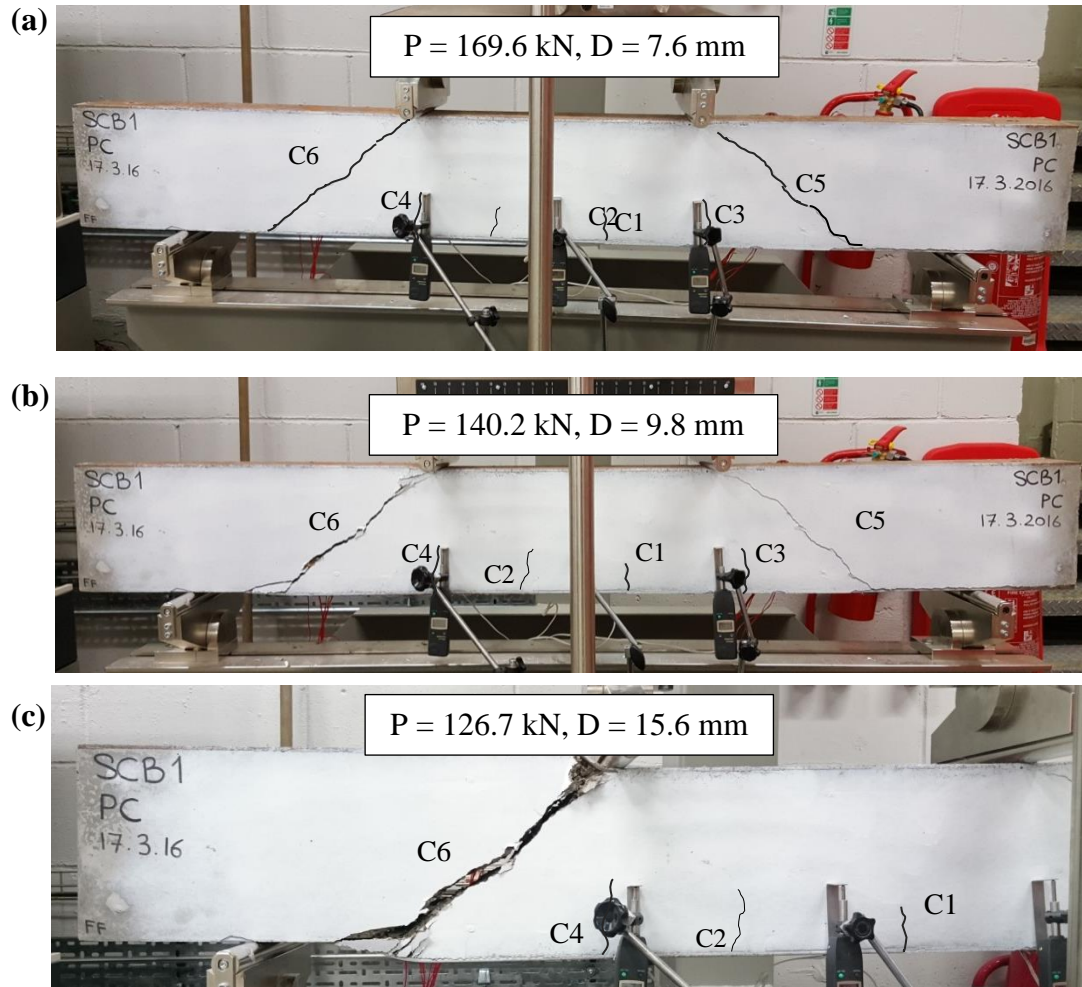


Figure 5.6. Crack development for SCB1

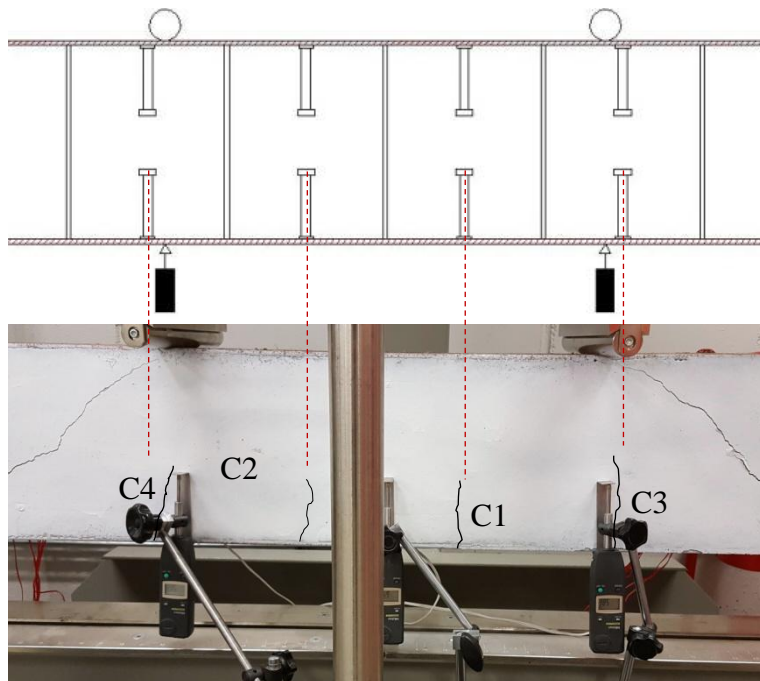


Figure 5.7. Flexural crack locations for SCB1

Vertical shear forces induce diagonal tension in the concrete core, and the section shear resistance is dependant on tie bars and concrete capacity. At 59% of the ultimate load ( $P = 100.2 \text{ kN}$ ) a full-length diagonal hairline crack (C5), also referred as shear crack, developed on the east shear span of the beam. The crack occurred in the vicinity of the right end support and extended to the right point load. With the progression of the applied load, similar diagonal haircrack (C6) developed on the west shear span at  $P=113.3 \text{ kN}$  (66.8% of the ultimate load). The occurrence of these diagonal shear cracks are apparent on the load-displacement graph where two small load drops took place at  $D = 3.6 \text{ mm}$  and  $D = 4.2 \text{ mm}$ , each associated with the east and west shear cracks respectively. As the test continued, diagonal shear cracks further widened and no additional cracks were observed on the beam. By reaching the ultimate capacity of the beam, shear crack C6 on the west side of the beam was widening faster than the east crack (C5) which resulted in a weaker concrete on the west side. During the post-peak stage, the load was decreasing gradually and the beam had negative stiffness due to loss of concrete core strength and resistance against shear force on the west side. Furthermore, with the onset of the post-peak stage and crack widening, local compression steel plate damage, crushing and spalling of concrete at both ends of crack C6 was initiated (Figure 5.6(b)) as depicted in Figure 5.8 with a closer view. Implying damage was generated and aggravated gradually throughout the post-peak stage.

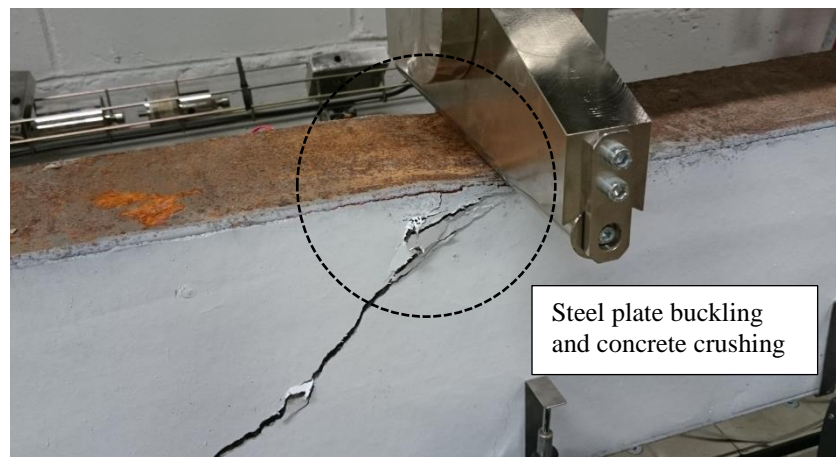


Figure 5.8. Steel plate local buckling of SCB1

At  $P = 136 \text{ kN}$ , and  $D = 15.6 \text{ mm}$ , there was a sudden small load drop of  $10 \text{ kN}$  to  $126 \text{ kN}$ . At this point the local buckling of steel plate in the vicinity of the left point load was maximised and concrete crushing was progressing under the point load and the

crack quickly opened up and resulted in the splitting of the concrete core into two sections (Figure 5.6(c)). At this stage, the concrete core fully lost its integrity and did not contribute to resisting shear force and flexural force, and the applied load was resisted by steel plates and tie bars which allowed the beam to have further displacement capacity as seen on the load-displacement curve.

There was another sudden load drop from 130 kN to 100 kN at  $D = 25$  mm displacement on the load-displacement curve (Figure 5.5) which occurred after an audible snapping noise. This was attributed to the fracture of tie bars crossing the shear crack, C6. Fractured tie bars are shown in Figure 5.9.



Figure 5.9. Fractured tie bars in SCB1

It should be noted that the number of flexural cracks stayed only a few and they did not develop in width or length throughout the test duration after the formation of the shear cracks. This is because the beam was governed by its shear capacity and the failure took place through shear modes of failure.

Figure 5.10(a) depicts SCB1 at the end of the test. The beam had substantial concrete core damage due to major shear crack opening and the concrete core was fully divided into two sections. Also, severe plastic deformation of the tension and compression steel plate at the west point load took place (see Figure 5.10(b) & (c)). A map of the final crack pattern for SCB1 at the end of the test is shown in Figure 5.11.



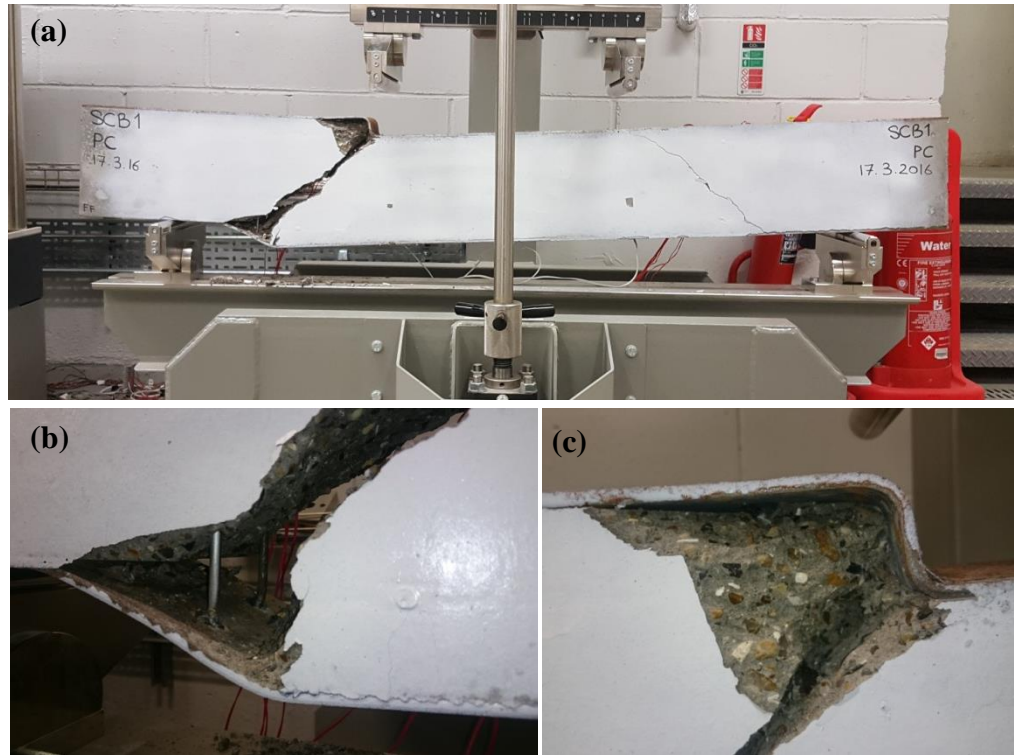


Figure 5.10. SCB1: (a) beam at the end of the test; (b) bottom plate plastic deformation at C6; (c) top plate deformation at C6

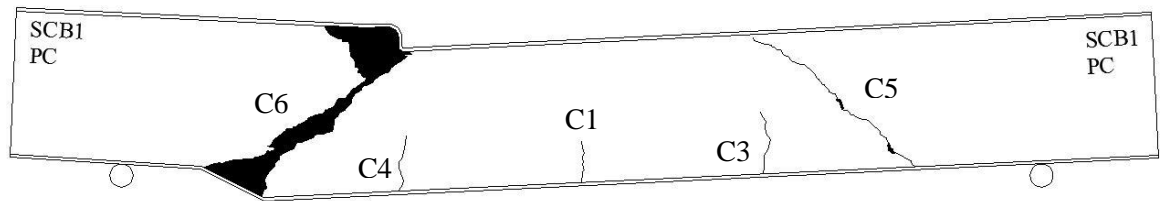


Figure 5.11. Crack map of SCB1 by the end of four-point bending test

#### 5.4.2. DG measurements

The displacement measurements from DGs corresponding to the right (DG-R) and left (DG-L) point loads for SCB1 are shown in Figure 5.12. The results are presented up to the maximum value that could be measured by the DG (i.e. stroke of the DG). The beam showed symmetrical deflection until the peak load was reached. During the post-peak stage, due to the development of the shear crack on the west side and local buckling of steel plate, the left side of the beam showed higher deflection. This deflection increased gradually and showed a higher value than the midspan deflection from  $D = 13.3$  mm resulting in an unsymmetric deflection.

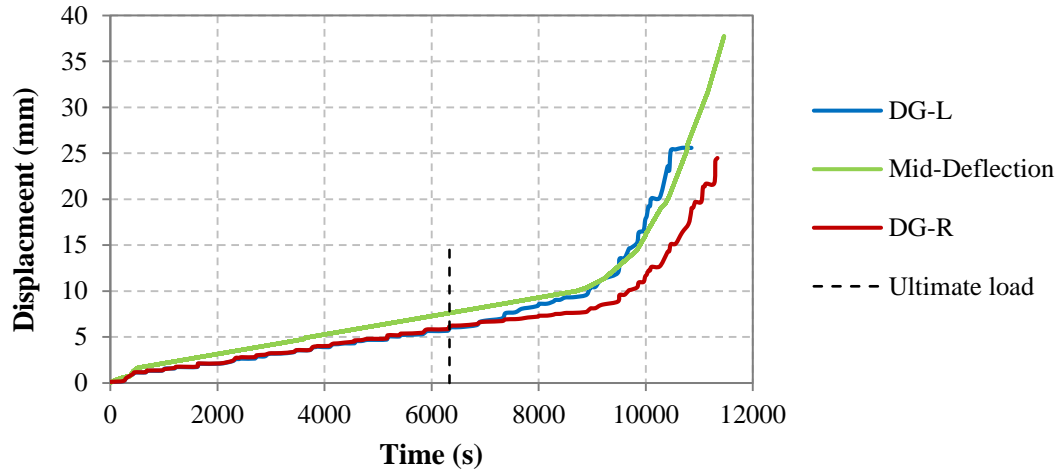


Figure 5.12. DG measurements for SCB1

### 5.4.3. Strain measurements

The strain induced in tie bars and steel plate for SCB1 are shown in Figure 5.13 and Figure 5.14. From observation of measured strain in tie bars, it is evident that a sudden increase in strain occurred for east bars at the same load level when the shear crack C5 became visible. Similarly, the strain of the west bars increased in an instant at which C6 appeared. This is due to the loss of concrete tensile strength which resulted in the shear crack formation, hence higher stresses were induced on tie bars as the concrete was losing its contribution in resisting shear. However, the bars did not undergo yielding at this stage ( $\epsilon_{y\text{-tie bar}} = 1925 \mu\epsilon$ ). G3 and G7 only recorded the strain up to a certain load level and they stopped recording any meaningful values possibly due to a damage of either the gauge or the gauge wires within the concrete.

Yielding of all tie bars took place prior to the peak load. Highest strain for inner bars was recorded by G4 which had a strain value of  $8505.5 \mu\epsilon$  at the ultimate load which increased to  $9729 \mu\epsilon$  at  $P = 166.2 \text{ kN}$  (post-peak stage) and from there onwards, the strain decreased gradually. On the opposite side, G14 and G10 reached the maximum strain of  $3005.6 \mu\epsilon$  and  $1621.5 \mu\epsilon$  respectively at the ultimate load and then decreased during the post-peak stage.

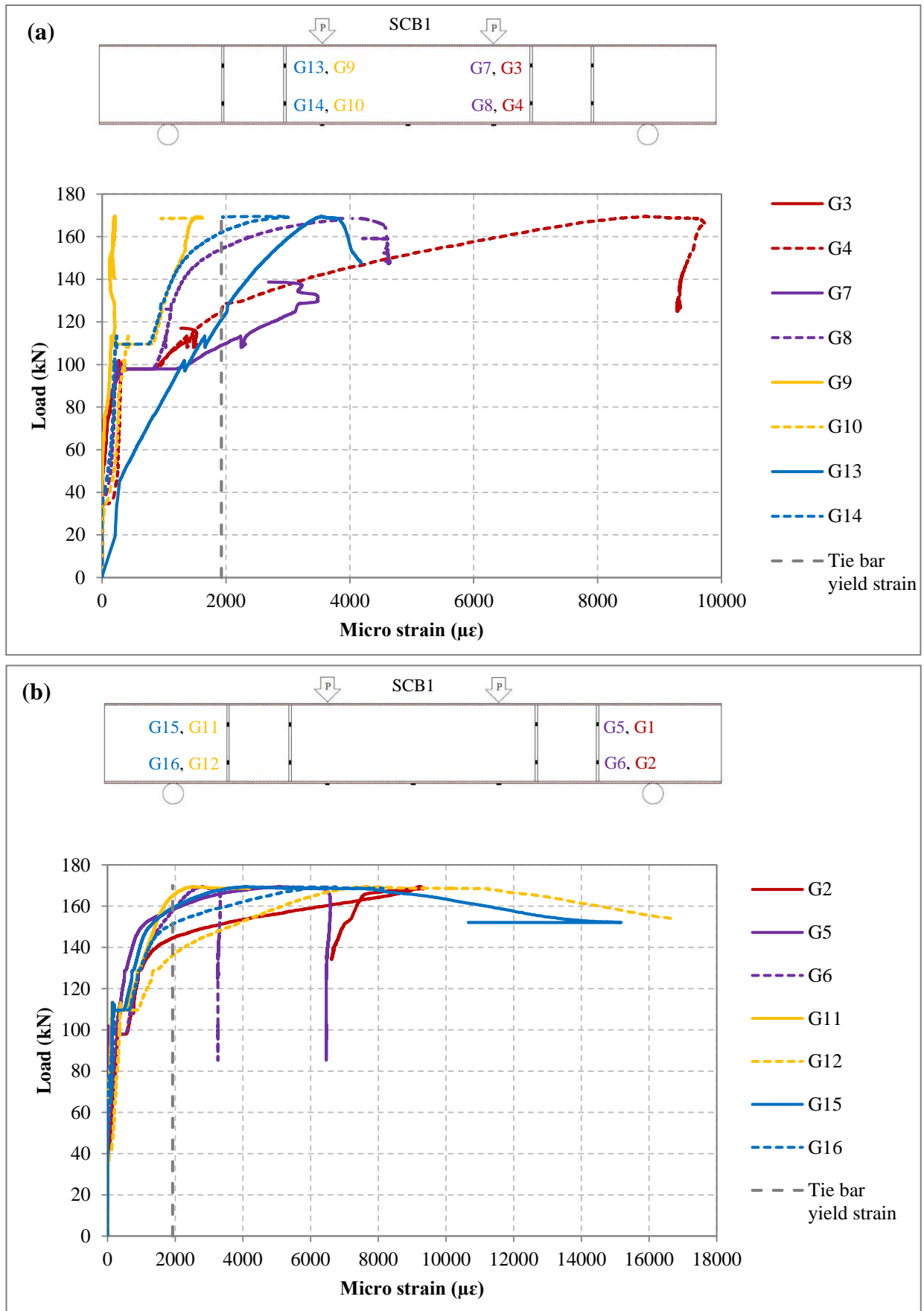


Figure 5.13. Measured strain for: (a) inner tie bars; (b) outer tie bars for SCB1



For the outer bars (Figure 5.13(b)), G11 and G15 had the smallest strain of  $2530.8 \mu\epsilon$  and  $4091.8 \mu\epsilon$  respectively at the ultimate load since they were away from the shear crack. G11 recorded maximum strain of  $4203.3 \mu\epsilon$  at  $P = 168.7 \text{ kN}$ , while G15 at  $P = 152.1 \text{ kN}$ , showed a sudden strain drop from  $10660.5 \mu\epsilon$  to  $9333.1 \mu\epsilon$  and strain decreases from that point onwards to  $3291 \mu\epsilon$  by  $P = 146 \text{ kN}$  on the post-peak branch. This is thought to be due to the excessive widening of C6 which caused core splitting. Thus, the induced strain on bars was reduced as energy dissipation on the left side of the beam took place by plate buckling.

G12 and G16 which were adjacent to the shear crack C6 showed yielding at an earlier stage of loading compared to other tie bars. G12 had the strain value of  $7628 \mu\epsilon$  at the peak load and increased to  $16800 \mu\epsilon$  at  $P = 153.7 \text{ kN}$ . G16 failed at  $P = 168.7 \text{ kN}$  with the maximum recorded strain of  $8146 \mu\epsilon$ .

From Figure 5.14, the tension steel plate reached the yielding strain ( $\epsilon_{y\text{-plate}} = 1545 \mu\epsilon$ ) first at the mid-span length recorded by G19 at  $P = 146 \text{ kN}$  (86% of the ultimate load), which was after tie bar yielding took place. The maximum strain recorded was  $1764 \mu\epsilon$ .

According to the failure criteria defined earlier, it can be concluded that the beam had shear failure since tie bars yielded excessively prior to tension steel plate. Also, the crack pattern and the load-displacement curve confirms the shear failure mode for SCB1.

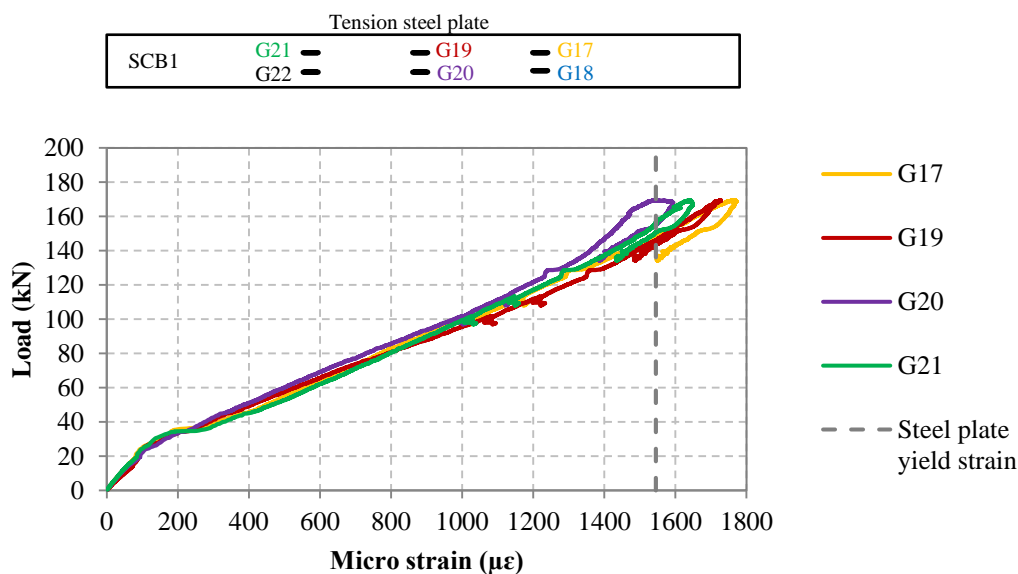


Figure 5.14. Measured strain in tension steel plate for SCB1

## 5.5. CATEGORY 1: SCB2-SCB4

### 5.5.1. SCB2: SFRC

Specimen SCB2 was made with SFRC concrete infill which had 0.5% volume fraction of end-hooked steel fibres. The compressive strength of SFRC concrete was 6.7% higher than PC and the split tensile strength was 32.6% higher due to the presence of fibres and their bridging effect in controlling tensile cracks.

The load-displacement curve for SCB2 is presented in Figure 5.15. The maximum load capacity of SCB2 was 191.9 kN which was 13.1% higher than SCB1. At the ultimate load capacity, the mid-span deflection of the beam was  $D = 7.4$  mm which was almost similar to SCB1.

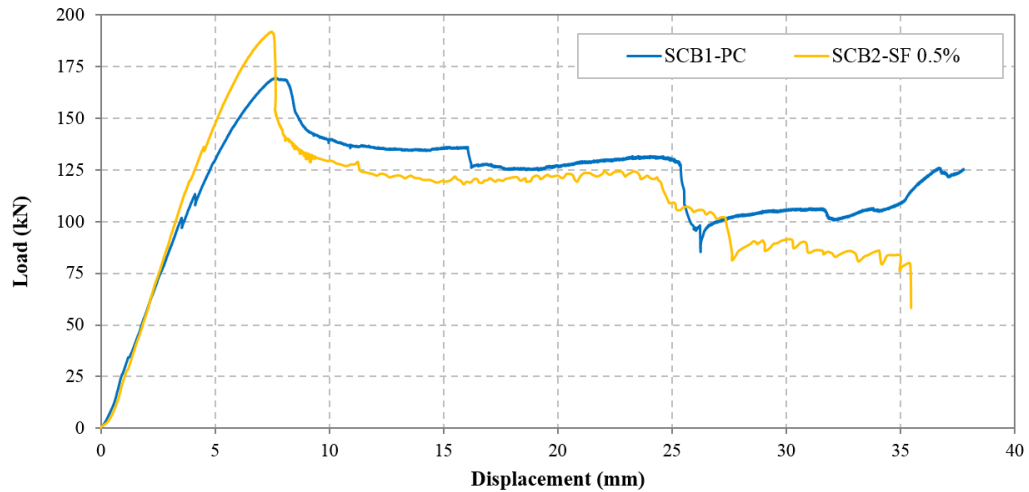


Figure 5.15. Load-displacement curve for SCB2

#### 5.5.1.1. Crack behaviour

The crack pattern of SCB2, shown in Figure 5.16, started with hairline vertical cracks (C1-C3) appearing at the centre and at the vicinity of the DG-L, at  $P = 33.6$  kN (17.5% of the ultimate load). This was slightly higher than the control specimen (which was at 11% of the ultimate load). These locations coincided with the shear stud position which was also seen found in SCB1. Central crack C1 appeared at 42.6% of the ultimate load. The beam developed full-length hairline diagonal shear crack on the west shear span of the beam (C4) simultaneously with the formation of the east shear crack (C5) at 71.4% of the ultimate strength ( $P = 137$  kN). The development of visible shear cracks was at 21.2% higher load level compared to SCB1; which was due to the presence of steel

fibres. The fibres increased the tensile strength of concrete to better resist diagonal tension stresses induced by shear forces.

The west shear crack increased in width as can be seen in Figure 5.16(c) (at around  $P = 190$  kN) as the load progressed towards the peak value. Simultaneously, the steel plate local buckling was originated when the maximum load was reached, and consequently concrete crushing took place. The structural stiffness was decreased due to the further crack development and plate buckling. This observation was similar to that of SCB1 at the peak load. After reaching the peak load, the load suddenly dropped and attained a steady value which was 60% - 70% of the peak load (see Figure 5.15). The sudden load drop was due to the crack opening of the shear crack C4 and transformation of the hairline crack into a major structural crack.

As the test progressed, during the post-peak stage, the shear crack increased slowly in width and vertical cracks increased in length towards the mid-height of the beam. The rate of crack growth decreased due to the presence of steel fibres in the concrete which controlled and delayed the crack opening. Due to the interruption of the crack opening, also the steel plate local buckling progression was better controlled compared to SCB1.

A new vertical crack (C6) under C4 was formed at  $P = 124$  kN,  $D = 11$  mm (Figure 5.15(d)), followed by a sudden snap sound which was due to the rupture of a tie bar crossing the cracked section at C4. This was due to an excessive local buckling and widening of C4 which in turn induced high tensile stress on the bars. C6 progressed until it joined C4 and the concrete triangle block in between C4 and C6 was formed at the bottom.

With the rupture of the bar, the beam became weaker in resisting the shear force, thus the shear crack was widened to an extent that the steel fibres lost their effect in bridging the crack (Figure 5.16(e)). Steel fibres were inefficient at this stage since they were pulled out or distorted (see Figure 5.17). The SFRC core lost its contribution in resisting the applied load at  $P = 120$  kN and  $D = 15.5$  mm and it was only the steel components of the SC beam contributing in resisting the applied force. As the test progressed, at  $D = 24.5$  mm and  $D = 27$  mm snapping noises were audible which caused the corresponding load drops on the load-displacement curve. This was attributed to the fracture of the tie bars. The rupture of the tie bar crossing the cracked section at C4 is depicted in Figure 5.19.

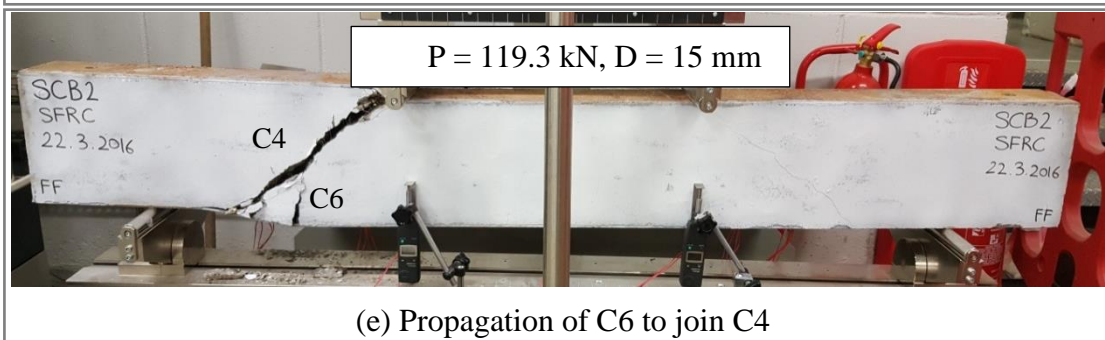
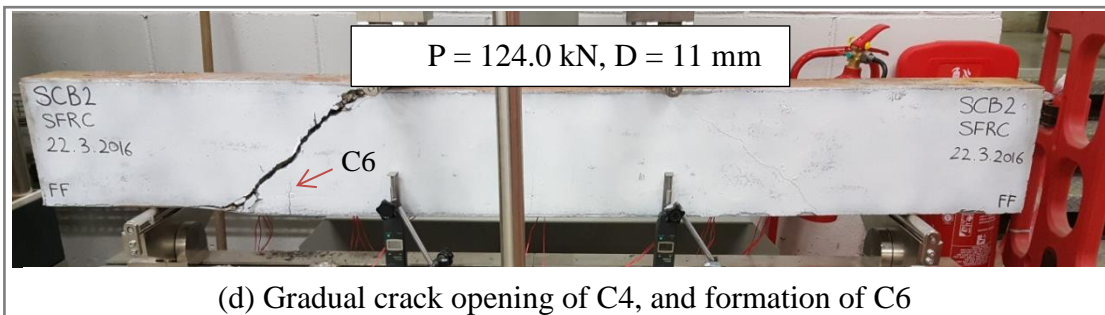
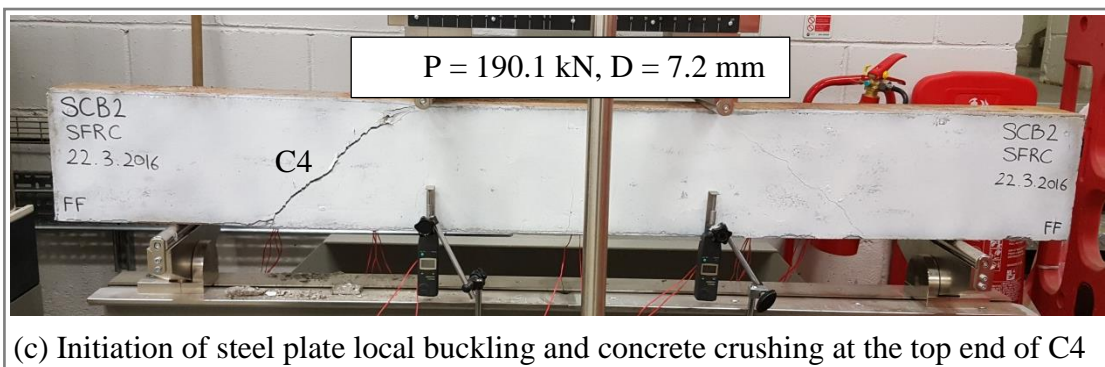
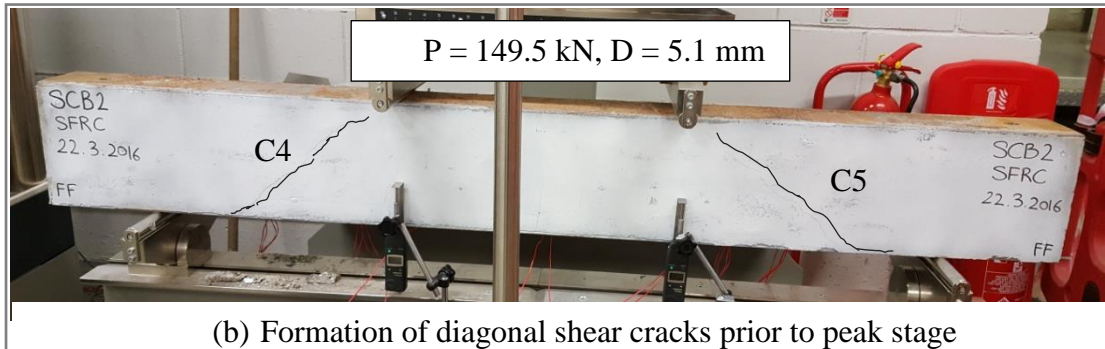
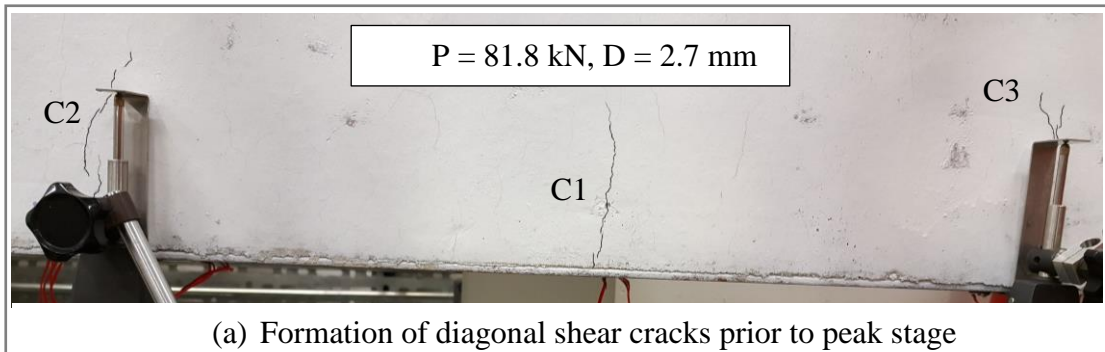


Figure 5.16. Crack progression for SCB2



Figure 5.17. Close view of steel fibre at the crack interface

The final crack pattern of SCB2 at the end of the test is shown in Figure 5.18. The damage to the concrete core was similar to SCB1 (i.e. shear crack damage), however, the length of the flexural vertical cracks was slightly higher in SCB2, which could mean that higher energy dissipation took place through flexural cracks. Also, the progression of damage was slightly delayed due to crack control effect of steel fibres.

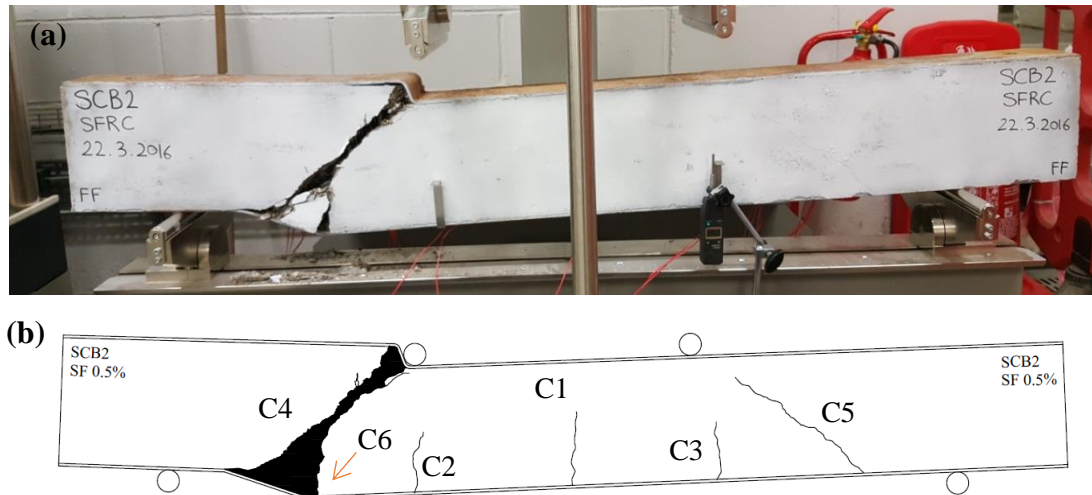


Figure 5.18. SCB2: (a) specimen after failure; (b) crack map of failed specimen





Figure 5.19. Fractured tie bars crossing C4

#### 5.5.1.2. DG measurements

From Figure 5.20 it is evident that the beam deflection was symmetric until DG-L increased with a higher rate than DG-R from  $D = 5.64$  mm at  $P = 182.5$  kN. This was shortly before the post-peak. Faster increase in the displacement of DG-L could indicate faster progression of shear crack width on the west side. From this point, the displacement of the left side of the beam became identical to the central displacement and with further buckling of top steel plate and increase in the width of C4, from  $D = 9.8$  mm, the displacement on the left side became higher than central deflection. This unsymmetrical displacement of the beam was similar to SCB1.

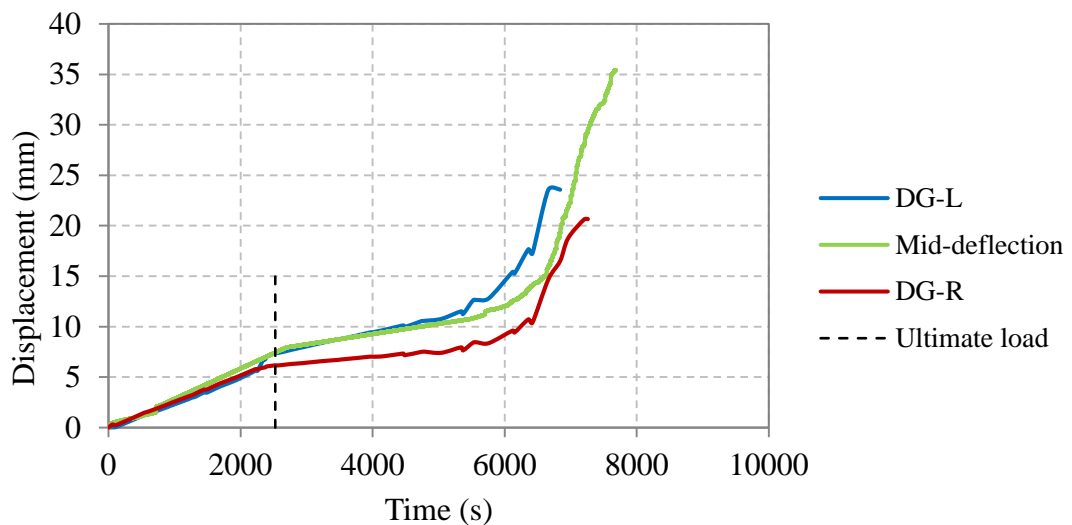


Figure 5.20. DG measurements for SCB2

### 5.5.1.3. Strain measurements

The strain values measured by the attached gauges on the inner and outer tie bars in the shear span are presented in Figure 5.21, and the strain readings for tension steel plate are shown in Figure 5.22. For this beam, G11 did not record any results which could have been due to possible damage of the gauge during casting concrete.

From Figure 5.21(a), yielding for inner bars took place at the top of the bars (G3 & G7) which were crossing shear crack C5, where tensile stress concentration is expected to be higher due to its proximity to the crack. On the other hand, the inner bar on the opposite side (G9 & G13) recorded higher strain at the peak load for the upper side of the bar adjacent to C4. G3 had a strain of  $3298 \mu\epsilon$ , while G13 recorded strain of  $6520 \mu\epsilon$  (twice as G3) at the ultimate load. This indicated that the west shear span were to develop the major crack. The strain value of G13 increased further to  $9690 \mu\epsilon$  and due to the severe crack opening of C4, the bar fractured at the top as shown in Figure 5.19.

Amongst the outer tie bars from Figure 5.21(b) (the maximum tensile strain displayed is limited to  $4000 \mu\epsilon$  for clarity of presentation), none of the tie bars underwent yielding prior to the peak load, except the west outer bar, in which G16 showed a strain value of  $2122 \mu\epsilon$  (exceeding  $\epsilon_{y-tiebar} = 1925 \mu\epsilon$ ). G12 and G16 which represented strain at the lower half of the outer west tie bars (near the shear crack C4) showed the highest strain of  $12075 \mu\epsilon$  and  $14100 \mu\epsilon$  respectively before they were damaged due to excessive crack extension. Similarly, the high strain value at these locations which are in the vicinity of the west shear crack reflected the concrete damage at C4 and loss of concrete contribution in resisting principal tension stress caused by vertical shear forces.

Overall, the strain measurements showed a sudden increase at the load at which the concrete started to develop shear cracks. Due to the diagonal cracks and strain localisation on bars at the location of the crack, higher stress was induced on the lower section of the outer tie bars and the upper section of the inner tie bars. This is because these locations were near the shear cracks (C4 & C5) and subjected to higher tensile stress. Comparison of the results with SCB1 revealed that tie bars in SCB2 had less strain value at the ultimate load in SCB2. More specifically, strain at locations away from the shear crack was significantly less in SCB2, which was due to the higher shear capacity of SFRC compared to PC. However, both samples had fractured tie bars by the end of the test.

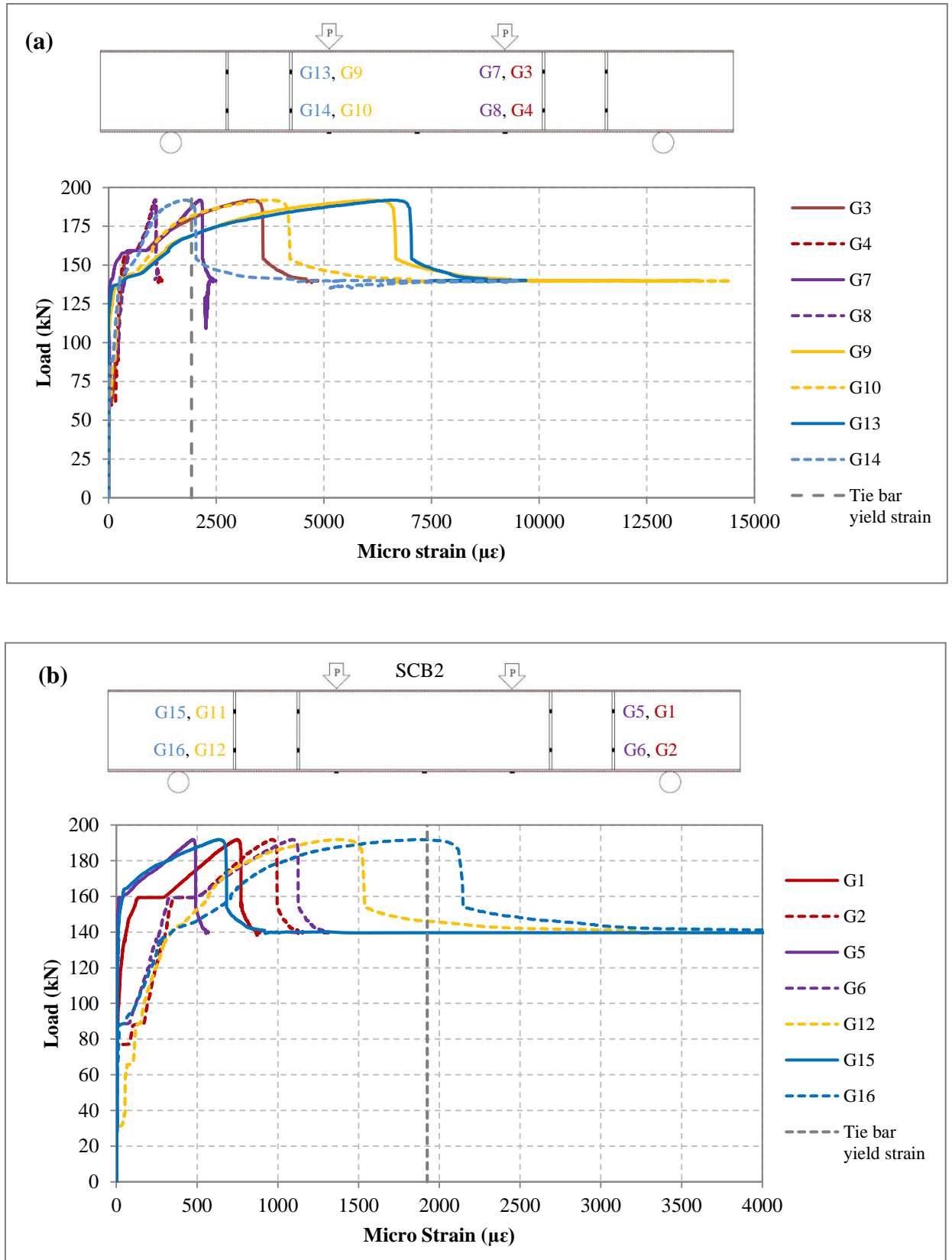


Figure 5.21. Measured strain for: (a) inner tie bars; (b) outer tie bars for SCB2



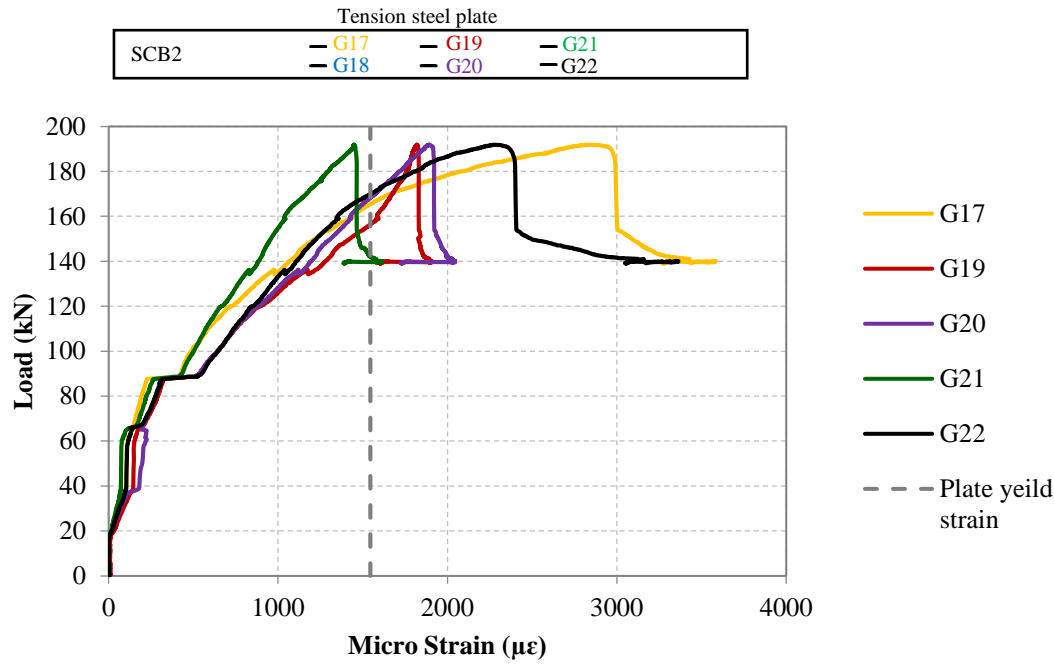


Figure 5.22. Measured strain in tension steel plate for SCB2

From Figure 5.22, the tension steel plate first yielded at the centre (G19) at  $P = 156.6$  kN (81.6% of the ultimate load). Some local variation in the steel plate strain can be observed which can be caused by asymmetrical concrete cracking. The steel plate showed yielding prior to peak load. However, at the peak load, when the damage was induced on the beam, and during the post-peak stage, the strain induced in steel plate was lower compared to west tie bars. Assessing the tension plate strain reveals that SCB2 performed better than SCB1, since the tension steel plate in SCB1 experienced less strain throughout the test, while more ductile energy dissipation took place for SCB2 through yielding of tension plate. This shows some improvement in the performance of SCB2 with 0.5% volume fraction of steel fibres, however, it was not sufficient to alter the failure mode. From the crack behaviour of the concrete core and the strain measurements, it can be concluded that shear failure limit state accompanied by fracture of the tie bars occurred and SCB2 failed in shear.

### 5.5.2. SCB3: CNFRC0.5

Specimen SCB3 was made with 0.5% volume fraction of carbon nanofibres (CNFRC0.5). The cube compressive strength of CNFRC was 11% less than PC. The split tensile strength of CNFRC was 4.8% higher than PC. The load-displacement curve of SCB3 is shown in Figure 5.23 and compared with the control beam SCB1.

The ultimate capacity of SCB3 was 136.1 kN which was 22.5% and 31.4% lower than SCB1 and SCB2 respectively. At the maximum load, the mid-span deflection of the beam was  $D = 6.47$  mm which was slightly lower than beams with PC core and SFRC core. The maximum displacement of this beam was 45 mm and at this stage, the maximum possible displacement limit of the testing machine was reached, thus the test was terminated.

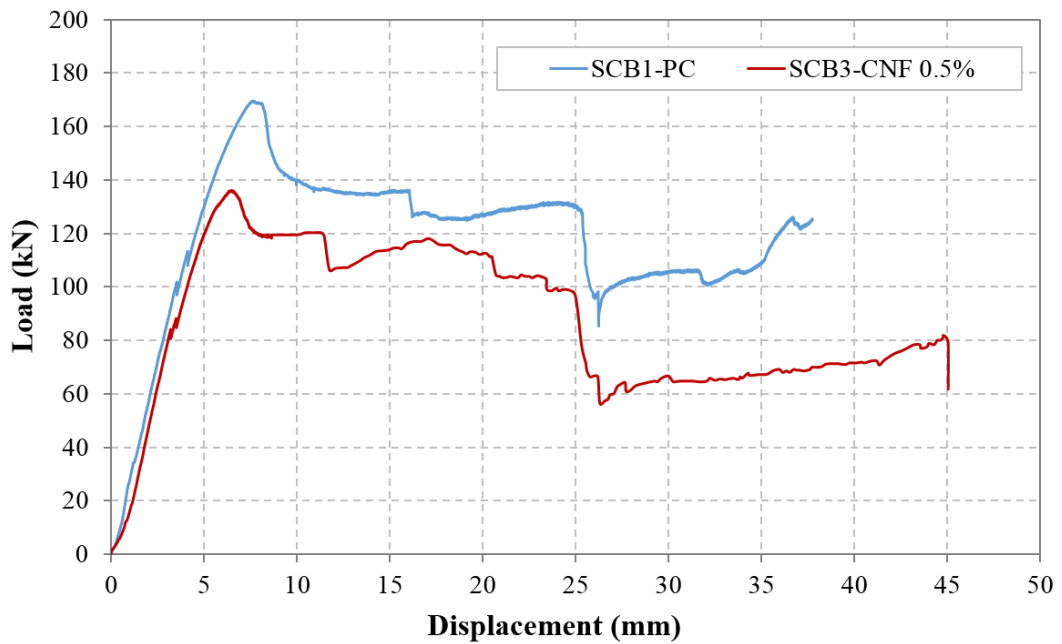


Figure 5.23. Load-displacement curve for SCB3

#### 5.5.2.1. Crack behaviour

The first cracks that appeared on the beam were very fine flexural cracks in the mid-span of the beam as shown in Figure 5.25(a) forming sequentially from C1 to C4. The location of these cracks coincided with the position of the shearing studs as for previous SC beams. The shear studs could have acted as crack inducers.

C1 appeared at 19.4% of the ultimate load ( $P = 25.5$  kN). This was 11% of the ultimate load for control specimen and 17.5% for SCB2. Therefore, CNFRC0.5 was successful in delaying the formation of initial flexural cracks. As the load increased, C2-C4 formed subsequently, however it should be mentioned that C4 was short in length and unlike C1-C3, it did not develop in length throughout the test.

The diagonal tension shear cracks C5 and C6 appeared at  $P = 82$  kN and  $P = 85$  kN on the west and east shear spans of the beam at 62.3% and 64.6% of the ultimate load respectively with a corresponding deflection of 3.5 mm. Compared to SCB1 with a shear crack appearance at 59% and 66.8%, it can be stated that CNFRC0.5 performed better in delaying the formation of the shear cracks as well, considering the lower compressive strength of the CNFRC0.5 than PC. On the other hand, SCB2 developed shear cracks at 71.4% of the ultimate load, which is slightly higher than SCB3. Since the effect of steel fibre on cracking shear strength is small, while the concrete strength influences the cracking shear more than the failure strength (Kwak et al., 2002), higher shear crack strength for SCB2 is mainly attributed to the higher compressive strength of SFRC (21.7% higher than SCB3) rather than the fibre effect. The occurrence of the shear cracks for SCB3 is also reflected in the load-displacement curve with a minor instant load drop during the linear stage (see Figure 5.23).

As the beam was reaching its ultimate strength, increase in crack width of C6 was noticeable and at this stage, the nanofibres become ineffective since the crack had progressed into a macro-size crack. Therefore, the beam had negative stiffness during the crack development. Followed by the increase in the crack width, the compression steel plate (top plate) started to buckle at  $P = 121.5$  kN and  $D = 7.56$  mm (post-peak stage) and the tension plate showed plastic deformation. Initial stages of plate buckling are shown in Figure 5.25(b). It can also be noticed in the figure that the width of C6 was larger than C5.

At  $P = 120.3$  kN and  $D = 11.3$  mm the load suddenly dropped to 106 kN, at which a sudden noise was heard. This was thought to be due to the fracture of a tie bar. At this moment, a small sudden downward movement of the beam on the west side was noticed as well as the formation of a new vertical crack (C7) close to C6 (see Figure 5.25(c)). The new crack further developed with increasing displacement and joined C6 and resulted in the formation of a triangular concrete block. The crack depth of C6 was

increasing gradually and at  $P = 109.5$  kN and  $D = 13.35$  mm the separation of the concrete core into two sections was visible. At this stage, after concrete failure occurs in the concrete core, the SC beam continued to resist load due to the membrane action in the steel plates preventing sudden failure of the beam and this allowed the beam to sustain a higher load at the large deflection range.

During the post-peak stage, at the load level of  $P = 98.7$  kN with a corresponding displacement of 24.7 mm, another snap sound was audible and a sudden marked load drop occurred on the load-displacement curve of the SCB3. This was due to the fracture of one or possibly two tie bars (see Figure 5.24). Despite the lower concrete strength of SCB3 compared to SCB1, this phenomenon occurred at similar displacement level for both samples. With further continuation of the test, the buckling of the compression plate was developing simultaneously with the plastic deformation of the tension plate under the damaged concrete core at C6. Concrete crushing was also progressing at the top end of C6 where the local buckling took place.

Figure 5.26 shows SCB3 after termination of the test and its crack map. It is evident from the crack pattern and the load-displacement curve that the beam failed in shear mode. The failure mode and damage pattern of SCB3 was similar to SCB1 and SCB2, in which symmetrical shear cracks appeared on the beam followed by a dramatic width and depth increase of a single shear crack resulting in the local buckling of the compression steel plates.



Figure 5.24. Fractured tie bars in SCB3 (east shear span)

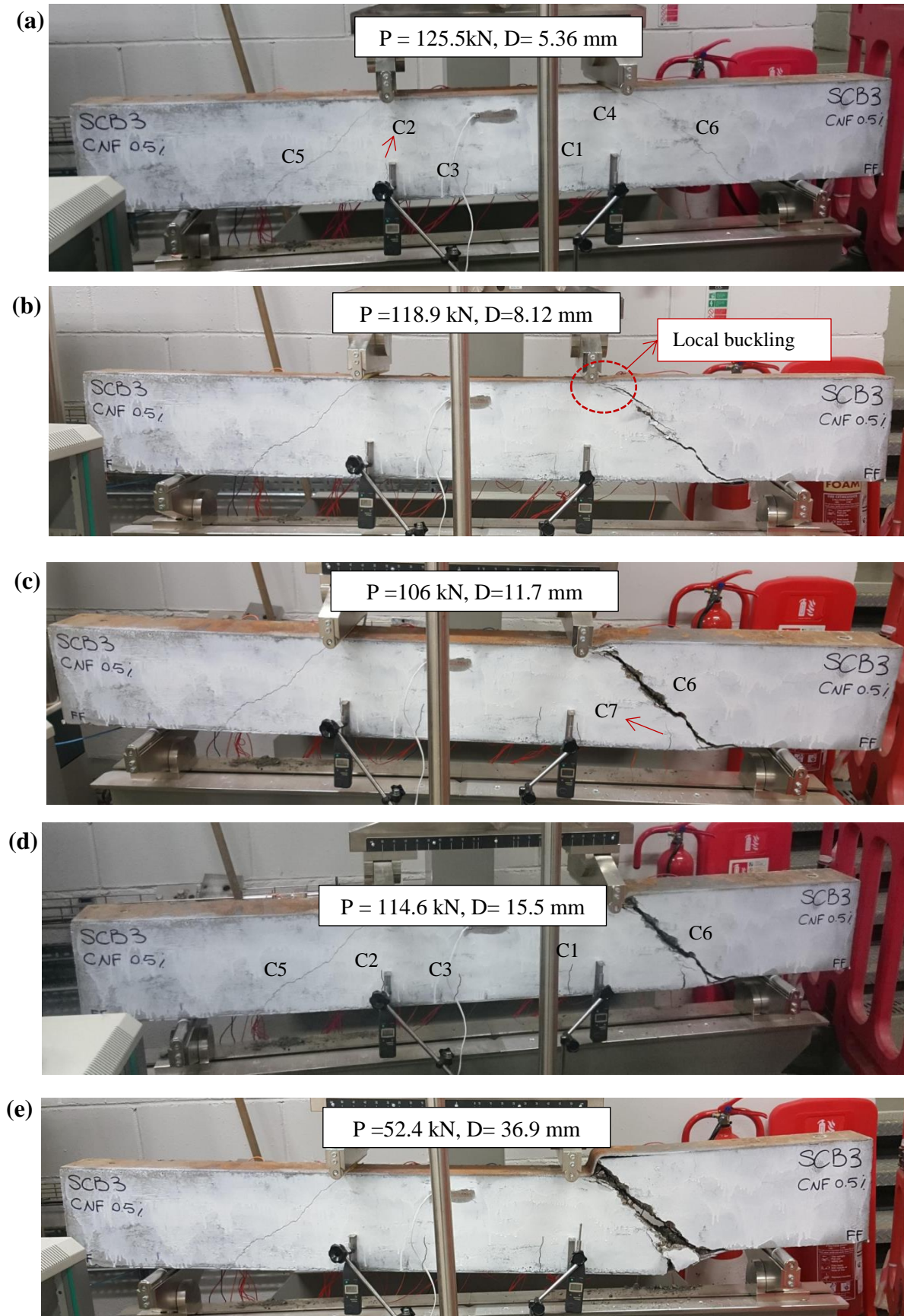


Figure 5.25. Crack progression for SCB3



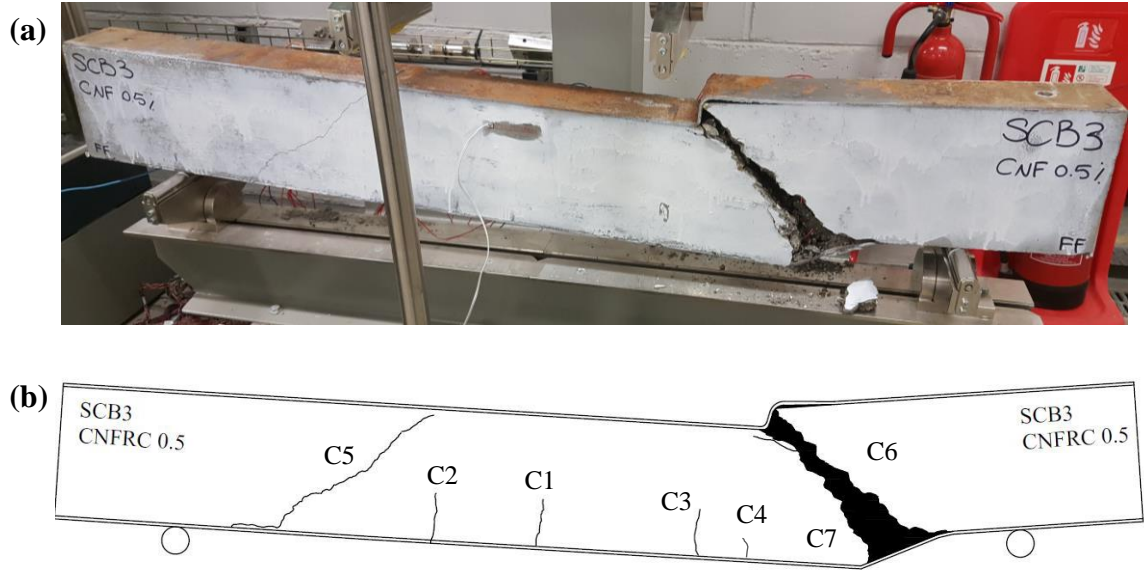


Figure 5.26. SCB3: (a) specimen after failure; (b) crack map of failed specimen

#### 5.5.2.2. DG measurements

The measured displacements throughout the test are presented in Figure 5.27. The displacement higher than 27 mm could not be captured because of DG stroke limit. It is evident from the curve that the measurements of DG-R shows deviation from the measurements of DG-L and reaches a value higher than mid-span deflection with a higher increasing rate. This increase was due to the formation of the east shear crack and buckling of the steel plates which caused excessive asymmetric deflection of the beam. This asymmetric deflection was also visually perceptible by the end of the test.

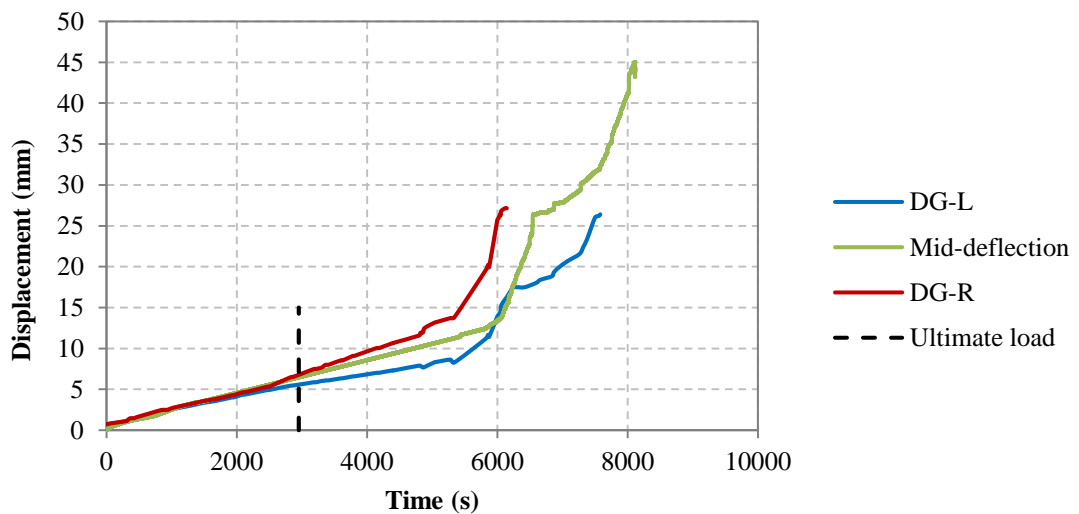


Figure 5.27. DG measurements for SCB3

### 5.5.2.3. Strain measurements

The measured strain for tie bars during the test for specimen SCB3 is shown in Figure 5.29. For this specimen, no readings were recorded for G3 and G9 due to gauge failure.

For this beam, all gauges exceeded yielding strain except G10. The strain values were increasing as the load reached to its ultimate value. Assessing the inner bars (Figure 5.29(a)), symmetrical strain value for both front bars (G7, G8, G13, G14) was observed and the upper half of the bars (G7 & G13) were experiencing higher strain at the same load level after shear crack occurred. Also, the outer tie bars showed higher strain at lower half (e.g. G12 & G2). These sections of the tie bars are the closest to C5 and C6 respectively, thus resulting in stress concentration on the upper half of the inner tie bars and lower half of the outer tie bars. Figure 5.28, backs up this stress concentration as the fracture of inner tie bars took place at the crack C6 interface.

The highest strain induced on tie bars at the ultimate load level ( $P = 136.1$  kN) was found to be for G2, G7 and G6 with values of  $9691.6 \mu\epsilon$ ,  $10847 \mu\epsilon$ , and  $11625.5 \mu\epsilon$  respectively on the east side of the beam. A dramatic increase in strain for G6 occurred from  $2000 \mu\epsilon$  to  $11625.5 \mu\epsilon$  when the load level increased from 125kN to 136kN prior to the peak load. During the post-peak stage with further crack (C6) development, the tie bar experienced increasing applied stress and it reached the greatest strain of  $13160.5 \mu\epsilon$  at  $P = 132.9$  kN on the post-peak curve. As shown in Figure 5.29, the location of these gauges (G2, G6 & G7) corresponds to the location of the major shear crack (C6).

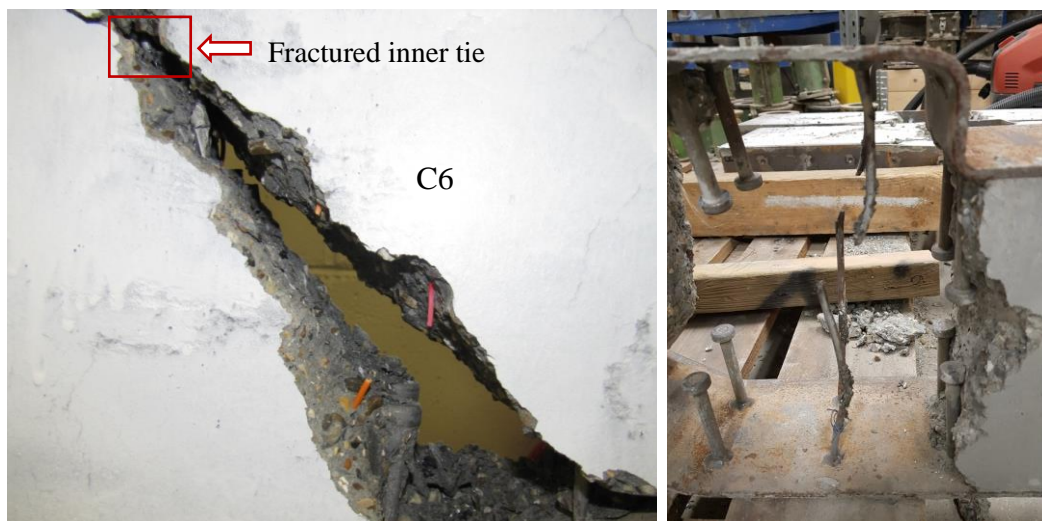


Figure 5.28. Fracture of a tie bar close to G7 for SCB3

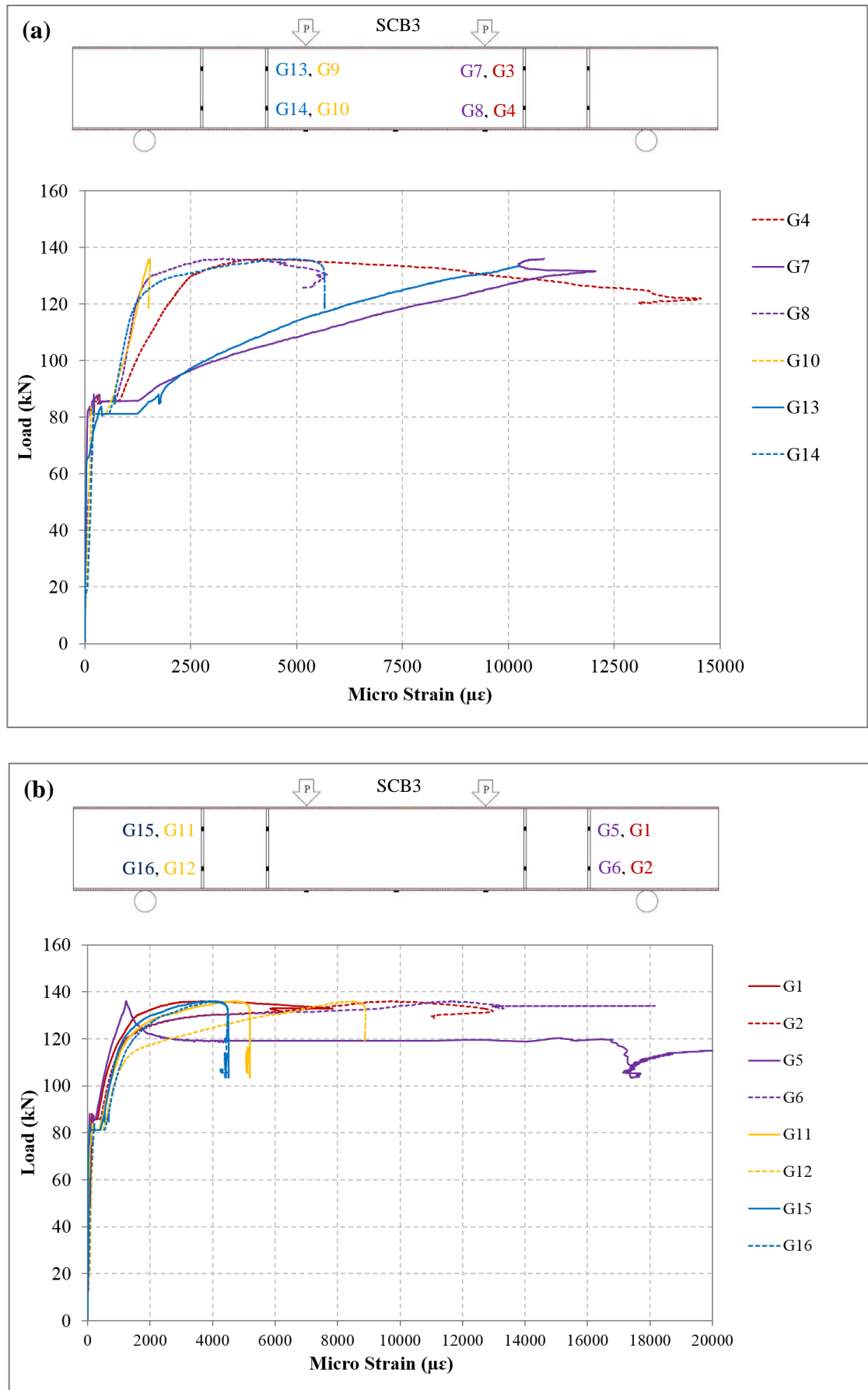


Figure 5.29. Measured strain for: (a) inner tie bars; (b) outer tie bars for SCB3



On the other hand, the highest strain on the west tie bars at ultimate load was measured by G12 and G13 which were  $8312.3 \mu\epsilon$  and  $10280.8 \mu\epsilon$  respectively. Similarly, these gauges cross the west shear crack C5. From these values, it is evident that the bars on the east side were under higher stresses at the ultimate load due to crack width progression at C6.

Comparing the results with SCB1, the strain induced on bars adjacent to the minor shear crack at the peak load for SCB1 had an average strain magnitude of  $6071 \mu\epsilon$  (G2 & G6), while SCB3 had an average value of  $6101.2 \mu\epsilon$  (G12 & G16). This shows that the strain induced for both beams were almost similar. This could be due to slightly higher split tensile strength of CNFRC. It can be concluded that the nanofibres were effective in the performance of concrete at the structural level by delaying the loss of concrete tensile strength, hence the strain induced on the bars were similar to the control sample. Contrariwise, SFRC performed better in SCB2 in resisting higher tensile stress, by controlling macro cracks, thus the bars had less strain at the peak load compared to both SCB1 and SCB3.

The measured strain for tension steel plate is shown in Figure 5.30. As can be seen from this figure, only the centre of the steel plate (G19 & G20) and G17 exceeded the yielding strain to some extent. SCB2 performed better than SCB3 in terms of tension plate yielding since the highest strain measured in SCB2 was  $1000 \mu\epsilon$  more than the measured strain in SCB3 tension plate. Considering this observation together with the significant yielding of the tie bars, it can be concluded that SCB3 failed in shear mode.

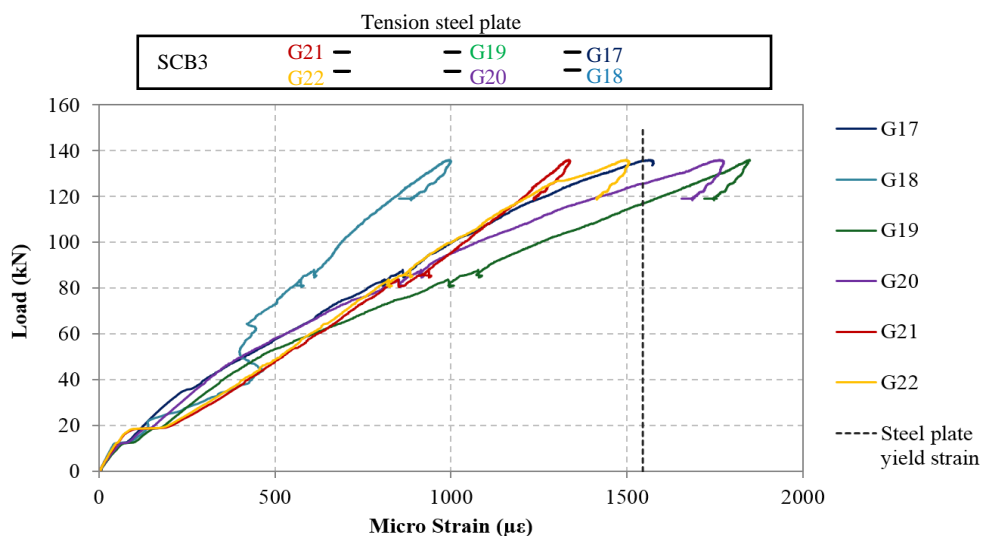


Figure 5.30. Measured strain in tension steel plate for SCB3

### 5.5.3. SCB4: CNFRC1.0

Specimen SCB4 was filled with carbon nanofibre reinforced concrete with 1.0% volume fraction of fibres (CNFRC1.0). The compressive strength and split tensile strength of CNFRC1.0 were respectively 11.4% lower and 7.1% higher than PC. The load-displacement curve for SCB4 is shown in Figure 5.31 and compared with the control sample SCB1.

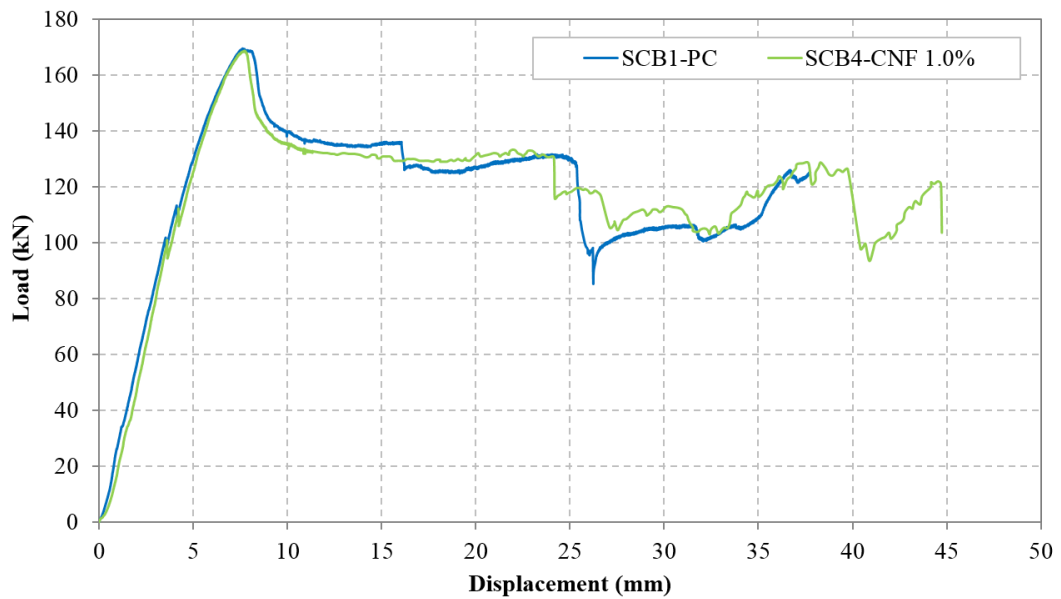


Figure 5.31. Load-displacement curve for SCB4

The ultimate load capacity of SCB4 was  $P = 168.8$  kN with the corresponding  $D = 7.72$  mm. It is interesting to note that although the compressive strength of CNFRC1.0 was lower than PC, the load-displacement behaviour of the beams was almost identical. From Figure 5.1, comparing SCB4 (CNFRC1.0) with SCB3 (CNFRC0.5), it is apparent that both samples had almost similar concrete mechanical properties. Accordingly, despite the identical mechanical properties, SCB4 performed better than SCB3 in terms of the ultimate load capacity (i.e. shear strength), displacement at the ultimate load, and energy dissipation of the system (i.e. area under the graph). This is associated with the volume fraction of fibres used and it shows that addition of 1.0% of CNF to the concrete had more pronounced effect on the structural performance of the SC beam than 0.5%.

### 5.5.3.1. Crack behaviour

The crack progression stages of sample SCB4 is shown in Figure 5.32. The first hairline crack appeared at  $P = 48.9$  kN (29% of the ultimate load) in the vicinity of the DG-R. This was significantly higher than previous samples which was 11% for SCB1, 17.5% for SCB2 and 19.4% for SCB3. The appearance of flexural cracks at higher load with relation to the ultimate load capacity for this sample manifests the effect of higher CNF in concrete and delaying the formation of flexural cracks by bridging (i.e. arresting) nano-cracks and micro-cracks. More vertical cracks started to appear in the mid-span (moment span) of the beam with increasing the applied displacement. Two very fine diagonal shear cracks appeared on the west (C5) and east (C6) side of the beam (Figure 5.32(a)) respectively at  $P = 101$  kN and  $P = 110.1$  kN, which was close to the control sample (100.2 kN and 113.3 kN). Minor load drops were evident on the load-displacement curve when these cracks appeared. The shear crack appearance was at higher load level compared to sample with 0.5% CNF (SCB3) which developed shear cracks at  $P = 82$  kN and  $P = 85$  kN. However, SCB2 had shear crack formation at  $P = 137$  kN, which was slightly higher than the SCB4. It is evident that 1.0% CNF was more effective than 0.5% CNF in delaying the formation of micro-cracks and consequently the flexural cracks, however, 0.5% SF performed slightly better for delaying the formation of shear cracks.

As the load progressed towards the peak load, similar to all previously described samples, the shear crack C5 increased in width, while vertical flexural cracks remained as a hairline crack (Figure 5.32(b)). With the shear crack opening, the beam started to show negative stiffness on the curve. At the same time, local buckling of the compression plate at the left point load was initiated. Figure 5.32(c) and Figure 5.32(d) show the plastic deformation of the compression plate during the post-peak stage and concrete crushing below the buckled plate.

The concrete contribution to resisting the load was diminished when the major shear crack C5 had progressed fully through the depth of the beam section at about  $P = 130$  kN and  $D = 15$  mm. Snap noises were heard at  $P = 129.6$  kN ( $D = 24.8$  mm),  $P = 116.8$  kN ( $D = 26.6$  mm), and  $P = 126$  kN ( $D = 39.8$  mm) consequently signified with small load drops on the load-displacement curve which were associated with tie bar fracture (Figure 5.33).

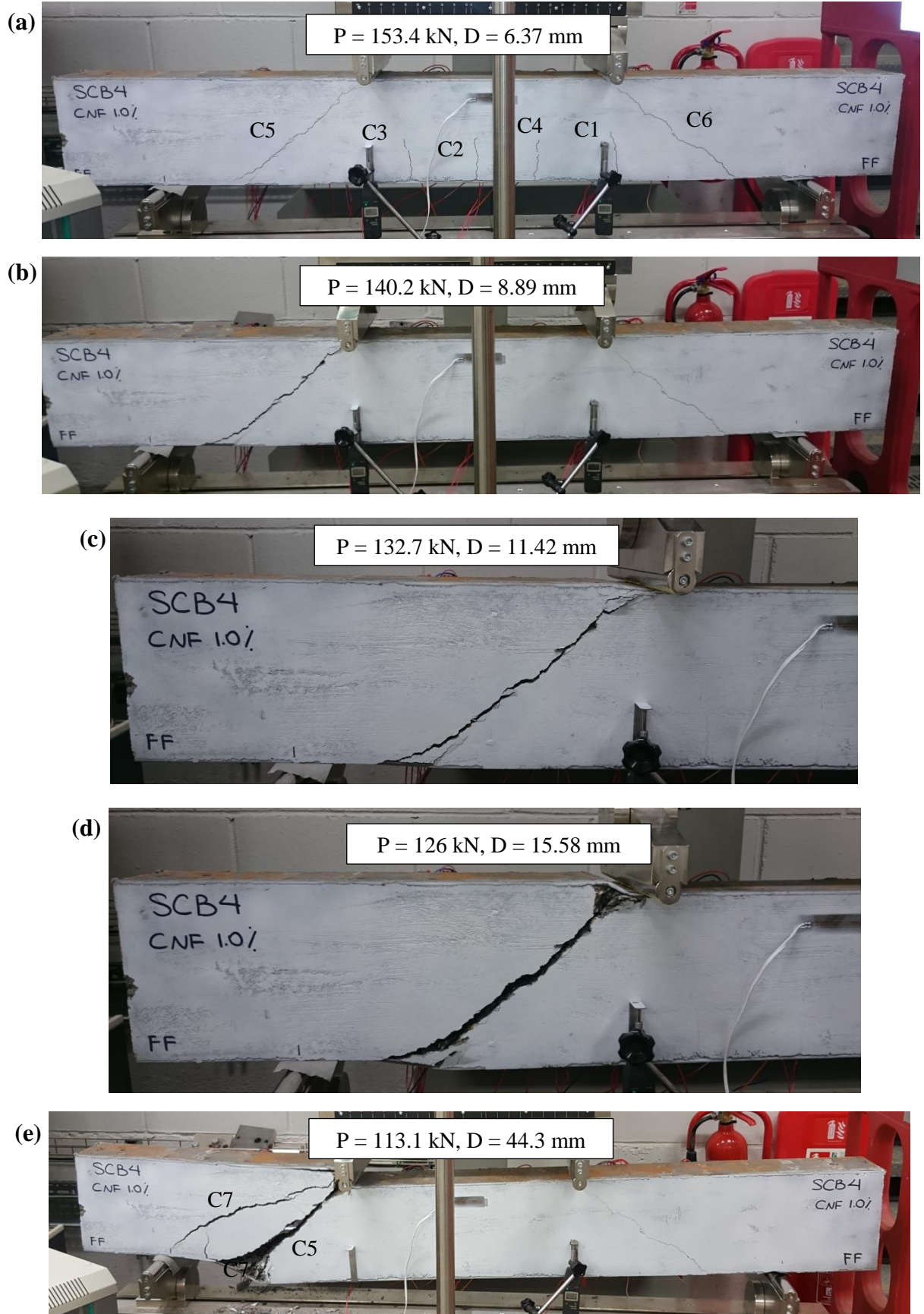


Figure 5.32. Crack progression for SCB4

It should be noted that the first tie bar fracture for SCB1 took place at lower displacement level of  $D = 15.5$  mm. The beam maintained its load capacity after the second tie bar fracture at 62.2% to 75% of the ultimate load. Followed by the third fracture noise which was thought to be associated with the west bars, a significant load drop to  $P = 97.8$  kN happened on the load-displacement curve. As a result of this tie bar fracture, a new abrupt diagonal crack (C7) adjacent to C5 formed across the support and the point load (see Figure 5.32(e)). After this phenomenon, there was an excessive beam deflection, thus the testing machine reached its displacement limit and the test was terminated. The final failure resulted in the separation of the concrete infill into two pieces at C5 as shown in Figure 5.34 with a closer view of C5 and C7.

From the crack pattern of the beam shown in Figure 5.35, it is evident that the beam failed in a shear mode similar to previous samples.



Figure 5.33. Fractured tie bar in SCB4





Figure 5.34. (a) Enlarged view of C5 and C7 for SCB4; (b) tie bars crossing C5 and C7 after demolition of the concrete core

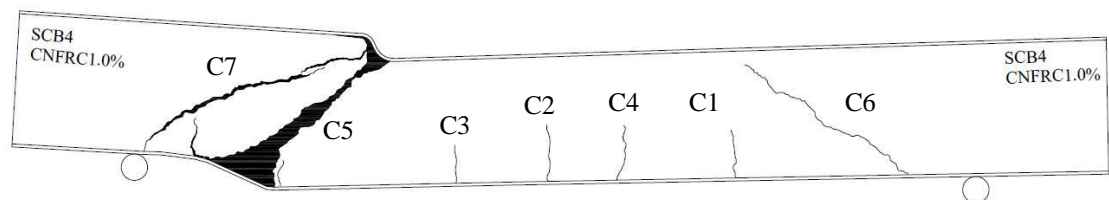


Figure 5.35. Final crack pattern for SCB4

### 5.5.3.2. DG measurements

The measured displacement by DGs and the mid-span deflection measured by the testing machine are presented in Figure 5.36. As expected from findings of previous samples, the displacement of the beam under the left point load showed divergence from symmetrical displacement compared to DG-R from ultimate load onwards. The displacement increased dramatically due to the damage progression on the west side of the beam and steel plate plastic deformation. This displacement eventually grew higher than the mid-span deflection.

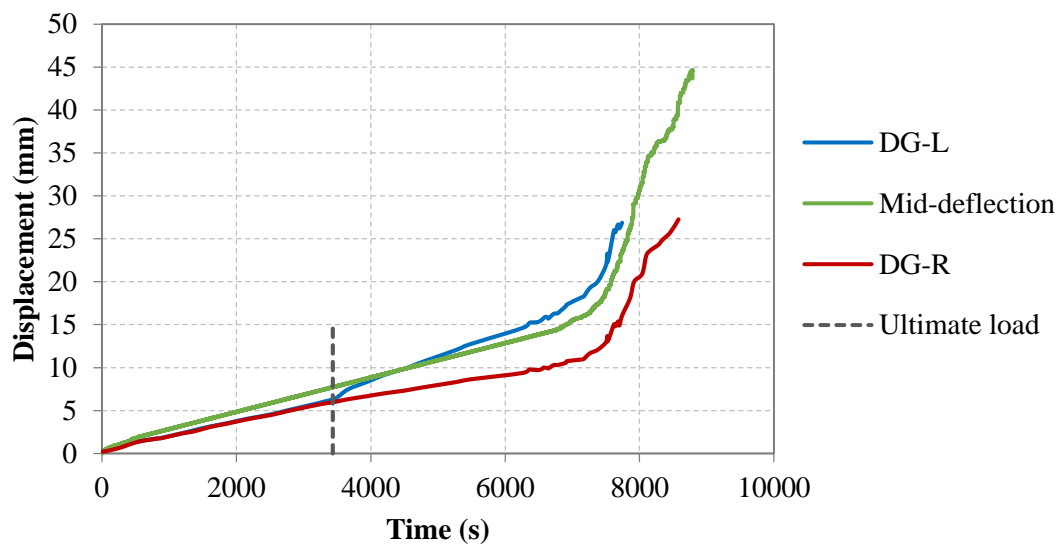


Figure 5.36. DG measurements for SCB4

### 5.5.3.3. Strain measurements

Measured strain for all tie bars for SCB4 is presented in Figure 5.37. the figure shows that all tie bars except G8 and G5 underwent yielding. As can be seen from Figure 5.37(a), the inner tie bars had higher strain at the top (G7, G3, G13, and G9). A sudden increase in strain for G13 was observed at  $P = 95$  kN, prior to the visibility of the shear crack, C5 at  $P = 100$  kN on the west side. Also, strain at the location of G7 at  $P = 110$  kN increased suddenly at which the east shear crack was formed. Moreover, an instant increase in the strain value of all gauges located at the bottom of the outer bars (G2, G6, G12 and G16) occurred at aforementioned load levels, which shows that due to the bar restraining the crack widening, the axial stress of the tie bar increased caused by

transmitting tensile stress across the crack. Thus, the strain in bar increased locally at the crack.

Comparison of the inner bars (e.g. G7 vs. G13) reveals that the tie bars on the west side showed higher strain values than the east side and this increase was more pronounced at higher load level towards the ultimate load. This indicated that the west crack was developing further, hence inducing higher stress in tie bars. In comparison to SCB3, which was made with CNFRC0.5, the strain induced on the tie bars crossing the cracks for SCB4 was lower at the ultimate load. G7 and G13 for SCB3 measured strain values ranging between 10000-12000  $\mu\epsilon$ , while SCB4 had 4200  $\mu\epsilon$  and 8300  $\mu\epsilon$  for similar gauges. This could be due to the effect of concrete with higher fibre dosage which was more effective in increasing concrete strength by controlling micro-cracks.

G16 and G12 at the lower half of the bars crossing the major shear crack showed strain value of 11270  $\mu\epsilon$  and 6981  $\mu\epsilon$  at the ultimate load. The strain value for SCB3, associated with the lower half of the bars at the major crack was 9691.6  $\mu\epsilon$  and 11625.5  $\mu\epsilon$ . The lower strain for SCB4 tie bars confirms better concrete resistance to the principal tension stresses, which resulted in less stress concentration on bars.

Figure 5.38 shows the measured strain for the tension steel plate of SCB4 throughout the test. All gauges, except G18, showed yielding of the tension plate in the moment region before the ultimate load capacity of the beam was reached. Yielding started from the centre of the beam and it expanded towards the sides. G22 showed a significant increase in strain, almost three times the strain in the middle (G20) at ultimate load compared to other gauges. The maximum strain reached for this beam was slightly higher than SCB3, which is considered to be an improved behaviour since energy dissipation through yielding of the plate is more favourable as a ductile behaviour. Also, the number of bars yielded in SSB4 was more than SCB3.

From the load-displacement curve, crack pattern, and the magnitude of strain induced on bars and steel plate, it can be concluded that SCB4 failed in shear mode.



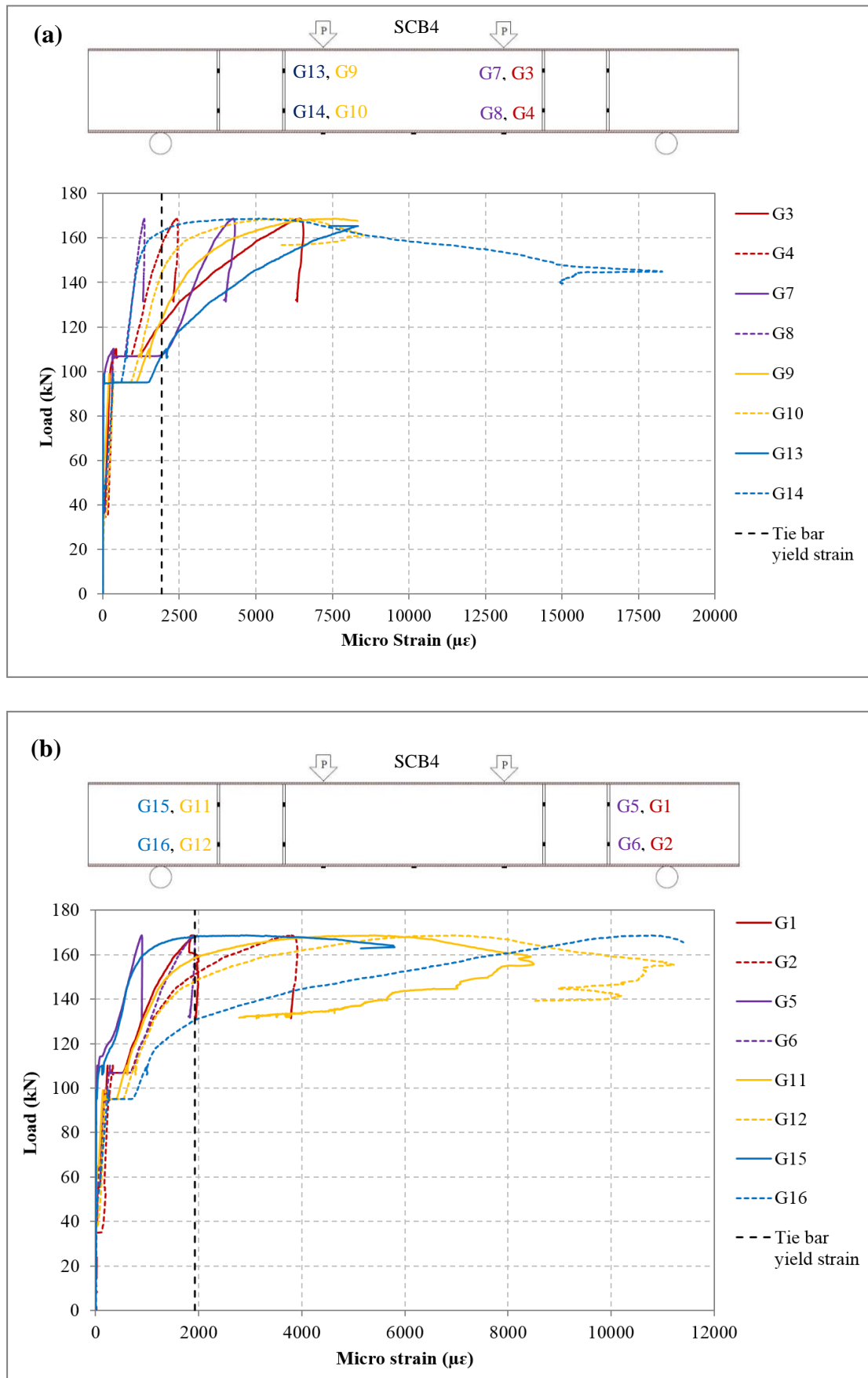


Figure 5.37. Strain measurements for: (a) inner tie bars; (b) outer tie bars for SCB4

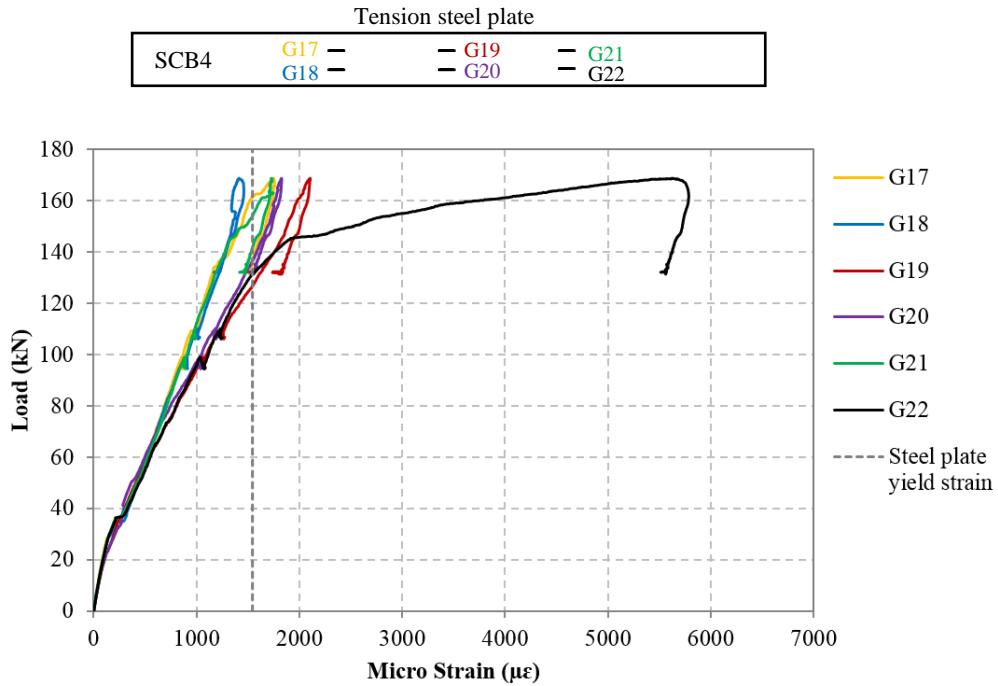


Figure 5.38. Measured strain in tension steel plate for SCB4

#### 5.5.4. Summary of category 1 SC beam test results

The load-displacement behaviour for all beams showed almost linear response up to 80% of the maximum load. All SC beams exhibited relatively uniform vertical flexural cracks under applied four-point flexural loading. The number of cracks increased with the formation of two diagonal shear cracks on both west and east shear span of the beam. The flexural cracks did not increase in length or width, while one shear crack showed gradual widening under increasing load and the load-displacement response became nonlinear. Limited number of flexural cracks and dominance of shear crack development in the beams in this category was due to lower shear capacity of the beam than the flexural capacity because of insufficient amount of vertical shear reinforcement (i.e. tie bars) and inadequate concrete strength. Hence, the shear failure occurred in advance and before further flexural damage (i.e. flexural cracks). For this category, the structural damage of all SC beams was marked by a major shear crack widening on one side of the beam at the peak load and by sudden load drop on the load-displacement curve. During the post-peak stage, followed by sever increase in crack width, local buckling of compression steel plate and concrete crushing took place and the concrete core was split into two sections. Hence, only steel plates and tie bars were contributing

in resisting the applied forces until maximum displacement limit of the testing machine was reached and the test was terminated.

The formation and subsequent opening of diagonal tension cracks in the concrete core describe the nature of a shear failure. A diagonal crack in the core can form at relatively low load. However, it should be noted that failure does not occur until the crack has opened significantly. The significant crack opening for all samples by splitting the concrete core into two sections signified the failure of the concrete core.

SFRC showed the highest energy dissipation through yielding of tension steel plate. CNFRC1.0 and CNFRC0.5 for SCB4 and SCB3 respectively, performed better in delaying the formation of flexural cracks compared to PC by 29% and 6.5% respectively. All FRC in this category delayed the formation of the first shear crack compared to the control sample SCB1. Amongst all, SFRC had the highest effect followed by CNFRC1.0 and CNFRC0.5 respectively. Furthermore, CNFRC1.0 performed better than CNFRC0.5 regarding the resistance of the core against applied shear forces as less strain values were monitored on tie bars. Having said that, the amount of fibres were insufficient to alter the failure mode of the SC beam.

Overall, the CNF fibres were more effective with 1.0% concentration in delaying the formation of the micro-cracks, especially the flexural cracks, while SF with 0.5% dosage was more effective in controlling the macro-size cracks and decelerating crack widening. It is evident that SF and CNF have been effective in enhancing the structural performance of the SC beam to some extent at different scales and they had different effects on the crack behaviour. This implies the need for benefiting from both improvements which can be obtained by combining the fibres within the matrix. The complementary action of nano- and micro-scale fibre reinforcement in concrete (rather than each of them individually) could render desired benefits to concrete material properties since they function at different scales. Also, according to few previous studies (Peyvandi et al., 2013; Willie and Loh, 2010), it is thought that nanofibres contribute to the interfacial stress transfer from macro fibres to the cementitious matrix and they can enhance the bonding and pull-out behaviour of macro-scale fibres.

Therefore, to better observe the effect of both fibres on the structural performance of SC beams, it was decided to use a hybrid fibre reinforced concrete combining both CNF and SF to enhance the material behaviour at two different scales and analyse their effect on the overall performance of the SC element. Accordingly, category 2 was then designed and tested, which will be further discussed in the following section.

## 5.6. CATEGORY 2: SCB5 & SCB6

In this category, both fibres (CNF & SF) were combined to make the hybrid fibre reinforced concrete core for the SC beams. The overall fibre volume fraction of 2% was considered for this category to see the effect of different fibre dosage on the behaviour of SC beam. SCB5 consisted of 1.0% volume fraction of each SF and CNF, while SCB6 had 1.5% SF and 0.5% CNF. The fibre dosage higher than 1.0% was not considered for CNF since the CNF threshold in this research according to the designed mix was 1.0%, and dispersion of higher dosage needs further material test to find the proper mix ratios. The load-displacement curve for both SCB5 and SCB6 is shown in Figure 5.39 and compared with SCB1. The results for each beam will be presented in the following subsections.

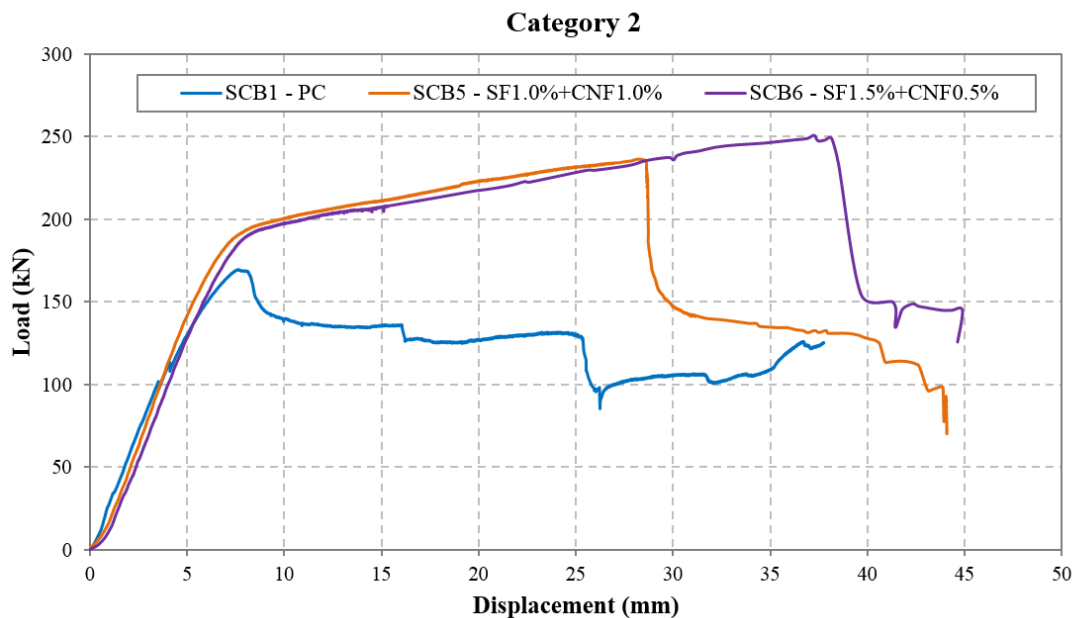


Figure 5.39. Load-displacement curve for beams in category 2

### 5.6.1. SCB5: SF1.0% + CNF1.0%

From Figure 5.39, the load-displacement response of SCB5 indicates that the specimen had an elastic-plastic behaviour with significant displacement ductility compared to SCB1. The compressive strength of the concrete core for this beam was 17% lower than PC and the tensile strength was 69% higher than PC. The ultimate load capacity of the beam was 236.5 kN with the corresponding displacement of 28.11 mm.

#### 5.6.1.1. Crack behaviour

The crack progression of the SCB5 is illustrated in Figure 5.40. Initially, few hairline flexural cracks were formed, as observed for previous beam samples, at  $P = 59.1$  kN in the moment span of the beam (C1-C3). This was higher than the control sample in which initial cracks occurred at  $P = 33.6$  kN. At the load level of  $P = 135.5$  kN with  $D = 4.77$  mm the formation of vertical cracks C4, C5 and C6 was noticed (Figure 5.40(a)). It should be noted that at this load level samples in category 1 already had developed two diagonal shear cracks at the shear spans. As the test progressed, new vertical hairline crack was formed within the moment span (C7). With increasing applied displacement, the length of flexural cracks (C1-C7) was developing further towards the top, hence moving the neutral axis towards the compression steel plate, while the crack width did not grow any further.

Crack C4 which initially formed as a flexural crack tended to change direction and propagated in an inclined direction towards the load point and it gradually increased in length as a flexure-shear crack. This also occurred for C5, which inclined towards the left point load as the test progressed. At  $P = 170$  kN with mid-span displacement of 6.22 mm, on the east shear span of the beam a short diagonal hairline shear crack (C8) started to form adjacent to the support extended towards crack C4. Similarly, on the west shear span of the beam, a new short diagonal hairline crack was formed (C9) in the mid-height of the beam depth. The length of C8 developed towards the top load point and it was more noticeable than C9 (see Figure 5.40(c)).

The mid-span crack width (C2) started to increase from the bottom gradually with increasing load (Figure 5.40(d)) and the load-displacement curve became non-linear from  $P = 140$  kN onwards. It should be noted that at this stage (transformation from linear to non-linear stage) the crack widths of all cracks, except C2, remained very fine and with increasing load the crack length increased while the crack width remained minimal. This signifies a good crack control of the hybrid FRC. The beam had hardening behaviour with decreased positive stiffness with the progression of the applied load.

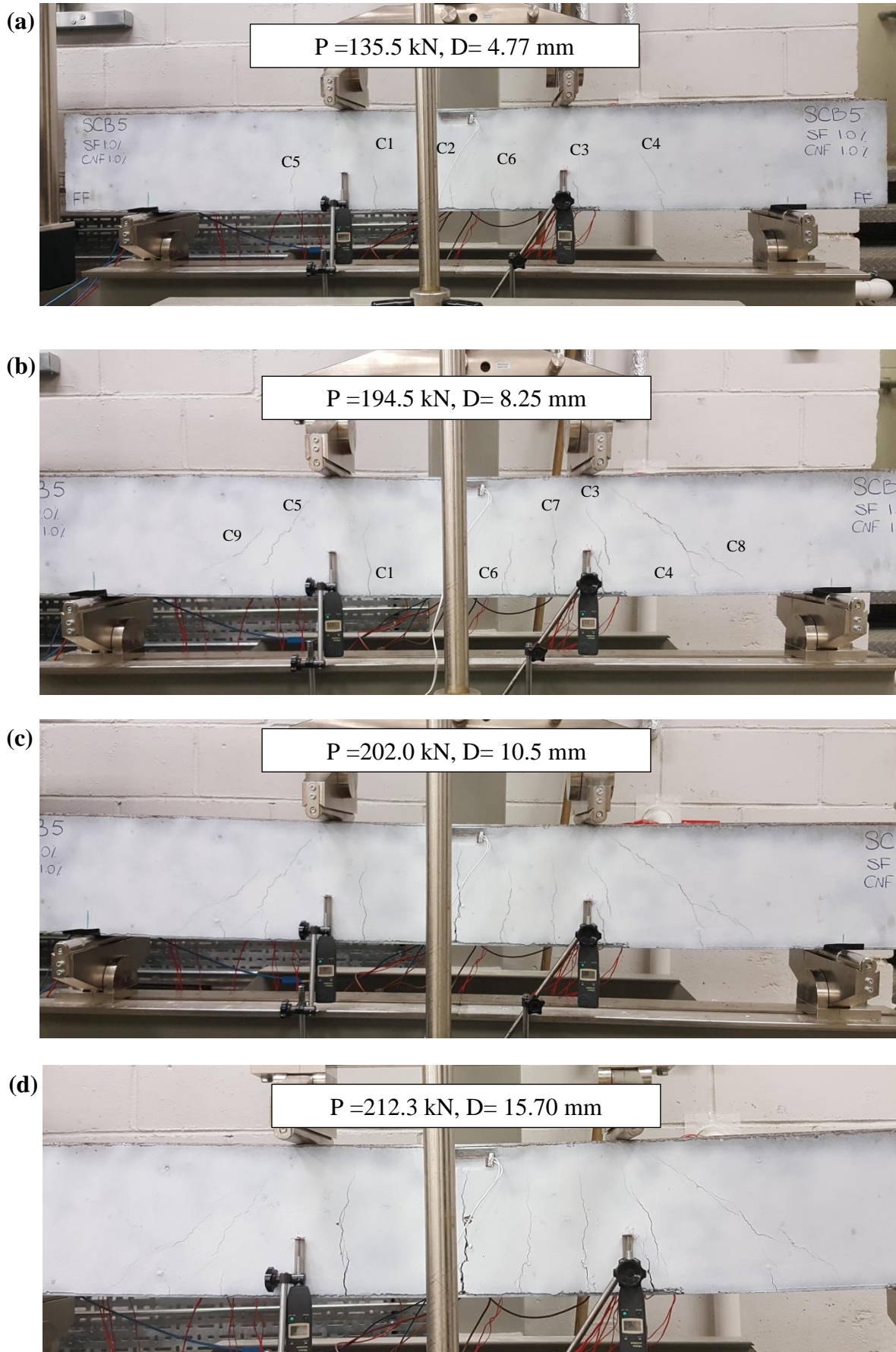


Figure 5.40. Crack progression for SCB5



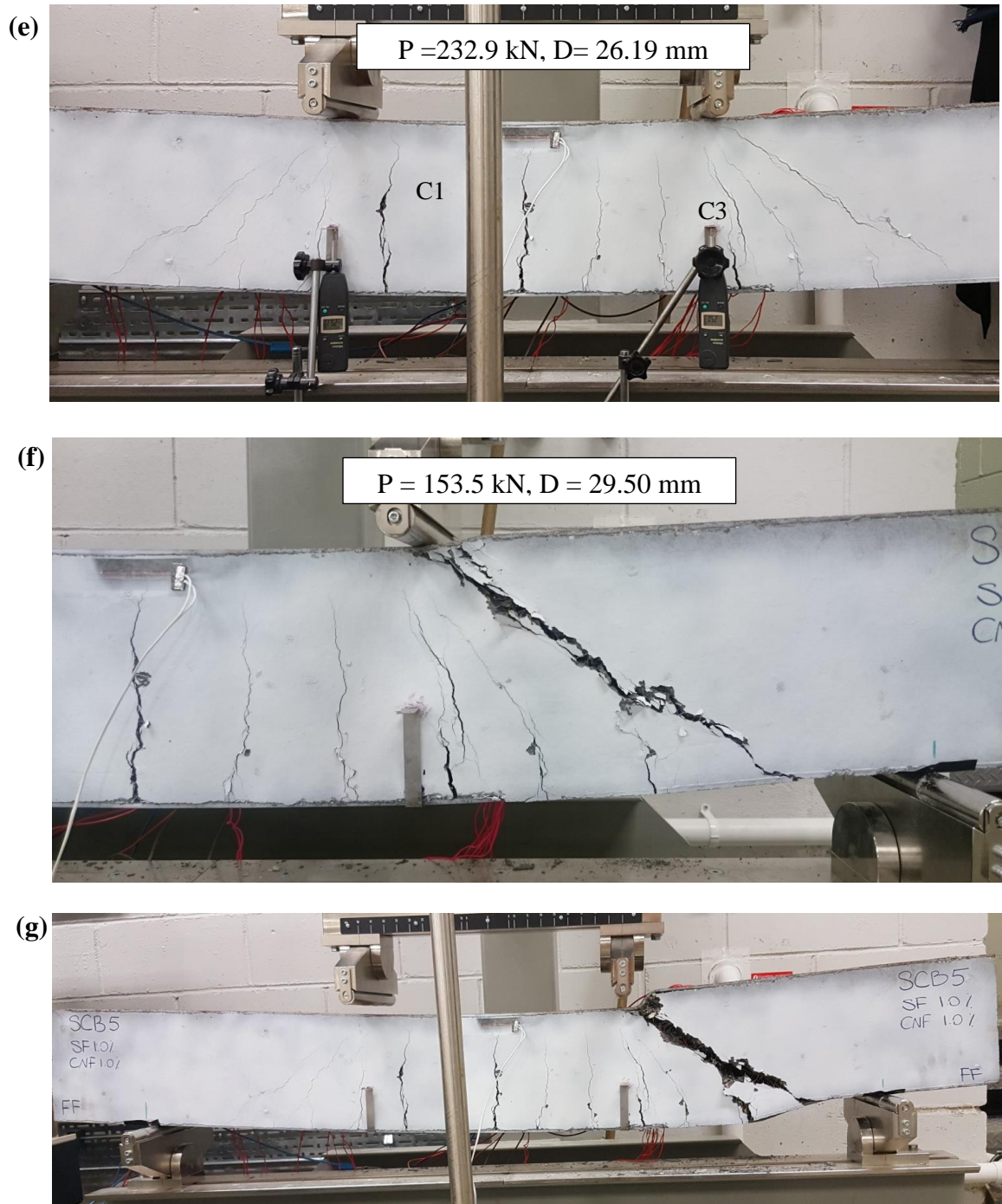


Figure 5.40. (continued)

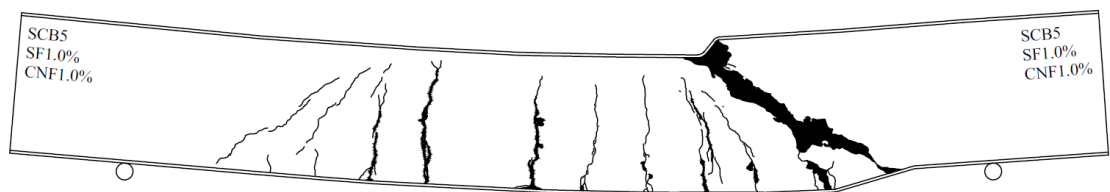


Figure 5.41. Schematic map of crack pattern for SCB5 after the test



The crack width of C2 increased to a certain extent and did not show significant crack opening due to the presence of steel fibres. Then C1, as well as C3, started to increase in width with the applied displacement (see Figure 5.40(d)). The steel fibres were successful in controlling any further increase in flexural crack widths. Vertical flexural cracks extended fully towards the top of the beam and the neutral axis at this stage reached close to the bottom edge of the compression steel plate. The moment capacity of the concrete core is zero at this stage and only steel plates contribute in resisting moment. At  $P = 231.2$  kN and  $D = 28.17$  mm, it was noticed that the width of the east shear crack (C8) started to increase gradually (Figure 5.40(e)). The beam achieved its ultimate loading capacity at  $P = 236.5$  kN and by an excessive increase in crack width of C8 and onset of steel plate local buckling at the east point load, the load capacity of the beam was governed by its shear capacity and a significant instant decrease in the load occurred on the load-displacement curve. Figure 5.40(f) shows the damage at shear crack C8 soon after the load drop.

Two snapping sounds were audible one after another during the final stages of the test at  $P = 142.6$  kN ( $D = 30.76$  mm) associated with the fracture of tie bars (see Figure 5.43), but unlike samples in category 1, no sudden load drop or sudden increase in crack width was observed and the steel fibres were bridging the concrete crack and resisted shear forces despite failure of tie bars. The crack suddenly increased in width due to fibre pull out at  $P = 100$  kN, therefore the concrete core was contributing in resisting shear forces up to this stage owing to the presence of SF. After the significant crack opening and fibre pull-out (Figure 5.42), concrete core lost its resisting capacity, while steel plates and tie bars could further contribute in resisting applied forces, however, the test was terminated at  $D = 44$  mm due to testing frame displacement limitations.

Figure 5.40(g) shows SCB5 at the end of the test and the final crack pattern for the beam is shown in Figure 5.41. From the crack behaviour of the SCB5, it can be concluded that the sample failed in flexure-shear mode.



Figure 5.43. Fractured tie bars in SCB5 (east shear span)



Figure 5.42. Closer view of the shear crack for SCB5

#### 5.6.1.2. DG measurements

The displacement vs. time for both DGs and mid-span displacement for SCB5 is presented in Figure 5.44. The beam showed symmetrical deflection during the test up to the maximum measured displacements of 25mm. It should be noted that by the end of the test, the right-hand side of the beam had higher deflection due to compression and tension steel plate deformation, and shear crack opening which occurred at higher displacement values that could not be measured by the DG. Comparison of the displacement for SCB5 with samples of category 1 shows that SCB5 had better performance in terms of symmetrical displacement up to higher deflection and less shear deflection. This was due to better crack control and delaying the shear crack opening by an adequate amount of fibres.

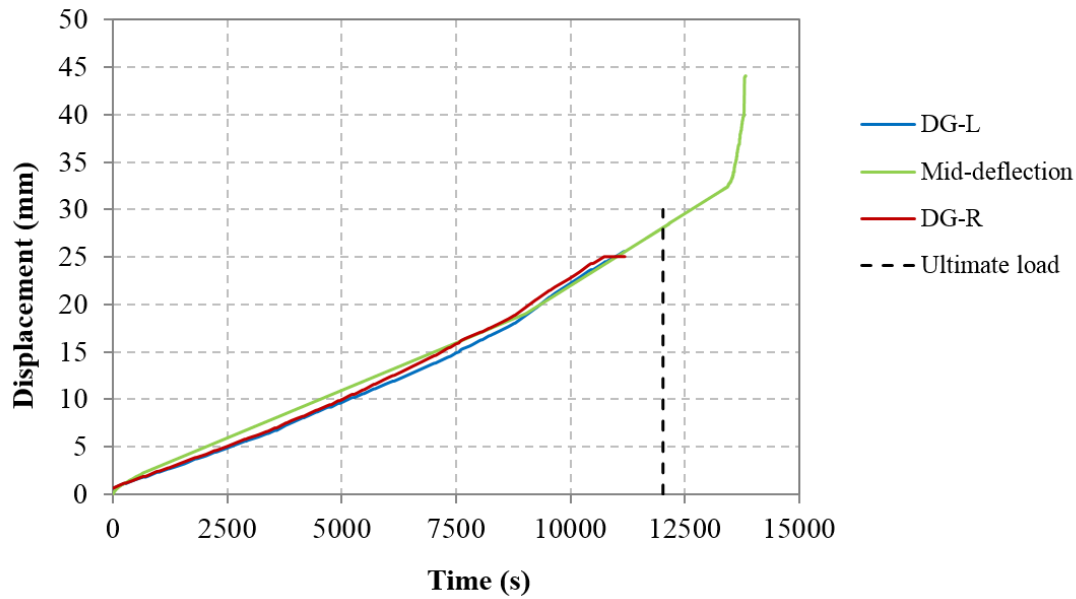


Figure 5.44. DG measurements for SCB5

### 5.6.1.3. Strain measurements

The measured strain for outer and inner tie bars vs. load are presented in Figure 5.45. For this specimen, G2, G3, and G10 were not working from the beginning of the test.

All inner tie bars underwent yielding at the plastic stage (i.e. hardening stage) of the load-displacement curve. These bars were in the vicinity of the vertical crack C4, C5, and the shear crack C8, hence due to higher stresses induced in this section, G3, G7 & G8 exhibited higher strain values compared to the west bars at any load point. The first yielding of bars occurred at G7 at  $P = 204$  kN. It is worth mentioning that the first yielding of the tie bar for the control sample occurred at the same location as SCB5 (i.e. G7; Figure 5.13) at  $P = 110$  kN, which was almost half the value for SCB5 with hybrid FRC.

At the ultimate load, when the load drop occurred due to the shear critical condition of the beam, the west tie bars (G13 & G14) showed strains of  $3500 \mu\epsilon$  and  $4700 \mu\epsilon$  respectively which was lower than the east bars. On the opposite side, the strain signal for G3 and G7 vanished before the beam reached its ultimate load capacity (i.e.  $236.5$  kN) and the maximum recorded strain for these were  $6660 \mu\epsilon$  and  $5800 \mu\epsilon$  at  $P = 232.8$  kN and  $P = 228.4$  kN respectively. However, G8 exhibited a strain of  $13600 \mu\epsilon$  at the ultimate load, indicating that the east tie bars were experiencing higher tensile stresses prior to the ultimate load and at the ultimate load due to the major concrete crack (C8)

and its widening. The maximum recorded strain by G8 was 24362  $\mu\epsilon$  after the major shear crack formation at  $P = 160.6$  kN.

In Figure 5.45(b) the strain value is presented up to 5000  $\mu\epsilon$  for clarity of presentation. G1, G5 and G6 reached a maximum strain value of 25000  $\mu\epsilon$  (at  $P = 128.4$  kN), 6700  $\mu\epsilon$  (at  $P = 157.4$  kN), and 13000  $\mu\epsilon$  (at  $P = 156.8$  kN) respectively. G6 had the highest strain due to its proximity to the major shear crack C8 and the bar crossing the major crack. In contrast to the inner tie bars, the outer tie bars on the west side did not yield throughout the test, while both east outer tie bars yielded after the load dropped corresponding to the significant opening of the east shear crack.

Overall, from the low strain level of tie bars during the test, up to ultimate load, it can be concluded that the shear forces and corresponding stresses were satisfactorily controlled and resisted up to the ultimate load mainly due to the concrete type used for the SC beam core which resulted in higher ultimate capacity of the beam. Thus, concrete contribution in resisting shear forces was significantly enhanced.

Figure 5.46 shows the strain in tension steel plate for SCB5. Plate yielding occurred prior to any tie bar yielding. By yielding of the tension steel plate and development of flexural cracks, the nonlinear stage of the load-displacement curve was originated. The maximum strain was reached at the ultimate load capacity of the beam (i.e.  $P = 236.6$  kN). The tensile steel plate first yielded at mid-span at G19 (at  $P = 121.7$  kN) and then spread towards the supports. Possibly the beam moved on the roller support and the left shear span length reduced, which increased the relative moment in the right shear span and caused the highest strain measured at G17 and G18. The strain varied from 26000  $\mu\epsilon$  to 31000  $\mu\epsilon$  at these locations. The strain induced on the tension plate was significantly higher than the measured strain in the tie bars throughout the test. Therefore, the desired ductile mode of energy dissipation took place by steel plate yielding.

Compared to the control sample and samples of category 1, the tension plate reached remarkably higher strain values (10 times higher than SCB2 and 17 times higher than SCB1). Therefore, the hybrid FRC was very effective in altering the structural behaviour of SC beam.

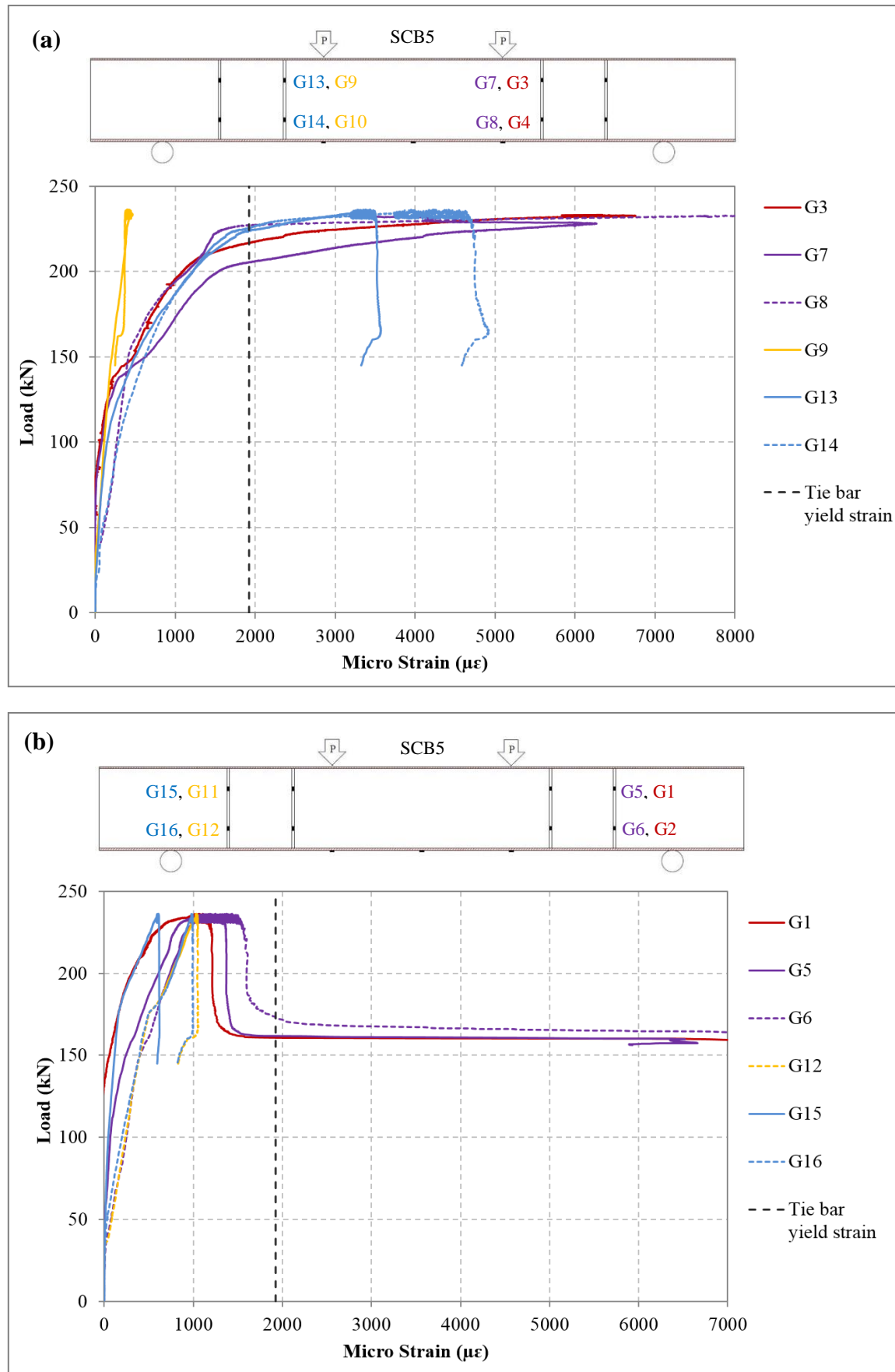


Figure 5.45. Measured strain for: (a) inner tie bars; (b) outer tie bars for SCB5

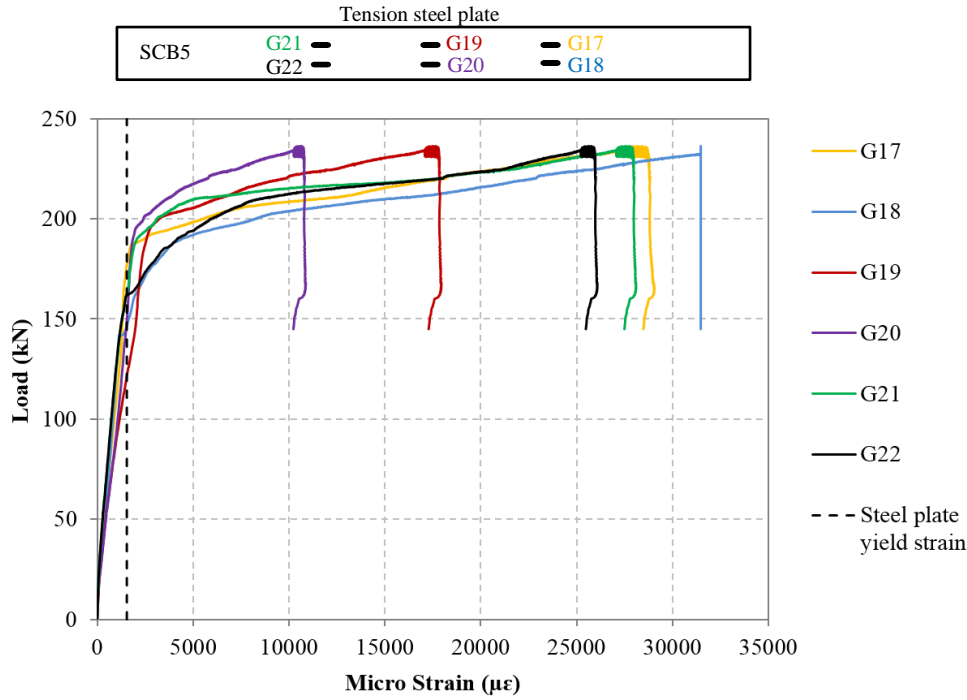


Figure 5.46. Measured strain in tension steel plate for SCB5

### 5.6.2. SCB6: SF1.5% + CNF0.5%

The compressive strength of concrete cubes for beam SCB6 tested on the testing day was 19% lower than PC, while the split tensile strength was 54.8% higher. The use of high steel fibre dosage has improved the tensile properties of the concrete remarkably.

The load-displacement curve for SCB6 (Figure 5.39) shows that this sample had the highest loading capacity of 251.9 kN with the corresponding displacement of  $D = 37.26\text{mm}$ . The ultimate load capacity and displacement at the ultimate load for SCB6 was increased by 6.5% and 32.5% respectively compared to SCB5 and by 48.5% and 390% respectively compared to the control sample.

### 5.6.2.1. Crack behaviour

The crack propagation for SCB6 is shown in Figure 5.47. For this sample, the initial hairline cracks (C1 & C2) were formed in the moment span at  $P = 66.2$  kN. Further hairline cracks (C3, C4 & C5) were developed at the mid-span and next to both DGs at  $P = 122.5$  kN and  $D = 4.7$  mm. It should be noted that for SCB5, these cracks developed at higher load level (i.e. 135.5 kN). Thus, the formation of the hairline flexural cracks was delayed in SCB5, which could be attributed to a higher percentage of CNF; twice as that in SCB6, which resulted in better micro-crack bridging and delaying the formation of the visible macro-cracks.

As the load progressed, cracks C1 and C2 further propagated towards the top. Also, a very fine diagonal hairline crack (C6) on the west shear span of the beam became visible as shown in Figure 5.47(b) at  $P = 160$  kN, and  $D = 6.3$  mm. The load at which the first diagonal tension crack that appeared on SCB5 was 170 kN, which was higher than that for SCB6. This is also attributed to the effect of nanofibres which delayed the formation of the shear crack by 6.3% higher load level. Shortly after, very fine vertical crack (C7) on the east shear span of the beam appeared.

The increase in central crack width was more obvious at the end of the linear stage and the behaviour became nonlinear on the load-displacement curve which was comparable with SCB5. Closer view of central cracks is shown at  $P=195.2$  kN and  $D = 9.26$  mm in Figure 5.47(d). As the applied displacement increased at the plastic stage, three cracks of C1, C2, and C4 located in the moment span were increasing in width from the bottom of the crack (see Figure 5.47(e)).

At the load level of 212.3 kN and  $D = 16.94$  mm, new diagonal hairline cracks (C8 & C9) parallel to each other appeared on the east shear span of the beam (Figure 5.47(f)). With the progression of the test, C7 joined C9 and further extended to the load point, and shear crack C6 further propagated from bottom of the beam to the point load. Finally, at  $P = 247.4$  kN and  $D = 38.01$  mm, the west shear crack was suddenly opened and the compression steel plate buckled at the load point causing concrete crushing. After the crack opening, the beam load capacity was governed by its shear capacity and the ultimate load was reached followed by a rapid load drop in the load-displacement curve. This behaviour was similar to SCB5, however at a displacement which was 32.5% higher than SCB5 and at a load which was 3.5% higher than SCB5.



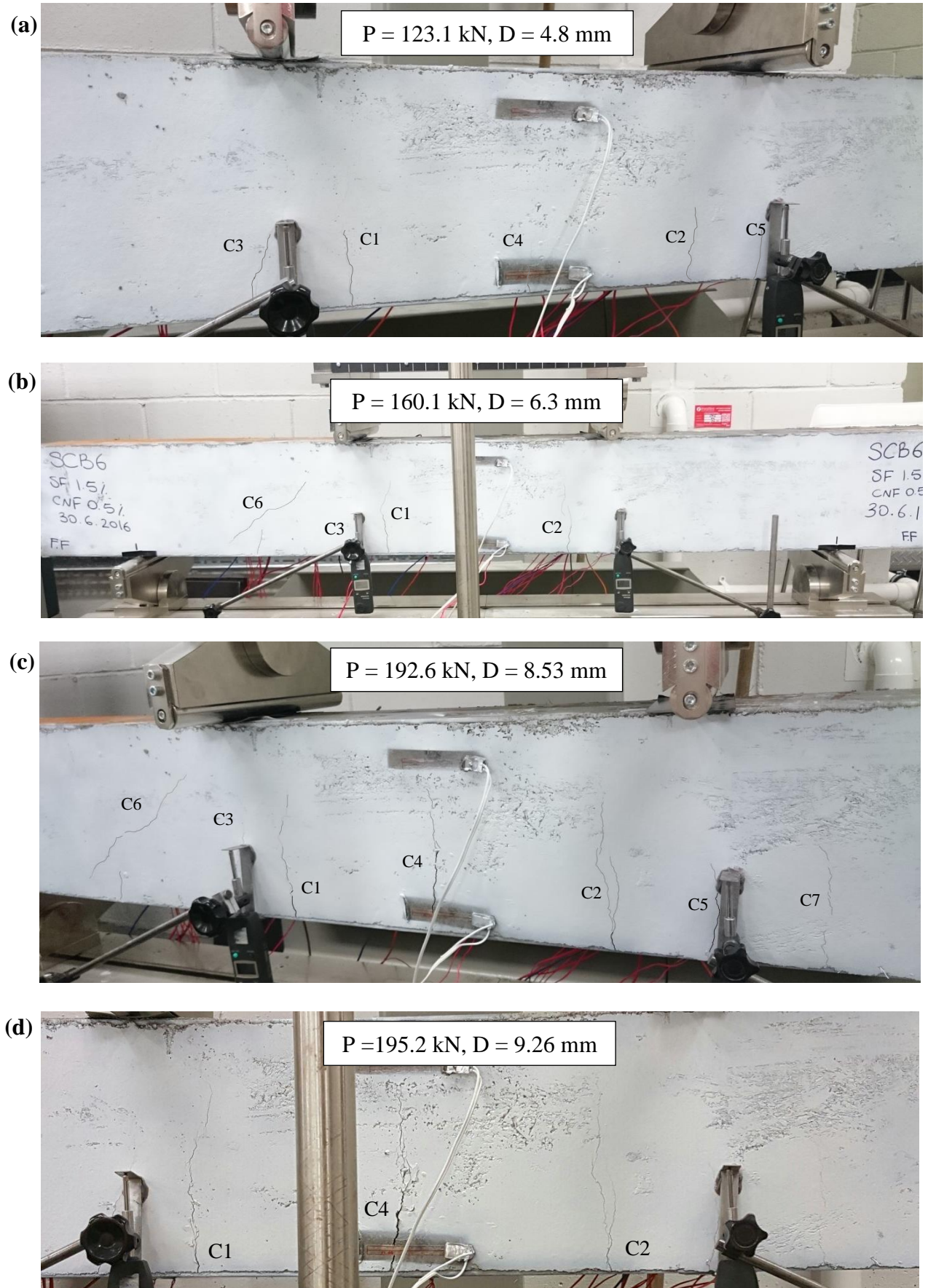


Figure 5.47. Crack progression for SCB6



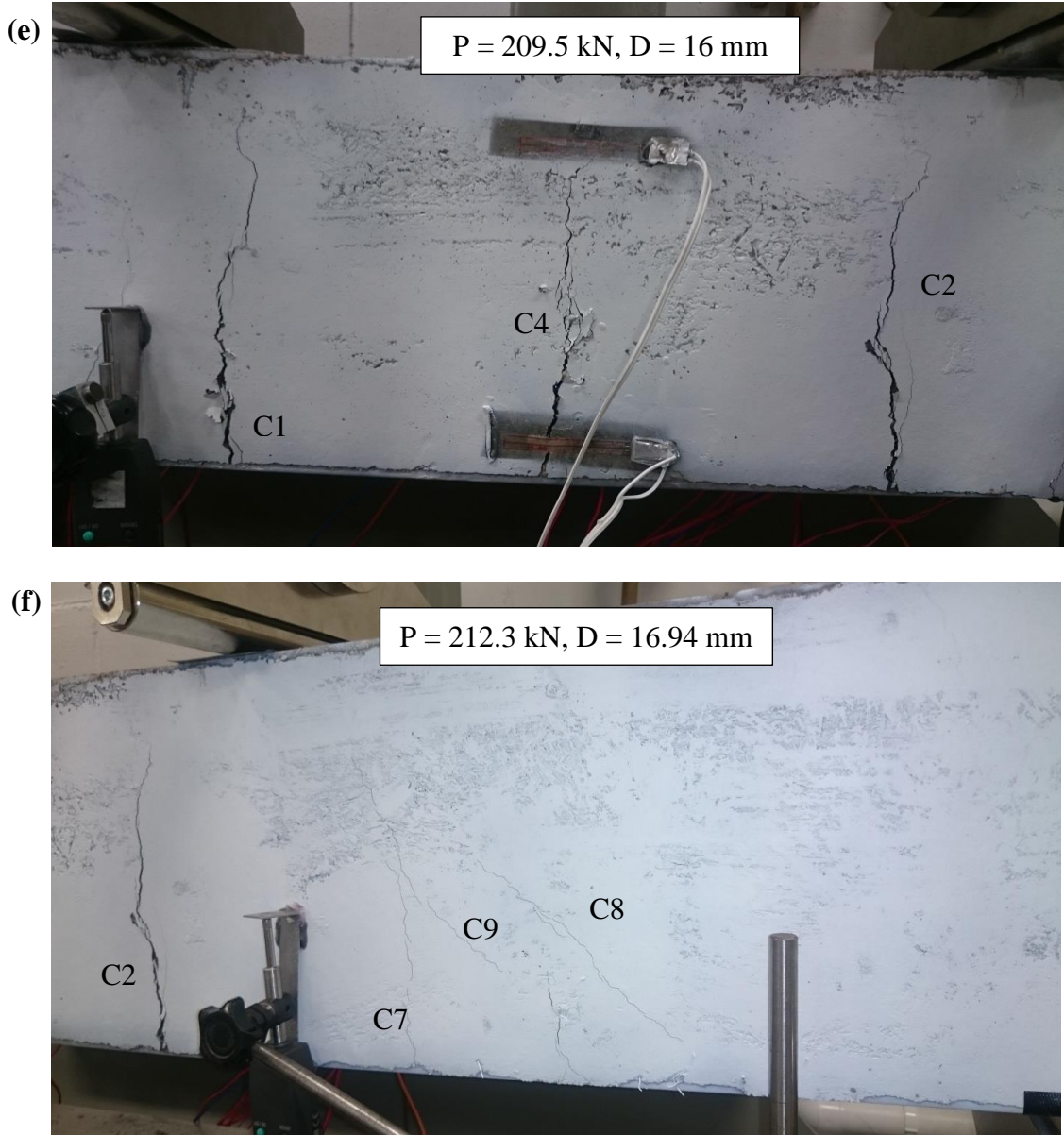


Figure 5.47. (continued)

It is worth mentioning that after the crack opening and the significant load drop, the concrete shear crack width was increased to an extent that the fibres were visible bridging the crack and the concrete core still had shear capacity due to bridging effect of 1.5% steel fibres (Figure 5.49). The beam maintained its resistance at a lower load level of 145 kN (57.6% of the ultimate load), however, the test was terminated as the maximum displacement capacity of the testing frame was reached. The photo of SCB6 after the test is presented in Figure 5.48(a) and the final crack map is illustrated in Figure 5.48(b). It is evident from this figure that the local buckling of the beam and the shear crack opening in SCB6 was less severe than SCB5 and higher steel fibre dosage could control the cracks from enormous crack width opening (as opposed to category 1).

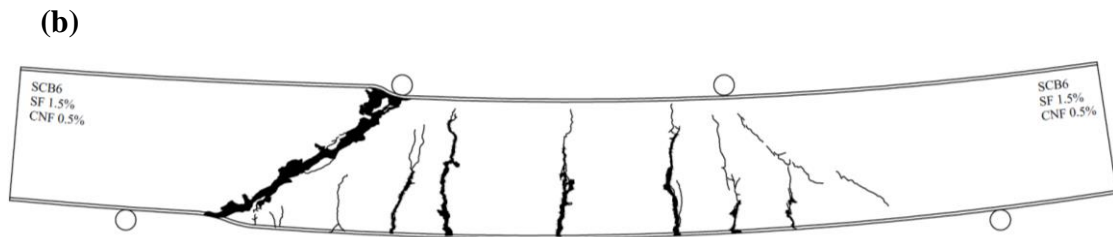
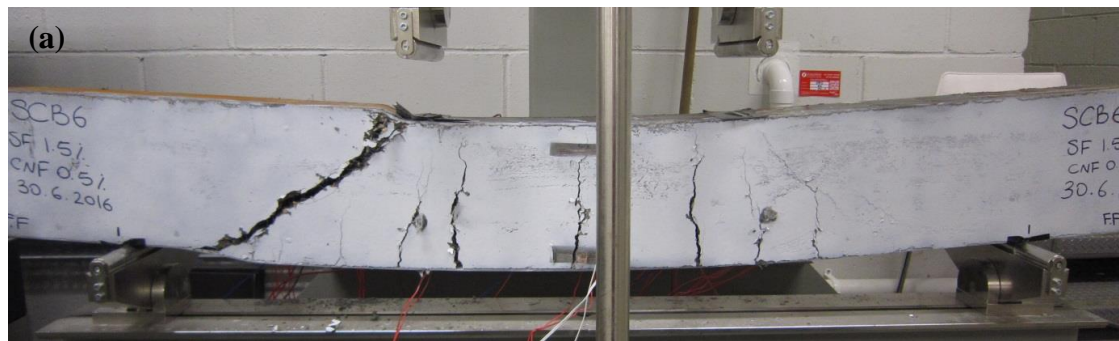


Figure 5.48. Crack pattern for SCB6 at the end of the test



Figure 5.49. Concrete shear crack view for SCB6

### 5.6.2.2. DG measurements

The displacement vs. time for both DGs and mid-span displacement for SCB6 is presented in Figure 5.50. It is evident that the measured displacements corresponding to load points were symmetric with no shearing displacement up to a large range of displacement. An increased rate of the displacement progression at all three locations could be detected from  $t = 9000$  s, which occurred at the onset of shear crack opening at the peak load. The maximum measured displacement by DGs was about 27 mm, however, from the trend of displacement increase it is thought that the displacement under the right point load outreached the mid-span deflection due to the shear crack of the beam.

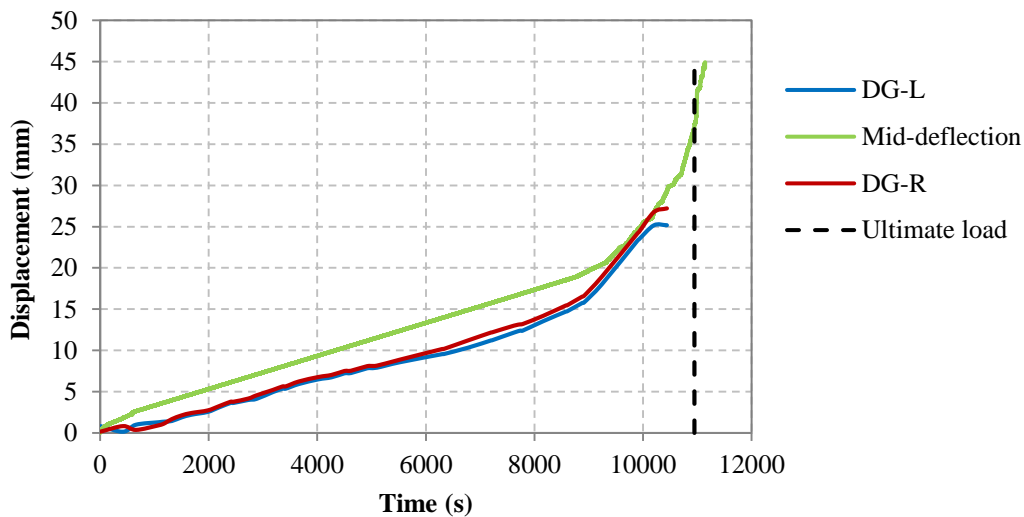


Figure 5.50. DG measurements for SCB6

### 5.6.2.3. Strain measurements

The measured strain for all tie bars is shown in Figure 5.51 for SCB6. In this sample, G1 and G2 were not working. As can be seen from Figure 5.51 (b), none of the outer tie bars yielded prior to the ultimate load. G11 and G12 showed yielding of the tie bars by sudden increase in strain to  $2476 \mu\epsilon$  and  $2940 \mu\epsilon$  respectively during the post-peak stage at  $P = 147.2$  kN. The yielding stage of the outer tie bars for SCB6 was similar to SCB5 (i.e. it occurred after the load drop). However, the maximum strain measured by the outer tie bars at the ultimate load level was  $1015 \mu\epsilon$  for SCB6, while SCB5 had a slightly higher strain of  $1540 \mu\epsilon$ . This was due to the higher shear resistance of SCB6 concrete core because of better macro crack bridging effect of steel fibres at higher volume fraction (1.5%).

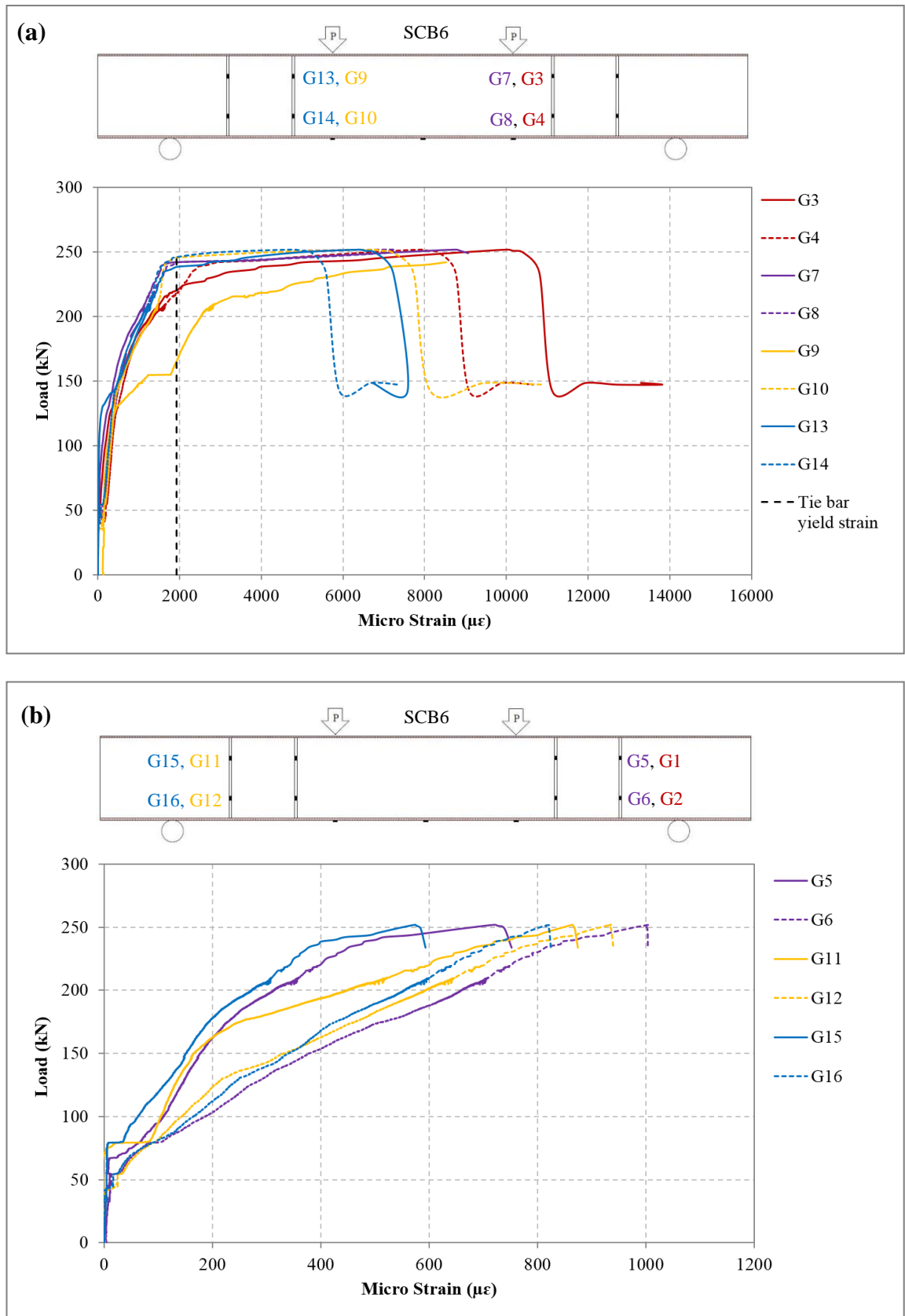


Figure 5.51. Measured strain for SCB6: (a) inner tie bars; (b) outer tie bars

From Figure 5.51(a), it is evident that the inner tie bars experienced higher strain than outer tie bars and they all underwent yielding at the beginning of the hardening stage (i.e. plastic stage) of the beam. At the ultimate load, the bar at the minor shear crack location, showed a measured strain of 10030.9  $\mu\epsilon$ , 8500  $\mu\epsilon$ , and 8760  $\mu\epsilon$  respectively for G3, G4 and G7 and the maximum measured strain by these gauges during the post-peak stage were 13809.6  $\mu\epsilon$ , 10654.4  $\mu\epsilon$ , and 9066.2  $\mu\epsilon$ . These gauge measurements were close to values previously observed for SCB3 (with 0.5% CNF) at its ultimate load of  $P = 136.1$  (8312  $\mu\epsilon$  and 10280  $\mu\epsilon$ ), however, it should be noted that the load level for SCB3 was 46% lower than SCB6. Therefore, the presence of SF at 1.5% volume fraction improved the performance to a great extent.

After the load drop, few strain data points were recorded by the gauges, which could be because of factors such as damage to the gauge, wire damage or de-bonding of the gauge from the tie bars. The measured strains on SCB6 for inner tie bars were higher than those in SCB5 and the reason is that the former resisted higher load. The measured strain for the inner bars was concentrated at the top of the bars, unlike the outer tie bars which had higher strain induced on the lower section of the bar. These locations are closer to the support and to the point load, at which the principal tension stress is causing the diagonal tension crack.

The measured strain of tension steel plate is shown in Figure 5.52. The tension plate yielded at the early stages of loading (around  $P = 100$  kN) prior to the hardening stage of the load-displacement curve. Yielding primarily occurred at the location parallel to the load points on the bottom steel plate. As the load increased, yielding progressed from the load point towards mid-span.

Compared to all previous SC beam samples, the plate yielding took place at lower load level. G17, G18, G21, and G22 showed identical strain values during the hardening stage up to ultimate load. This reveals the symmetrical stress distribution in the bottom steel plate. The maximum strain measured by these gauges was 31442  $\mu\epsilon$  due to the gauge measurement limit. This value was recorded before the ultimate load was reached at  $P = 234$  kN and it is expected that the maximum strain at the ultimate load would have been higher. The maximum strain at the centre of the plate was 23600  $\mu\epsilon$  and 25500  $\mu\epsilon$ . The tension plate for SCB6 showed highest measured strain for the plate amongst all previous samples, which reflects higher energy dissipation of the system

through tension plate yielding, which is the desirable structural performance. According to the observations from strain measurements, it can be concluded that SCB6 had ductile flexural behaviour up to the ultimate load and after the ultimate load the shear failure took place. Hence, the beam failed in combined flexure-shear mode.

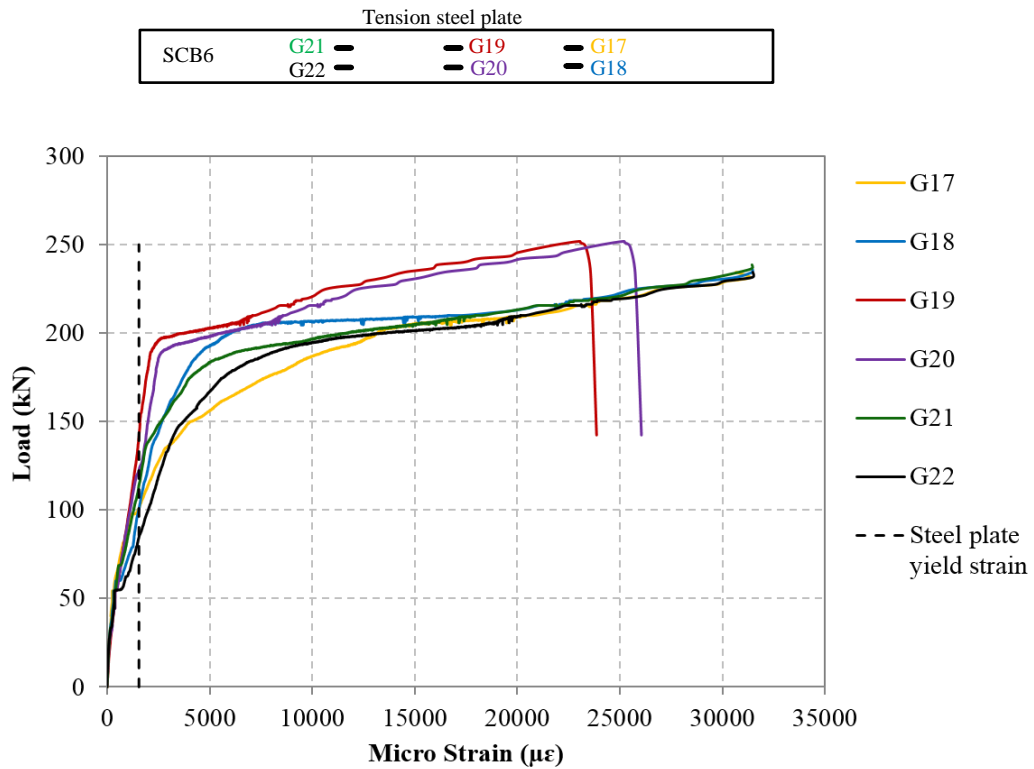


Figure 5.52. Measured strain in tension steel plate for SCB6

### 5.6.3. Summary of category 2 SC beam test results

Samples in category 2 with overall 2.0% fibres showed flexure-shear failure. Both beams had an elastic-plastic load-displacement curve and after reaching the ultimate load, the load resistance of the beam was governed by the shear capacity of the beam and an increase in a single shear crack width resulted in a load drop. The beam maintained its loading capacity at about 60% of the ultimate load, but due to the limited displacement of the testing machine, the test was terminated at around  $D = 45$  mm.

In comparison to category 1, both SCB5 and SCB6 showed significant tension steel plate yielding, hence there existed a ductile mode of energy dissipation. Moreover, the width of the shear cracks after the crack opening was significantly less compared to the

width of major shear cracks for the control specimen and beams in category 1. As a consequence of better crack control, category 2 showed less severe compression plate buckling, hence the overall displacement of the beam was symmetric with smaller shear deformation within a great displacement range.

Despite the higher compressive strength and tensile strength of SCB6 than SCB5, flexural cracks and shear cracks for SCB5 were further delayed during the test and they formed at higher load level. This is because higher CNF dosage was used in SCB5 and nanofibres were bridging the nano-cracks and micro-cracks more efficiently, therefore they were effective in giving a better crack pattern to SCB5 as opposed to SCB6. When the cracks reached the macro size, steel fibres were responsible for bridging the cracks and preventing excessive crack opening, where SCB6 performed better in terms of the ultimate strength and ductility due to higher steel fibre dosage.

Overall, the addition of 2.0% hybrid fibres to the concrete successfully altered the failure mode of the beam from diagonal tension failure to flexural-shear failure and significantly improved the ductility of the SC element. This was due to the increased shear capacity of the concrete core. To further investigate the effect of lower fibre concentration, which is more desirable in terms of cost and concrete weight, and whether the ductile failure mode observed for category 2 could be achieved with less fibre concentration, the overall fibre concentration of 1.5% was investigated. Category 3 then was designed and prepared accordingly, and SC beams were tested to investigate whether their response would be in any way superior or different to that of category 2.



### 5.7. CATEGORY 3: SCB7 & SCB8

The experimental investigation on category 3 focused on the use of hybrid fibre using both nano and macro fibres for the SC beam concrete core similar to category 2. However, in this category overall fibre volume fraction of 1.5% was chosen to further investigate the effect of the fibre dosage on the behaviour of the beam and its failure mode. SCB7 concrete core consisted of 1.0% volume fraction of SF and 0.5% CNF, while SCB8 had 0.5% volume fraction of SF and 1.0% CNF. The load-displacement curve for both SCB7 and SCB8 is shown in Figure 5.53 and compared with the control sample SCB1.

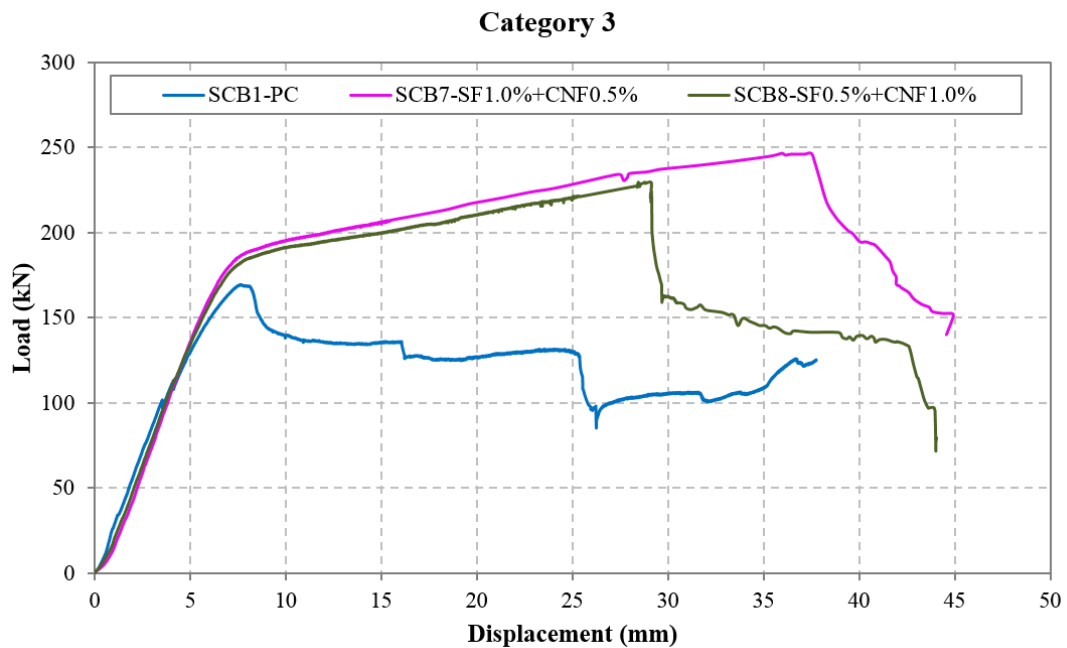


Figure 5.53. Load-displacement curve for category 3

#### 5.7.1. SCB7: SF1.0% + CNF0.5%

The compressive strength of concrete core for SCB7 tested on the testing day was 13.7% lower than PC, while its split tensile strength was increased by 78.6%. This shows that the combination of both nano and macro fibres have worked efficiently in improving the tensile properties of the concrete significantly.

The load-displacement curve for SCB7 shows that the ultimate loading capacity of the beam was 247.9 kN with the corresponding displacement of  $D = 35.9$  mm. These values were very close to that of SCB6 (251.9 kN and 37.3mm) from category 2 with 0.5%



higher steel fibre. It can be concluded that 0.5% steel fibres did not affect the load-displacement behaviour of the beam and 1.0% SF could be the sufficient volume fraction of steel fibre to be used in combination with CNF.

#### 5.7.1.1. Crack behaviour

The crack propagation of SCB7 is shown in Figure 5.54. For this sample, the first crack (C1) became visible at  $P = 56.1$  kN in the moment span adjacent to the DG-R. This was slightly weaker than SCB5 ( $P = 59.1$  kN), which had the same SF dosage as SCB7 but combined with doubled CNF dosage (1%). At  $P = 108.8$  kN and  $D = 4.1$  mm short vertical cracks C2, C3 and C4 were formed (Figure 5.54(a)). For SCB5 further flexural cracks formed at higher load level of  $P = 135.5$  kN (higher by 24.5%). This shows the effect of higher CNF dosage in the concrete affecting the load at which initial cracks form. As the load progressed the cracks in the moment region increased in length.

A very short diagonal crack (C5) on the east side of the beam was visible at  $P = 161$  kN with the corresponding displacement of 5.98 mm (this was  $P = 170$  kN for SCB5) and C3 propagated in a diagonal direction towards the loading point due to combined action of shear and flexure in the shearing span. As the crack width of C2 widened, the beam showed hardening followed by an increase in the width of C1 (see Figure 5.54(c)). Additional flexure cracks C6 and C7 occurred at the location of DGs at  $P = 179$  kN. The crack widths of C1, C2, and C4 increased gradually with the applied displacement (Figure 5.54(d)), while other cracks remained as hairline cracks. This is because the propagation of crack width was controlled by end hooked steel fibres and the crack length reached the top surface of the beam. As the flexural cracks were extended through the entire depth of the beam section, at these sectors at failure, the concrete had no contribution to the section flexural capacity and the neutral axis had risen from the mid-height (at early stages of loading) to higher up along the section near or at the bottom edge of the compression steel plate with increasing load.

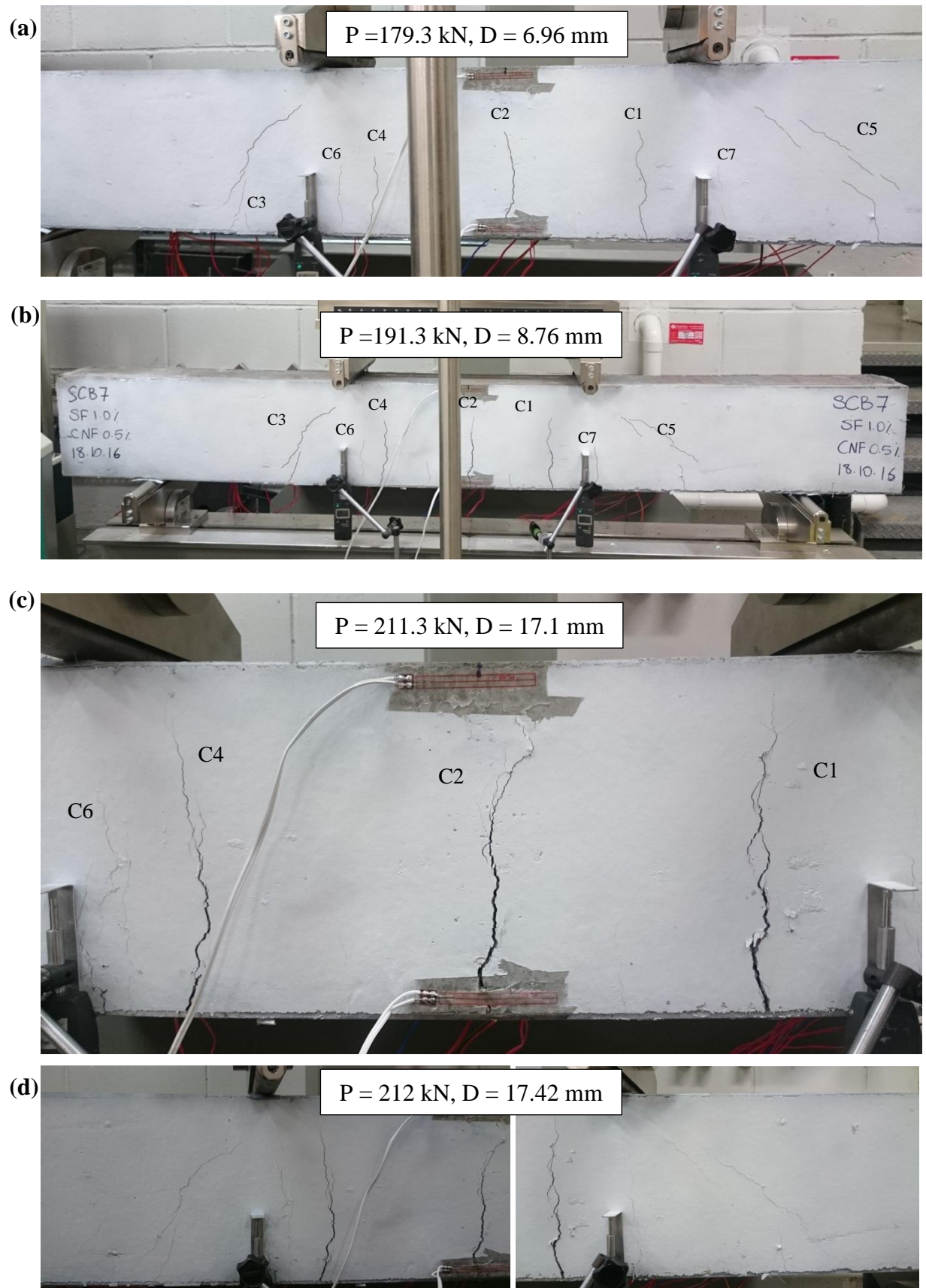


Figure 5.54. Crack progression for SCB7

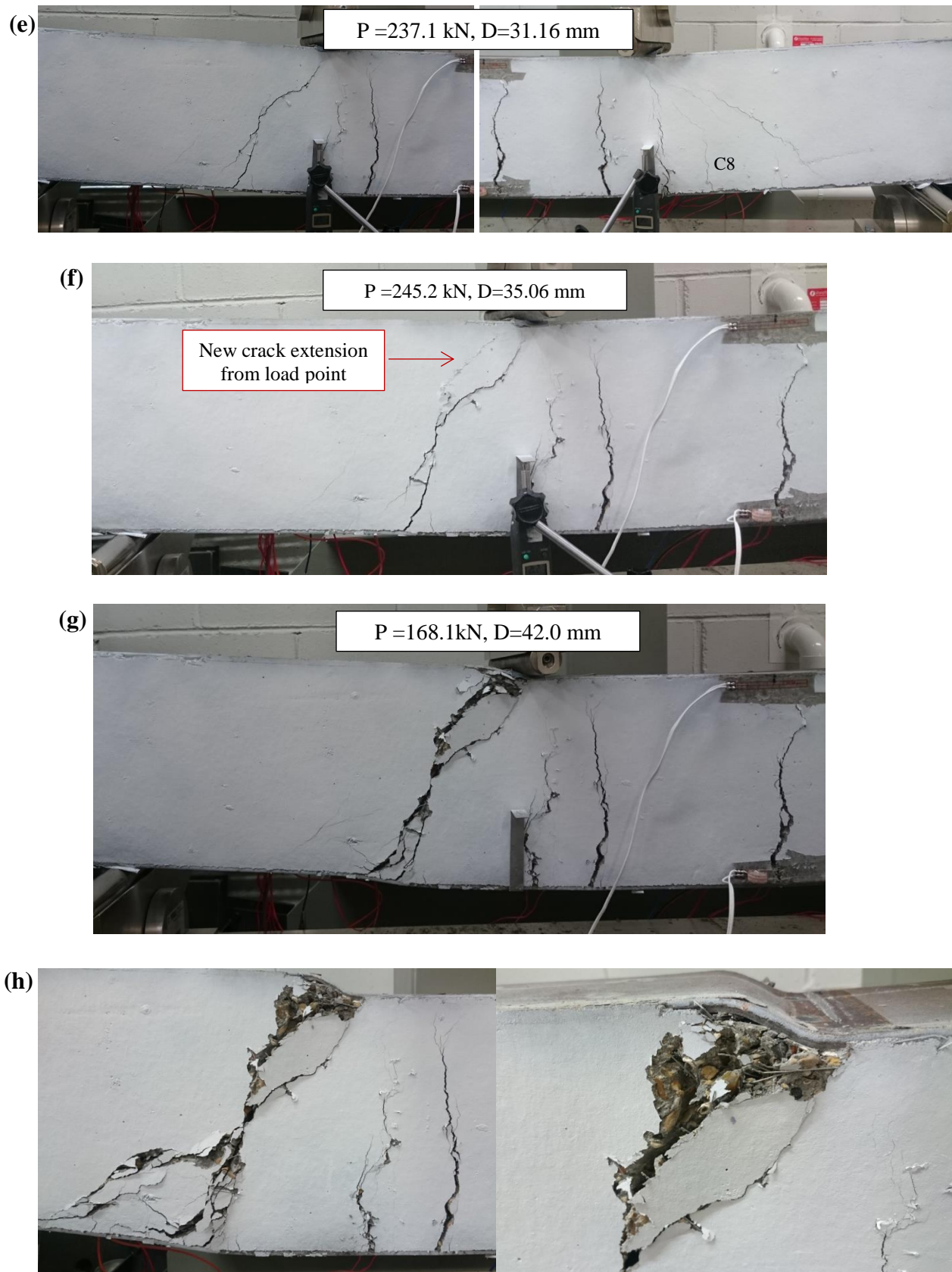


Figure 5.54. (continued)

Fracture noises were also heard for this beam at  $P = 230$  kN with corresponding  $D = 22.38$  mm, however, no excessive increase in any crack width was observed which means that the steel fibres could control crack opening in an event of tie bar failure. Cracking noises could be heard at  $P = 230.1$  kN and  $D = 25.46$  mm from inside the concrete core. With the progression of applied displacement, C1 showed an increase in width at  $P = 236.2$  kN and  $D = 28.33$  mm. Meanwhile, C5 on the east side increased in length towards the point load and a new crack C8 appeared between C7 and C5 as shown in Figure 5.54(e). At the large deflection range, the cracks in moment span reached the top plate. Moreover, small scattered cracks in the vicinity of C6 and C7 in the proximity of DGs were developing. Two fracture noises were audible at  $P = 239.8$  kN ( $D = 31.66$  mm) and  $P = 241.4$  kN ( $D = 32.76$  mm) before the ultimate load was reached. Despite the few tie bar failures, the beam still showed hardening behaviour until  $P = 247.9$  kN which signposts the concrete ability in controlling cracks and structural damage under high shear stress.

At the load 245.2 kN with the corresponding displacement of  $D = 35.06$  mm a diagonal crack from the left point load joined C3 and created a concrete block under the left point load (see Figure 5.54(f)). At the ultimate load, this section of the beam started to show increased damage and compression steel plate deformation was induced by the opening of C3. The beam showed negative stiffness and the load decreased on the load-displacement curve. With decreased capacity of the beam, concrete crushing and spalling were happening as shown in Figure 5.54(h). Although the beam did not fail, the test was terminated automatically as the displacement capacity of the test frame was reached. It can be seen from Figure 5.55, showing SCB7 at the end of the test and its crack map, that major cracks on the concrete core, did not show large crack width as significant as previous beams. Also, the major crack C3 was ineffectual in splitting the concrete core into two sections. Thus, there was a significantly enhanced crack behaviour of the SC beam with the addition of 1.5% hybrid fibres in the concrete core.

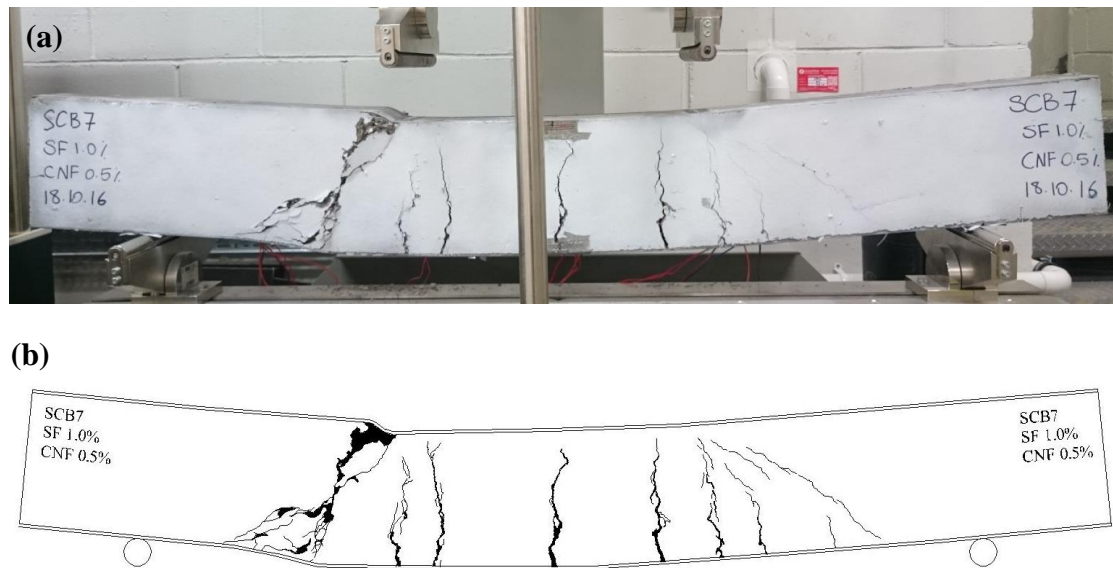


Figure 5.55. SCB7: (a) after the test; (b) crack map after the test

#### 5.7.1.2. DG measurements

The measured displacements by DGs are shown in Figure 5.56. The displacement of the SCB7 was symmetrical throughout the test, up to the ultimate load and the maximum displacement that could be measured by the DGs were reached just before the ultimate load was reached and before the shear crack widening and local buckling took place. The displacement of the beam increased gradually and proportionally and this was due to the distributed discrete number of flexural cracks along the beam and ductile performance of the beam. This behaviour was in contrast to the performance of the control specimen and singly-reinforced beams in category 1 which showed displacement deviation at one side of the beam at the early stages of loading due to the shear crack formation.



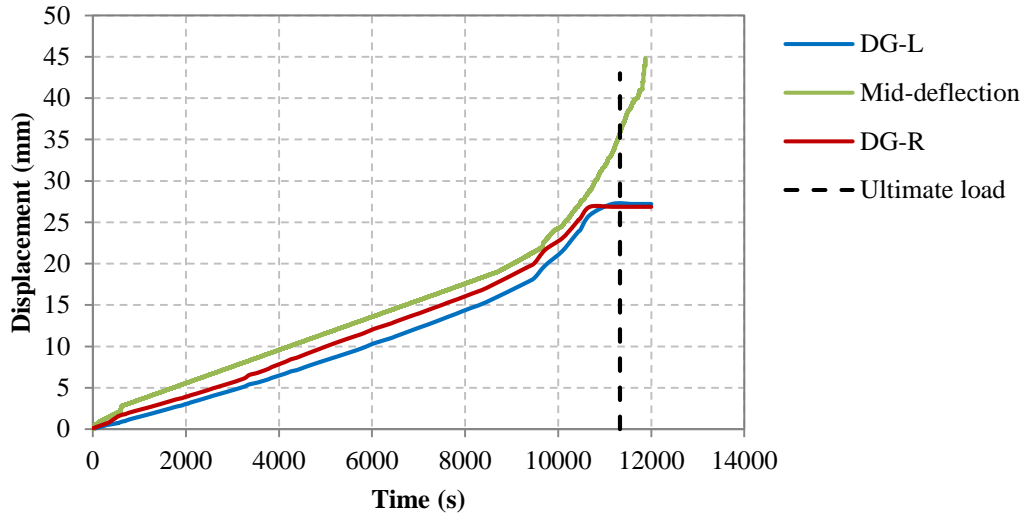


Figure 5.56. DG measurements for SCB7

### 5.7.1.3. Strain measurements

The measured strain for all tie bars, except G2 and G6 which did not function, is shown in Figure 5.57 for SCB7. The results for the inner tie bar (Figure 5.57(a)) show that G3, G7, G8, G10, and G14 exceeded yielding strain and first yielding took place at about  $P = 209$  kN as recorded by G7. This value is comparable to results from G7 in SCB5, at which initial yielding occurred at  $P = 204$  kN which was at an almost similar load level.

By getting closer to the ultimate load capacity of the beam, G8 showed a sudden increase from  $2000 \mu\epsilon$  (at  $P = 242.2$  kN) to  $5240 \mu\epsilon$  (at  $P = 245.5$  kN) and G14 had an increase in strain from  $1959 \mu\epsilon$  ( $P = 238.1$  kN) to  $8411 \mu\epsilon$  ( $P = 246.9$  kN). Also, the strain for G10 increased significantly from  $2047 \mu\epsilon$  (at  $P = 238$  kN) to  $8876 \mu\epsilon$  at ( $P = 242$  kN). G10 and G14 with an average strain value of  $9013 \mu\epsilon$  showed the highest strain value at the ultimate load capacity of the beam, representing the strain of the lower section of the west inner bars which were crossing flexure-shear crack C3.

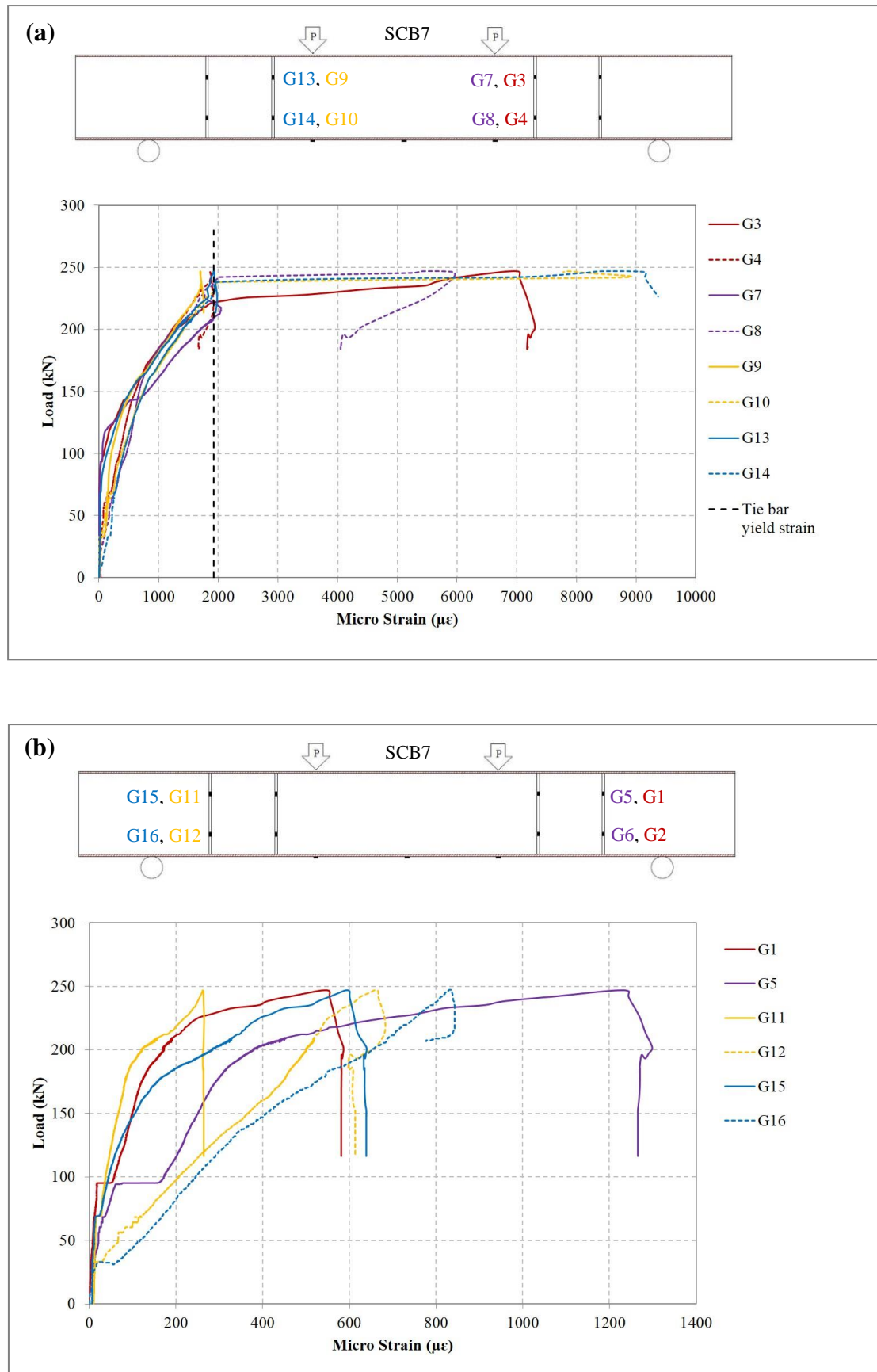


Figure 5.57. Measured strain for SCB7: (a) inner tie bars; (b) outer tie bars

G8 adjacent to C8 showed strain of  $5936\mu\epsilon$  which was 29.4% less than opposite gauge (G14) at the ultimate load. It was clear that C8 was not as severe as C3 (see Figure 5.54(e)) hence the strain induced on the west tie bar adjacent to C3 was higher. Overall the inner tie bars had a substantial increase in their strain from approximately  $P = 240$  kN just before the ultimate load at which the concrete shear capacity was reached. In Figure 5.57(b), it is shown that none of the outer tie bars yielded and they were strained up to a comparatively small value. The maximum strain reached for these bars were for bottom gauges of west bars, G16 and G12 which were  $824\mu\epsilon$  and  $657.5\mu\epsilon$  respectively.

The measured strain for the tension steel plate for SCB7 is shown in Figure 5.58. Steel plate yielding started at  $P = 125$  kN. As one might expect, this was earlier for SCB6 (at  $P = 84.8$  kN) with 0.5% higher SF dosage. On the other hand, it was close to the behaviour of SCB5 (SF1.0+CNF1.0) with initial plate yielding at  $P = 121.7$  kN. The strain increased gradually at the linear stage of the loading and all gauges reached  $31450\mu\epsilon$  (i.e. the maximum bound for the strain gauge sensor) at almost the maximum load capacity of the beam. Comparing the strain induced on tension steel plate throughout the test with the tie bars reveals that the energy dissipation took place by yielding and plastic deformation of the bottom plate while the strain in tie bars was generally minimal compared to steel plate until the peak load was reached. This ductile behaviour is a favourable structural performance achieved by the SC beam with the aid of hybrid fibre reinforced concrete core. Finally, SCB7 failed in a flexure-shear mode.

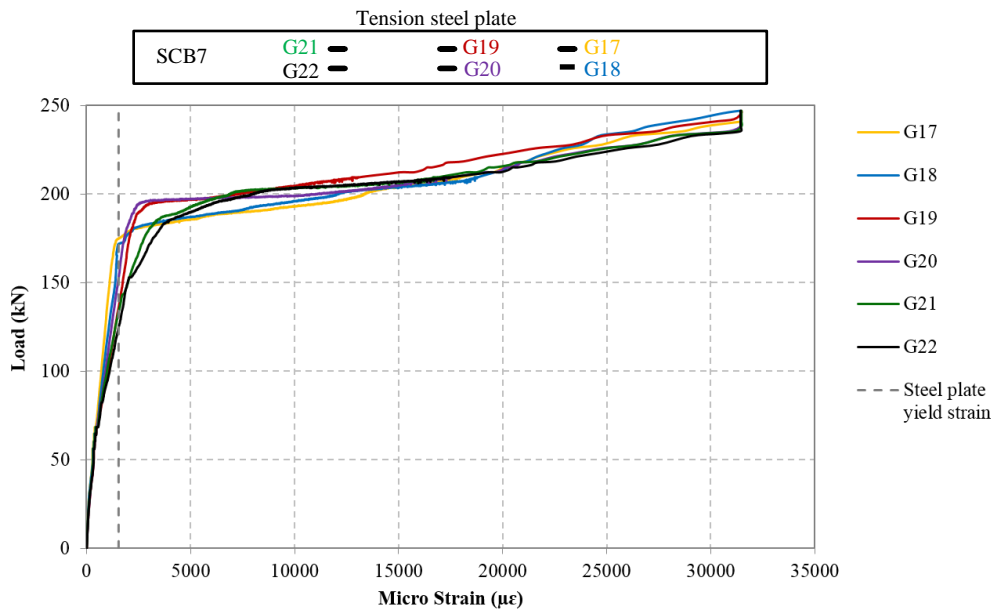


Figure 5.58. Measured strain in tension steel plate for SCB7



### 5.7.2. SCB8: SF0.5% + CNF1.0%

The compressive strength of concrete core used for SCB8 was 14.3% lower than the PC, whereas the split tensile strength was 50% higher. According to the load-displacement curve for SCB8 (Figure 5.53), the beam had the ultimate loading capacity of 230 kN with the corresponding displacement of 28.42 mm. The capacity of this beam compared to SCB2 with similar SF dosage was improved by 19.9%, which shows the beneficial effect of adding 1.0% CNF to the concrete matrix.

#### 5.7.2.1. Crack behaviour

Crack progression for SCB8 is illustrated in Figure 5.59. Initially, cracks C1 and C2 were formed in the moment span at  $P = 68.8$  kN ( $D = 2.67$  mm). Cracks C3 and C4 were also flexure cracks which formed at  $P = 139.6$  kN ( $D = 5.2$  mm) as shown in Figure 5.59(a). The load at which flexural cracks (C1-C4) appeared for SCB8 was higher than SCB7 by 16.4% and 28.3%. This can be attributed to the higher  $V_f$  of CNF present in the concrete, which delayed the formation and initiation of cracks by bridging micro-cracks. On the other hand, the initial crack formation behaviour was similar to SCB5 with the same CNF dosage as SCB8.

Diagonal hairline cracks shown in Figure 5.59(b) started to appear on the west shear span (C5) and east shear span (C6) at  $P = 169.2$  kN ( $D = 6.6$  mm) and  $P = 171.8$ , ( $D = 6.72$  mm) respectively. This occurred at higher load compared to SCB7, which had its initial shear crack at  $P = 161$  kN, whereas it was similar to SCB5 which had the first shear crack at  $P = 170$  kN. Vertical crack C7 (Figure 5.59(e)) adjacent to left DG was also formed followed by the shear crack formations.

As the load-displacement curve exhibited the hardening behaviour, the width of C1 and C4 slightly increased from the bottom (see Figure 5.59(d)). At  $P = 192.1$  kN ( $D = 10.37$  mm) a new short vertical flexural crack (C8) appeared next to C7 as well as C9 in the vicinity of west shear crack; C5 (Figure 5.59(e)). With the progression of applying displacement, the increase in width of C1 and C4 became more profound.

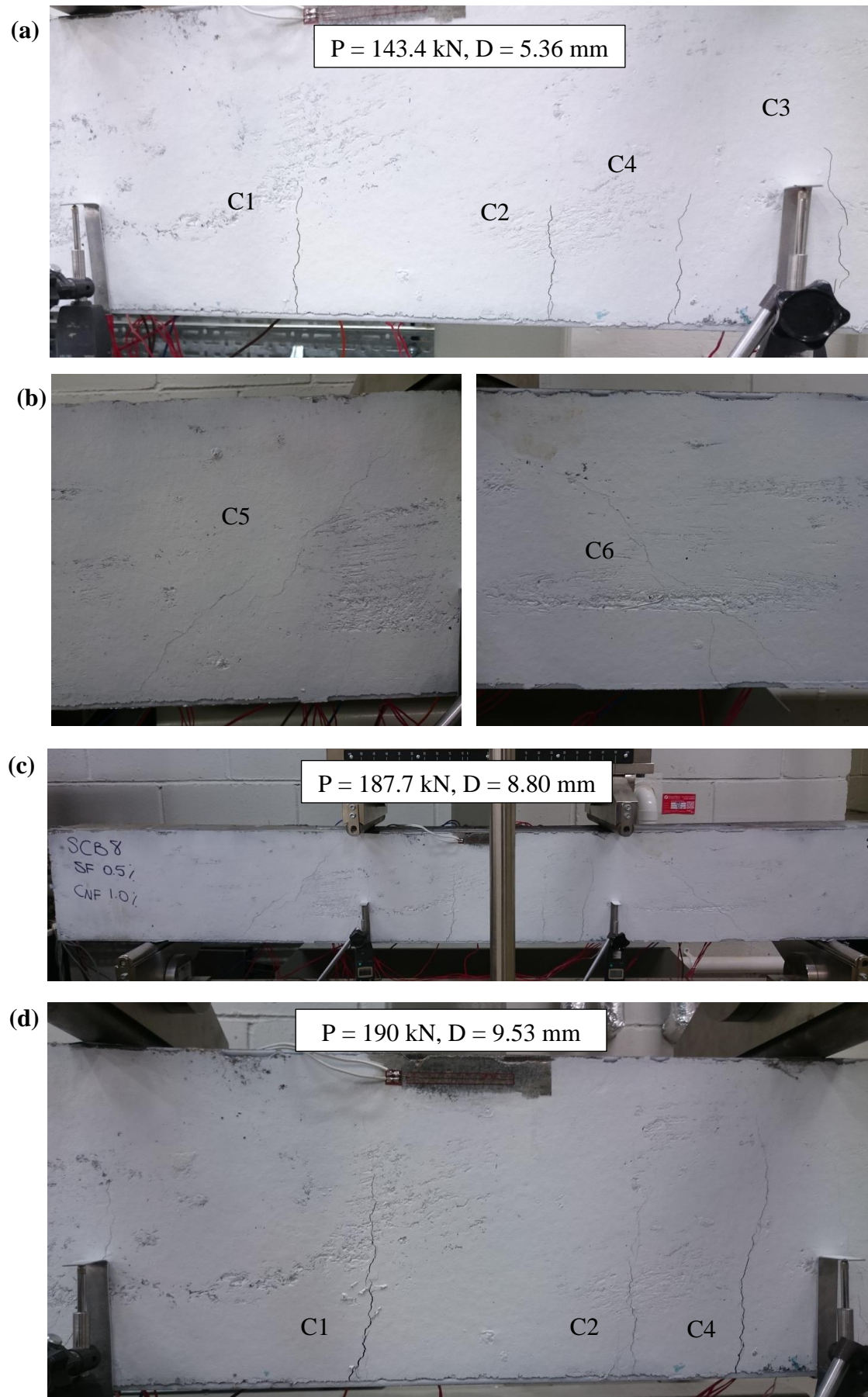


Figure 5.59. Crack progression for SCB8

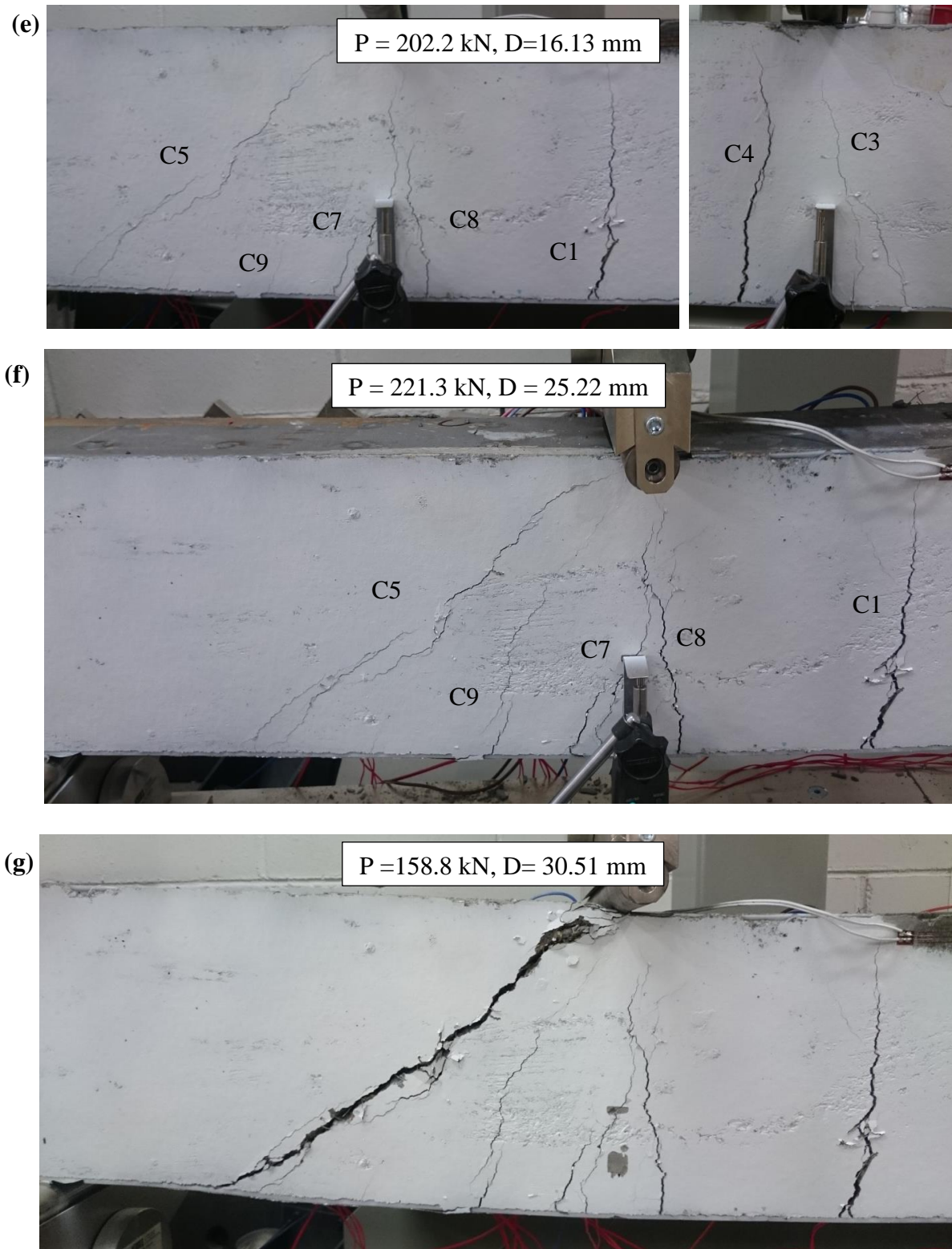


Figure 5.59. (continued)

Through the second half of the plastic stage of the load-displacement curve, the changes in the width of cracks were unnoticeable, while the length of flexural cracks, C7, C8, and C3, was further progressing towards the top surface of the beam. By approaching the ultimate load at  $P = 221.3$  kN and  $D = 25.22$  mm, C9 increased in length towards the top and C5 increased in width gradually (Figure 5.59(f)).

When the beam reached its ultimate capacity, the shear crack C5 showed an increase in width (steel fibre pull-out) and steel plate plastic deformation accompanied by concrete crushing took place. At the onset of the major cracking of the specimen, the load abruptly jumped to a smaller load value and the beam maintained its strength at 59%-74% of the ultimate load. Figure 5.59(g) shows C5 immediately after the peak load.

After the load drop and crack widening, both concrete and steel plates were still contributing in resisting the applied load. The propagation of crack C5 was controlled through the presence of steel fibres. The test was terminated automatically by the testing machine as the ultimate displacement capacity of the frame was reached. It was expected that the beam could continue to maintain load, characterised by large deformations and further shear crack damage development.

From close observation of crack C5 (see Figure 5.60(a)) it could be found that some steel fibres were pulled out at the crack surface, while some were still bridging the crack. However, at some locations, the crack width was extended to a limit that the fibre length was shorter than the crack width. Also, the west inner bars crossing this crack were fractured as shown in Figure 5.60(b). Sample SCB8 after the test with its crack pattern is shown in Figure 5.61. The crack pattern reveals a flexure-shear failure mode for SCB8.

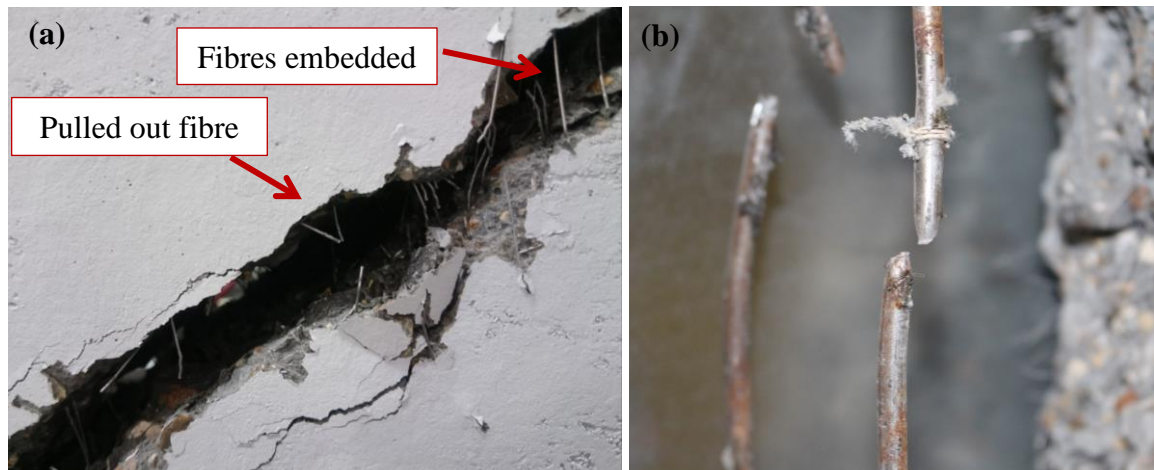


Figure 5.60. Close observation of (a) shear crack C5; (b) tie bar fractured at C5



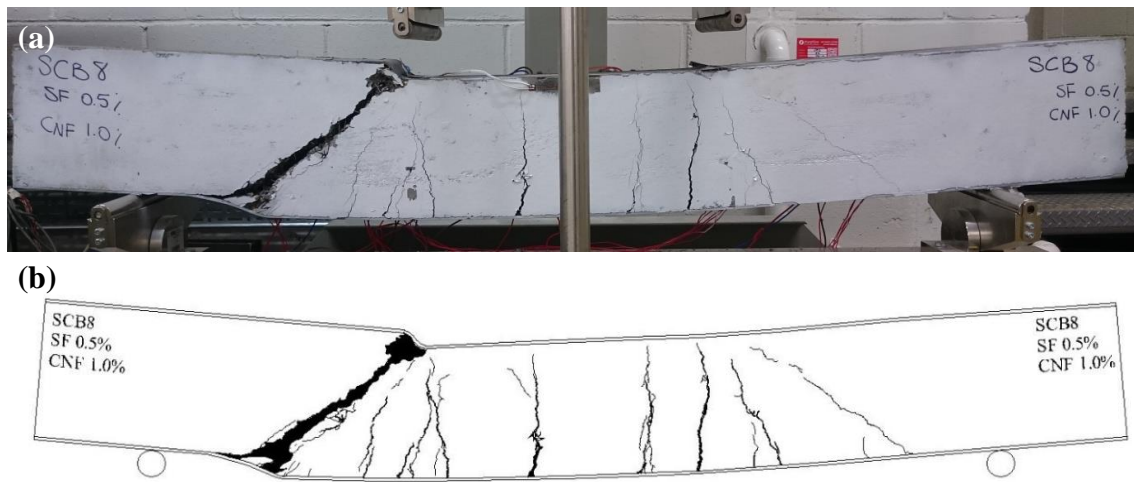


Figure 5.61. SCB8: (a) after the test; (b) crack map after the test

### 5.7.2.2. DG measurements

The measured displacement for SCB8 shown in Figure 5.62 reveals that the beam was displaced symmetrically throughout the test until the peak load was reached prior to the local buckling. It is however expected from the observations and the local damage of the beam that the displacement of DG-L increased further than other two locations following local buckling of the plate. This trend was similar to SCB7.

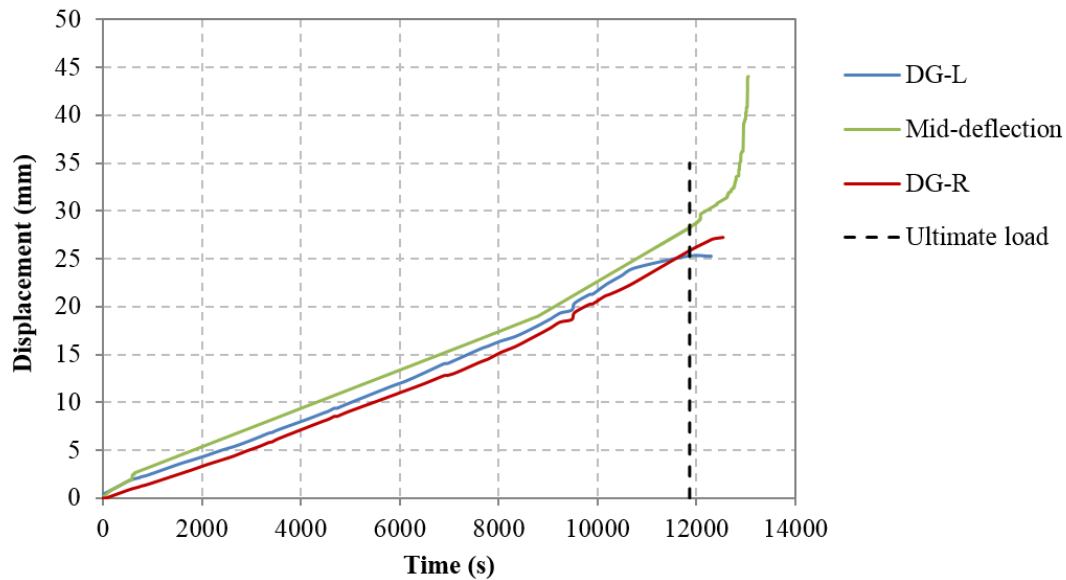


Figure 5.62. DG measurements for SCB8

### 5.7.2.3. Strain measurements

The measured strain in tie bars for SCB8 is presented in Figure 5.63. It is evident that none of the outer tie bars yielded and they all maintained a low level of strain, this behaviour of outer tie bars was similar to SCB7. However, the strain at the ultimate load for outer tie bars of SCB7 had lower level ranging from 550-1250  $\mu\epsilon$ , while the outer bars for SCB8 had strains ranging from 900-1640  $\mu\epsilon$ . In SCB2, which was singly-reinforced with 0.5% steel fibre without CNF, with higher compressive strength, the outer bars showed a limit of 500-2080  $\mu\epsilon$ . The maximum strain for SCB8 was slightly less which could be due to the effect of CNF in enhancing the concrete capacity in resisting higher forces by bridging micro-cracks. It is important to note that although the bridging effect of nanofibres diminish after the formation of macro-cracks as the fibre pull-out takes place, these fibres are still effective in improving the steel fibre pull-out process. Therefore, another prominent reason could be that nanofibres enhanced the bonding and pull-out behaviour of steel fibres, hence they contributed to the interfacial stress transfer from fibres to the cementitious matrix.

Assessing the strain measured for inner bars in Figure 5.63(a) also revealed that yielding took place on the upper section of the bars, however, maximum strain reached for non-yielding bars was close to the yield strain at the ultimate load level. G9 and G13, located at where the bar fracture occurred shown in Figure 5.60, yielded simultaneously earlier than any other tie bar at  $P = 192.1$  kN and they had a maximum recorded strain of 18100  $\mu\epsilon$  and 3200  $\mu\epsilon$  respectively. This was comparable to first yielding load for SCB7, which showed the first yielding at  $P = 209$  kN. On the other hand, G9 in SCB6 first yielded at  $P = 165.4$  kN followed by yielding of G3 at  $P = 219$  kN. G9 and G13 ceased to function and record any further strain after this point due to possible gauge damage and it is expected that the strain for these bars at the ultimate load (230 kN) was slightly higher. It can be concluded that the crack widening of C5 on the west side of the beam was more pronounced at the top adjacent to the left point load which resulted in high stresses induced on the upper part of the inner tie bar.

East inner bars for SCB8, unlike SCB7, showed lower strain level with no sudden significant increase of the strain prior to the ultimate load. This indicates that the crack opposite the major shear crack was better controlled, hence inducing less stress in tie bars.

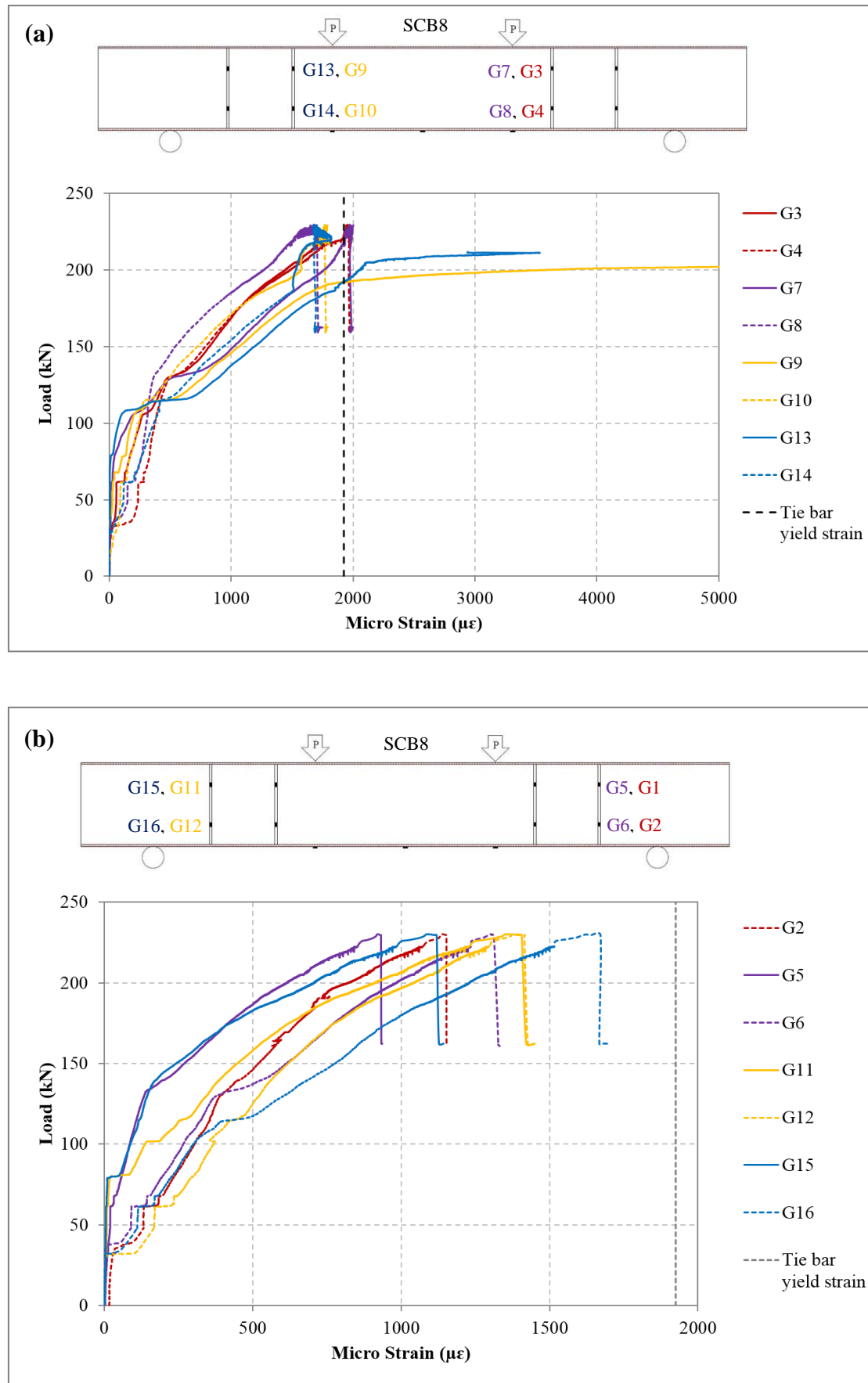


Figure 5.63. Measured strain in tie bars for: (a) outer bars; (b) inner bars for SCB8

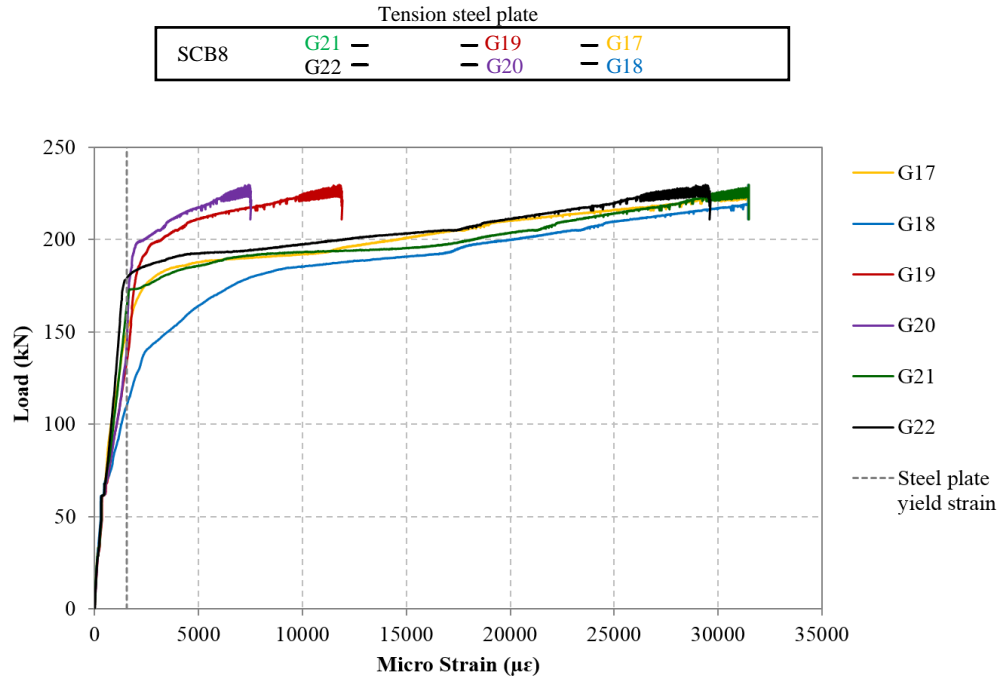


Figure 5.64. Measured strain in tension steel plate for SCB8

The strain measured in the bottom steel plate for SCB8 is shown above. It is evident that the steel plate underwent yielding at early stages of loading. First G18 reached the yielding strain at  $P = 110$  kN (lower than SCB7; 125 kN) and G17 measured yielding strain at  $P = 150$  kN. G19 and G20 showed yielding at  $P = 140$  kN simultaneously. G21 and G22 recorded yielding strain at  $P = 162$  kN, and  $P = 178$  kN respectively.

The gauges parallel to the load points showed higher strain increase as the ultimate load was approached as opposed to the centre of the beam and they reached a value of about 31500  $\mu\epsilon$  which was the maximum strain that could be measured by the gauges used in the test. G19 and G20 had their lowest strain of 11900  $\mu\epsilon$  and 7500  $\mu\epsilon$  respectively at the ultimate load. G21 and G22 had a strain value of 31483  $\mu\epsilon$  and 28900  $\mu\epsilon$  at ultimate load respectively. Furthermore, G17 and G18 had 31446  $\mu\epsilon$  at  $P = 222$  kN and 31440  $\mu\epsilon$  at  $P = 218$  kN respectively. The strain at the centre for this beam was less compared to SCB7, which had higher energy dissipation through plate yielding.

Overall, SCB8 showed a ductile behaviour by yielding of the tension steel plate at earlier loading stage in comparison to tie bars, therefore the failure mode of this beam considering the crack pattern of the beam is classified as a flexure-shear mode of failure.



### 5.7.3. Summary of category 3

The crack pattern for both beams was following similar progression stages in which initial vertical flexural cracks appeared followed by a short diagonal hairline crack in the shear span. The occurrence of several flexural cracking also increased the magnitude of the longitudinal strains measured in the steel faceplates. At the hardening stage of the load-displacement curve, the length and width of flexural cracks were increasing while at the ultimate load one shear crack showed an increase in the width resulting in negative stiffness and a reduction of the loading capacity of the beam.

Despite similar trend observed for the crack behaviour of both beams; SCB8 had a lower shear capacity which is attributed to lower steel fibre dosage of this beam against SCB7. At  $V_f$  of 1.0% SF, concrete core performed better in controlling the macro-size crack propagation at higher load level. On the other hand, it is interesting to note that the formation of the initial flexural and shear cracks was further delayed in SCB8. This was due to the effect of higher  $V_f$  of nanofibres. Furthermore, the strain induced on tie bars within the shear span with minor shear crack, was lower for beam with higher CNF dosage, which signifies the effect of CNF on the structural performance by micro-crack bridging. Overall, both beams were successful in altering the shear failure mode of the control beam with plain concrete core into a ductile mode of failure.

## 5.8. SEM ANALYSIS OF SC CONCRETE CORE

To gain insight into the microstructure of the concrete, for each SC beam, concrete pieces as samples, taken from the cracked sections (see Figure 5.65) were inspected by the Scanning Electron Microscopy (SEM) method at Queen Mary University. Initially, few samples both unpolished and polished on the top side were examined. From the observations, nanofibres were clearly visible in the unpolished areas and it seemed that they were destroyed by polishing the surface or they were covered with the attrition material and therefore they were not visible in the SEM image. Thus, all samples were inspected as taken from the specimen without any polishing. Below is the discussion on the SEM observations for each sample. Further SEM images of samples can be found in Appendix B.

Studying the microstructure of the concrete would provide details regarding the dispersion of the nanofibres within the concrete and their distribution status. A well-

dispersed nanofibre is identified by observing individual fibres within the matrix without any agglomeration and dense bundles of the nanofibres. In the observations, the accumulation of CNF bundles in large sizes of 100-500  $\mu\text{m}$  as referenced by Kim et al. (2014) was considered as an agglomeration of fibres within the matrix.



Figure 5.65. Example of samples taken from SCB4 beam for SEM analysis

SEM images of SCB3 concrete core reinforced with 0.5% CNF is shown in Figure 5.66. In the figure, a net-like distributed mixed CNFs within the concrete matrix was observed. The interaction between the fibres and the hydration products (C-S-H) could be observed from the embedded CNF (arrows) between the hydration products. Similarly, the SEM images of core samples from SCB4 (with 1.0% CNF) illustrated in Figure 5.67(a), which depicts the insertion of CNFs (arrows) between hydration products, did not show any clumps and the interfacial interaction between the nanofibres and C-S-H could be observed.

The density of the CNF in the similar sized community (20000 $\times$  magnification) of embedded CNFs within observed surface was less in some cases as can be seen from Figure 5.67(b) and (c). The CNF dispersion at some parts was denser, while at other location, a single fibre was observed. Despite the difference in the dispersion density of CNF within the matrix, CNFs are not considered agglomerated in the matrix as the size of the CNF bundles observed in Figure 5.67(b) was not within the reference range of 100-500  $\mu\text{m}$ . The difference between the two observations reveals that the dispersion of fibres was not completely homogenous within the matrix and the fact that a perfect

single fibre distribution within the matrix was not achieved. Identifying individual fibres such that shown in Figure 5.67(c), however, on the fractured surface proves the satisfying dispersion of CNF, since the agglomeration and formation of bundles were prevented. This was also shown in Konsta-Gdoutos et al. (2010) for MWCNT for samples with a surfactant to MWCNT ratios ranging in 4.0-6.25 (Figure 5.68).

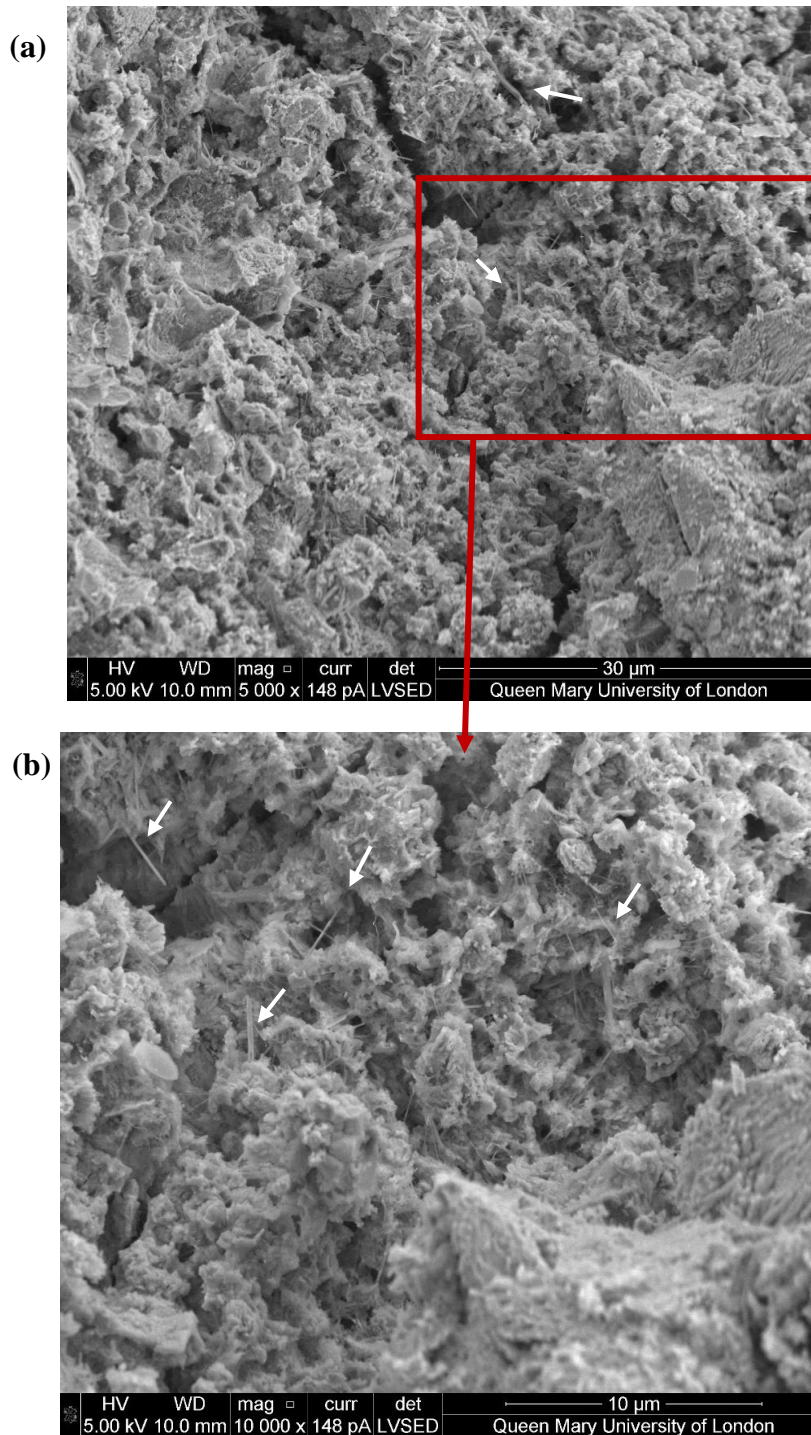


Figure 5.66. SEM micrographs of SCB3 core sample with 0.5% CNF at magnifications: (a) 5000 $\times$ ; (b) 10000 $\times$

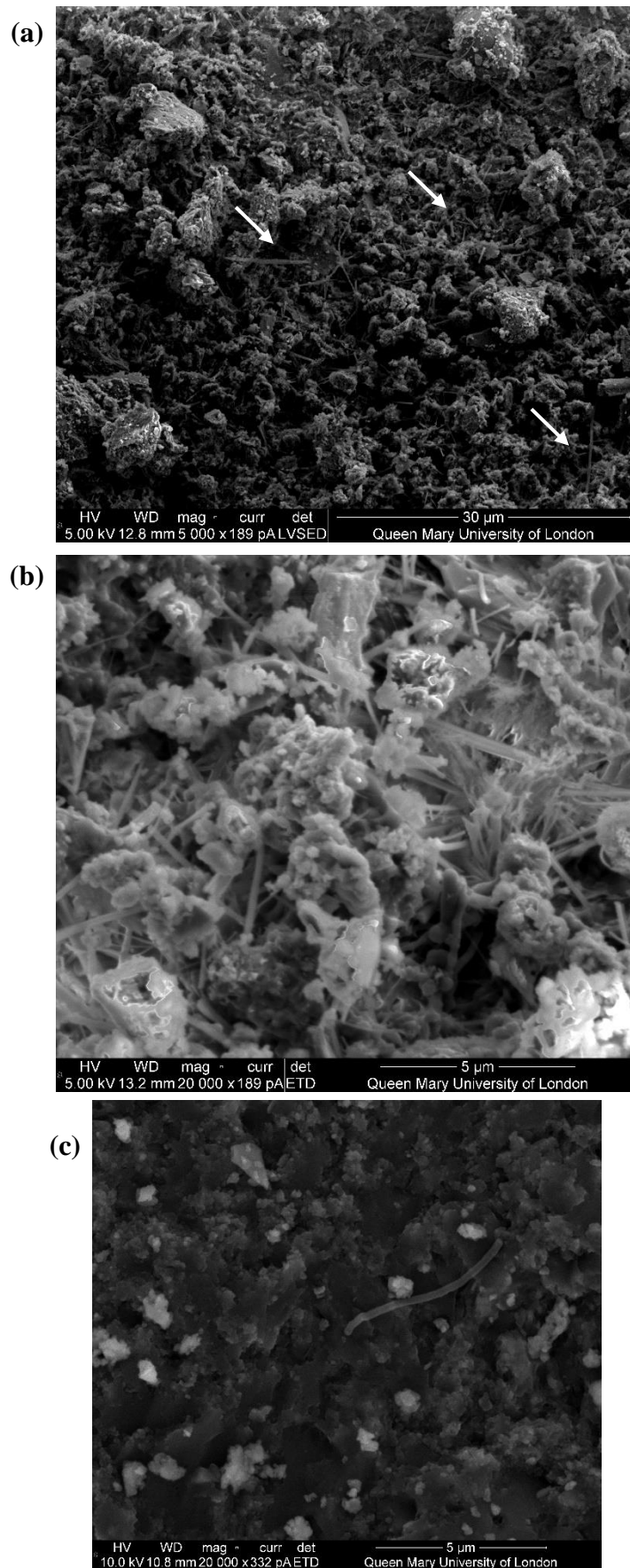


Figure 5.67. SEM micrographs of SCB4 core sample with 1.0% CNF at magnifications: (a) 5000 $\times$ ; (b) 20000 $\times$ ; (c) 20000 $\times$ ; (d) 50000 $\times$

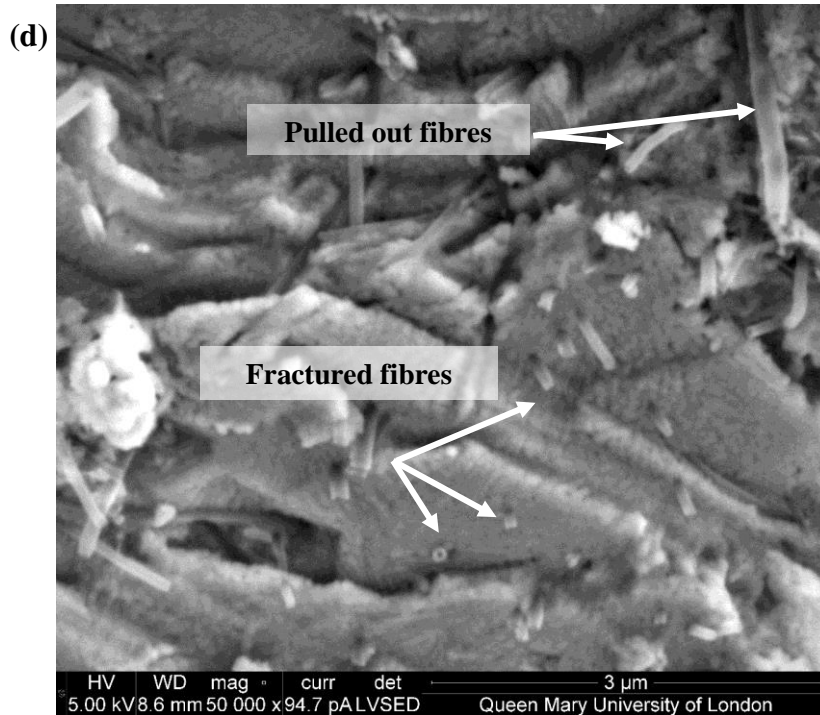


Figure 5.67. (continued)

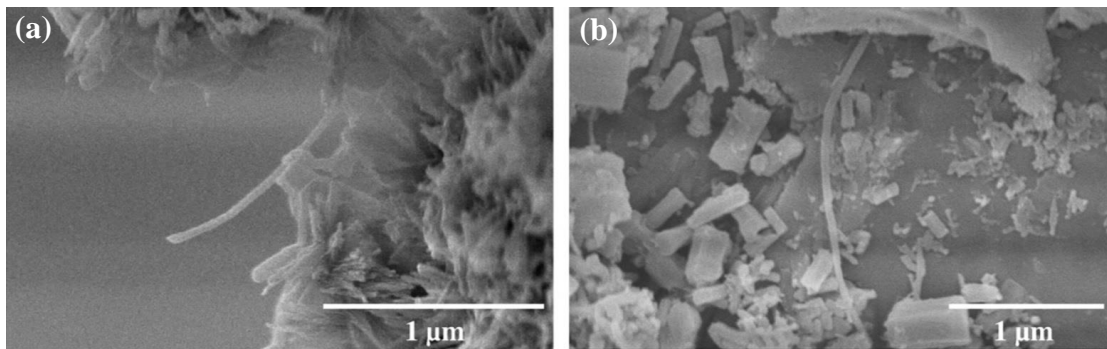


Figure 5.68. Surfactant concentration effect on nanotube dispersion: (a) dispersant to MWCNT weight ratio of 4.0 and; (b) 6.25 (Konsta-Gdoutos et al., 2010)

Figure 5.67(d) shows the fractured surface of the specimen (SCB4). It can be observed from this figure that some fibres have broken at the same level of the crack surface, which indicated that the fibres have not been pulled out. Some fibres, however, were pulled out as shown. The fractured fibres indicate good fibre-matrix interfacial bond, which could be due to the roughened surface of fibres as a result of sonication as Yazdanbakhsh et al. (2009) stated. This also indicates that the bond strength was controllable and can reach a high value to prevent fibre slippage. The energy dissipation takes place at the nanofibre-matrix interface when the fibres are pulled out at the crack surface with the increase in applied load. This is thought to be the reason for higher crack load obtained for CNFCR samples, particularly SCB4.

The SEM images of core samples for SCB5 is represented in Figure 5.69. From the figure, distribution of CNF with less density was observed for this sample compared to SCB4, while both had similar CNF volume fractions. From Figure 5.69(b), also individual fibres embedded within the matrix was detected, meaning that good dispersion was achieved for the sample. In addition to this observation, for some samples taken from SCB5, no fibre could be detected on the surface or close to micro-cracks (see Appendix B). Once again, this could be an indication of nonhomogeneous dispersion of fibres. However, it should be noted that these images do not represent the distribution of CNFs in the whole matrix. But, the samples taken from different sections of the beams are regarded as a representative and they can estimate the average dispersion quality of the CNF within the concrete.

The SEM images of core samples for SCB6, SCB7, and SCB8 are represented in Figure 5.70, Figure 5.71, and Figure 5.72, respectively. No CNF clump was detected for any of these samples. CNF dispersed as individual fibres were abundantly found in the concrete matrix of SCB6 (Figure 5.70(a)). The presence of the CNF was also spotted adjacent to the steel fibre in this sample as can be seen in Figure 5.70(c). The CNF fibre seemed to be fractured in the mid-length (Figure 5.70(d)). This could mean that the embedded CNF, in the vicinity of SF, contributed in the energy dissipation of the sample, and also it aided the SF in energy dissipation. In addition, they enhance the performance of SF by reinforcing the matrix surrounding the steel fibres.

The analysis of SEM images of the SCB7 depicted in Figure 5.71 shows that fibres partially filled the micro-voids. Such phenomenon would reduce the permeability by void compaction and this could result in higher compressive strength.

None of the observed samples showed any CNF clumps or agglomerations such as that observed in previous researches (e.g. Mo and Howser Roberts, 2013; Yazdanbakhsh, 2012) as shown in Figure 5.73(a) and Figure 5.74(a). The distribution of nanofibres in this study was found to be similar to what has been referred as well-dispersed by previous researchers such as that shown in Figure 5.73(b) and Figure 5.74(b).



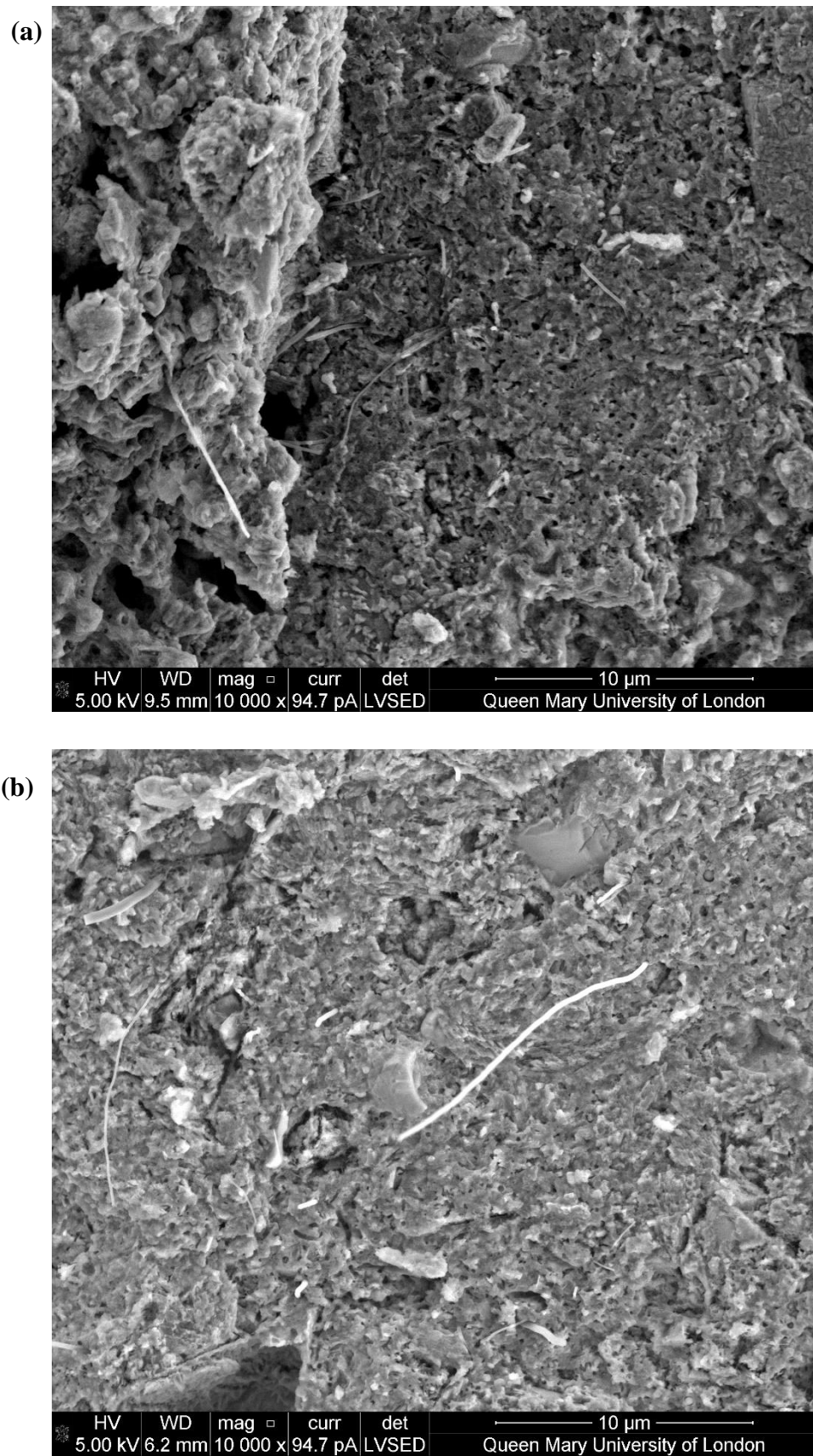


Figure 5.69. SEM micrographs of SCB5 core sample with 1.0% SF + 1.0% CNF at 10000 $\times$  magnification

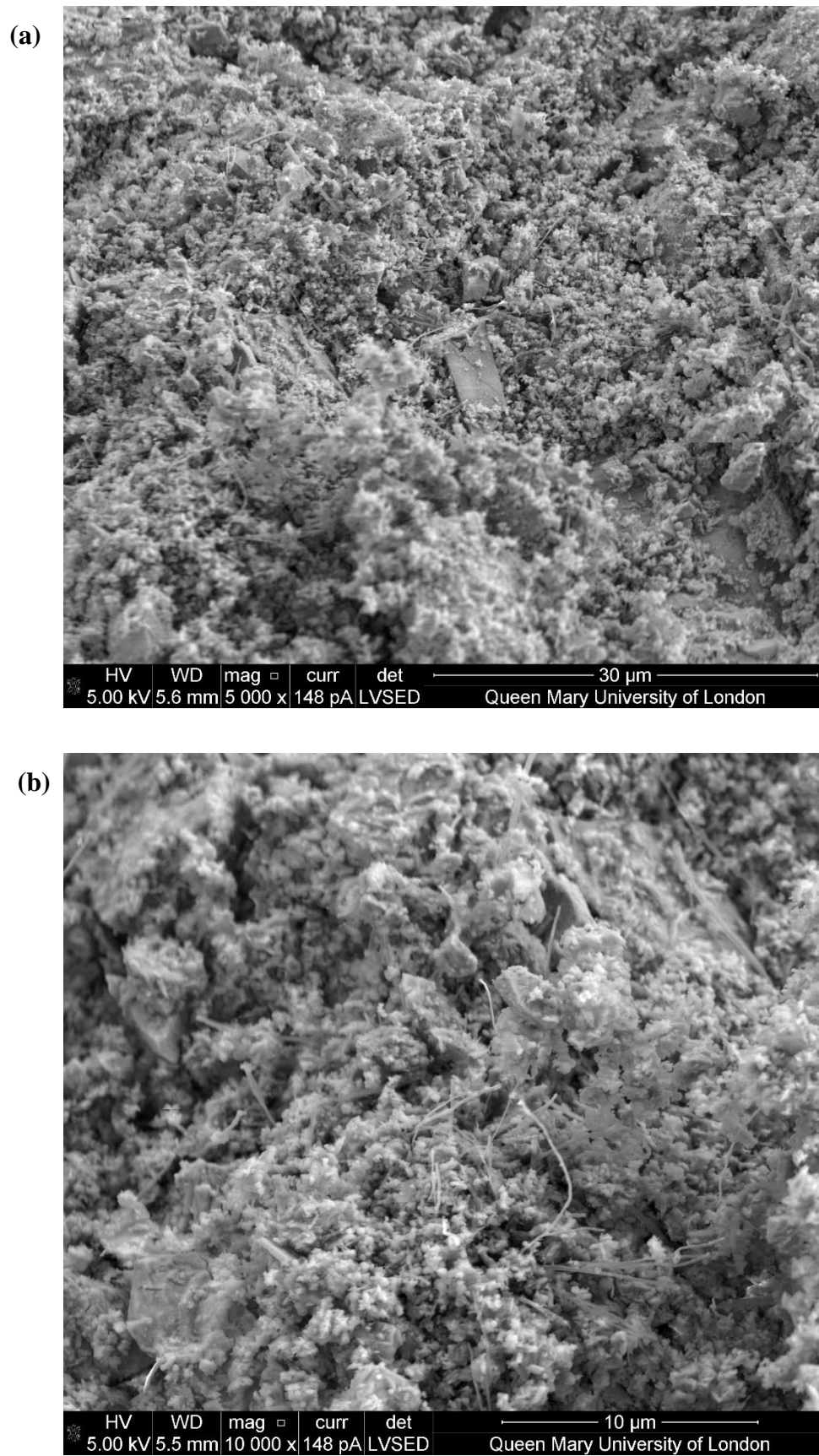


Figure 5.70. SEM micrographs of SCB6 core sample with 1.5% SF + 0.5% CNF at magnifications: (a) 5000×; (b) 10000×; (c) 5000× with steel fibre





Figure 5.70. (continued)

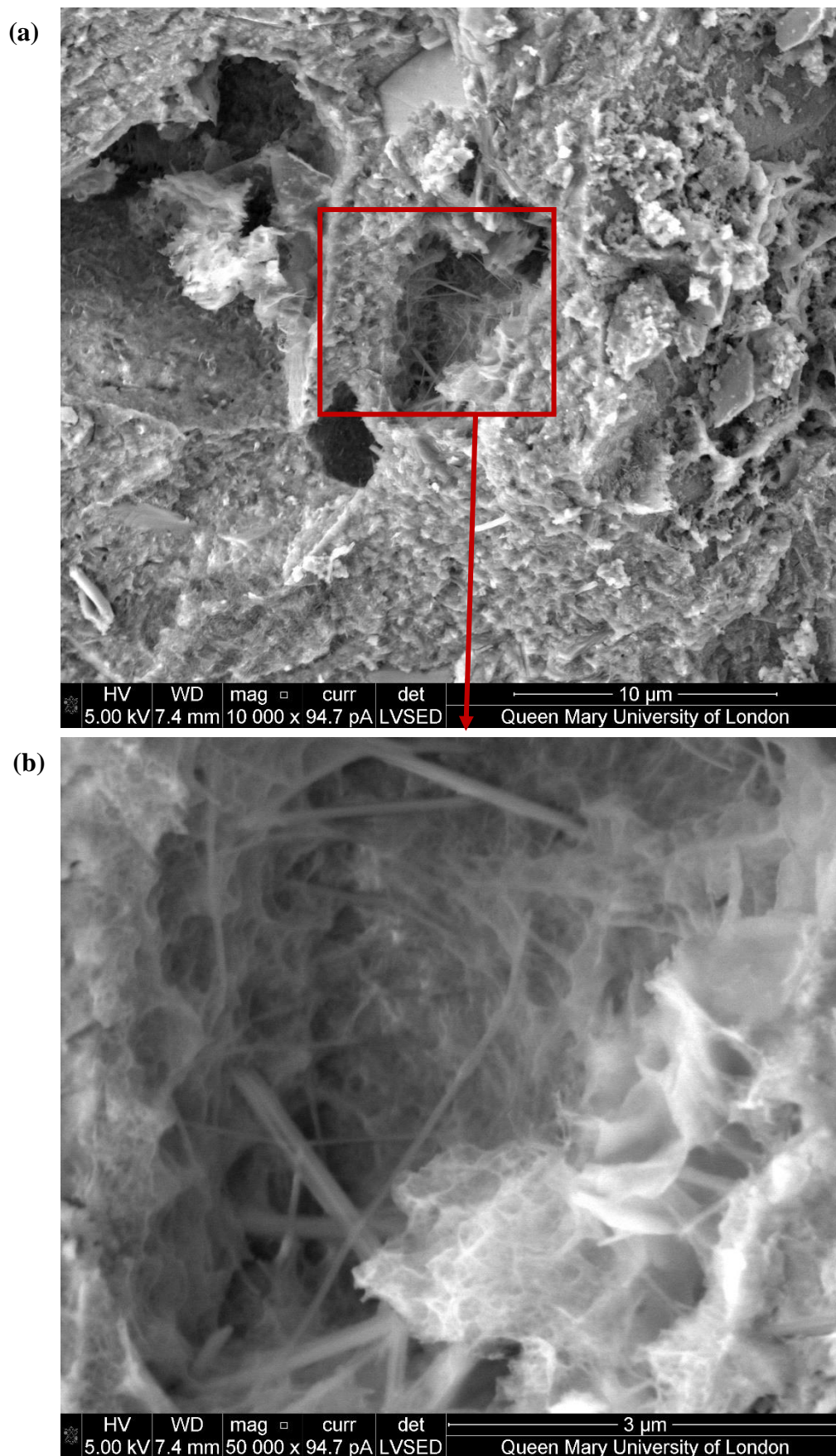


Figure 5.71. SEM micrographs of SCB7 core sample with 1.0% SF + 0.5% CNF at magnifications: (a) 10000 $\times$ ; (b) 50000 $\times$

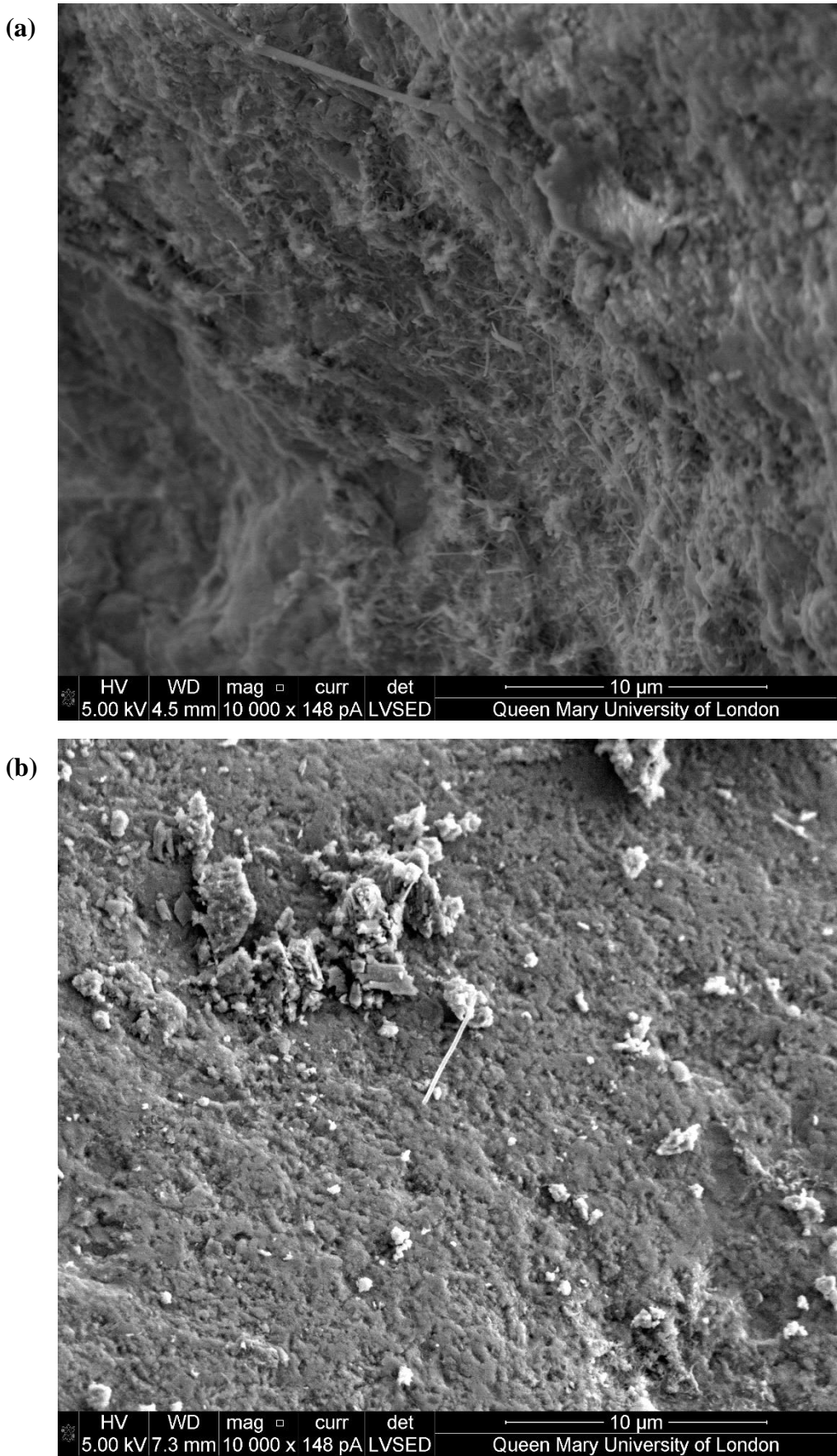


Figure 5.72. SEM micrographs of SCB8 core sample with 0.5% SF + 1.0% CNF at 10000× magnification



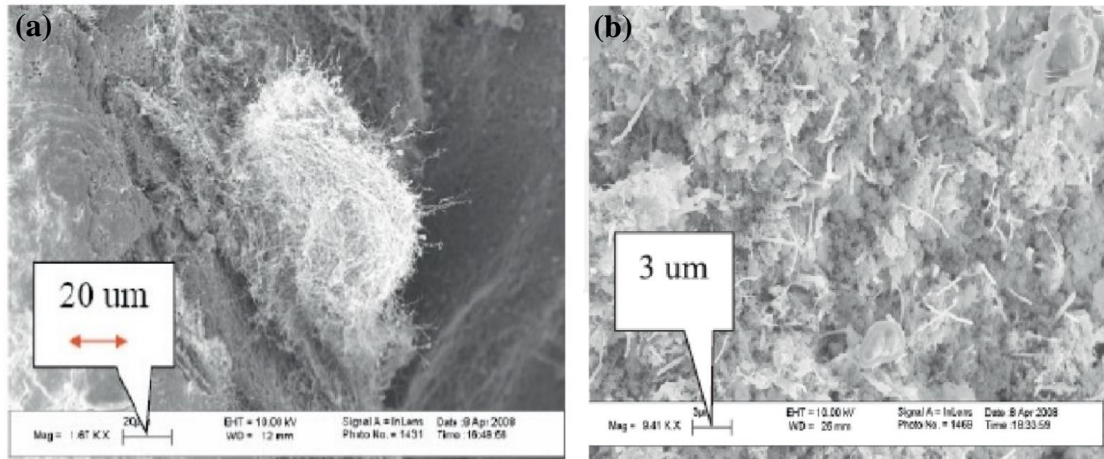


Figure 5.73. (a) Scanning Electron Microscope Image of CNF Clump in Normal Cement (1670× Magnification), (b) Scanning Electron Microscope Image of Well Dispersed CNF in a Uniform Self-Consolidating Cement (9410× Magnification). (Mo and Howser Roberts, 2013)

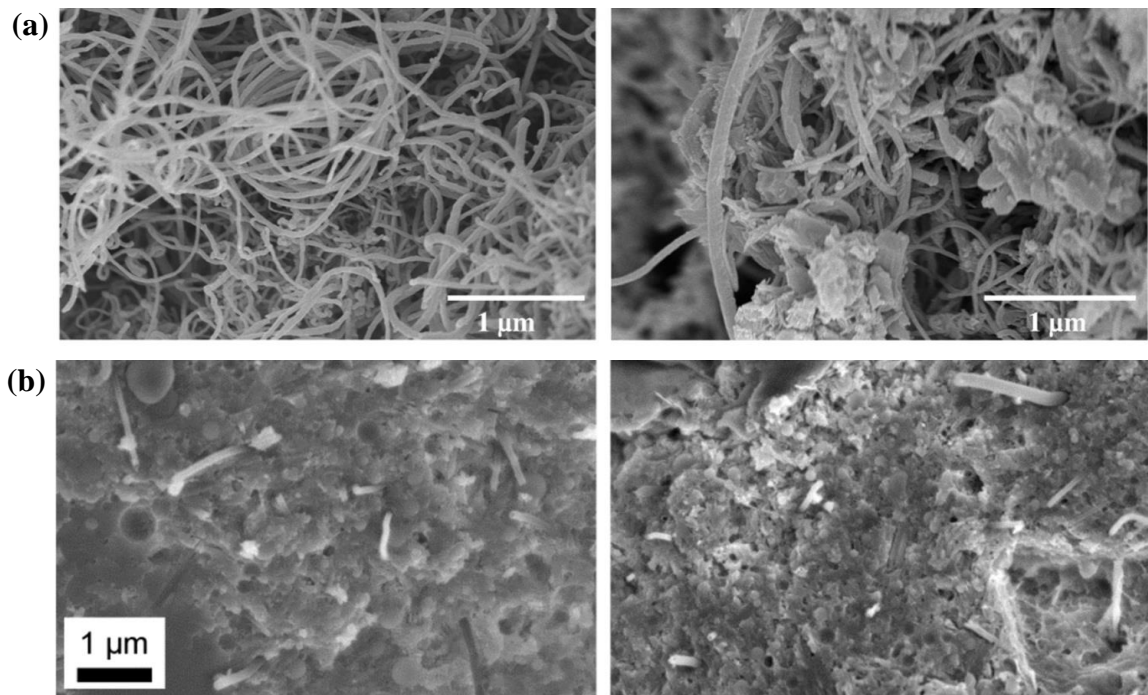


Figure 5.74. (a) SEM images of fractured surface of hardened silica fume paste SF-3, indicating the uniform dispersion of CNFs. (b) SEM images of fractured surface of hardened silica fume paste SF-3, indicating the uniform dispersion of CNFs. (Yazdanbakhsh, 2012)

## 5.9. OVERVIEW OF THE RESULTS

To compare the results for all eight samples, the results were normalized as shown in Figure 5.75. To normalize the load-displacement curves, the total applied load ( $P$ ) was divided by the concrete compressive strength at 28d ( $f'_c$ ). The displacement was normalised as  $D/L$ , where  $D$  is the mid-span deflection and  $L$  is the flexural span length.

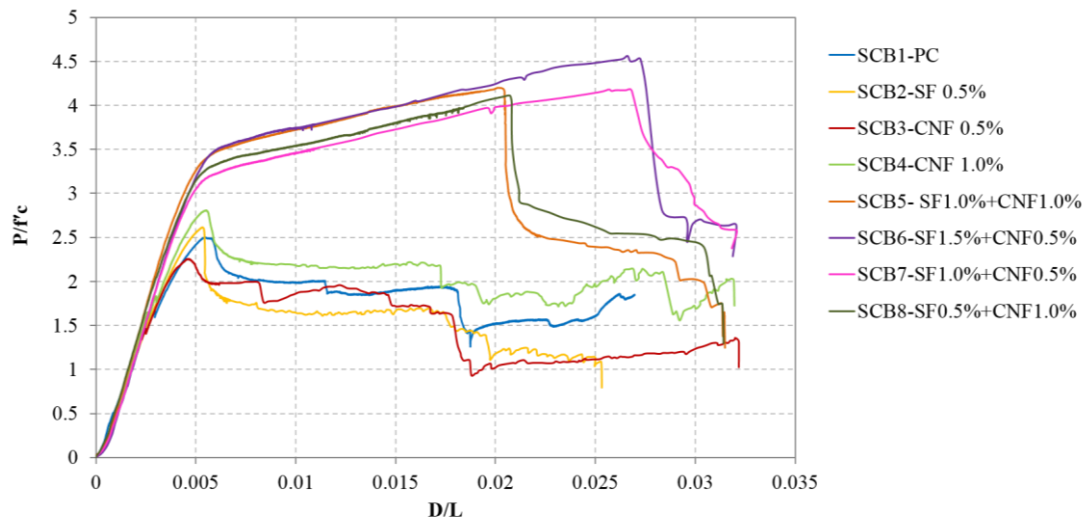


Figure 5.75. Normalised load-displacement curve for all tested SC beams under four-point bending

From the figure above, it can be seen that CNFRC1.0 performed better than other specimens amongst singly-reinforced FRC samples with higher strength and higher energy dissipation. Amongst hybrid fibre reinforced samples, those with higher  $V_f$  of macro fibre showed better ductility, while the strength of samples with less steel fibre was maintained due to the combined effect of nanofibres and macro fibres.

For the control specimen, flexural cracks appeared at early stages of loading, i.e., about 11% of the shear force capacity of the specimens. This early flexural cracking indicates the relatively quick transition from uncracked to cracked section, which is important to consider in structure stiffness evaluation.

The control sample, as well as beams in category 1, failed in shear mode. For these SC beams crack normally appeared first at the moment span in the extreme lowest fibre of the concrete core. They only showed few number of cracks short in length which were formed as flexure cracks. Shear cracks appeared following the flexural cracks. The onset of the major diagonal shear crack opening was observed at the peak load resulting

in negative stiffness for the beam. Soon after the load drop, the shear crack widened and the core split in two sections. For SCB2, the macro steel fibres were found to be ineffective in delaying the initiation and progression of macro cracks which can be due to the relatively large spacing between fibres. A critical factor for the control beam and those in category 1 with shear failure was the inadequate tensile strength of concrete, which was exceeded in the principal direction at the maximum load obtained on the curve. The ductility of this category was less than other categories.

On the other hand, there was evidence of good curvature formed during the test and a good deal of ductility in the behaviour of beams in category 2 and category 3. The load-displacement responses indicate that both categories had elastic-plastic behaviour with significant displacement ductility due to flexural yielding of the tension steel plate and the overall tie bar strains were small and much smaller than those in category 1. All beams in these two categories began to display rapid loss of stiffness corresponding to tension steel plate yielding. For beams with hybrid FRC concrete core, at the ultimate load as well as flexural yielding of the tension (bottom) steel plate, the concrete was still contributing in resisting load due to the presence of steel fibres; therefore, the ultimate resistance was governed by both concrete and steel plates.

By comparing the results for SCB8 (SF0.5%+CNF1.0%), SCB2 and SCB4, it can be seen that there has been a significant enhancement in ductility of the beam for SCB8 owing to the combined action of both fibres. As experimentally investigated by Wright et al, (1991) the low concrete compression strength did not change the fundamental failure mode of the double skin composite beams under four-point bending but only the level at which failure occurred. It can be emphasised that for SC beams in category 2 and category 3 with less concrete compressive strength than control specimen, which showed different failure mode, the change in the failure mode was strictly due to the presence of fibres.

Summary of the results obtained from load-displacement curves for all eight SC beams is summarised in Table 5.1. From the table, it can be concluded that 1.0% CNF was successful in delaying the formation of the shear cracks by the act of bridging nano-cracks and micro-cracks. The evidence for this observation comes from the comparison of the  $P_{s,crack}$  for both categories 2 and 3 in which the beam with 1.0% of CNF in each

category showed higher load level. The shear force margin between the appearance of the flexural crack and brittle shear crack was at its maximum for SCB5.

Table 5.1. Summary of test results for SCB1-SCB8

Beam sample		Concrete type	$P_{f.crack}^*$ (kN) (% of $P_{max}$ )	$P_{s.crack}^{**}$ (kN) (% of $P_{max}$ )	$P_{max}$ (kN)	$D_u^{***}$ (mm)	Failure mode
SCB1 Control Sample		PC	18.8 (11.1%)	100.2 (59%)	169.6	7.6	Vertical Shear
							Diagonal shear crack
Category 1	SCB2	SFRC 0.5	33.6 (17.5%)	137 (71.4%)	191.9	7.4	Vertical Shear
							Diagonal shear crack
	SCB3	CNFRC0.5	25.5 (19.4%)	82 (62.3%)	131.6	6.5	Vertical Shear
							Diagonal shear crack
	SCB4	CNFRC1.0	48.9 (29.0%)	101 (59.8%)	168.8	7.7	Vertical Shear
							Diagonal shear crack
Category 2	SCB5	SF1.0 + CNF1.0	59.1 (25%)	170.0 (71.9%)	236.5	28.1	Flexure-shear
							Tension steel plate yielding followed by shear crack
	SCB6	SF1.5 + CNF0.5	66.2 (26.3%)	160.0 (63.5%)	251.9	38.18	Flexure-shear
							Tension steel plate yielding followed by shear crack
Category 3	SCB7	SF1.0 + CNF0.5	56.1 (22.6%)	161 (65.3%)	247.9	35.9	Flexure-shear
							Tension steel plate yielding followed by shear crack
	SCB8	SF0.5 + CNF1.0	68.8 (30%)	169.2 (72.3%)	230	28.4	Flexure-shear
							Tension steel plate yielding followed by shear crack

\*Load at the first concrete flexural crack

\*\*Load at the first concrete core shear crack

\*\*\* Displacement at ultimate load

The effectiveness of the CNF as flexural reinforcement was more pronounced for singly-reinforced FRC core (category 1), as opposed to shear reinforcement. The mechanism of the CNF within the concrete as Gdoutos et al. (2016) also described, is that they enhance the material's ability to control the coalescence of cracks at the nano-scale and the subsequent formation of micro-cracks, hence a higher amount of energy

is required to initiate cracking. Also, damage localisation is avoided by fibres arresting crack growth upon the initiation of matrix cracking; thereby, ‘energy is dissipated through the formation of a dense field of micro-cracks (with widths less than 100  $\mu\text{m}$ )’ (Hou and Lynch, 2005).

This observation is confirmed by the comparison between the  $P_{f.crack}$  of SCB4 and other beams, in which 1.0% CNF had the highest enhancement with 29% increase in initial flexural crack load. While the greatest effect on the initial shear crack formation was recorded for SCB2 with 0.5% steel fibres. The load at which initial flexural crack occurred for SCB8 was higher than SCB7, which could be attributed to higher CNF concentrations; however, in category 2, for SCB6 with 1.5% of steel fibres the initial flexural crack appeared at 26.3% of the ultimate load and this phenomenon occurred at 25% of the ultimate load for SCB5. This could be due to the high steel fibre dosage that has had a slight effect on the load level. From another viewpoint, SCB6 had the highest w/c ratio due to the high volume fraction of fibres and it had the lowest slump, and the handling and compacting the concrete in the structural element was very difficult and the chance of fibre interlocking is increased. Also, the density of this concrete (Figure 5.3) was the highest amongst all. In the construction industry, concrete which has good workability (e.g. self-consolidating concrete) and has lower weight (e.g. lightweight concrete) are more desirable especially for structures that use SC system, in which the consolidation of the concrete could be challenging. Therefore, this could be a drawback for beam SCB6 which could increase the weight of the structure especially in massive structural elements, thus it would be less practical for SC applications. Furthermore, the shearing deformation for beams in categories 2 and 3 was less than those in category 1.

In terms of load capacity of the beams, there is limited literature on the effect of fibres on SC beams. However, in review of the available results from past studies, Liew and Soheli (2009) studied the addition of PVA fibres to the SC beams with J-hook connectors and they showed that the load carrying capacity was increased by 25%. In this research study, in a descending order, the load carrying capacity was enhanced by 48.5%, 46.2%, 39.4%, 35.6%, and 13.1% for SCB6, SCB7, SCB5, SCB8 and SCB2 respectively which was greater than the aforementioned research finding.

Figure 5.76 shows the crack map for all eight SC beams. From the figure, it is evident that the number of flexural cracks increased for category 2 and category 3 beams which



had hybrid FRC core. Also, the shear crack at the end of the test had greater width for beams in category 1, because the use of hybrid fibres especially with SF dosage higher than 0.5% were more effective in controlling crack width. Within category 1, SCB4 showed more cracks with less spacing along the span than other singly-reinforced beams and SCB1. This shows a better flexural crack distribution with higher CNF fibre.

For the beams with hybrid core, SCB5 showed more cracks distributed along the length (with less crack spacing), while for SCB6 the width of flexural cracks was larger than those in SCB5. Also, SCB7 showed higher flexural crack width than SCB8, while SCB8 developed more cracks. This observation provides deeper insight into the contribution of higher CNF dosage in giving more crack distribution, while higher SF dosage helps with energy dissipation through increased crack width.

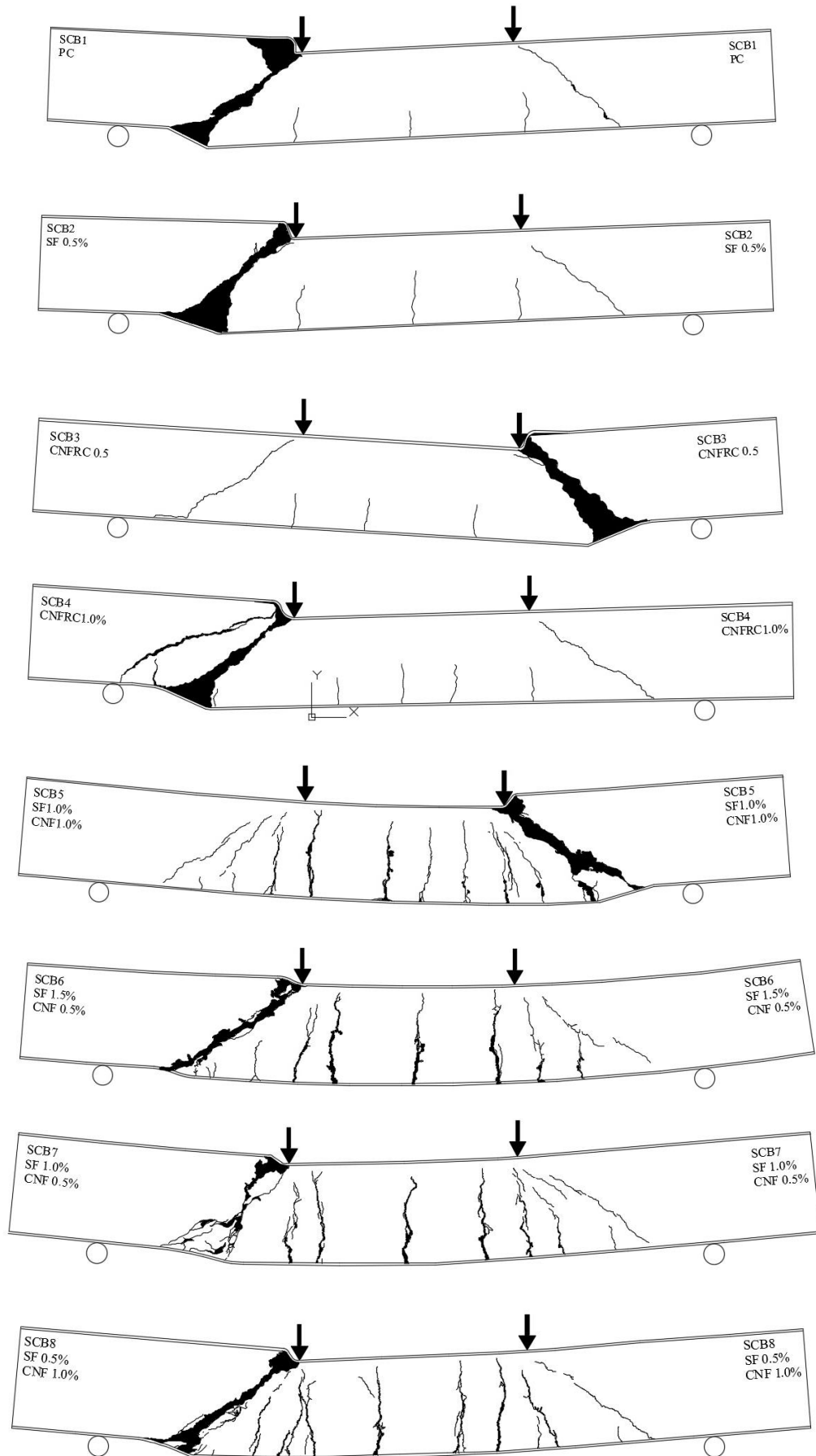


Figure 5.76. Crack map for all tested SC beams under four-point bending

## 5.10. CONCLUSIONS

To conclude the findings of the experimental investigation carried out in this chapter, the effect of each fibre type and their performance in combination with the second type fibre is outlined. The results indicated that steel fibres used in this study enhanced the shear capacity of the beam after initial cracking, hence improving the ductility at the post-peak stage, while during the early stages of loading, nanofibres provided the material with the ability to carry a higher load as well as improving SF performance throughout the entire loading phase (which was attained through enhanced C-S-H and interfacial interaction of fibres as observed in SEM images). The initial performance was best improved for each category as follows.

Category 1: 1.0% CNF showed the best results in delaying the formation of both initial flexural cracks and shear cracks.

Category 2: 1.0% CNF combined with 1.0% SF showed better performance in delaying the formation of initial shear crack, while the initial flexure crack was controlled at similar load level as concrete with 0.5% CNF and 1.5% SF.

Category 3: 1.0% CNF showed the best result in delaying the formation of both initial flexural cracks and shear cracks.

It is concluded that 1.0% CNF showed a good effect on the performance of the beam, both in singly reinforced concrete as well as in combination with SF. The experimental investigation carried out showed that the combination of nano (CNF) and macro size fibres (SF) improved the structural response, both for category 2 beams ( $V_f = 1.5\%$ ) and category 3 beams ( $V_f = 2.0\%$ ), so much that an adequate content of fibres could change the failure mode from shear to flexure-shear. Moreover, it was found that the strain induced on tie bars was minimised as opposed to control sample, while the strain induced on plate was maximised. The combination of fibres at two scales, provided a delay in the formation of cracks and higher post cracking stiffness because of a better crack-arresting mechanism and higher tension stiffening of the concrete. It should be noted that due to better crack control at macro scale, other shear resisting mechanism of the concrete namely the aggregate interlock is improved, providing more shear resisting capacity. The brittle failure of the concrete core was prevented and large

flexural deflection range (28-38mm) without severe plate deformation (i.e. shear deformation) was obtained.

In the review of the works on the use of hybrid fibres, Metaxa et al. (2010) indicated that using hybrid fibres of CNF and PVA in cement paste caused in higher load carrying capacity and a highly ductile behaviour at the post-peak stage because of microfibres, while, nanofibres enhanced the ability of the material to carry higher load during the early stages of loading. The findings of this experimental programme revealed a similar effect of fibres on the structural performance of SC elements constructed with CNFRC, which contributes to the knowledge in this area and shedding light on the effect of nanofibre reinforced cementitious composites at the structural level.

To conclude, the use of overall  $V_f$  of 1.5% is recommended for the design of SC with FRC concrete core as opposed to 2% since this category proved to be sufficient to alter the failure mode of the beam and achieving a high ductility and energy dissipation. Using less fibre content in the structural element is preferred due to better workability as well as less self-weight of the concrete. On the other hand, the use of higher CNF content in the hybrid fibre reinforced concrete (e.g. SCB5 & SCB8) is recommended, if one wish to obtain better self-health monitoring properties within the structural element which will be extensively discussed in the next chapter.

## CHAPTER 6

### SELF-SENSING PROPERTIES OF CNF REINFORCED CONCRETE

---

#### 6.1. INTRODUCTION

Monitoring the service life of structures is an essential task. It is hard to check the service life of filled SC walls or other structural elements by means of the visual inspection or sampling examination from the member core since the wall is enveloped by the steel plates. The aim of this chapter is to study the structural damage sensing capability of CNF in imparting smartness to concrete, by using CNFRC in a structural member considered for this research. For this task, SC beams (SCB3-SCB8) which were constructed with CNF reinforced concrete were aimed at the investigation conducted in this section.

#### 6.2. EXPERIMENTAL PROGRAMME OUTLINE

The self-sensing capability of the smart concrete can be evaluated by its piezoresistivity properties. Piezoresistive (electrical resistance changes with strain) behaviour is expressed using fractional change in resistance. In the experimental programme conducted for eight SC beams, the resistance was monitored at three different locations by means of embedding copper electrodes and using the two-probe method, described in Chapter 4, to record the change in the electrical resistance of the concrete core for each SC beam during loading. Some researchers (Han et al., 2014; Reza et al., 2003) pointed out that although the true resistance of the composites may be lower than the measured resistance value from the two-probe method due to the effect of the contact resistance, but it does not affect the capability of the two-probe method to detect changes in resistance of the composite under loading. On the other hand, this method is simpler and more convenient to use compared to a four-probe method and it is still widely used in research.

In addition, there are few environmental factors which could affect the resistivity of the concrete, which are temperature, moisture content of concrete, and environmental humidity. In this experimental program, all samples were left to completely dry out after they were removed from the water tank for the test. Also, all samples were tested in the similar laboratory environment, in which the temperature was kept at room temperature and the humidity of the environment was not variable, hence, the environmental effect on the electrical resistance of the samples were minimal.

A constant current was applied through electrodes incorporated within each SC beams containing carbon nanofibers. The voltage (V) was measured and electrical resistance (R) was calculated according to Ohm's law. It should be emphasised that one characteristic of the electrode to be mentioned is that the resistance of the matrix measured by the electrode is independent of the electric field direction. Also, it is important to note that those sections at which the electrical resistance, R, is calculated are in a stress state that is different from free sensors which were studied under uniaxial compression or tension in previous studies.

To better understand and analyse the outcome of the two-probe test, two key parameters of strain and electrical resistance variation (ERV) were studied and their relationship was analysed by regression analysis. The following results are presented and discussed for each individual electrode used in the beams.

- Trend line: the best-fit curve for the strain vs. ERV relationship.
- Correlation coefficient ( $R^2$ ): this is the squared value of the Pearson's correlation coefficient (R). The correlation coefficient of linear regression curve for the data is a measure of the linear distribution of the data. This statistical measure represents the linear interdependence of ERV and strain and shows the accuracy degree to which the change in the value of ERV could predict the change in the value of strain. This is obtained by:

$$R^2 = \left( \frac{\sum(x-\bar{x})(y-\bar{y})}{\sqrt{\sum(x-\bar{x})^2 \sum(y-\bar{y})^2}} \right)^2 \quad (\text{Eq. 6.1})$$

A value of +1 indicates a strong linear distribution and perfect linear correlation, which means that a change in the value of ERV will predict a change (increase or decrease) in applied strain. The closer the value of  $R^2$  is to +1, the stronger the linear correlation.

### 6.3. ELECTRICAL RESISTANCE OF CONCRETE FOR SC BEAMS

The initial electrical resistance for each beam before loading is presented in Figure 6.1. The fiber loading for each beam is demonstrated at the top of each bar. The initial electrical resistance of each beam is calculated from the average value of electrical resistance of two electrodes with identical applied current and identical distance between electrode poles. This consideration is aimed at eliminating the effect of current magnitude and electrode pole distance on the resistance. The concrete resistivity for each CNFRC is presented in Table 6.1 which is measured according to the following:

$$\rho = R \times A/L$$

Where  $\rho$  is the electrical resistivity,  $A$  ( $=40 \times 40 \text{ mm}$ ) is the area of electrode pole, and  $L$  ( $=90 \text{ mm}$ ) is the length between the two electrode poles. Previous study (Madhavi and Annamalai, 2016) indicated that moist concrete behaves as a semiconductor with resistivity of the order of  $100 \text{ } \Omega \cdot \text{m}$  while oven-dried concrete behaves as an insulator with resistivity of the order of  $10^9 \text{ } \Omega \cdot \text{m}$ . From Table 6.1 it is evident that all CNFRC has better resistivity compared to concrete.

From the figure, it can be seen that the use of 1.0% CNF in SCB4 was more effective in reducing the concrete resistance as opposed to SCB3 with 0.5% CNF. Doubling the amount of CNF in concrete matrix from 0.5% to 1.0% decreased the electrical resistance of the concrete by 35.5%.

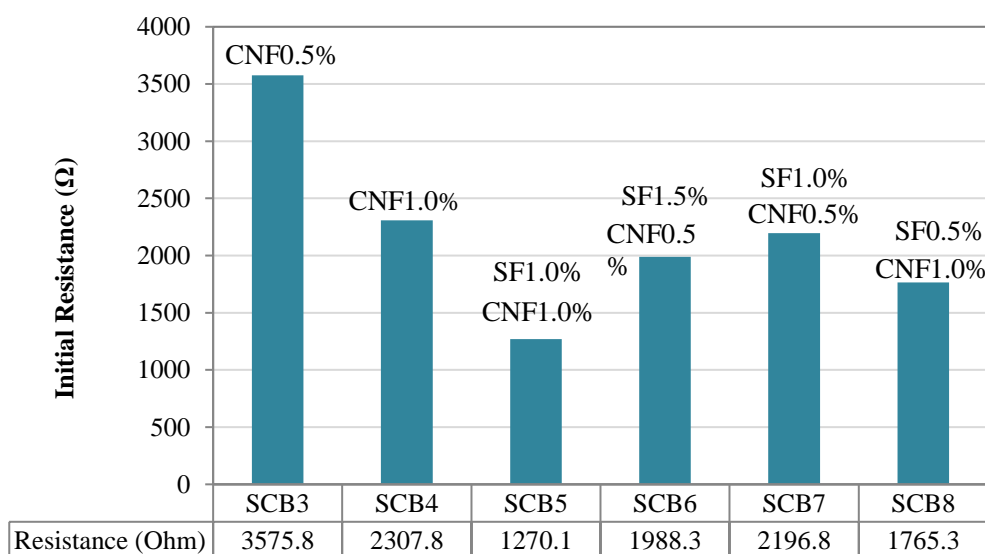


Figure 6.1. Electrical resistance of concrete core for all SC beams before loading

Table 6.1. CNFRC electrical resistivity

	<b>SCB3</b>	<b>SCB4</b>	<b>SCB5</b>	<b>SCB6</b>	<b>SCB7</b>	<b>SCB8</b>
<b><math>\rho</math> (<math>\Omega\cdot\text{m}</math>)</b>	63.5	41	22.6	35.4	39	31.4

Amongst specimens with 1.0% CNF (SCB4, SCB5, and SCB8), SCB5 showed the least electrical resistance, which could be due to the effect of additional 1.0% steel fiber in the matrix assisting the nanofibers in increasing electrical conductivity of concrete. Compared with SCB4, the addition of 0.5% SF to the CNFRC1.0 in SCB8, decreased the electrical resistance by 23% while adding 1.0% SF to the CNFRC1.0 in SCB5 decreased the electrical resistance by 45%.

Amongst specimens with 0.5% CNF (SCB3, SCB6, and SCB7), the addition of 1.0% and 1.5 % SF to the concrete core, was successful in decreasing the electrical resistance of the concrete by 38.5% and 44.4% compared to SCB3 with no SF. Although adding steel fiber to the concrete with 0.5% CNF was effective in enhancing the conductivity of concrete, comparing SCB5 and SCB7 reveals that CNF with 1.0% loading is more effective in enhancing the conductivity of the smart concrete since its combination with 1.0% SF showed lower resistance than the combination of 0.5% CNF with 1.0% SF. Increasing the steel fiber volume fraction from 1.0% to 1.5% within CNFRC0.5, decreased the electrical resistance of the FRC by only 9.5%. A possible reason for this insignificant effect could be that 0.5% steel fiber does not greatly affect the conductivity of concrete and these fibers are not as effective as CNF.

From the dispersion point of view, Konsta-Gdoutos and Aza (2014) stated that:

‘It is possible that conductivity/resistivity measurements besides being a valuable tool in evaluating the smart properties of the nanocomposites may provide a good correlation between the resistivity values measured and the degree of dispersion of the material in the matrix.’ (p.167)

Therefore, the successful effect of CNF on decreasing electrical resistance of the concrete could mean that the nanofiber dispersion has been satisfactory as it was also concluded from the SEM analysis of the concrete core (refer to section 5.8).



Overall, 1.0% CNF showed the best result and its combination with 1.0% SF was found to outperform the performance of other samples in decreasing the smart concrete electrical resistance. This fiber combination accommodated CNF bridging the existing pathways between the SF and created a more uniform conduction path. Thus, having the CNF in combination with SF could improve the accuracy of the self-sensing properties of concrete.

#### 6.4. SC BEAM RESULTS

The results for each beam is presented in this section by analysing the change of electrical resistance variation (i.e.  $ERV = (R - R_0)/R_0$ ) measured in situ during four-point bending test of the beam for each electrode at three previously specified locations (T, M, and B). The magnitude of ERV is then compared to the corresponding relevant strain values. The assumption of 100% composite action between tie bars and concrete implies strain compatibility between the tie bar and concrete. Therefore, for the Electrodes T and B, which were located in between the tie bars, the measured ERV was compared with the corresponding strain values measured from the strain gauges on adjacent tie bars, assuming that full bond between the bars and concrete exists. Electrode M was used to measure the electrical resistance in the horizontal direction at the upper half of the beam section at the centre of the moment span. Since the concrete and the top steel plate were experiencing compressive stress at the upper section of the beam the change in the electrical resistance was expected to be due to the change in compressive strain. The comparison for this electrode is then made against the compressive strain monitored with the concrete strain gauge wherever results were available. The results for each beam are presented in the following sub-sections.

##### 6.4.1. SCB3: CNFRC0.5

The electrode positions within the SCB3 concrete core are shown in Figure 6.2. The approximate position of shear cracks on this beam is represented in this figure with a dashed line. For this sample, the major shear crack occurred on the east shear span of the beam close to Electrode B. At the end of the test the damaged wires of the Electrode B due to the extreme shear crack opening were noticed as shown in Figure 6.3.

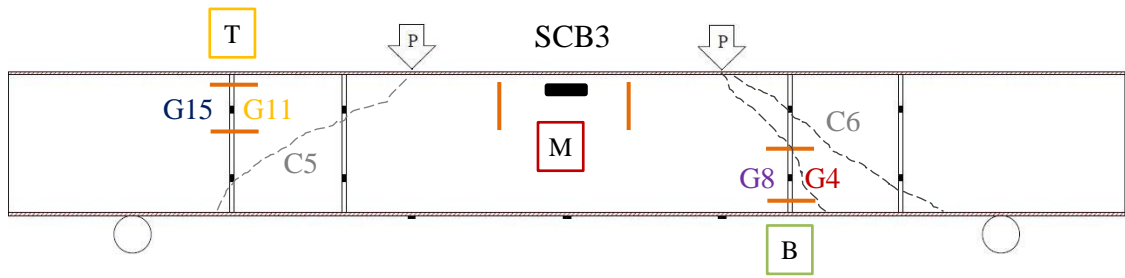


Figure 6.2. Electrode positions for SCB3

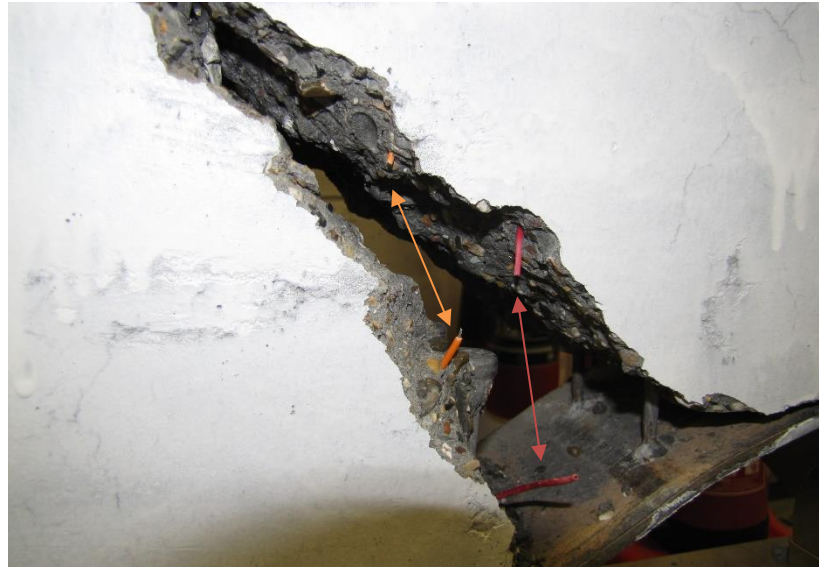


Figure 6.3. Damaged wires of Electrode B at east shear crack for SCB3

#### 6.4.1.1. Electrode T

The electrode resistance variation, ERV, for the top electrode (Electrode T) is shown in Figure 6.4 as a function of time. For ease of conception of instantaneous strain level, strain measurements on adjacent tie bars are also included as a left-hand side y-axis. The behaviour depicted in the figure manifests that the ERV did not vary smoothly with the strain variation and it can be stated that the piezoresistivity of the concrete was unstable and noisy. On the other hand, it is evident that the changing trend of the ERV followed the same trend of adjacent tie bar strains (G11 and G15). For example, the significant increase in strain from  $t = 1300\text{s}$  to  $t = 3000\text{s}$  was simultaneous with an increase in the ERV magnitude during this time of loading. It is interesting to note that  $t = 1300\text{s}$  corresponds to the formation of the shear crack on the west side until the ultimate load capacity of the beam was reached at  $t = 3000\text{s}$ . The constant strain value

following the significant increase in strain depicts the failure of the tie bar gauges at ultimate load capacity. Likewise, the electrode did not show a significant change in the ERV trend.

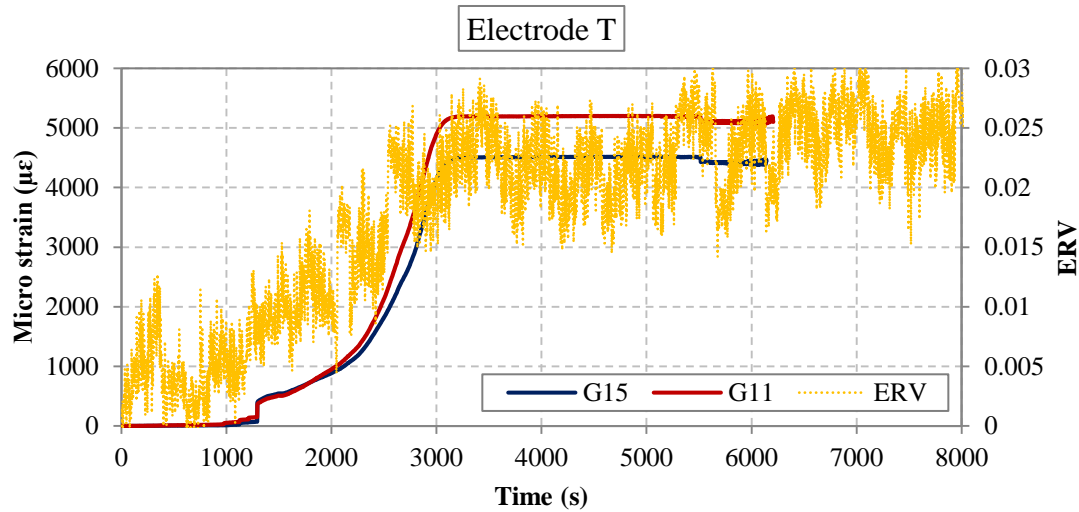


Figure 6.4. Electrode T results for SCB3

ERV increased with positive sign for this electrode. This means electrical resistance was increased, which was previously observed for samples under monotonic uniaxial tension. Under such situation the ERV increases as the fillers tend to separate. It can be concluded that concrete experienced tension in the direction of the electrode and filler separation was happening as well as formation of micro-cracks which interrupted the electrical circuit and in turn caused an increased electrical resistance of the concrete.

To better understand the direct relationship between ERV and strain, the ERV as a function of strain for Electrode T was plotted and is shown in Figure 6.5. The curve was then divided into two stages to investigate whether a linear line could be fitted into the curve as shown in Figure 6.6. Due to the noisy results of the ERV, the relation between ERV and strain could not be correlated with either a straight line or a parabola and as can be seen from the figure the error margin is large. The best  $R^2$  value amongst the two stages was as low as 0.64 which does not represent a good linear relationship. It is probable that the scatter result in the ERV response is due to the inconsistencies in the dispersion pattern of CNF in the concrete matrix throughout the specimen volume. This was also observed in the SEM micrographs of the SCB3 concrete core, which showed denser distribution of fibers at some observed surfaces (see Appendix B). Therefore, non-homogenous dispersion could be the reason for unstable measurements.

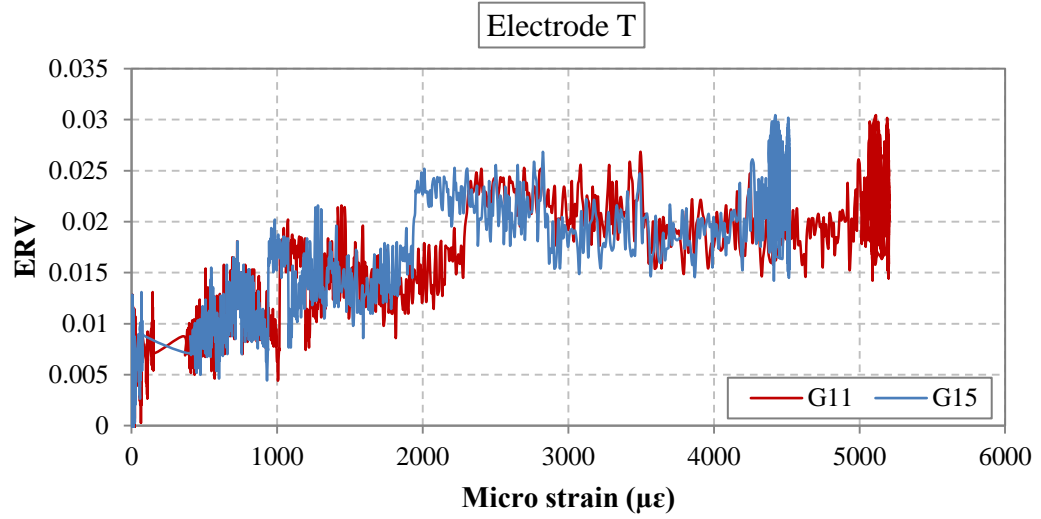


Figure 6.5. ERV vs. strain for electrode T for SCB3

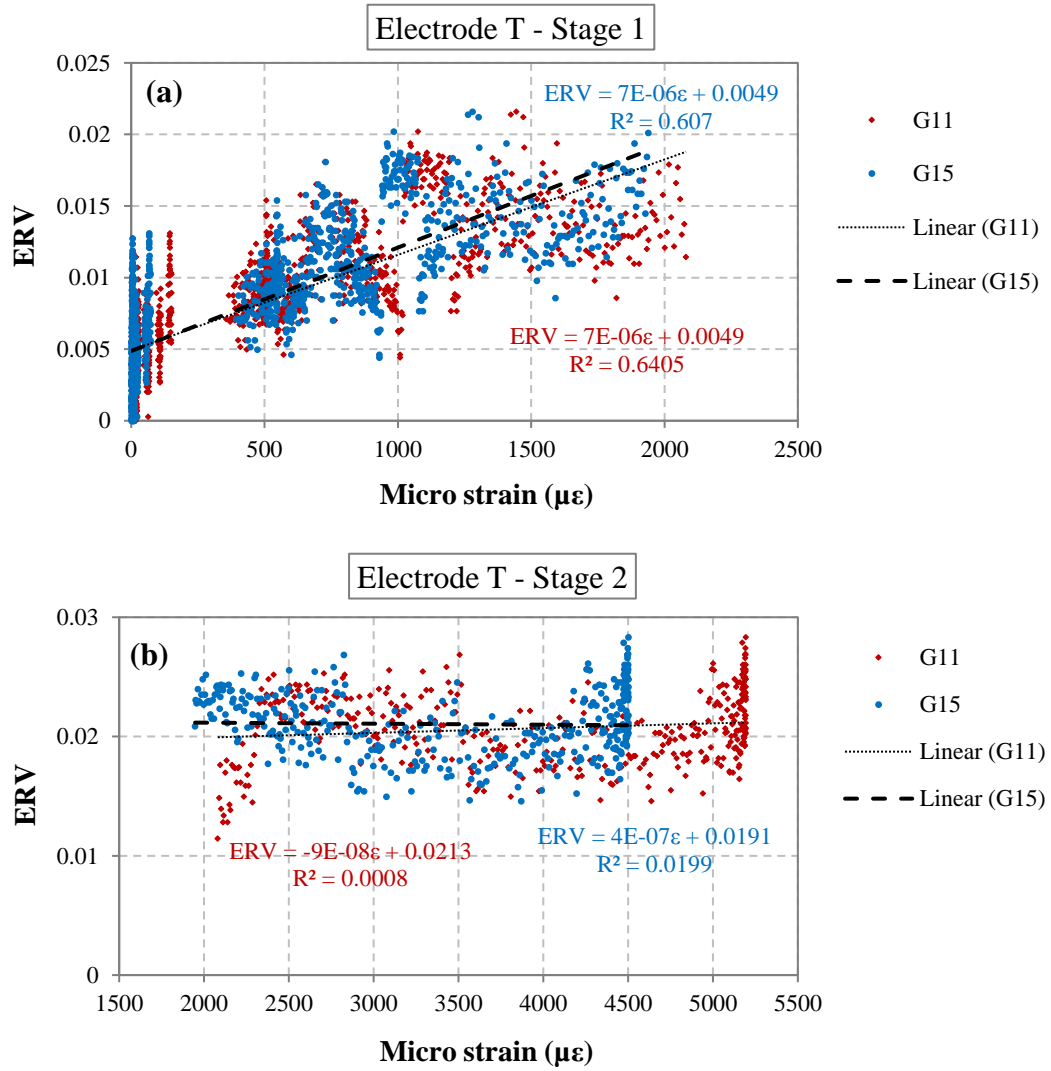


Figure 6.6. ERV vs. strain for Electrode T: (a) stage 1; (b) stage 2

#### 6.4.1.2. Electrode B

The electrode resistance variation, ERV, for Electrode B (located at the bottom half of the beam) is shown in Figure 6.7. The recorded results for this electrode also showed noisy measurements similar to Electrode T. The significant increase in strain, following a low-level strain value, was captured by the change in ERV up to the maximum strain measured by the strain gauges at the post-peak stage. The gauges then had a slight drop and then failed to function at this point ( $t = 3600s$ ). However, the electrical resistance of the concrete was still being recorded during the post-peak stage of loading (after  $t = 3000s$ ) and the ERV showed further increase in electrical resistance but at a lower rate. Finally, towards the end of the test at  $t = 7000s$  (corresponding to  $D = 28$  mm), the result showed a sudden drop in the ERV which is attributed to the failure of the electrode due to wire damage during the sudden crack opening of the east shear crack as shown in Figure 6.3. Overall, the ERV showed a dramatic change from the moment the shear crack formed until the ultimate capacity for the beam was reached and the strain reached its ultimate measurement. During the post-peak stage of loading, the ERV increased gradually with a lower rate which reflects decreased sensitivity of the concrete due to the presence of tensile stresses and cracks.

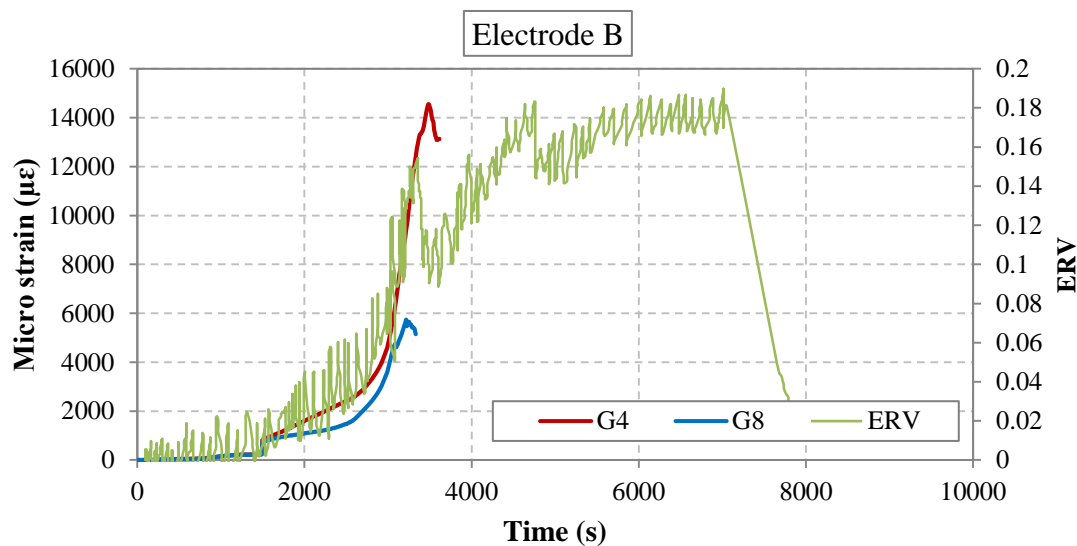


Figure 6.7. Electrode B results for SCB3

The relationship between ERV and measured strain by each gauge (G4 and G8) is shown in Figure 6.8. There is no perfect linear relationship between the two variables. However, it is evident that despite the unstable ERV, the best  $R^2$  value is 0.81 which is

not too low. This electrode showed a better correlation with changing strain as opposed to Electrode T of this specimen. This could be due to more homogenous fiber distribution in the area.

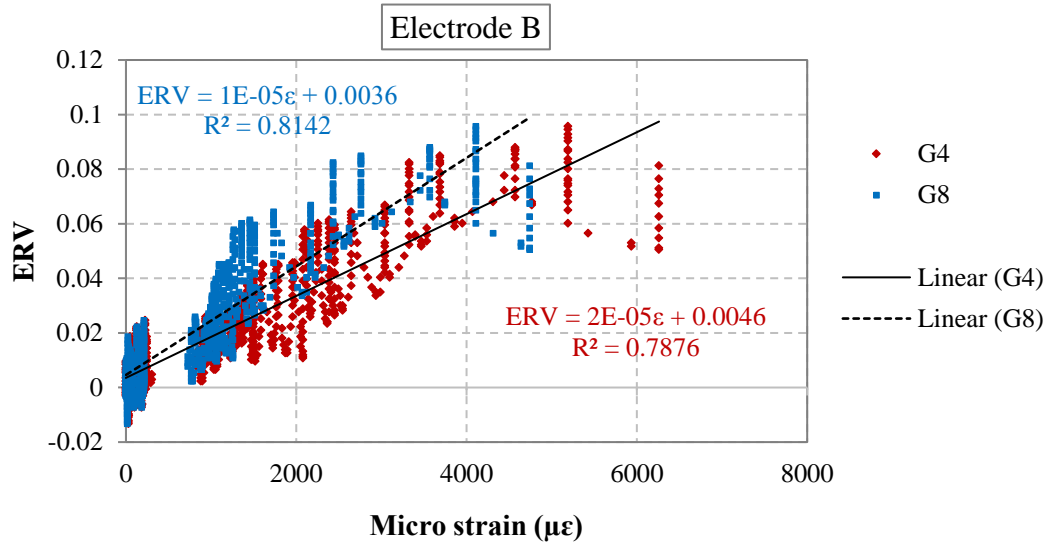


Figure 6.8. ERV vs. strain for Electrode B in SCB3

#### 6.4.1.3. Electrode M

The ERV, for Electrode M, located at the centre of the beam at the top section is shown in Figure 6.9. The concrete strain gauge failed at early stages and the results from the electrode could not be correlated with the strain value. Overall the variation of the ERV was in the range of -0.002 to -0.006 which is very small. It is concluded that the change in compressive strain was either unremarkable or another reason could be that the concrete could not perfectly capture the change in strain. Another plausible reason for small ERV with no reasonable trend could be the distance of the electrode poles in Electrode M (180 mm), which was three times greater than poles in Electrodes B and T (60 mm). This could be the reason for a weak circuit and it can be said that 0.5% CNF was not sufficient to create a circuit with high sensitivity at 180 mm distance. Nevertheless, the results for Electrode T and Electrode B showed that despite the unstable result, the concrete could capture the same changing trend in strain by its electrical resistivity.

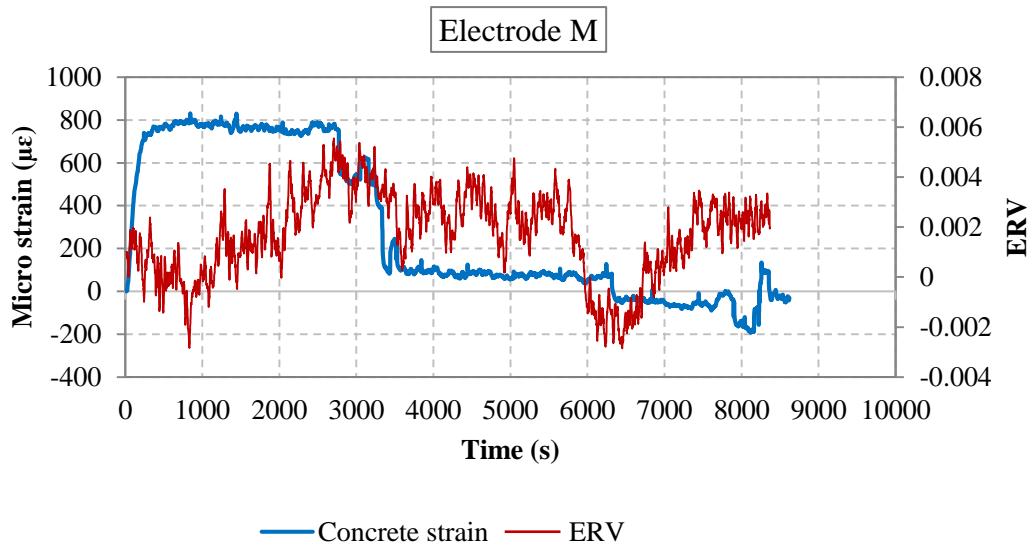


Figure 6.9. Electrode M results for SCB3

#### 6.4.2. SCB4: CNFRC1.0

The electrode positions for SCB4, with CNFRC1.0 concrete core, are shown in Figure 6.10 along with the approximate position of the shear cracks near the electrodes. For this sample, the major shear crack occurred on the west shear span of the beam close to electrode B.

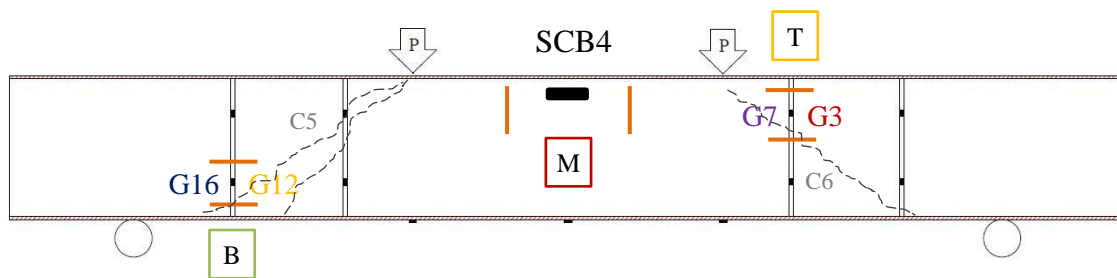


Figure 6.10. Electrode positions for SCB4

##### 6.4.2.1. Electrode T

The electrode resistance variation, ERV, for Electrode T is shown in Figure 6.11. There was no fluctuation in the piezoresistive response of SCB4. It can be seen from the figure that the ERV was changing homologically with the measured strain in the adjacent tie bars. The trend for ERV was closer to the trend of measured strain by G7. This could mean that G7 had closer strain value to the strain of the surrounding concrete.

The strain in bars at the proximity of the east shear crack location suddenly increased after the shear crack formation at around  $t = 1500$ s, the ERV also increased suddenly, which shows the sensitivity of the concrete to the formation of the hairline shear crack at the pre-peak stage. The sudden increase in electrical resistance can provide early warning of upcoming material failure. When the strain reached its peak value, which corresponded to the ultimate load level, the ERV also reached a peak value and then the ERV showed a slight decrease in resistance and an almost constant value from  $t = 4500$ s- $6500$ s. This behaviour can be due to a more stable condition with no change in resistance. After  $t = 6500$ s, the ERV increased which is attributed to a small increase in depth of C6 within the concrete which weakened the piezoresistivity effect of the CNFRC by interrupting the conduction path which was not captured by the gauges.

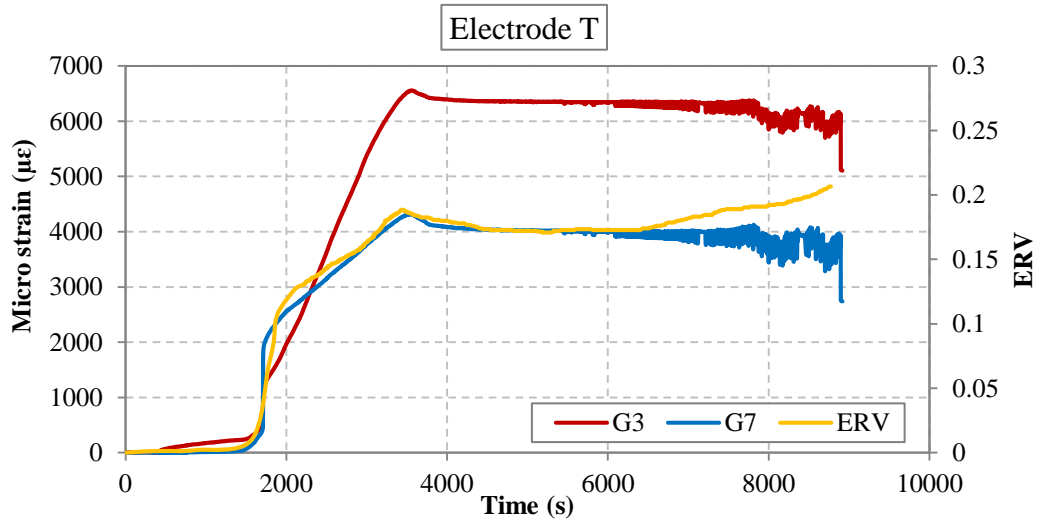


Figure 6.11. Electrode T results for SCB4

The direct relationship between ERV and strain measurements of G3 and G7 is shown in Figure 6.12. A linear trend line was drawn for the data points. A Linear relationship is observed between ERV and strains up to the formation of the shear crack, which was signified by a sudden increase in strain and ERV in Figure 6.11. According to this figure, the piezoresistive response of the concrete core can be categorised into the steps during the loading as follows:

1. *Stage 1*: Elastic phase; there is a linear relationship between ERV and strain from the start of loading to a strain of  $\epsilon_{G3} = 1300\mu\epsilon$ , and  $\epsilon_{G7} = 2300\mu\epsilon$ . This



- phase belongs to the pre-peak loading stage up to the formation of the shear crack.
2. *Transition phase*: there is a transition phase between the two stages, at which nonlinear relationship is found with lower sensitivity, indicating that the number and size of microcracks begin to increase at this stage. This phase is shown with a coloured background in Figure 6.12.
  3. *Stage 2*: near-linear relationship between ERV and strain is found during the second stage until failure. The sensitivity at this stage is lower than stage 1 due to increased number and size of micro-cracks.

These stages are also referred to for other SC beams analysed in the following sections. The correlation coefficient for both gauges at both stages was about 0.99 (very close to 1). This shows that there is a very good correlation between the ERV and strain which means that the change in strain is accurately captured with the change in electrical resistance of the smart concrete.

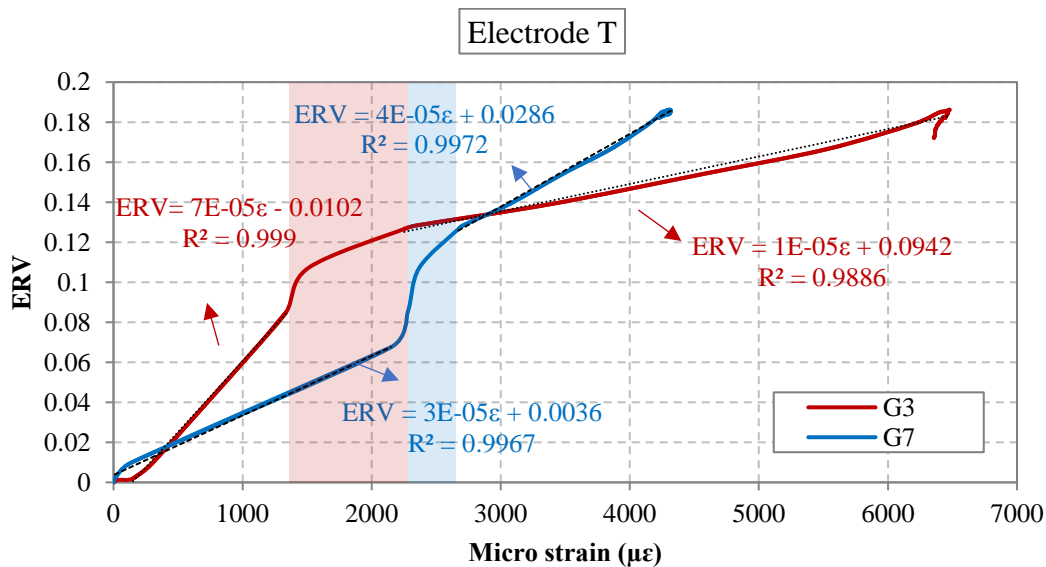


Figure 6.12. ERV vs. strain for electrode T for SCB4

#### 6.4.2.2. Electrode B

The electrode resistance variation, ERV, for Electrode B is shown in Figure 6.13. The location of this electrode was close to the major west shear crack, C5. The change in ERV was minimal initially as the strain value was low before the formation of the shear crack. With the shear crack formation (C5) and the sudden increase in strain (at  $t = 1380$  s), the ERV also showed a sudden increase. This change in ERV by the formation of

the crack shows that the concrete itself could sense the formation of the shear crack and the corresponding increase in strain. After the formation of C5 the rate in the strain growth was increased, likewise, the ERV increased with higher rate until the peak strain was reached at the ultimate loading capacity of the beam ( $t = 3400s$ ). After the peak load was reached, the maximum strain was recorded, and the gauges were not able to measure strain after this point, while the electrodes were recording more data during the post-peak stage. This could be regarded as an advantage of the smart concrete to monitor its damage while the gauges failed at an earlier stage. The ERV was increasing during the post-peak stage, however, the rate of increase was smaller than the rate of ERV increase from the crack formation to the peak load due to lower sensitivity during this phase because crack extension and widening within the concrete weakened the piezoresistivity effect of the CNFRC.

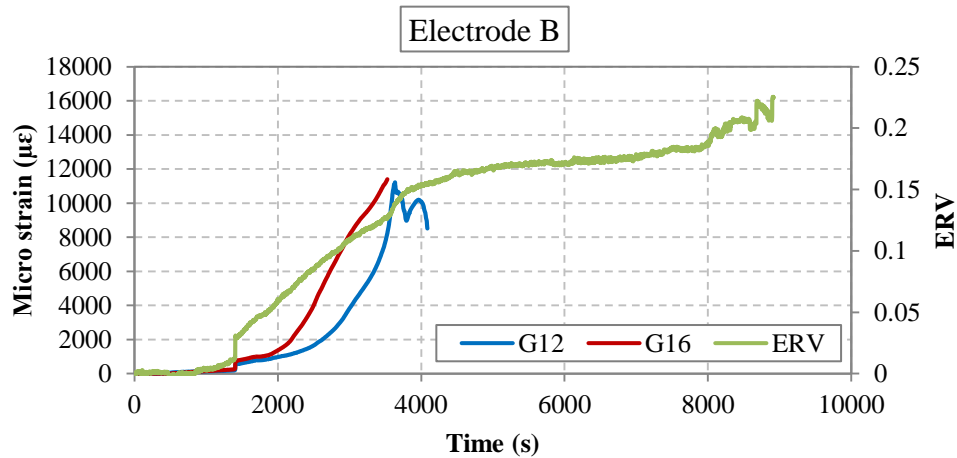


Figure 6.13. Electrode B results for SCB4

The direct relationship between ERV and both G12 and G16 strain measurements is shown in Figure 6.14. Similar to Electrode T, the relationship can be divided into two stages. It is evident that the main difference between the two stages is the slope of the curve. The small change in ERV (less slope) during the second stage is due to increased number and size of micro-cracks in the CNF concrete with strain, which causes the increased resistance of smart concrete and causes less sensitivity of the concrete as opposed to the first stage.

The figure also shows the linear relationship at each stage with the  $R^2$  correlation coefficient for the linear relationship between ERV and strain. Very good correlation between the ERV and strain is observed ( $R^2 > 0.99$ ). According to this result, it can be concluded that the CNFRC1.0 was successful in monitoring the change in strain by its electrical conductivity properties. The behaviour of this specimen was better than SCB3 with CNFRC0.5 since a stronger correlation between ERV and applied strain was observed.

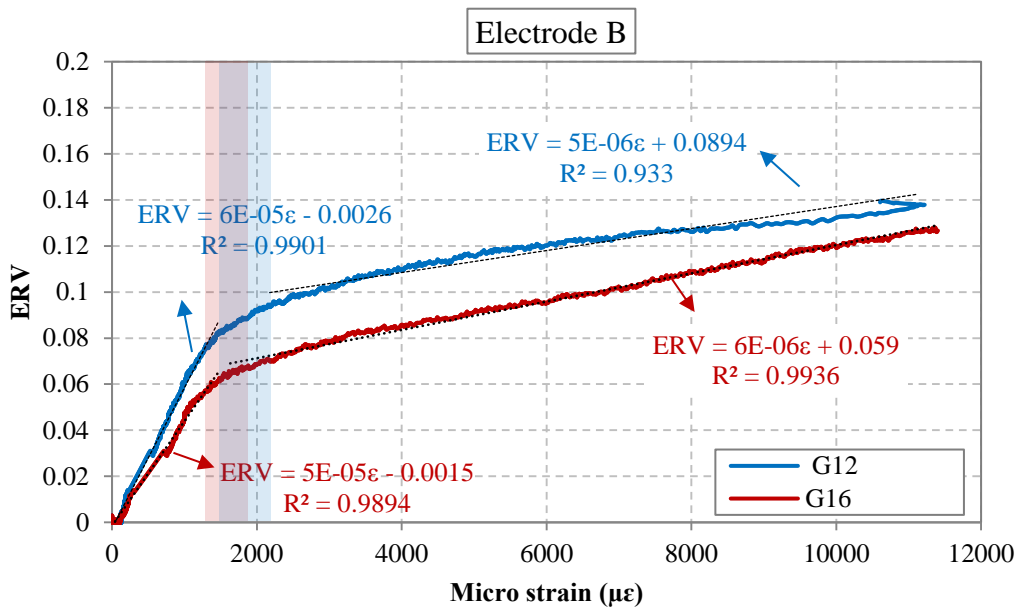


Figure 6.14. ERV vs. strain for Electrode B in SCB4

#### 6.4.2.3. Electrode M

The electrode resistance variation, ERV, for Electrode M, embedded in SCB4 is shown in Figure 6.15. The concrete strain gauge for this sample failed to function, however, the ERV measurements showed linear change during the loading. Since this electrode was measuring the compressive strain in the horizontal direction, the electrical resistance of concrete was expected to decrease as the pressure compaction causes functional fillers to approach each other, thus improving the conductive network inside the concrete. Due to a decrease in electrical resistance of the concrete, the ERV has a negative sign. This was also observed for specimens studied and presented in Chapter 3. The increase in the ERV was constant and the maximum absolute ERV value measured for SCB4 with CNFRC1.0 was 0.065.

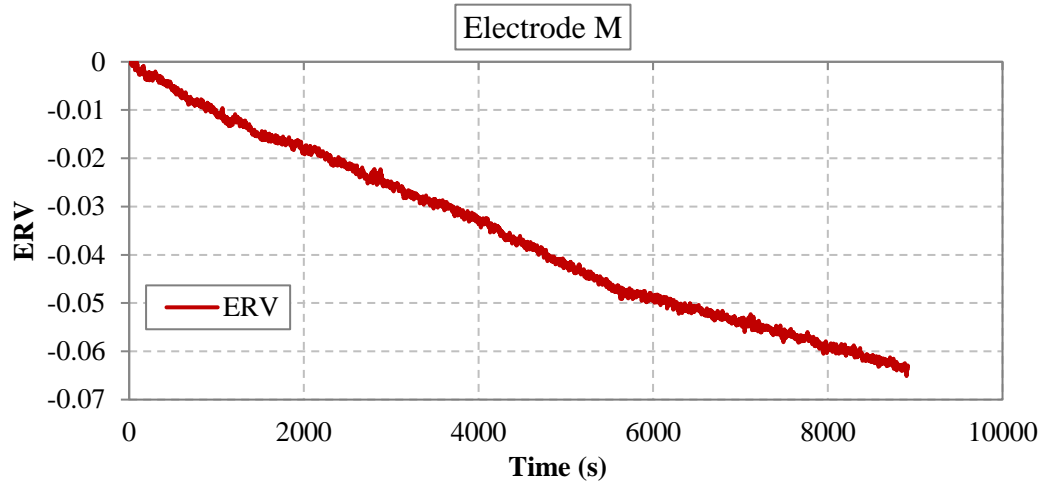


Figure 6.15. Electrode M results for SCB4

#### 6.4.3. SCB5: SF1.0% + CNF1.0%

The electrode positions for SCB5, with hybrid fiber reinforced concrete core are shown in Figure 6.16 as well as the approximate location of the shear cracks. The major shear crack for this sample formed at the east shear span towards the end of the test.

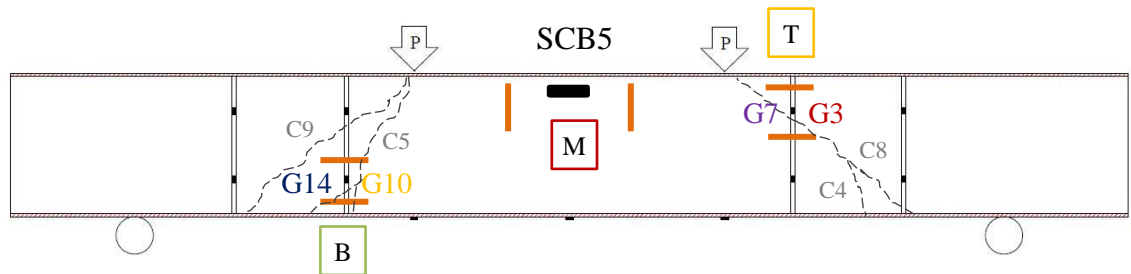


Figure 6.16. Electrode positions for SCB5

##### 6.4.3.1. Electrode T

The electrode resistance variation, ERV, for Electrode T adjacent to G3 and G7 is shown in Figure 6.17. For clarity of the presentation of results, the electrical response of this electrode is divided into two stages and shown in Figure 6.17. Stage 1 (Figure 6.17(b)) represents the stage before the significant increase in strain due to progression of diagonal cracks on the east side (C8) prior to the ultimate capacity of the beam and stage 2 (Figure 6.17(b)) depicts the phase in which the shear crack on the east side increased in width towards reaching the ultimate capacity of the beam (reached at  $t = 11000s$ ).

Both figures show that the ERV results are highly related to the strain values which are equal to the concrete strain at the location of the electrode. From the overlapping results, it can be claimed that the ERV of the smart concrete was capable of capturing the change of strain in concrete with high accuracy, hence this parameter can be used for predicting the varying strain during loading.

The direct relationship between the strain and ERV can be better examined from Figure 6.18. Similar to SCB4, a linear relationship was observed between ERV and strain prior

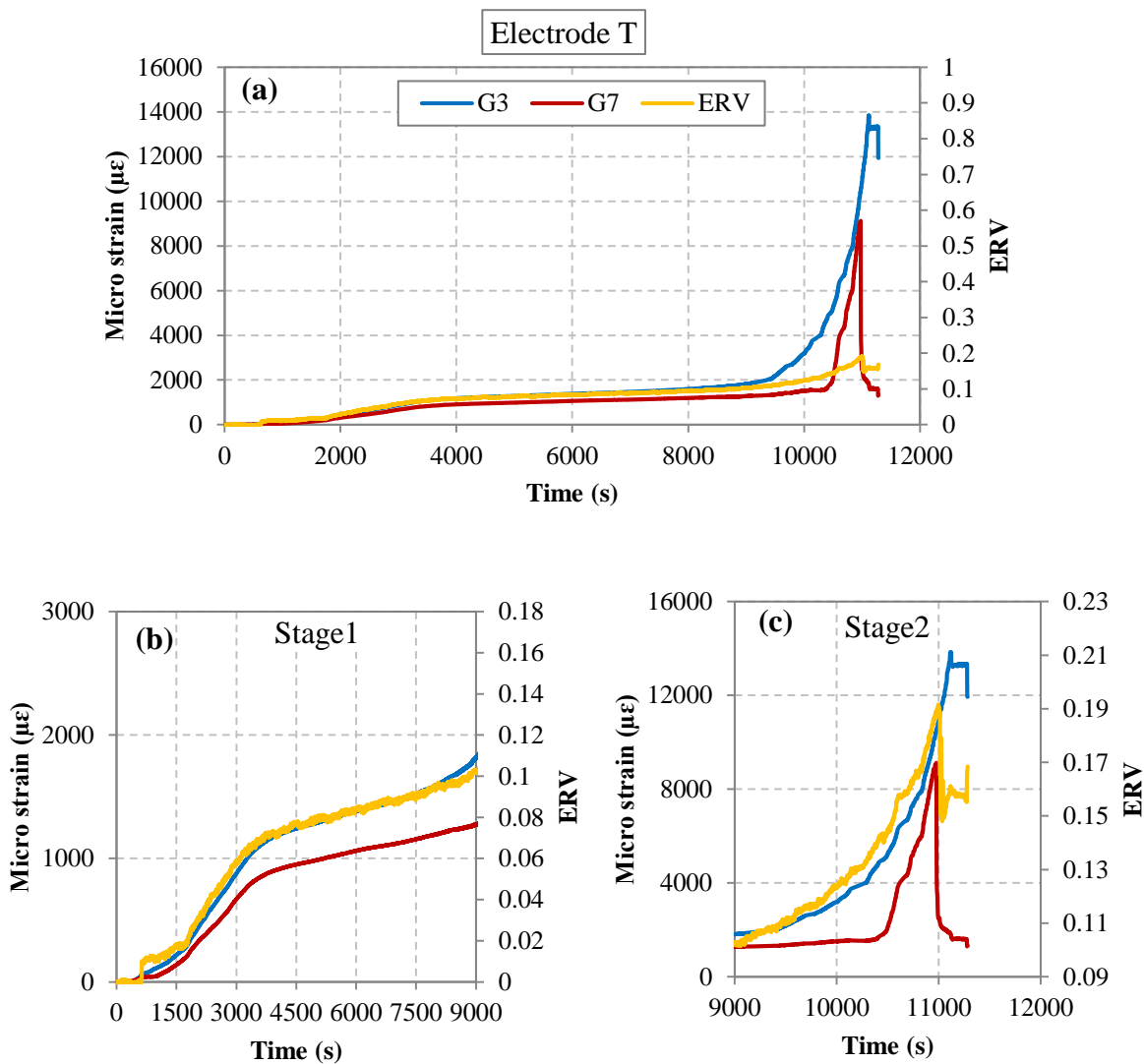


Figure 6.17. ERV vs. strain for Electrode T for SCB5

to the flexure-shear crack formation in the proximity of Electrode T (C8, close to the right point load) and the sensitivity of the concrete was higher during stage 1. After the transformation from stage 1 to stage 2, at which crack in the concrete was developed, the relationship between the ERV and strain were still linear but with lower slope due

to the lower sensitivity of the concrete because of the presence of the major crack which increased the electrical resistance.

The figure above shows that the fractional change in electrical resistance is highly correlated with strain with correlation coefficients higher than 0.99. The transition

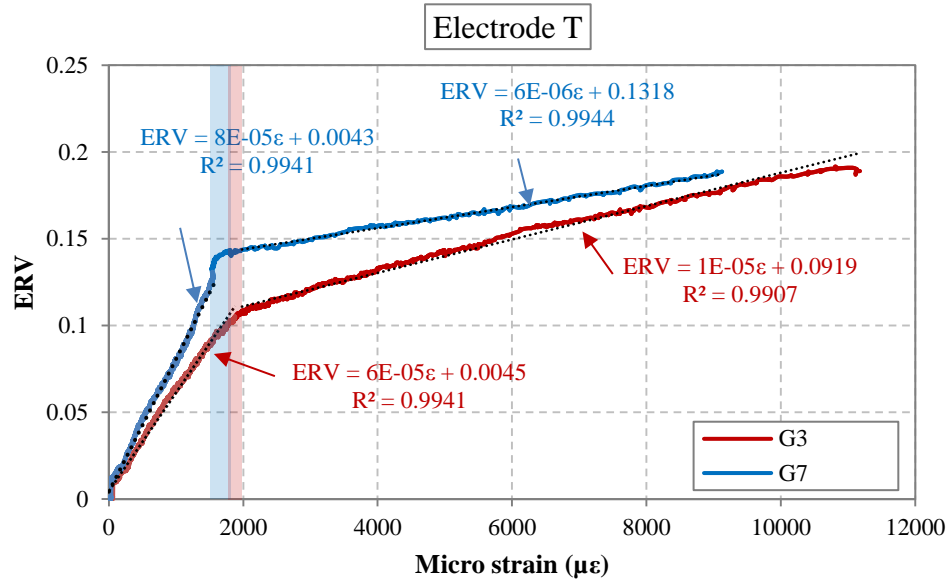


Figure 6.18. Electrode T results for SCB5

phase, in this case, is very small. From these results, it is evident that the electrical properties of a smart concrete with 1.0% CNF and 1.0% SF is highly correlated to the strain of the concrete. This implies that having the ERV value the strain can be predicted.

#### 6.4.3.2. Electrode B

The ERV for Electrode B on the west side of the beam is shown in Figure 6.19. The location of this electrode was close to the west shear crack. The figure shows that the ERV had correlation with the measured strain in adjacent bars (G10 and G14) and at every instance, the strain increased the ERV increased as well. For clarity of presentation, the ERV at two stages are shown in Figure 6.20(b) and (c); the former shows the results prior to the sudden increase in strain due to shear crack progression in concrete. The strain increased until the ultimate capacity of the beam was reached.

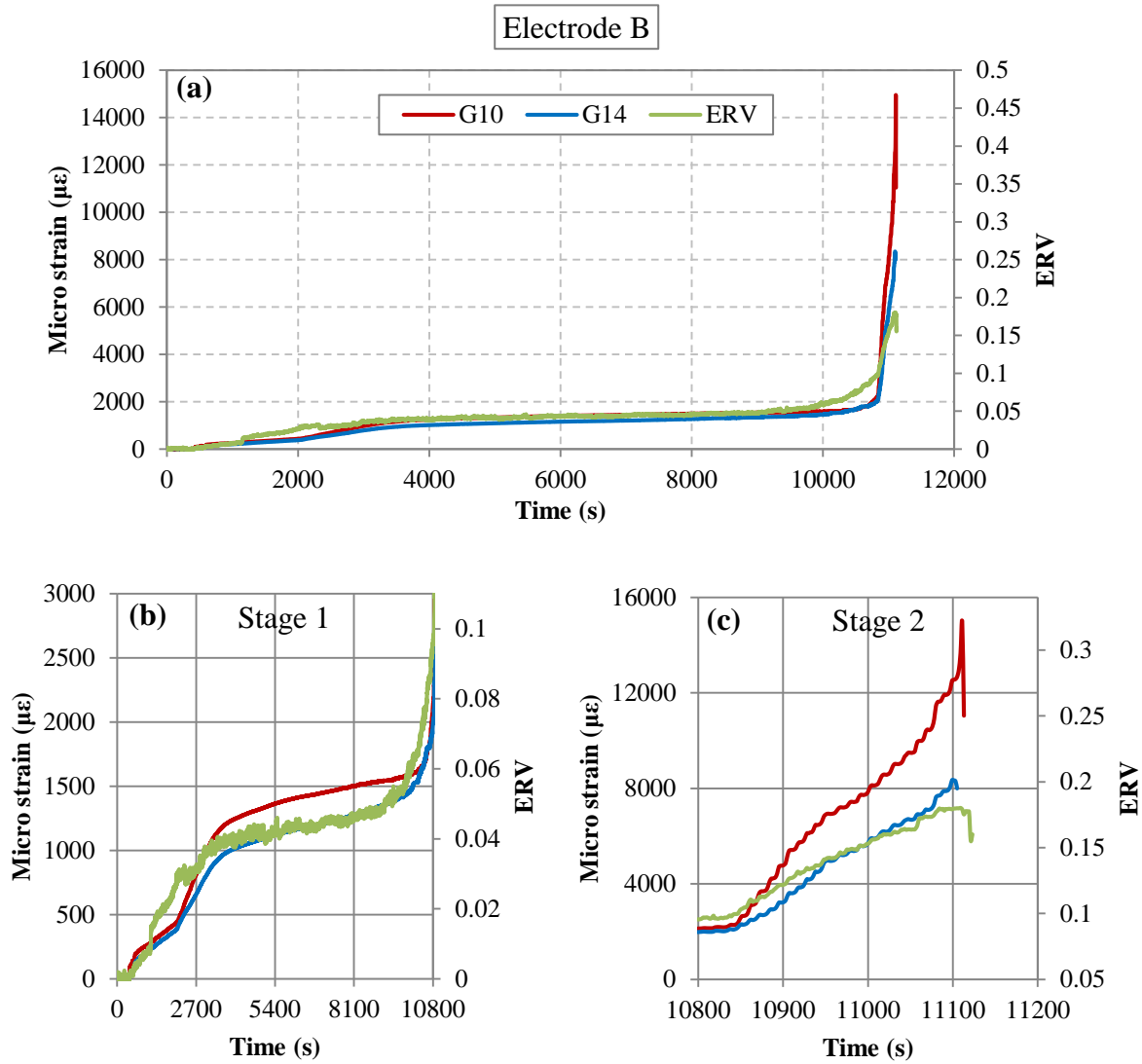


Figure 6.19. Electrode B results for SCB5

ERV as a function of strain is shown in Figure 6.20. The initial stage showed a linear relationship between the ERV and strain, which could be defined by three different lines. These lines lie in between strain ranges of 0-400  $\mu\epsilon$ , 400-1500  $\mu\epsilon$ , and 1500-1900  $\mu\epsilon$ . This could be due to the difference between the measured strain on tie bars and the actual strain concrete was experiencing during this stage. The transition stage, in which the west crack was further developed, took place over a narrow strain range. After the transition from stage 1 to stage 2, the concrete electrical resistance was increased, and a linear relationship between the ERV and strain was obtained with high correlation coefficient ( $R^2 > 0.98$ ).

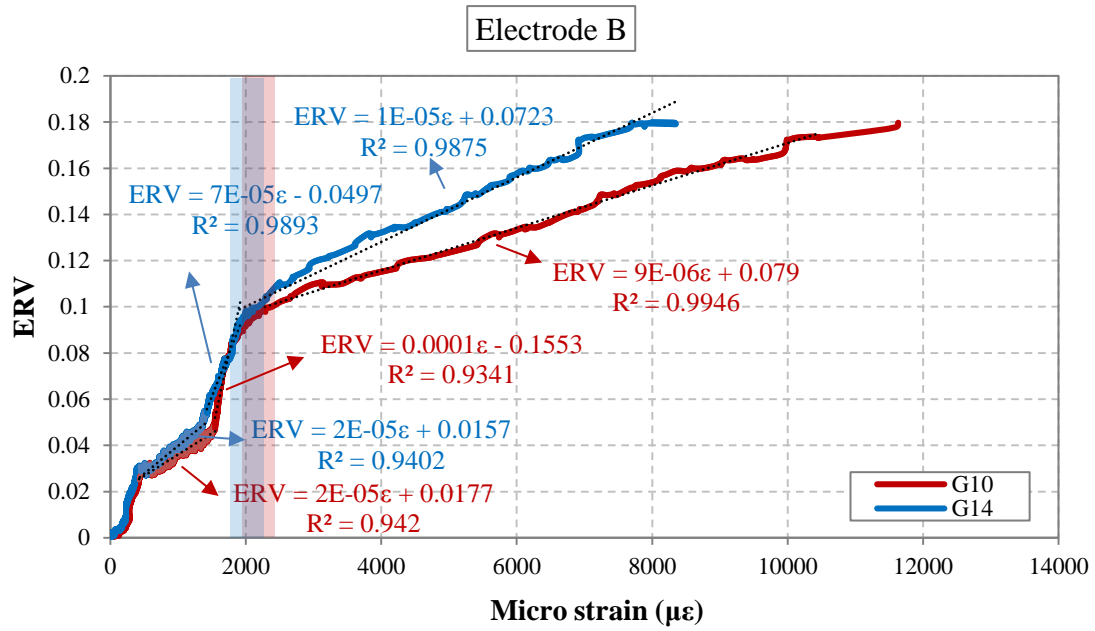


Figure 6.20. ERV vs. strain for Electrode B for SCB5

Similar to previously observed electrode results for other SC beams, the sensitivity of the concrete decreased during stage 2 due to the merging of micro-cracks in the vicinity of this electrode which interrupted the conductive network.

#### 6.4.3.3. Electrode M

The electrode resistance variation, ERV, for Electrode M, positioned in SCB5 is shown in Figure 6.21. The concrete gauge in this specimen had noisy signal output and the results could not be used for correlation. Similar to SCB4, the ERV decreased linearly with a negative sign, until the maximum capacity of the beam was reached. The maximum absolute measured ERV was 0.1 for this sample which was higher than SCB4 (ERV= 0.06). From this, it can be stated that the strain induced in this sample was higher at the ultimate load ( $t = 11000s$ ) than SCB4 as the ERV showed higher absolute value.



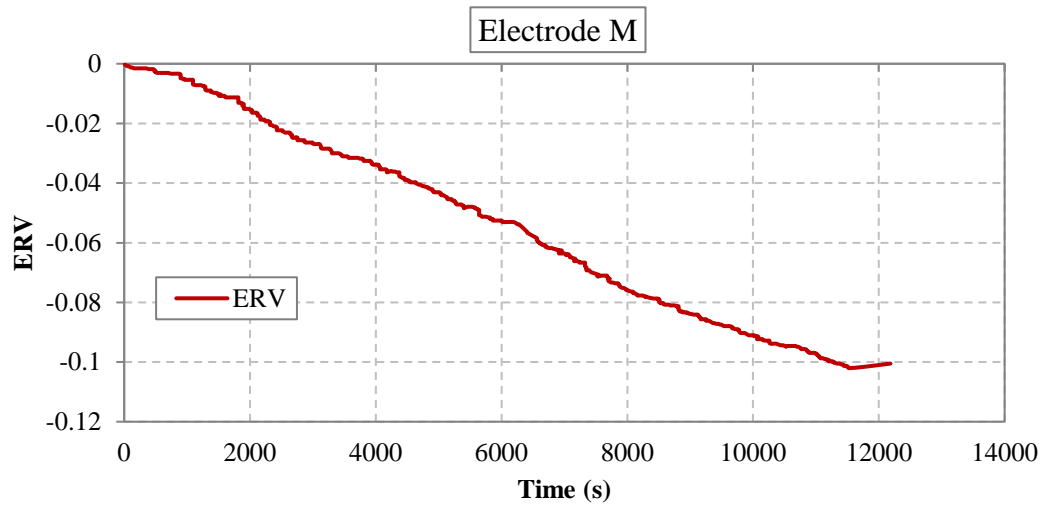


Figure 6.21. Electrode M results for SCB5

#### 6.4.4. SCB6: SF1.5% + CNF0.5%

The electrode positions for SCB6, with hybrid fiber reinforced concrete core (SF 1.5% and CNF 0.5%) are shown in Figure 6.22. This sample showed a ductile behaviour with flexure-shear failure and the major shear crack formed at the west shear span close to electrode B.

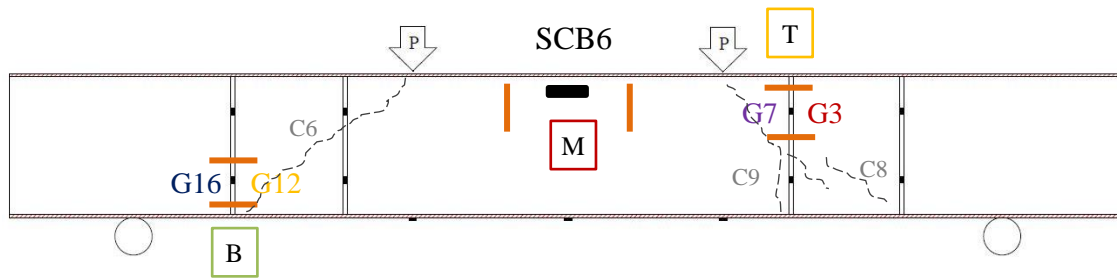


Figure 6.22. Electrode positions for SCB6

##### 6.4.4.1. Electrode T

The electrode resistance variation, ERV, for Electrode T adjacent to G3 and G7 is shown in Figure 6.23 along with the measured strain from G3 and G7 during the test. The gauges showed a slight increase at  $t = 2000$ s from the strain of  $180 \mu\epsilon$  to  $640 \mu\epsilon$ . This signified increased applied stress and hence formation of cracks in the vicinity of these gauges. The strain continued increasing gradually until the beam was close to reaching

its ultimate capacity at  $t = 11780$  s. While the gauges failed prior to the ultimate load, the electrode could capture the change in strain when the strain started to increase from  $t = 2000$ s. Therefore, the electrode could measure more data for longer than the gauges and also beyond the ultimate load of the beam which indicates that the concrete strain was increasing.

Direct relationship between the strain and ERV can be better examined from Figure 6.24. Two linear stages were marked for each gauge. The relationship of the ERV with G3 appeared to be better correlated since the correlation coefficient for the developed linear trend line was higher than that for G7. The correlation coefficient for this specimen was lower than SCB4 and SCB5, which could mean that the latter two beams had higher sensitivity to the change of strain, in another word, they had better piezoresistive behaviour due to higher CNF dosage. Having said that, the concrete in this beam could predict the strain by its ERV with a reasonable accuracy.

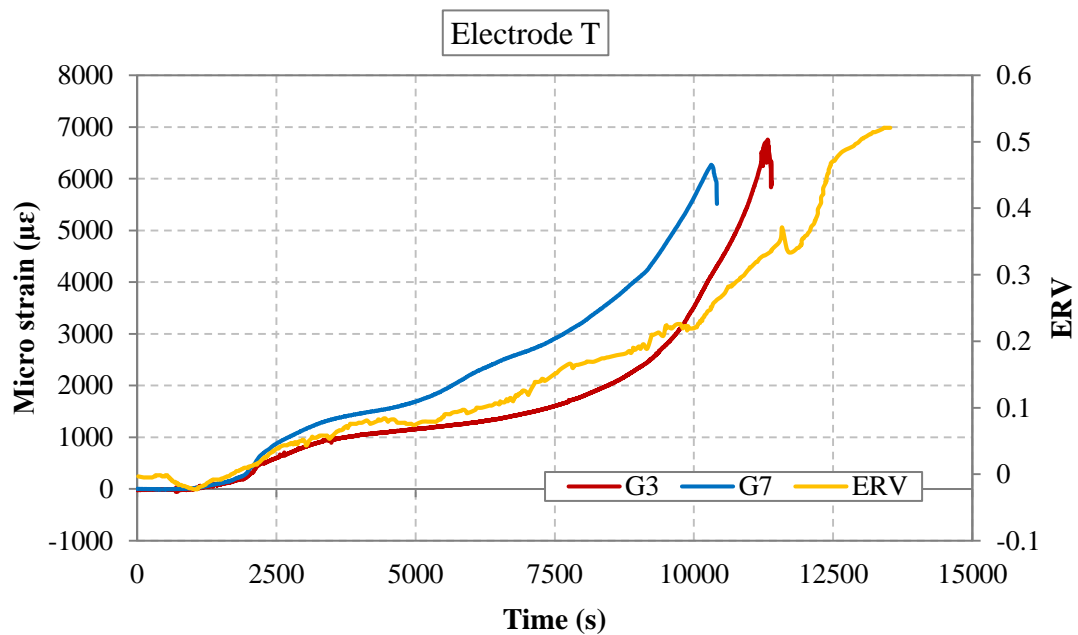


Figure 6.23. Electrode T results for SCB6

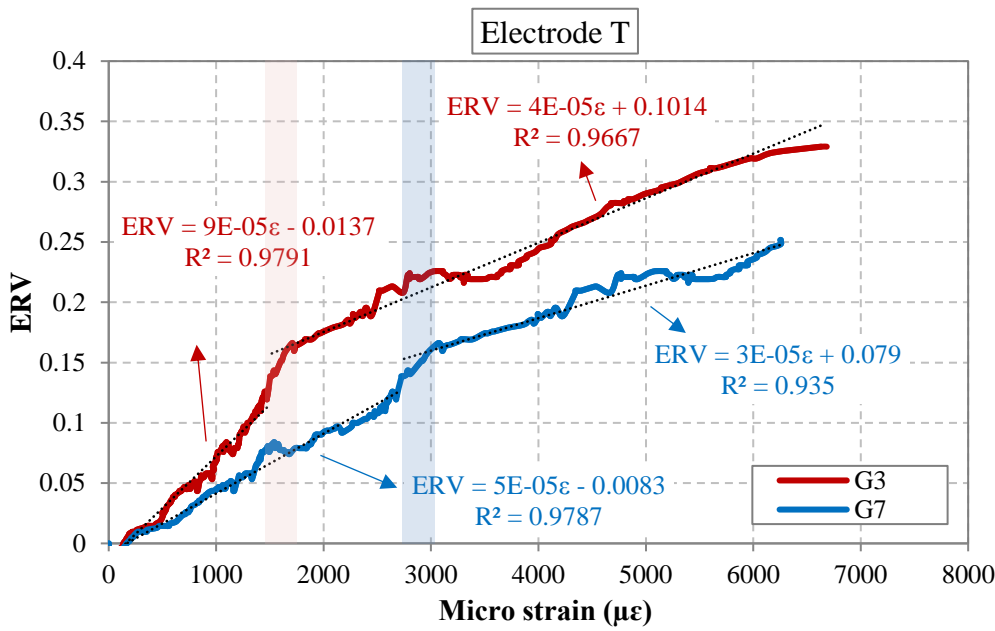


Figure 6.24. ERV vs. strain for Electrode T for SCB6

#### 6.4.4.2. Electrode B

The electrode resistance variation, ERV, for Electrode B on the west side of the beam is shown in Figure 6.25. It can be seen from the figure that the ERV has traced the strain change very well and there can be a relationship between the two parameters. Initially, the gauges showed a small strain value and the ERV was progressing with no increase or decrease in the value until the strain started to increase by a small sudden increase in the value. This increase in strain was captured by the ERV with a sudden increase, which reflected the increase in electrical resistance due to the tensile stresses and formation of micro-cracks. After this point, both strain and ERV increased consistently until the maximum load capacity of the beam was reached at  $t = 11780s$ . After the formation of the major shear crack (C6) and its widening, the strain induced on the concrete at which the electrical resistance was being measured decreased since the load was being resisted by the steel components and no stress was induced in concrete, therefore, the ERV showed decrease in the resistance variation after the peak load was reached.

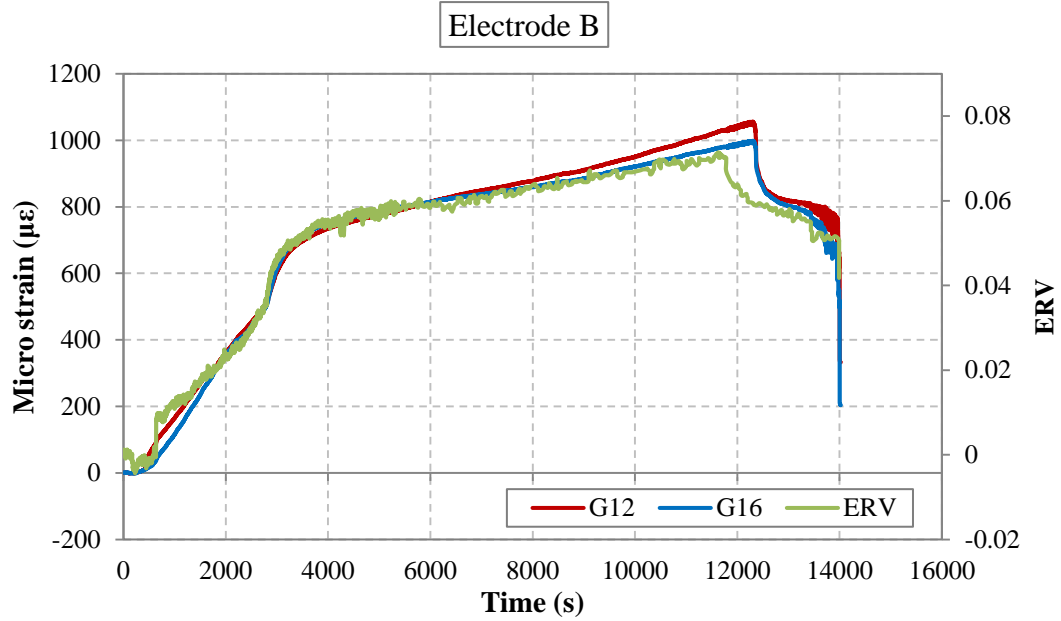


Figure 6.25. Electrode B results for SCB6

The plot shown in Figure 6.26, shows the ERV as a function of strain. From the overall low strain magnitude induced on bars, it can be concluded that the area at which the electrode was active, did not experience high strains and therefore, few cracks only formed and did not further develop. From the figure, it can be seen that the pattern up to the ultimate value captured by ERV at the ultimate load was almost linear without any noticeable apparent change in the slope of the curve. This observed behaviour could mean that despite the vicinity of the electrode to the major shear crack, the crack did not interrupt the conduction path, and no further cracks developed within the concrete

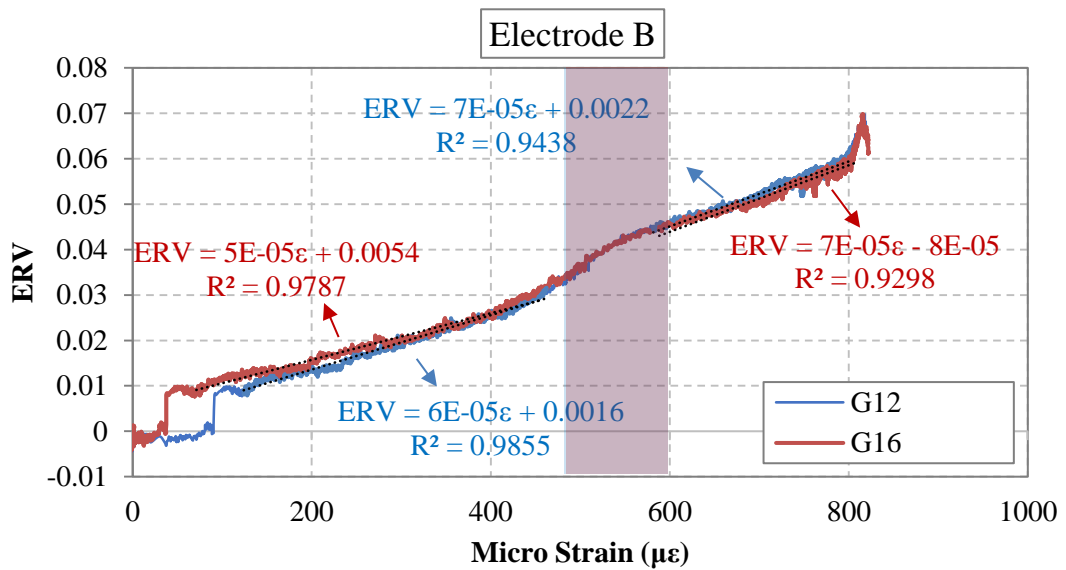


Figure 6.26. ERV vs. strain for Electrode B for SCB6

in the electrode zone to affect the piezoresistive behaviour of the concrete. Therefore, the variation of the electrical resistance of the concrete remained stable. Only, a slight change in the ERV vs. strain relationship was noticed at a strain of about  $500 \mu\epsilon$ , which could be attributed to the formation of a micro-crack. For evaluating the results with better accuracy, the linear behaviour was assessed before and after strain margin of 500-600  $\mu\epsilon$ . The correlation coefficient inscribed in Figure 6.26, shows that a somewhat strong linear relationship existed between ERV and strain during the initial stage. This correlation was slightly affected during the final stages of the strain monitoring (after 600 $\mu\epsilon$ ). This could be due to less CNF fiber in this matrix as opposed to previous specimens. Fewer fibers within the matrix were affected by the micro-cracks more profoundly, hence resulting in less sensitivity of the matrix and lower linear correlation coefficient. However, the values of 0.93-0.94 are still regarded as a good linear relationship.

#### 6.4.4.3. Electrode M

The electrode resistance variation, ERV, for Electrode M, positioned in the mid-span is shown in Figure 6.27. The behaviour of this electrode was different than previous specimens, therefore, the load was also presented on the left y-axis to better understand the result obtained from the electrode. The concrete gauge failed to function well during the test and the results could not be used for correlation.

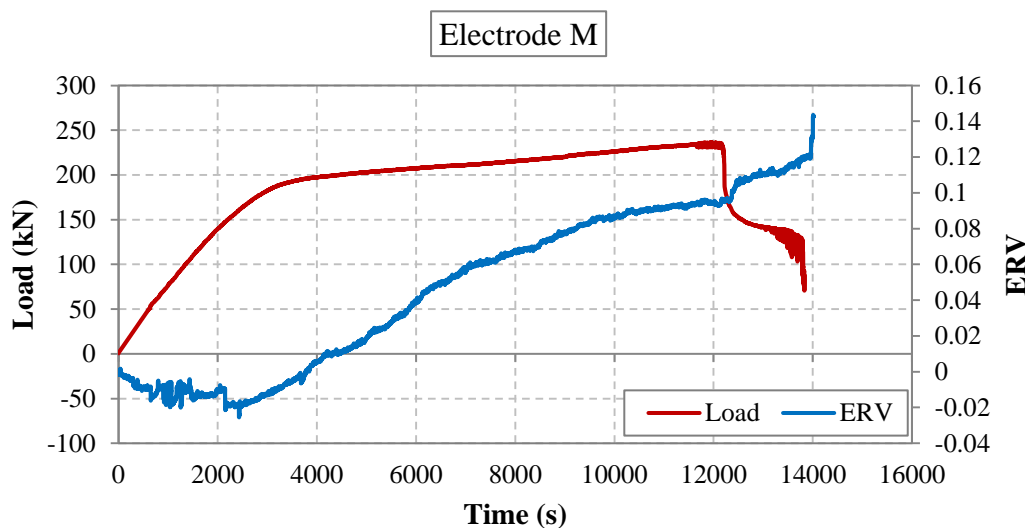


Figure 6.27. Electrode M results for SCB6

From Figure 6.27, it is evident that the ERV decreased due to compressive strain up to the load level of 180 kN, at which the beam yielding took place and flexural cracks were propagating. During the hardening stage of the beam up to the ultimate load, the ERV increased. A possible reason for this could be the extension of the flexural cracks in the moment span towards the top reaching, which then moved the neutral axis to higher up through the depth of the concrete and resulted in the transformation of compressive strain to tensile strain and the change in the ERV magnitude. The ERV behaviour reveals the ability of this method in capturing the change in strain type.

#### 6.4.5. SCB7: SF1.0% + CNF0.5%

The electrode positions for SCB7, with hybrid fiber reinforced concrete core (SF 1.0% and CNF 0.5%) are shown in Figure 6.28. The major shear crack for this sample formed at the west shear span after the beam reached its ultimate strength.

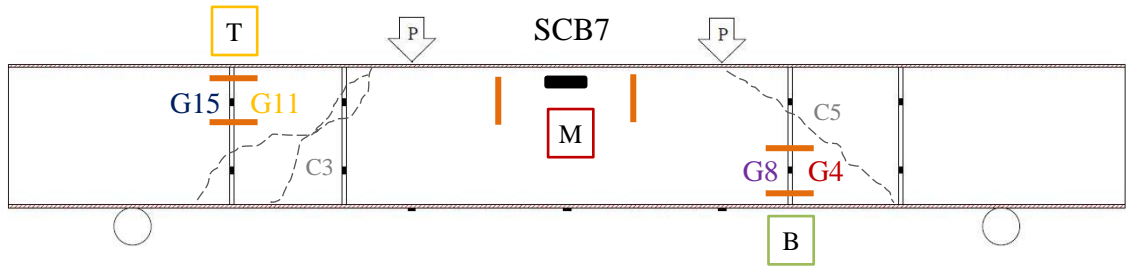


Figure 6.28. Electrode locations for SCB7

##### 6.4.5.1. Electrode T

The electrode resistance variation, ERV, for Electrode T is shown in Figure 6.29. As can be seen from the figure, this electrode monitored the results up to  $t = 600$ s and with the slight increase in strain at the time, the ERV had an abrupt increase. The increase in ERV can be regarded as an indication that the damage within the concrete in the form of micro-crack has taken place. However, this was unlikely since the change in the ERV was unexpectedly significant. From this point onward, the ERV remained constant which means that the conductivity was interrupted. The significant increase in ERV followed by the constant outcome could be due to wire damage as this occurred at early stages of the test and it is unlikely that the formation of cracks was the reason for the loss of conduction path. Another possible reason is that after the application of the load

and formation of cracks in the beam, the copper mesh had contact with other steel components, hence resulting in a constant electrical resistance.

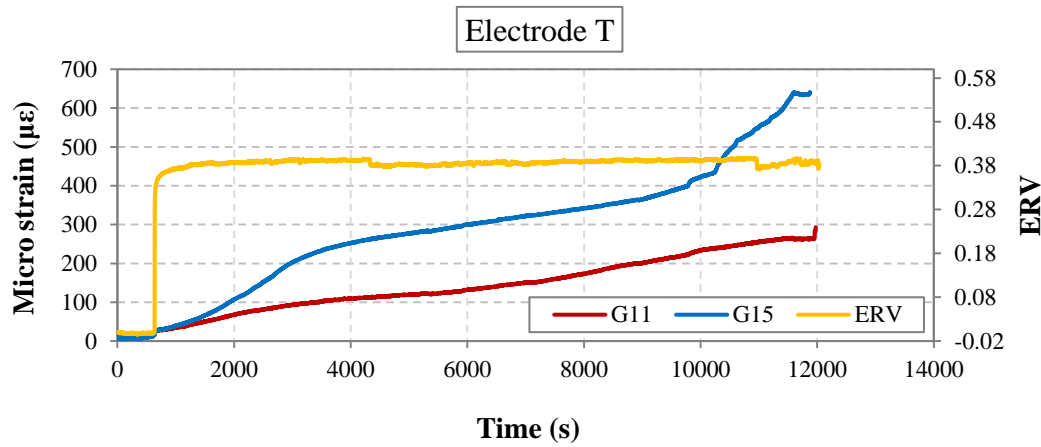


Figure 6.29. Electrode T results for SCB7

The correlation coefficient for ERV against strain was calculated for the stages before the abrupt increase in ERV, and the  $R^2$  value for the linear correlation between ERV and measured strain from G11 and G15 was 0.9855 and 0.9770 respectively. It can be concluded that the concrete had good self-sensing property before the electrode ceased to function well.

#### 6.4.5.2. Electrode B

The electrode resistance variation, ERV, for Electrode B is shown in Figure 6.30. For this electrode, some fluctuation is observed in the ERV results at some points. This could be due to the low CNF dosage. Having said that, the ERV results showed a similar trend as strain and concrete with 1.0% steel fibers and 0.5% CNF could monitor the change in strain satisfactorily.

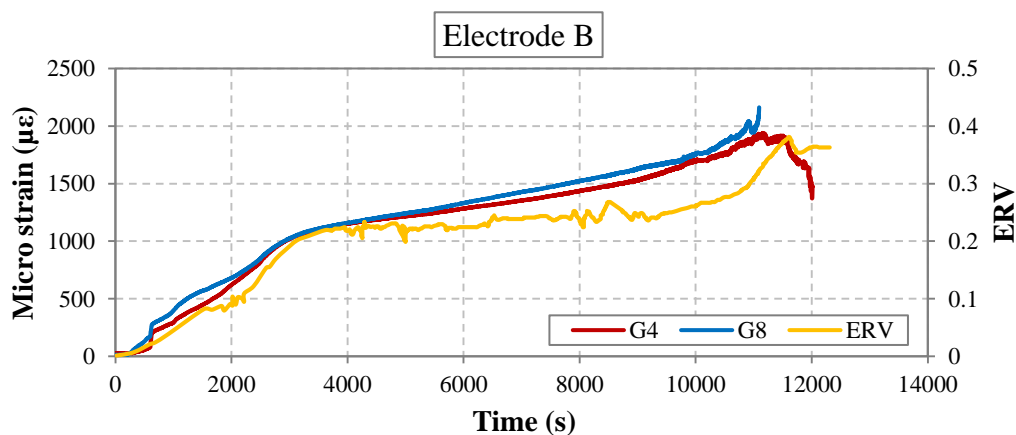


Figure 6.30. Electrode B results for SCB7

The ERV as a function of strain is shown in Figure 6.31. Since there was some fluctuation in the results of ERV, the relationship between the ERV and strain also showed instabilities in the strain ranging from 1000-1700 $\mu\epsilon$ . The linear relationship was detected for three stages. Similar to previous samples the first stage had the highest sensitivity and a good correlation coefficient was observed (about 0.97-0.98). During the transition phase (coloured block), also the relationship was close to linear, unlike previous samples which showed nonlinear transition. However, the two parameters did not show a strong correlation ( $R^2 = 0.79$ ), which could be attributed to the noisy response at this stage. This is due to the appearance of micro-cracks which caused a less sensitive response (lower slope of the curve). The amount of fibers seemed to be inadequate to produce a strong correlation between ERV and strain during the transition phase.

During stage 2, G4 did not show increasing strain, hence the result is compared with measurements from G8. At this stage, in which the merging of micro-cracks takes place the ERV is at its lowest, as observed for previous specimens. At this stage, the self-sensing capability of the concrete was at its lowest. Overall, the self-sensing capability of SCB7 was weaker than SCB4, SCB5, and SCB6, because of the lower correlation coefficient obtained for this beam as well as the noisy response observed at some points.

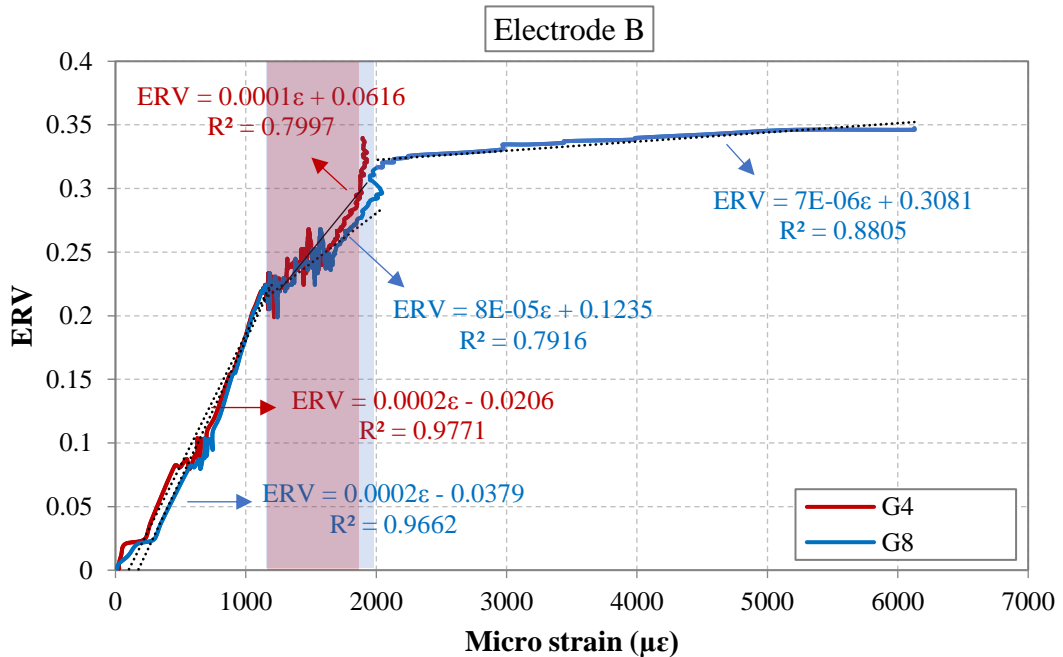


Figure 6.31. ERV vs. strain for Electrode B for SCB7



#### 6.4.5.3. Electrode M

The results for Electrode M is shown in Figure 6.32 and compared against the measured concrete strain. Similar to previous samples the ERV had negative sign. This is because the compressive stress at the upper section of the beam resulted in the compaction of the concrete and therefore better conductivity was achieved with lower electrical resistance, therefore, the ERV decreased. From this sample with 1.0% SF and 0.5% CNF, more stable results with decreased level of noise were obtained in contrast to SCB3 which was singly-reinforced with 0.5% CNF. Hence, the addition of 1.0% steel fibers has been effective in improving the conductivity of the beam by assisting the CNFs. Another reason could be a better dispersion of CNF fibers in the matrix for SCB7 since the electrical resistance response of a material could be a representation of the dispersion quality.

The figure shows that the compressive strain in concrete increased gradually in an almost linear manner. The change in the ERV showed an almost linear increase up to  $t = 3800s$ . A sudden increase in ERV was evident which owed to an increase in the electrical resistance. The increase in electrical resistance means that a defect in the concrete matrix (such as micro-crack) has affected the conductivity of the circuit. This is also evident from the rate of change of ERV after this point. It was noticed that the strain monitored by the concrete gauge showed higher increase in strain during  $t = 3800s$  and  $t = 12000s$  from  $100\mu\epsilon$  to  $1500\mu\epsilon$ . This can be regarded as an appearance of inner micro-cracks, hence, the ERV decreased with the progression of the test but at a slower rate. Also, the behaviour seemed less linear and more similar to a parabola. The maximum absolute ERV value was 0.12. This value was very close to the value obtained for SCB5 ( $|ERV_{max}| = 0.1$ ).

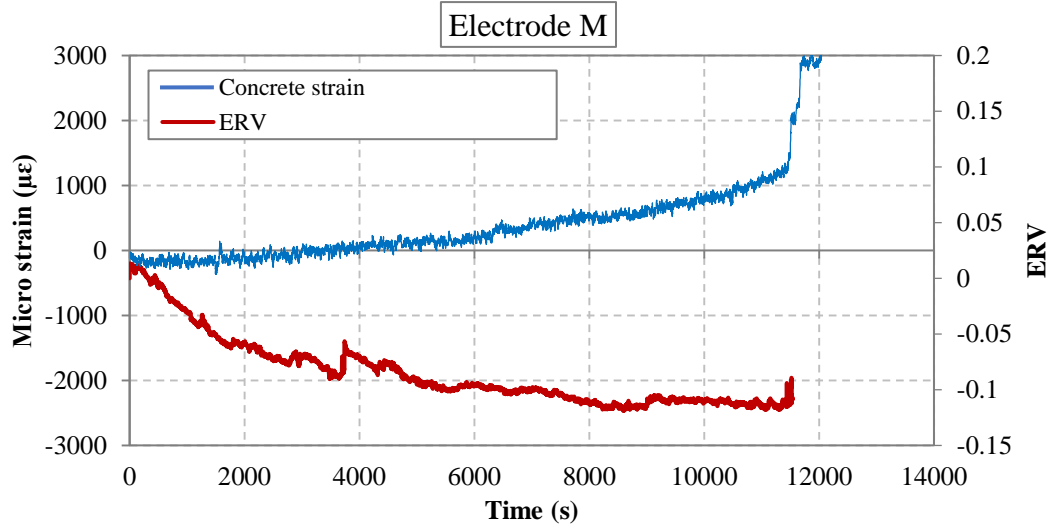


Figure 6.32. Electrode M results for SCB7

#### 6.4.6. SCB8: SF0.5% + CNF1.0%

The electrode positions for SCB8, with hybrid fiber reinforced concrete core (SF 0.5% and CNF 1.0%) are shown in Figure 6.33. The major shear crack (C5) for this sample formed at the west shear span and its width extended towards the end of the test. The location of Electrode T was very close to this crack (C5). Electrode B was in the vicinity of flexure-shear crack C3 and shear crack C6 on the east side.

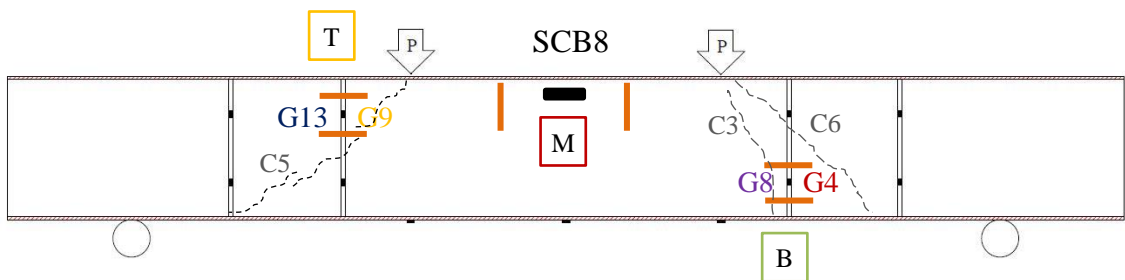


Figure 6.33. Electrode positions for SCB8

##### 6.4.6.1. Electrode T

The electrode resistance variation, ERV, for Electrode T adjacent to G9 and G13 is shown in Figure 6.34. It is evident that the ERV variation behaviour is closer to strain measurements by G13. It is likely that the recorded strain by G13 was closer to the strain of the surrounding concrete. Both G13 and G9 failed before the ultimate load capacity of the beam was reached and before the widening of C5.

Widening of C5 (which was adjacent to Electrode T) occurred at  $t = 12000$ s (at which the maximum load capacity of the beam was reached), and ERV showed a sudden increase from 0.13 to 0.2. After the initiation of the crack widening (this occurred by a sudden load drop on the load-displacement curve presented in Chapter 5) the ERV continued to show monitoring the change in resistance at the  $ERV = 0.224$  level.

Shortly after, the ERV showed an abrupt increase to a high value in few steps because the resistance increased significantly, and this was attributed to further widening of the crack C5 which affected the conduction path. Overall, the ERV showed that the concrete core was capable of monitoring the change in the concrete behaviour from monitoring small variation in strain during initial stages to sensing formation of macro scale cracks as well as warning for major crack damage induced within the concrete by an abruptly increased value.

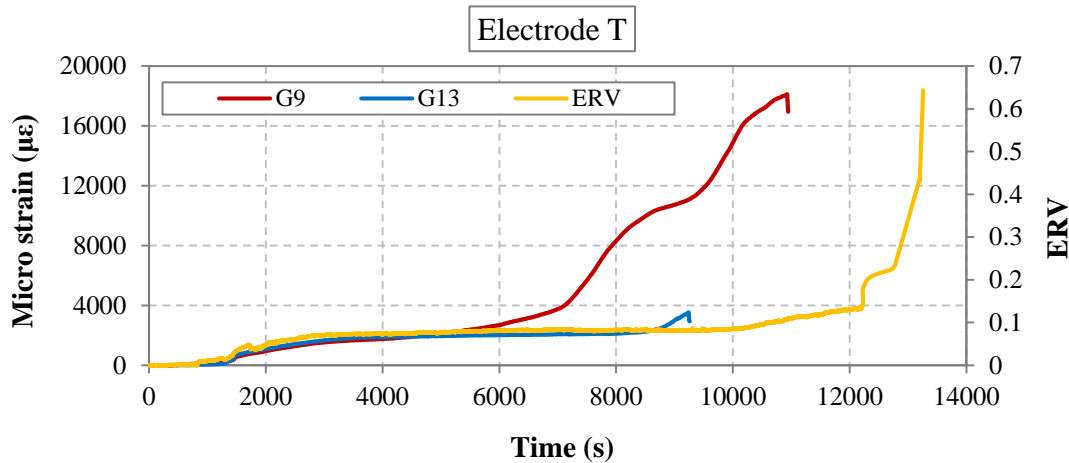


Figure 6.34. Electrode T results for SCB8

The ERV vs. strains measured by both G9 and G13 is shown in Figure 6.35. Since G13 failed before G9 and it only measured up to a maximum strain of  $3400\mu\epsilon$ , the ERV against G13 could only be obtained up to the maximum measured strain. The linear relationship during stage 1 showed high sensitivity with a correlation coefficient of 0.98 which confirms a strong relationship between the two variables. This phenomenon shows that the ERV could be used for determining the strain within the concrete. Also, this correlation coefficient was higher than specimen SCB7. This could be because of higher CNF dosage used in SCB8 at 1.0% volume fraction.

Stage 2, which represents the stage at which the sensitivity of the concrete was decreased, was simultaneous with the appearance of the shear crack C5. The magnitude of ERV remained almost constant from  $t = 3000$ s-8500s (at which G13 also showed

constant strain; Figure 6.34), therefore a straight line was observed during the second stage for increasing strain value of G9 in Figure 6.35. This shows that the strain at G9 was not correlated with ERV. Since the behaviour of the ERV was shown to be closer to G13, it can be assumed that the strain in concrete was closer to measured values by G13. Therefore, the result for G9 could be neglected as an appropriate result for comparing the ERV to the concrete strain.

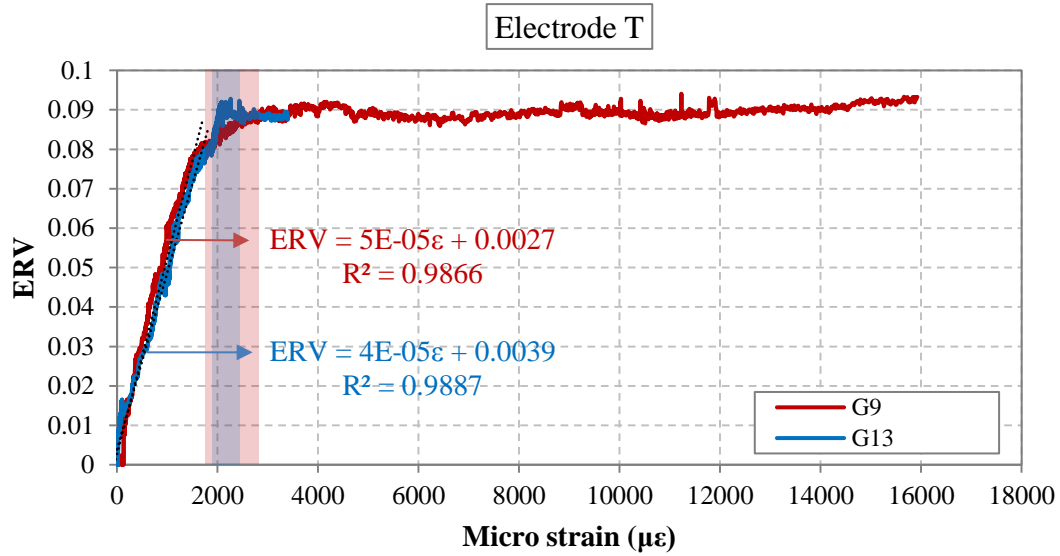


Figure 6.35. ERV vs. strain for Electrode T in SCB8

#### 6.4.6.2. Electrode B

The electrode resistance variation, ERV, for Electrode B is shown in Figure 6.36. For more clear observation of the ERV variation against strain variation by time, Figure 6.36(b) and Figure 6.36(c) are presented. The ERV was closer to the strain measured by G4 during the initial stages of loading. From Figure 6.36(b) a sudden increase in both strains were noticed at  $t = 400s$ . At this point, the ERV also showed a sudden increase. This phenomenon occurred at quite early stages of loading and no cracks were visible on the concrete surface. This increase in ERV could be a warning that the crack was forming within the concrete depth in the electrode region or at its proximity which has resulted in a significant increase in resistance.

With the appearance of the shear crack C6, the strain increased from  $t = 1800s$ . From Figure 6.36(c), it is evident that the ERV captured the change in strain and the increase in strain due to the formation of the shear crack. The increase in ERV continued with

strain until the end of the test. The ERV showed a rapid increase from  $t = 10000$ s which seemed to be higher than the change in the strain. This could mean that the concrete damage was further developed after this time since the beam was reaching its ultimate capacity at  $t = 12000$ s.

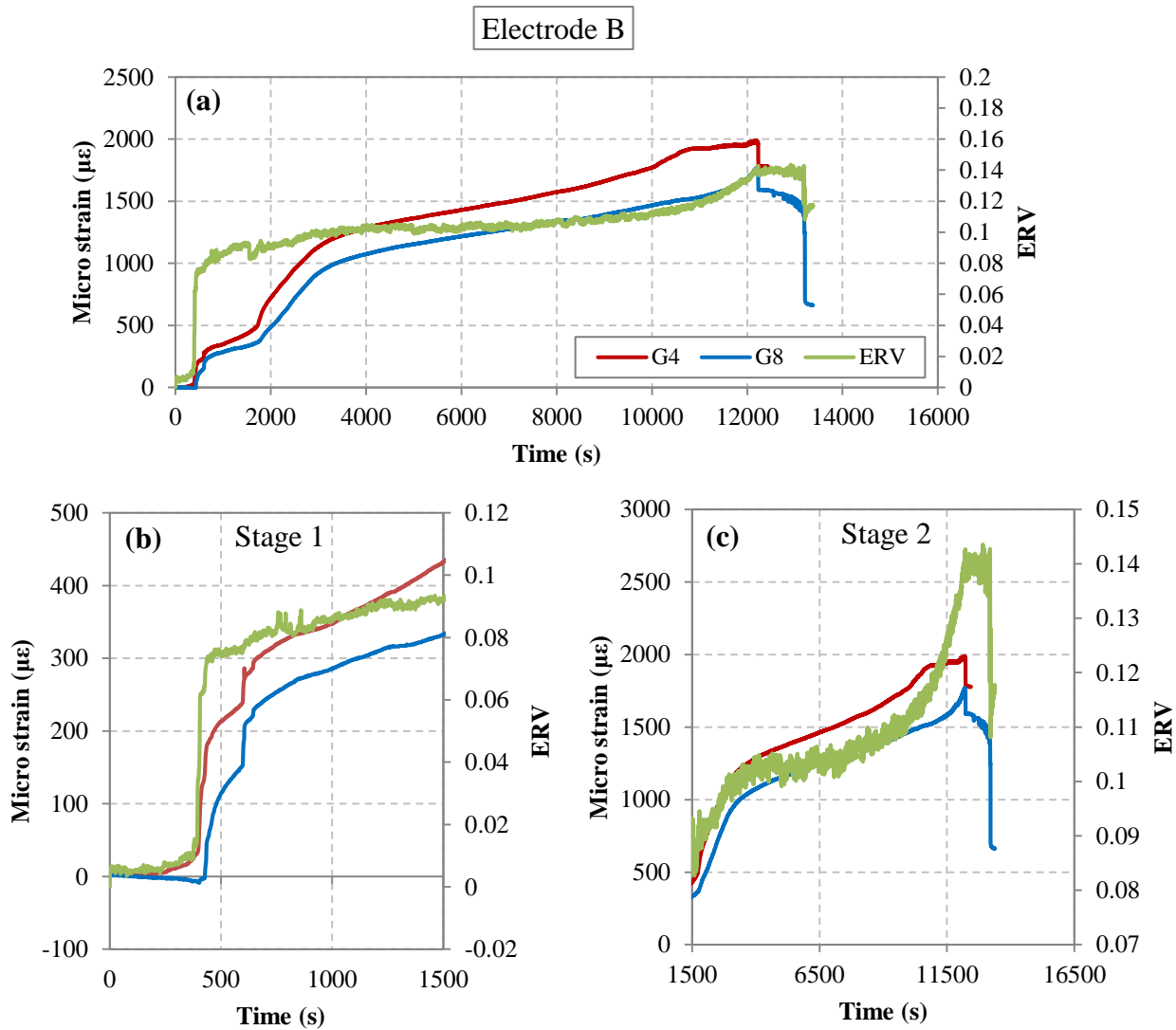


Figure 6.36. Electrode B results for SCB8

The relationship between ERV and strain shown in Figure 6.37 reveals that the ERV was linearly related to strain upto a strain value of about  $60\mu\epsilon$  (for G8) and  $200\mu\epsilon$  (for G4) at which the sudden increase in strain value was observed (Figure 6.36(b)). During the first stage, ERV showed closer behaviour to G4, which could mean that G4 reflected the concrete strain more accurately. Therefore, the relationship between ERV and G4 was considered to be more reliable. The slope of the curve was at its highest (i.e. high

sensitivity) prior to the formation of the crack within concrete. After this stage, the aforementioned sudden increase in strain took place (Figure 6.36(a)), which was captured by a significant decrease in ERV slope during the transition phase. This was thought to be due to inner cracks that were not visible on the surface. Crack C3 became visible at  $t = 1900$ s, at which the strain gauges G8 and G4 had values of 460 and 500  $\mu\epsilon$  respectively where a distinct change of strain was observed. From this strain onwards, the slope of the ERV slightly decreased further than the transition stage, which is attributed to the merging of micro-cracks, and possible crossing of C3 over the electrode zone, which in turn caused reduced sensitivity.

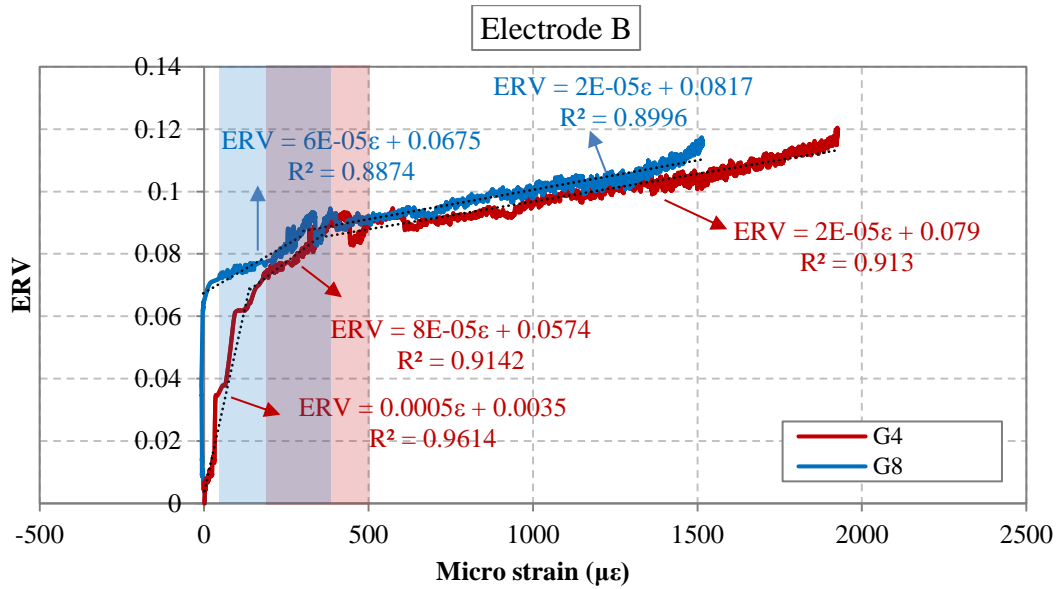


Figure 6.37. ERV vs. strain for Electrode B for SCB8

Overall, a good correlation was observed between ERV and strain measurements by G4 with a correlation coefficient higher than 0.9. The first stage, however, showed the best correlation between the strain measurements and the ERV of G4.

Overall, it can be concluded that SCB8 was successful in sensing its own damage and the electrical resistance variation could be an indicator of the change in the concrete strain and it was capable of capturing the formation of cracks within concrete.

### 6.4.6.3. Electrode M

The electrode resistance variation, ERV, for Electrode M is shown in Figure 6.38 along with the strain measurements by the concrete gauge. The ERV values were negative as the compressive strain was being measured by this electrode, therefore the results on the secondary axis are multiplied by -1.

The ERV showed an almost linear trend as did the concrete strain. At the initial stage of the test the change in the concrete strain was small and from  $t = 4000$ s the strain increased proportionally and linearly. The ERV results showed that the concrete was capable of monitoring the change of compressive strain induced on the upper section of the beam. The maximum absolute ERV value that was measured was 0.5. This value was five times larger than that measured by SCB5 and SCB7 which had absolute values of 0.1 and 0.12 respectively. Since the maximum strain level for SCB7 and SCB8 was similar (about  $1000\mu\epsilon$ ) the difference in the magnitude of the maximum ERV could be an indication that higher CNF dosage in SCB8, resulted in a higher sensitivity of the concrete and enhancing the conductivity of the matrix.

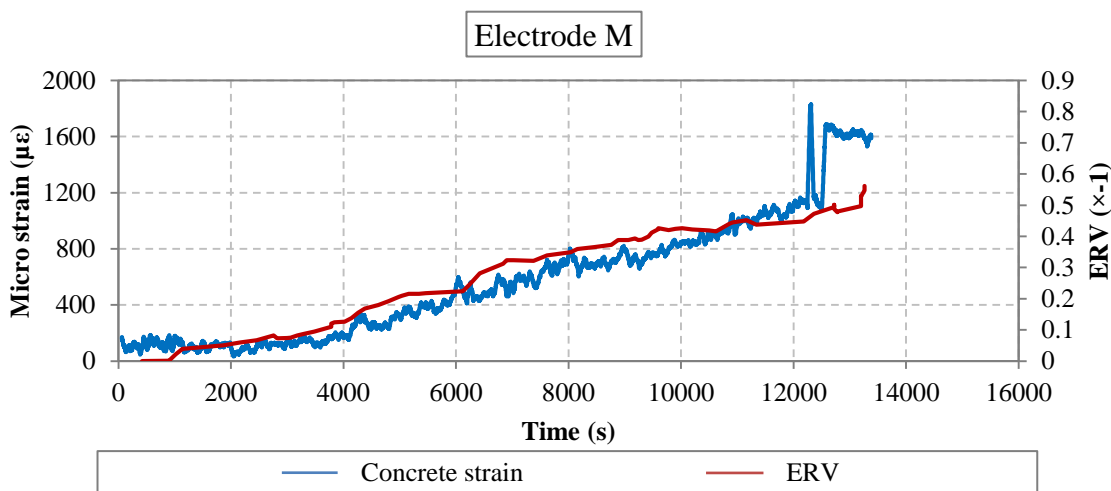


Figure 6.38. Electrode M results for SCB8

## 6.5. CONCLUSIONS

The self-sensing capability of tested SC beams was monitored by means of measuring the electrical resistance of the concrete using a two-probe method by embedding three electrodes in the concrete for each beam. ERV and strain measurements were analysed for each electrode.

The results for SCB3 with 0.5% CNF showed an unstable fractional change in electrical resistance of the concrete and the highest correlation coefficient recorded was  $R^2 = 0.8$ , which was not a strong correlation. The fluctuation of the ERV could be primarily attributed to the nonhomogeneous dispersion of the fiber. A more plausible explanation may include the possibility of an insufficient fiber loading within the matrix.

Overall, specimen reinforced with 1.0% CNF (SCB4, SCB5, and SCB8) showed higher correlation coefficient (about 0.98-0.99) which concludes that better piezoresistivity response (change in ERV with a change of strain) was obtained. On the other hand, the accuracy of concrete with 0.5% CNF could be further improved by means of adding at least 1.0% steel fiber to the matrix (SCB6 and SCB7) in which the steel fibers aided the CNF in creating a conduction path for monitoring the electrical resistance variation with satisfactory accuracy.

The direct relationship between ERV and strain showed that there was an almost linear relationship between the variables and the curve could be divided into two zones during the whole loading process. The first stage was during the elastic stage prior to any severe crack formation wherein concrete showed higher sensitivity. The second stage was after formation of fresh cracks and it involved merging of multiple crack paths and the widening of cracks which resulted in the breakdown of the conductive network. This stage involved a smaller increase in resistance as opposed to stage 1 since the concrete was less sensitive. If no increase in ERV was observed, either the complete collapse of the conductive network was attained, or the strain remained unchanged.

Overall, the succession of the two stages demonstrated a remarkable damage sensing potential of the embedded nanofibers and it showed the potential of the smart concrete with good self-sensing capability to predict its own strain by means of ERV as well as its own damage. In both stages, any sudden change in strain was followed by a sudden change in ERV which proved the timely response of the electrical resistance variation



of the smart concrete with varying strain. Consequently, the increase in ERV (i.e. increased electrical resistance,  $R$ , of concrete) can be treated as an early warning of upcoming material catastrophe.

It should be noted that despite the good correlation between the values of ERV and strain, the measured strains were from tie bars which were assumed to represent the concrete strain that the electrode was measuring. But, the exact concrete strain could vary slightly with that measured by tie bar gauges, especially when the damage takes place within the concrete. Therefore, this degree of correlation ( $>0.9$ ) between the ERV and strain measured from tie-bars is considered satisfactory.

From the results of this chapter, it is concluded that the CNFRC is sensitive to applied strain even under complex loading condition (such as Electrode T and Electrode B). Furthermore, the CNFRC concrete core of the SC beam could sense the applied strain at different locations until failure and by means of observing the fractional change in the electrical resistance (ERV) of the CNF reinforced concrete, damage of the SC beams can be monitored without the need for strain gauges.

In addition to the experimental work reported to this point, a companion analytical study is undertaken to better understand the behaviour of SC elements which will be presented in the next chapter.

## CHAPTER 7

### FINITE ELEMENT ANALYSIS OF SC BEAMS

---

#### 7.1. INTRODUCTION

Finite element models were created with the intention of investigating SC design parameters by parametric study. In order to numerically simulate the structural behaviour of SC beams with various type of concrete core, 2-dimensional fiber-based analytical models were established using the user developed FE programme FEAP (Finite Element Analysis Programme). Tested specimens with hybrid fiber reinforced concrete (category 2 and category 3) with ductile behaviour reported in Chapter 5 were modelled and then validated against experimental results. The finite element analysis reported here aimed at expanding the knowledge base for the effect of FRC on the structural performance of SC. The validated models were then used to conduct parameter study and a single case study.

#### 7.2. FE METHOD

The tested SC beam specimens were modelled using a fiber model and their load-displacement behaviour was examined against the experimental data. The fiber model approach was used because experimental observations did not indicate any local buckling of the compression steel plates due to excessive compression stress, or significant slip at the shear connector locations. This is important because the current fiber model assumes plane sections remain plane and perpendicular to the neutral axis before and after bending, which would be violated by local buckling and significant slip.

Also, the fiber model approach was selected because of its reasonably accurate prediction and its ability to deal efficiently with concrete tensile cracking, which would be difficult to model effectively with the 3D finite element method. Therefore, each SC beam was modelled with a 2D fiber beam-column element. The elements were force

based since force-based formulation requires a lower number of elements (i.e. lower number of DOFs) to produce accurate results as opposed to displacement-based formulation.

### 7.2.1. Fiber beam-column element

Force based (i.e. flexibility based) fiber beam elements are known to be the most promising models for nonlinear analysis of RC members (Taucer et al., 1991). As shown in Figure 7.1, in these models, a cross section is defined for the 2D beam element which comprises two nodes with three degrees of freedom at each node which are x-displacement, y-displacement, and z-rotation. The element cross-section is defined in the local y-z coordinate system and the section is segmented into longitudinal fibers with corresponding location and fiber area and the appropriate material constitutive models are assigned to the fibers. Each element is divided into 5 sections along the length, which are the control points of the numerical integration. Every section represents one Gauss-Lobato integration point, which allows for two integration points to coincide with the end sections of the element (see Figure 7.1). The constitutive relation of the section is derived by integration of the response of the fibers which follows the material stress-strain relationship of a particular material it is associated with, and the response of the element is then derived by integration of the response of sections along the length of the element.

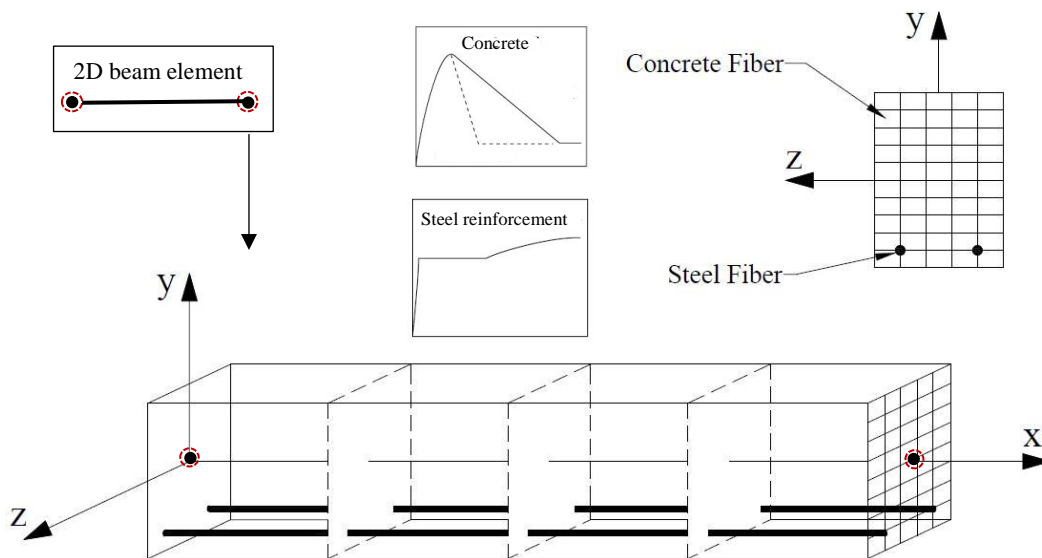


Figure 7.1. Fiber beam element; distribution of control sections and section subdivision into fibers

The fiber-beam column formulation for the element is briefly presented here and a comprehensive formulation can be found in Mullapudi and Ayoub (2010). Total stiffness of the section is derived from the sum of concrete and steel stiffness:

$$[K_{section}] = \sum_1^{nc} (K_{section})_c + \sum_1^{ns} (K_{section})_s \quad (\text{Eq. 7.1})$$

Where  $nc$  and  $ns$  are the numbers of concrete and steel fibers in a section. The element stiffness calculated by numerical integration is as follows:

$$[K_{element}] = J \int_{-1}^{+1} B(x)^T k(x)_{section} B(x) \partial \xi \quad (\text{Eq. 7.2})$$

$$= J \sum_{ii=1}^{nIP} W_{ii} B(x_{ii})^T k(x_{ii})_{section} B(x_{ii}) \quad (\text{Eq. 7.3})$$

Where  $J$  is the Jacobian,  $B(x)$  is the force interpolation function,  $W$  is the Gaussian weight, and  $nIP$  is the number of integration points. The total force of the section is the sum of concrete and steel forces in their respective directions:

$$\{F_{section}\} = \sum_1^{nc} (F_{section})_c + \sum_1^{ns} (F_{section})_s \quad (\text{Eq. 7.4})$$

The element forces are then calculated with numerical integration as follows:

$$\{F_{element}\} = J \int_{-1}^{+1} B(x)^T F(x)_{section} \partial \xi \quad (\text{Eq. 7.5})$$

$$= J \sum_{ii=1}^{nIP} W_{ii} * B(x_{ii})^T F(x_{ii})_{section} \quad (\text{Eq. 7.6})$$

Where  $J$  is the Jacobian,  $W$  is the Gaussian weight, and  $nIP$  is the number of integration points.

### 7.2.2. Theory behind the FE model

Various analytical models and shear theories have been developed to obtain the response of an RC element and to predict the load-deflection behaviour in the past

decades. Constitutive models play a vital role in the proposed models. The main assumption in models was in equilibrium equations and it was assumed that the stress in concrete and the stress in steel bars to be smeared. To relate the smeared stress to smeared strain in the constitutive law, large-scale panel tests were conducted. First, in 1981 such constitutive law was conducted by Vecchio and Collins, and they proposed Compression Field Theory (CFT). This model did not account for tension stiffening of the concrete material. The researchers improved their model by taking into account the tension stiffening of concrete and proposed Modified Compression Field Theory (MCFT).

A different approach for taking into account the tension stiffening effect of concrete was developed by Belarbi and Hsu (1995) and Pang and Hsu (1995) and they proposed the Rotating-Angle Softened-Truss Model (RA-STM). In this model, shear stress is assumed along the crack direction. In practice, new cracks form at different angles to previous cracks as loading increases. In the RA crack approximation, initial cracks in the model are assumed to form at the angle of principal tensile stress before cracking. But, after cracking the average stress directions may no longer align with this axis. This approach allows the angle of the crack to change as the analysis progress.

By the development of the proposed RA-STM, and assuming the cracks to be at a fixed angle meaning that the angle of the crack is forced to remain constant after initial cracking, the new Fixed-Angle Softened-Truss Model (FA-STM) was proposed which was also capable of predicting concrete contribution to shear resistance (Hsu and Zhang, 1996; Zhang and Hsu, 1998).

Later the researchers Hsu and Zhu (2002) improved the FA-STM model by taking into account the poison effect of cracked reinforced concrete which led to the development of the Softened Membrane Model (SMM). They characterised this property by Hsu/Zhu ratio using the strain control feature of the universal panel tester (Hsu and Mo, 2010). The Hsu/Zhu ratio is the modified Poisson's ratios of cracked RC members.

The outline of the two most recent developed shear theories RA and FA for a 2D membrane RC element is shown in Figure 7.2 (adapted from Hsu and Mo, 2010). The RC element is split into two elements of a concrete element and a steel grid element as shown in Figure 7.2. The system is defined by three coordinate systems as follows:

- i.  $x - y$  coordinate: local coordinate of the fiber (Steel grid element)
- ii.  $1 - 2$  coordinate: principal coordinate for applied stresses (RC element)
- iii.  $r - d$  coordinate: principal coordinate for concrete stresses<sup>1</sup> in which the concrete shear stress  $\tau_{12}^c = 0$  (Concrete element)

The  $x - y$  coordinate is the stationary coordinate system which also specifies the direction of the longitudinal and transverse steel.

The applied principal stresses for the RC element (Figure 7.2(a)), are defined as  $\sigma_1$  and  $\sigma_2$ , based on the  $1 - 2$  coordinate system as shown in Figure 7.2(d). The angle from the  $x - y$  coordinate to the  $1 - 2$  coordinate is defined as the fixed angle  $\alpha_1$  because this angle does not change when the three in-plane stresses  $\sigma_x$ ,  $\sigma_y$  and  $\tau_{xy}$  increase proportionally.

The principal stresses for the concrete element (Figure 7.2(b)), are defined as  $\sigma_r$  and  $\sigma_d$ , based on the  $r - d$  coordinate system as shown in Figure 7.2(e). The angle from the  $x - y$  coordinate to the  $r - d$  coordinate is defined as the rotating angle,  $\alpha_r$ , because this angle will rotate when the three in-plane stresses  $\sigma_x$ ,  $\sigma_y$  and  $\tau_{xy}$  on the RC element increase proportionally.

The steel bars do not affect the behaviour of RC element before cracking. Therefore, the principal stresses in the concrete element ( $\sigma_r$  and  $\sigma_d$ ) coincide with the applied principal stresses  $\sigma_1$  and  $\sigma_2$ . When the tensile strength of concrete is reached by principal tensile stress  $\sigma_1$ , as shown in Figure 7.2(f), cracks will appear and the concrete element will be divided into a series of concrete struts in the 2-direction by the cracks. If the longitudinal ( $\rho_x f_x$ ) and transverse steel reinforcements ( $\rho_y f_y$ ) have different amounts in the  $x$ - and  $y$ -directions (Figure 7.2(c)), then the  $r - d$  coordinate after cracking will deviate from the  $1 - 2$  coordinate of the applied principal stresses on the RC element. Figure 7.2(g) shows the cracking pattern based on the  $r - d$  coordinate after cracking.

---

<sup>1</sup> Principal stresses are defined as the normal stresses on the face oriented in such a way that the shear stress vanishes.

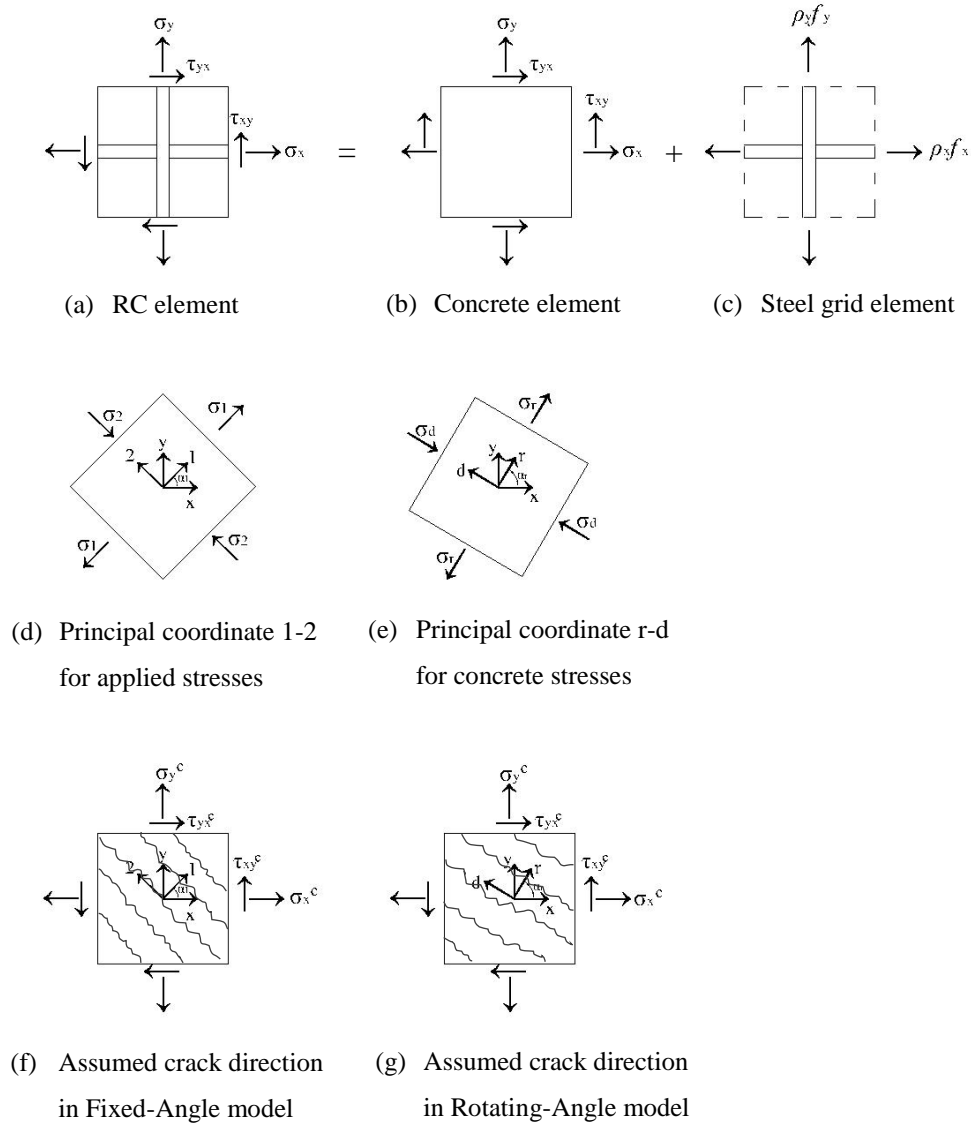


Figure 7.2. Reinforced concrete membrane elements subjected to in-plane stress (Hsu and Mo, 2010)

The difference between the RA theory and FA theory becomes evident here. In the RA theory, the direction of cracks is governed by the  $r - d$  coordinate and it is assumed that the cracks form perpendicular to the principal tensile stress in the concrete element ( $\sigma_r$ ), as shown in Figure 7.2(g). Therefore, the derivation of all the equilibrium and compatibility equations are based on the  $r - d$  coordinate.

In contrast, in the FA theories, the direction of cracks is represented by the  $1 - 2$  coordinate system and it is assumed that the direction of subsequent cracks is perpendicular to the applied principal tensile stress ( $\sigma_1$ ), as shown in Figure 7.2(f).

Therefore, the derivation of all the equilibrium and compatibility equations are based on the 1 – 2 coordinate (Hsu and Mo, 2010).

It should be noted that:

‘The term fixed angle simply means that the angle  $\alpha_1$  remains unchanged when the applied stresses ( $\sigma_x$ ,  $\sigma_y$  and  $\tau_{xy}$ ) are increased proportionally. It does not mean that the applied stresses ( $\sigma_x$ ,  $\sigma_y$  and  $\tau_{xy}$ ) cannot produce a different  $\alpha_1$  angle, when the applied stresses are increased in a non-proportional manner. Nor does the term imply that the observed crack angles are fixed in the subsequent cracking process.’ (Hsu and Mo, 2010, p.140)

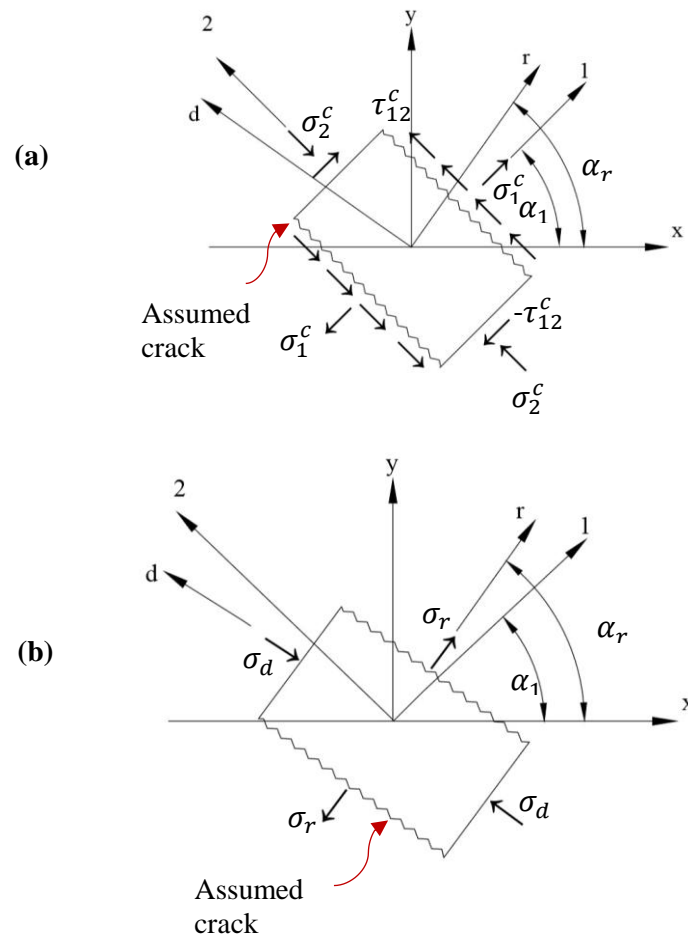


Figure 7.3 Stress states in (a) fixed-angle theory and; (b) rotating-angle theory (adopted from Hsu and Mo, 2010)



Regarding the contribution of concrete in shear resistance ( $V_c$ ), as illustrated in Figure 7.3, the RA theory is incapable of estimating the  $V_c$  since the cracks are governed by the  $r - d$  coordinate, which rotates with increasing proportional loading in such a way that the concrete shear stress ( $\tau_{12}^c$ ) vanishes and hence  $V_c = 0$ . While, for FA theory, because the crack angle is based on the principal coordinates of the applied stresses of the RC element, a concrete strut is subjected to both axial compressive stress  $\sigma_2^c$  and concrete shear stress  $\tau_{12}^c$  (i.e. the source of the  $V_c$ ) in the direction of the cracks.

To conclude, the FA theory is more complicated than the RA theory, however, it is more accurate since it can predict the  $V_c$  and it is found more suitable for this study since different FRC used in this study are expected to have different  $V_c$  which affected the behaviour of the structural member.

SMM model implemented in the fiber-beam column element used in this study follows the FA theory taking into account the Poisson ratio in the constitutive relationship of the material. Two Hsu/Zhu ratios ( $\mu_{12}$ ,  $\mu_{21}$ ) are used, where  $\mu_{12}$  is the ratio of the resulting tensile strain increment in the principal 1- direction to the source compressive strain increment in the principal 2-direction, and  $\mu_{21}$  is the ratio of the compressive strain increment in the principal 2- direction to the tensile source strain increment in the principal 1-direction. Before cracking Hsu/Zhu ratio is  $\mu_{21}=0.2$  and, after cracking the Hsu/Zhu ratio  $\mu_{21}=0$ , indicating that the tensile strain does not have any effect on the compressive strain.

### 7.2.3. Shear-based fiber beam-column element

Mullapudi and Ayoub (2010) developed a shear-based 2D fiber beam-column element for shear critical elements with distributed inelasticity, adopting the shear theory Softened Membrane Model (SMM) as well as Timoshenko beam theory to account for shear deformation effects in the formulation of the fiber beam element. This theory proved to ‘satisfactorily predict the entire monotonic response of the load-deformation curves, including both pre-cracking and post-cracking responses as well as the ascending and descending branches’ (Hsu and Mo, 2010; Mullapudi and Ayoub, 2010). The finite element formulation was based on the force method of analysis since this method is advantageous as opposed to displacement-based method due to model robustness and lower number of degrees of freedom. The element was developed using the Finite Element Analysis Program FEAP (Taylor, 2012).

Initially, the problem is solved for each fiber as summarised below:

- The concrete local stiffness matrix in the principal direction (1 – 2 direction) is determined by relating the stress and strain in local coordinate at each fiber.
- The matrix is then transformed into global x-y coordinate by a rotation matrix  $R$  which is a function of  $\alpha_1$ .
- Then the total global stiffness of the fiber is determined by the summation of concrete stiffness and transverse steel stiffness.

Next, sectional stiffness matrices are determined from fiber discretisation. For each element, five control sections along the length of the element were defined as shown in Figure 7.1. Each section stiffness matrix is obtained by:

- Total stiffness of the section is derived from the summation of concrete fiber and steel fiber stiffness (Eq. 7.1)
- Sectional forces due to concrete fibers and sectional forces due to longitudinal steel fiber are calculated by summation of  $(\sigma_{\text{fiber}} \times \text{Area of fiber})$ ,
- The total force of the section is the summation of concrete and steel forces (Eq. 7.4).

By obtaining sectional stiffness and forces, the element stiffness (Eq. 7.2 and Eq. 7.3) and forces (Eq. 7.5 and Eq. 7.6) are then calculated by numerical integration of sectional stiffnesses and sectional forces respectively. The structural stiffness matrix and global resisting forces are then assembled. The complete formulation and analysis procedure of the element is out of the scope of this study and duly described in Mullapudi (2010), Mullapudi and Ayoub (2010), and Mullapudi, Charkhchi and Ayoub (2013).

This FE model follows the smeared crack model. One great advantage of using the smeared crack concept is that the cracked concrete can be treated as a continuous material. In these models, the equilibrium equations assume the stresses in the concrete element and steel bars to be smeared. Similarly, the strains of steel and concrete are also smeared, and are obtained by averaging the strains along a steel bar that crosses several cracks.

### 7.3. SC BEAM FE MODEL

To model the tested SC beams in this study the developed shear-based fiber beam-column element (Mullapudi and Ayoub, 2010) described previously was used in FEAP. To evaluate the effect of design parameters on the performance of the beam, specimens with ductile behaviour (SCB5-SCB8) were chosen to be analysed. In the model, perfect bond is assumed between concrete core and steel plates implying full compatibility between concrete and steel strains.

#### 7.3.1. Material constitutive model

Developing a model for the behaviour of a brittle material namely concrete is a must difficult task. Concrete has different behaviour in compression and tension. It is important to bear in mind that the cracked concrete can still initially carry some tensile stresses in the direction normal to the crack known as tension-stiffening. To describe the post-cracking response of concrete, tension-stiffening effect is considered in the FE model. Tension stiffening can be included by considering the tensile resistance of concrete. ‘The concrete model is based on a smeared approach of cracked continuous orthotropic concrete with the inclusion of Poisson effect’ (Mullapudi and Ayoub, 2010). Concrete model is defined with tensile strength and linear tension softening as shown in Figure 7.4 with the following parameters:

$f'_c$ : concrete compressive strength at 28 days (compression is negative)

$\epsilon_0$ : concrete strain at maximum strength (compression is negative)

$f_{cu}$ : concrete crushing strength (compression is negative)

$\epsilon_u$ : concrete strain at crushing strength (compression is negative)

$f_t$ : tensile strength

$E_{ts}$ : tension softening stiffness

$f_{cu}$  is assumed to be 20% of the  $f'_c$ . Other material properties that were validated and used in the FE model are presented in Table 7.1. These values were obtained from the mechanical test on materials samples while the tension softening parameters were assumed by validation of FE models for each material. For FRC, the cracking stress and strain were altered slightly to adhere to the presence of the steel fibers and crack bridging enhancement. Since these fibers are oriented randomly, the contribution of these fibers was included in the tensile constitutive properties.

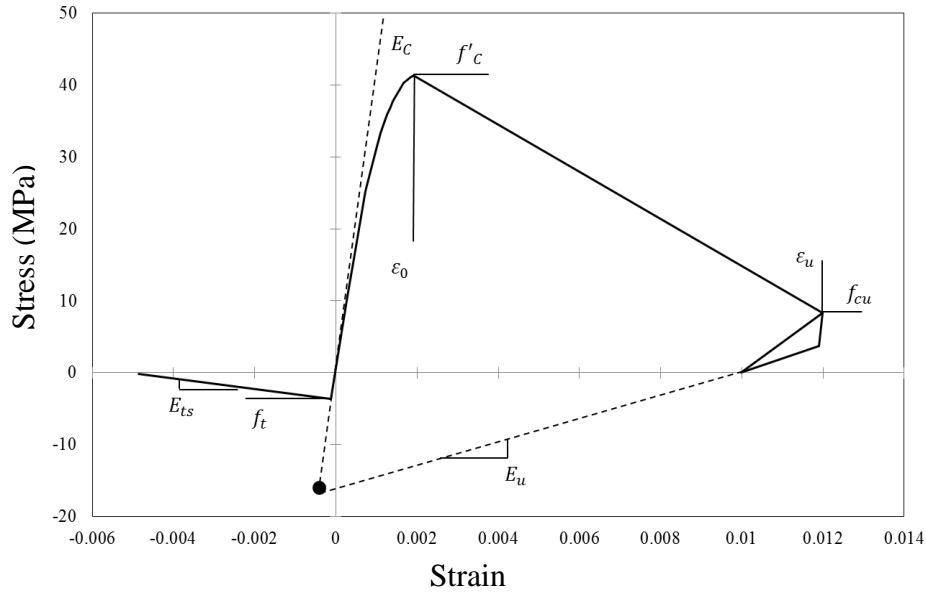


Figure 7.4. Concrete material model used in FE analysis

Table 7.1. Concrete material properties used in the FE models

	$f'_c$ (MPa)	$\epsilon_0$	$\epsilon_u$	$f_t$ (MPa)	$E_{ts}$ (MPa)
<b>SCB5 (SF1.0+CNF1.0)</b>	45.04	0.0013	0.025	7.1	15000
<b>SCB6 (SF1.5+CNF0.5)</b>	43.92	0.0013	0.038	6.5	15000
<b>SCB7 (SF1.0+CNF0.5)</b>	46.80	0.0013	0.030	7.5	15000
<b>SCB8 (SF0.5+CNF1.0)</b>	46.48	0.0013	0.024	6.3	22000

Steel material constitutive law follows the Giuffré-Menegotto-Pinto model with isotropic strain hardening shown in Figure 7.5. Key parameters are:

$f_y$ : yield strength

$E$ : Young's modulus

$b = E_p/E$  : strain hardening ratio

$R$ : exponent that controls the transition between elastic and hardening branch (suggested values between 10 and 20)

Yield strength for the tie bars and steel plate were provided by the manufacturer as well as the modulus of elasticity. Parameter  $b$  and  $R$  were validated according to the FE results. The adopted values are presented in Table 7.2.

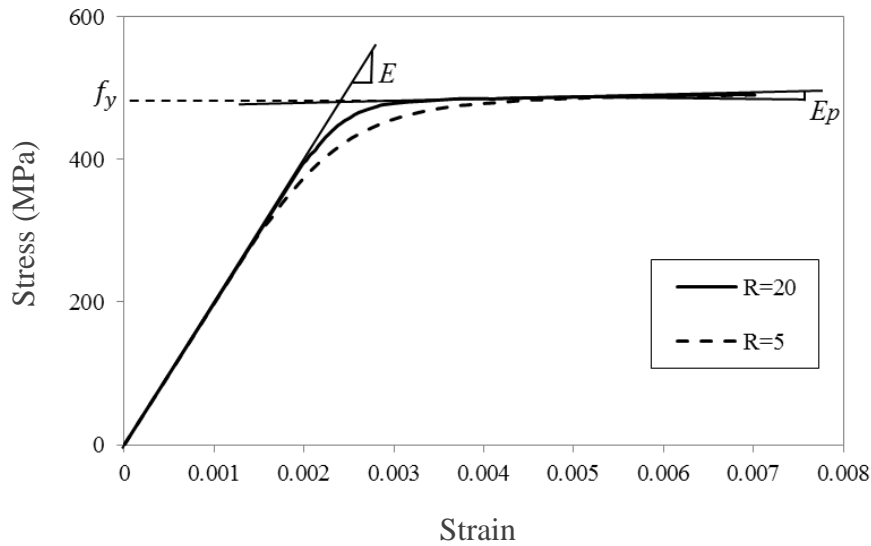


Figure 7.5. Steel material model used in FE analysis

Table 7.2. FE steel material model properties

	$f_y$ (MPa)		$E$ (GPa)	$b$	$R$
	<i>Tie bar</i>	<i>Steel plate</i>			
<b>Shear element</b>	385	309	200	0.019	15

#### 7.4. FE MODEL VALIDATION OF SCB5 - SCB8 SPECIMENS

All FE models for SC beams are validated in this section. For each validation, the load-displacement curves obtained from the FE model were compared against the test results. Key parameters of the curve namely, peak load ( $P_{max}$ ), displacement at the peak load ( $D_{max}$ ) and the load at which yielding occurred ( $P_y$ ) were compared. An error below 5% between the predicted values by the FE model and the actual results was considered acceptable. Furthermore, for each beam, the load vs. strain of tension plate responses were graphically compared.

All beam cross-section in the FE model was divided into 10 fibres and the sensitivity study (Appendix C) showed that higher number of fibers would not affect the results. All beam models showed higher stiffness than tested sample and the discrepancies in the slopes of the experimental and analytical shear force-displacement response were probably due to the discrete concrete cracking in the specimens, which was modelled using smeared cracking approach in the FE models (Sener et al., 2016), as well as

possible marginal slip that might have occurred in the test, could be the possible reasons for lower stiffness in the test. Additionally, the displacement of the beam was calculated theoretically for the initial elastic region of the curve from Eq. 7.7.

$$D = \frac{Pa}{48EI} (3L^2 - 4a^2) \quad (\text{Eq. 7.7})$$

Where P is the total applied load, a is the shear span, L is the span, E is the material young's modulus, and I is the moment of inertia. The results are compared with both FE model and experiment (Appendix D). As shown in Appendix D, the theoretical calculation shows identical results to the FE model, which implies that the less stiff behaviour of the beam during the experiment is due to the nature of experiment and its set up which causes slip during the application of the load.

#### 7.4.1. SCB5 model

The load-displacement curves for both FE model and experiment is shown in Figure 7.6 and validated parameters are presented in Table 7.3. The strain comparison for the bottom plate is shown in Figure 7.7. Comparing the curves in Figure 7.6 and values in Table 7.3 reveals that the FE model showed good agreement with the experiment results and the failure load and displacement at the ultimate load were also close to the experimental value. The failure mode predicted by the FE model was in accordance with the observed failure mode for the beam. The strain at the bottom plate for fiber 18 of the model, which was the fiber at the centre point of the plate, was compared with the strain measurements of the gauges. Considering the various strain ranges for the

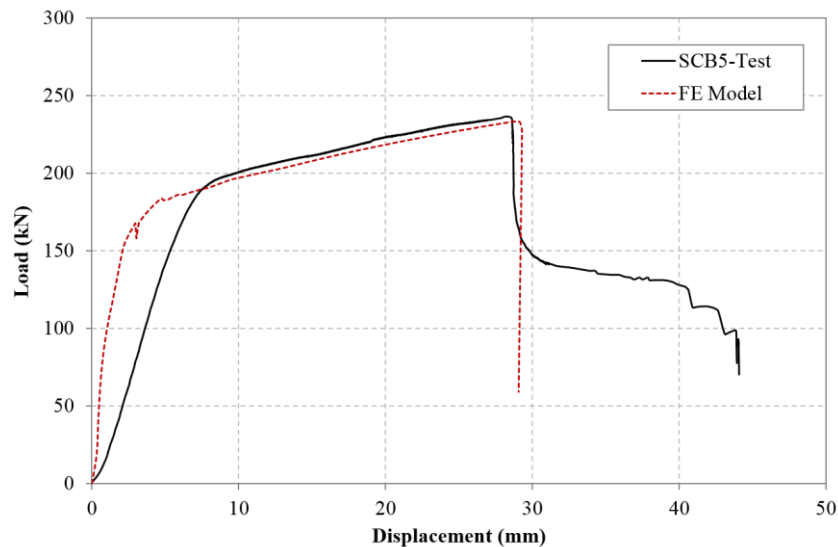


Figure 7.6. Validation of FE model with experimental result for SCB5

bottom plate, the FE prediction lies within the same strain range as the gauges, hence it is regarded as an acceptable prediction by the FE model.

Table 7.3. Validation of FE model with test results for SCB5

	$P_{\max}$ (kN)	$D_{\max}$ (mm)	$P_y$ (kN)
<b>SCB5- EXP</b>	236.5	28.12	127
<b>FE Analysis</b>	233.28	29.29	122.7
<b>Error</b>	-1.36%	+4.16%	-3.38%
<b>Model Factor</b> ( $P_{\text{EXP}}/P_{\text{FE}}$ )	1.01	0.96	1.04

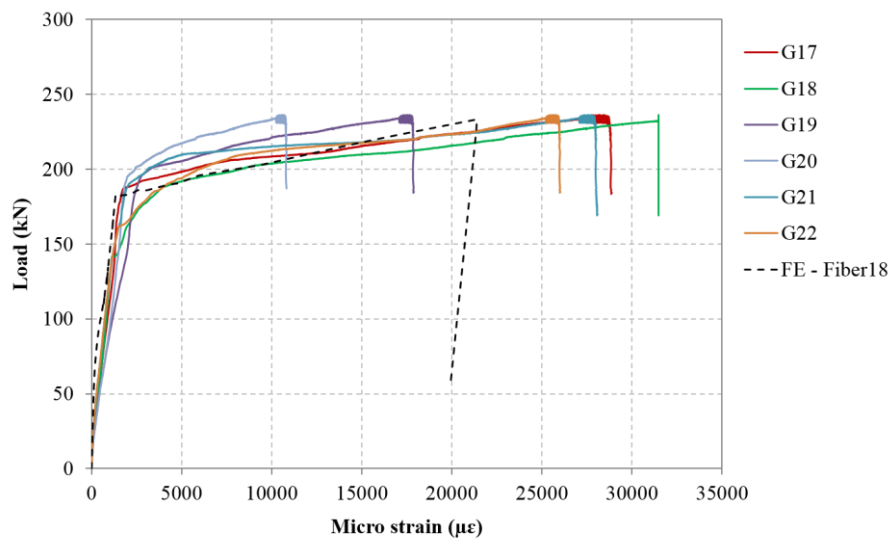


Figure 7.7. Strain measurements for SCB6: FE model vs. Test

#### 7.4.2. SCB6 model

The load-displacement curve and the strain measurements at the bottom steel plate obtained from the finite element model for SCB6 are illustrated in Figure 7.8 and Figure 7.9 respectively. The key parameters of the load-deflection curve are compared in Table 7.4. The ultimate load predicted by the FE model compares conservatively with the experimental results with maximum error margin of 2.9%. The model factor is very close to the value of 1 reflecting the good prediction of the FE model.

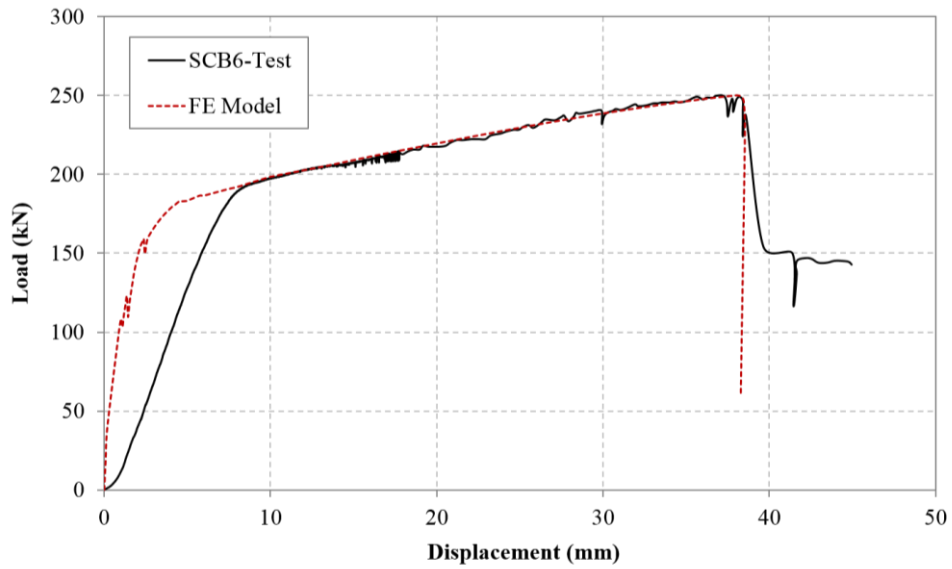


Figure 7.8. Validation of FE model with experimental result for SCB6

Table 7.4. Validation of FE model with test results for SCB6

	$P_{\max}$ (kN)	$D_{\max}$ (mm)	$P_y$ (kN)
<b>SCB6- Test</b>	251.9	38.18	141.4
<b>FE Analysis</b>	250.1	38.08	145.6
<b>Error</b>	-0.71%	-0.26%	+2.9%
<b>Model Factor</b> ( $P_{\text{EXP}}/P_{\text{FE}}$ )	1.007	1.002	0.97

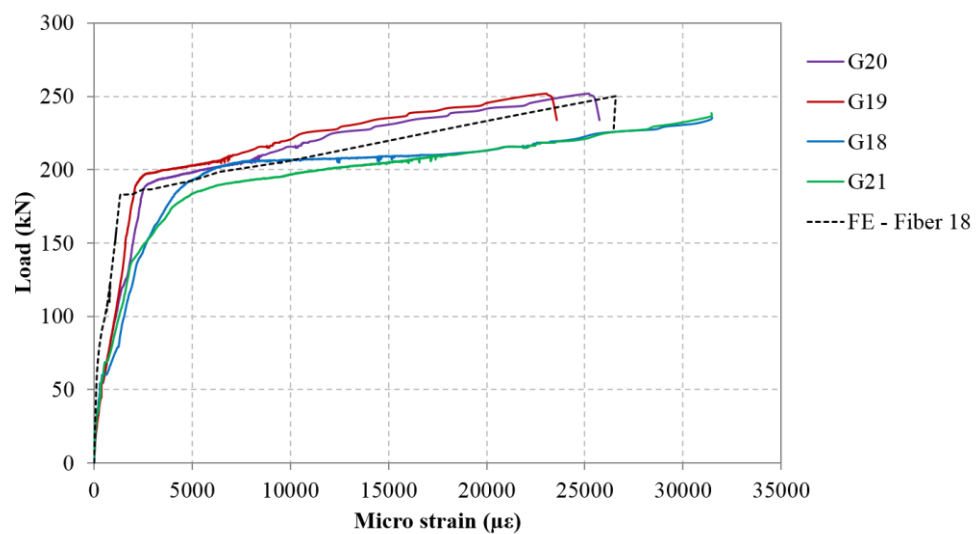


Figure 7.9. Strain measurements for SCB6: FE model vs. Test



Figure 7.9 shows the strain at the bottom steel plate measured by the strain gauges and the strain obtained from the FE model at the centre of the bottom plate. The FE model values lies within the same strain range compared to FE model and hence considering all these comparisons, the material model was validated for FRC with 1.5% SF and 0.5% CNF.

#### 7.4.3. SCB7 model

The load-displacement curve and the strain measurements at the bottom steel plate obtained from the FE model for SCB7 are shown in Figure 7.10 and Figure 7.11 respectively. Table 7.5 compares the key parameters of the load-deflection curve. It is evident that the FE model could satisfactorily predict the ultimate load capacity, load at which yielding occurred, and the displacement at which the beam had shear failure with a minimal error and high model factor.

The strain at the bottom steel plate also compared well with experimental values (Figure 7.11). It can be concluded that material model used for this beam was validated for FRC with 1.0% SF and 0.5% CNF.

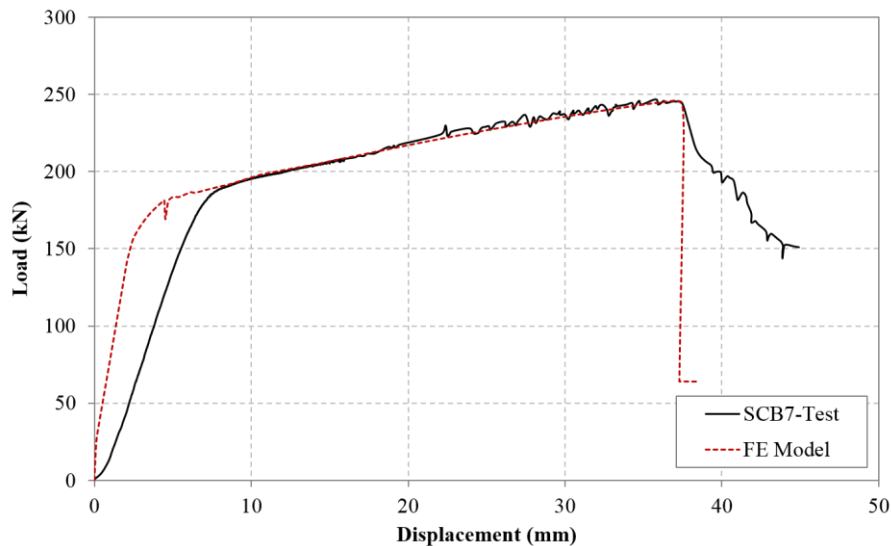


Figure 7.10. Validation of FE model with experimental result for SCB7

Table 7.5. Validation of FE model with test results for SCB7

	$P_{\max}$ (kN)	$D_{\max}$ (mm)	$P_y$ (kN)
<b>SCB7- Test</b>	247.9	37.19	148
<b>FE Analysis</b>	246.1	37.12	144
<b>Error</b>	-0.73%	-0.19%	-2.7%
<b>Model Factor</b> ( $P_{\text{EXP}}/P_{\text{FE}}$ )	1.007	1.002	1.03

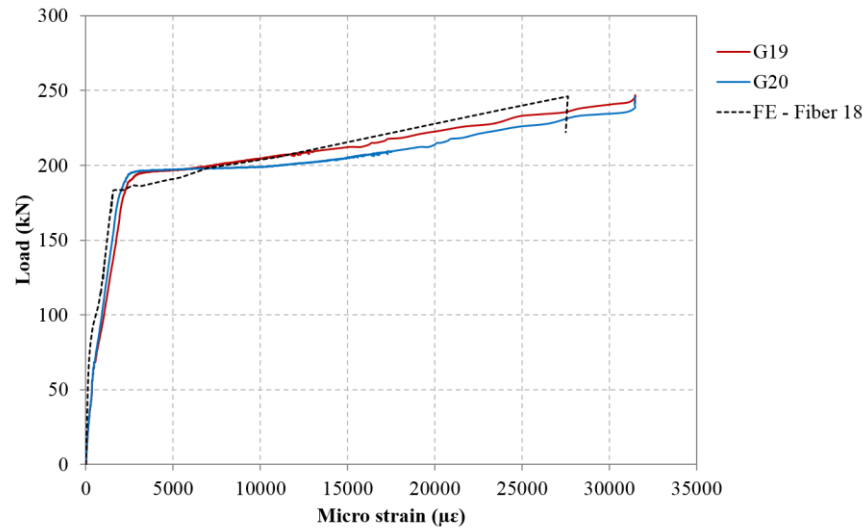


Figure 7.11. Validation of FE model with experimental result for SCB7

#### 7.4.4. SCB8 model

The load-displacement curve and the strain measurements at the bottom steel plate obtained from the finite element model for SCB8 are shown in Figure 7.12 and Figure 7.13 respectively. The small error between the FE model and the experimental results presented in Table 7.6 reveals that the FE model could satisfactorily predict the ultimate load capacity, yielding load and the displacement at which the beam had shear failure.

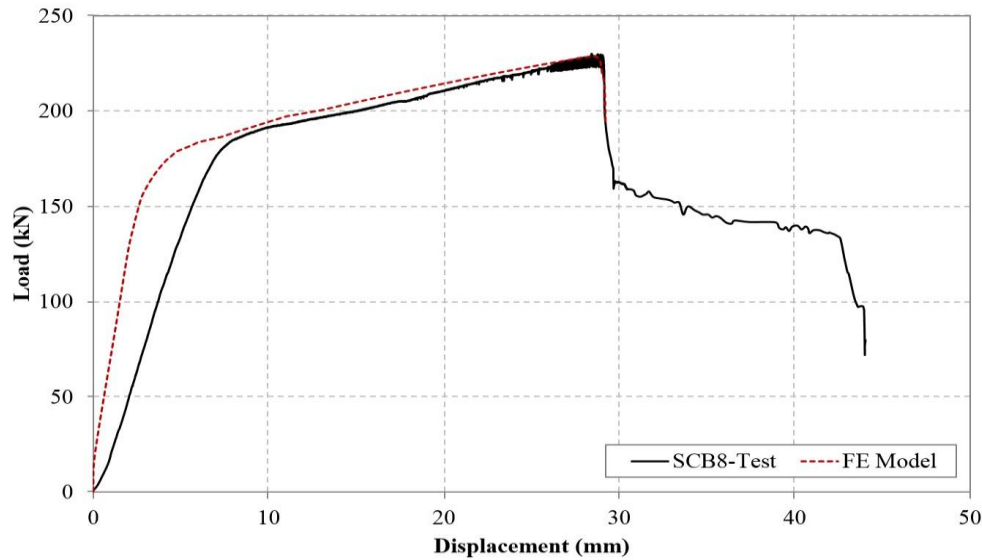


Figure 7.12. Validation of FE model with experimental result for SCB8

Table 7.6. Validation of FE model with test results for SCB8

	$P_{\max}$ (kN)	$D_{\max}$ (mm)	$P_y$ (kN)
<b>SCB8- Test</b>	230	28.9	131.5
<b>FE Analysis</b>	228.6	29.0	132
<b>Error</b>	-0.6%	+0.35%	+0.38%
<b>Model Factor</b> ( $P_{\text{EXP}}/P_{\text{FE}}$ )	1.006	0.997	0.996

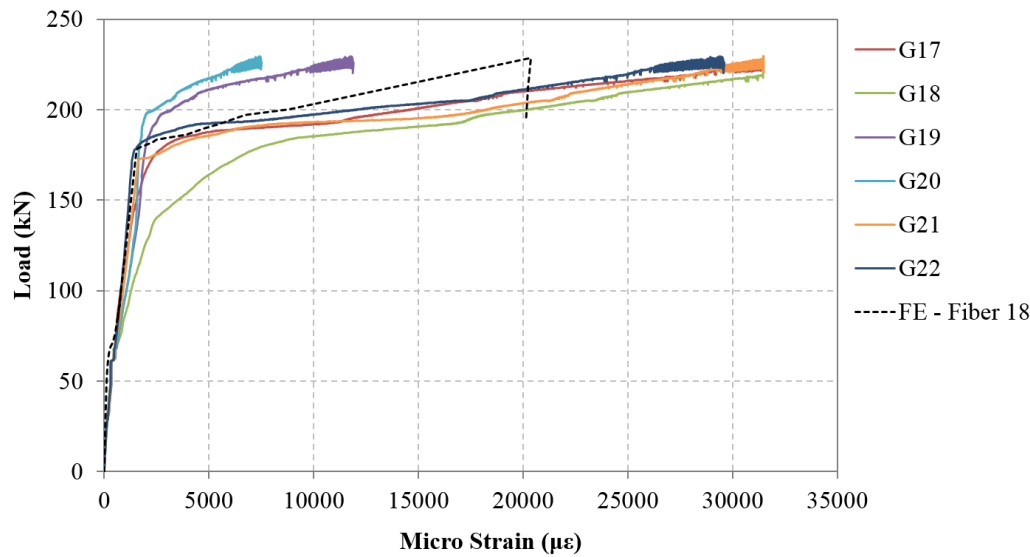


Figure 7.13. Strain measurements for SCB8: FE model vs Test

The experimental data of strain measurements at the bottom steel plate showed discrepant values for G19 and G20 located at the centre compared to other gauges. However, the FE results lied within the strain range captured for all gauges and it was considered as a reasonable prediction by the FE model. Therefore, the concrete material properties used in this model was considered satisfactory for FRC with 0.5% volume fraction of SF combined with 1.0% volume fraction of CNF.

Followed by the validation of the material properties for each hybrid fiber reinforced concrete materials in SC specimens, the next phase of the FE study (parametric analysis) was conducted which is explained in the following section.

### 7.5. PARAMETRIC STUDY

Parametric analyses on parameters which were thought to have a major effect on the behaviour of the SC beam were studied in this section as described in Table 7.7. Each validated beam models for SCB5-SCB8 were considered for the parametric study. The two parameters which were chosen to be studied were: 1) steel plate thickness ( $t_p$ ) which affects the longitudinal reinforcement ratio of an SC beam, and 2) tie bar spacing ( $S$ ) which affects the vertical shear reinforcement ratio of an SC beam.

Table 7.7. Parameters for parametric study

Parameter	Values
Steel plate thickness ( $t_p$ )	4, 6, 8 mm
Spacing of tie bars ( $S$ )	100, 200, 300 mm

The range considered for the plate thickness affects the longitudinal reinforcement ( $\rho = 2t_p/t_{sc}$ ) and it covers  $0.026 \leq \rho \leq 0.07$ . The recommendation by AISC N690-Appendix9 is  $0.015 \leq \rho \leq 0.05$ . Since a thickness smaller than 3 is not recommended, smaller values are neglected. The plate slenderness ratio which is defined as ( $s/t_p$ ), where  $s$  is the stud spacing, decreases by increasing plate thickness.

The values considered for bar spacing creates a range of  $0.45 \leq S/h_c \leq 1.36$ , which is within the range for most practical applications (i.e.  $0.5 \leq S/h_c \leq 2$ ).

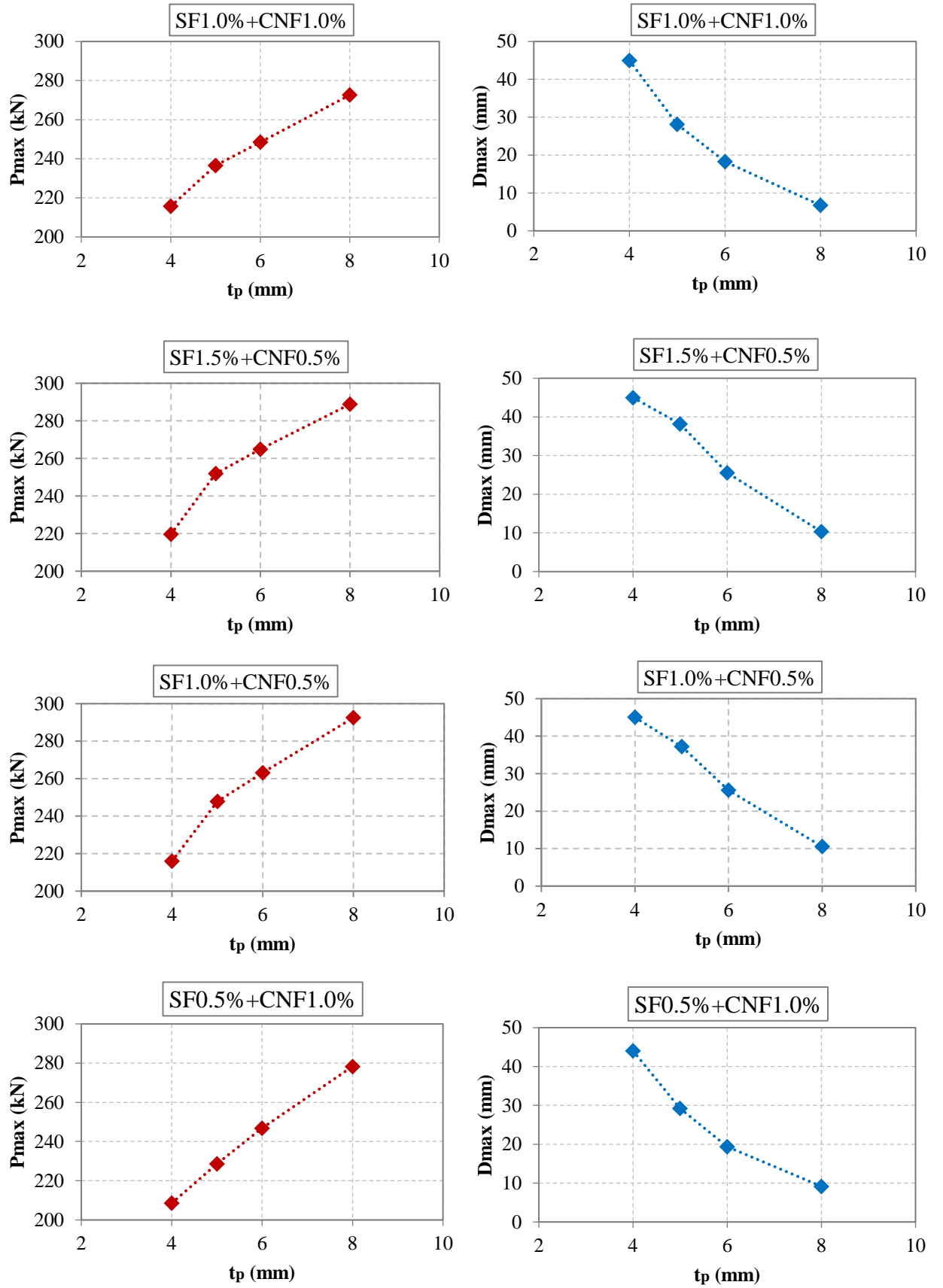
For each case, the ultimate load capacity of the SC beam and the maximum displacement before failure with various parameters were compared to analyse the effect of these two parameters on the beam strength and ductility.

### 7.5.1. Steel plate thickness

The results for beams SCB5-SCB8 are shown in Figure 7.14 for varying the plate thickness  $t_p$ , from 4 mm to 8 mm. As can be seen from the figure, increasing the steel plate thickness resulted in an increase in the strength of the beam, while the maximum displacement decreased. Lower displacement reflects the less ductile behaviour of the beam. This behaviour (i.e. increased strength with decreased ductility) is similar to a specimen that is over-reinforced. The results provided in a study by Oduyemi and Wright (1989), Wright et al. (1991b) and Anandavalli et al. (2013) corroborate similar finding that a reduction in ductility occurs as the steel plate area increases. Also, they stated that as the bottom steel area increased, strains recorded in the bottom steel at the last load stage (before collapse) increased.

Moreover, the initial stiffness increased insignificantly with increased steel plate thickness. This confirms the findings of Ozaki et al. (2001). They also stated that increased plate thickness resulted in an inconsiderable increase in cracking strength, while maximum shear strength increased noticeably. Sener et al. (2016) found that increasing the longitudinal reinforcement by increasing plate thickness by 50%, increased the shear strength of the beam. This was attributed to the larger contribution of aggregate interlock associated with smaller crack width. Bruhl and Varma (2017) also found that increasing plate thickness results in higher moment capacity and stiffness, deformation, and curvature ductility were also increased.

FE analysis conducted by Zhang et al. (2014) on SC wall showed that for reinforcement ratio ( $\rho$ ) of 1.5%, the composite action was 90%, and for  $\rho$  values of 2.5%, 3.3% and 4.2% the corresponding composite actions decreased to 75%, 60%, and 52% respectively. Foundoukos and Chapman (2008) studied the effect of tension plate thickness on transverse shear resistance of the Bi-steel beam. It was summarised that the truss contribution in shear resistance of the beam under truss analogy remained constant, since the geometry was the same, while the concrete contribution increased for thicker plates. Thicker plates resulted in an increase in the un-cracked concrete area and corresponding reduction in concrete stresses.

Figure 7.14. Parametric study results for varying parameter  $t_p$

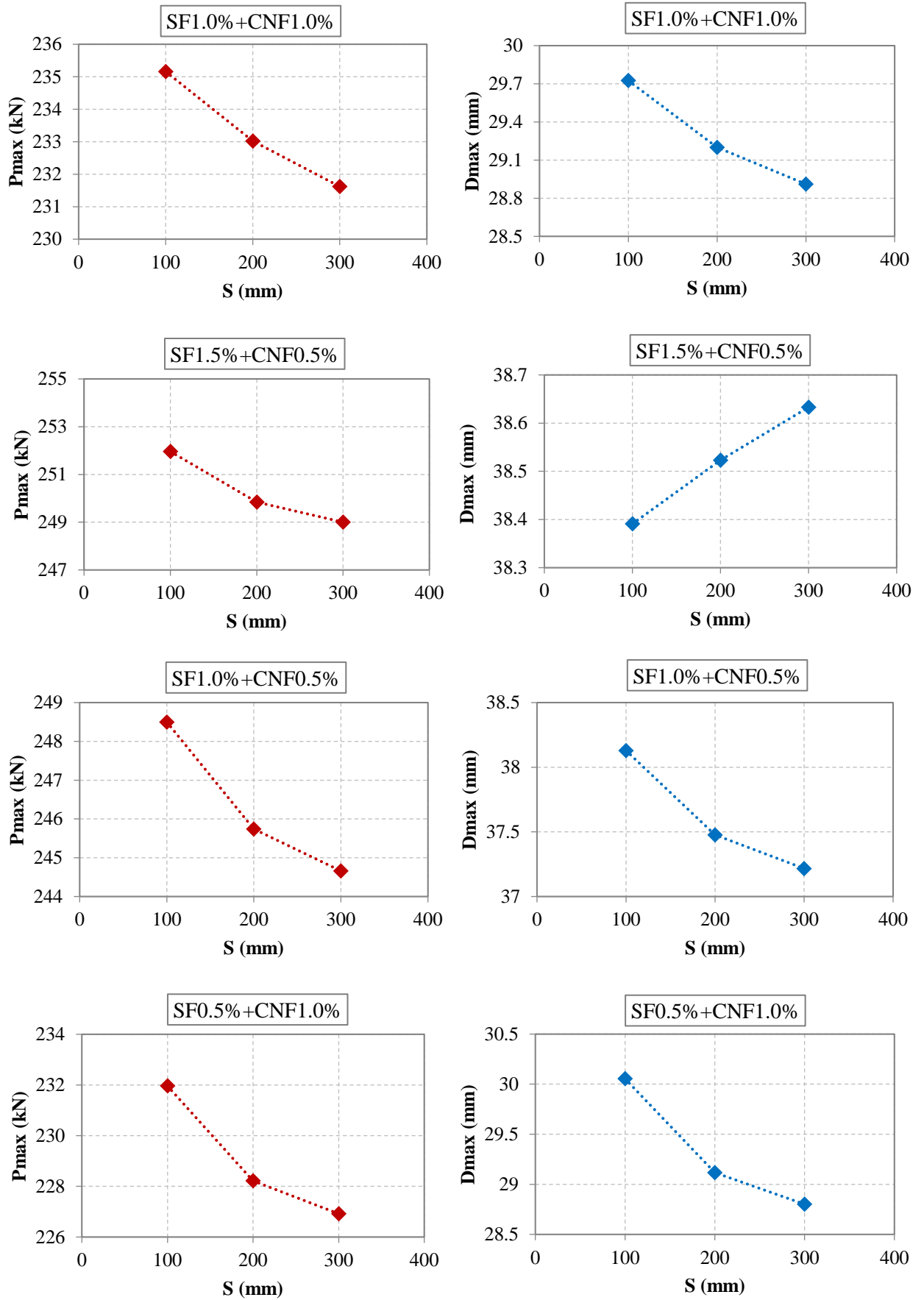
### 7.5.2. Tie bar spacing

The results of beams SCB5-SCB8 are shown in Figure 7.15 for different vertical shear reinforcement (tie bar) spacing, varying from 100 mm to 300 mm. As can be seen from the figure, increasing the tie bar spacing resulted in a decrease in the ultimate load capacity (i.e. shear strength) of the beam, as well as lower displacement capacity. However, it should be noted that the change in both strength and displacement by varying the tie bar spacing was marginal. The smallest change in strength by increasing the tie bar spacing was as small as 0.84% (for SCB6:SF1.5%+CNF0.5%) and the highest decrease was as small as 2.2% reduction in strength (for SCB8:SF0.5%+CNF1.0%). Also, the highest reduction in displacement was for SCB8, with 4.2% reduction in displacement when  $S=100$  was increased to  $S=300$ . The smallest change in displacement was for SCB6 with 0.6% increase in displacement when  $S=100$  was increased to  $S=300$ .

Overall, from the marginal changes in both strength and displacement, it can be concluded that the effect of the tie bar spacing ( $S$ ) on the behaviour of the SC element is minimal when FRC with adequate fiber is used as a concrete infill. Amongst the samples the behaviour of specimen (SCB6) with highest steel fiber (1.5% SF+0.5% CNF) showed the least dependence to the tie bar spacing, and the specimen (SCB8) with the minimum SF dosage (0.5% SF + 1.0% CNF) showed most dependency to the tie bar spacing, although this dependency was minimal.

Foundoukos and Chapman (2008) studied the Bi-Steel SC system with varying bar spacing to concrete thickness ratio between 0.5 and 2 ( $0.5 \leq S/h_c \leq 2$ ). It was found that the average shear stress at failure decreased with increasing  $S/h_c$ . Also, it was found that the concrete contribution to transverse shear under truss analogy remained approximately constant with changing  $S/h_c$  in contrast to the previous case where  $\rho$  was effective on concrete contribution.

In contrast to the finding of this research, Anandavalli et al. (2013) found an increase in displacement of SC beam with bi-directionally inclined connector when the spacing of the connectors was increased above 225mm. This difference is attributed to the different type of connector used in their study as well as different concrete type. On the other hand, the load carrying capacity had marginal change with varying connector spacing which was consistent with the finding of this study.

Figure 7.15. Parametric study results for varying parameter  $S$



### 7.6. A CASE STUDY ON SC BEAM

In this section, the effect of FRC concrete core (those studied in this research) on the behaviour of SC beams with no vertical shear reinforcement (i.e. tie bars or long/overlapping studs) was analysed by studying the SC beam tested by Sener et al. (2016). The vertical shear capacity of SC composite beams without shear reinforcement is dependent on concrete strength, bottom steel plate area, shear span/effective depth ratio and bottom connection ratio (Oduyemi and Wright, 1989). The SC beam named SP1-3 tested by Sener et al. (2016) was chosen for this case study, which had full composite action with no vertical shear reinforcement. Also, the beam had an out-of-plane shear failure mode. The tested specimen was infilled with normal concrete with a compressive strength of 42.1 MPa. This compressive strength is close to the compressive strength of FRC used in this research. All of the beam specimen features, including the geometry and the steel plate material properties, were identically modelled as of the experiment condition and the validated concrete material properties of this study were used to analyse the effect of hybrid fiber (SF + CNF) reinforced concrete on the behaviour of an SC beam with no shear reinforcement. The schematic drawing of the specimen is shown in Figure 7.16 and dimensional measurements and material properties are given in Table 7.8.

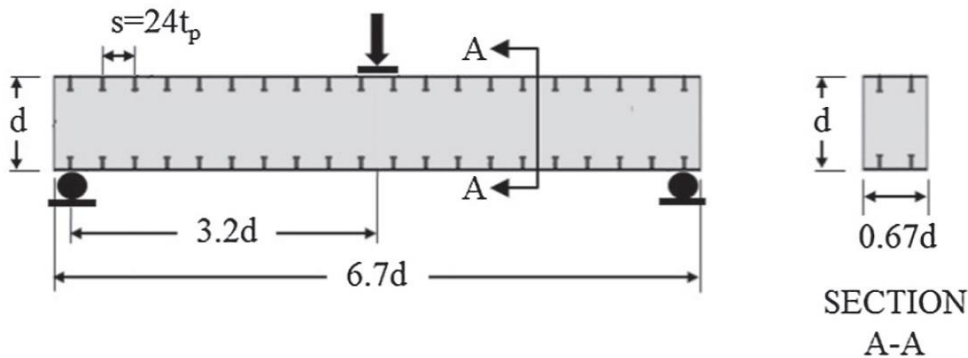


Figure 7.16. Schematic drawing of tested specimen SP1-3 (Sener et al., 2016)

Table 7.8. Details of SC beam SP1-3 tested by Sener et al. (2016)

Specimen	d (mm)	Width (mm)	$t_p$ (mm)	$\rho = 2t_p/d$ (%)	$f_y$ (MPa)	Failure mode
SP1-3	457.2	306.3	9.5	4.17	448.2	Out-of-plane shear

The results of the FE model for SP1-3 with different concrete types are shown in Figure 7.17. It is clearly evident from the figure that the fiber reinforced concrete affected the behaviour of the SC beam with no vertical shear reinforcement. The behaviour of the beam infilled with all hybrid fiber reinforced concrete was similar in altering the failure mode, however, the displacement at failure for each beam varied. The ultimate load capacity of the beam was also enhanced as well as the ductility. It is observed that using overall 2.0% of fibers with equal volume fraction of nanofibers and macro fibers showed the highest displacement. Increasing the steel fiber dosage from 0.5% to 1.0% in combination with 0.5% CNF had the lowest enhancement amongst others and the smallest ductility was observed for sample with the least steel fiber dosage.

It is concluded that hybrid fiber reinforced concrete can alter the failure mode of the beam by increasing its shear capacity owing to the presence of fibers within the concrete matrix when no transverse shear reinforcement is used.

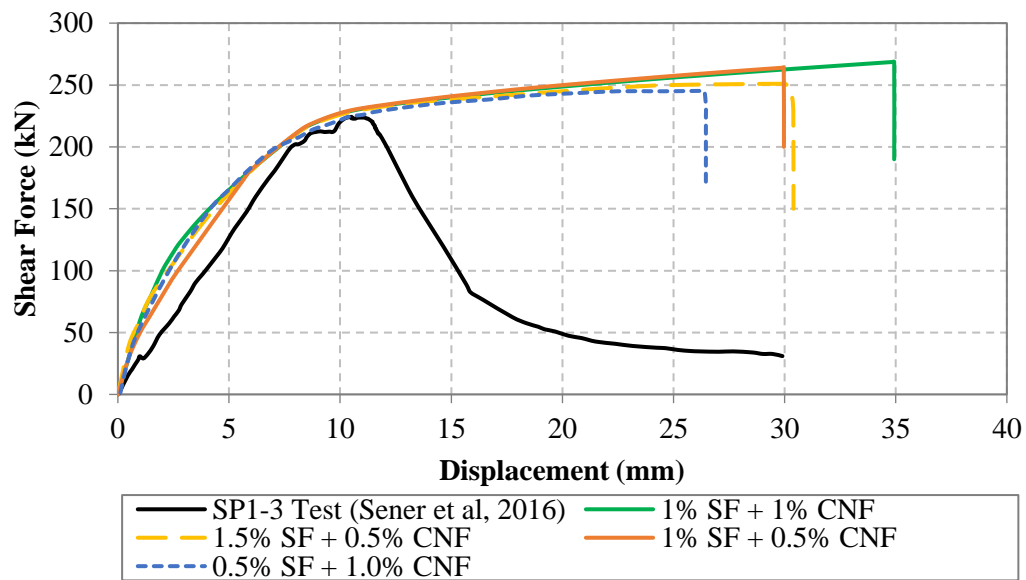


Figure 7.17. FE study on tested SC beam by Sener et al. (2016)

## 7.7. CONCLUSIONS

A summary of the theoretical approach to the 2D shear based fiber beam element used for the finite element study of this research was outlined at the beginning of this chapter. Material properties of the concrete for beams in category 2 and category 3 described in Chapter 5 were validated against experimental results. The validated models were further used for conducting a parametric study to examine the effect of steel plate

thickness and tie bar spacing on the behaviour of the SC beam. It was concluded that increasing the plate thickness (4mm – 8mm) results in higher shear capacity of the beam, which is partially associated with smaller crack width and larger contribution of aggregate interlock, while, the ductility was decreased. The effect of tie bar spacing (100mm – 300mm) was minimal on both strength (as small as 2.2% reduction) and ductility (as small as 4.2% reduction), which was attributed to the effect of fiber reinforced concrete infill and higher shear capacity of the concrete, due to crack control by the presence of fibers, as well as enhanced mechanical properties of SFRC, which in turn minimised the effect of tie bars on the behaviour of the beam. This was also confirmed by the results of a case study conducted. An FE case study on an SC beam tested by previous researchers showed that the use of hybrid fiber reinforced concrete infill (with overall  $V_f = 1.5\%$  and  $2.0\%$ ) in SC beam without any vertical shear reinforcement could be effective in changing the shear failure mode of the specimen to a ductile mode of failure by increasing both the maximum shear strength and maximum ductile displacement during the hardening stage.

## CHAPTER 8

### CONCLUSIONS AND RECOMMENDATIONS

---

#### 8.1. INTRODUCTION

The overall aims and objectives of the work in this thesis were set out in the introduction. The completed work addresses the effect of carbon nanofibers on concrete in both material and structural level. This chapter reviews, firstly, a summary of the key findings of the research work followed by the significance of findings for practical application and research development. There are several lines of research arising from this work which should be pursued. These recommendations are included at the end of this chapter.

#### 8.2. SUMMARY OF KEY FINDINGS

The primary objective of this research was to investigate the effect of CNF on mechanical properties of concrete; and in particular, to examine its effect on the structural performance of SC wall system. The secondary aim of the study was to examine the self-sensing capability of CNFRC. Followed by the review on the literature in Chapter 2, the first series of test reported in Chapter 3, sought to compare the mechanical performance of CNFRC material with plain concrete and the second series (reported in Chapter 5) focused on structural performance of SC wall system with CNFRC and hybrid FRC infill for the beam. Self-health monitoring properties of the CNFRC was then analysed in Chapter 6 followed by FE parametric study conducted on SC structural elements in Chapter 7. The findings of this study contribute to the field of nanoreinforced cementitious composite research by adding to the knowledge with regards to the behaviour of nanoreinforced concrete materials by presenting the enhanced effect of CNF on the mechanical properties of concrete. It was found that all mechanical properties of the CNFRC were affected and improved by the addition of 0.25%-1.0% CNF by the volume of binder. Moreover, this study addressed the lack of

earlier studies on the use of nano materials in concrete for structural health monitoring applications by contributing to the understanding of electrical properties of CNFRC and concluding that CNF could be used in concrete for making a structural element itself a potential sensor to sense its own change in strain as well as its own damage. The key findings of each chapter are summarised below.

Chapter 3:

- The material test conducted on two groups: Group A and Group B, showed that the mixing method adopted in Group B was more suitable. It was observed that mixing CNF with the whole amount of water required for the designed mix, resulted in a more uniform concrete mixture rather than mixing the CNF with only a portion of the water.
- Addition of 1.0% CNF (amongst 0.25%, 0.5% and 0.75% volume fractions) into concrete resulted in the highest compressive strength improvement by 39% as well as better post-peak behaviour for stress-strain relationship under uniaxial compression. Also, this amount of fiber showed the best flexural strength with the magnitude of 6.30 MPa. This increase in the flexural capacity of the beam with the addition of 1.0% fibers showed that the nanofibers were effective in increasing the flexural capacity of the beam to a great extent.
- The flexural strength was more influenced by CNF dosage amongst the CNFRC samples as opposed to other mechanical properties. Whereas, the split tensile strength was the least affected by varying the CNF dosage. Having said that, the split tensile strength was improved by 22.2% with the addition of only 0.25% volume fraction of CNF.
- The peak displacement of concrete under four-point bending test was improved for CNFRC mixes. The greatest achievement was observed for 0.5% and 1.0% CNF reinforced concrete up to 170% higher than PC, which is crucial to structural applications in which higher ductility and strain capacity to failure is needed.
- Regarding the damaged samples, specimens with 0.75% and 1.0% fiber in concrete showed better integrity in compression test and surface damage was observed rather than severe crushing and explosion of the cylinder samples.

- From the self-sensing point of view, increasing the fiber dosage from 0.25% to 1.0% decreased the electrical resistance of the concrete by almost 50% from 8.78 k $\Omega$  to 4.19 k $\Omega$ .
- The electrical resistance of the CNFRC showed a reverse relationship with compressive strain. As the compressive strain decreased, the resistance increased, while with increasing compressive strain, the resistance decreased.
- The electrical resistance variation (ERV) for PC showed no relation with applied strain, while the ERV for all CNFRC had a linear relation with compressive strain prior to reaching the ultimate load with the correlation coefficients ( $R^2$ ) above 0.9.
- The gauge factor obtained for CNFRC0.25, CNFRC0.5, CNFRC0.75, and CNFRC1.0 was 645, 664, 760, and 1264 respectively. These high values confirm the piezoresistive properties of CNFRC and their high strain sensibility with aforementioned CNF dosages. Hence, the potential of carbon nanofiber reinforced concrete as damage sensor is verified. This was also manifested by a dramatic increase in electrical resistivity under four-point bending test, at loading instances as early as the maximum load, hence providing timely failure warnings.

#### Chapter 5:

Assessment of the structural performance of SC walls with fiber reinforced concrete was completed by conducting four-point bending test on beams. The following conclusions were made from this study:

- The failure mode of SC wall with plain concrete infill under four-point bending was localised concrete core failure by a major shear crack together with local buckling of top steel plate adjacent to the major shear crack which indicated brittle failure mode.
- Using singly-reinforced concrete with either CNF or SF at dosages of up to 1.0% and 0.5% respectively did not affect the shear failure mode of the SC beam under four-point flexural test. However, the load at which initial cracks (flexural or diagonal shear cracks) were formed was increased due to the bridging effect of fibers.

- From the behaviour of single fiber reinforced concrete it was concluded that the fibers were not sufficient in enhancing the structural behaviour to a great extent that a ductile behaviour could be observed, while using hybrid composite (combination of macro steel fiber and nano carbon fiber) was successful in enhancing the performance of the beam.
- SC beams with hybrid fiber reinforced concrete (category 2 and category 3), with combined fiber volume fractions of 1.5% and 2.0%, showed significant improvement in the overall performance of the beam by altering the shear failure mode of the beam to a flexure-shear failure mode.
- For beams with hybrid fiber reinforced concrete, pronounced formation of curvature and good ductile behaviour of the load-displacement curve, tension steel plate yielding, and better crack control were clear hallmarks of the beams. These beams were extremely ductile and had higher ultimate load capacity and could sustain a very large deflection until the flexural cracks in the concrete core grew towards the top plate followed by the opening of the shear crack towards the ultimate load capacity of the beam.
- From the crack behaviour and load-displacement graphs of the hybrid composite, it was observed that the pre-peak mechanical behaviour of the hybrid specimens was mainly controlled by the CNFs, while macro steel fiber had great influence on the post-peak response. Therefore, it is concluded that the incorporation of CNFs and macro SF results in a stronger (especially in tension) and more ductile concrete for the use in SC structural element compared to the singly-reinforced concrete or plain concrete.
- The post-cracking stage was mainly associated with fiber pull-out behaviour; however, the CNF could still affect the behaviour of the element by helping the steel fiber to better bind with the matrix. This enhancement to the bond strength due to the presence of nanofibers, as stated by researchers (Meng and Khayat, 2016), can be attributed to the ‘modification of the interface due to the presence of nanofilaments that can provide additional sites for the nucleation of hydrates.’ The presence of nanofibers in the proximity of steel fibers was also observed in the SEM images (e.g. for SCB6).

- The cracking pattern for beams with hybrid fiber reinforced concrete showed more flexural cracks and better crack distribution along the span as opposed to the singly-reinforced concrete with a minimum number of cracks.
- From the SEM observations, it was clearly seen that the CNFs were effectively dispersed reinforcing the matrix within the concrete and no agglomeration was spotted. However, the dispersion was not perfectly homogeneous.

#### Chapter 6:

The study reported in this chapter, consisted of validation of conductivity-based strain monitoring by analysing the electrical resistance of concrete at different locations within tested SC beams and concludes the following:

- From the initial concrete electrical resistance, it was found that having the CNF in combination with SF could improve the accuracy of the self-sensing properties of concrete by giving the least electrical resistance. However, this effect was minimal.
- All SC beams reinforced with CNF fibers (used individually or in combination with SF), except the specimen with 0.5% CNF reinforcement showed correlation between ERV and the strain induced in the material. The sample with 0.5% CNF, had weak sensitivity with noisy resistance response. This was attributed to either dispersion issues for the CNF or inadequate fiber dosage. Nevertheless, the latter is less likely to be the reason since the results of the material test in Chapter 3 revealed that 0.5% CNF was successful in increasing electrical conductivity of the concrete. The error margin for this sample was the highest with the least correlation coefficient between ERV and strain. It is fair to assume that had the CNF been dispersed in a more uniform way, not forming any clusters, the concrete would have exhibited more superior results.
- Overall, 1.0% CNF showed the best result and its combination with 1.0% SF was found to outperform the performance of other samples in decreasing the smart concrete electrical resistance. This fiber combination possibly had the highest opportunity for fibers to be in contact with each other to pass the current.
- In this work, the correlation coefficient ( $R^2$ ) values were over 0.9 and close to 1 for all hybrid fiber reinforced concretes as well as the beam with 1.0% CNF



reinforcement, which shows the strong linear relationship between the electrical resistance change and strain.

- The damage localisation could be easily identified from a drastic change in the materials ERV. By the formation of cracks, the ERV vs strain relationship showed less sensitivity which was apparent in the reduced slope of the curve.
- The ERV showed that (i.e. specimen SCB8) the concrete core was capable of monitoring the change in the concrete behaviour from monitoring small variation in strain to sensing formation of macro scale cracks as well as warning the formation of major crack induced within the concrete. This is beneficial for the SC system since the concrete face is covered by the steel plate and initial cracks cannot be identified from the surface. Therefore, the self-sensing capability of the concrete is a great advantage to give information about the health of the concrete within the structural element.
- The ERV changed reversely with compressive strain, due to decreased electrical resistance which is caused by better conduction path under compressive strain. This finding was similar to that in Chapter 3.
- The piezoresistive properties of the CNF reinforced concrete were shown to be an accurate measure of the material strain by finding a good correlation between the ERV and strain. In addition, changes in conductivity with variations in strain were also shown to be correlated to crack damage in the structural element. Therefore, the concrete has the potential to predict its own strain from the ERV measurements.

#### Chapter 7:

The FE analysis conducted in this chapter led to the following concluding remarks:

- Increasing the plate thickness resulted in stronger but less ductile SC beam when hybrid fiber reinforced concrete types that were studied in this research were used.
- The tie bar spacing did not show significant change in either strength or ductility, which was attributed to the effect of fiber reinforced concrete infill and the higher shear capacity of the concrete
- The FE case study on an SC beam tested by previous researchers showed that using the hybrid fiber reinforced concrete infill in SC beam could eliminate the

need for vertical shear reinforcement or minimise the number of tie bars required while achieving a ductile mode of failure.

To conclude, this research has made a contribution towards understanding the effect of CNF as fiber in concrete as well as SC system behaviour when such fibers are used. Despite some conflicts present in the experimental results available in the literature due to use of different fiber types and dispersion methods, nanofiber reinforced composites showed they are a promising area of material applications. It was shown that using smart concrete in a structural member allows for inner damage detection, hence eliminating the need for embedding, attaching or remote sensing systems. This work is the first and essential step towards understanding the potential of the CNFRC to be used at the structural level in the construction industry and comprehensive research programme is required before CNFRC is fully incorporated into the industry. This study has raised a number of interesting research areas, that if developed further would increase the understanding of the effect of CNF on mechanical properties of concrete, structural performance of CNFRC structural elements as well as their self-sensing ability. The following section presents the recommendations for further research.

### **8.3. RECOMMENDATIONS FOR FUTURE WORK**

Based on the work conducted in this research the following can be recommended for future work:

- Further experimental work is suggested to be conducted to find the optimum mixture ratios such as CNF/Water ratio.
- Obtaining the best sonication properties such as amplitude, sonication time, and total applied energy for achieving the best possible dispersion for various fiber loadings.
- It is suggested that the effect of CNF on different types of concrete such as reactive powder concrete (RPC), Ultra-high performance concrete (UHPC), self-consolidating concrete (SCC), and lightweight concrete (LWC) be investigated. In addition, the self-sensing of such advanced smart concrete is recommended to be investigated.
- Additional investigation on the effect of aggregate proportions of the mix design on the electrical conductivity of the CNFRC as well as investigation on the effect

of the coarse aggregate size on the piezoresistive properties of concrete is recommended.

- Further research is required to establish the direct relationship (e.g. formula) between ERV and strain for different CNF dosage within concrete by conducting material tests under different stress states.
- The use of CNFRC in structural elements other than SC is recommended to be examined.
- Implement the CNFRC and hybrid FRC material model in finite element analytical models, and further investigate the performance of structural elements under different loading conditions including hazard loads (e.g. seismic loads, blast, and impact).
- Experimentally investigate the behaviour of structural elements when partially reinforced with CNFRC (i.e. at critical locations; e.g. base of a column, beam-column joints, etc.).

#### **8.4. LIMITATIONS OF THE WORK**

The author tried her best to bring success to this research project. This study was valuable in providing a comprehensive investigation on the effect of CNF on the performance of concrete and behaviour of SC system under monotonic flexural load. Yet, due to the limitations confronted during the experimental programme, some obstacles were confronted during the course of research as acknowledged below.

- Sonication of CNF solution was limited to be conducted for a maximum liquid volume of 4L as of the instructions given for the ultrasonic processor equipment.
- The designed SC beam could only have a limited dimension to be compatible with the flexural testing frame.
- The possible measured voltage for the electrodes by the data logger was ranging between -10 v and +10 v, hence limiting the magnitude of applied constant current to the electrodes.

Despite the above limitations, attempts were made to maximise achieving the findings that were primarily the aim of the study. It is believed that the present study has generated rich data, which has contributed to the knowledge on the mechanical, electrical and structural performance of CNFRC.

## REFERENCES

### A

---

Abu Al-Rub, R.K., Ashour, A.I. and Tyson, B.M. (2012) On the aspect ratio effect of multi-walled carbon nanotube reinforcements on the mechanical properties of cementitious nanocomposites. *Construction and Building Materials*. 35, 647-655.

Adams, P.F. and Zimmerman, T.J.E. (1987) Design and Behaviour of Composite Ice-Resisting Walls, Steel/Composite Structural Systems. In: *Proceedings of a special symposium held in conjunction with POAC '87, Fairbanks, Alaska, 9th International Conference on Port and Ocean Engineering under Arctic Conditions*.

American Concrete Institute (2006) ACI 234R-06. *Guide for the Use of Silica Fume in Concrete*. Farmington Hills, MI, ACI.

American Concrete Institute (2006) ACI 349-06. *Code Reqs. for Nuclear Safety Related Conc. Struct. and Comm.* Farmington Hills, Michigan.

American Concrete Institute (2006) ACI 349M-06. *Code Requirements for Nuclear Safety-Related Concrete Structures and Commentary*. Farmington Hills, MI, ACI.

American Institute of Steel Construction (2013) AISC N690-Appendix N9. *Specification for Design of Steel-Plate Composite (SC) Walls in Safety-Related Structures for Nuclear Facilities*. Chicago, IL, AISC.

Anandavalli, N., Rajasankar, J., Prakash, A. and Sivaprasad, B. (2013) Static Response of Steel-Concrete-Steel Sandwich Beam with Bi-Directionally Inclined Connectors. *American Journal of Civil Engineering and Architecture*. 1 (1), 15-20.

Applied Science Inc. Pyrograf Products (2013). Available from: <http://www.pyrografproducts.com> [Accessed 20<sup>th</sup> March 2013].

Azhari, F. and Banthia, N. (2012) Cement-based sensors with carbon fibers and carbon nanotubes for piezoresistive sensing. *Cement and concrete Composites*. 34 (7), 866-873.

Azhari, F. and Banthia, N. (2017) Carbon Fiber-Reinforced Cementitious Composites for Tensile Strain Sensing. *ACI Materials Journal*. 114 (1), 129-136.

### B

---

Bal, S. and Saha, S. (2015) Fabrication and characterization of carbon nanofiber (CNF) based epoxy composites. *IOP Conference Series: Materials Science and Engineering*. 75 (2015). Available from: doi: 10.1088/1757-899X/75/1/012018 [Accessed 1<sup>st</sup> December 2015].

Bazgir, A. (2016) *The Behaviour of Steel Fiber Reinforced Concrete Material and Its Effect on Impact Resistance of Slabs*. MPhil Thesis. City University of London, United Kingdom.

Belarbi, A. and Hsu, T.T.C. (1995) Constitutive Laws of Softened Concrete in Biaxial Tension-Compression. *ACI Structural Journal*. 92 (5), 562–573.

Booth, P.N. (2008) *Behaviour of SC wall subjected to combined thermal and mechanical loads*. MS Thesis. Purdue University, West Lafayette, Indiana.

Braverman, J., Morante, R. and Hofmayer, C. (1997) Assessment of Modular Construction for Safety-Related Structures at Advanced Nuclear Power Plants. Manuscript Prepared for Division of Engineering Technology Office of Nuclear Regulatory Research U.S. Nuclear Regulatory Commission, Washington, DC, 1-34.

British Standards Institution (2000) BS EN 12350-1:2000. *Testing fresh concrete; Sampling*. London, BSI.

British Standards Institution (2000) BS EN 12390-5:2000. *Testing hardened concrete; Flexural strength of test specimens*. London, BSI.

British Standards Institution (2002) BS EN 12390-3:2002. *Testing hardened concrete; Compressive strength of test specimens*. London, BSI.

British Standards Institution (2004) BS EN 1992-1-1:2004. *Eurocode 2. Design of concrete structures. General rules and rules for buildings*. London, BSI.

British Standards Institution (2004) BS EN 1994-1-1:2004. *Eurocode 4. Design of composite steel and concrete structures. General rules and rules for buildings*. London, BSI.

British Standards Institution (2009) BS EN 12390- 6:2009. *Testing hardened concrete; Tensile splitting strength of test specimens*. London, BSI.

Bruhl, J.C. and Varma, A.H. (2017) Experimental Resistance and Available Ductility of Steel-Plate Composite Walls in One-Way Bending. *Journal of Structural Engineering*. 143(4).

Burgan, B. (1997) *Double skin composite construction for submerged tube tunnels, Phase 3*. European Commission; technical steel research. Report number: Final report.

## C

---

Camacho-Ballesta, C., Garces, O. and Zornoza, E. (2016) Performance of cement based sensors with CNT for strain. *Advanced Cement Research*. 28(4), 274-284.

Cao, J. and Chung, D.D.D. (2001) Carbon fiber reinforced cement mortar improved by using acrylic dispersion as an admixture. *Cement & Concrete Research*. 31(11), 1633-1637.

Chen, P.W. and Chung, D.D.L. (1996) Carbon fiber reinforced concrete as an intrinsically smart concrete for damage assessment during static and dynamic loading. *ACI Materials Journal*. 93(4), 341-350.

Cwirzen, A., Habermehl-Cwirzen, K. and Penttala, V. (2008) Surface Decoration of Carbon Nanotubes and Mechanical Properties of Cement/Carbon Nanotube Composites. *Advances in Cement Research*. 20 (2), 65-73.

## D

---

D'Alessandro, A., Rallini, M., Ubertini, F., Materazzi, A.L. and Kenny, J.M. (2016) Investigations on scalable fabrication procedures for self-sensing carbon nanotube cement matrix composites for SHM applications. *Cement Concrete Composites*. 65, 200-213.

Dalla, P.T., Dassios, K.G., Tragazikis, I.K., Exarchos, D.A. and Matikas, T.E. (2016) Carbon nanotubes and nanofibers as strain and damage sensors for smart cement. *Materials Today Communications*. 8, 196-204.

Ding, Y., Chen, Z., Han, Z., Zhang, Y. and Pacheco-Torgal, F. (2013) Nano-Carbon black and carbon fiber as conductive materials for the diagnosing of the damage of concrete beams. *Construction and Building Materials*. 43, 233-241.

Ding, Y., Zhang, F., Torgal, F. and Zhang, Y. (2012) Shear behaviour of steel fibre reinforced self-consolidating concrete beams based on the modified compression field theory. *Composite Structures*. 94, 2440-2449.

## F

---

Feng, L., Xie, N. and Zhong, J. (2014) Carbon Nanofibers and Their Composites: A Review of Synthesizing, Properties, and Applications. *Materials*. 7, 3919-3945.

Foundoukos, N. and Chapman, J.C. (2008) Finite element analysis of steel–concrete–steel sandwich beams. *Journal of Constructional Steel Research*. 64, 947–961.

## G

---

Galao, O., Baeza, F.J., Zornoza, E. and Garces, P. (2014) Strain and damage sensing properties on multifunctional cement composites with CNF admixture. *Cement & Concrete Composites*. 46, 90-98.

Gao, D., Sturm, M. and Mo, Y.L. (2009) Electrical resistance of carbon-nanofiber concrete. *Smart Materials and Structures*. 18.

Gay, C. and Sanchez, F. (2010) Performance of Carbon Nanofiber-Cement Composites with a High-Range Water Reducer. *Transportation Research Record: Journal of the Transportation Research Board*. 2142, 109-113.

Gdoutos, E.E., Konsta-Gdoutos, M.S. and Danoglidis, P.A. (2016) Portland Cement mortar nanocomposites at low carbon nanotube and carbon nanofiber content: A fracture mechanics experimental study. *Cement and Concrete Composites*. 70, 110-118.

Ge, M. and Sattler, K. (1994) Observation of fullerene cones. *Chemical Physics Letter*. 220, 192–196.

## H

---

Han, B., Guan, X. and Ou J. (2007) Electrode design, measuring method and data acquisition system of carbon fiber cement paste piezoresistive sensors. *Sensors and Actuators A*. 135, 360-369.

Han, B., Sun, S., Ding, S., Zhang, L., Yu, X. and Ou, J. (2015). Review of nanocarbon-engineered multifunctional cementitious composites. *Composite: Part A*. 70, 69-81.

Han, B., Yu, X. and Ou, J. (2014) *Self-Sensing Concrete in Smart Structures*. UK, Elsevier Science & Technology.

Hoheneder, J.A. (2012) *Smart Carbon Nanotube/fiber and Pva Fiber-Reinforced Composites for Stress Sensing and Chloride Ion Detection*. Master Thesis, University of Wisconsin Milwaukee.

Hou, T.C. and Lynch, J.P. (2005) Conductivity-based strain monitoring and damage characterization of fiber reinforced cementitious structural components. In: *Proceedings of SPIE 12th Annual International Symposium on Smart Structures and Materials, San Diego, CA, March 6-10*. Available from: <http://www-personal.umich.edu/~jerlynch/papers/SPIE2005Conductivity.pdf> [Accessed 14 October 2015].

Howser Roberts, R. and Mo, Y. (2016) Development of carbon nanofiber aggregate for concrete strain monitoring. *Innovative development of advanced multifunctional nanocomposites in civil and structural engineering*. Chapter 2. 9-45.

Howser, R., Dhonde, H.B. and Mo, Y.L. (2011) Self-sensing of carbon nanofiber concrete columns subjected to reversed cyclic loading. *Smart Materials and Structures*. 20, 1-13.

Hsu, T.T.C. and Mo, Y.L. (2010) *Unified Theory of Concrete Structures*. United Kingdom, John Wiley & Sons.

Hsu, T.T.C. and Zhang, L.X. (1996) Tension Stiffening in Reinforced Concrete Membrane Elements. *Structural Journal of the American Concrete Institute*. 93 (1), 108–115.

Hsu, T.T.C. and Zhu, R.R.H. (2002) Softened Membrane Model for Reinforced Concrete Elements in Shear. *Structural Journal of the American Concrete Institute*, 99 (4), 460–469.

Hunashyal, A.M., Tippa, S.V., Quadri, S.S. and Banapurmath, N.R. (2011) Experimental Investigation on Effect of Carbon Nanotubes and Carbon Fibres on the Behavior of Plain Cement Mortar Composite Round Bars under Direct Tension. *ISR/N Nanotechnology*. 2011. Available from: <http://dx.doi.org/10.5402/2011/856849> [Accessed 36th June 2013].

## **J**

---

“JEAG-4618: Technical Guidelines for Seismic Design of Steel Plate Reinforced Concrete Structures - Buildings and Structures,” by Japan Electric Association’s Nuclear Standard Committee, 2005.

## **K**

---

Kang, I., Heung, Y.Y., Kim, J.H., Lee, J.W., Gollapudi, R., Subramaniam, S., Narasimhadevara, S., Hurd, D., Kirikera, G.R., Shanov, V., Schulz, M.J., Shi, D.,

Boerio, J., Mall, S. and Ruggles-Wren, M. (2006) Introduction to carbon nanotube and nanofiber smart materials. *Composites: Part B*. 37, 382-394.

Kim, H.K., Nam, I.W. and Lee, H.K. (2014) Enhanced effect of carbon nanotube on mechanical and electrical properties of cement composites by incorporation of silica fume. *Composite Structures*. 107, 60-69.

Konsta-Gdoutos, M.S. and Aza, C.A. (2014) Self sensing carbon nanotube (CNT) and nanofiber (CNF) cementitious composites for real time damage assessment in smart structures. *Cement & Concrete Composites*. 53, 162-169.

Konsta-Gdoutos, M.S., Metaxa, Z.S. and Shah, S.P. (2010) Highly dispersed carbon nanotube reinforced cement based materials. *Cement and Concrete Research*. 40 (7), 1052-1059.

Korea Electric Association (2010) KEPIC-SNG. *Specification for Safety-related steel plate concrete structures for nuclear facilities*. Board of KEPIC Policy, Structural committee.

Kowald, T. (2004) Influence of surface-modified carbon nanotubes on ultra-high performance concrete. In: *Proceedings of International Symposium on Ultra High Performance Concrete, Kassel, Germany*. 195–202. Available from: <http://www.uni-kassel.de/upress/online/frei/978-3-89958-086-0.volltext.frei.pdf> [Accessed 24th May 2013].

Kwak, Y.K., Eberhard, M.O., Kim, W.S. and Kim, J. (2002) Shear strength of Steel Fiber – Reinforced Concrete Beams without Stirrups. *Structural Journal*. 99 (4), 530-538.

## **L**

---

Li, C., Thostenson, E.T. and Chou, T.W. (2007) Dominant role of tunnelling resistance in the electrical conductivity of carbon nanotube-based composites. *Applied Physics Letters*. 91 (22).

Li, G.Y. Wang, P.M. and Zhao, X. (2005) Mechanical Behaviour and Microstructure of Cement Composites Incorporating Surface-Treated Multi-Walled Carbon Nanotubes. *Carbon*. 43(6), 1239-1245.

Lie, H., Ziao, H. and Ou, J. (2006) Effect of compressive strain on electrical resistivity of carbon black-filled cement-based composites. *Cement & Concrete Composites*. 28 (9), 824-828.

Liew, J.Y.R. and Soheli, K.M.A. (2009) Lightweight steel-concrete-steel sandwich system with J-hook connectors. *Engineering Structures*. 31, 1166-1178.

Liew, J.Y.R., Soheli, K.M.A. and Koh, C.G. (2009) Impact tests on steel-concrete-steel sandwich beams with lightweight concrete core. *Engineering Structures*. 31, 2045-2059.

Loh, K.J. and Gonsalez, J. (2015) Cementitious composites engineered with embedded carbon nanotube thin films for enhanced sensing performance. *Journal of Physics:*



*Conference Series*. 628 (2015). Available from: doi: 10.1088/1742-6596/628/1/012042 [Accessed 1<sup>st</sup> December 2015].

Lourie, O. and Wagner, H.D. (1998) Transmission Electron Microscopy Observations of Fracture of Single-Wall Carbon Nanotubes Under Axial Tension. *Applied Physics Letters*. 73 (24), 3527-3529.

## M

---

Madhavi, T.Ch. and Annamalai, S. (2016) Electrical Conductivity of Concrete. *ARPJ Journal of Engineering and Applied Sciences*. 11(9), 5979-5982.

Manzur, T. and Yazdani, N. (2010) Strength Enhancement of Cement Mortar with Carbon Nanotubes: Early Results and Potential. *Journal of the Transportation Research Records*. 2142, 102-108.

Matterazzi, A.L., Ubertini, F. and D'Alessandro, A. (2013) Carbon nanotube cement-based transducers for dynamic sensing of strain. *Cement & Concrete Composites*. 37, 2-11.

McKinley, B. (2002) *Large Deformation Structural Performance of Double Skin Composite Construction using British Steel's "Bi-Steel"*. PhD Thesis. City University London, London.

McKinley, B. and Boswell, L.F. (2002) Behaviour of double skin composite Construction. *Journal of constructional steel research*. 58, 1347-1359.

Mehta, P.K. and Monterio, P.J.M. (2014) Fiber reinforced concrete. *Concrete: Microstructure, Properties, and Materials*. Available from: <http://www.retawprojects.com/uploads/fibers.pdf> [Accessed 15<sup>th</sup> June 2015].

Meng, W. and Khayat, K.H. (2016) Mechanical properties of ultra-high-performance concrete enhanced with graphite nanoplatelets and carbon nanofibers. *Composites Part B*. 107, 113-122.

Metaxa, Z.S. Konsta-Gdoutos, M.S. and Shah, S.P. (2010) Mechanical properties and nanostructure of cement-based materials reinforced with carbon nanofibers and polyvinyl alcohol (PVA) microfibers. In: *ACI Spring 2010 Convention*. Chicago, IL: American Concrete Institute. pp. 115-126.

Metaxa, Z.S., Konsta-Gdoutos, M.S. and Shah, S.P. (2013) Carbon nanofiber cementitious composites-effects of debulking procedure on dispersion and reinforcing efficiency. *Cement and Concrete Composites*. 36, 25-32.

Mo, Y.L. and Howser Roberts, R. (2013) Advances in Nanofibers. In: Maguire, R. (Ed.) *Carbon Nanofiber Concrete for Damage Detection of Infrastructure*. InTech. pp.125-143. Available from: <https://www.intechopen.com/books/advances-in-nanofibers/carbon-nanofiber-concrete-for-damage-detection-of-infrastructure> [Accessed 1st December 2015].

Mullapudi, T.R.S. (2010) *Seismic Analysis of Reinforced Concrete Structures Subjected to Combined Axial, Flexure, Shear and Torsional Loads*. PhD Thesis. University of Houston. Texas.

Mullapudi, T.R.S. and Ayoub, A. (2010) Modelling of the seismic behavior of shear-critical reinforced concrete columns. *Engineering Structures*. 32, 3601-3615.

Mullapudi, T.R.S., Charkhchi, P. and Ayoub, A. (2013) Behaviour of Shear-dominant thin-walled RC structures. *Thin-Walled Structures*. 63, 134-146.

Mullapudi, T.R.S., Gao, D. and Ayoub, A. (2013) Nondestructive Evaluation of Carbon-Nanofiber Concrete. *Magazine of Concrete Research*. 65(18), 1081-1091.

## N

---

Nadarajah, A., Lawrence, J.G. and Hughes, T.W. (2008) Development and Commercialization of Vapor Grown Carbon Nanofibers: A Review. *Key Engineering Materials*. 380, 193-206.

Nam, I.W., Kim, H.K. and Lee, H.K. (2010). Investigation of high-strength and electromagnetic wave shielding properties of a mortar incorporating carbon nanotube (CNT). In: *IV European conference on computational mechanics (ECCM IV)*, 16–21 May, Paris, France.

Narayanan, R., Wright, H.D., Francis, R.W. and Evans, H.R. (1987). Double skin composite construction for submerged tube tunnels. *Steel Construction Today*. 1, 185–189.

Nasibulin, A.G., Shandakov, S.D., Nasibulina, L.I., Cwirzen, A., Mudimela, P.R., Habermehl-Cwirzen, K., Grishin, D.A., Gavrilov, Y.V., Malm, J.E.M., Tapper, U., Tian, Y., Penttala, V., Karppinen, M.J. and Kauppinen, E.I. (2009) A Novel Cement-Based Hybrid Material. *New Journal of Physics*, 11 (2), 1-11. Available from: doi: 10.1088/1367-2630/11/2/023013 [Accessed 8<sup>th</sup> December 2014].

Nie, J.G., Hu, H.S., Fan, J.S., Tao, M.X., Li, S.Y. and Liu, F.J. (2013) Experimental Study on Seismic behaviour of high-strength concrete filled double-steel-plate composite walls. *Journal of Constructional Steel Research*. 88, 206-219.

Nochaiya, T. and Chaipanich, A. (2011) Behavior of multi-walled carbon nanotubes on the porosity and microstructure of cement-based materials. *Applied Surface Science*. 257(6), 1941-45.

Noiseux-Lauze, G. and Akhras, G. (2013) Structural health monitoring using smart nano cement sensors. In: *International workshop on smart materials, structures NDT for the energy industry*, October 7-10, Calgary, Alberta, Canada.

## O

---

Oduyemi, T.O.S. and Wright, H.D. (1989) An Experimental Investigation into the Behaviour of Double-Skin Sandwich Beams. *Journal of Construction Steel Research*. 14 (3), 197-220.

Ozaki, M., Akita, S., Niwa, N., Matsuo, I. and Usami, S. (2001) Study on Steel Plate Reinforced Concrete Bearing Wall for Nuclear Power Plants Part 1: Shear and Bending Loading Tests of SC Walls. In: *SMIRT 16*. Washington, DC, August 2001.

Ozkan, T., Chen, Q., Naraghi, M. and Chasiotis, I., (2008) Mechanical and Interface Properties of Carbon Nanofibers for Polymer Nanocomposites. In: *International SAMPE Technical Conference, 2008 SAMPE Fall Technical Conference and Exhibition - Multifunctional Materials: Working Smarter Together, SAMPE '08, Memphis, TN, United States*.

Ozkan, T., Naraghi, M. and Chasiotis, I. (2009) Mechanical Properties of Individual Carbon Nanofibers. In: *Proceedings of the SEM Annual Conference, June 1-4, 2009 Albuquerque New Mexico, USA*.

## **P**

---

Pang, X.B. and Hsu, T.T.C. (1995) Behavior of Reinforced Concrete Membrane Elements in Shear. *ACI Structural Journal*. 92 (6) 665–679

Parveen, S., Rana, A. and Fanguero, R. (2013) Review Article: A review on Nanomaterial Dispersion, Microstructure, and Mechanical Properties of Carbon Nanotube and Nanofiber Reinforced Cementitious Composites. *Journal of Nanomaterials*. 2013. Available from: <http://dx.doi.org/10.1155/2013/710175> [Accessed 29th September 2013].

Peyvandi, A., Sbiya, L.A., Soroushian, P. and Sobolev, K. (2013) Effect of the cementitious paste density on the performance efficiency of carbon nanofiber in concrete nanocomposites. *Construction and Building Materials*, 48, 265-269.

Pryer J.W. and Bowerman, H.G. (1998) The development and use of British steel Bi-Steel. *Journal of Constructional Steel Research*. 46 (1-3), 15.

## **R**

---

Reza, F., Batson, G.B., Yamamuro, J.A. and Lee, J.S. (2003). Resistance Changes During Compression of Carbon Fiber Cement Composites. *Journal of Material Civil Engineering, ASCE*. 15, 476-483.

Rhee, I. and Roh, Y.S. (2013) Properties of normal-strength concrete and mortar with multi-walled carbon nanotubes. *Magazine of Concrete Research*. 65 (16), 951-961.

Roberts, T.M., Edwards, D.N. and Narayanan, R. (1996) Testing and Analysis of steel-concrete-steel sandwich beams. *Journal of Constructional Steel Research*. 38(3), 257-279.

## **S**

---

Salvetat, J.P. and Kuik, A.J. (1997) Electronic and Mechanical Properties of Carbon Nanotubes. *Advanced Materials*. 22 (7).

Sanchez, F. and Ince, C. (2009) Microstructure and macroscopic properties of hybrid carbon nanofiber/silica fume cement composites. *Composites Science and Technology*. 69 (7-8), 1310-1318.

Sanchez, F. and Sobolev, K. (2010) Nanotechnology in concrete – A review. *Construction and Building Materials*. 24 (11), 2060-2071.

Sánchez, M., Rams, J., Campo, M., Jiménez-Suárez, A. and Ureña, A. (2011) Characterization of carbon nanofiber/epoxy nanocomposites by the nanoindentation technique. *Composites Part B: Engineering*. 42 (4), 638–644.

Sasmal, S., Ravivarman, N., Sindu, B.S. and Vignesh, K. (2017) Electrical conductivity and piezo-resistive characteristics of CNT and CNF incorporated cementitious nanocomposites under static and dynamic loading. *Composites: Part A*. 100, 227-243.

Sener, K.C., Varma, A.H. and Seo, J. (2016) Experimental and numerical investigation of the shear behaviour of steel-plate composite (SC) beams without shear reinforcement. *Engineering Structures*. 127, 495-509.

Shah, S. (2011) Nanoscale Modification of Cementitious Materials. In: *Public Seminar on Recent Advances in Concrete Material Technologies, NTU, Singapore, 16 August 2011*.

Shi, L., Lu, Y. and Bai, Y. (2017) Mechanical and electrical characterisation of steel fiber and carbon black engineered cementitious composites. *Procedia Engineering*, 188, 325-332.

Siddique, R. and Mehta, A. (2014) Effect of carbon nanotubes on Properties of cement mortars. *Construction and Building Materials*. 50, 116-129.

Sivakumar, M.V.N. (2011) Performance characteristics of Carbon Nanofiber Blended Self Compacting Concrete. *International Journal of Advanced Structural Engineering*. 3 (2), 179-186.

Sobolkina, A., Mechtcherine, V., Khavrus, V., Mair, D., Mende, M., Ritschel, M. and Leonhardt, A. (2012) Dispersion of carbon nanotubes and its influence on the mechanical properties of the cement matrix. *Cement and Concrete Composites*. 34 (10), 1104–1113.

Sohel K.M.A., Liew J.Y.R. and Koh C.G. (2007) Steel-concrete-steel sandwich structures subjected to impact loads. In: Beale, R.G. (ed.) *Steel and Aluminium Structures, ICSAS'07: Proceedings of 6th international conference on steel and aluminium structures*. Oxford Brook University. pp. 506-513.

Sohel, K.M.A. and Liew, J.Y.R. (2011) Steel–Concrete–Steel sandwich slabs with lightweight core - Static performance. *Engineering Structures*, 33 (3), 981-992.

Sohel, K.M.A., Liew, J.Y.R., Yan, J.B., Zhang, M.H. and Chia, K.S. (2012) Behavior of Steel–Concrete–Steel sandwich structures with lightweight cement composite and novel shear connectors. *Composite Structures*. 94 (12), 3500-3509.

Sun, M.Q., Liew, R.J.Y., Zhang, M.H. and Li, W. (2014) Development of cement-based strain sensor for health monitoring of ultra-high strength concrete. *Construction and building Materials*. 65, 630-637.

## T

---

Takeuchi, M., Narikawa, M., Matsuo, I., Hara, K. and Usami, S. (1998) Study on a concrete filled structure for nuclear power plants. *Nuclear Engineering and Design*. 179 (2), 209-223.

Taucer, F.T., Spacone, E. and Filippou, F.C. (1991) *A Fiber Beam–Column Element for Seismic Response Analysis of Reinforced Concrete Structures*. University of California, Berkeley. Report UCB/EERC-91/17.

Taylor, R.L. (2012) *FEAPpv User Manual v.3.1*. Department of Civil and Environmental Engineering, University of California, Berkeley. Available from: <http://projects.ce.berkeley.edu/feap/feappv/manual.pdf> [Accessed 23rd March 2013].

Tchoul, M.N., Ford, W.T., Lolli, G., Resasco, D.E. and Arepalli, S. (2007) Effect of Mild Nitric Acid Oxidation on Dispersibility, Size, and Structure of Single-Walled Carbon Nanotubes. *Chemistry of Materials*. 19 (23), 5765–5772.

Teomete, E. and Kocyigit, O.I. (2013) Tensile strain sensitivity of steel fiber reinforced cement matrix composites testes by split tensile test. *Construction and Building Materials*. 47, 962-968.

Teychenne, D.C., Franklin, R.E. and Erntroy, H.C. (1997) Part two: The mix design process. In: Marsh, B.K (ed.) *Design of Normal Concrete Mixes*. 2<sup>nd</sup> edition. Watford, Construction Research Communications Ltd, pp. 9-16.

Thomas Swan & Co. Ltd. Available from: <http://www.thomas-swan.co.uk> [Accessed 3<sup>rd</sup> May 2013].

Tyson, B.M., Abu Al-Rub, R.A., Yazdanbakhsh, A. and Grasley, Z. (2011) Carbon Nanotubes and Carbon Nanofibers for Enhancing the Mechanical Properties of Nanocomposite Cementitious Materials. *Journal of Materials in Civil Engineering*. 23 (7), 1028–1035.

## V

---

Varma, A.H., Malushte, S.R., Sener, K.C., Boot, P.N. and Coogler, K. (2011b) Steel-Plate Composite (SC) Walls: Analysis and Design Including Thermal Effects. In: *The 21st International Conference on Structural Mechanics in Reactor Technology, SMiRT 21, Paper No. 761, 6<sup>th</sup>-11<sup>th</sup> November 2011. New Delhi, India*.

Varma, A.H., Sener, K.C., Zhang, K., Coogler, K. and Malushte, S.R. (2011a) Out-Of-Plane Shear Behavior Of SC Composite Structures. In: *The 21st International Conference on Structural Mechanics in Reactor Technology, SMiRT 21, paper No. 76, 6<sup>th</sup>-11<sup>th</sup> November 2011. New Delhi, India*.

Vecchio, F.J. and Collins, M.P. (1981) *Stress-Strain Characteristic of Reinforced Concrete in Pure Shear*. IABSE Colloquium, Advanced Mechanics of Reinforced Concrete, Delft, Final Report, International Association of Bridge and Structural Engineering, Zurich, Switzerland, pp. 221–225.

## W

---

Weitzenböck, J.R. and Grafton, T. (2010) *Assessment of the INCA Steel-concrete-steel sandwich technology - Public Report*. DNV China. Report Number: 2010-1284.

Wen, S. and Chung, D. (2007) Piezoresistivity-Based Strain Sensing in Carbon Fiber-Reinforced Cement. *ACI Materials Journal*. 104 (2), 171-179.

Wen, S. and Chung, D.D.L. (2000) Uniaxial tension in carbon fiber reinforced cement, sensed by electrical resistivity measurement in longitudinal and transverse directions. *Cement and Concrete Research*, 30 (8), 1289-1291.

Wen, S. and Chung, D.D.L. (2001) Uniaxial compression in carbon fiber-reinforced cement, sensed by electrical resistivity measurement in longitudinal and transverse directions. *Cement and Concrete Research*. 31 (2), 297-301.

Wen, S. and Chung, D.D.L. (2003) A comparative study of steel- and carbon-fibre cement as piezoresistive strain sensors. *Advances in Cement Research*. 15(3), 119-128.

Westinghouse Electric Company LLC, AP1000. Available from: <http://www.ap1000.westinghousenuclear.com/> [Accessed 13<sup>th</sup> July 2013].

Willie, K. and Loh, K.J. (2010) Nanoengineering Ultra-High-Performance Concrete with Multiwalled Carbon Nanotubes. *Journal of the Transportation Research Board*. 2142, 119-126. Available from: DOI: 10.3141/2142-18 [Accessed 15<sup>th</sup> April 2013].

Wright, H.D., Oduyemi, T.O.S. and Evans, H.R. (1991a) The Design of Double Skin Composite elements. *Journal of Constructional Steel Research*. 19 (2), 111-132.

Wright, H.D., Oduyemi, T.O.S. and Evans, H.R. (1991b) The Experimental Behaviour of Double Skin Composite Elements. *Journal of Constructional Steel Research*. 19 (2), 97-110.

## X

---

Xie, M. and Chapman, J.C. (2006) Developments in Sandwich Construction. *Journal of Constructional Steel Research*. 62 (11), 1123–1133.

Xie, M., Foundoukos, N. and Chapman, J.C. (2007) Static tests on steel-concrete-steel sandwich beams. *Journal of Constructional Steel Research*. 63 (6), 735–750.

## Y

---

Yakovlev, G.I. Skripkiunas, G. Polianskich, I.S. Lahayne, O. Eberhardsteiner, J. Urkhanova, L.A. Pudov, I.A. Sychugov, S.V. Karpova, E.A. and Senkov, S.A. (2017) Modification of Cement Matrix Using Carbon Nanotube Dispersions and Nanosilica. *Procedia Engineering*. 172, 1261-1269.

Yazdanbakhsh, A. (2012) *Production, Characterization, And Mechanical Behavior of Cementitious Materials Incorporating Carbon Nanofibers*. PhD thesis. Texas A&M University. Texas.

Yazdanbakhsh, A. and Grasley, Z. (2014) Utilization of silica fume to stabilize the dispersion of carbon nanofilaments in cement paste. *Journal of Materials in Civil Engineering*. 26 (7).

Yazdanbakhsh, A., Grasley, Z., Tyson, B. and Abu Al-Rub, R.A. (2010) Distribution of Carbon Nanofibers and Nanotubes in Cementitious Composites. *Journal of the Transportation Research Board, Transportation Research Board of the National Academies*. 2142, 89–95. Available from: DOI: 10.3141/2142-13 [Accessed 3<sup>rd</sup> April 2013].

Yazdanbakhsh, A., Grasley, Z., Tyson, B. and Abu Al-Rub, R.K. (2009) Carbon Nano Filaments in Cementitious Materials: Some Issues on Dispersion and Interfacial Bond. *Nanotechnology of Concrete: The Next Big Thing Is Small*. Available from: DOI: 10.14359/51663280 [Accessed 3<sup>rd</sup> April 2013].

Yazdani, N. and Mohanam, V. (2014) Carbon Nano-Tube and Nano-Fiber in Cement Mortar: Effect of Dosage Rate and Water-Cement Ratio. *International Journal of Material Science (IJMSCI)*. 4 (2), 45-52.

Yu, M.F., Lourie, O., Dyer, M.J., Moloni, K., Kelly, T.F. and Ruoff, R.S. (2000) Strength and Breaking Mechanism of Multiwalled Carbon Nanotubes Under Tensile Load. *Science*. 287 (5453), 637-640. Available from: <http://science.sciencemag.org/content/287/5453/637.long> [Accessed 15th April 2013].

## **Z**

---

Zhang, K., Varma, A.H., Malushte, S.R. and Gallocher, S. (2014) Effect of shear connectors on local buckling and composite action in steel concrete composite walls. *Nuclear Engineering and Design*. 269, 231-239. Available from: <http://dx.doi.org/10.1016/j.nucengdes.2013.08.035> [Accessed 28th August 2014].

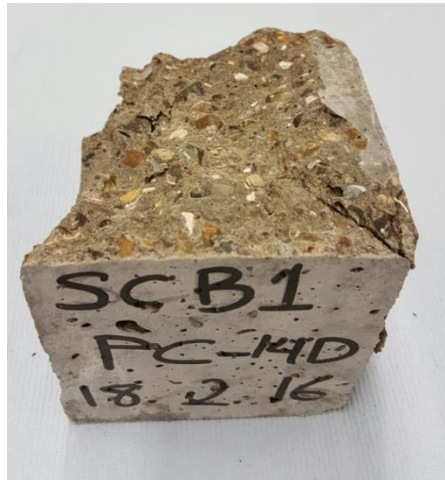
Zhang, L.X. and Hsu, T.T.C. (1998) Behavior and Analysis of 100 MPa Concrete Membrane Elements. *Journal of Structural Engineering*. 124 (1), 24-34.

## APPENDIX A: SC BEAM MATERIAL TEST PHOTOS

### SCB1- Cube Compression Test

14 Day

---



28 Day

---





## SCB1- Split Tensile Test

14 Day



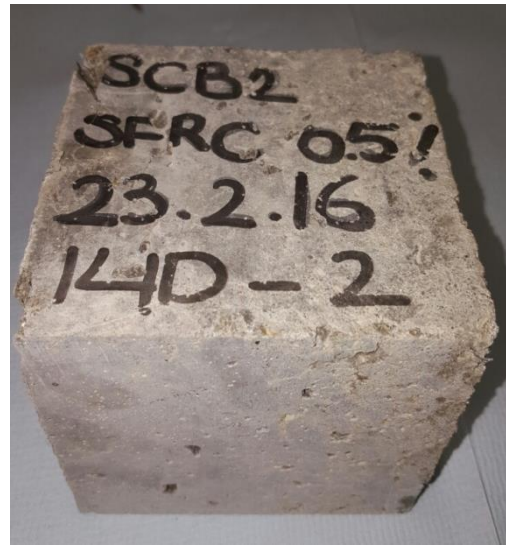
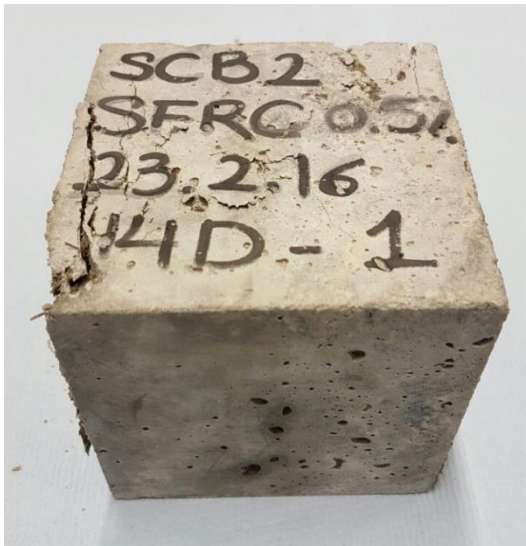
28 Day



## SCB2- Cube Compression Test

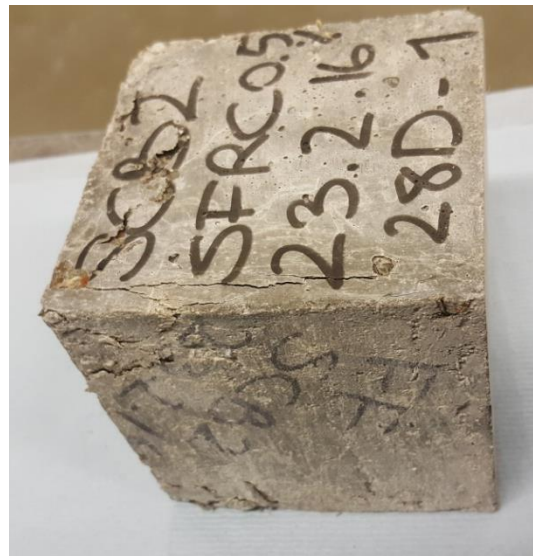
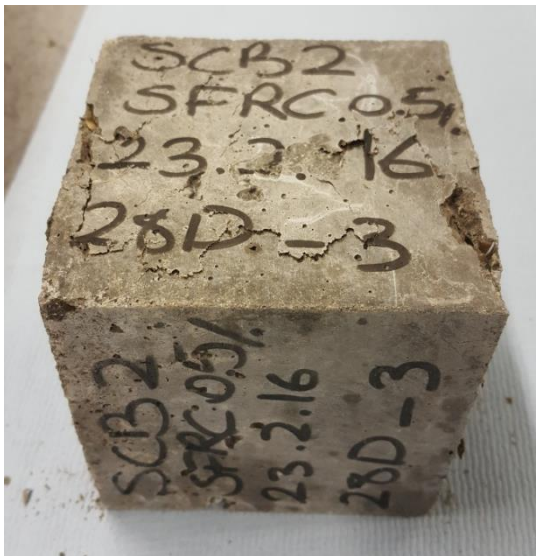
14 Day

---



28 Day

---

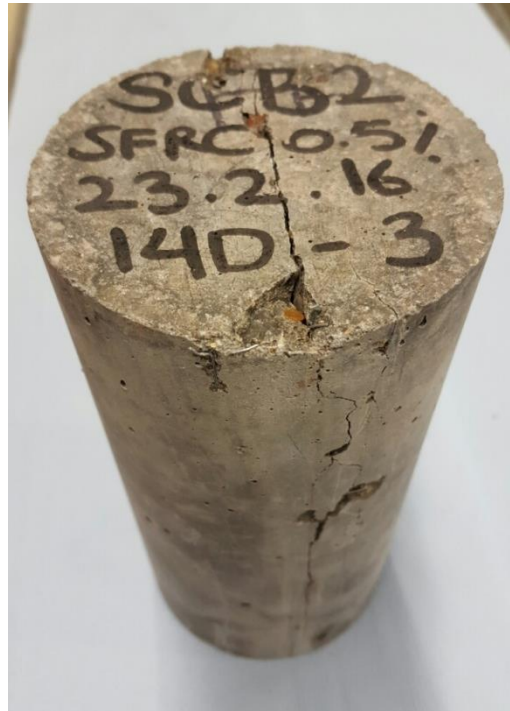
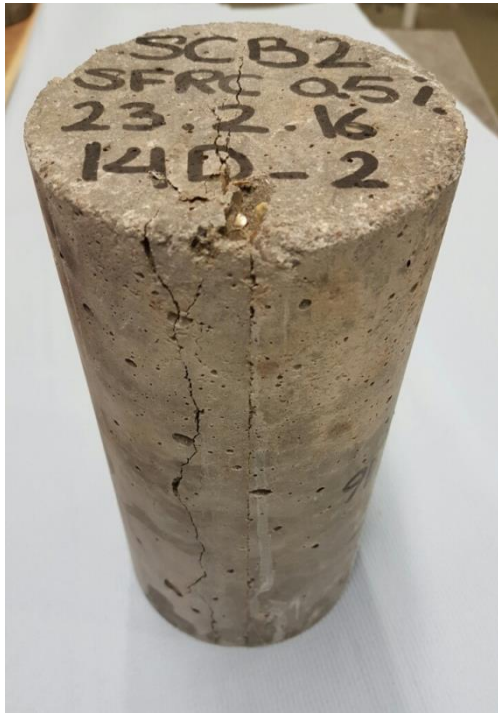




## SCB2- Split Tensile Test

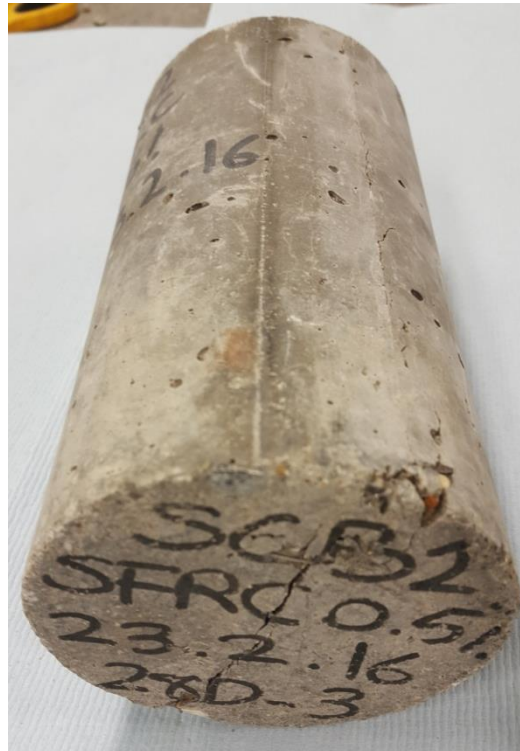
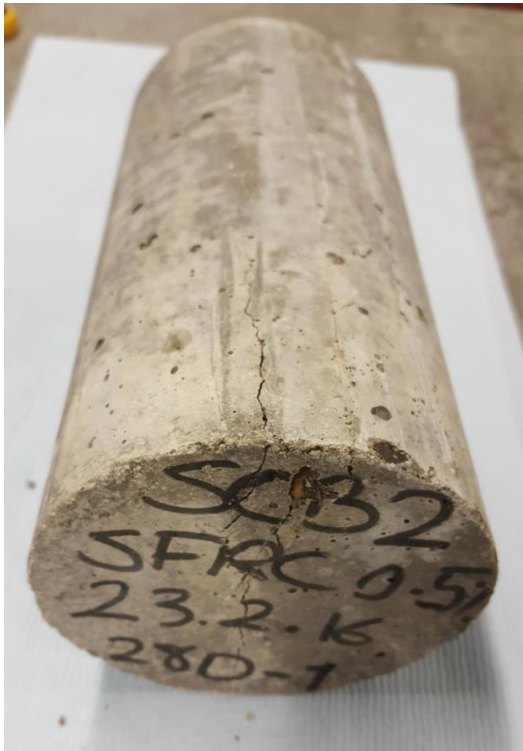
14 Day

---



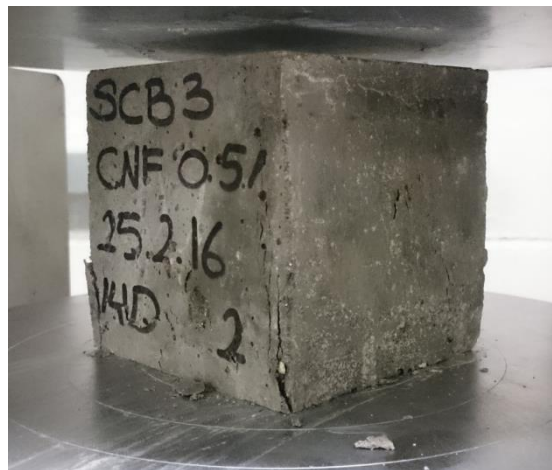
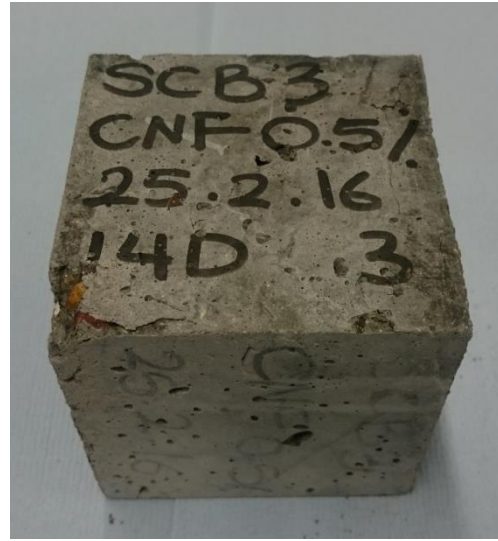
28 Day

---

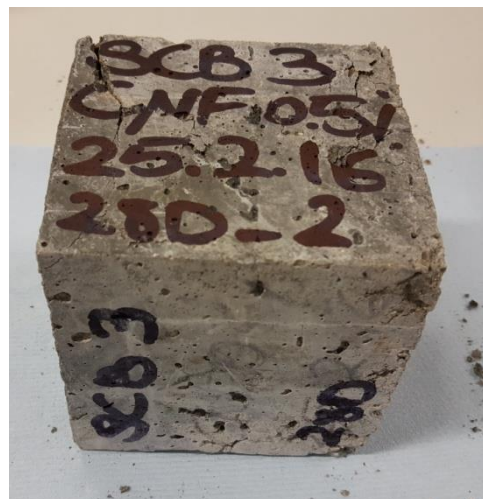
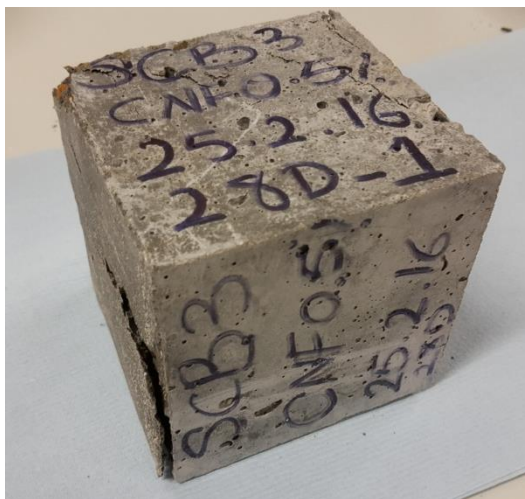


## SCB3- Cube Compression Test

14 Day



28 Day





## SCB3- Split Tensile Test

14 Day

---



28 Day

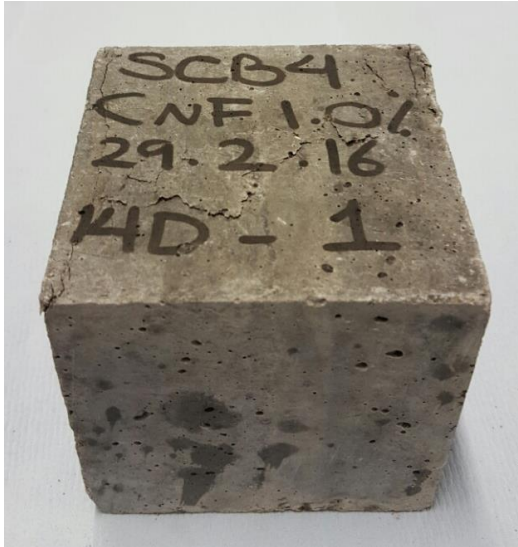
---



## SCB4- Cube Compression Test

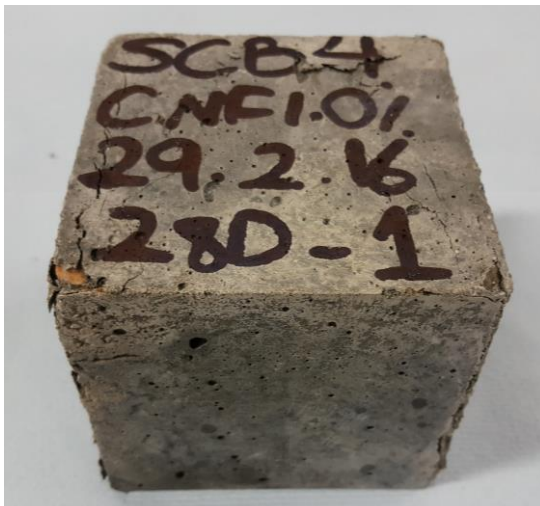
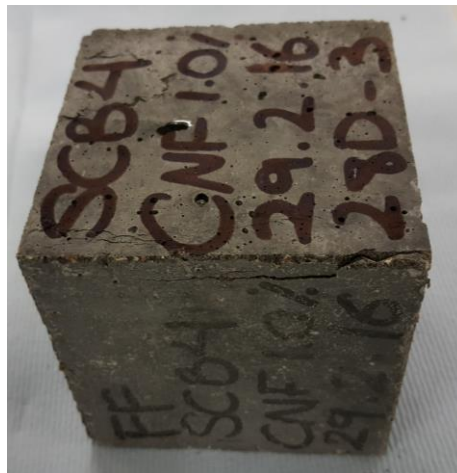
14 Day

---



28 Day

---





## SCB4- Split Tensile Test

14 Day

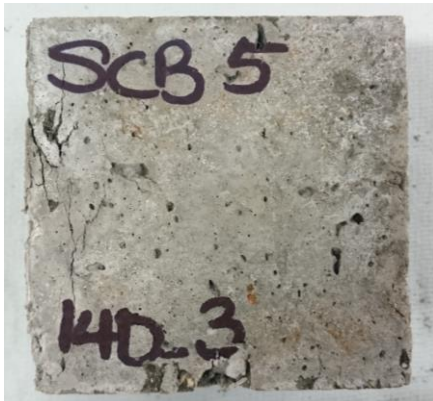
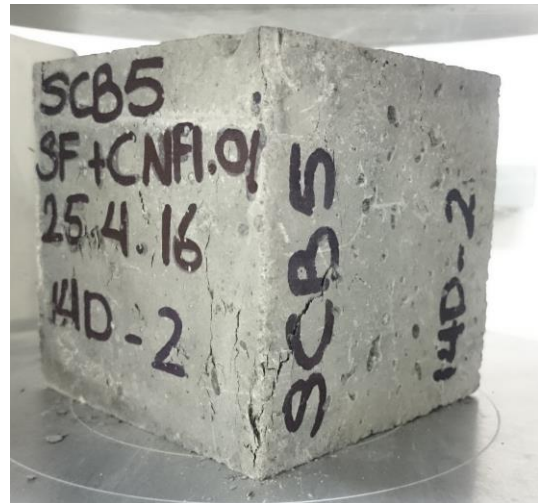


28 Day

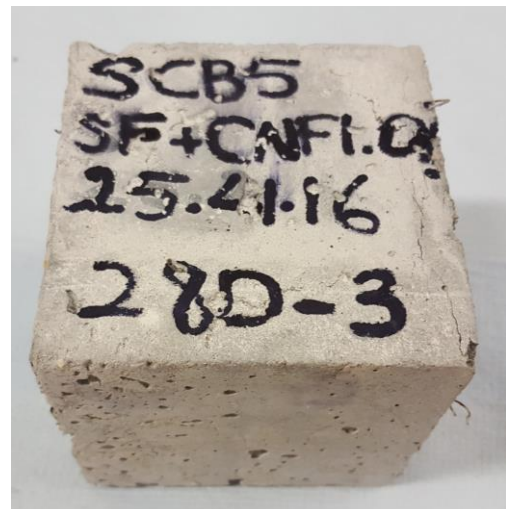
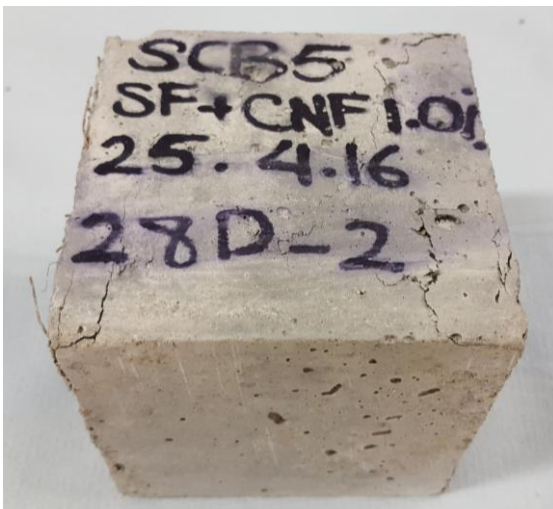


## SCB5- Cube Compression Test

14 Day



28 Day



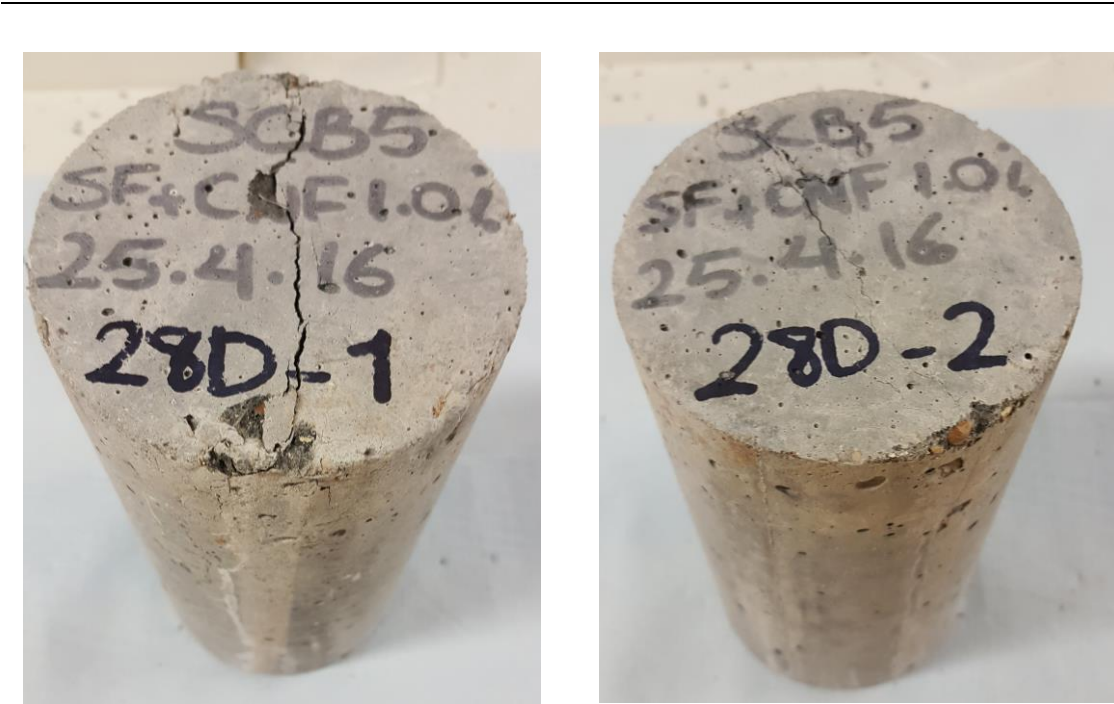


SCB5 - Split Tensile Test

14 Day



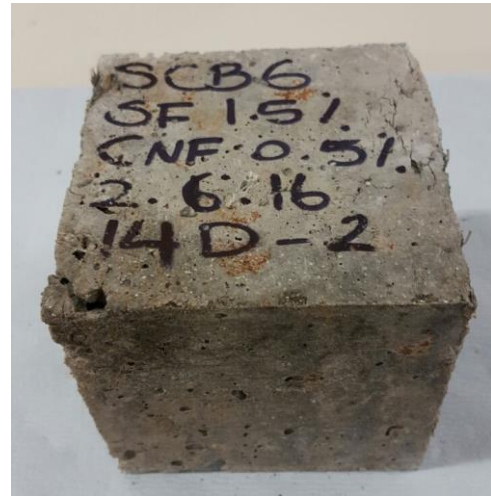
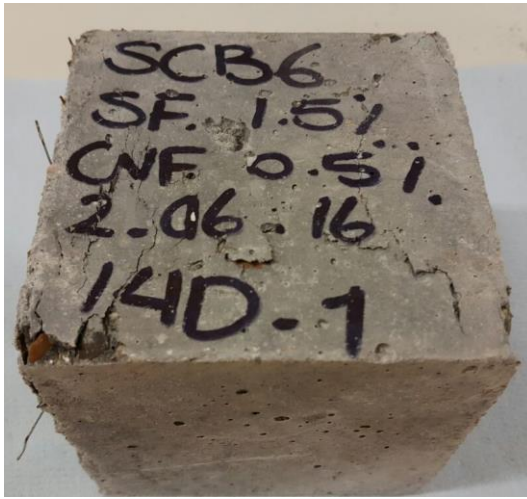
28 Day



## SCB6 – Cube Compression Test

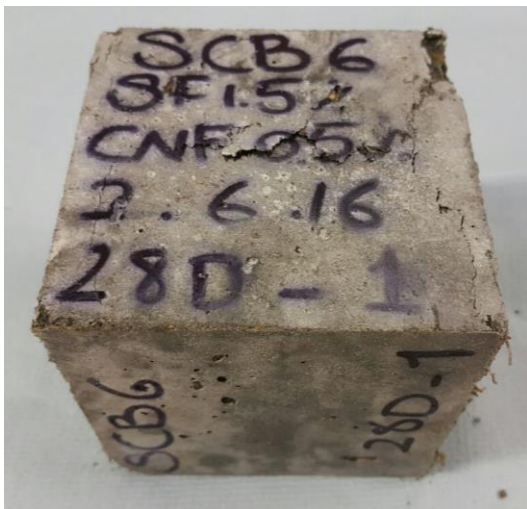
14 Day

---



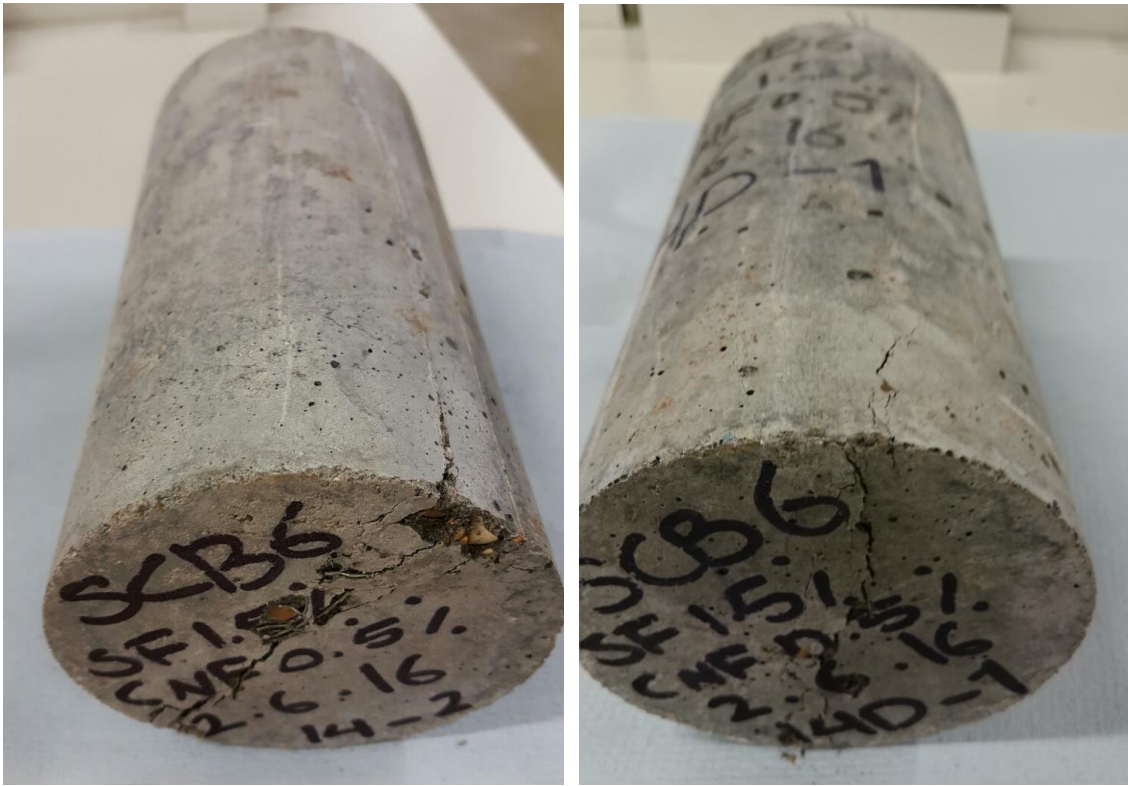
28 Day

---

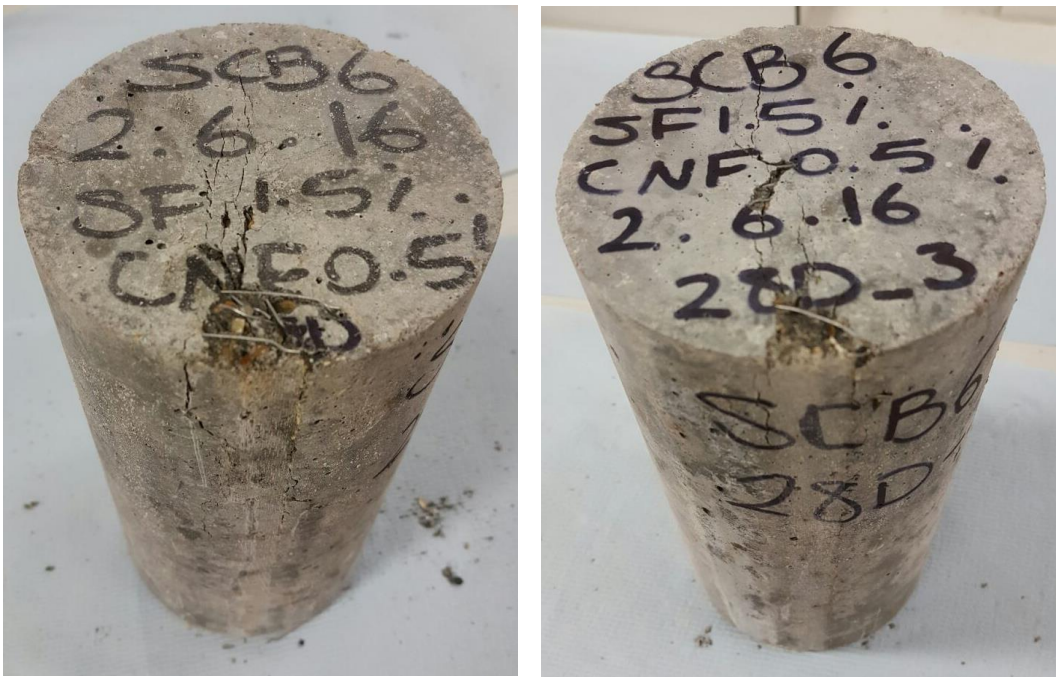


SCB6 – Split Tensile Test

14 Day



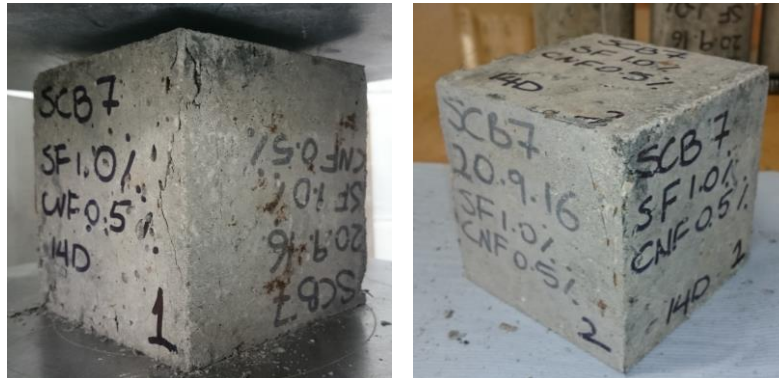
28 Day



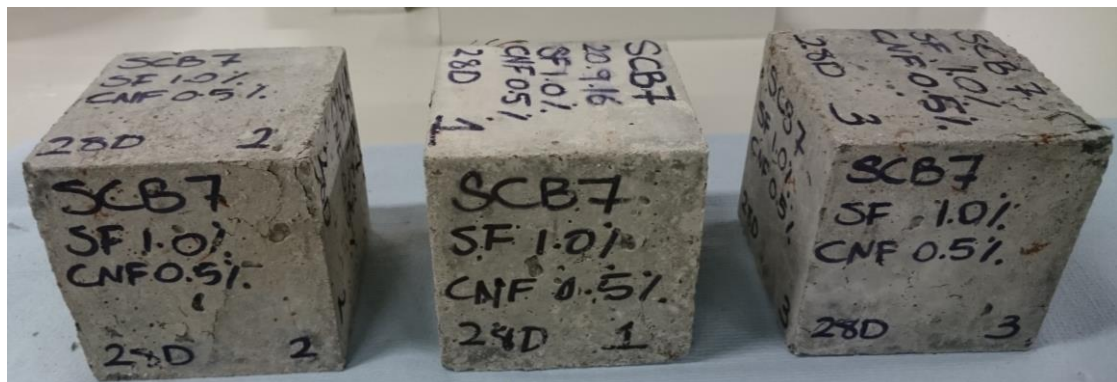


## SCB7- Cube Compression Test

14 Day



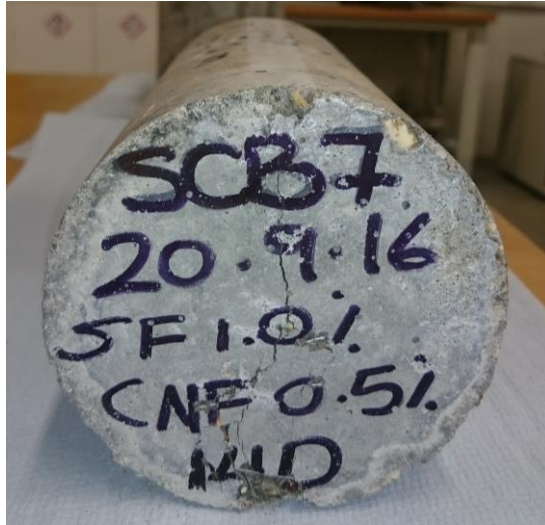
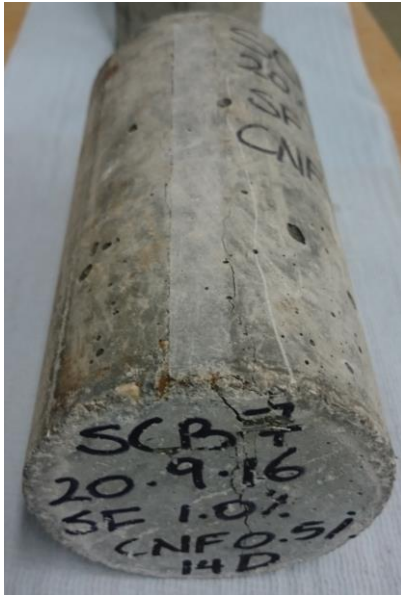
28 Day



## SCB7 – Split Tensile Test

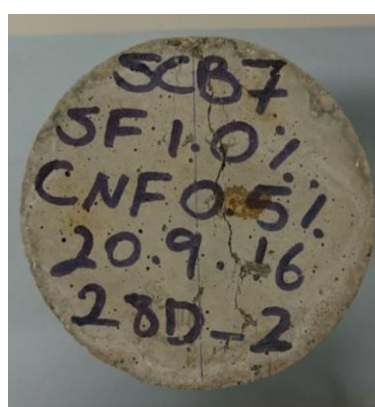
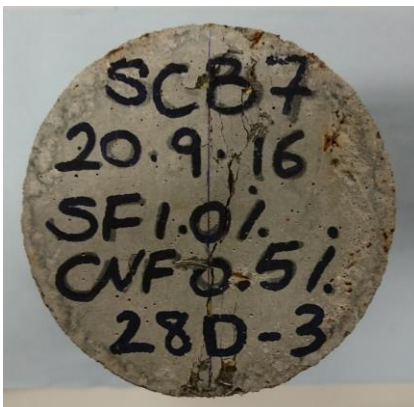
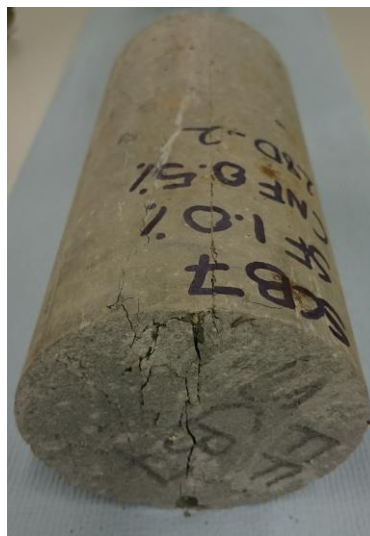
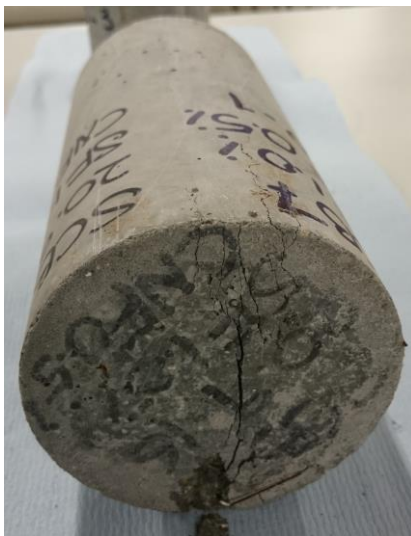
14 Day

---



28 Day

---

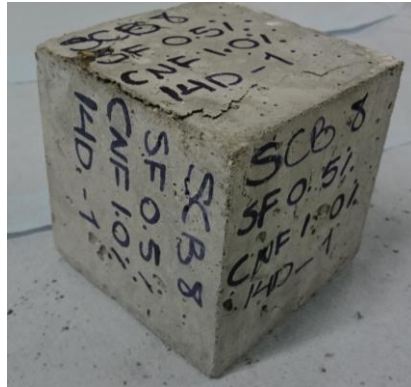




## SCB8- Cube Compression Test

14 Day

---



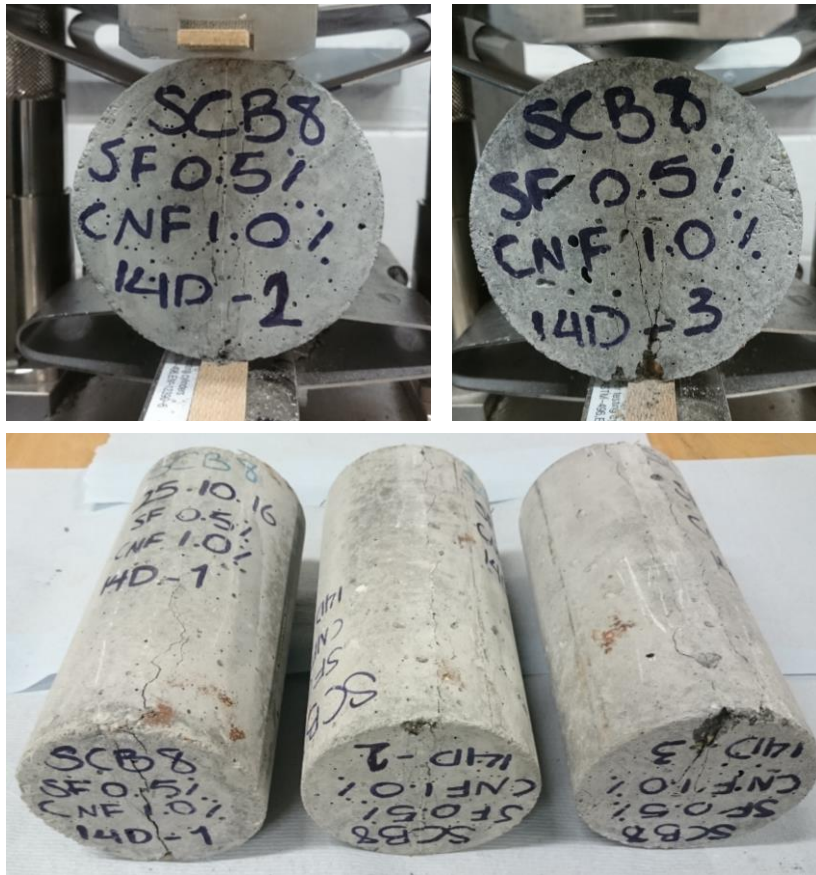
28 Day

---

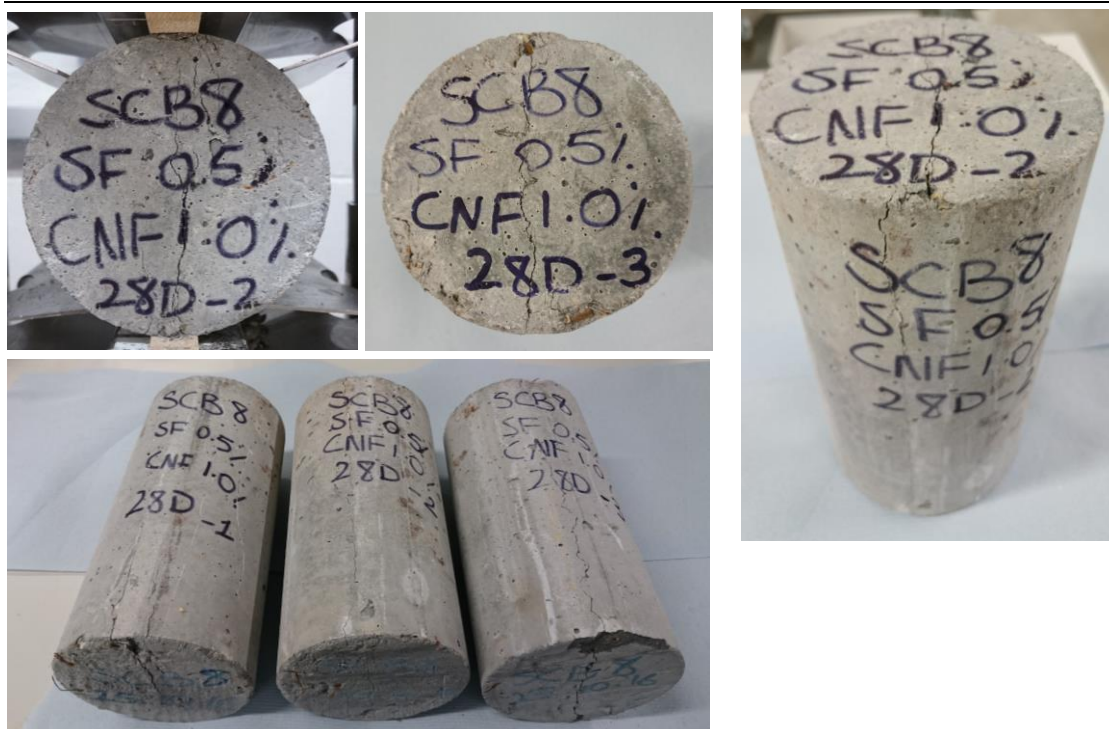


## SCB8- Split Tensile Test

14 Day

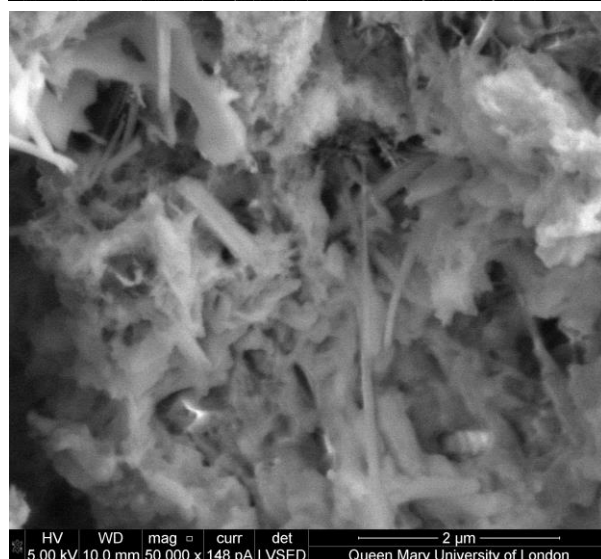
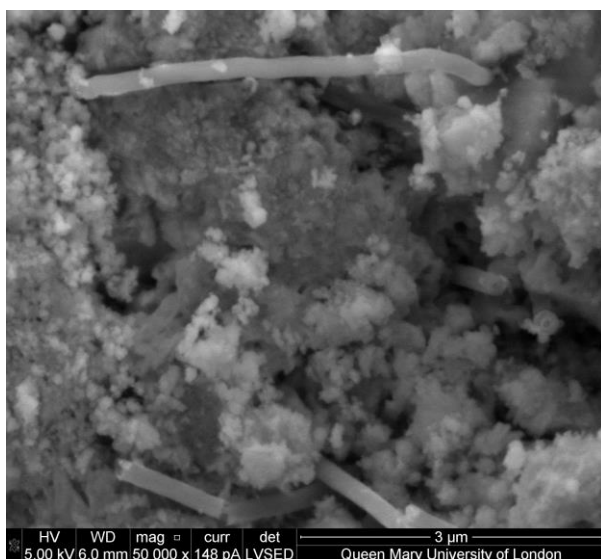
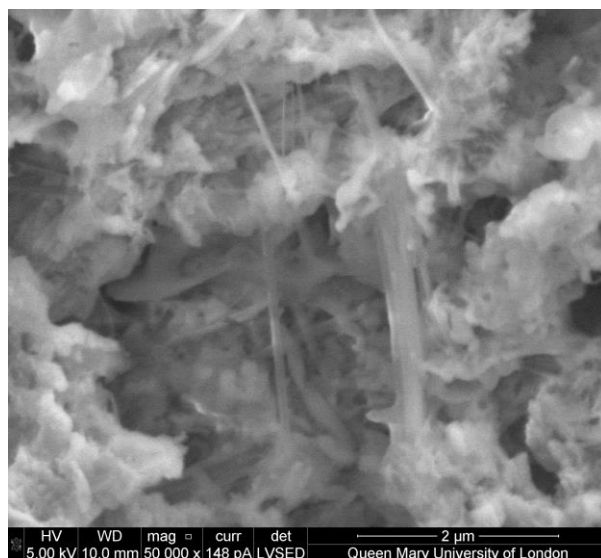
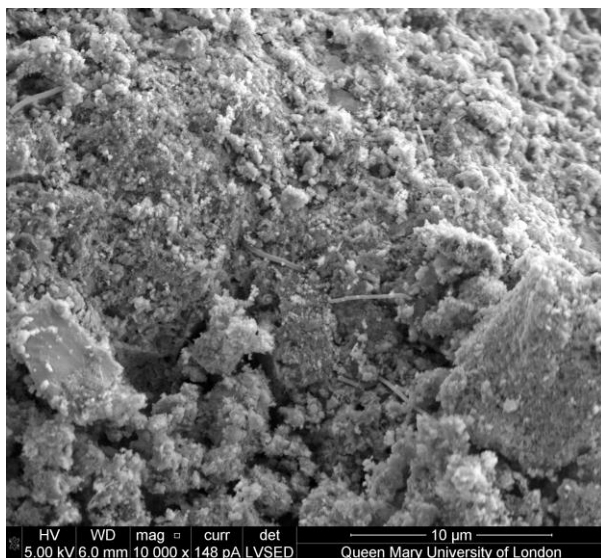


28 Day



## APPENDIX B: SEM IMAGES

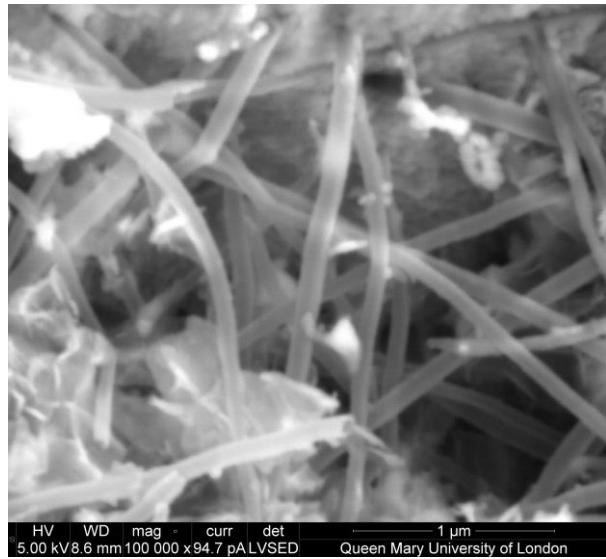
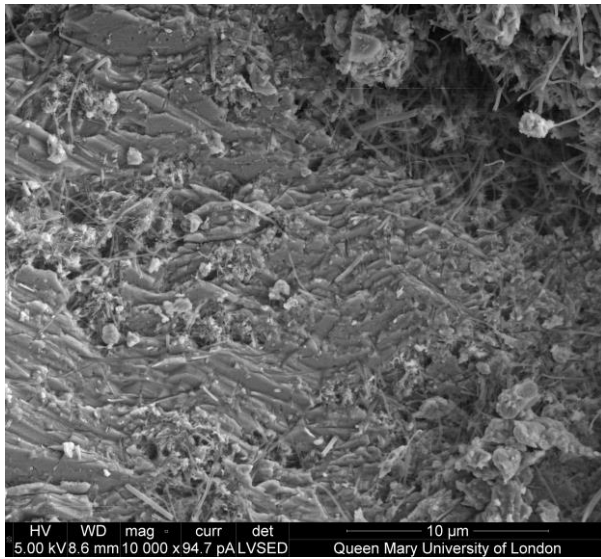
SCB3





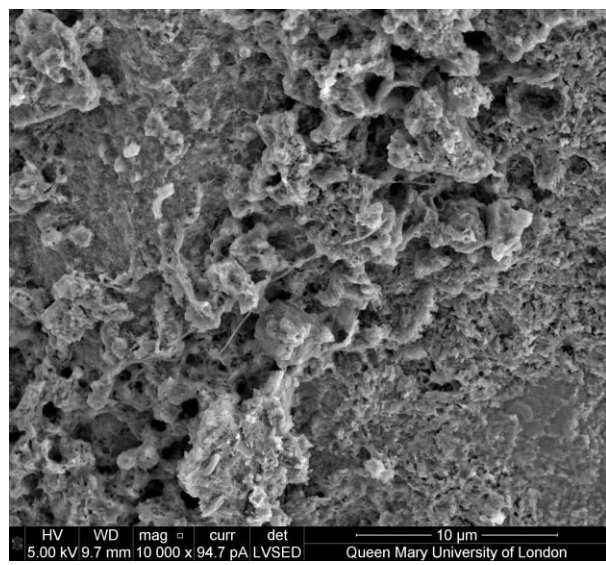
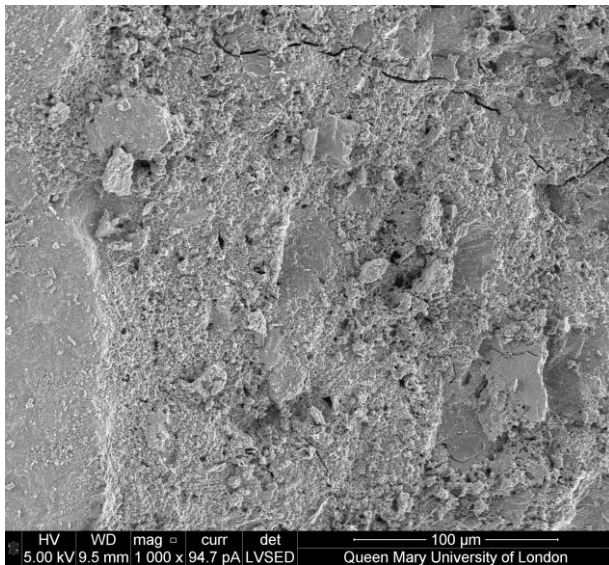
## SCB4

---

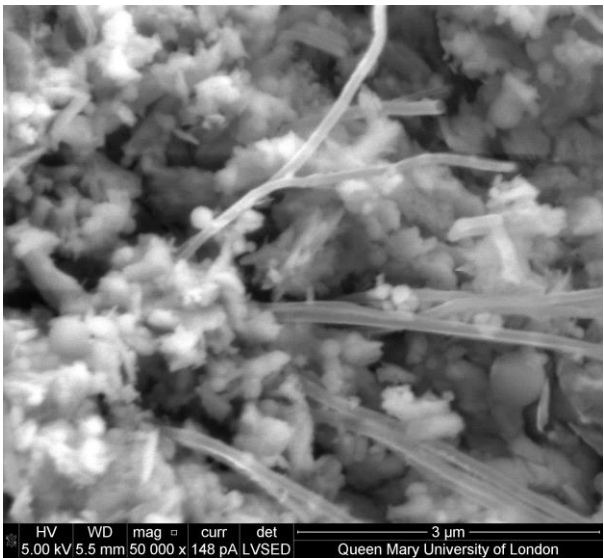
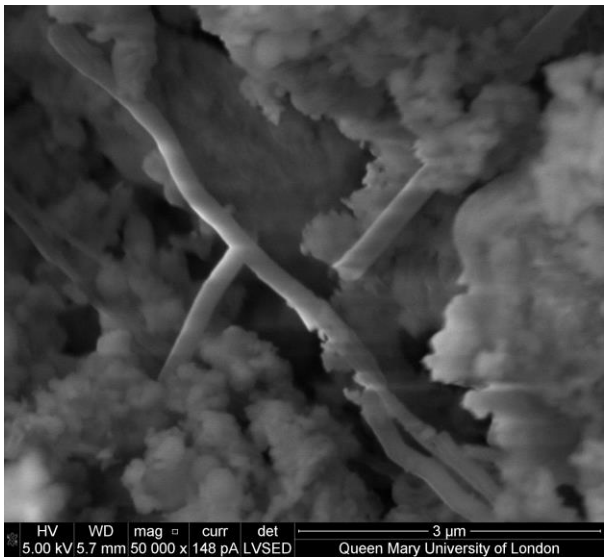


## SCB5

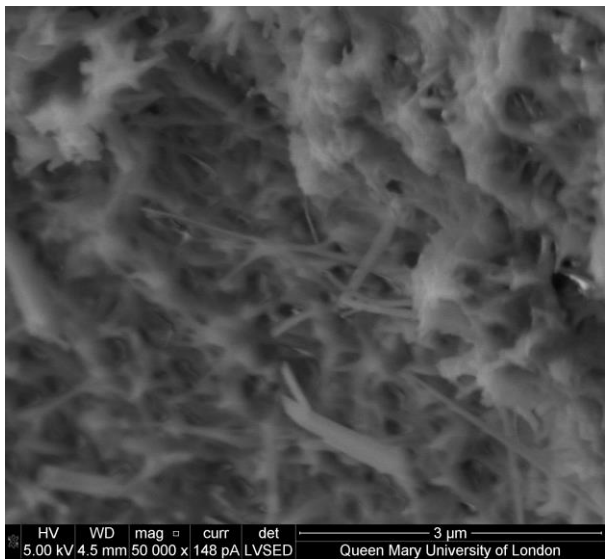
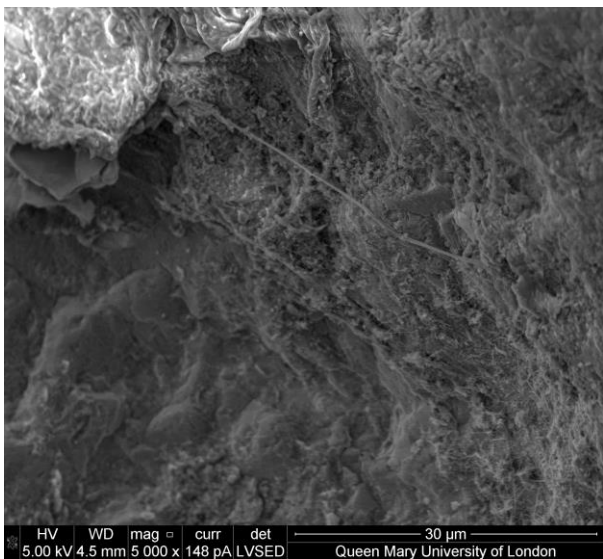
---



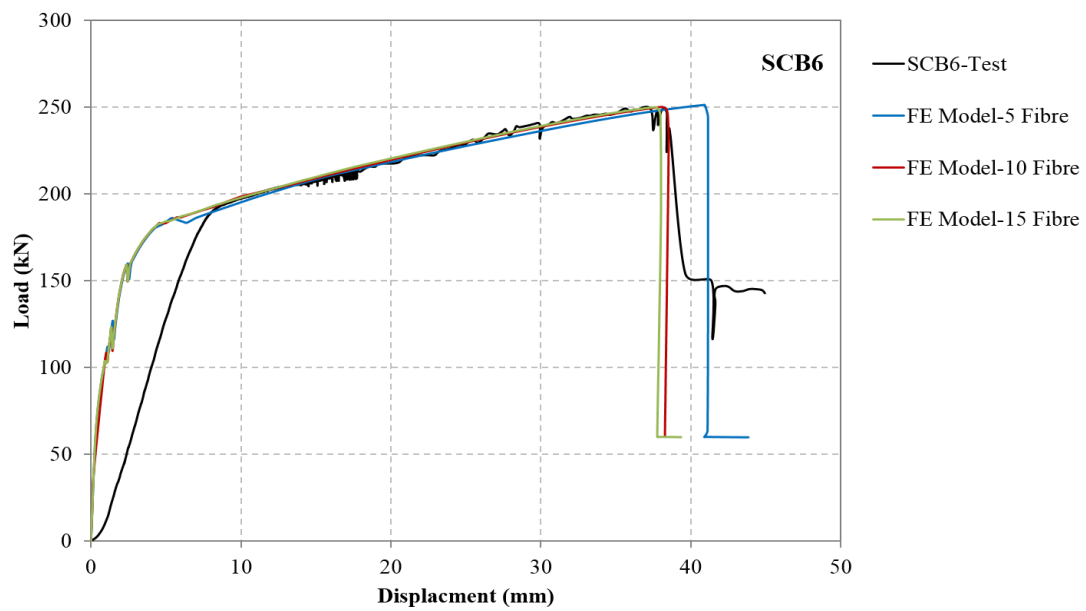
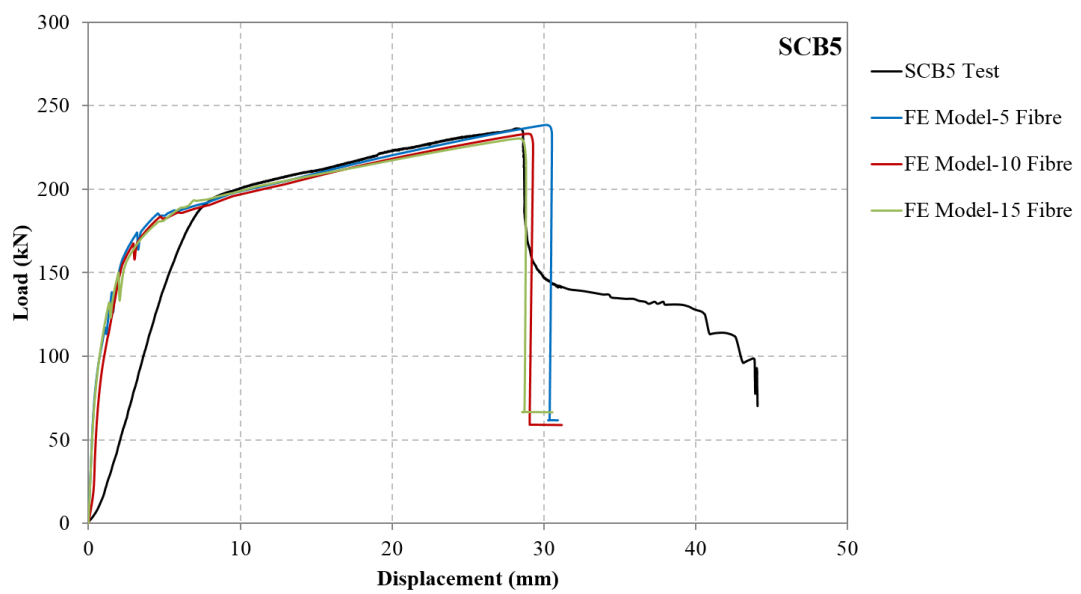
SCB6



SCB8



# APPENDIX C: FE SENSITIVITY STUDY ON SCB6



# APPENDIX D: THEORETICAL SC BEAM MID-DISPLACEMENT

